Lecture Notes in Computer Science 2674
Edited by G. Goos, J. Hartmanis, and J. van Leeuwen

Springer
*Berlin*
*Heidelberg*
*New York*
*Barcelona*
*Hong Kong*
*London*
*Milan*
*Paris*
*Tokyo*

Isabelle E. Magnin  Johan Montagnat
Patrick Clarysse  Jukka Nenonen
Toivo Katila (Eds.)

# Functional Imaging and Modeling of the Heart

Second International Workshop, FIMH 2003
Lyon, France, June 5-6, 2003
Proceedings

Springer

Volume Editors

Isabelle E. Magnin
CREATIS, INSERM
Johan Montagnat
Patrick Clarysse
CREATIS, CNRS
INSA, bâtiment Blaise Pascal
20, avenue Albert Einstein, 69621 Villeurbanne cedex, France
E-mail: {Isabelle.Magnin/Johan.Montagnat/Patrick.Clarysse}@creatis.insa-lyon.fr

Jukka Nenonen
Toivo Katila
Helsinki University of Technology
Institute of Biomedical Engineering
P.O. Box 2200, 02015 Hut, Finland
E-mail: {Jukka.Nenonen/Toivo.Katila}@hut.fi

Cataloging-in-Publication Data applied for

A catalog record for this book is available from the Library of Congress.

Bibliographic information published by Die Deutsche Bibliothek
Die Deutsche Bibliothek lists this publication in the Deutsche Nationalbibliografie; detailed bibliographic data is available in the Internet at <http://dnb.ddb.de>.

CR Subject Classification (1998): I.4, J.3, I.6, I.2.10

ISSN 0302-9743
ISBN 3-540-40262-4 Springer-Verlag Berlin Heidelberg New York



Springer-Verlag Berlin Heidelberg New York
a member of BertelsmannSpringer Science+Business Media GmbH

http://www.springer.de


Printed in Germany

Typesetting: Camera-ready by author, data conversion by PTP-Berlin GmbH
Printed on acid-free paper SPIN: 10927519 06/3142 5 4 3 2 1 0

# Preface

The first international conference on Functional Imaging and Modeling of the Heart[1] (FIMH) was held in Helsinki, Finland, in November 2001, thanks to the strong scientific collaboration between France and Finland. This event was a first attempt to federate the heart imaging community and to encourage collaboration between scientists in signal and image processing, applied mathematics and physics, biomedical engineering and computer science, and experts in cardiology, radiology, biology, and physiology, in Europe and beyond. The conference has encountered considerable success. The outstanding research works presented have demonstrated a very active research field with complex modeling and image analysis problems to be solved. One of the outcomes was the special issue of the Medical Image Analysis journal based on a selection of the conference's best papers, to appear in the second half of 2003.

The FIMH 2001 meeting was the starting point of a discussion for federating the European research effort in cardiac imaging, heart modeling, and cardiac image analysis. It was very successful, and a large coalition was created around the e-Heart[2] proposal for a Network of Excellence in the European Sixth Framework Program. The e-Heart network has already gathered about 200 researchers from 100 institutes. A project proposal has been submitted to the European Union.

It was decided in the first meeting to organize a regular biennial conference. Subsequently, these proceedings have gathered the contributions from the participants to the second FIMH conference, held in Lyon in June 2003, under the auspices of the 30-year-old French-Finnish Association for Scientific and Technical Research (AFFRST). For this second edition, there has been a significant increase in the number of papers submitted. Papers accepted to the conference were distributed over 4 oral and 2 poster sessions. A session dealt with anatomical modeling and a second with motion estimation. Two sessions were dedicated to cardiac mechanics and electric modeling and analysis. An image registration session and an image analysis session also took place. Finally, we saw some works on data acquisition and experimental studies.

We hope to meet you at the next FIMH meeting, planned for 2005.

June 2003

Johan Montagnat
Patrick Clarysse
Jukka Nenonen
Toivo Katila
Isabelle Magnin

[1] http://www.creatis.insa-lyon.fr/FIMH/
[2] http://www.creatis.insa-lyon.fr/e-Heart/

# Acknowledgments

The members of the program committee deserve special thanks for their work in reviewing all the papers, and for their support in the organization of the conference.

We thank the members of the CREATIS unit in Lyon and the Laboratory of Biomedical Engineering in Helsinki for their involvement and support in the organization of this conference.

## Conference supported by

Institut National des Sciences Appliquées de Lyon (INSA), France
Helsinki University of Technology (HUT), Finland
French-Finnish Association for Scientific and Technical Research (AFFRST)
French National Center for Scientific Research (CNRS), France
Science Academy of Finland, Graduate School "Functional Research in Medicine"
Scientific Department of the French Embassy in Helsinki
French Biomedical Engineering Society (SFGBM)
Joint incentive action "Beating Heart" of the ISIS research group (CNRS)
Conseil Général du Rhône
Conseil Régional Rhône Alpes
Lyon City
University Claude Bernard Lyon 1

# Organization

FIMH 2003 was co-organized by the CREATIS Laboratory, CNRS UMR 5515, Lyon, France, and the Laboratory of Biomedical Engineering at the Helsinki University of Technology, Finland.

## Conference Chairs

| | |
|---|---|
| Isabelle E. Magnin | CREATIS, CNRS UMR 5515, Lyon, France |
| Toivo Katila | Laboratory of Biomedical Engineering, Helsinki University of Technology, Finland |

## Organization Committee

| | |
|---|---|
| Johan Montagnat | CREATIS, CNRS UMR 5515, Lyon, France |
| Patrick Clarysse | CREATIS, CNRS UMR 5515, Lyon, France |
| Jukka Nenonen | Laboratory of Biomedical Engineering, Helsinki University of Technology, Finland |

## Program Committee

| | |
|---|---|
| T. Arts | University of Technology of Eindhoven, The Netherlands |
| N. Ayache | INRIA Sophia-Antipolis, France |
| M. Barlaud | I3S, Sophia-Antipolis, France |
| B. Bijnens | MIC, Katholieke Universiteit Leuven, Belgium |
| E. Canet | CREATIS, Lyon, France |
| P. Clarysse | CREATIS, Lyon, France |
| P. Claus | Katholieke Universiteit Leuven, Belgium |
| J.-L. Coatrieux | LTSI, Rennes, France |
| L. Cohen | CEREMADE, Paris, France |
| P. Croisille | CREATIS, Lyon, France |
| J. D'hooge | MIC, Katholieke Universiteit Leuven, Belgium |
| R. Fenici | Catholic University of Rome, Italy |
| A. Frangi | Universidad de Zaragoza, Spain |
| D. Friboulet | CREATIS, Lyon, France |
| M. Garreau | LTSI, Rennes, France |
| P. Grangeat | CEA, Grenoble, France |
| A. Holden | University of Leeds, UK |
| T. Katila | Laboratory of Biomedical Engineering, Helsinki, Finland |
| K. Lauerma | Helsinki University Central Hospital, Finland |
| S. Loncaric | University of Zagreb, Croatia |
| J. Lötjönen | VTT Technology, Tampere, Finland |
| I.E. Magnin | CREATIS, Lyon, France |
| M. Mäkijärvi | Helsinki University Central Hospital, Helsinki, Finland |

## Program Committee (continuation)

| | |
|---|---|
| J. Montagnat | CREATIS, Lyon, France |
| J. Nenonen | Helsinki University of Technology, Finland |
| A. Noble | Medical Vision Laboratory, Oxford, UK |
| N. Rougon | ARTEMIS, INT Evry, France |
| F. Sachse | University of Karlsruhe, Germany |
| G. Sutherland | MIC, Katholieke Universiteit Leuven, Belgium |
| B. Tilg | University of Graz, Austria |
| M. Viergever | Utrecht University, The Netherlands |

# Table of Contents

## Invited Speakers

Tagged MRI-Based Studies of Cardiac Function . . . . . 1
*L. Axel*

A Novel Method for Quantifying the Contribution of Different Intracellular Mechanisms to Mechanically Induced Changes in Action Potential Characteristics . . . . . 8
*O. Solovyova, N. Vikulova, V.S. Markhasin, P. Kohl*

## Session 1: Anatomy Extraction and Description

Automatic Construction of Biventricular Statistical Shape Models . . . . . 18
*F. Frangi, D. Rueckert, J.A. Schnabel, W.J. Niessen*

Visualising Cardiac Anatomy Using Constructive Volume Geometry . . . . . 30
*M. Chen, R.H. Clayton, A.V. Holden, J.V. Tucker*

Evaluation of a 3D Segmentation Software for the Coronary Characterization in Multi-Slice Computed Tomography . . . . . 39
*A. Larralde, C. Boldak, M. Garreau, C. Toumoulin, D. Boulmier, Y. Rolland*

A Levelset Based Method for Segmenting the Heart in 3D+T Gated SPECT Images . . . . . 52
*A. Charnoz, D. Lingrand, J. Montagnat*

## Session 2: Modeling of the Cardiac Mechanics and Functions

Modeling of Electro-mechanical Coupling in Cardiac Myocytes: Feedback Mechanisms and Cooperativity . . . . . 62
*F.B. Sachse, K. Glänzel, C. Seemann*

Simulating Cardiac Mechanoenergetics in the Left Ventricle . . . . . 72
*M. Vendelin, P.H.M. Bovendeerd, V. Saks, J. Engelbrecht, T. Arts*

Towards Patient Specific Models of Cardiac Mechanics: a Sensitivity Study 81
*L. Geerts, R. Kerckhoffs, P.H.M. Bovendeerd, T. Arts*

Does the Collagen Network Contribute to Normal Systolic Left Ventricular Wall Thickening? A Theoretical Study in Continuum Mechanics 91
*J. Ohayon, C. Bourdarias, S. Gerbi*

## Session 3: Electro-physiology, Electro-, and Magnetography

Regularization in Cardiac Source Imaging . . . . . 101
*T. Lunttila, J. Nenonen, E. Somersalo*

On the Influence of a Volume Conductor on the Orientation of Currents in a Thin Cardiac Tissue . . . . . 111
*R. Weber dos Santos, F. Dickstein*

First 36-Channel Magnetocardiographic Study of CAD Patients in an Unshielded Laboratory for Interventional and Intensive Cardiac Care . . . . 122
*D. Brisinda, A.M. Meloni, R. Fenici*

Heterogeneous Sinoatrial Node of Rabbit Heart – Molecular and Electrical Mapping and Biophysical Reconstruction . . . . . 132
*H. Zhang, H. Dobrzynski, A.V. Holden, M.R. Boyett*

## Session 4: Motion Estimation

Construction of a Cardiac Motion Atlas From MR Using Non-rigid Registration . . . . . 141
*A. Rao, G.I. Sanchez-Ortiz, R. Chandrashekara, M. Lorenzo-Valdés, R. Mohiaddin, D. Rueckert*

Motion-Compensation of Cardiac Perfusion MRI Using a Statistical Texture Ensemble . . . . . 151
*M.B. Stegmann, H.B.W. Larsson*

Measuring Myocardial Deformations in Tagged MR Image Sequences Using Informational Non-rigid Registration . . . . . 162
*C. Petitjean, N. Rougon, F. Prêteux, P. Cluzel, P. Grenier*

Parametric Analysis of Main Motion to Study the Regional Wall Motion of the Left Ventricle in Echocardiography . . . . . 173
*C.R. Dominguez, F. Frouin, O. Gérard, P. Lim, B. Diebold, A. Herment*

Modeling and Tracking of the Cardiac Left Ventricular Motion by a State Space Harmonic Model in MRI Sequence . . . . . 184
*M. Oumsis, Q.-C. Pham, A.D. Sdigui, B. Neyran, I.E. Magnin*

## Session 5: Image Registration and Image Analysis

A Strategy to Quantitatively Evaluate MRI/PET Cardiac Rigid Registration Methods Using a Monte Carlo Simulator . . . . . 194
*N. Pauna, P. Croisille, N. Costes, A. Reilhac, T. Mäkelä, O. Cozar, M. Janier, P. Clarysse*

Spatio-temporal Alignment of 4D Cardiac MR Images ..... 205
*D. Perperidis, A. Rao, M. Lorenzo-Valdés, R. Mohiaddin, D. Rueckert*

Automatic Registration of MR First-Pass Myocardial Perfusion Images .. 215
*L. Bracoud, F. Vincent, C. Pachai, E. Canet, P. Croisille, D. Revel*

Evaluation and Comparison of Surface and Intensity Based Rigid Registration Methods for Thorax and Cardiac MR and PET Images ..... 224
*T. Mäkelä, M. Pollari, J. Lötjönen, N. Pauna, A. Reilhac, P. Clarysse, I.E. Magnin, T. Katila*

Left Ventricular Flow Dynamics and Transmural Gradients in Myofiber Shortening with MRI-Tagging ..... 234
*T. Arts, T. Delhaas, A. Van Susteren, G. Snoep, F.W. Prinzen*

Intravascular Ultrasound Images Vessel Characterization Using AdaBoost 242
*O. Pujol, M. Rosales, P. Radeva, E. Nofrerias-Fernández*

Motion Analysis of 3D Ultrasound Texture Patterns ..... 252
*W. Yu, N. Lin, P. Yan, K. Purushothaman, A. Sinusas, K. Thiele, J.S. Duncan*

**Session 6: Data Acquisition, Experimental, and Modeling Studies**

Estimation of the Diastolic Intraventricular Relative Pressures Using MRI Acceleration Measurements ..... 262
*F. Balleux, O. Jolivet, A. De Cesare, A. Herment, J.-P. Tasu, E. Mousseaux*

Magnetic Resonance Fusion Imaging of Chronic Myocardial Ischemia .... 272
*M. Nahrendorf, K.-H. Hiller, A. Greiser, S. Köhler, T. Neuberger, K. Hu, C. Waller, G. Ertl, A. Haase, W.R. Bauer*

The Relationship between Regional Integrated Backscatter Levels and Regional Strain in Normal, Acutely Ischemic, and Reperfused Myocardium ..... 278
*J. D'hooge, O. Turschner, C. Dommke, P. Claus, B. Bijnens, J. Thoen, F. Van de Werf, G.R. Sutherland, P. Suetens*

Why Ischemic Hearts Respond Less to Cardiac Resynchronisation Therapy. A Modeling Study ..... 287
*P. Claus, B. Bijnens, O.-A. Breithardt, G.R. Sutherland*

Finite Element Models for Mechanical Simulation of Coronary Arteries .. 295
*J. Rodríguez, J. M$^a$Goicolea, J.C. García, F. Gabaldón*

**Author Index** ..... 307

# Tagged MRI-Based Studies of Cardiac Function

Leon Axel

Dept. Radiology
NYU School of Medicine
New York, NY 10016
leon.axel@med.nyu.edu

**Abstract.** Tagged MRI provides a potentially powerful new way to non-invasively assess the regional function of the heart. Although its potential has not yet been fully realized, due to remaining technical limitations in image acquisition and analysis, good progress is being made to overcome these limitations. Current research focuses on improving imaging methods to obtain high resolution 3D spatially registered tagged images, designing more efficient methods to extract the heart wall contours and tag positions within the wall from the tagged images, and implementing efficient ways to reconstruct the 3D motion of the heart from this data. In addition to the new regional motion and deformation data that tagged MRI can provide on normal and abnormal cardiac function, we can potentially use this motion data to model the corresponding forces within the heart wall.

## Introduction

Traditional non-invasive methods to evaluate regional cardiac function have been significantly limited by the scarcity of natural landmarks within the heart. This has largely limited conventional tomographic imaging to assessment of the radial motion of the endocardial surface or wall thickening. Thus, any non-radial components of the motion or transmural variation of the motion cannot be measured. This limited data is further compromised by the possible effects of motion of the curved heart wall through the plane of the image, which can result in alteration of the apparent motion due to the changing location of the intersection of the wall with the image plane. Tagged MRI provides a means to non-invasively create synthetic landmarks within the heart that can be used to track the full 3D wall motion.

## 1 Magnetization-Tagged MRI

### 1.1 Principles of Tagged MRI

The introduction of magnetization tagging in magnetic resonance imaging (MRI) has made it possible to determine correspondence of material points at different cardiac cycle phases, by visibly marking otherwise identical appearing portions of the heart wall [1–3]. The basic principle of tagged MRI is the creation of localized perturbation of the magnetization. This can be done selectively, similarly to the selective excitation process used for image slice location, or non-invasively, using spatial modulation of

I. Magnin et al. (Eds.): FIMH 2003, LNCS 2674, pp. 1–7, 2003.

magnetization (SPAMM). SPAMM efficiently creates a periodic modulation of the magnetization along a desired direction by applying a series of non-selective excitation pulses, allowing the phase of the magnetization to evolve under the influence of a magnetic field gradient along the desired direction between excitations. The profile of the tagged magnetization regions can be controlled by adjusting the relative amplitudes of the excitation pulses. The intersections of the sheets of tagged magnetization with the image plane will be seen as dark lines in the subsequent images; the tag lines will move with the underlying tissue. The tags thus provide a 1D sample of the heart wall motion. The tag lines will fade over time due to magnetic relaxation, but they can last for most or all of the cardiac cycle.

## 1.2 Improvements in Tagged MRI Methods

Technical improvements in imaging methods can improve the resulting function analysis. Some ways in which we are seeking to improve tagged imaging include improved physiologic motion synchronization, faster imaging methods and 3D image acquisition.

### 1.2.1 Physiologic Motion Synchronization

Synchronization of tagged imaging with the cardiac cycle is important for good quality tagged images. Reliable detection of the QRS complex of the ECG is required in order to tag at a consistent phase of the cycle, as well as to produce sharp images. Flow-related artefacts that can be seen in the ECG when the subject is in the imaging magnet can degrade performance of the QRS detection; we have developed a correlation filtering method to help detect the QRS complexes in the presence of such interference. Respiratory motion can also degrade image quality. While imaging in times short enough to suspend respiration is possible, it limits the attainable image resolution and makes registration of images obtained at different breath holds potentially difficult. We are working on methods for joint synchronization of the imaging with both the cardiac and respiratory cycles in order to avoid these limitations [4].

### 1.2.2 Faster Tagged MR Imaging

In order to achieve high quality 2D tagged images at fast heart rates, as in stress testing and pediatric cardiac imaging, it is important to increase the temporal resolution, enhance tag contrast, and/or decrease the breath-hold duration. These goals can be accomplished using a hybrid fast gradient-echo/echo-planar imaging (FGRE-EPI) pulse sequence [5]. Although FGRE-EPI improves the data acquisition efficiency and tag contrast compared to fast gradient-echo (FGRE) imaging, it is also more susceptible to image artifacts due to various phase discontinuities that can arise in the acquisition of the image data; care must be taken in designing the imaging method to avoid or minimize such discontinuities. Figure 1 shows end-systolic, long-axis tagged images of one volunteer acquired using an improved FGRE-EPI sequence at baseline and peak dobutamine stress (heart rate = 150 bpm), where a significant increase in myocardial contraction and a change in the geometry of the heart can be appreciated in the peak stress image.

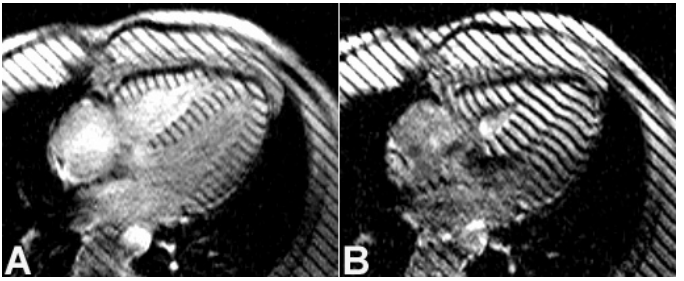


**Fig. 1.** Hybrid fast gradient echo-EPI tagged images (A) at rest and (B) under dobutamine stress. (Image courtesy of D. Kim)

### 1.2.3 3D Imaging

One potential application of the combination of faster imaging and cardiac and respiratory gating is 3D tagged image acquisition. While still under development, this should permit improved registration of images of tags acquired in different orientations.

## 2 Tagged Image Data Extraction

A variety of approaches have been explored for extraction of wall contour and tag position data from tagged MR images. Manual interactive methods are robust but too slow to be practical except for correction of the results of more automated methods. Active contours provide faster interactive tracking of contours or tags, through smooth spline curves that can move under image-derived forces and user-supplied interactions [6,7]. Optical flow approaches can speed up the tag tracking, although with some loss of control over the process [8]. Fourier–based approaches to tag tracking are fast but also hard to control and subject to artefacts.

### 2.1 Tagged MR Contour Extraction

The presence of the tags in the image of the wall can interfere with extraction of the wall contours. The regional intensity variations in the image resulting from the commonly used local surface receiver coils can also interfere with contour extraction. We have used a combination of morphologic image processing and image intensity normalization with anisotropic image filtering to derive edge-related gradients, in order to automatically find the contours of the heart wall; we can use a priori knowledge of the ventricle topology to guide the process and reject unrelated features [9]. We can further speed up the process and make it more robust by extending the contour extraction process directly to the 3D tagged image data set, using a deformable model moving under the wall gradient forces (Fig. 2), as has been used for untagged images [10,11]. The extracted contours can then be used to restrict the tag tracking to follow tags within the heart wall.

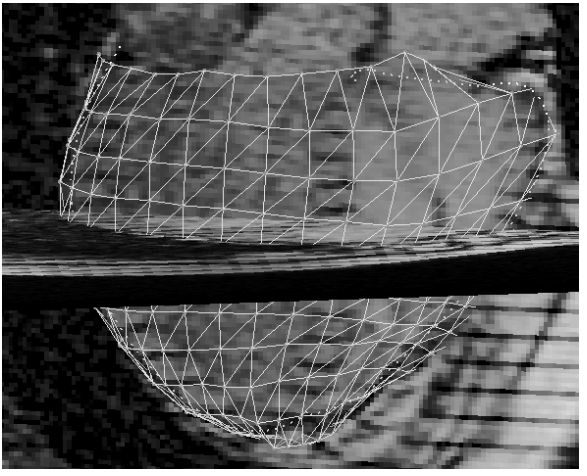

**Fig. 2.** Deformable 3D model of epicardium (colored shell), simultaneously fit to long and short axis tagged images (selected images shown)

## 3 Motion Analysis from Tagged MRI Data

The tracked tag locations can be used to analyze the local wall motion. The intersections of a tag grid can be used to tesselate the image of the heart wall with triangles; the motion of the vertices of the triangles can be used to calculate the rigid body motion and homogeneous strain of each triangle [12]. The 3D motion data inherent in tagged images acquired in different orientations can be combined to reconstruct the 3D motion, using finite element techniques [13–15]. We can use a combined deformable model of the left and right ventricles to recover the 3D motion of both ventricles from the tagged data [16,17] (Fig. 3). The model is constructed by fitting a finite element model to the contours at end diastole, imbedding the initial tag planes in the model at end diastole, and then having the model move under the influence of forces from the tags through the cardiac cycle.

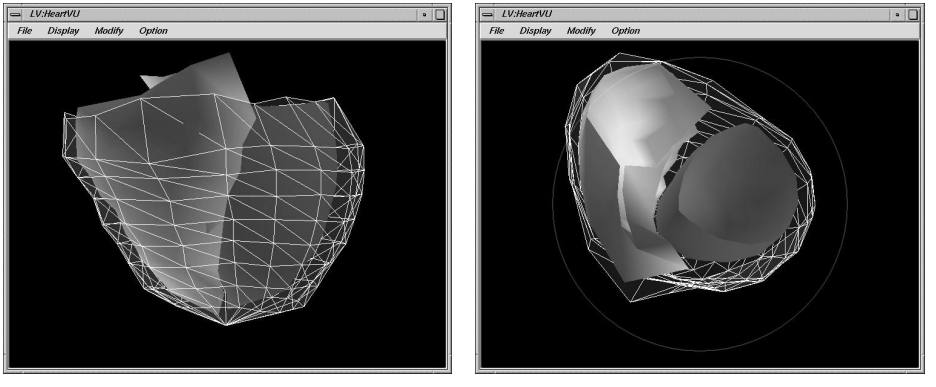


**Fig. 3.** Front (left) and top (right) views of representative phase of biventricular model (RV yellow, LV red), reconstructed from multiplanar tagged MRI data

## 4 Mechanics Modelling

While there is no reliable way to directly measure the forces within the heart wall during the cardiac cycle, we can seek to model the stress-strain relationships in the heart wall, using the observed strain data for the tagged images, coupled with "historical" data on the material properties of the heart wall and the pressure boundary conditions. As part of this effort, we can map the typical distribution of the muscle fiber angles across the heart wall; this can be transformed to later deformed states (Fig. 4). Assuming we have an estimate of the passive material properties and the initial residual strain in the wall, we can estimate the active force needed to be generated along the fibers in order to balance the other forces in the wall, for the strains observed at the successive cardiac configurations [18]. If this can be carried out successfully, we can extend this approach to the prediction of motion for a given active contraction pattern, and compare the results to the observed strains.

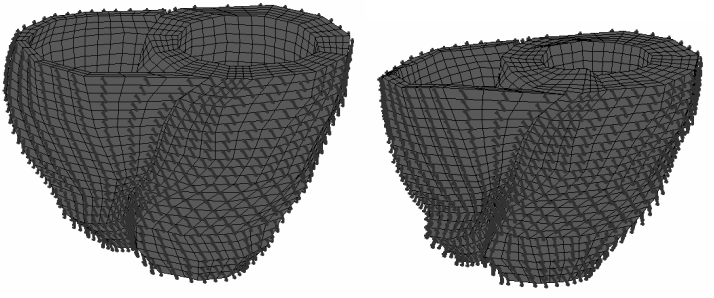

**Fig. 4.** 3D model reconstructed for normal ventricles with superimposed assumed epicardial muscle fiber orientations initialized at end diastole (left) and transformed to end systole (right)

## 5 Future Challenges

An important challenge for the future is further improving the tagged MR image resolution, both spatially and temporally. Ongoing developments in cardiac MRI, such as faster and stronger gradients, parallel image data acquisition from array coils, and higher imaging field strengths, will be applicable to tagged MRI as well. A major limitation of current tagged MRI studies is the amount of time required for image analysis; this is still generally too long for clinical applicability. However, ongoing developments in image analysis methods, such as joint tag and contour extraction combined with model fitting, promise to reduce image analysis times significantly, so that this should be less of a concern in the future. The need to acquire spatially well-registered data for 3D motion reconstruction requires very cooperative subjects, although improvements in physiologic synchronization of imaging and 3D data acquisitions should reduce this problem. A general challenge is the need to handle and visualize the large amounts of image data acquired and the high dimensional data sets that can result from the analysis. To take full advantage of the motion data we are able to

acquire, we will need to register them to other kinds of image-derived data and integrate them into a broader view of the normal and abnormal physiology of the heart.

## Conclusions

Tagged MRI of the heart can provide potentially valuable data on regional cardiac function. While it is still not quite ready for widespread application, ongoing development of improved imaging and image analysis methods is very promising for the near future.

## References

1. E. Zerhouni, D. Parish, W. Rogers, et al., Human heart: tagging with MR imaging- a method for non-invasive assessment of myocardial motion. In *Radiology,* vol. 169, pages 59–63, 1988.
2. L. Axel, L. Dougherty, MR imaging of motion with spatial modulation of magnetization, In *Radiology,* vol. l7l, pages 84l–845, l989.
3. L. Axel, L. Dougherty, Improved method of spatial modulation of magnetization (SPAMM) for MRI of heart wall motion, In *Radiology,* vol. l72, pages 349–350, l989.
4. Q. Yuan, L. Axel, E.H. Hernandez, L. Dougherty, J.J. Pilla, D.H. Scott, V.A. Ferrari, and A.S. Blom, Cardiac-respiratory gating method for magnetic resonance imaging of the heart, In *MRM*; vol. 43, pages 314–318, 2000.
5. F.H. Epstein, S.D. Wolff, A.E. Arai, Segmented k-space fast cardiac imaging using an echo-train readout, In *Magn Reson Med,* vol. 41(3), pages 609–613, 1999.
6. M. Kass, A. Witkin, D. Terzopolous, Snakes: active contours, In *Intl J Computer Vision*, vol 1, pages 321–331,1988.
7. D.L. Kraitchman, A.A. Young, C.-N. Chang, L. Axel, Semi-automatic tracking of myocardial motion in MR tagged images, In *IEEE-TMI* vol. 14, pages 422–423, 1995.
8. L. Dougherty, J.C. Asmuth, A.S. Blom, L. Axel, R. Kumar, Validation of an optical flow method for tag displacement estimation, In *IEEE Trans Med Imag*, vol 18, pages 359–363, 1999.
9. A. Montillo, D. Metaxas, L. Axel. Automated segmentation of the left and right ventricles in 4D cardiac SPAMM images, In *MICCA 2002*, LNCS 2488, pages 620–633, 2002
10. T. McInerney,D. Terzopoulos, A dynamic finite element surface model for segmentation and tracking in multidimensional medical images with application to cardiac 4D image analysis, In *Computerized Medical Imaging and Graphics*, vol. 19(1), pages 69–83, 1995.
11. J. Montagnat, H. Delingette, Spatial and temporal shape constrained deformable surfaces for 3D and 4D medical image segmentation, In *INRIA research report 4078*, 2000.
12. L. Axel, R. Gonçalves, D. Bloomgarden, Regional heart wall motion: Two-dimensional analysis and functional imaging of regional heart wall motion with magnetic resonance imaging, In *Radiology*, vol. 183(3), pages 745–750, 1992.
13. A.A. Young, L. Axel, Three-dimensional motion and deformation of the heart wall: estimation with spatial modulation of magnetization – a model based approach, In *Radiology*, vol 185, pages 241–247, 1992.
14. A.A. Young, D.L. Kraitchman, L. Dougherty, L. Axel, Tracking and finite element modeling of stripe deformation in magnetic resonance tagging, In IE*EE-TMI,* vol 14, pages 413–421, 1995.

15. J. Park, D. Metaxas, L. Axel, Analysis of left ventricular wall motion based on volumetric deformable models and MRI-SPAMM, In *Medical Image Analysis,* vol. 1, pages 53–71, 1996.
16. I. Haber, D. Metaxas, L. Axel, Three-dimensional motion reconstruction and analysis of the right ventricle using tagged MRI, In *Medical Image Analysis,* vol. 4, pages 335–355, 2000.
17. K. Park, D.N. Metaxas, L. Axel, LV-RV shape modeling based on a blended parameterized model, In *MICCAI 2002*, LNCS 2488, pages 753–761, 2002.
18. Z. Hu, D. Metaxis, L. Axel, In-vivo strain and stress estimation of the heart left and right ventricles from MRI images, In *Medical Image Analysis* (accepted 2003).

# A Novel Method for Quantifying the Contribution of Different Intracellular Mechanisms to Mechanically Induced Changes in Action Potential Characteristics

Olga Solovyova[1], Nathalie Vikulova[1], Vladimir S. Markhasin[1], and Peter Kohl[2]

[1] Institute of Immunology and Physiology, Ural Division of the Russian Academy of Sciences
Pervomayskaya ul. 91, Ekaterinburg 620219, Russia
{oas,nath,vsm}@cranium.uran.ru
[2] The Cardiac Mechano-Electric Feedback Group, University Laboratory of Physiology
Parks Road, Oxford OX1 3PT, UK
peter.kohl@physiol.ox.ac.uk
http://www.physiol.ox.ac.uk/~pk

**Abstract.** We introduce the Difference-Current Integral (DCI) method as a tool for quantitative assessment of contributions by individual model components to dynamic responses at the system's level. Using a detailed model of cardiac electrophysiology and mechanics, we assess the relative effects of mechano-sensitive ion channels and intracellular calcium handling to stretch-induced changes in action potential (AP) characteristics. DCI supports the hypothesis that some of the experimentally observed variability in cardiac AP responses to mechanical stimulation may be caused by differences in activation of underlying mechanisms, rather than solely species or technical differences. In particular, the model suggests that systems with a pronounced reverse mode $Na^+$-$Ca^{2+}$ exchange during the AP will respond to mechanical interventions that affect primarily cellular $Ca^{2+}$ handling with AP shortening, whereas a predominant contribution of mechano-sensitive ion channels, in particular cation non-selective ones, may cause late AP prolongation and cross-over of repolarisation.

## 1 Introduction

Biological systems – and their mathematical models – involve dynamic interactions of multiple interdependent components. This high level of interdependency often makes it difficult to establish chains of events, to identify causal interrelations, or to assess the relative contribution of individual components to complex system behaviour.

This applies, without reservation, to the study of cardiac electro-mechanical interactions, including the relatively novel field of mechano-electric feedback (MEF). MEF investigates how the mechanical environment affects cardiac electrophysiology. The relevance of MEF derives from the theoretical understanding that electrical control of cardiac mechanical activity requires a feedback loop in order to give rise to a regulatory system, as well as from numerous clinical reports on mechanical induction, and termination, of heart rhythm disturbances [1].

Experimental studies into mechanical modulation of cardiac action potential duration (APD) have yielded a wide variety of results, including action potential (AP)

I. Magnin et al. (Eds.): FIMH 2003, LNCS 2674, pp. 8–17, 2003.

shortening, crossover of repolarisation, AP lengthening, and early or late after-depolarisation-like events [2]. This variability is believed to be related to differences in species, and/or experimental techniques used to mechanically stimulate and to electrically record from cardiac preparations.

Mechanisms that give rise to MEF include a range of mechano-sensitive ion channels (MSC), and mechanical modulation of cellular calcium ($Ca^{2+}$) handling. These are interdependent, as ion channels and transporter activity is affected by cellular $Ca^{2+}$ concentration, which, in turn, is influenced by channels and transporters.

Any of these mechanisms may directly affect the membrane potential, and thus APD. In turn, any changes in membrane potential will affect a multitude of voltage-sensitive mechanisms in cardiac cells, including ion channel activity, so that primary effects on APD will lead to secondary and tertiary ones, making it exceedingly difficult to quantify and compare observations.

Using a novel mathematical model of cardiac electro-mechanical interactions [3], we investigate the hypothesis that the experimentally observed variability in mechanically-induced APD responses may, in fact, arise from differences in the relative contribution of underlying cellular mechanisms of MEF. In particular, we suggest that the interplay between (i) mechanical effects on the cooperative modulation of troponin C (TnC) affinity for $Ca^{2+}$ and (ii) mechanical activation/inactivation of MSC determines responses at the cellular level, including APD changes.

In order to quantify the relative contribution of individual mechanisms, we developed the 'Difference-Current Integral' (DCI) method, to provide insight into the dynamic contribution of individual model components to system behaviour. Using the DCI approach, we identify the difference in total charge, carried by individual intracellular mechanisms in response to mechanical stimulation. Comparison of DCIs allows one to elucidate the relative significance of individual mechanisms for the overall response to mechanical stimulation, as expressed by changes in APD.

## 2 Methods

### 2.1 Model of Ventricular Mechano-Electric Interactions

A new mathematical model of mechano-electric interactions in ventricular cardiomyocytes has been developed [3], which inherits the description of the electrical activity from the Noble'98 ventricular cell model [4] and the description of cellular $Ca^{2+}$ kinetics and mechanical activity from the Ekaterinburg model family [5].

The combined model realistically reproduces mechanical and electrical activity of cardiomyocytes during isometric and afterloaded contractions, and allows implementation of complex mechanical protocols, such as acute length changes during contraction, as well as simulation of electrical interventions, such as patch clamp. The model includes mechano-dependent cooperativity of the kinetics of $Ca^{2+}$ - troponin C (TnC) binding. This is a principal link between cardiac mechanics and $Ca^{2+}$ handling. Three types of experimentally-established cooperativity of $Ca^{2+}$ activation [6] are taken into account in the model [7]. Thus, the affinity of TnC for $Ca^{2+}$ increases i) with the concentration of strongly-bound crossbridges and ii) with increasing concentration of $Ca^{2+}$-TnC complexes; while, iii), availability of actin sites for crossbridge formation increases nonlinearly due to end-to-end interaction between adjacent tropomyosins.

These mechanisms allow one to simulate a wide range of experimental observations on mechano-mechanical coupling (such as the effects of mechanical load on muscle relaxation) and mechano-$Ca^{2+}$ coupling (e.g. length- and load-dependence of $Ca^{2+}$ transients). In addition, mechanical modulation of $Ca^{2+}$ transients (due to mechano-dependent $Ca^{2+}$-TnC kinetics) links through to mechanical and electrical activity, via $Ca^{2+}$-dependent ion currents. The model reproduces the effects of mechano-electrical coupling as an influence of muscle length on APD during isometric contractions, the APD dependence on the muscle load during afterloaded contractions, and certain APD changes caused by passive deformation [3].

Our model findings support experimentally derived conclusions [8] on the central role of the $Na^{+}$-$Ca^{2+}$ exchanger (NCX) in the sequence of events underlying MEF. For the present study we extend our model by adding a description of MSC, to study the interplay between these two major mechanisms of cardiac MEF [9].

**MSC Model**. We used a description of the net current through MSC based on [10]:

$$I_{MSC} = g_{MSC} \cdot \frac{1}{1 + K_{MSC} \cdot e^{-\gamma_{MSC} \cdot (L - L_{ref})}} \cdot (E - E_{MSC}) \ . \quad (1)$$

where E is the membrane potential, $E_{MSC}$ is a user-defined MSC reversal potential (here -20 mV to simulate cation non-selective channels [9]), and $g_{MSC}$ is the maximum whole cell MSC conductance (which itself is a product of single channel conductance, ion channel density, and cell area). We varied the value of $g_{MSC}$ to simulate different relative contributions of MSC. Stretch activation of the channels is implemented by the factor depending on deviation of the current cell length, L, from a reference length, $L_{ref}$, where $\gamma_{MSC}$ is a sensitivity parameter and $K_{MSC}$ an equilibrium constant determining the current at $L_{ref}$.

Here we present some model simulations of stretch effects on APD and analyze the relative contribution of different intracellular mechano-sensitive mechanisms to macroscopic manifestations, such as APD changes, using the quantitative DCI method described below.

### 2.2 Difference-Current Integral (DCI) Method

Difference-currents are a standard experimental approach to illustrating the effects of an intervention on electrophysiology. Difference-currents are obtained by subtracting a current measured in control conditions from the corresponding current during the intervention. It is important to realise that a difference-current therefore signifies *how much more* de- or repolarising a particular current is during the intervention, rather than whether the current itself is directed outward (repolarising) or inward (deploarising). In other words – a 'repolarising difference-current' may signify either i) an increase in a repolarising current, or ii) a reduction in a depolarising one. Crucially, the net effect of both scenarios on AP characteristics will be comparable.

Any changes observed during an intervention (such as mechanical stimulation) are determined by the dynamic changes in net current, which is equal to the sum of individual difference-currents. Thus, the relative contribution of individual currents to net changes can be calculated, in particular using mathematical models.

Let $E_X$ be the membrane potential measured during a given condition X (for example stretch). If $i_X$ is an individual current, contributing to the net current through the membrane, then the total charge carried by this individual current, $Q_{i,X}$, can be calculated as the integral of the current over time, from $t_0$ to t:

$$Q_{i,X}(t) = \int_{t_0}^{t} i_X(\tau) d\tau \ . \tag{2}$$

The magnitude of membrane potential changes over this time is determined by the sum of all charges, transferred by all currents:

$$E(t) = E(t_0) + (-\frac{1}{C}) \sum_i Q_{i,X}(t) \ . \tag{3}$$

Let us consider, for example, stretch as an intervention causing AP modulation. Using equation (3) it is easy to calculate the potential difference $\Delta E(t)$ between membrane potentials measured during stretch, $E_{stretch}(t)$, and control, $E_{cont}(t)$:

$$\Delta E(t) = E_{stretch}(t) - E_{cont}(t) = \Delta E(t_0) + (-\frac{1}{C}) \sum_i \Delta Q_i(t) \ . \tag{4}$$

where $\Delta Q_i(t)$ is the additional charge carried by the current i during stretch, contributing to the total modulation of AP parameters. Obviously, $\Delta Q_i(t)$ is equal to the integral of the difference-current $\Delta i(t)$, obtained by subtracting the control current from the current during stretch:

$$\Delta Q_i(t) = \int_{t_0}^{t} \Delta i(\tau) d\tau = \int_{t_0}^{t} (i_{stretch}(\tau) - i_{control}(\tau)) d\tau \ . \tag{5}$$

Together with the charge increment, carried by an individual current during stretch, we also calculate a value for the voltage modulation provided by the charge flux:

$$\Delta E_i(t) = -\frac{1}{C} \cdot \Delta Q_i(t) \ . \tag{6}$$

Comparison of cumulative effects $\Delta E_i(t)$ of the difference-currents on the membrane potential $\Delta E(t)$ allows one to quantify the significance of mechanisms contributing to mechano-dependent feedback in cardiomyocytes.

## 3 Results

Stretch effects on AP shape and duration were modelled and analyzed using DCI. The modelled muscle contracted isometrically, either at control length, $L_{cont}$ (sarcomere length of 1.84 μm) or, after elongation, at $L_{stretch}$ (2.13 μm), with three different maximum whole cell conductances of MSC: $g_{MSC}$ = 0.0 μS (absence of MSC), 0.013 μS (low MSC density), and 0.09 μS (high MSC density).

### 3.1 Role of $Na^+$-$Ca^{2+}$ Exchange Currents in Stretch Effects on Action Potential

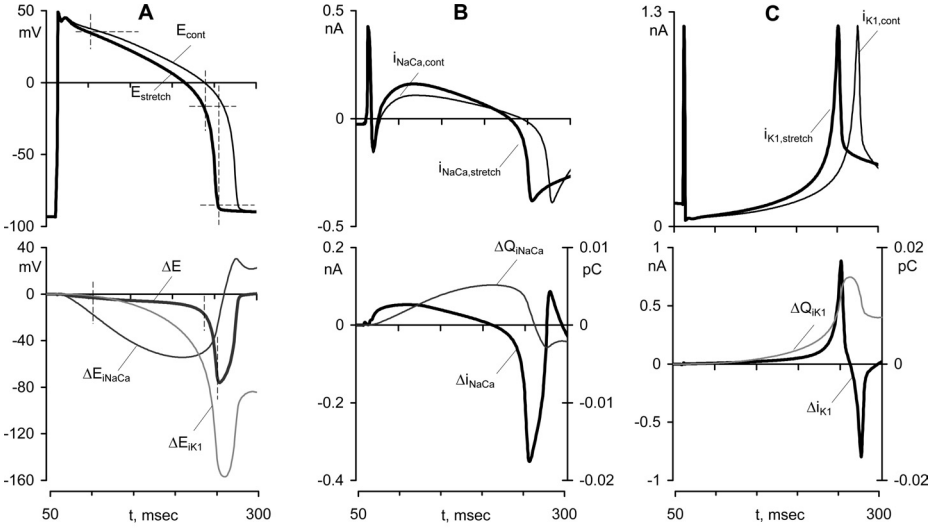


**Fig. 1.** Stretch effects on ventricular cardiomyocyte electrophysiology, simulated in the absence of mechano-sensitive ion channels (MSC). **A**: Stretch, targeted at mechanisms other than MSC, may cause reduction in action potential duration (APD), as evident from the time-course of membrane potentials during stretch, $E_{stretch}$, and control, $E_{cont}$ (*top panel*). The negative difference in membrane potential integrals, $\Delta E$ (*thick line, bottom panel*) is a result of membrane potential changes driven by variation in $Na^+$-$Ca^{2+}$ exchange current, $\Delta E_{iNaCa}$, and inward rectifying $K^+$ current, $\Delta E_{iK1}$. **B** and **C**: Time course of $i_{NaCa}$ (*B*) and $i_{K1}$ (*C*) during stretch and in control conditions (*top panels*). Bottom panels illustrate the difference-currents, $\Delta i_{NaCa}$ and $\Delta i_{K1}$, and the additional charge, $\Delta Q_{NaCa}$ and $\Delta Q_{K1}$, carried by those currents during stretch

Stretch effects, mediated via mechanical modulation of cellular $Ca^{2+}$ handling alone (i.e. where $g_{MSC} = 0$) may cause AP shortening, if there is sufficiently large reverse mode NCX, as shown in Fig. 1A and B. Similar AP shortening has been seen in isolated cardiomyocytes, strips of myocardium, and whole heart [11, 12, 13]. The APD at 10%, 50%, and 95% repolarisation ($APD_{10}$, $APD_{50}$, and $APD_{95}$) decreased, under these conditions, by 28% (from 57 ms to 41 ms), 11% (from 203 ms to 180 ms) and 11% (from 217 ms to 194 ms), respectively (Fig. 1A, see dotted horizontal lines).

The time-course of membrane potential differences, $\Delta E(t)$, between stretch, $E_{stretch}(t)$, and control, $E_{cont}(t)$, are presented in the bottom panel of Fig. 1A. The difference increases with time from -4 mV at $APD_{10}$ (of the stretched cell), to -19.5 mV at $APD_{50}$, and -75.8 mV at $APD_{95}$ (see dotted vertical lines in Fig. 1A). This membrane potential change is determined by the sum of additional charges, carried by individual currents in response to mechanical stimulation of the cell (for detail see Table 1).

Key contributors to the stretch-induced negative (repolarising) $\Delta E(t)$ during the AP are the NCX current, $i_{NaCa}$, and the inward rectifying $K^+$ current, $i_{K1}$ (Fig. 1B, C). These currents allow for an additional efflux of positive charges from the cell during stretch, which results in repolarisation and APD shortening. Difference-currents and total charge carried ($\Delta Q_i(t)$, see equation (5)) are shown in the bottom panels of

Fig. 1B and C. It is evident, that the dynamic contribution of both currents to the total negative ΔE(t) varies over the course of the AP. The initial effect is caused mainly by a relative increase in repolarising (outward) current via the NCX (see $\Delta i_{NaCa}$ in Fig. 1B and $\Delta E_{iNaCa}(APD_{10})$ in Table 1), which causes a decrease in early AP plateau amplitude (see Fig. 1A and ΔE(t) in Table 1). This, in turn, accelerates the voltage-dependent activation of the repolarising $i_{K1}$ (Fig. 1C), which shortens APD.

### 3.2 Contribution of MSC to Stretch Effects on Action Potential

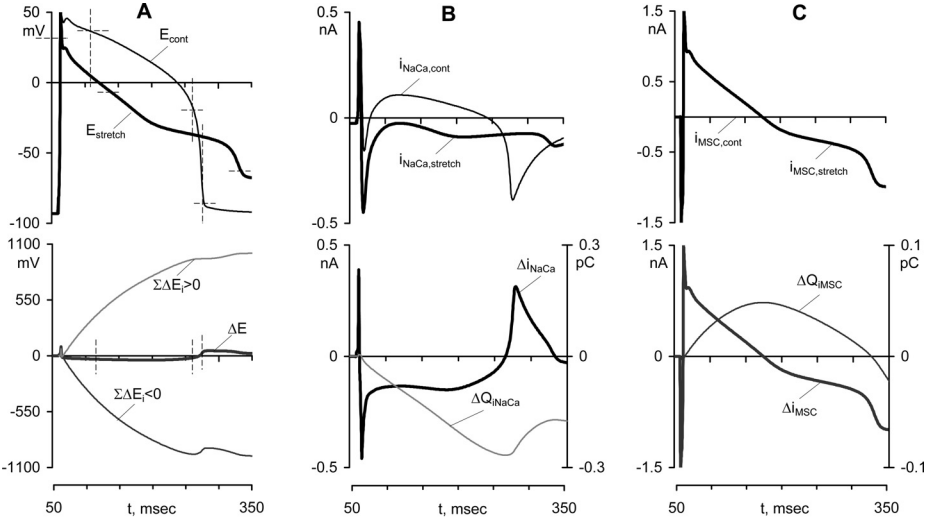


**Fig. 2.** Stretch effects in the presence of MSC. **A**: Stretch effects, mediated via MSC, cause diastolic depolarization, early AP repolarisation, and – if large enough – cross-over of late AP repolarisation (*top*), as witnessed by the bi-phasic response of the membrane potential difference, $\Delta E$ (*thick line, bottom panel*). **B**: Stretch-induced differences in $i_{NaCa}$ are of the opposite polarity, compared to Fig. 1, as the instant reduction in early AP amplitude (Fig. 2A) prevents reverse mode NCX. **C**: The stretch activated MSC current (*top, set to zero in control conditions*) causes a significant early influx of repolarising charges (*bottom panel*) and is the cause for responses illustrated in **A** and **B**. The sum of repolarising $\Delta E_{MSC}$ and $\Delta E_{K1}$ (*bottom of panel A,* $\Sigma\Delta E_i < 0$) determines the fast initial decrease in AP amplitude, while the sum of depolarising effects (*bottom of panel A,* $\Sigma\Delta E_i > 0$) underlies late AP prolongation cross-over

The experimental protocol of 3.1 was repeated in the presence of MSC. Using a small conductance for MSCs, $g_{MSC}$ = 0.013 µS (not shown), we observed a decrease in APD, which was determined by coordinated repolarising effects of both $\Delta i_{NaCa}$ and $\Delta i_{MSC}$ during the early plateau of the AP. The development of a depolarising MSC current after the membrane potential passed the reversal potential of MSC (-20 mV) did not counterbalance the repolarising effect of $\Delta i_{NaCa}$ and $\Delta i_K$, so that APD declined.

In contrast, simulated stretch in the presence of a large whole-cell MSC peak conductance ($g_{MSC}$ = 0.09 μS) induced crossover of late AP repolarisation (Fig. 2A). This reproduces another facet of experimentally observed behaviour [14, 15]. In this case, $APD_{10}$ decreased by 93% (from 57 ms to 4 ms), $APD_{50}$ decreased by 57% (from 203 ms to 87 ms), while $APD_{95}$ increased by 27% (from 217 ms to 276 ms). Note, that crossover of repolarisation occurred at a potential of -33 mV, which is lower than the reversal potential for MSC, illustrating multifactorial MEF responses.

DCI analysis shows that the contribution of MSC currents during stretch dominates the response to mechanical stimulation in the presence of a large MSC conductance (see Table 1), and even causes a reversal of the relative contribution of NCX to APD. The early reduction in AP amplitude prevents the outward mode of NCX and causes a depolarising $\Delta i_{NaCa}$ (see $\Delta E_{iNaCa}$ in Table 1 and compare $\Delta i_{NaCa}$ in Fig. 1B and 2B). In addition, it causes an increase in depolarising L-type $Ca^{2+}$, $i_{Ca,L}$, and persistent $Na^+$ current, $i_{pNa}$, as well as a decrease in the delayed rectifying $K^+$ current, $i_K$, compared to control (not shown). Nonetheless, the large $g_{MSC}$ allows MSC to dominate the response and to maintain a reduction in AP amplitude up and until the membrane potential passes the MSC reversal potential. At this point, MSC start to provide a depolarising current, which – together with the above – eventually causes crossover of repolarisation (at about –33 mV, Fig. 2).

**Table 1.** Contribution (cumulative effects) of individual difference-currents to voltage changes, $\Delta E_i$, relative to the stretch-induced changes in total membrane potential, $\Delta E$, assessed at different stages of AP repolarisation (as identified in Figs. 1 and 2)[1]

| | $\Delta E_i(APD_{10})$, mV | | $\Delta E_i(APD_{50})$, mV | | $\Delta E_i(APD_{95})$, mV | |
|---|---|---|---|---|---|---|
| ***Current*** | $g_{MSC}$ = 0 μS | $g_{MSC}$ = 0.09 μS | $g_{MSC}$ = 0 μS | $g_{MSC}$ = 0.09 μS | $g_{MSC}$ = 0 μS | $g_{MSC}$ = 0.09 μS |
| $i_{MSC}$ | 0.0 | **-379.0** | 0.0 | **-293.4** | 0.0 | -238.6 |
| $i_{NaCa}$ | **-24.6** | 91.0 | **-48.1** | 280.8 | **-21.4** | **265.4** |
| $i_{CaL}$ | 11.0 | 173.6 | 26.6 | 193.4 | 21.4 | **192.5** |
| $i_{bCa}$ | 0.9 | 4.2 | 5.4 | 22.1 | 7.2 | **22.1** |
| $i_K$ | 0.3 | **-2.3** | 3.1 | 36.6 | 12.1 | **39.8** |
| $i_{K1}$ | **-3.0** | **-65.7** | **-68.7** | **-675.1** | **-150.2** | -674.7 |
| $i_{to}$ | 2.0 | 29.9 | 3.5 | 49.9 | 3.6 | **49.9** |
| $i_{KL}$ | 1.7 | 20.4 | 3.7 | 31.7 | 3.9 | **31.7** |
| $i_{Na}$ | 0.2 | **-6.0** | 0.4 | 10.6 | 1.2 | **14.8** |
| $i_{pNa}$ | 4.8 | 62.6 | 43.5 | 255.8 | 32.4 | **272.2** |
| $i_{NaL}$ | 2.0 | 29.3 | 4.4 | 29.5 | 3.4 | **29.3** |
| $i_{bNa}$ | 0.7 | 8.3 | 6.6 | 42.6 | 10.5 | **42.0** |
| $i_p$ | 0.0 | **-0.1** | 0.1 | **-1.0** | 0.1 | -1.1 |
| ***Total ΔE(t), mV*** | **-4** | **-33.8** | **-19.5** | **-16.5** | **-75.8** | **45.3** |

[1] Columns present either absence of MSC (shaded), or presence of strong MSC effects ($g_{MSC}$ = 0.09 μS). Contributors to the overall response with matching polarity are highlighted.

# 4 Discussion

## 4.1 Role of $Ca^{2+}$-Handling in MEF

Results obtained in the absence of MSC ($g_{MSC}$ = 0.0 μS) illustrate the critical role of mechanical modulation of NCX currents for APD shortening during stretch. The observed reduction in APD is caused, in the model, by complex interactions between contractile element lattice spacing and $Ca^{2+}$ handling (see [3] for further detail), which affects the $Ca^{2+}$ dependent NCX current. Stretch causes a cooperative increase in TnC affinity for $Ca^{2+}$ (see Sect. 2.1) and thus slows $Ca^{2+}$ dissociation from $Ca^{2+}$–TnC complexes. This, in turn, leads to a slight decrease in the amplitude of $Ca^{2+}$ transients and a significant acceleration of cytosolic $Ca^{2+}$ decay during stretch. Reduced $Ca^{2+}$ transients favour increase in reverse mode (repolarising) NCX and shorten the AP (Fig. 1B). Model simulations of stretch effects on $Ca^{2+}$ transients correspond well with experimental data obtained in muscle strips and isolated cells [11, 12].

## 4.2 MSC Effects on the Action Potential

Mechanical modulation of $Ca^{2+}$ handling in the presence of significant reverse mode NCX can explain a range of experimentally observed responses to mechanical stimulation [3,5], but it does not explain stretch-induced AP prolongation, cross-over of repolarisation, or afterdepolarisation-like events. Introduction of a simple description of MSC (equation (1)) allows one to begin addressing other aspects of the above-mentioned diversity of stretch-induced effects on APD. Small stretch-activated conductances can enhance the reduction in APD, while larger activation of MSC may cause crossover of repolarisation (Fig. 2).

All known cardiac MSC have reversal potentials that are negative to AP plateau levels. They contribute, therefore, to early AP repolarisation, while their effect on late AP shape depends on MSC type and amplitude. Here, we model only one sub-type of MSC (cation non-selective, $E_{MSC}$ = -20 mV) and consider it as a charge carrier only (no effect on ion concentrations). This has previously been shown to be acceptable for the simulation of immediate stretch effects [10]. Still, the response to MSC activation emerges from complex interactions with other currents, such as $i_{NaCa}$, $i_{Ca,L}$, and $i_{pNa}$. This, together with a strong dependence on preceding AP effects, may explain some of the experimentally observed diversity in stretch effects, and help to explain the close links between MSC and cellular $Ca^{2+}$ handling observed in single cells [16].

Further variability of electrical responses to stretch arises from stretch timing, where early stretch contributes to repolarisation, while late stretch – in particular if applied when membrane potentials have returned to levels near $E_{MSC}$ – may prolong the late AP, or cause afterdepolarisation-like behaviour, as concluded before [10].

## 4.3 Interplay of MEF Mechanisms

Analysis of the interplay of individual mechano-sensitive mechanisms in the response to stretch was helped by application of the DCI method, which allows one to quantify and compare charges, carried by individual cellular mechanisms, during control and

stretch. Comparison of the cumulative effects of individual charge carrying mechanisms, and their development in time, provides a useful tool for the identification of primary and secondary responses, such as effects of changes in AP shape on voltage dependent currents.

Thus, we found that in the presence of no or very small MSC conductances, the stretch-induced decrease in APD is largely caused by a $Ca^{2+}$-dependent modulation of NCX. In this case, the affinity of TnC for $Ca^{2+}$ is the primary mechanical sensor.

In the presence of high MSC conductances, the situation is changed by a sudden reduction in early AP amplitude, which exceeds the potential contribution of mechanical modulation in $Ca^{2+}$ handling and, subsequently, affects all other voltage-dependent mechanisms in the system. Here, MSC act as the primary mechanical sensor.

In order to exclude secondary effects of stretch-induced AP changes on ionic currents, we also conducted a study where an AP, recoded under control conditions, was re-applied as a command voltage during stretch – an approach know from experimental studies as the 'AP clamp technique'. This technique is based on recording the compensation current required to maintain control AP characteristics during an intervention, such as stretch. This current is the *inverse* of the mechanically induced current component, and it can be used to calculate the actual influence of primary effects on AP configuration. AP clamp findings confirmed that NCX and MSC currents are key targets of mechanical stimulation in our model.

### 4.4 Conclusions

A quantitative method for the assessment of contributions by different intracellular mechanisms to mechanically induced changes in AP characteristics has been developed, based on the comparison of difference-current integrals. This method allows one to analyse dynamic interactions of interdependent mechanisms in complex models of cardiac electro-mechanical activity. The model proposed here may in its own right be seen as a useful tool for further studies into cardiac electro-mechanics. In combination with the DCI method, the model allows theoretical testing of various MEF scenarios, with the aim of identifying causal chains of events and pinpointing lead targets for experimental study. This illustrates the role mathematical modelling can play as an integrated tool for biological research.

**Acknowledgements.** The authors thank Mrs Patricia J Cooper for helpful comments on the manuscript. This work is subject of a Wellcome Trust Research Development Award (#061115) and was further supported by a grant from the Russian Foundation for Basic Research (03-04-48260). NV holds a Young Scientists Award of the Ural Division of the Russian Academy of Sciences. PK is a Royal Society Research Fellow.

## References

1. Kohl, P., Nesbitt, A.D., Cooper, P.J., Lei, M.: Sudden Cardiac Death by *Commotio Cordis*: Role of Mechano-Electric Feedback. Cardiovasc. Res. **50** (2001) 280–289

2. Kohl, P., Hunter, P., Noble, D.: Stretch-Induced Changes in Heart Rate and Rhythm: Clinical Observations, Experiments and Mathematical Models. Prog. Biophys. Mol. Biol. **71.1** (1999) 91–138
3. Solovyova, O., Vikulova, N., Katsnelson, L.B., Markhasin, V.S., Noble, P.J., Garny, A.F., Kohl, P., Noble, D.: Mechanical Interaction of Heterogeneous Cardiac Muscle Segments in Silico: Effects on $Ca^{2+}$ Handling and Action Potential. Int. J. Bifurcation and Chaos (2003) in press
4. Noble, D., Varghese, A., Kohl, P., Noble, P.: Improved Guinea-Pig Ventricular Cell Model Incorporating a Diadic Space, Ikr and Iks, and Length- and Tension-Dependent Processes. Can. J. Cardiol. **14.1** (1998) 123–134
5. Solovyova, O., Katsnelson, L., Guriev, S., Nikitina, L., Protsenko, Y., Routkevitch, S., Markhasin, V.: Mechanical Inhomogeneity of Myocardium Studied in Parallel and Serial Cardiac Muscle Duplexes: Experiments and Models. Chaos, Solitons & Fractals **13.8** (2002) 1685–1711
6. Gordon, A.M., Regnier, M., Homsher, E.: Skeletal and Cardiac Muscle Contractile Activation: Tropomyosin "Rocks and Rolls". News Physiol. Sci. **16** (2001) 49 –55
7. Katsnelson, L.B., Markhasin, V.S.: Mathematical Modeling of Relations between the Kinetics of Free Intracellular Calcium and Mechanical Function of Myocardium. J. Mol. Cell. Cardiol. **28.3** (1996) 475–486
8. Hongo, K., White, E., Le Guennec, J.Y., Orchard, C.H.: Changes in $[Ca^{2+}]_I$, $[Na^{+}]_I$ and $Ca^{2+}$ Current in Isolated Rat Ventricular Myocytes Following an Increase in Cell Length. J. Physiol. **491.3** (1996) 609–619
9. Kohl, P., Sachs, F.: Mechano-Electric Feedback in Cardiac Cells. Phil. Trans. R. Soc. Lond. A **359** (2001) 1173–1185
10. Kohl, P., Day, K., Noble, D.: Cellular Mechanisms of Cardiac Mechano-Electric Feedback in a Mathematical Model. Can. J. Cardiol. **14.1** (1998) 111–119
11. Lab, M.J., Allen, D.G., Orchard, C.H.: The Effects of Shortening on Myoplasmic Calcium Concentration and on the Action Potential in Mammalian Ventricular Muscle. Circ. Res. **55.6** (1984) 825–829
12. White, E., Le Guennec, J.Y., Nigretto, J.M., Gannier, F., Argibay, J.A., Garnier, D.: The Effects of Increasing Cell Length on Auxotonic Contractions; Membrane Potential and Intracellular Calcium Transients in Single Guinea-Pig Ventricular Myocytes. Exp. Physiol. **78.1** (1993) 65–78
13. Hansen, D.E.: Mechanoelectrical Feedback Effects of Altering Preload, Afterload, and Ventricular Shortening. Am. J. Physiol. **264** (1993) H423–H432
14. Kamkin, A., Kiseleva, I., Isenberg, G.: Stretch-Activated Currents in Ventricular Myocytes: Amplitude and Arrhythmogenic Effects Increase with Hypertrophy. Cardiovasc. Res. **48.3** (2000) 409–420
15. Zabel, M., Koller, B.S., Sachs, F., Franz, M.R.: Stretch-Induced Voltage Changes in the Isolated Beating Heart: Importance of the Timing of Stretch and Implications for Stretch-Activated Ion Channels. Cardiovasc. Res. **32** (1996) 120–130
16. Belus, A., White, E.: Streptomycin and Intracellular Calcium Modulate the Response of Single Guinea-Pig Ventricular Myocytes to Axial Stretch. J. Physiol. **546.2** (2003) 501–509

# Automatic Construction of Biventricular Statistical Shape Models

A.F. Frangi[1], D. Rueckert[2], J.A. Schnabel[3], and W.J. Niessen[4]

[1] Division of Biomedical Engineering, Aragon Institute of Engineering Research
University of Zaragoza. Zaragoza, Spain
[2] Visual Information Processing Group, Department of Computing
Imperial College of Science, Technology and Medicine, London, UK
[3] Computational Imaging Science Group, Division of Radiological Sciences
Guy's Hospital, King's College London, London, UK
[4] Image Sciences Institute, University Medical Center Utrecht, The Netherlands

**Abstract.** This paper presents a method for the generation of landmarks in three-dimensional shapes and the construction of the corresponding 3-D statistical shape models. The technique relies on establishing shape correspondances via a volumetric non-rigid registration technique using multi-resolution B-spline deformations. This approach presents some advantages over previously published methods: it can treat multiple-part structures, and it requires less restrictive assumptions on the structure's topology. In this paper we address the problem of building a three-dimensional statistical shape model of the left and right ventricles of the heart from 3-D Magnetic Resonance (MR) images. This application demonstrates the robustness and accuracy of the method in the presence of large shape variability and multiple objects.

## 1 Introduction

Statistical models of shape variability or Active Shape Models (ASM) [1] have been successfully applied to perform segmentation and recognition tasks in two-dimensional images. In building statistical models, a set of segmentations of the shape of interest is required, as well as a set of corresponding landmarks defined over the set of training shapes.

Manual segmentation and determination of point correspondences are time consuming and tedious tasks. This is particularly true for three-dimensional applications where the amount of image data to analyze and the amount of landmarks required to describe the shape increases dramatically in comparison to two-dimensional applications. This work aims at automating the landmarking procedure. That is, we still rely on the existence of a manual segmentation of the shapes but the process of landmark extraction will be automated.

To our knowledge, only few authors have addressed the problem of automatic construction of 3-D ASMs using non-rigid registration [2,3,4,5,6]. The frameworks proposed by Brett and Taylor [2,3] are closely related to this work. In these approaches, each shape is first converted into a polyhedral representation.

I. Magnin et al. (Eds.): FIMH 2003, LNCS 2674, pp. 18–29, 2003.

In the first approach [2], shape pairs are matched using a symmetric version of the Iterative Closest Point (ICP) algorithm by Besl and McKay [7]. Using this method, the authors were able to build 3-D ASMs by automatically finding corresponding landmarks between surfaces. This method is prone to obtain shape models with surface folding due to some landmark groups (triples) matched in different order between training examples as a consequence of the use of the ICP technique which is a purely local registration technique and does not incorporate any connectivity constraints. In Brett and Taylor [3] this problem is addressed by transforming the surface to a planar domain using harmonic maps where connectivity constraints can be explicitly enforced. This technique however is only applicable to single-part shapes that are topologically isomorphic to a disk. The work by Fleute and Lavallée [4,5] is also closely related to our work. They use a multi-resolution non-rigid registration technique based on octree-splines. Finally, Subsol et al. [6] reported on a method for automatically constructing 3D morphometric anatomical atlantes which is based on the extraction of line and point features and their subsequent non-rigid registration. Recently, Davies *et al.* [8] have published a method to automatically extract a set of optimal landmarks using the Minimum Description Length (MDL) principle. Although this is a promising method that has a sound mathematical formulation, it is still required to elucidate whether the optimal landmarks in the MDL sense are also optimal in the sense of anatomical correspondence.

In this paper a technique is introduced that tries to address the shortcomings of point- or surface-based registration where no overall connectivity constraints are imposed. Our method introduces global constraints by matching shapes via a volumetric non-rigid registration technique using multi-resolution B-spline deformation fields [9,10]. Owing to the multi-resolution nature of the deformation field, the mappings between matched shapes have been shown to be smooth [10]. Although in our experience this is not essential, an additional smoothness penalty can be incorporated which further prevents folding when recovering the deformation field. An important feature of our approach is that the same method for establishing correspondences can be simultaneously applied to all the parts of a composite object. This has not been previously investigated in [4,5,2,3]. As an application, we show the use of this technique to create three-dimensional statistical shape models describing the shape of the left and right ventricles of the heart.

## 2 Statistical Shape Models

Let $\{\mathbf{x}_i; i = 1 \cdots n\}$ denote $n$ shapes. Each shape consists of $m$ 3-D landmarks, $\{\mathbf{p}_j = (p_{1j}, p_{2j}, p_{3j}); j = 1 \cdots m\}$ that represent the nodes of a surface triangulation. Obtaining those $m$ 3-D landmarks is a non-trivial task and presents the main topic of this paper. Each vector $\mathbf{x}_i$ is of dimension $3m$ and consists of the landmarks $(p_{11}, p_{21}, p_{31}, p_{12}, p_{22}, p_{32}, \cdots, p_{1m}, p_{2m}, p_{3m})$. Moreover, assume that the positions of the landmarks of all shapes are expressed in the same coordinate system. These vectors form a distribution in a $3m$-dimensional space. The goal

is to approximate this distribution with a linear model of the form

$$\mathbf{x} = \hat{\mathbf{x}} + \mathbf{\Phi}\mathbf{b} \tag{1}$$

where $\hat{\mathbf{x}}$ is the average landmark vector, $\mathbf{b}$ is the shape parameter vector of the model, and $\mathbf{\Phi}$ is a matrix whose columns are obtained by performing a Principal Component Analysis (PCA) of the covariance matrix $\mathbf{S}$. The principal components of $\mathbf{S}$ are calculated as its eigenvectors, $\phi_i$, with corresponding eigenvalues, $\lambda_i$ (sorted so that $\lambda_i \geq \lambda_{i+1}$). If $\mathbf{\Phi}$ contains the $t < \min\{m, n\}$ eigenvectors corresponding to the largest non-zero eigenvalues, we can approximate any shape of the training set, $\mathbf{x}$, using Equation (1) where $\mathbf{\Phi} = (\phi_1|\phi_2|\cdots|\phi_t)$ and $\mathbf{b}$ is a $t$ dimensional vector given by $\mathbf{b} = \mathbf{\Phi}^T(\mathbf{x} - \hat{\mathbf{x}})$.

## 3 Automatic Landmarking

**Overview.** Ideally, a landmark is an anatomically characteristic point that can be uniquely identified on a set of shapes. However, anatomical landmarks are usually too sparse to accurately describe a 3-D shape. Therefore, we will consider pseudo-landmarks, *i.e.* landmarks lying on the shape's surface and determining its geometry.

Assume that $n$ segmented shapes of the structure of interest are available. These segmentations constitute the training set, $\mathcal{S}_n = \{L_i\}$ where $i = 1 \cdots n$. Each shape in the training set is represented by a *labeled image* whose voxel values belong to a label set $\mathcal{L}$. To generate the landmarks for the $n$ shapes, a shape atlas $A$ is constructed, landmarked, and these landmarks are finally propagated back to the $n$ shapes. The following sections describe these three steps in detail and a pictorial overview is given in Fig. 1.

**Pre-processing.** The automatic landmarking algorithm can be applied to a set of previously segmented structures. In our application, three main structures of the heart have been segmented from a number of volunteer scans. Each segmentation consists of manual identification of the background ($BG$), the left ventricular blood pool ($LV_{bp}$) and myocardium ($LV_{myo}$), and of the right ventricular blood pool ($RV_{bp}$). In the segmentation of the left ventricle, the papillary muscles are considered part of the blood pool as is customary in functional cardiac analysis. Each segmentation is represented as a labeled image, where each voxel is labeled according to the tissue type to which it belongs ($\mathcal{L} = \{BG, LV_{bp}, LV_{myo}, RV_{bp}\}$).

Owing to the large voxel anisotropy in MR short-axis acquisitions of functional cardiac data sets, manual segmentations have significant staircase artefacts in the direction of the long axis of the heart. In order to facilitate image registration and to smooth out those artefacts, shape-based interpolation [12] has been applied to obtain labeled images of isotropic voxel size.

**Atlas Construction in Single Object Shapes.** Let us assume that a set of $n$ training shapes, $\mathcal{S}_n$, is available and that each shape is represented by a bi-valued

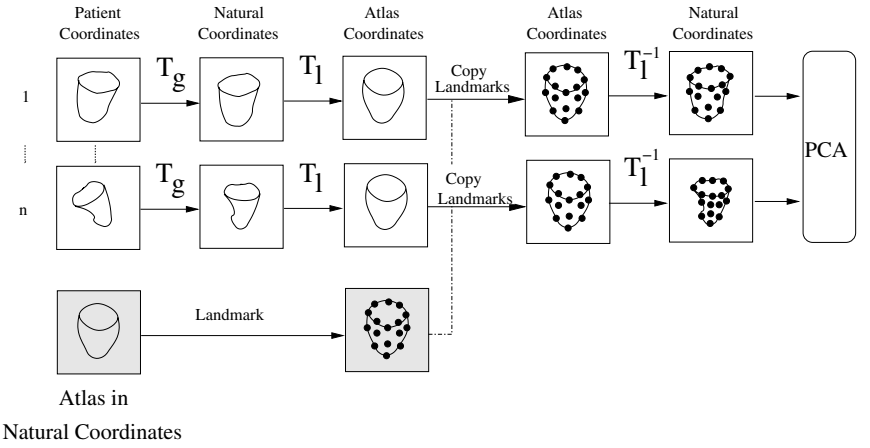


**Fig. 1.** Overview of the automatic landmarking framework. All individual data sets are matched to an atlas via an affine transformation ($\mathbf{T}_g$) and an non-rigid transformation ($\mathbf{T}_l$). The landmarks in the atlas can then be copied to the individual patients. The non-rigid deformation is subsequently reversed. Thus, Principal Component Analysis (PCA) is carried out in a space where all shapes are aligned with the atlas. The principal modes of variation will therefore account for non-rigid deformations and not for pose or size differences

labeled image, $B_i$. That is, the label set contains only two labels corresponding to the object and background segmentations. For the sake of simplicity, we assume that $\mathcal{S}'_n$ is the set of shapes $\mathcal{S}_n$ after they have been aligned to a reference coordinate system.

Let $B'_i$ and $\mathcal{DT}(B'_i)$ denote the shape in atlas-aligned coordinates and its signed Euclidean distance transform [13] respectively. The signed distance transform of an average shape, $B_{av}$, can be obtained by computing $\mathcal{DT}(B_{av}) = \frac{1}{n}\sum_{i=1}^{n}\mathcal{DT}(B'_i)$. The average shape can be retrieved by thresholding the distance transform map to its zero-level set. We coin this averaging procedure *shape-based blending*.

As was mentioned earlier, prior to shape-based blending all shapes have to be aligned into an atlas-aligned coordinate system. As the atlas is still to be constructed, the initial coordinate system can be chosen arbitrarily to coincide with that of any of the shapes in the training set $\mathcal{S}_n$. In order to reduce the bias introduced by the selection of the initial reference shape, an iterative algorithm has been developed. In the first iteration, one shape of the training set is randomly selected to be the atlas. Subsequently, all other shapes in the set are registered to the current atlas using the global registration technique presented in Appendix A, Sec. A.1, and the label-based similarity measures introduced in Sect. A.2 of the same appendix. After registration, all shapes are blended and a new atlas is generated. This new atlas then becomes the current atlas and the

process is iterated until the difference between the current and new atlas falls below a certain threshold.

**Atlas Construction in Multiple-Part Shapes.** Let us assume that a set of $n$ training shapes, $\mathcal{S}_n$, is available and that each shape is represented by a labeled image, $L_i$, in which $l$ objects are represented by distinctive labels.

The atlas construction algorithm as described above applies to bi-valued labeled images for which the distance transform is defined. However, it is possible to generalize the method to multiple-part shapes, which is needed for cardiac modeling. In fact, to extend the method of the previous subsection we only need to specify a method for shape-based blending of multi-valued images. The atlas alignment procedure used in this work readily extends from single-object to multiple-object labeled images. In the following, we discuss our method for shape-based blending in cardiac labeled images.

This heart model can be decomposed into three sub-shapes: the $LV_{bp}$, the $LV_{bp} \bigcup LV_{myo}$ and the $RV_{bp}$. By construction the $LV_{bp} \bigcup LV_{myo}$ always embeds the $LV_{bp}$, and both of them are non-overlapping structures with respect to the $RV_{bp}$. Each one of these sub-shapes can now be represented as a separate bi-valued labeled image. This transforms the problem of shape-based blending of a multi-valued labeled image into $l$ problems of shape-based blending of bi-valued labeled images. After the $l$ average sub-shapes have been generated, all of them are combined into a new labeled image by taking the initial arrangement and labeling into account.

**Landmark Extraction.** After an atlas has been constructed and mapped into the atlas space, it needs to be landmarked. In this paper we shall consider surface landmarks only. For cardiac modeling, landmarks for the endocardial and epicardial wall of the left ventricle, and for the endocardial wall of the right ventricle can be extracted. In order to landmark the atlas automatically, the *marching cubes* [14] algorithm is applied. By using this algorithm, a dense and approximately even distribution of landmarks is obtained.

**Landmark Propagation.** Once the atlas is constructed, mapped to atlas space, and landmarked, its landmarks can be propagated to the individual shapes. This is carried out by warping each sample labeled volume into the atlas with a transformation, $\mathbf{T} = \mathbf{T}_g + \mathbf{T}_l$, that is composed of a quasi-affine ($\mathbf{T}_g$) and a non-rigid ($\mathbf{T}_l$) transformation. The transformation $\mathbf{T}_g$ accounts for global (pose and size) differences between the atlas and each sample volume while the transformation $\mathbf{T}_l$ accounts for local shape differences. The recovering of $\mathbf{T}$ is carried out using the algorithms described in Appendix A A.

Once the full transformation $\mathbf{T}$ has been found, the landmarks of the atlas can be propagated to the natural coordinate system by applying the inverse of the non-rigid transformation ($\mathbf{T}_l^{-1}$). This process is repeated for each sample shape. As a result, a set of landmarks is obtained that describes shape variations

with respect to the atlas. Since these landmarks are now in natural coordinates, pose and size variations are explicitly eliminated from further analysis. These transformed landmarks are subsequently used as the input for PCA.

## 4 Results

**Data Sets.** Fourteen adult subjects, free of clinical cardiovascular disease, were scanned on a 1.5 Tesla MR scanner (Phillip's ACS-NT, PowerTrak 6000 Gradient System, Philips Medical Systems, Best, The Netherlands) using an ECG-triggered Echo Planar Imaging (FFE-EPI) sequence. From the acquired temporal sequence of each volunteer, the end diastolic frame was manually segmented. Subsequently, all segmentations were resampled to isotropic voxels with size equal to the in-plane resolution (1.2 mm) using shape-based interpolation [12].

**Atlas Construction.** Figure 2 shows the result of the atlas building process described in previously. The shape-based blending procedure captures the global shape of the ventricles without an apparent bias in the wall thickness at any particular sector.

The convergence of the iterative atlas construction and the effect of different initial shapes in the generation of the atlas have also been studied. Figure 3 plots the $\kappa$ statistic between two successive iterations of the algorithm of Sect. 3. The same curves were generated for the 14 atlantes obtained by using each of the 14 subjects as initial shapes. For each atlas, and both registration measures used in the atlas building procedure, we show the evolution of both metrics as a function of the iteration number. After two iterations the agreement is excellent ($\kappa > 0.94$) and the label consistency very high (LC $> 0.99$).

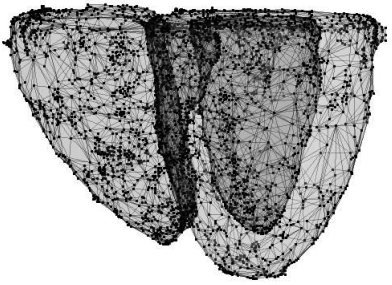

**Fig. 2.** Atlas construction and landmarking. Surface rendering of the atlas with the wire frame joining the extracted landmarks. The landmarks have been extracted using marching cubes with subsequent mesh decimation (95% decimation factor)

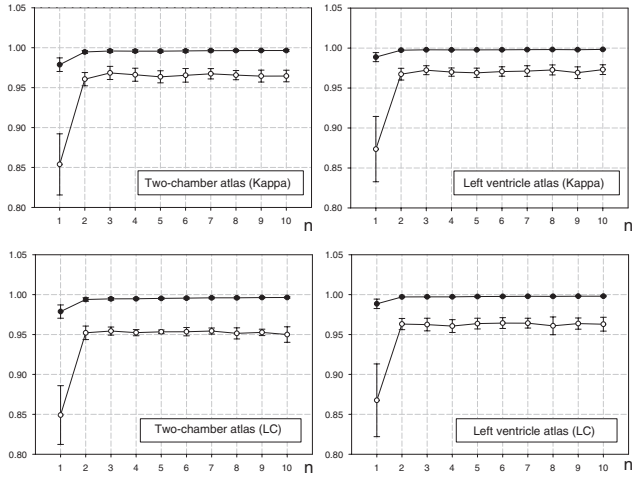


**Fig. 3.** Convergence of the atlas construction algorithm. The $\kappa$ statistic and the *label consistency* similarity measures between two consecutive atlases as a function of the iteration number $n$. In the in-set of each plot the similarity measure is indicated. The graph denoted with (•) corresponds to the evolution of the *label consistency* measure while the one with (∘) corresponds to the evolution of the $\kappa$ statistic. Each curve is the average of the convergence curve resulting from initializing the atlas building procedure with one of the 14 shapes

### 4.1 Statistical Shape Models

To construct a statistical model from the cardiac atlas, landmarks were extracted automatically from the atlas using marching cubes and subsequent mesh decimation (95% decimation ratio). This procedure yielded 1352 (Kappa) and 1304 (LC) landmarks for the left ventricular epicardial surface, 679 (Kappa) and 631 (LC) landmarks for the endocardial surface, and 1841 (Kappa) and 1693 (LC) landmarks for the right ventricular endocardial surface.

After automatic atlas landmarking, a Principal Component Analysis (PCA) was performed on the set of propagated landmarks to the 14 shapes. Figure 4 show the first three modes of variation of a combined left and right ventricle model built using the kappa statistic.

In order to quantitatively assess the performance of the constructed models we have analyzed the reconstruction error by performing several leave-one-out experiments. The landmarks of all but one data set were used to build a statistical model. This model was subsequently used to reconstruct the set of landmarks not included in the PCA. The same experiment was repeated by taking out from the PCA, one in turn, each of the sets of landmarks. Finally, the average reconstruction error over the leave-one-out experiments was computed. Figure 5 shows the mean square reconstruction error as a function of the number of modes used in shape reconstruction. Since our training set is relatively small and the

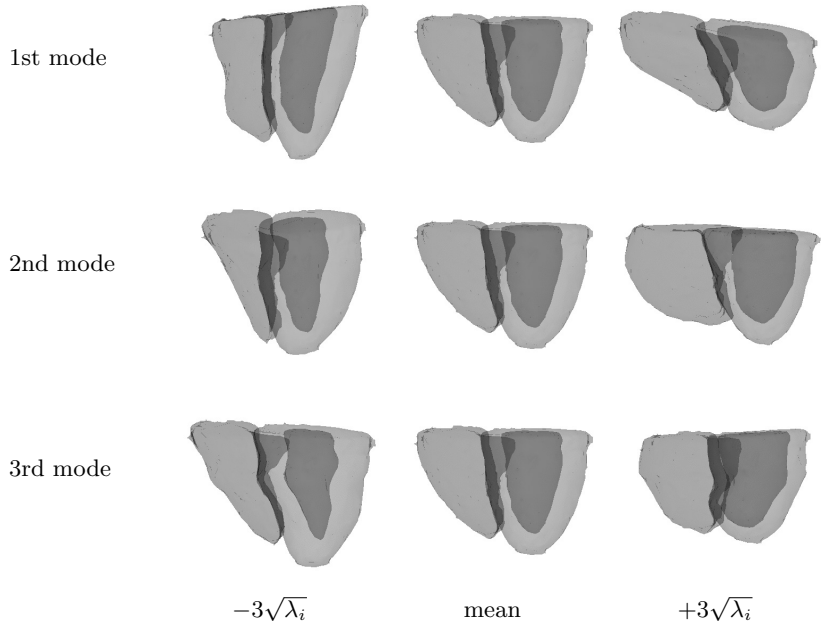


**Fig. 4.** Shape instances generated using the 3-D two-chamber model and the kappa statistic registration measure from 14 cardiac data sets. The instances are generated by varying a single shape parameter, fixing all others at zero standard deviations from the mean shape

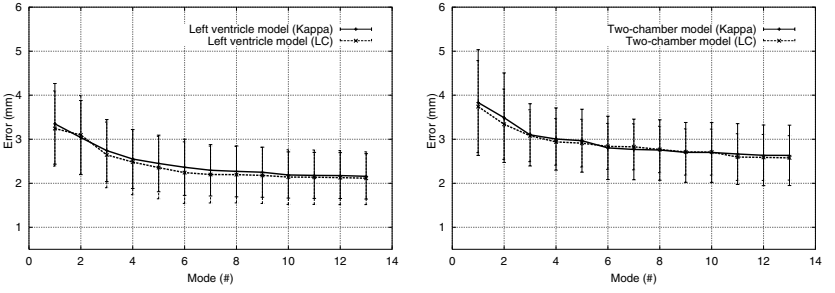


**Fig. 5.** Reconstruction error in the leave-one-out experiments for the left ventricle and two-chamber models and different registration measures used in model building

shape variability is quite large, these experiments do not reveal much information on the generalization ability of the models. However, they provide a first estimate that could be refined by enlarging the database of shapes.

## 5 Conclusions

This paper has presented a method for the automatic construction of 3-D statistical shape models. The technique is based on the automatic extraction of a dense mesh of landmarks in an atlas constructed from a set of training shapes. These landmarks are subsequently warped by a non-rigid deformation field to each shape in the training set. The method is able to treat single- and multiple-part shapes.

This work has shown that the combination of our atlas generation method and the multi-resolution FFD non-rigid registration algorithm is able to cope with the large deformations involved in inter-subject matching of cardiac shapes. We had previously experimented with a single-level version of the FFD registration technique. Although with that approach we were able to propagate the landmarks of anatomical structures with moderate shape variability (deep structures of the brain and bone structures) [15], it was unsuccessful in the application presented in this paper. In order to cope with large shape variations, a multi-resolution extension [10] of the free-form registration algorithm proposed by Rueckert *et al.* [9] was applied. In this approach, the non-rigid transformation is recovered by increasing the mesh resolution by subsequent subdivision. Gross shape warping takes place at the coarsest resolution while shape details are captured at the finest resolution.

Our future work will focus on applying our method to model-based cardiac image segmentation and analysis. A strategy has to be devised to adapt the model mesh to segment cardiac MR images. This could be achieved, for instance, by applying a method similar to the two-dimensional deformation procedure of active shape models [1]. For each landmark in the model, a statistical model of the intensity profile (or some other suitable image feature) along the surface normal can be computed. The model mesh could be deformed by moving the nodes along the direction of the normals to the position best matching the intensity with the statistical profile model. This method would provide an image-derived displacement for each node. The displacements applied to update the mesh can be obtained by projecting the suggested displacements onto the sub-space spanned by the main modes of variation. This projection step would naturally incorporate shape constraints in the deformation of the mesh.

In conclusion, a method was presented to construct a shape atlas and to derive a statistical model of three-dimensional shape variability. We have demonstrated that this method is applicable to the construction of a statistical shape model of the cardiac chambers. To the best of our knowledge, this work is the first one which uses three-dimensional statistical shape models to describe the left and right ventricles of the heart. Our future work will concentrate on the application of this model to cardiac image segmentation and analysis.

**Acknowledgments.** The work of AFF is sponsored by the Spanish Ministry of Science and Technology (FEDER-MCYT TIC2002-04495-C02) and a Ramon y Cajal Research Fellowship. DR is supported by EPSRC grant no GR/N24919.

# A Appendix: Multi-resolution Non-rigid Registration

The matching algorithm summarized here is a multi-resolution free-form non-rigid registration algorithm which was formulated by Rueckert *et al.* [9] and further developed by Schnabel *et al.* [10]. This algorithm manipulates a shape by embedding it into a subsequently refined volumetric mesh which defines a continuous deformation field through a set of B-spline basis functions. For each location in the reference shape, the corresponding locations in the individual shapes are found to obtain an optimal match. The corresponding optimal deformation field is obtained by maximizing a voxel similarity measure on the basis of the corresponding labels. This maximization is carried out using a standard gradient ascent algorithm. The registration method and two novel similarity measures for labeled images are briefly summarized in the following paragraphs.

## A.1 Transformation Model

Let $\mathbf{T} : (x, y, z) \mapsto (x', y', z')$ be a transformation that maps any point $(x, y, z)$ in the source image into the corresponding target image coordinates $(x', y', z')$.

In order to accommodate for non-rigid deformations, $\mathbf{T}$ will consist of a global transformation $\mathbf{T}_g$ and a non-rigid transformation obtained in a coarse-to-fine manner, $\mathbf{T}_l^H$ where $H$ is the number of mesh subdivisions that take place in the multi-resolution strategy,

$$\mathbf{T}(x, y, z) = \mathbf{T}_g(x, y, z) + \mathbf{T}_l^H(x, y, z) \tag{2}$$

**Global Transformation.** The global transformation describes the pose and size of the transformed shape with respect to the atlas. This can be accomplished with a global transformation in the form of a quasi-affine model. For a quasi-affine transformation, only nine parameters are independent (rigid transformation, $\{t_x, t_y, t_z, r_x, r_y, r_z\}$, plus anisotropic scaling, $\{s_x, s_y, s_z\}$ ).

**Local Transformation.** In order to accommodate for detailed shape differences, the global deformation field has to be supplemented with a local deformation model. The local deformation field is represented by a free-form deformation (FFD) based on B-splines. We use a multi-level FFD. At each level of mesh resolution, $h$, the FFD is represented by a tensor-product B-spline using a grid of control points with uniform spacing $\delta_h = \delta_o/2^h$, where $\delta_o$ is the initial mesh spacing. The control points act as parameters of the B-spline and the degree of non-rigid deformation which can be modeled depends on the resolution level $h$. In our experiments with cardiac data sets, we have used a deformation field with three mesh subdivisions ($H = 3$) and an initial spacing $\delta_o = 20$ mm.

## A.2 Similarity Measure for Labeled Image Registration

Since the correspondences of structures across both images are encoded explicitly in the labeling, we are only interested in maximizing the overlap of structures

denoted by the same label in both images. Therefore we have used two registration measures that favor the mapping of identical labels. We have coined these measures *label consistency* and $\kappa$ *statistic*.

**Label Consistency.** Assume that $P_{AB}(i,j)$ is the joint probability of labels $i$ and $j$ in the source (A) and target (B) shapes, respectively. This can be estimated as the number of voxels with label $i$ in image $A$ and label $j$ in image $B$ divided by the total number of voxels in the overlap region of both images. The label consistency measure is then defined as

$$\mathcal{C}_{LC}(A,B) = \sum_{i=1}^{l} P_{AB}(i,i) \tag{3}$$

**The $\kappa$ Statistic.** The measure is inspired in a statistic used frequently in biomedical research to assess the agreement between two raters measuring the same quantity or performing a classification task [11]. For a given voxel, each image can be considered as an observer who assigns a class label to it. Therefore, comparing labeled images is equivalent to comparing the agreement between two observers. This statistic is defined as follows:

$$\kappa = \frac{p_a - p_c}{1 - p_c} \tag{4}$$

$$p_c = \sum_{i=1}^{l} P_A(i) P_B(i) \tag{5}$$

$$p_a = \sum_{i=1}^{l} P_{AB}(i,i) \tag{6}$$

where $P_{AB}(i,j)$, $P_A(i)$, and $P_B(i)$ are the joint probability density and marginal probability densities for the labels in the images $A$ and $B$. The $\kappa$ statistic is a measure of agreement between two classifications, $p_a$, that is corrected for chance agreement $p_c$.

## References

1. T. F. Cootes, C. J. Taylor, D. H. Cooper, and J. Graham, "Active Shape Models - their training and application," *Comp Vis Image Underst*, vol. 61, no. 1, pp. 38–59, 1995.
2. A. D. Brett and C. J. Taylor, "A method of automated landmark generation for automated 3D PDM construction," *Imag Vis Comp*, vol. 18, no. 9, pp. 739–48, 2000.
3. A. D. Brett and C. J. Taylor, "Automated construction of 3D shape models using harmonic maps," in *Medical Image Understanding and Analysis*, S. Arridge and A. Todd-Pokropek, Eds., London, July 2000, pp. 175–78.

4. M. Fleute and S. Lavallée, "Building a complete surface model from sparse data using statistical shape models: applications to computer assisted knee surgery," Boston, USA, Sept. 1998, vol. 1496 of *Lect Notes Comp Science*, pp. 879–87, Springer Verlag.
5. M. Fleute and S. Lavallée, "Incorporating a statistically based shape model into a system for computer-assisted anterior cruciate ligament surgery," *Med Image Anal*, vol. 3, no. 3, pp. 209–22, 1999.
6. G. Subsol, J-P. Thirion, and N. Ayache, "A scheme for automatically building three-dimensional morphometric anatomical atlases: application to a skull atlas," *Med Image Anal*, vol. 2, no. 1, pp. 37–60, 1998.
7. P.J. Besl and N.D. McKay, "A method for registration of 3D shapes," *IEEE Trans Pattern Anal Machine Intell*, vol. 14, no. 2, pp. 239–55, Feb. 1992.
8. R. H. Davies, C. J. Twining, T. F. Cootes, J. C. Waterton, and C. J. Taylor, "A minumum description length approach to statistical shape modelling," *IEEE Trans Med Imaging*, vol. 21, no. 5, May 2002, in press.
9. D. Rueckert, L. I. Sonoda, C. Hayes, D. L. G. Hill, M. O. Leach, and D. J. Hawkes, "Non-rigid registration using free-form deformations: Application to breast MR images," *IEEE Trans Med Imaging*, vol. 18, no. 8, pp. 712–721, Aug. 1999.
10. J. A. Schnabel, D. Rueckert, M. Quist, J. M. Blackall, A. D. Castellano-Smith, T. Hartkens, G. P. Penney, W. A. Hall, H. Liu, C. L. Truwitt, F. A. Gerritsen, D.L.G. Hill, and D.J. Hawkes, "A generic framework for non-rigid registration based on non-uniform multi-level free-form deformations," Utrecht, NL, Oct. 2001, vol. 2208 of *Lect Notes Comp Science*, pp. 573–81, Springer Verlag.
11. D.G. Altman, *Practical Statistics for Medical Research*, Chapman & Hall, 1991.
12. G.T. Herman, J. Zheng, and C.A. Bucholtz, "Shape-based interpolation," *IEEE Comp Graph & Appl*, pp. 69–79, May 1992.
13. P.E. Danielsson, "Euclidean distance mapping," *Comp Graph Imag Proces*, vol. 14, pp. 227–248, 1980.
14. W.E. Lorensen and H.E. Cline, "Marching cubes: a high resolution 3D surface reconstruction algorithm," *Computer Graphics: SIGGRAPH'87 Conference Proceeding*, vol. 21, pp. 163–9, July 1987.
15. A.F. Frangi, D. Rueckert, J.A. Schnabel, and W.J. Niessen, "Automatic 3D ASM construction via atlas-based landmarking and volumetric elastic registration," in *Inf Proces Med Imag*, M. F. Insana and R. M. Leahy, Eds., 2001, vol. 2082, pp. 78–91.

# Visualising Cardiac Anatomy Using Constructive Volume Geometry

Min Chen[1], Richard H. Clayton[2], Arun V. Holden[2], and John V. Tucker[1]

[1] Department of Computer Science, University of Wales Swansea, SA2 8PP, UK
[2] School of Biomedical Sciences, University of Leeds, LS2 9JT, UK

**Abstract.** In this paper, we describe the application of a new volume graphics technique, namely constructive volume geometry, to the visualisation of cardiac anatomy and electrophysiology. We exploit the fact that field-based data types underlie the computational process in both the virtual engineering of the heart and volume graphics. We demonstrate the capability of constructive volume geometry in generating combinational visualisations that depict meaningful information extracted from different cardiac data sets. We also show the capability of volume graphics in displaying the interiors of anatomical structures through effective use of opacity and combinational operators.

## 1 Introduction

One component in the complete virtual engineering of the entire beating heart is the development of advanced visualisation tools for the display of electrochemical wave phenomena – both scalar (potential, intra- and extracellular ionic concentrations) and vector (current densities) fields – within a moving, anisotropic geometry that has mechanical vector variables (stresses, strains), and that encloses a changing volume of moving blood. Local perfusion, metabolic variables and coronary system flow also need to be added. The data to be visualised comes from both simulations and clinical or experimental recordings, with different spatial and temporal resolutions.

The passive geometry of the ventricle itself raises problems of visualising the surfaces and interiors of a complicated geometric object that can be segmented into different tissues (contractile muscle, conducting tissue, connective tissue) and organised into interconnected sheets. The fibre orientation of muscle cells and the spatial distribution of the expression of different proteins through the tissue may need to be visualised.

The propagation of waves of electrochemical activity through such a static geometry requires the visualisation of the scalar field of transmembrane potential through the tissue, and perhaps its decomposition into intra- and extracellular potentials, and derived quantities, such as iso-surfaces corresponding to wave fronts and wave backs. The pattern of activity can be further decomposed into the spatio-temporal distribution of action potential duration, and for re-entrant activity, the phase, and the phase singularity or filament around which it is propagating, and the local twist or tension of the filament.

I. Magnin et al. (Eds.): FIMH 2003, LNCS 2674, pp. 30–38, 2003.

The mechanical activity (motions, stresses and strains) derived from clinical visualisation methods or computed from an electro-mechanical model are of vector fields within a moving geometry. The electrical and electro-mechanical vector fields may need to be used to compute observable time series, or computationally steered by observed times series.

The visualisation of haemodynamic variables – pressures and flows within the cardiac chambers, aorta and coronary circulation – may need to be superimposed on, or coupled to computational generators of, these vector fields.

This series of problems can be considered both in terms of a methodological challenge – how to construct combinational visual representations that extract meaningful information from different field data sets as well as in terms of a technological challenge – how to deliver such visualisations to laboratory on clinical standard workstations.

Volume graphics [6] is concerned with graphics scenes defined in field-based data types, where a model is specified by a mass of points instead of a set of surfaces. The underlying mathematical definition of such a model is a set of scalar fields, that define the geometrical and physical properties of every point in three-dimensional space. As true 3D representations, field-based data types possess more descriptive power than surface data types, and are morphologically closer to data types used in many scientific fields, such as the modelling and simulation of the entire beating heart. One important development in volume graphics is the formulation of the theory and practice of *Constructive Volume Geometry (CVG)* [5], which can offer an effective tool for visualising complex data sets in a combinational manner. This paper presents an interdisciplinary effort for applying the CVG technique to the visualisation of cardiac anatomy and electrophysiology.

## 2 Constructive Volume Geometry

Constructive solid geometry (CSG) [11] is one of the most important modelling methods in computer graphics and computer aided design (CAD). It allows complicated objects to be built as various ordered "union", "intersection" and "difference" of simpler objects, which may be bounded primitives or half-spaces. It is supported by Boolean algebra and a set of well-understood regularised set operations.

Constructive volume geometry (CVG) [5] is a major generalisation of CSG. Unlike CSG, CVG does not limit itself to geometrical operations only, and it can be employed to manipulate physical properties that are associated with objects. Its combinational operations, mostly defined in the real domain, can be used to model complex internal structures of objects and amorphous phenomena in a constructive manner.

The discrete and bounded nature of raw volumetric field data, such as a digitised heart or a simulated current density field, is the main obstacle to a consistent specification of combinational operations. In order to equip volume data types with such operations, CVG introduces a set of concepts that map

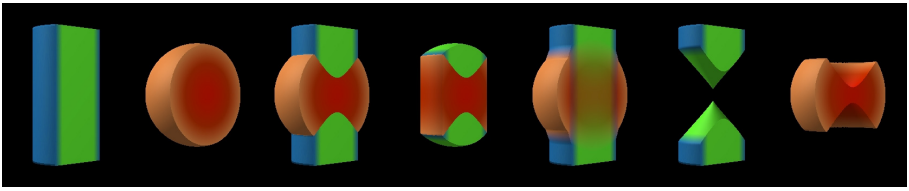

**Fig. 1.** The seven images illustrate the effect of combinational operations to the interior of the objects. From left to right, they are: cylinder, sphere, their union, intersection, blending and difference of two different orders.

field data sets to more inter-operable *spatial objects*, which are defined at every point in 3D Euclidean space $\mathbb{E}^3$. Each spatial object is a tuple of scalar fields, including an opacity field and other attribute fields such as colour, rendering parameters, etc. For example, a spatial object has the form

$$\mathbf{o} = (O, A_1, \ldots, A_n)$$

where $O$ is the opacity field and $A_1, \ldots, A_n$ are other attribute fields.

The opacity field "implicitly" defines the "visible geometry" of the object. Any point that is not entirely transparent is potentially visible to a rendering algorithm. Considering different applications may define spatial objects with different attributes. CVG utilises an algebraic concept called signature [5] to describe the algebraic structure of a particular graphics model in a consistent manner. Although conceptually it is not necessary because of the dominant role of the opacity field, CVG also allows the specification of additional geometry fields to suit the needs of some applications. In visualisation, such fields typically represent some physical properties obtained from digitisation, measurement or computer simulation.

In CVG, combinational operators are defined upon unbounded spatial objects, and are constructed from simple arithmetic operations on scalars through a series of operational decomposition. The operations on scalars are normally defined in the real domain. Table 1 gives the definition of some basic CVG operators, including union $\boxed{\cup}$, intersection $\boxed{\cap}$, difference $\boxed{-}$, and blending $\boxed{\oplus}$, which are illustrated in Fig. 1. With the flexibility and accuracy of the real domain, complex operators, such as those for data filtering and volume deformation, can easily be specified.

In Fig. 1, two simple spatial objects, sphere and cylinder, are used to illustrate the constructive and combinational operations of CVG. CVG operations can be applied to any spatial object that is composed of a set of scalar fields. Such scalar fields can be mathematically defined (e.g., Fig. 1) or specified using discrete data sets. Figure 2 shows an example of combining spatial objects built from different types of scalar fields. The heart object is built from a 3D volume data set (a discrete specification), and the cylindrical object is built upon a mathematical scalar function (a continuous specification).

**Table 1.** Basic CVG operators on spatial objects and their decomposition.

| *Operation on Spatial Objects* – $\mathbf{o}_a = (O_a, A_{a,1}, \ldots, A_{a,n})$, $\mathbf{o}_b = (O_b, A_{b,1}, \ldots, A_{b,n})$ |
|---|
| $\boxed{\cup}(\mathbf{o}_a, \mathbf{o}_b) = (\mathbf{max}(O_a, O_b), \mathbf{select}(O_a, A_{a,1}O_b, A_{b,1}), \ldots, \mathbf{select}(O_a, A_{a,n}O_b, A_{b,n}))$ |
| $\boxed{\cap}(\mathbf{o}_a, \mathbf{o}_b) = (\mathbf{min}(O_a, O_b), \mathbf{select}(O_a, A_{a,1}O_b, A_{b,1}), \ldots, \mathbf{select}(O_a, A_{a,n}O_b, A_{b,n}))$ |
| $\boxed{-}(\mathbf{o}_a, \mathbf{o}_b) = (\mathbf{sub}(O_a, O_b), A_{a,1}, \ldots, A_{a,n})$ |
| $\boxed{\oplus}(\mathbf{o}_a, \mathbf{o}_b) = (\mathbf{add}(O_a, O_b), \mathbf{mix}(O_a, A_{a,1}O_b, A_{b,1}), \ldots \mathbf{mix}(O_a, A_{a,n}O_b, A_{b,n}))$ |
| *Operation on Fields* – $S_a, S_b, T_a, T_b : \mathbb{E}^3 \rightarrow [0,1]$ |
| $\forall p \in \mathbb{E}^3, \mathbf{max}(S_a, S_b)(p) = max(S_a(p), S_b(p))$ |
| $\forall p \in \mathbb{E}^3, \mathbf{min}(S_a, S_b)(p) = min(S_a(p), S_b(p))$ |
| $\forall p \in \mathbb{E}^3, \mathbf{sub}(S_a, S_b)(p) = sub(S_a(p), S_b(p))$ |
| $\forall p \in \mathbb{E}^3, \mathbf{add}(S_a, S_b)(p) = add(S_a(p), S_b(p))$ |
| $\forall p \in \mathbb{E}^3, \mathbf{select}(S_a, T_a, S_b, T_b)(p) = select(S_a(p), T_a(p), S_b(p), T_b(p))$ |
| $\forall p \in \mathbb{E}^3, \mathbf{mix}(S_a, T_a, S_b, T_b)(p) = mix(S_a(p), T_a(p), S_b(p), T_b(p))$ |
| *Operation on Scalars* – $s_a, s_b, t_a, t_b \in [0,1]$ |
| $max(s_a, s_b) = s_a$ if $s_a \geq s_b$, or $s_b$ if $s_a < s_b$ |
| $min(s_a, s_b) = s_a$ if $s_a \leq s_b$, or $s_b$ if $s_a > s_b$ |
| $sub(s_a, s_b) = max(0, s_a - s_b)$ |
| $add(s_a, s_b) = min(1, s_a + s_b)$ |
| $select(s_a, t_a, s_b, t_b) = t_a$ if $s_a \geq s_b$, or $t_b$ if $s_a < s_b$ |
| $mix(s_a, t_a, s_b, t_b) = (t_a s_a + t_b s_b)/(s_a + s_b)$ if $s_a + s_b \neq 0$, or $(t_a + t_b)/2$ if $s_a = s_b = 0$ |

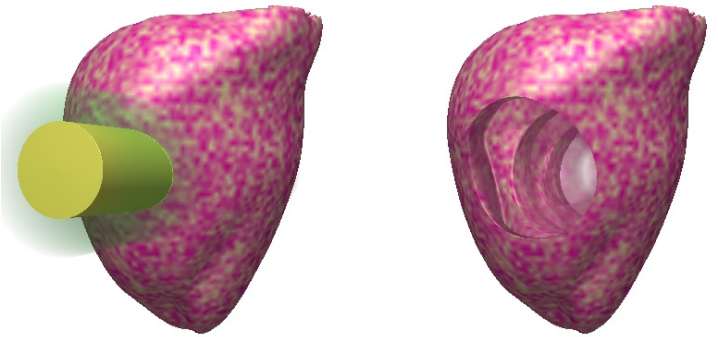

**Fig. 2.** The application of CVG operations (i.e., a union operation on the left and a difference operation on the right) to spatial objects built from different types of scalar fields.

In comparison with CSG, CVG offers a comprehensive algebraic framework for a variety of field-based models. In fact, it has been shown that the CSG model based on union $\cup$, intersection $\cap$ and difference $-$ is embedded in a simple CVG model, that is, the Boolean opacity only model based on volume operations $\boxed{\cup}$, $\boxed{\cap}$ and $\boxed{-}$ [5]. CVG operates on the interior as well as the exterior of objects, and therefore preserves the main geometrical properties in field data sets such as volume density and multiple iso-surfaces. Physical properties such as colours

are defined and manipulated in the same way as geometry. It accommodates objects that are defined mathematically by scalar fields as well as those built from digitised field data sets. Images can be naturally integrated into a scene as a degenerated field object. Scenes specified in CVG can be rendered directly by a sophisticated volume rendering engine [5], or may be voxelised into volume buffers as the input to general-purpose volume rendering systems.

## 3 Combinational Visualisation

Virtual tissue engineering – the computational electrophysiology and electromechanics of cardiac tissue – requires models of cardiac geometry and fibre orientation: propagation of the rising phase of the action potential is anisotropic, and is up to five times faster along the fibre axis, and contraction is in the direction of the fibre axis. Two public domain models of ventricular geometry and anisotropy that were obtained by quantitative histology are the Auckland canine ventricle [9] and the UCSD (University of California, San Diego) rabbit ventricle [13]. Here we use the UCSD rabbit data set from http://cmrg.ucsd.edu, where the fibre orientation at each node of a 1mm, 3D Cartesian lattice for points within the ventricle is specified. This provides the ventricular geometry, from which the endocardial and epicardial surfaces can be extracted, and within which computational simulation of excitation and contraction can be performed, and the sampled fibre orientation.

The fibre orientation changes through about 120° passing radially through the ventricular wall, and changes smoothly within the sheets forming the ventricular wall. Rough manual dissection of the heart after boiling in 1% acetic acid [12] shows cardiac fibres in the left ventricular wall in bundles that spiral around and through the ventricle: these fall on geometric geodesics, in which epicardial fibre bundles, in an idealised geometry, are continuous with endocardial fibre bundles. This conjecture has been supported by the analysis of fibre orientation in the human foetal left ventricle [10]. Here we use CVG operations to digitally dissect and display the fibre orientation of the UCSD rabbit ventricle, by choosing a point at random, and following the same fibre orientation vector within a tolerance.

Given a vector field $F^v(p)$ and the seed position $s$ of a particle in $\mathbb{E}^3$ we can trace a discrete path by following the seed through $F^v(p)$ as:

$$p_0 = s; \quad p_i = p_{i-1} + F^v(p_{i-1}) \cdot \delta$$

where $\delta$ is a user-definable parameter specifying the interval distance of each particle movement. The path is normally terminated when the particle is surrounded locally by a small domain of zero vectors. In our application, it is also necessary to obtain a backward trace from each seed position by following the opposite direction of the vector field $F^v(p)$, as we have no prior knowledge about the end points of each path. Each particle movement is represented as a distance field of a line segment, and the union of all sections of a path results in an approximation of a field representation of a fibre bundle. The advantages of using a

field rather than a tubular surface include the flexibility of altering the thickness of the tubes during rendering and smoother joining of tubular sections.

Figure 3 shows three sets of fibre bundles, each generated using 40 seeds, and displayed in purple, blue and yellow respectively. A further application of a CVG union operation to three field data sets give us a combinational visualisation of all 120 fibre bundles, from which the shape of a heart is recognisable. To visualise traced fibre bundles against the passive geometry of the dead heart, one may construct a combinational visualisation as shown in Fig. 4, where the corresponding CVG tree is also shown to illustrate the modelling process. One of the strength of volume graphics is its ability to model and display internal structure of a volume object in a more accurate manner. The set of images in Fig. 5 demonstrates the use of this feature. In the figure, the trace of a single fibre bundle is shown as a set of spheres, which are display with the corresponding heart anatomy. The heart is modelled as a translucent object in order for viewers to visualise the relative position of the fibre bundle in the heart.

An important feature of CVG is that the actual combination of different data sets does not take place until the composite objects are being rendered. In fact, the representations of spatial objects are never combined. It is the sampling process in volume rendering that evaluates a CVG tree that defines the combinations of spatial objects. Without using CVG, one would have great difficulties to create such visualisations as shown in Figs. 3, 4, and 5, without physically combining all the data representations together. This would lead to loss of data quality or excessive space consumption.

The digital dissection of the smooth vector field of fibre orientation into bundles with almost the same fibre orientation shows that fibre bundles that wind around and through the heart do follow the course similar to that expected for the geodesic conjecture, and allow quantitative questions to be posed, e.g., how many bundles do begin on the epicardial and end on the endocardial surface. Algorithmic digital dissection of a smoothly varying tissue data set is distinct from segmentation of the data set into different tissue types, and this method could be applied to fibre orientation data sets obtained from diffusion tensor imaging. For the purpose of computational simulation of electrical activity, the fibre orientation field provides the diffusion coefficient tensor for voltage, or the conductivity tensor. In three-dimensional media re-entrant activity propagates as a scroll wave around curved, rod-like filaments that may end on the medium surfaces, or be closed. The motion of these filaments even in homogenous media is complicated, and is influenced by filament twist and local curvature. In anisotropic, homogenous media filaments align themselves, asymptotically with time, along a geodesic whose metric is the inverse conductivity tensor of the medium, i.e., the fibre orientation tensor [14]. Filament geometry can be extracted from computed data [7] or tomographically visualised using the methods described in [1], and so deviations between filament alignment along geodesics, due to electrophysiological heterogenities, could be isolated and quantified by measuring the deviation between filaments and fibre bundles.

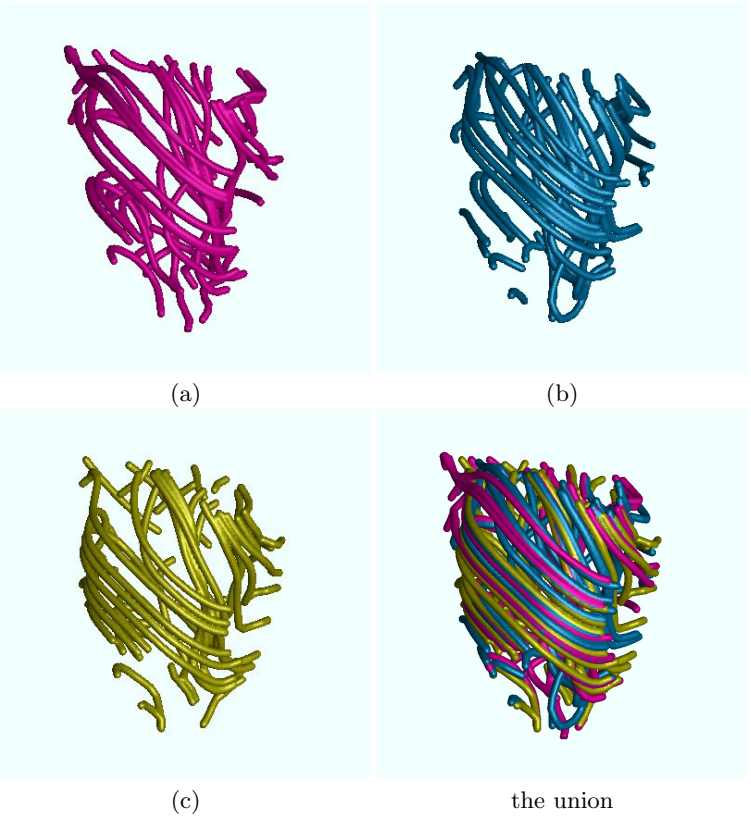


**Fig. 3.** The union of three field data sets representing the individual sets of fibre bundles shown in (a), (b) and (c) respectively.

## 4 Conclusions

We have described the core of a volume graphics technique, namely *Constructive Volume Geometry (CVG)*, and its application to combinational visualisation of field-based data obtained from both digitisation and computational simulation. CVG provides a powerful, general purpose tool for constructing and decomposing data of continuous field representations of function and structure, and so for synthesising images based on discrete field data sets obtained from different imaging modalities, such as echocardiolography, magnetic resonance imaging and histology, and computational simulation of electrical and mechanical activities. It thus provides a powerful framework for the integrative functional visualisation of cardiac structure and activity, and the fusion of simulation and non-invasive visualisation data streams. It has been applied to visualising electrophysiology within anatomically and histologically ventricular tissue models in [2].

One very recent development in volume graphics is to equip CVG with the capability of deformation, through the use of spatial transfer functions [3,4]. This

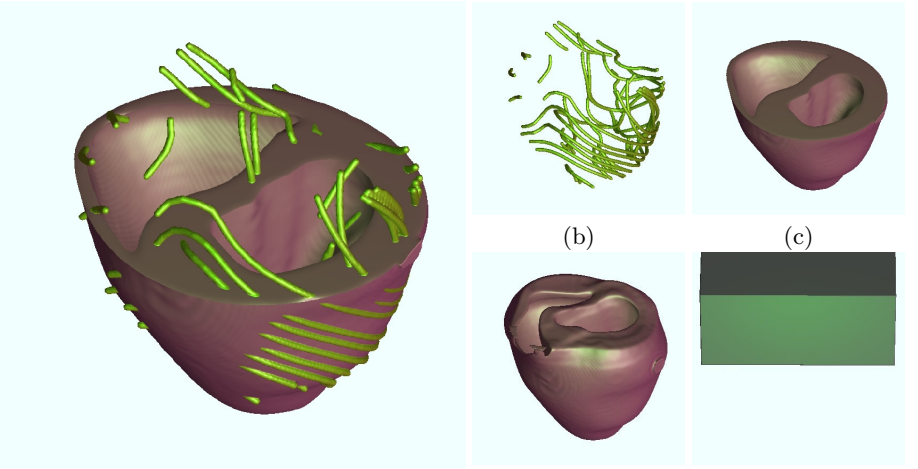


**Fig. 4.** The specification of a combinational visualisation using a CVG tree which is defined as (a) = (b) union (c) = (b) union {(d) diff (e)}.

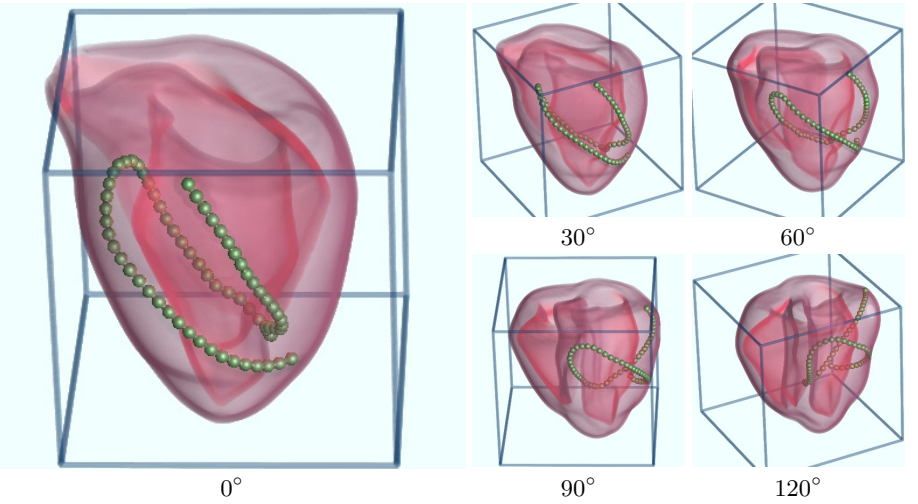


**Fig. 5.** Five rotational views, about the z-axis, depicting the position a traced fibre bundle relative to the corresponding heart anatomy.

technique has also been applied to cardiac visualisation for digital dissection and manipulation of anatomical structures [2].

## References


1. Baxter, W.T., Moronov, S.F., Zaitsev, A.V., Jalife, J., Pertsov, A.M.: Visualising excitation waves inside cardiac muscle using transillumination. Biophysical J. **80** (2001) 516-530
2. Chen, M., Clayton, R.H., Holden, A.V., Tucker, J.V.: Constructive volume geometry applied to visualisation of cardiac anatomy and electrophysiology. Int. J. Bifurcation and Chaos **12** (2003) in press
3. Chen, M., Winter, A.S., Rodgman, D., Treavett, S.M.F.: Enriching volume modelling with scalar fields. Data Visualization: The State of the Art, Post, F., Nielson, G., Bonneau, G.-P. (eds). Kluwer Academic Publishers (2003) 345–362
4. Chen, M., Silver, D., Winter, A.S., Singh, V., Cornea, N.: Spatial transfer functions – a unified approach to specifying deformation in volume modeling and animation. to appear in Proc. Volume Graphics 2003, Tokyo, Japan (2003)
5. Chen, M., Tucker, J.V.: Constructive volume geometry. Computer Graphics Forum **19:4** (2000) 281–293
6. Chen, M.: Volume graphics. Encyclopedia of Microcomputers, Kent, A., Williams J.G. (eds). Marcel Dekker, New York (2000) 363–387
7. Clayton, R.H., Holden, A.V.: Dynamics and interaction of filaments in a computational model of re-entrant ventricular fibrillation. Physics in Medicine and Biology **47** (2002) 1777–1792
8. Kaufman, A., Cohen, D., Bagel, R.: Volume graphics. IEEE Computer **26:7** (1993) 51–64
9. Leg rice, I., Hunter, P., Young, A., Small, B.: The architecture of the heart: a data-based model. Phil. Krans. Roy. Soc. Blond. A **359** (2001) 1217–1232
10. Mourad, A., Baird, L., Caillerie, D., Jouk, P.-S., Raoult, A., Szafran, N., Usson, Y.: Geometrical modelling of the fibre organisation in the human left ventricle. Functional Imaging and Modelling of the Heart. (eds) Katila, T., Magnin, I.E., Clarysse, P., Montagnat. J. Nenonen, J. LNCS 2230 Springer Verlag, Berlin. (2002) 32–38
11. Requicha, A.A.G.: Representations for rigid solids: theory, methods and systems. ACM Computing Surveys **12:4** (1980) 437–464
12. Torenrent-Guasp, F.: The Cardiac Muscle Madrid: Fundacion Juan. March (1973)
13. Vetter, J.J., McCulloch, A.D.: Three-dimensional analysis for electrophysiological models of myocardium. Progress in Biophysics and Molecular Biology **69** (1998) 157–183
14. Wellner, M., Berenfeld, O., Jalife, J., Pertsov, A.M.: Minimal principal for rotor filaments. Proc. Nat. Acad. Sci. USA **99** (2002) 8015–8018

# Evaluation of a 3D Segmentation Software for the Coronary Characterization in Multi-slice Computed Tomography

A. Larralde[1], C. Boldak[2,3], M. Garreau[2], C. Toumoulin[2], D. Boulmier[4], and Y. Rolland[1]

[1] DRIMS, Hopital Sud, CHU Rennes, France
[2] LTSI, bat 22, Campus de Beaulieu, Université de Rennes 1, 35O42, Rennes cedex, France
[3] Computer Science Department, Institute of Bialystok, Bialystok, Poland
[4] Dépt. de Cardiologie, Service d'hémodynamique et de cardiologie interventionnelle, CHU Rennes, France
mireille.garreau@univ-rennes1.fr

**Abstract.** A new generation of sub-second multi-slices computed tomography (MSCT) scanners, which allow a complete coronary coverage, is becoming widely available. Nevertheless, they need to be associated with 3D processing tools to quantify the coronary diseases. This study proposes to evaluate a new 3D moment-based method for the extraction of the coronary network and the calcification localization in MSCT. We called on two medical experts respectively in coronarography and radiology to carry out this evaluation. It was based on a comparison between extracted vessels and original scan data with objective and subjective criteria. This preliminary study has been performed on a set of six data sets, which included pathological patterns such as dense and scattered calcifications. These results confirm the good performances of the method with high scores of sensitivity and constitute a first step toward the detection of coronary networks in MSCT data.

**Keywords:** 3D angiography, MSCT, pathology extraction, 3D vessel detection, medical evaluation

## 1 Introduction

Providing a noninvasive coronary imaging is today a real challenge which is not easy to achieve due to the difficulties inherent to the observation of cardiac vascular vessels (moving and twisting structures, small diameters, connectivity with cavities and veins of the heart). Conventional X-ray coronary angiography still remains the standard of reference for the assessment of coronary-artery disease. The procedure is invasive and potentially harmful with a risk of serious event evaluated to 2% (arrhythmia, stroke, coronary-artery dissection, ...). Furthermore, the catheterization procedure involves admission to hospital and discomfort for the patient. The feasibility of noninvasive coronary imaging has been explored using different modalities, such as electron beam computed tomography (EBCT) [1] and magnetic resonance imaging (MRI) [2]. The EBCT modality gives a high temporal resolution (100 ms), with a moderate spatial resolution (0.8 x 0.8 mm).

I. Magnin et al. (Eds.): FIMH 2003, LNCS 2674, pp. 39–51, 2003.

The MRA modality is not ionizing but has low resolution and contrast, especially with regard to the visibility of small diameter (i.e. 1 up 2 millimeters). It needs a compromise between spatial and temporal resolution (high resolution with thin slices versus apnea duration) leading to a long time of acquisition. In fact, despite encouraging results, neither of them is yet considered suitable for a clinical routine use. The recent significant advances of multi-slices computed tomography scanners (augmented gantry rotation rate – 0.5s/tr –, higher spatial and temporal resolutions with respective values such as 0.35 x 0.35 x 0.6 $mm^3$ and 105 ms), multi-detectors (from 4 to 16 detectors), retrospectively ECG-gated image reconstruction), give to this modality the means to lead to high quality cardiac and vascular examinations, providing noninvasive coronary angiography [3–4]. The clinical application field of MSCT is large including the studies of the vascular wall and the lumen as well as the analysis of the vascular environment (cardiac cavities, myocardium) from only one exam.

Most of these systems offer interactive tools to facilitate the visual analysis of 3D data set. Slice-by-slice presentation, image sequence display, or three-dimensional rendering (surface or voxel based) is now widely available and marketed. Maximum Intensity Projection (MIP) is a commonly used technique for 3D angiographies and provides a 2D projection of the 3D vessel network along a given direction. But the inherent 2D nature of the resulting image limits the value of such technique: visual occultation of vessels, artificial crossings, masking of low-intensity structures by high-intensity ones are some of the drawbacks of this technique. Simple procedures have been explored to face these difficulties by looking for the optimal viewing direction allowing disambiguating complex vessel patterns. These first steps make easier the visual reading of the image volume to the radiologist but they lead to subjective interpretation and not to quantitative features. Quantification tools still call on manual drawing and are far from fitting to the users needs. Their use requires an important effort to extract the vessel borders, compute their diameter and their cross-sectional area with enough accuracy to correctly characterize pathologies. The accurate determination of the vessel width relies on robust, precise, reproducible segmentation and characterization methods. They are expected to overcome the intra- and inter-observer variability and to improve both the diagnosis stage and the therapeutic solutions.

This paper proposes to evaluate a semi-automatic 3D moment-based method to extract the coronary network and to localize calcifications in multi-slice scanner volume data. This evaluation is done on a set of six data volumes, which contain several complex pathological cases (stenoses, calcifications, aneurysms …). The study was led on the 16 vascular segments defined according to the classification established by the American Heart Association (AHA). A comparison was completed between the segments observed in the original 3D image and those extracted from the semi-automatic method. This comparison was based on a set of objective (robustness, computing time, interactivity) and subjective (vascular permeability, calcification) criteria, with the computing of the commonly used kappa coefficient to evaluate the similarity of information. The outline of this paper is as follows. Section 2 gives a brief overview of the current works in 3D segmentation for the extraction of vessels and describes the method based on the 3D geometrical moments. Section 3 presents the tools used for the evaluation of the vascular extracted segments. In Sect. 4, results on several data sets are provided and their analysis, conducted by two medical experts, is reported. A discussion and some prospects for future work are finally addressed in Sect. 5.

## 2 3D Geometrical Moment-Based Method

### 2.1 Related Work

Several methods have been proposed to segment the vessels in an image volume. Some tackled it in 2D by extracting the vessels contours independently on each slice, and reconstituting the volume information through an inter-slice tracking; others directly processed the volume with the advantage of exploiting more fully the 3D connectivity. The segmentation techniques can be classified into five categories:

**Region growing** approaches combine a threshold criterion with a connectivity restriction. From a given seed pixel (or voxel), all the neighbours (sharing a face, an edge or a vertex in 3D) are explored and added to the region if the decision rule is verified. Such methods can be applied to surface element search and avoid the exploration of the whole data sets. An ordered region growing (ORG) algorithm has been proposed by [5], where the growth direction is limited toward the voxels with the highest intensity level. An acyclic graph is built whose edges and nodes represent respectively the centrelines and the bifurcations of small vessels in cerebral and abdominal MRA.

- **Multiscale filters** aim at coping with the varying width of the vessels. They make use of a set of different order derivative operators to extract the medial axes of the vessel at different scales [6]. A number of assumptions are generally made: the vessel is circular with a radius equal to some empirical function of scale. The discretization of the scale parameter determines the accuracy of the extraction at each level. The problem is that the number of decomposition levels is generally reduced to decrease the computational load. Nevertheless, this class of methods allows extracting the vessel tree structure.
- **Deformable models** are derived into two families: parametric (active contour or snake) and geodesic (level sets). Parametric deformable curves are local methods based on an energy-minimizing guided by external and image forces, which pull or push a set of nodes toward the lines or edges of the structure [7]. This approach was applied in [8] to extract the abdominal aorta borders from consecutive CT slices. The Level Set technique is a front propagation method also based on energy minimization but makes use of geodesic or minimal cost curves/surfaces. The curves or fronts' moving is governed by the curvatures. These methods have the particularity of being adaptable to the topology change (curves split and merge) but they are very time-consuming [9]. Contributions based on level sets have been reported in MRA for 2D vessel contour detection in slices [10] and for a fully 3D extraction [11].
- **Vessel tracking** aims at following the object along its principal direction. Manual initialisation allows choosing a seed point for the central axis tracking. The local orientation of the vessel is computed at each step. A 2D analysis can be performed by locally exploring the plane orthogonal to this direction and estimating the centreline point. A location refinement is got from the computation of the mass centre [12–13]. In [13], the tracking process is based on a grey level mask of the vascular network where the background has been removed. The local search area is a box built from the estimated point and its direction. The dimension of the box is adaptive and the horizon of the parallelepiped evolves inversely

proportional to the local curvature computed between the previous and current estimated points. The extracted points are then interpolated by a second-order B-spline curve. A similar approach is used in [14] to analyse CT and MR angiograms, where the first estimation of the next point is corrected in the 2D orthogonal plane to the estimated direction, by selecting the voxel that maximises the "Centre Likelihood": the voxel probability of being a vessel central point is computed using the signed directional gradient along the 2D radii going from this voxel and equally dividing the 2D plane space. Calcifications in CTA and ringing artefacts in MRA images are taken into account through the rejection of all pixels with positive gradients.

- **Hybrid methods** combine several techniques with the idea to take benefit of their different advantages while minimising their potential drawbacks. Gerig [15] described a thinning algorithm for MRA with an hysteresis thresholding in order to get a consistent 1-voxel-wide skeleton representing the centrelines of the vessel tree. The skeleton is further compiled into a graph structure and complex information on the vessel architecture and properties is supplied. The transposition to CTA is not obvious due to other high-intensity structures (like bones and calcifications).

Very few quantitative evaluations have been reported in the literature. This points out the difficulty of obtaining accurate measurements from the results of the vessel extraction, especially in presence of pathologies.

### 2.2 Model-Based Vessel Tracking

The vessel is locally modelled by a cylinder of diameter d and orientation $\alpha$ and $\beta$ in the 3D space (Fig. 1).

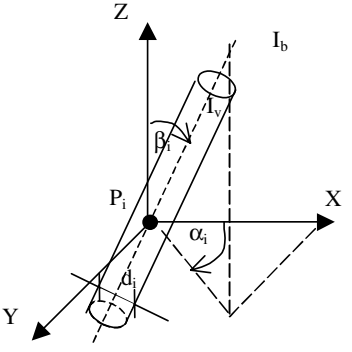


$\alpha_i$, $\beta_i$ – two angles giving the orientation in 3D space
$P_i$ – vessel centre-point, in its neighbourhood the vessel is locally considered as an ideal cylinder
$d_i$ – cylinder diameter, approximating the vessel diameter
$I_v$, $I_b$ – intensities of the vessel and of the background

**Fig. 1.** Local vessel approximation. $\alpha$ is the angle between the projection on Oxy of the axis cylinder and Oz, $\beta$ is the angle between the axis of the cylinder and Oz

The inside and outside cylinder respectively representing the vessel and the background were assumed to be homogeneous with two constant intensities $I_v$ and $I_b$. The three-dimensional geometrical moments of up to order 2 led to analytical expressions of the orientation of the cylinder axis, its diameter, and the estimated mean gray levels

inside and around the vessel. The discrete computation of these moments was performed on the set of elementary volumes (e.g. voxels) arranged on an isotropic grid using a spherical window, associated to a subvoxel decomposition. This way, the computation was reduced to mask convolutions. The tracking was performed by shifting the computation window according to the estimated orientation, and the stopping rule was stated as a decision between two hypotheses, presence or absence of the vessel. This method initially applied to low field MRA data [16] has been modified to deal with some specific features of CT images: the presence of more than two tissues in the surrounding of the vessels and the presence of pathology such as stenosis and calcification, where the ideal cylinder assumption does not hold anymore and, consequently, the computation of the vessel diameter is biased [17].

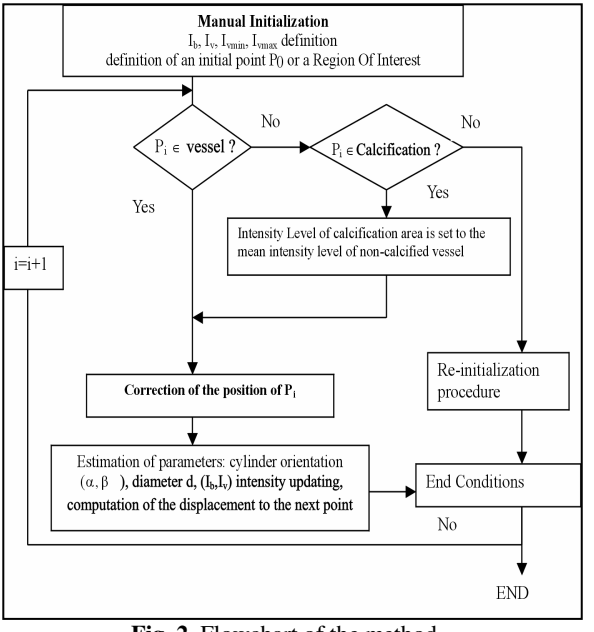


**Fig. 2.** Flowchart of the method

The flowchart of the method is reported in Fig. 2. The initialization is performed interactively by pointing inside a vascular branch of interest or defining a region in any of the three orthogonal cross-sections. Initial values are prior set to the intensities $I_b$ and $I_v$ as well as the range of value specifying the maximum and minimum vessel levels $I_{max}$ and $I_{min}$ . This range was defined to take into account the variability of the density inside the vessel.

From each extracted seed point, the position $P_i$ inside the cylinder corresponds to the center of gravity of the spherical window. Nevertheless, the orientation estimated at a given position of the window does not guarantee a precise positioning at the next point along the vessel in particular when highly curved vessels are tracked. An iterative centering was therefore performed based on the first order moments to move the point toward the vessel center. The incremental displacement between two points is made adaptive and depends on the vessel size and curvature.

**Window Size Adjustment:** The size of the vessels can widely vary (from 20 to a very few voxels) when large segments of the body are explored or when diseases are concerned. In addition, the analytical diameter formulation as reported in [16] depends directly on the window size as well as the precision of the localisation of the vessel centre $P_i$. The vessel must always be included in the investigation window: its size has been made adaptive during the vessel tracking. The adjustment is performed at each step according to the previously computed vessel diameter.

**Multi-Region Handling:** In CTA, the vessels cross several organs and tissues (muscle, fat, …), and can be located at the boundaries of several ones. In order to take into account the diversity of the crossed surroundings, the background was made adaptive. The vessel surrounding was investigated at each step along equally spaced directions (eight in total) in a plane perpendicular to the currently estimated vessel axis. The profiles along these directions were explored and the highest mean intensity level among the eight's, was used to set the background value to almost zero. An additional constraint consisted in checking that $I_v$, the current intensity at the point $P_i$, be greater than $I_b$ (if not the tracking is stopped).

**Intensity Range Overlapping between the Vessels and Anatomical Structures:** A vessel may be located nearby to an anatomical structure, whose intensity ranges in the same interval as the vessel's. This is the case with bones located in the immediate neighbourhood of a calcified vessel or with the ventricle when coronaries are concerned. The investigation window includes then the two structures. Consequently, when distances are very small (less as 5 voxels), the tracking process is susceptible to jump to the other structure. A solution consisted in forecasting this situation by examining step by step the surrounding of the estimated points. A region growing performed on a restrictive area (but larger than the area corresponding to the vessel's) allows then to compute the volume of the investigated structures and check if it comes out in the same density scale than the vessel volume. In case of doubt, another criterion was applied based on the second order moments. For a cylindrical object oriented along the OZ axis, the second order moment $M_{002}$ is maximum with respect to $\alpha$ and $\beta$ whereas $M_{020}$ and $M_{002}$ are minimum. After having estimated the orientation of the vessel in the 3D space, the second order moment test allows to check if the estimated point lies or not on the medial axis of the vessel.

**Pathological Situation Handling:** Vascular abnormalities (like calcification and stenoses or aneurysms) involve some deviations from the ideal cylindrical model and may have a strong impact on the tracking efficiency and the vessel features estimation. The calcification is generally fixed on the inner wall of the vessel. They all are usually asymmetric and may have different appearances in the images. If the tracking process is applied on the part of the non-calcified vessel after a preliminary delineation of the calcification area, the location of the central points and the estimation of the diameter appear erroneous. A solution consisted in:

(1) Delimiting the calcification area: at each step, if any voxel with intensity level above $I_{max}$ and located inside the extracted vessel was detected, a region growing technique was applied from this point using the threshold $I_{max}$ . At each boundary of this region an intensity profile along a line perpendicular to its surface was derived to determine the inflection point: all voxels along this line with higher in-

tensity were incorporated into the region. A morphological closing operation was then performed to fill the gaps.

(2) Bringing down the intensity level in the calcified area to the mean density associated to the non-pathological part of the vessel.

(3) Applying the tracking process onto the whole of the reconstituted vessel. The central point is thus computed on a shape close to the cylinder. The quality and the precision of the extraction were consequently improved and the diameter fully contains the calcified area.

**Re-initialisation Procedure:** The tracking can be stopped when the model does not fit to the local shape (bifurcation, high curvature of small vessels), in presence of artefacts or very severe stenosis. A cubic box, twice the size of the computation window, centred on the endpoint, is then open and an intersection of vessels with the faces of the box is searched. The previously visited voxels are marked in order to avoid a potential backtrack.

**End Conditions:** The stopping conditions, checked at each step, allow testing the location of the estimated point (inside/outside). This decision relies on the mean intensity and standard deviation values estimated within the current tracking window compared to a reference corresponding to a minimal diameter vessel $d_{min}$ that can be detected. In any case, the vessel intensity must be higher than the background one ($I_v > I_b$);

## 3 Analysis and Evaluation Tools

Two software were used in this study, which were designed in our laboratory. The first one, named 3Dbase allows the loading, the visualization (of 2D slices and MIP projections in the axial, sagittal and coronal planes) and the recording of raw data or DICOM formatted data volume. It integrates a number of processing routines for vascular extraction using the 3D geometrical moment-based method, parietal calcification detection, vascular diameter computation, bone structure removal (to get a better observation of the vascular network when a MIP visualization is achieved). This software was initially developed for multi-detector spiral CTs and targeted to the normal and calcified vessels of lower limbs [18]. The second one (Icon) is also a 3D data processing software, which provides a 2D projection of a 3D object along any direction. It was here employed to compute MIP projections in the planes usually viewed by the cardiologists in clinical practice for the right and left coronary network analysis (Right Anterior Oblique (RAO) 30°, RAO 15° with a 15° cranio-caudal angle, Left Anterior Oblique (LAO) 60°, LAO 60° with a 20° caudo-cranial angle and left or transverse profile) in order to facilitate their interpretation.

A first objective evaluation was carried out by means of three criteria. The first one consisted in testing the robustness of the vascular extraction both in terms of reproducibility of the results and of good performance (extraction errors). A second criterion concerned the time needed to fully process a data volume and get a satisfactory result (submitted to the expert decision). An intermediate index corresponding to the time required to extract the three main coronaries trunks (right coronary artery, Left Anterior Descending artery (LAD) and Circumflex (CX)) without their collaterals was recorded.

The third criterion characterized the number of seed points (or interactive pointing) needed to get a sufficiently elaborated vascular structure to allow the analysis.

A subjective analysis was then performed by an interventional cardiologist to evaluate the quality of the extraction. It was based on the classification established by the American Heart Association, which divides the coronary vascular network into 16 segments. This evaluation was carried out on each vascular segment by comparing the result of the semi-automatic extraction with respect to the visual perception that could have the expert of this segment in the original volume (before processing). The observation, which relied on the MIP or slice visualization of the vascular segments, aimed at labeling the extracted vascular segments with regard to their permeability analysis (a coding was set to 0 for non-visualized, occluded or truncated segments, and to 1 for those totally visualized), and cataloguing the parietals calcifications ((0) absence of calcification, (1) presence but with small size and in reduced number, (2) presence but with large size and numerous).

An agreement test was performed between segments of reference (observed in the original data) and extracted segments. It aimed at verifying the conformity between the segments respectively identified non-permeable and permeable (visible) and led to the calculation of a Cohen kappa coefficient (computed from the SPSS software release 10.0.5). Segments were thus classified into: good / over-detected (respectively categorized True Positive versus False Positive segments), not detected (because no segment) / under-detected (present but not detected) (also respectively labelled as True Negative versus False Negative segments). This test was globally performed for the set of the sixteen segments in all the data volumes in order to get a global index of the quality of extraction, and independently, for each segment for the set of the data volumes in order to obtain a trend indicator on the bias of the extraction and to determine the reproducibility of these biases with regard to some vascular areas.

## 4 Results

Six angio-scanners were acquired on a Siemens Somatom volume zoom 4 detectors. They were acquired with identical protocols and with the following acquisition parameters: collimation of 0.6 mm, table displacement of 1.5 mm/rotation, reconstruction increment of 0.6 mm, size of the matrix 512x512 with an average of 350 slices and a pixel size from 0.33x0.33 to 0.4x0.4 mm. The resolution is 8 bits and the slice thickness of 1.25 mm.

These data were acquired on an aged men population having pretty much diffused vascular lesions. When reading axial slices, no coronary network looked healthy: we observed the presence of (1) a slender distal network, particularly at the Postero-lateral left level (bases 4,5,6), (2) thrombosed and calcified aneurysms on the right coronary artery with a partial downstream over tacking by a marginal artery and collaterals compensated dilation of the LAD (base 3), (3) a stent on the mean segment of the LAD (base 1) and (4), a double transplant respectively mammary on the LAD and venous on the Posterior Descending artery (base 2). A preliminary study, which aimed at assessing the quality of the data sets, showed that 90% of the segments (i.e. 87/96 (16 segments * 6 bases)) was correctly visualized. On the remaining nine, thromboses appeared on three of them and six corresponded to collaterals of main coronary trunks (posterior descend-

ing artery, second diagonal, first, second and third marginal), for which the non-visible segments were related to either anatomical variability or acquisition system limitations. Two had thus kinetic artifacts on the right coronary artery indicating an unsuitable reconstruction delay. The examination of these data volume pointed out that, as a whole, the injection of the different coronary segments was satisfactory, as well as the cardiac cavity enhancement. No stripe artifacts were detected at the atrium level as it can be seen in some cases of high-iodised concentration, disturbing thus the right coronary artery viewing. The good quality of the injection was due to a systematic use of a test bolus for the optimal determination of the acquisition outset. This step was essential to allow making the differences between segments with thrombosis (base 3) and the other non-visualized segments.

The extraction of the coronaries was then performed for each of the six data volumes with the 3Dbase software. Results on two of them are drawn through a MIP visualization in the coronal plane, with a red colored marking of parietal calcifications (Fig. 3b and 4b). Figure 3 pictures the base number 6, where two atherosclerotic plaques appear on the Proximal LAD artery. Three segments were not visible in the axial slices in the original volume (Posterior descending, second and third marginal arteries). Figure 4 shows the base number 1, on which a stent can be seen on the Mid LAD artery. One segment was not visible in the original base (first marginal artery). These results were then loaded on the Icon station in order to visualize the extracted coronary network in the standard 2D views. Nevertheless, the extracted calcifications were not visible in these views (Figs. 3c and 4c).

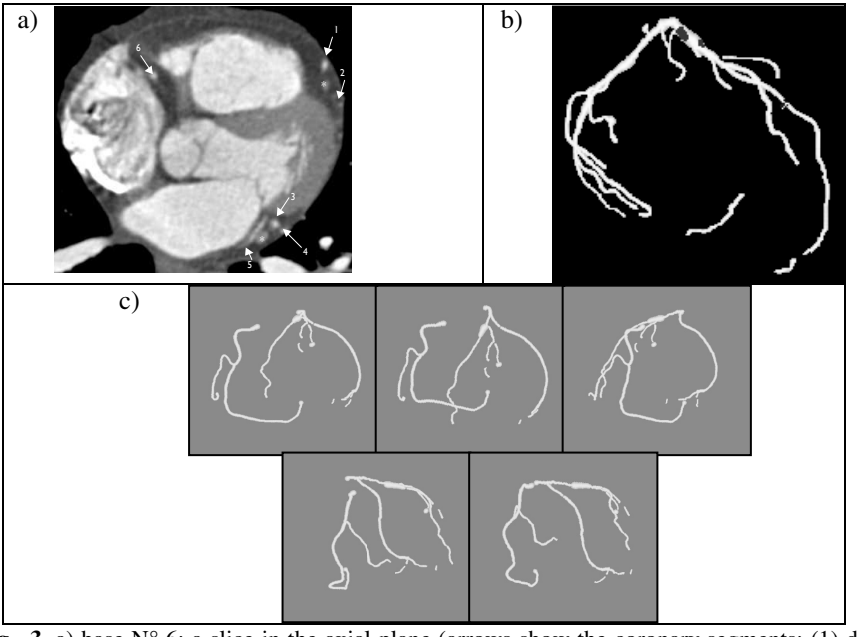


**Fig. 3.** a) base N° 6: a slice in the axial plane (arrows show the coronary segments: (1) distal LAD, (2) diagonal $2^d$, (3) and (4) Marginal $2^d$ and $3^d$, (5) distal CX, (6) distal right coronary, (*) large vein of the heart). b) MIP projection in the coronal plane of the extracted network including calcification marks in red (completed with 3Dbase), c) MIP standard projections (from left to right, top to down: LAO 60°, LAO 60° with a 20° caudo-cranial angle, transverse profile, RAO 30°, RAO 15° with a 15° cranio-caudal angle (computed with Icon)

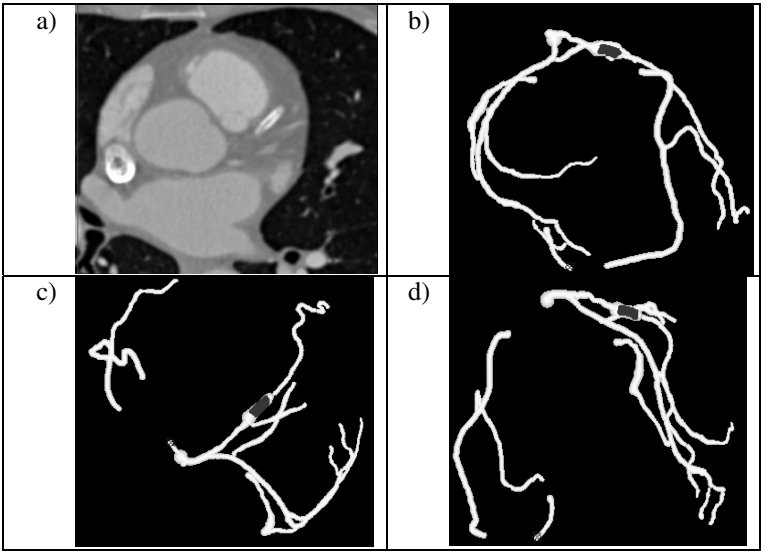


**Fig. 4.** a) Base N°1: a slice in the axial plane at the stent level, b-d) MIP projections in the coronal, axial and sagittal planes of the extracted network, including in red the stent on the mid LAD artery (completed with 3Dbase)

### 4.1 Objective Analysis

All the six data sets were successfully processed, without any complex manipulation. Parameters were initially set up to take into account the characteristics of the vessels, which are the intensity range $[I_{vmin},I_{vmax}]$, the initial vessel and background intensities $I_v$ and $I_b$. The extraction procedure consisted then in interactively selecting seed points (or defining a region of interest) for initiating the tracking process. Each time the process stopped, the expert could restart it interactively till getting a satisfying description of the coronary tree. No unexpected stopping happened during the extraction procedure. In case of wrong selection of the seed point, the operator could come back to the previous step (removing thus the detected structure, issued from an incorrect pointing). The reproducibility of the results was studied on two data volumes by renaming and presenting them again to the expert after several days. This experience has shown a very good concordance between the two extractions with very little variability ($0.83 <$ Kappa coefficient $< 1$).

The global time needed to process a volume and get a satisfying extraction, included: (1) the slices or MIP observation to choose the best suitable area for the interactive selection of the seed points (sometimes, the tortuous aspect of the arteries and their connectivity with some veins made this choice difficult), (2) the tracking procedure for each selected seed point, (3) the MIP visualization process. The mean time was evaluated to 15 minutes for the most complete extraction and 6 minutes for the intermediate time (see section III). These relatively high times are mainly related to the interactive selection: the observation of the data by the expert and the MIP visualization process were performed several times during the extraction in order to draw the results at each step. The extraction method, in itself, was very fast. For instance,

the time needed to process the right lower limb vessels, which was acquired on the same MSCT system (size matrix 256x256 pixels, 494 slices, 12 bits resolution) was about 10 seconds [Boldak, 02] while the current manual method used by the radiologist can take about three hours. The high complexity of the cardiac network when comparing with the lower limb vascular network is without common measure and can justify of a longer process time. The last objective criterion was related to the number of seed points required to perform the detection. In average, 25 selections were needed to process the whole network and 14 for the main arteries extraction while only 2 to 4 seed points and 2 ROI definitions were enough to extract the right or left lower limb vessels.

### 4.2 Subjective Analysis

The vascular permeability was then determined for each segment after the extraction process. Over the 96 processed segments, four were removed because of kinetic artefacts and too restrictive acquisition volume (segments located at the limit of the base). On the remaining ones, only 78 were found in agreement when comparing with the initial data volumes. This means that a good matching was obtained for 83% of the segments (coefficient of kappa Cohen of 0.46). The sensitivity of the method was then established to 84.3%, its specificity to 88.9%, the positive predictive value (PPV), 98.6% and the negative predictive value (NPV), 38%. Among the last fourteen segments, one had a thrombosed and a calcified aneurysm, considered as permeable because partially extracted by the method, and thirteen were related to negative false (they were located on the collateral segments). These segments corresponded to marginal branches, which were too thin or tortuous to be detected, or to the Posterolateral left branch, whose size and proximity to the coronary sinus and to the mid vein of the heart made difficult the extraction. Considering now the main coronary trunks only, the detection results provide 51 segments in agreement over a total of 54 segments (equivalent to a good detection rate of 94.5%) (the number of non-permeable segments being not sufficient to compute a kappa coefficient). The sensitivity and the NPV were of 100%, the specificity 66.7% and the PPV 98%.
Regarding calcifications, an excellent agreement was found with 90 good interpretations over the 96 original vascular segments (93.7%) and a kappa coefficient value equals to 0.88. The segments not in agreement corresponded to (1) undetected calcifications (2) calcified segments, which were under- or overestimated according to the initial classification carried out on the original data, for which the assigned code did not match. This error was linked to the subjective visual evaluation of the calcification severity. By conducting the analysis with only two classes (presence or absence of calcification), the kappa coefficient would increase to 0.93, the sensitivity to 91.8%, with a NPV equal to 92.2%, a specificity and a PPV to 100%.

## 5 Conclusion and Discussion

A fast, efficient model-based solution has been proposed for the 3-D tracking of vessels in MSCT images. It provides a first approximation of the vascular patterns even in presence of severe calcifications and, as such, presents a real clinical interest. The

software platforms offer an easy to use interface where the interaction with the user (pointing or region delimitation, parameter setting) is very limited and can fulfil the clinical requirements. A first evaluation has been completed for the coronary tree extraction and the localization of calcifications with the participation of two experts in coronarography and radiology. The method was proved to be robust, giving excellent results when dealing with the main coronary trunks and good results if we consider the whole vascular tree. It makes appear high sensibility and specificity measures in the assessment of the vascular permeability. The diameter of the branches, even if not evaluated here, was available. It was not included in the study because no objective tools were defined to quantify the accuracy of the measure. The number of pointing (25) required to process the coronary tree varies according to the complexity of the vessel shapes to be extracted. It was not considered as a handicap by the expert but remains largely reasonable with respect to the manual procedure.

The method of detection of coronary vessels is going to be tested on more data sets and cross validated with conventional X-ray coronary angiography. The work in progress is also aimed at quantifying the degree of stenoses and characterizing the calcifications.

**Acknowledgements.** The authors are grateful to Brigitte Le Bruno from Siemens France, for supporting this work and for providing the image data. They also express their thanks to Jean Louis Dillenseger, the Icon designer, for his help. The authors are also grateful to the anonymous reviewers for their suggestions to improve this paper.

## References

[1] S. Achenbach, W. Moshage, D. Ropers, J. Nossen, W.G. Daniel, Value of electron-beam computed tomography for the noninvasive detection of high-grade coronary-artery stenoses and occlusions. N. Engl. J. Med., 339 (27), pp. 1964–71, 1998.

[2] W.Y. Kim, P.G. Danias, M. Stuber, S.D. Flamm, S. Plein, E. Nagel, and al. Coronary magnetic resonance angiography for the detection of coronary stenoses. N. Engl. J. Med., 345(26), pp. 1863–1869, 2001.

[3] T.C. Gerber, R.S. Kuzo, N. Karstaedt, G.E. Lane, R.L. Morin, P.F. Sheedy, R.E. Safford, J.L. Blackshear, J.H. Pietan, Current results and new developments of coronary angiography with use of contrast-enhanced computed tomography of the heart, Mayo Clin. Proc., 77 , pp. 55–71, 2002.

[4] A. Blum; Scanner volumique multicoupe: principe, applications et perspectives, ITBM-RBM, vol 23, N°4, pp. 189–262, 2002.

[5] P.J. Yim, P.L. Choyke, R.M. Summers; Grey-scale skeletonisation of small vessels in magnetic resonance angiography; IEEE Transactions on Medical Imaging, vol. 19, no. 6, pp. 568–576; June 2000.

[6] Y. Sato,. S. Nakajima, N.Shiraga, H. Atsumi, S. Yoshida, T. Koller, G. Gerig. R. Kikinis, 3-D multi-scale line filter for segmentation and visualization of curvilinear structures in medical images, Medical Image Analysis, 2, 2, pp. 143–168, 1998.

[7] T. McInerney, D. Terzopoulos; Deformable models in medical image analysis: a survey; Medical Image Analysis, vol. 1, no. 2, pp. 91–108, 1996.

[8] V. Juhan, B. Nazarian, K. Malkani, R. Bulot, J. M. Bartoli, J.Sequeira; Geometrical modelling of abdominal aortic aneurysms; CVRMed, pp. 243–252, 1997.

[9] J.S. Suri, K. Liu, S. Singh, S.N. Laxminarayan, X. Zeng, L. Reden; Shape recovery Algorithms using level sets in 2-D/3-D medical imagery: A state of the art review, IEEE Transactions on Information Technology in Biomedicine, vol. 6, N°1, pp. 8–28, March 2002.

[10] K.C. Wang, R.W. Dutton, Ch.A Taylor; Improving geometric model construction for blood flow modeling; IEEE Engineering in Medicine and Biology, vol. 18(6), pp. 33–39, 1999.

[11] L.M. Lorigo, O.Faugeras, W.E.L. Grimson, R. Keriven, R. Kikinis, C.-F. Westin; Co-dimension 2 geodesic active contours for MRA segmentation; IPMI; pp. 126–139, Lecture Notes in Computer Science, vol. 1613, Springer 1999.

[12] Y. Trousset, D. Schieber, J. Knoplioch; An algorithm for tracking vessels in three-dimensional angiograms; Proc. of the 14th IEEE-EMBS conf., Paris, vol. 5, pp. 2053–2054, October 1992.

[13] N. Flasque, M. Desvignes, J-M Constans, M. Revenu; Aquisition, segmentation and tracking of the cerebral vascular tree on 3D magnetic resonance angiography images, Medical Image Analysis, Eds. Elsevier, vol. 5, pp. 173–183, 2001.

[14] O. Wink, W.J. Niessen, M.A. Vierger; Fast Delineation and Visualisation of Vessels in 3-D Angiographic Images; IEEE Transactions on Medical Imaging, vol. 19, no. 4, pp. 337–346, April 2000.

[15] G. Gerig, Th. Koller, G. Székely, Ch. Brechbühler, O. Kübler; Symbolic description of 3-D structures applied to cerebral vessel tree obtained from MR angiography volume data; Information Processing in Medical Imaging, pp. 94–111, 1993.

[16] P. Reuzé, J.L. Coatrieux, L.M. Luo, J.L. Dillenseger; A 3-D moment based approach for blood vessel detection and quantification in MRA; Technology and Health Care, 1, pp. 181–188, 1993.

[17] C. Toumoulin, C. Boldak, J-L Dillenseger, J-L Coatrieux, Y. Rolland; Fast detection and characterization of vessels in very large 3-d data sets using geometrical moments, IEEE Transactions on Biomedical Engineering, vol. 48, 5, 604–606, 2001

[18] Bołdak C., Rolland Y., Toumoulin C.,. Coatrieux J.L: An improved model-based vessel tracking algorithm with application to Computed Tomography Angiography; Journal of Biocybernetics and Biomédical Engineering, vol .3, (1), pp. 41–64, 2003.

# A Levelset Based Method for Segmenting the Heart in 3D+T Gated SPECT Images

Arnaud Charnoz[1], Diane Lingrand[1], and Johan Montagnat[2]

[1] CReATIVe, I3S, CNRS/UNSA
B.P.121 – F06903 Sophia Antipolis Cédex – France
lingrand@i3s.unice.fr
[2] Creatis, CNRS/INSA Lyon
F69621 Villeurbanne Cédex – France
johan@creatis.insa-lyon.fr

**Abstract.** Levelset methods were introduced in medical images segmentation by Malladi et al. in 1995. In this paper, we propose several improvements of the original method to speed up the algorithm convergence and to improve the quality of the segmentation in the case of cardiac gated SPECT images.
We studied several evolution criterions, taking into account the dynamic property of heart image sequences. For each step of the segmentation algorithm, we have compared different solutions in order to both reduce time and improve quality.
We have developed a modular segmentation tool with 3D+T visualization capabilities to experiment the proposed solutions and tune the algorithm parameters. We show segmentation results on both simulated and real SPECT images.

## 1 Motivations

Cardiovascular pathologies are the first cause of mortality in industrialized countries. Functional imaging of the heart such as gated SPECT images provide low invasive inspection methods useful for cardiac diagnosis. However, high noise level and low resolution make these images difficult to interpret. Moreover, the dynamic properties of 3D heart image sequences make manual analysis of the images extremely tedious.

In this paper, we propose an automated segmentation method of the heart boundaries based on the levelset method. The resulting models can be used for quantitative dynamic parameters computation useful for medical diagnosis such as the left ventricle volume variations or walls thickness variations. These parameters allow to compute precise estimates of well established clinical indicators such as the ejection fraction. Combining the SPECT intensity information with the model geometry allows to precisely locate necrosed myocardial area, and estimate the tissue viability.

In the following sections we focus on the first step of this process which is the segmentation. Making the segmentation automatic in SPECT images is known

I. Magnin et al. (Eds.): FIMH 2003, LNCS 2674, pp. 52–61, 2003.

to be a hard problem due to the lack of information (low resolution), blurred boundaries, high noise level, low contrast, and the need for reliable results.

We use a model driven approach in order to segment the heart. Different geometrical models exist (see [10] for a survey). The original model-based segmentation methods were 2D explicit contours [8] later on extended to surfaces in 3D [15,3]. The levelset method is an alternative implicit surface representation due to Osher and Sethian [11] and Caselles [1]. It has been introduced for segmenting medical images by Malladi and Sethian [9].

Most shape recognition algorithms need to know the topology of objects to recover. The levelset method allows to perform topology changes during the segmentation process without introducing additional complexity. It has been widely used in segmentation [2,4,12,7,5,6].

## 2 The Levelset Method for Segmentation

In the levelset method, the model $C$ is implicitly defined as the zero levelset of a higher dimension function $u$. Starting from a given shape $C_0$, the model is able to evolve toward the shape of the object to segment, according to the first order evolution law:

$$\frac{\partial C}{\partial t} = F\vec{\mathbf{N}} = (F_{int} + F_{ext})\vec{\mathbf{N}} \tag{1}$$

with $F$ the force applied on the surface and $\vec{\mathbf{N}}$ the surface normal vector. This force may be decomposed into two components:

- an internal component $F_{int}$, enforcing a regularity constraint over the surface
- an external component, $F_{ext}$, taking into account the image to enforce the convergence of the model shape toward the data.

For simplicity, we will explain the levelset approach in case of 2D images. Given an initial contour $C_0$, the levelset function is $u(x, y) = d((x, y), C_0)$ where $d$ is a signed distance (see Fig. 1). The initial contour is indeed defined as $C = \{(x, y)|u(x, y) = 0\}$. $u$ is therefore represented as a distance map. Outside the contour, map values are positive. Inside, they are negative.

The level set method shows that the model evolution (Eq. (1)) corresponds to an evolution of the distance map satisfying [9]:

$$\frac{\partial u}{\partial t} = F \, \|\nabla u\| = (F_{int} + F_{ext}) \, \|\nabla u\| \tag{2}$$

where $u(x, y, t)$ is the evolutive distance map. This equation is only valid at the model location. As a consequence, the distance map property of $u$ will not be preserved. In order to cope with this problem, we need to reinitialize $u$ periodically so that it corresponds to a distance map, *i.e.* to constrain $\|\nabla u\| = 1$.

The level set formulation extends straight forward in 3D with a higher dimension distance map. We can therefore consider surface model for 3D and 3D+T images segmentation. Equation (2) is discretized using an explicit scheme for numerical implementation.

The segmentation algorithms steps are:

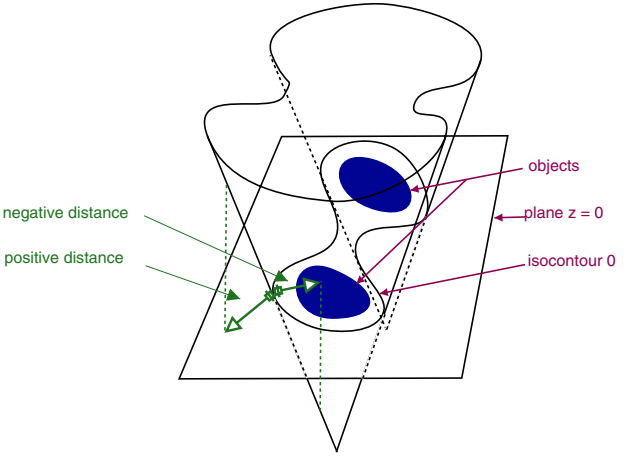


**Fig. 1.** Distance map $u$, in dimension 2

**Initialization:** the initial location of the surface
**Loop:**
**Compute the forces:** defined by a criterion
**Make the distance map evolve:** using (Eq. (2)
**Reinitialize the distance map:** in order to enforce $\|\nabla u\| = 1$.
**Convergence:** iterate until the algorithm converges (need a stop criterion)

In the following sections, we study each of these steps in order to optimize the segmentation algorithm. We use synthetic data (with or without white noise) made from simple geometric forms or more realistic forms (shape similar to the heart left ventricle) for experiments. We have also used simulated images by the MCAT method [13] and real SPECT data provided by the Pr J. Darcourt of the Pasteur hospital (Nice, France).

## 3 Initialization

A basic idea for initialization is to take a sphere centered in the volume with a diameter equal to half image dimension. However, this naive approach initializes the model far from the actual object boundaries and the convergence time is long.

The segmentation process time has been decreased by using simple image processing techniques to obtain a closer approximation of the object. The image is first filtered with a Gaussian kernel in order to reduce noise. The mean and variance of image intensity are estimated and a threshold is computed as the sum of these two parameters, in order to eliminate a large part of the background. Thereafter, a morphomathematic opening operation is performed, using this threshold, in order to eliminate small objects due to noise and fuse close

components. We extract the surface splitting the resulting binary image in order to initialize the distance map (see Sect. 5). A similar approach was proposed for the balloon model by Cohen [3].

## 4 Evolution Criterions and Parameters

Most evolution criterions proposed in levelset-based segmentation methods are spatial [7]. In the case of dynamic images, they only allow to segment each volume independently of the others. The first criterion that we implemented uses only intensity information. It makes the hypothesis that the image is composed of a uniform intensity region (the object to segment) and a uniform background:

$$\begin{cases} \dfrac{\partial u}{\partial t} = \left(4\,(I-\mu_{int})^2 - (I-\mu_{out})^2 + \lambda\kappa\right)\ \|\nabla u\| \\ \text{with: } \kappa \text{ the curvature,} \\ \qquad \mu_{out} \text{ mean of image external part,} \\ \qquad \mu_{int} \text{ mean of image internal part,} \\ \qquad \text{and } I \text{ image intensity.} \end{cases} \tag{3}$$

This approximation is only roughly valid for SPECT images due to the image noise, the inhomogeneity of the heart and the perfusion deficiencies causing signal drops.

A more elaborated criterion uses both information on intensity and variance of intensity allowing the segmentation of non uniform regions (textured region).

$$\begin{cases} \dfrac{\partial u}{\partial t} = \Big(2\,log(1+\sigma_{int}^2) - log(1+\sigma_{out}^2) \\ \qquad + 2\,\dfrac{(I-\mu_{int})^2 - \sigma_{int}^2}{1+\sigma_{int}^2} - \dfrac{(I-\mu_{out})^2 - \sigma_{out}^2}{1+\sigma_{out}^2} + \lambda\kappa\Big)\,\|\nabla u\| \\ \text{with: } \kappa \text{ the curvature,} \\ \qquad \mu_{out} \text{ mean of image external part,} \\ \qquad \mu_{int} \text{ mean of image internal part,} \\ \qquad \sigma_{out} \text{ variance of image external part,} \\ \qquad \sigma_{int} \text{ variance of image internal part,} \\ \qquad \text{and } I \text{ image intensity} \end{cases} \tag{4}$$

Equation (5) presents a spatial and temporal criterion [5]. Let $I_n$ represent the image at instant $n$. The whole sequence is used in order to filter noise and determine the mean background intensity ($B$):

$$\begin{cases} \dfrac{\partial u_n}{\partial t} = \left(2\,(I_n - \mu_{int_n})^2 - (B-I_n)^2 + \lambda\kappa_n\right)\ \|\nabla u_n\| \\ \text{with: } \kappa_n \text{ the curvature,} \\ \qquad B \text{ the whole sequence mean background intensity,} \\ \qquad \mu_{int_n} \text{ mean of image n internal part,} \\ \qquad \text{and } I_n \text{ image n intensity.} \end{cases} \tag{5}$$

### 4.1 Influence of the Curvature

Using the evolution criterion (3), different weights $\lambda$ of the curvature have been experimented. Figure 2 shows that for segmentation quality and segmentation time, we need to find a compromise for the $\lambda$ value.

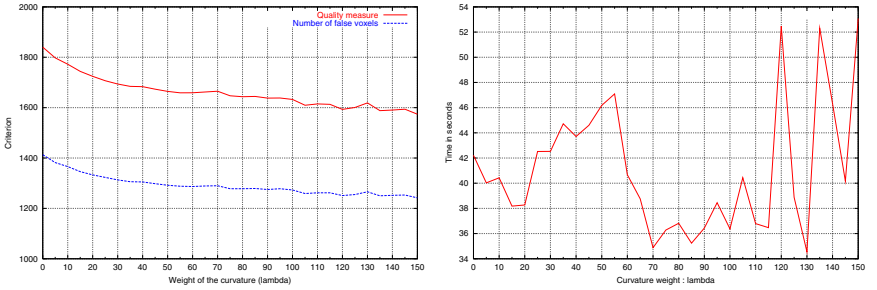


**Fig. 2.** On the left: evaluation of the quality on the final segmentation for different values of $\lambda$. We observe that the larger the curvature weight is, the better the final segmentation is. On the right: segmentation time. For large values of $\lambda$, the numerical scheme is unstable. A good compromise is to take a $\lambda$ value around 100

### 4.2 Do We Need to Recompute the Distance Map Gradient $\|\nabla u\|$?

The distance map gradient $\|\nabla u\|$ is used in the evolution Eq. (2). If the distance map is a real distance map or if we reinitialize it often, $\|\nabla u\| = 1$ and we do not need to compute it. However, frequent reinitializations are costly.

If we do not reinitialize $u$ frequently, the distance map is false as soon as we update $u$ according to the evolution equation. We observed that the levelset surface becomes sharp and the gradient is high near the isolevel+0. The pixels need a greater force to move from outside to inside the object (and conversely).

A naive approach would consist in introducing the computed value of the gradient into the evolution equation. However, we observed that this quickly makes the explicit numerical scheme unstable. A diminution of the time step is then needed at the cost of an increased convergence time.

It appears that using $\|\nabla u\| = 1$ leads to a more stable algorithm and the distance map only need to be periodically reinitialized.

## 5 Reinitialization

As seen before, the Eq. (5) is only true at the model location. This is illustrated in Fig. 3. In order to preserve the distance map, we need to reinitialize it regularly, every $n$ iterations.

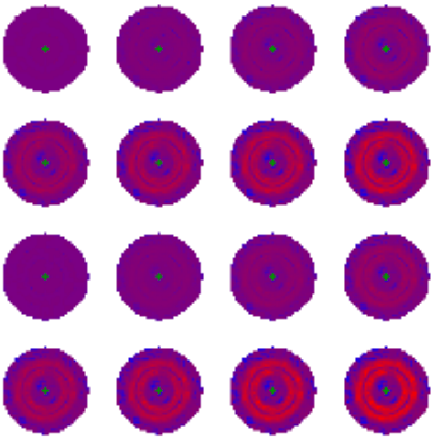

**Fig. 3.** Evolution of the distance map gradient in the model neighborhood during the segmentation of a synthetic ventricle. The reinitialization is made every 8 iterations. From left to right and top to bottom, we show the 16th first iterations. The blue color corresponds to a gradient value 0, the purple 1 and the red 10, which is the maximum value. The other colors are interpolated from these values

### 5.1 Classical Reinitialization

Usually, the distance map is reinitialized using the Sussman *et al* [14] equation:

$$\frac{\partial u}{\partial t} = \text{sign}(u) \times (1 - \|\nabla u\|) \quad \text{where:} \quad \begin{array}{l} \text{if } u < 1, \text{sign}(u) = -1 \\ \text{else if } -1 < u < 1, \text{sign}(u) = |u| \\ \text{else sign}(u) = 1 \end{array} \tag{6}$$

The withdraw of this method is the computation cost. It can be limited using the narrow band method [9]. But is is even more efficient to proceed to a faster reinitialization that is presented in the following section.

### 5.2 Fast Reinitialization

This method involves 2 steps. The first step cuts the distance map just around the model: using 8-connexity in 2D or 26-connexity in 3D, we preserve only pixels or voxels that have a neighbor with an opposite sign in the distance map values. The second step expands this to all the distance map: we begin with distance map values around the edges and propagate the values using distances.

In this case, we reduce the computation cost without reducing the segmentation quality. We can also restrict the reinitialization to a narrow band around the model, but the gain is not as important as in the case of classical reinitialization: distances greater than the narrow band size are not computed and voxels outside the narrow band are assigned a constant upper value.

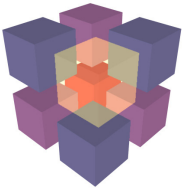

*Distances values with respect to the yellow transparent voxel: the blue voxels are at distance 1, the purple $\sqrt{2}$ and the red $\sqrt{3}$.*

## 6 Stopping the Segmentation Process

We studied several stop conditions: the variation of the surface, the variation of the volume, and the variations of energy criterions. The two first criterions are necessary but not sufficient (when the model converges, its surface and volume are constant). The last one is sufficient (the equation evolution corresponds to a minimization of the model energy with a gradient descent method). However, computing the model volume or surface is much cheaper than computing its energy, and it is very unlikely that the model will evolve significantly for several iterations while its surface and its volume remain constant. Therefore, we used surface and volume variation as stop conditions as well.

We observe periodic oscillations (see Fig. 4) due to the variation of energy which is caused by the distance map reinitializations: after each reinitialization the distance map is flatten, the surface encounters less resistive gradients, and evolves more than before reinitialization (when we need larger forces to move).

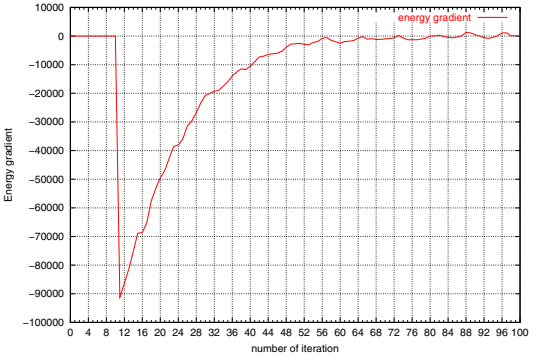


**Fig. 4.** Energy variation during the segmentation process, using reinitialization every 8 steps. We observe oscillations corresponding to the reinitialization frequency

## 7 Experiments

We present in Figs. 5, 7, and 6 the result of the segmentation of a real SPECT image of the heart left ventricle. The sequence is composed by 8 frames of dimension 64x64x28 voxels. Each voxel has a dimension of 2.5x2.5x5 $mm^3$. When the heart muscle relaxes (diastole), the contrast between muscle intensity and background decreases. On contrary, the contrast is better when the muscle contracts (systole).

Due to this low contrast in diastole images, a small portion of the right ventricle is also segmented in frames 4 to 7 using criterion 3 or 4 (Figs. 5 and 7). Spatial criterions fail to take into account image intensity variations along the sequence. Using criterion (5) improves the segmentation by taking into account the intensity variation of the ventricle in the whole sequence (see Fig. 6). We could further improve this result by taking into account the fact that the myocardium is hardly compressible and that the model volume should be constant in all time frames.

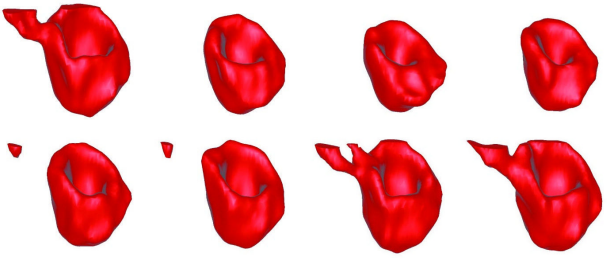

**Fig. 5.** From left to right and top to bottom, segmentation results from frame 0 to frame 7 of the cardiac sequence, using criterion (3)

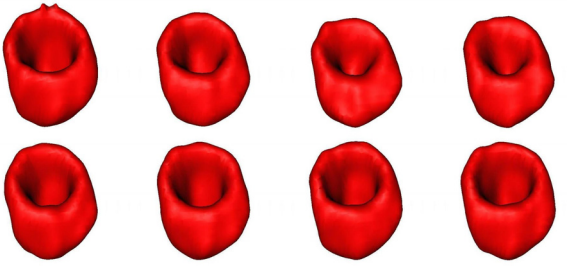

**Fig. 6.** From left to right and top to bottom, segmentation results from frame 0 to frame 7 of the cardiac sequence, using criterion (5)

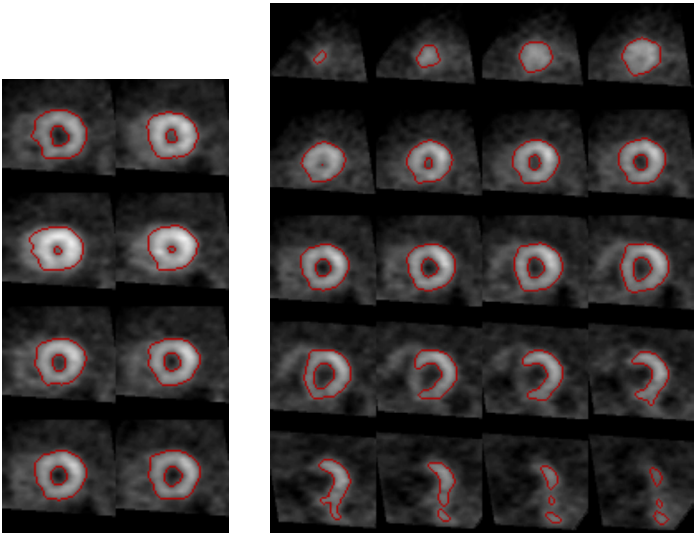

**Fig. 7.** On the left, the whole cardiac sequence viewing plane Z=11 with segmentation result superimposed (using criterion (3)). On the right, data of frame 6 with segmentation result superimposed. We observe the two stages of a heart beat: the systole (frames 1 to 3) and the diastole (frames 4 to 7 and 0)

## 8 Discussion and Perspectives

In this study, we have improved the segmentation (i) in quality by improving the robustness to noise and (ii) in time: we have reduced the total algorithm time by 85%. We have studied in details each step of the algorithm. Various parameters such as the reinitialization frequency or the curvature weight were analyzed and tuned for reducing the computation time to a minimum.

This study of the mathematical parameters now need to be further investigated on clinical data. A more thorough validation involving comparison to segmentation results by medical experts on a larger dataset is needed. Additional constraints taking into account the physiology of the heart such as the almost incompressibility of the muscle could also be implemented. The method could then be used to extract quantitative functional parameters.

**Acknowledgments.** The authors would like to thank Pr. J. Darcourt for fruitful discussions.

This work is partly financed by the CNRS (French National Center for Scientific Research) STIC department as a multilaboratory Project (Creatis in Lyon, I3S in Sophia Antipolis and Pasteur Hospital in Nice).

## References


1. V. Caselles, F. Catte, T. Coll, and F. Dibos. A geometric model for active contours in image processing. In *Numerische Mathematik*, volume 66, pages 1–33, 1993.
2. V. Caselles, R. Kimmel, and G. Sapiro. Geodesic active contours. *International Journal of Computer Vision*, 22(1):61–79, 1997.
3. L.D. Cohen and Isaac Cohen. Finite element methods for active contour models and balloons for 2-D and 3-D images. *IEEE Transactions on Pattern Analysis and Machine Intelligence, PAMI*, 15, November 1993.
4. L.D. Cohen and Ron Kimmel. Global minimum for active contour models: A minimal path approach. *Int. J. of Computer Vision*, 24(1):57–78, 1997.
5. E. Debreuve, M. Barlaud, G. Aubert, I. Laurette, and J. Darcourt. Space time segmentation using level set active contours applied to myocardial gated spect. In *International Conference on Medical Imaging (MIC99), Vancouver*, Octobre 1999.
6. J. Gomes and O.D. Faugeras. Reconciling Distance Functions and Level Sets. *Journal of Visual Communication and Image Representation*, 11:209–223, 2000.
7. S. Jehan-Besson, M. Barlaud, and G. Aubert. A 3-step algorithm using region-based active contours for video objects detection. *EURASIP Journal of Applied Signal Processing*, 2002(6):572–581, 2002.
8. M. Kass, A. Witkin, and D. Terzopoulos. SNAKES: Active contour models. *International Journal of Computer Vision*, 1:321–332, January 1988.
9. R. Malladi, J. A. Sethian, and B.C. Vemuri. Shape modeling with front propagation: A level set approach. *IEEE Transactions on Pattern Analysis and Machine Intelligence*, 17(2):158–175, February 1995.
10. J. Montagnat and H. Delingette. A review of deformable surfaces: topology, geometry and deformation. *Image and Vision Comput.*, 19(14):1023–1040, Dec. 2001.
11. S. Osher and J. Sethian. Fronts propagating with curvature dependent speed : algorithms based on the Hamilton-Jacobi formulation. *Journal of Computational Physics*, 79:12–49, 1988.
12. Nikos Paragios and Rachid Deriche. Geodesic active contours and level sets for the detection and tracking of moving objects. *IEEE Transactions on Pattern Analysis and Machine Intelligence*, 22(3):266–280, March 2000.
13. P.H. Pretorius, W. Xia, M. A. King, B. M. W. Tsui, T.-S. Pan, and B.J. Villegas. Determination of left and right ventricular volume and ejection fraction using a mathematical cardiac torso phantom for gated blood pool spect. *Journal of Nuclear Medicine*, 37:97, 1996.
14. M. Sussman, P. Smereka, and S. Osher. A level set approach for computing solutions to incompressible two-phase flow. *J. Comput. Physics*, 114:146–159, 1994.
15. D. Terzopoulos, A. Witkin, and M. Kass. Constraints on deformable models : Recovering 3d shape and non rigid motion. *Artificial Intelligence*, 36(1):91–123, 1988.

# Modeling of Electro-mechanical Coupling in Cardiac Myocytes: Feedback Mechanisms and Cooperativity

F.B. Sachse, K. Glänzel, and G. Seemann

Institut für Biomedizinische Technik, Universität Karlsruhe (TH), Germany

**Abstract.** Modeling of mechanisms involved in electrophysiology and tension development of cardiac myocytes can enhance the understanding of physiological and pathophysiological cardiac phenomena. Interactions of divers components are necessary for cellular electro-mechanics. Particularly, the interactions between proteins in the cell membrane, sarcoplasmic reticulum and sarcomere are of importance. In this work hybrid electro-mechanical models of cardiac myocytes were derived on basis of recently developed models as well as of measurements ranging from protein to multi-cell level. The models quantify dynamically the electrophysiology and tension development by states, partly associated to configurations of the involved proteins, and the transition between these states. The models allow the reconstruction of electro-mechanical phenomena. Results of simulations with the hybrid models were performed illustrating their properties. The models may help to clarify feedback and cooperativity mechanisms, pathophysiological changes and metabolism of myocytes.

## 1 Introduction

Cardiac myocytes show complex electrical and mechanical properties, i.e. electrical excitability and development of tension, respectively. The electrical excitation is strongly coupled with the tension development. Vice versa mechanical contraction influences electrophysiology.

An electrical excitation of myocytes leads to an increase of transmembrane voltage and of concentration of cytoplasmic calcium. This calcium transient initiates and modulates the development of tension in the contractile units, i.e. the sarcomeres. The excitation process and the resulting concentration changes are affected primarily by proteins, e.g. ion pumps, exchanger and channels, which control the flow of different ions from and to spatial domains, as well as tropomyosin, troponin, myosin II and actin, which are found in the contractile unit.

A multitude of studies of electrophysiology and tension development of cardiac myocytes was performed in recent years yielding knowledge concerning physiological and pathophysiological cardiac phenomena. This knowledge is partly transformed in mathematical models, which describe different aspects of cellular

I. Magnin et al. (Eds.): FIMH 2003, LNCS 2674, pp. 62–71, 2003.

electro-mechanics. The models describe the interactions of several components, particularly, the interactions between proteins in the cell membrane, sarcoplasmic reticulum and sarcomere.

In this work hybrid models of electro-mechanics in cardiac myocytes are derived from different modes as well as from measurements of proteins, single cells and cell clusters. The hybrid models provide knowledge of basic mechanisms and can enhance the understanding of physiological and pathophysiological cardiac phenomena. The models offer interfaces to models of cellular metabolism and signaling pathways. Simulations with the hybrid models explore the reconstructability of experimental studies of myocardium.

## 2 Cellular Electrophysiology

*Mechanisms* A cardiac myocyte can be electrically excited, i.e. the transmembrane voltage raises from the resting voltage of approx. $-90\ mV$ to $30\ mV$. The raise can be initiated by a sufficiently large influx of positive ions into the cell. This influx can occur through gap junctions from attached excited myocytes or by specific ion channels located in the sarcolemma. The first mechanism is significant for excitation propagation, the secondary for initiation of excitation in pace maker cells. The initial influx leads to a raise of transmembrane voltage up to a threshold voltage. Afterwards the opening of specific ion channels allows passage of specific ions, which determine the shape, amplitude and length of the action voltage.

The excitation process acquires the whole sarcolemma, particularly the transversal tubuli, where in consequence the sarcolemmal voltage-gated L-type calcium ion channels open initiating a positive feed back mechanism [1]. In mammalian myocytes a high density of L-type calcium ion channels (and of Na-Ca exchangers) is reported at the end of transversal tubuli, which intrude into the myocyte as a specialization of the sarcolemma and end at adjacencies of Z disks.

The influx of calcium ions through the L-type calcium ion channels triggers the opening of sarcoplasmic calcium release channels leading to calcium sparks. The sarcoplasmic reticulum is a determinant for the intracellular calcium handling. The sarcoplasmic reticulum is decomposed in the terminal cisternae and longitudinal tubuli. The longitudinal tubuli surround mesh-like the sarcomeres. The terminal cisternae located at the Z disks act primarily as buffer for calcium and show a high density of the protein calsequestrin. The sarcoplasmic reticulum includes different proteins controlling the calcium flux through the membrane. Sarcoplasmic calcium release channels are gated by cytoplasmic calcium concentration and allow the efflux of calcium from the junctional sarcoplasmic reticulum into the cytoplasm. Sarcoplasmic calcium pumps remove calcium ions from the cytoplasm into the sarcoplasmic reticulum consuming adenosine triphosphate (ATP).

Numerous calcium sparks sum up to a significant increase of the concentration of cytoplasmic calcium. The release channels show a refractory period, which stops the positive feed back mechanism. The calcium is re-uptaken by

calcium specific pumps into the sarcoplasmic reticulum. Smaller amounts are transported extracellularly via the sarcolemmal Na-Ca exchangers and calcium pumps.

*Modeling* In the last years a large number of electrophysiological models of myocytes was constructed [2] with increasing abilities to reconstruct quantitatively and detailed the underlying mechanisms. In this work the Noble-Varghese-Kohl-Noble model was applied, which describes the electrophysiology of a ventricular myocyte of guinea-pig [3, 4]. The model includes effects on ionic channels by the concentration of ATP and acetylcholine (ACh) as well as by stretch or tension, i.e. stretch-activated ion conductances, modulation of calcium binding to troponin C, and modulation of sarcoplasmic leak current. Furthermore, a tension generation model is included. A description of the diadic space is incorporated.

Different variants and configurations of the model exist. The variant applied in this work is based on neglecting ATP and ACh activated ionic channels as well as using only the electrophysiological part of the model. Furthermore, only length dependencies of the electrophysiological parameters are included. Stretch activated ion channels were deactivated.

## 3 Cellular Tension Development

### 3.1 Experimental Studies

The combination of experimental studies and modeling of active muscular behavior started with A. V. Hill in 1938 [5], who measured, analyzed and described in a mathematical manner the interdependencies between speed of shortening, tension and heat production in skeletal muscles of frog. In these experiments the muscle load was varied. The muscle was clamped at both ends, its length was fixed and noted. The muscle was tetanized isometrically by electrical stimulation. After quick release of the fixation the muscle shortened and the shorting velocity was measured.

In the past 30 years similar and advanced experiments were performed with single myocytes (table 1). Experiments with intact and skinned myocytes can be distinguished. Skinning of myocytes permits the direct control of the environment inside of the cells. A classical work was carried out by Fabiato and Fabiato [6], who measured the tension of skinned myocytes and its interdependencies with calcium release and re-sequestrations by the sarcoplasmic reticulum. A single skinned myocyte was located in a perfusion chamber with the two ends of the cell attached to glass micro-needles. One micro-needle was fixed, the other connected to the lever of a force transducer. Force as well as length and width of the cell were measured. Furthermore, a mean sarcomere length was determined. Several conclusions were drawn from these and subsequent measurements: Cellular tension is a direct effect of the concentration of free intracellular calcium. Tension is developed regardless deletion of the sarcoplasmic reticulum. A significant calcium sink exists in the cell, which was identified as the sarcoplasmic

**Table 1.** Force measurements of cardiac myocytes.

| Date | Publisher | Myocyte type | Species | Reference |
|---|---|---|---|---|
| 1975 | Fabiato, Fabiato | skinned ventricular | rat | [6] |
| 1977 | De Clerck, Claes, Brutsaert | - | rat | [7] |
| 1989/90 | Harrison, Bers | skinned ventricular | rabbit, frog, guinea pig, rat | [8] |
| 1993 | White, Guennec, Nigretto, Gannier, Argibay, Garnier | ventricular | guinea-pig | [9] |
| 1993 | Gannier, Bernengo, Jacquemond, Garnier | ventricular | guinea-pig | [10] |
| 1995 | White, Boyett, Orchard | ventricular | guinea-pig | [11] |
| 1995 | Bluhm, McCulloch, Lew | left ventricular | rabbit | [12] |
| 1998 | Brandt, Colomo, Piroddi, Pogessi, Tesi | skinned atrial and ventricular | frog | [13] |
| 1999 | O'Rourke, Kass, Tomaselli, Kaab, Tunin, Marbán | left ventricular | canine | [14] |
| 2001 | Yasuda, Sugiura, Kobayakawa, Fjita, Yamashita et al. | ventricular | rat | [15] |

reticulum. Physiologically, calcium is re-sequestrated in the sarcoplasmic reticulum after contraction. The release of calcium from the sarcoplasmic reticulum is triggered by concentration of free calcium. The amplitude of contraction is increased by increasing of the triggering concentration of free calcium.

### 3.2 Excitation-Contraction Coupling

A physiological initiation of tension development in the sarcomere is performed by an increase of the intracellular concentration of calcium subsequent to an electrical excitation of the myocyte. The calcium binds to troponin C resulting in shifting of the troponin-tropomyosin complex followed by structural changes of the tropomyosin-actin configuration [8]. The changes allow the binding of a myosin head to actin, the so-called cycling of cross bridges or actin-activated myosin II ATPase cycle (figure 1).

In absence of ATP the actin-myosin binding is arrested. By binding and hydrolysis of ATP the motor protein performs four steps:

- Binding of ATP to myosin head resulting in its unbinding from actin
- Rebinding of myosin head at adjacent actin while ATP hydrolysis
- Changing of the angle of myosin heads to neck and tails, whereby phosphate $P_i$ is released into the cytoplasm
- Unbinding of ADP from myosin and its release into the cytoplasm

If ATP is available, a binding to the myosin is occuring. If the calcium concentration is sufficiently large, the procedure can be repeated.

Different step lengths and tensions are reported for several types of myosin and myocytes. Step lengths, which are multiple of a minimal length, and back

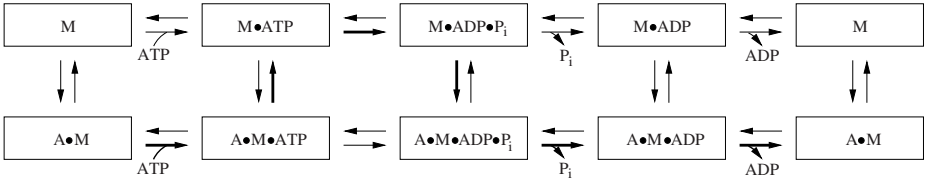


**Fig. 1.** States and transitions of actin-activated myosin II ATPase cycle (adapted from [8, 22]). M and A symbolize myosin and actin, respectively. ATP, ADP and $P_i$ represent adenosine triphosphate, adenosine diphosphate and phosphate, respectively. Arrows indicate possible transitions. Bold arrows signify the normal transitions. Closed circles indicate binding.

steps are reported in recent experimental works. For myosin II one up to five substeps per hydrolyzed ATP are performed by folding of the head-neck junction, whereby the multiple steps are still controversial and partly probably attributed to the measurement equipment [16]. Each folding of myosin II leads to substeps with a length of circa 5.3 $nm$ in direction of the actin filament [17] and a summary force of $1 - 5$ $pN$ [18].

Three different cooperativity mechanisms for force development are reported:

- cross-bridges increase affinity for binding of calcium to troponin C (XB-TN) [19]
- cross-bridges support the building of cross-bridges in the neighborhood (XB-XB) [20]
- shifting of tropomyosin leads to shifting of attached tropomyosins (TM-TM) [21]

### 3.3 Modeling of Tension Development

Of special interest for biophysically motivated modeling are descriptions of cellular tension development, which base on the concentration of intracellular calcium $[Ca_{2+}]_i$ delivered e.g. by electrophysiological cell models. The concentration $[Ca^{2+}]_i$ is used to define rate coefficients, which depict the interaction between states of actin and myosin. The state variables describe e.g. the binding of intracellular calcium to the troponin complex and the cross bridge cycling. Further parameters influencing the rate coefficients are the sarcomere length and the state variables.

*Hybrid model* The hybrid model combines a description of the binding of intracellular calcium $[Ca^{2+}]_i$ to troponin C, the configuration change of tropomyosin, and the interaction of actin and myosin [23]. The calcium binding to troponin C is similarly described as in the 3rd model of Rice et al. [24]. The interaction of actin and myosin is adopted from Gordon et al. [25], Bers et al. [8], and Spudich [22]. The cooperativity mechanisms XB-TN, XB-XB, and TM-TM are incorporated in the hybrid model.

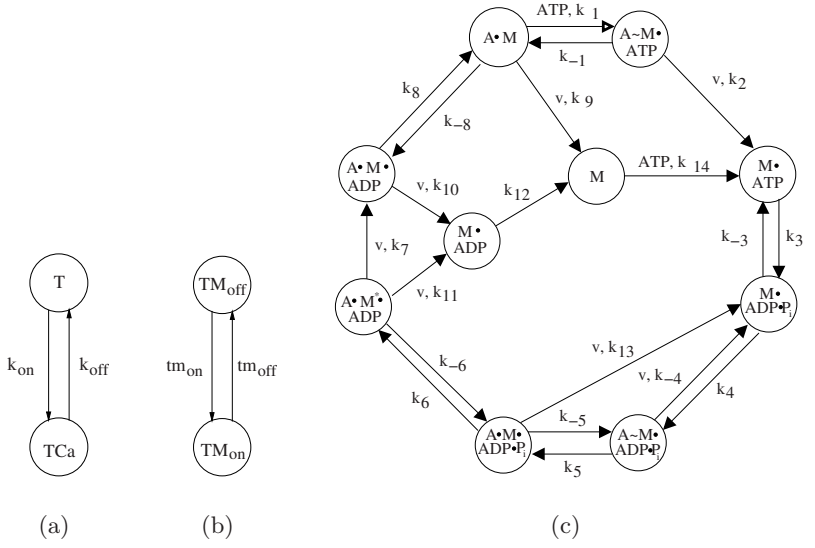


**Fig. 2.** State diagram of hybrid model. (a) Two state variables quantify the calcium binding to troponin C. (b) Two further state variables describe the configuration of tropomyosin. (c) Ten state variables detail the interaction of actin and myosin as well as the hydrolysis of adenosine triphosphate. M and A symbolize myosin and actin, respectively. ATP, ADP and $P_i$ represent adenosine triphosphate, adenosine diphosphate and phosphate, respectively. The transition between states is depicted by an arrow, strong binding by a closed circle, and weak binding by a tilde. The arrows are labeled with constants $k_x$, ATP and stretch velocity v, which are parameters of the rate coefficients functions.

The model uses 14 state variables, which are coupled by rate coefficients. Two state variables, $T$ and $TCa$, detail the binding of intracellular calcium $Ca^{2+}$ to troponin C (figure 2a). The state variable $T$ describes the normalized concentration of troponin C with no bound calcium, $TCa$ the normalized concentration of troponin C with bound calcium. The normalization leads to $T + TCa = 1$. Two further state variables, $TM_{on}$ and $TM_{off}$, quantify the configuration of tropomyosin (figure 2b). The state variable $TM_{on}$ describes the concentration of tropomyosin in permissive configuration, $TM_{off}$ the normalized concentration in non permissive. The normalization leads to $TM_{on} + TM_{off} = 1$. Ten state variables are used to quantify the interaction between actin and myosin, particularly the cross-bridge cycling (figure 2c). These variables describe normalized concentrations of myosin. The condition, that the variables sum up to 1, is used as normalization.

The power stroke is performed during transition from $A \bullet M \bullet ADP \bullet P_i$ to $A \bullet M^* \bullet ADP$. The normalized concentration of myosin strongly bound to actin $S_{A \bullet M}$ is quantified by:

$$S_{A \bullet M} = A \bullet M \bullet ADP \bullet P_i + A \bullet M^* \bullet ADP + A \bullet M \bullet ADP + A \bullet M$$

The interaction between the states of the model is described by a system of 1st order differential equations:

$$\frac{\partial}{\partial t}\begin{pmatrix} T \\ TCa \\ TM_{off} \\ TM_{on} \\ M \bullet ATP \\ M \bullet ADP \bullet P_i \\ A \sim M \bullet ADP \bullet P_i \\ A \bullet M \bullet ADP \bullet P_i \\ A \bullet M^* \bullet ADP \\ A \bullet M \bullet ADP \\ A \bullet M \\ A \sim M \bullet ATP \\ M \\ M \bullet ADP \end{pmatrix} = \boldsymbol{R} \begin{pmatrix} T \\ TCa \\ TM_{off} \\ TM_{on} \\ M \bullet ATP \\ M \bullet ADP \bullet P_i \\ A \sim M \bullet ADP \bullet P_i \\ A \bullet M \bullet ADP \bullet P_i \\ A \bullet M^* \bullet ADP \\ A \bullet M \bullet ADP \\ A \bullet M \\ A \sim M \bullet ATP \\ M \\ M \bullet ADP \end{pmatrix}$$

with the $14 \times 14$ matrix $\boldsymbol{R}$ consisting of rate coefficients. Partly, the rate coefficients are dependent on the sarcomere stretch velocity $v$, the sarcomere stretch $\lambda$ and the intracellular calcium concentration $[Ca^{2+}]_i$. The sum of force generating states $T_{AM}$ is given by:

$$T_{AM} = A \bullet M + A \bullet M \bullet ADP + A \bullet M^* \bullet ADP$$

The normalized force $F$ is determined by

$$F = \alpha \frac{T_{AM}}{F_{max}}$$

with the sarcomere overlap function $\alpha = \alpha(SL)$ and maximal force $F_{max}$, which are tissue and species specific.

## 4 Results and Discussion

### Static Simulation of Coupled Electro-mechanics

Results of static simulations with a combination of the Noble-Varghese-Kohl-Noble model of cellular electrophysiology and the hybrid model of force development are shown in figure 3. The binding of calcium to troponin C is managed by the hybrid model. The cytosolic concentration of calcium serves in conjunction with the sarcomere stretch as input parameter for the force model. Stretch dependent differences are found for transmembrane voltage, intracellular calcium concentration, and force. These difference can be attributed to stretch dependence of troponin C's affinity for free intracellular calcium. The differences of transmembrane voltage and intracellular calcium concentration are relatively small in comparison to the difference of force, which results significantly from the sarcomere overlap function $\alpha$.

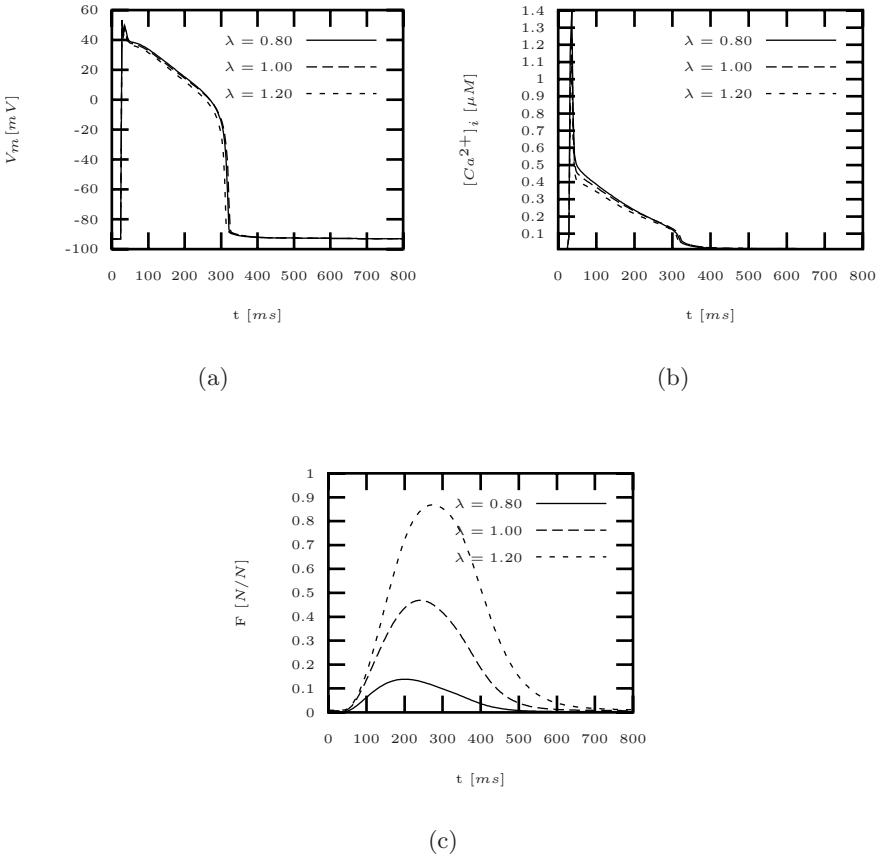


**Fig. 3.** Static simulation of coupled electro-mechanics in cardiac myocytes. (a) Transmembrane voltage, (b) intracellular calcium concentration $[Ca^{2+}]_i$, and (c) normalized force are reconstructed for different stretches $\lambda$. A stimulus current was applied at $t = 25\ ms$ to the electrophysiological model.

### Cooperativity Mechanisms

Cooperativity mechanisms are evaluated by simulations, whereby the calcium concentration was varied and a stretch of $\lambda = 1$ was applied. The simulations are performed with a combination of the Noble-Varghese-Kohl-Noble model of cellular electrophysiology and the hybrid model of force development. Results with and without incorperation of the mechanisms are shown in figure 4. The influence of the different cooperativity mechanisms is quantified by the Hill parameters $Ca_{50}$ and $N$. All mechanisms lead to a left shift and steepening of the calcium-force relationship, which is indicated by a decrease of the parameter $Ca_{50}$ and an increase of the parameter $N$.

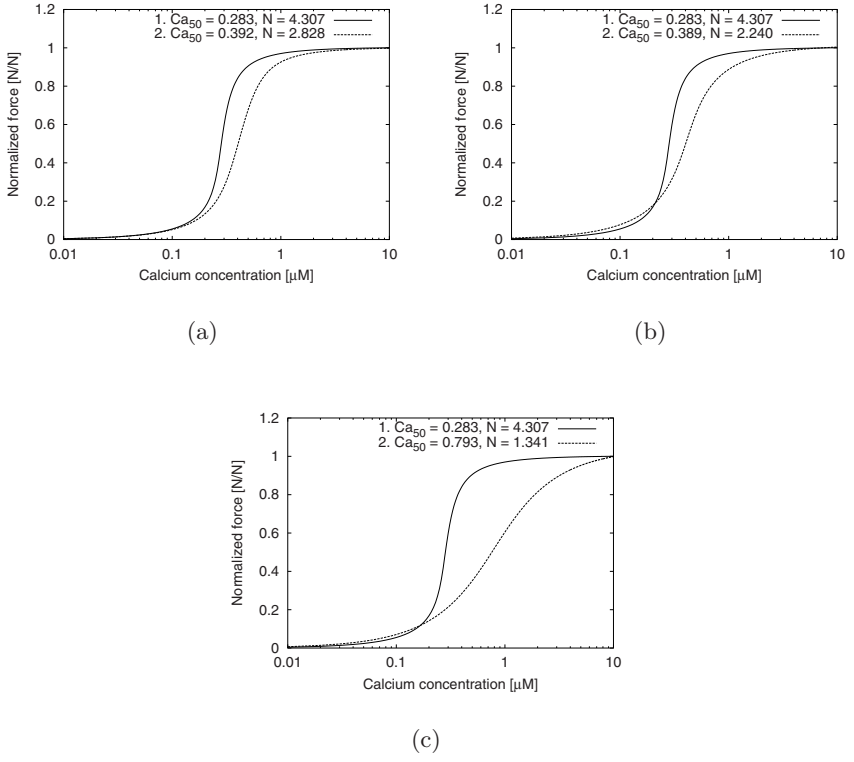


**Fig. 4.** Evaluation of cooperativity mechanisms (adapted from [23]). Simulations are performed (1) with and (2) without the mechanisms (a) XB-TN, (b) XB-XB, and (c) TM-TM. The Hill parameters $Ca_{50}$ and $N$ quantify the differences resulting from incorporating the different mechanisms.

## References

1. Bers, D.M.: Cardiac excitation-contraction coupling. Nature **415** (2002) 198–205
2. Sachse, F.B.: Modeling of the mammalian heart, Universität Karlsruhe (TH), Institut für Biomedizinische Technik (2002) Habilitationsschrift.
3. Noble, D., Varghese, A., Kohl, P., Noble, P.: Improved guinea-pig ventricular cell model incorporating a diadic space, $I_{Kr}$ and $I_{Ks}$, and length- and tension-dependend processes. Can. J. Cardiol. **14** (1998) 123–134
4. Noble, P.: -. personal communication (2000)
5. Hill, A.V.: The heat of shortening and the dynamic constants of muscle. Proc. R. Soc. Lond. **B126** (1938) 136–195
6. Fabiato, A., Fabiato, F.: Contractions induced by a calcium-triggered release of calcium for the sarcoplasmic reticulum of single skinned cardiac cells. J. Physiol. Lond. **249** (1975) 469–495
7. de Clerck, N.M., Claes, V.A., Brutsaert, D.L.: Force velocity relations of single cardiac muscle cells. J. Gen. Physiol. **69** (1977) 221–241

8. Bers, D.M.: Excitation-Contraction Coupling and Cardiac Contractile Force. Kluwer Academic Publishers, Dordrecht, Netherlands (1991)
9. White, E., Guennec, J.Y.L., Nigretto, J.M., Gannier, F., Argibay, J.A., Garnier, D.: The effects of increasing cell length on auxotonic contractions; membrane potential and intracellular calcium transients in single guinea-pig ventricular myocytes. Experimental Physiol. (1993) 65–78
10. Gannier, F., Bernengo, J.C., Jacquemond, V., Garnier, D.: Measurements of sarcomere dynamics simultaneously with auxotonic force in isolated cardiac cells. IEEE Transactions on Biomedical Engineering **40** (1993) 1226–1232
11. White, E., Boyett, M.R., Orchard, C.H.: The effects of mechanical loading and changes to length on single guinea-pig ventricular myocytes. J. Physiol. (1995) 93–107
12. Bluhm, W.F., McCulloch, A.D., Lew, W.Y.W.: Active force in rabbit ventricular myocytes. J. Biomechanics **28** (1995) 1119–1122
13. Brandt, P.W., Colomo, F., Piroddi, N., Poggesi, C., Tesi, C.: Force regulation by $Ca^{2+}$ in skinned single cardiac myocytes of frog. Biophys J **74** (1998) 1994–2004
14. O'Rourke, B., Kass, D.A., Tomaselli, G.F., Kaab, S., Tunin, R., Marbán, E.: Mechanisms of altered excitation-contraction coupling in canine tachycardia-induced heart failure, I experimental studies. Circ. Res **84(5)** (1999) 562–570
15. Yasuda, S., Sugiura, S., Kobayakawa, N., Fjita, H., Yamashita, H., Katoh, K., Seaki, Y., Kaneko, H., Suda, Y., Nagai, R., Sugi, H.: A novel method to study contraction characteristics of a single cardiac myocyte using carbon fibers. Am. J. Physiol. **281** (2001) H1442–H1446
16. Irving, M., Goldman, Y.E.: Another step ahead for myosin. Nature **398** (1999) 463–465
17. Kitamura, K., Tokunaga, M., Iwane, A.H., Yanagida, T.: A single myosin head moves along an actin filament with regular steps of 5.3 nanometeres. Nature **397** (1999) 129–134
18. Lodish, H., Berk, A., Zipursky, S.L., Matsudaira, P., Baltimore, D., Darneell, J.: Molekulare Zellbiologie. Spektrum Akademischer Verlag, Heidelberg, Berlin (2001)
19. Allen, D., Kurihara, S.: The effects of muscle length on intracellular calcium transients in mammalian cardiac muscle. J. Physiol. **327** (1982) 79–94
20. Nagashima, H., Asakura, S.: Studies on co-operative properties of tropomyosin-actin and tropomyosin-troponin-actin complexes by use of N-ethylmaleinide-treated and untreated species of myosin subfragment. J. Mol. Bio. **155** (1982) 409–428
21. Tobacman, L.: Thin filament mediated regulation of cardiac contraction. Ann. Rev. Physiol. **58** (1996) 447–481
22. Spudich, J.A.: TIMELINE: The myosin swinging cross-bridge model. Nature Reviews Molecular Cell Biology **2** (2001) 387–392
23. Glänzel, K.: Kraftentwicklung im Sarkomer unter Berücksichtigung elektromechanischer Kopplung. Diploma Thesis, Institut für Biomedizinische Technik, Universität Karlsruhe (TH) (2002)
24. Rice, J.J., Winslow, R.L., Hunter, W.C.: Comparison of putative cooperative mechanisms in cardiac muscle: length dependence and dynamic responses. Am. J. Physiol. Circ. Heart. **276** (1999) H1734–H1754
25. Gordon, A., Regnier, M., Homsher, E.: Skeletal and cardiac muscle contractile activation: Tropomyosin "rocks and rolls". News Physiol. Sci. **16** (2001) 49–55

# Simulating Cardiac Mechanoenergetics in the Left Ventricle

M. Vendelin[1], P.H.M. Bovendeerd[2], V. Saks[4], J. Engelbrecht[1], and T. Arts[2,3]

[1] Intitute of Cybernetics at Tallinn Technical University, Akadeemia 21
12618 Tallinn, Estonia
markov@ioc.ee
[2] Department of Biomedical Engineering, Eindhoven University of Technology
The Netherlands
[3] Cardiovascular Research Institute, Maastricht University, The Netherlands
[4] Laboratory of Fundamental and Applied Bioenergetics, INSERM E0221
Joseph Fourier University, Grenoble, France

**Abstract.** Distribution of myocardial perfusion and oxygen consumption within the cardiac wall is spatially heterogeneous. The cause of this heterogeneity is still unclear, but it is expected to be in close relation with the heterogeneity in mechanical function in the heart. In order to study the mechanical contraction and energy consumption by the cardiac wall, we developed a finite element model of the left ventricle with active properties described by the Huxley-type cross-bridge model. Here we present an overview of the developed model and the following simulation results obtained by the model. First, an important property of energy transformation from biochemical form to mechanical work in the cardiac muscle, the linear relationship between the oxygen consumption and the stress-strain area, is replicated by a cross-bridge model. Second, by using the developed cross-bridge model, the correlation between ejection fraction of the left ventricle and heterogeneity of sarcomere strain, developed stress and ATP consumption in the left ventricular wall is established. Third, an experimentally observed linear relationship between oxygen consumption and the pressure-volume area can be predicted theoretically from a linear relationship between the oxygen consumption and the stress-strain area.

## 1 Introduction

Myocardial perfusion within the cardiac wall is spatially heterogeneous, the relative dispersion (standard deviation divided by the mean) being about 25% [2]. The heterogeneity persists with changing workload [7, 15], but interindividually no consistent location of low and high flow regions has been found. Correlation between regional perfusion and energy consumption has been identified [10, 19], indicating heterogeneous distribution of energy consumption in the cardiac wall. The cause of the heterogeneity is still unclear, but a close relation with heterogeneity in mechanical function is expected [2, 19]. To study the relationships

I. Magnin et al. (Eds.): FIMH 2003, LNCS 2674, pp. 72–80, 2003.

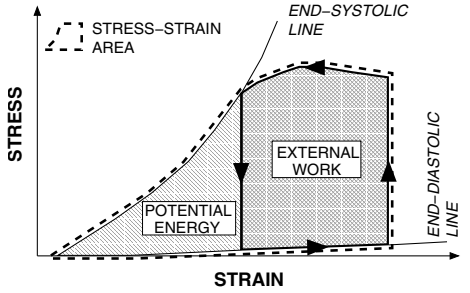


**Fig. 1.** A schematic representation of regional stress-strain trajectory loop during ejecting contraction. Stress-strain area (SSA) is the specific area in the stress-strain (SS) diagram surrounded by the end-systolic SS line, the end-diastolic SS line, and the systolic segment of the SS trajectory during ejection. According to the definition, SSA is the sum of external work and so-called "potential energy"

between mechanical contraction and oxygen consumption within the heart, models describing these aspects of heart physiology on tissue and left ventricle levels have been developed. Here, we give an overview of the developed models and present some results obtained in our simulations. All results have been published earlier [25, 26, 27].

## 2 Tissue Properties: Contraction of the Cardiac Muscle Fiber

Several models of muscle contraction exist, from phenomenological models that describe certain macroscopic properties of the muscle contraction [1, 13] to cross-bridge models which are often used to gain insight into the mechanisms of the muscle contraction. Actually, cross-bridge models include a phenomenological description as well, but at a finer level. The cross-bridge models have been used in cardiac muscle research for more than three decades to relate the development of the mechanical stress to ATP consumption by the muscle [22, 23, 29].

One important property of the cardiac muscle, which links the energy consumption of the muscle with mechanical output, is as follows. The oxygen consumption of the ventricle is linearly related to the pressure-volume area (PVA), the specific area in the pressure–volume (PV) diagram surrounded by the end-systolic PV line, the end-diastolic PV line, and the systolic segment of the PV trajectory for a contraction [21]. A similar relationship was identified at the tissue level — the oxygen consumption of the cardiac muscle per unit of tissue volume is linearly related to the stress-strain area (SSA, see Fig. 1), an analog of PVA [12]. To reproduce this property of cardiac muscle, we composed a model consisting of a three-state Huxley-type model for cross-bridge interaction and a phenomenological model of $Ca^{2+}$-induced activation [26]. Our model is based on the thermodynamic theory of the muscle contraction developed by

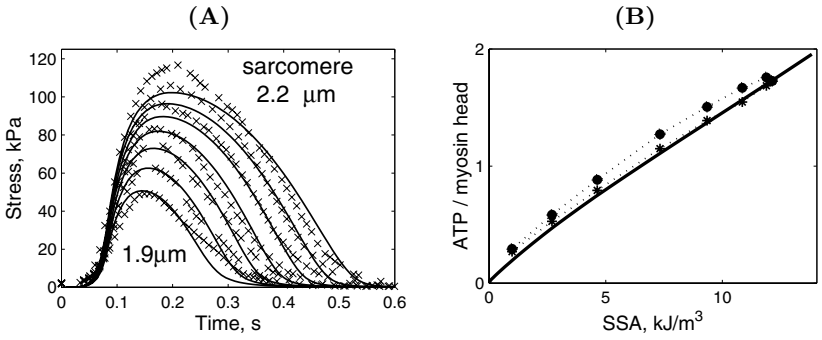


**Fig. 2.** Simulations performed with the Huxley-type model of cardiac muscle. Subplot A: Computed stress (solid lines) during the isometric contraction as a function of time at sarcomere length of 1.9, 1.95, 2.0, 2.05, 2.1, 2.15, and 2.2 $\mu$M. The simulation results are compared with the measurements (crosses) by Janssen and Hunter [14]. Subplot B: Total amount of consumed ATP molecules per myosin head during a cardiac cycle as a function of SSA for isometric (bold line) and two types of shortening contractions (thin dashed lines with dots and stars). Adapted from [26]

T.L. Hill and Eisenberg [8, 11]. The models, developed on the basis of this theory, take into account the free energy available from the hydrolysis of ATP, the amount of mechanical work performed by cross-bridges and the free energy of the different cross-bridge configurations. The studies performed with this type of models by Pate, Cooke, and White successfully reproduced several important aspects of skeletal muscle contraction including the influence of metabolite levels on the contraction [5, 17] and ATP consumption of rapidly contracting muscles [6].

To reproduce the linear oxygen consumption–SSA relationship, we used an approach which was different from what has been used earlier. Instead of computing ATP consumption using prescribed cross-bridge cycling rates as in Taylor et al. [22], Taylor et al. [23], we treated the linear relationship between ATP consumption and SSA as a fundamental property of the muscle and determined cross-bridge cycling rate constants and the activation parameters with which this macroscopical property of the muscle could be reproduced. When this approach was applied the following properties of the cardiac muscle were reproduced [26]: (a) the relationship between ATP consumption and SSA is linear, with contractile efficiency close to the measured one; (b) the computed isometric active stress during a beat replicates the measured stress in isosarcometric contractions at different sarcomere length values [14]; (c) the contraction duration is smaller in the isotonic case if compared with the isometric case, in agreement with isotonic contraction experiment results [4]; (d) the end-systolic point in the stress-strain diagram in isotonic contraction lies close to the end-systolic line computed for the isometric case [12]. The model was able to predict the following properties of the muscle: (a) the shortening velocity–afterload

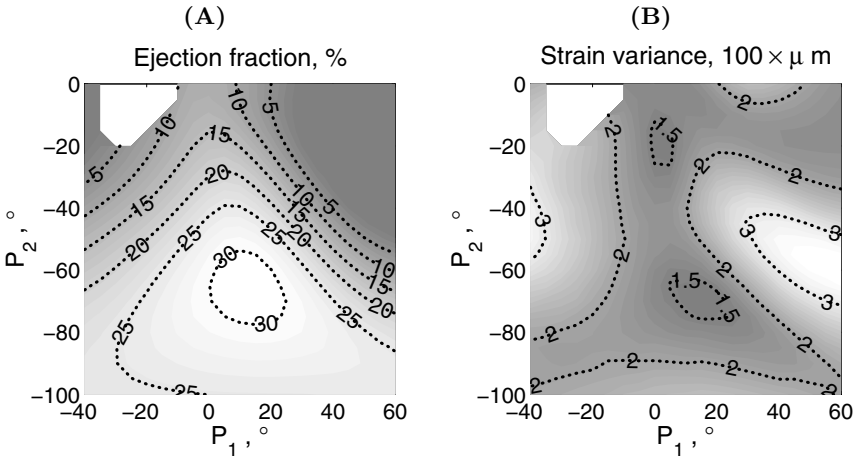


**Fig. 3.** The computed ejection fraction (subplot A) and variance of half-sarcomere length (subplot B) for the left ventricle at different helix fiber orientations. The helix fiber angle is quantified by angle value in the midwall ($P_1$) and the difference between values of the angle in the endocardial and epicardial surface ($2 \cdot P_2$). The mechanical activation was taken the same as electrical activation of the ventricle. Adapted from [26]

relationship at afterloads higher than 2.5 kPa [24]; (b) the drop of ATP consumption by the cross-bridges during a cycle by about 40% if the muscle is released at the time of peak force [12]. The computed ATP consumption–SSA relationship and stress development during isometric twitch is shown in Fig. 2. It is important to note, that the set of the parameters found by optimization may be not unique, as discussed in [26]. For example, one can find cross-bridge rates with different shapes and still obtain good results. In our work, we tried to find the rates with as simple shapes as possible to fit the desired data.

## 3 Simulations of Mechanoenergetic Properties of the Left Ventricle

A finite element model similar to [3] was developed with active properties described by the Huxley-type cross-bridge model [26]. The model computes the deformation of the ventricle, local strains, passive and active stress, and ATP consumption in the ventricular wall. The governing equations were discretized using the finite element method in conjunction with Galerkin's method. The fiber orientation was quantified by two angles: the helix fiber angle, describing the crossover of fibers between base and apex of the heart, and the transverse angle, describing the crossover of fibers between inner and outer layers of the

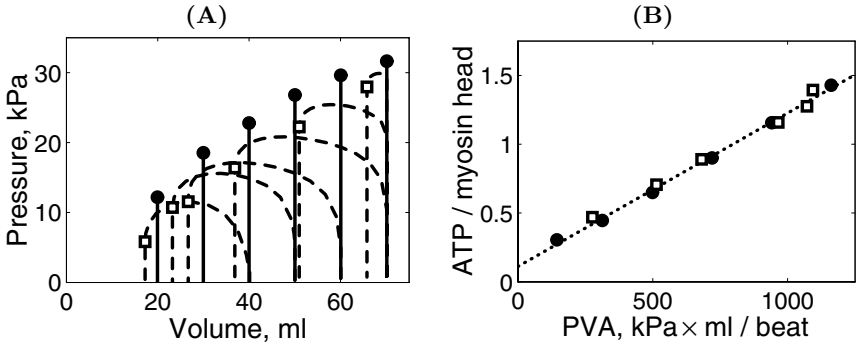


**Fig. 4.** Subplot A: The pressure-volume relationship computed for isovolumetric and ejecting contractions of the left ventricle. Subplot B: ATP consumption of the complete left ventricle as a function of the pressure-volume area (PVA) for isovolumetric (solid dots) and ejecting (open squares) contractions. Adapted from [26]

cardiac wall. According to our simulations [25], the variances of the sarcomere length, developed stress and ATP consumption during a beat have very similar dependencies on transmural course of the helix fiber angle. The optimal transverse angle value is also similar if the variance of the sarcomere length or developed stress is minimized. The dependency of sarcomere length, developed stress and ATP consumption variances on the helix fiber angle distribution is not simple: the variances have several minima at different helix fiber angle distributions. However, we identified only one region in the studied design space with a high ejection fraction of the left ventricle and relatively homogeneous distributions of sarcomere strain, developed stress and ATP consumption within the ventricular wall (see Fig. 3). This region corresponds to the physiological distribution of the helix fiber angle in the LV wall [16, 20]. From our analysis we concluded that if the fiber orientation is regulated by strain or stress distribution, the adaptation process should be stable and lead to the ventricles with high ejection fraction provided the difference between actual and optimal fiber orientation is relatively small.

Using our model [25], we reproduced a linear PVA–ATP consumption relationship (see Fig. 4). Since the tissue properties are described by a cross-bridge model [26] which produced a linear SSA–ATP consumption relationship, the measured PVA–ATP relationship can be expected. The computed ATP consumption distribution was similar to the distribution of oxygen consumption estimated from phosphocreatine (PCr)/ATP ratio measurements by NMR. According to the measurements, PCr/ATP ratio is slightly higher in the epicardial layer than in the endocardial layer and, with a midwall layer value between these two [9, 30]. From the available PCr/ATP ratio measurements, one can conclude that oxygen consumption in epicardial layers is lower than in endocardial layers. According to our simulations, the highest ATP consumption rate is

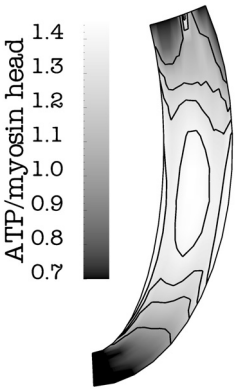


**Fig. 5.** ATP consumption distribution within the left ventricular wall during a heart beat predicted by the model. Adapted from [26]

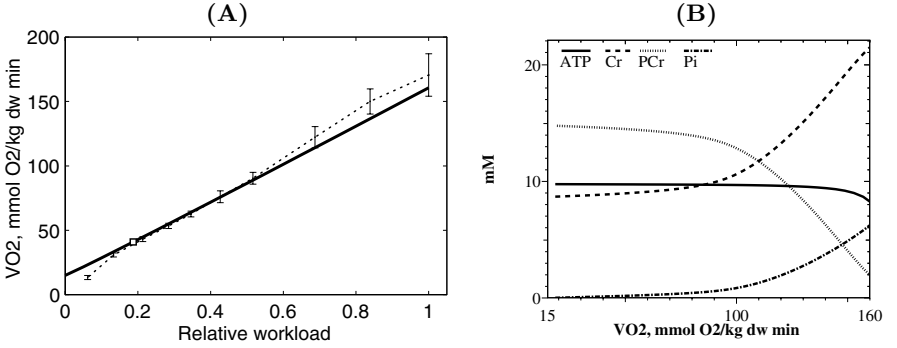


**Fig. 6.** Subplot A: Oxygen consumption is almost linearly related to ATPase activity (workload). Model simulation results (solid line) are compared with the measurements by Williamson et al. [28] (dashed line). Subplot B: Average ATP, PCr, Cr, and Pi levels over cardiac cycle at different workloads computed by the model. Adapted from [27]

between the midwall and endocardial layers and the smallest ATP consumption in sub-epicardial layer (see Fig. 5)

Predicted ATP consumption rates can be compared with the measured oxygen consumption distribution or NMR measurements of PCr/ATP ratio. Namely, assuming that ATP consumption by excitation-contraction coupling and basal metabolism is almost constant regardless of SSA in given contractile state [21] and taking into account the almost linear relationship between ATP and oxygen consumption (see Fig. 6A and [28]), it is possible to relate ATP consumption rate to the oxygen consumption by muscle. In addition, metabolite levels can be

estimated from the measurements (see [18] for overview) or using kinetic models of intracellular energy fluxes (see Fig. 6B and [27]).

## 4 Conclusions

We have developed the model which is able to predict distribution ATP consumption rate by the cross-bridges, regional stress and strain within the left ventricular wall. The model has been used to reproduce several important mechanoenergetic properties of the cardiac muscle and the left ventricle such as linear dependency of oxygen consumption on stress-strain area (tissue level) and on pressure-volume area (organ level). In addition, we identified the correlation between ejection fraction of the left ventricle and heterogeneity of sarcomere strain, developed stress and ATP consumption in the left ventricular wall.

## References

[1] T. Arts, P.C. Veenstra, and R.S. Reneman. Epicardial deformation and left ventricular wall mechanisms during ejection in the dog. *Am J Physiol*, 243 (3):H379–H390, 1982.

[2] J.B. Bassingthwaighte, D.A. Beard, and Z. Li. The mechanical and metabolic basis of myocardial blood flow heterogeneity. *Basic Res Cardiol*, 96(6):582–594, 2001.

[3] P.H.M. Bovendeerd, J.M. Huyghe, T. Arts, D.H. van Campen, and R.S. Reneman. Influence of endocardial-epicardial crossover of muscle fibers on left ventricular wall mechanics. *J Biomech*, 27(7):941–951, 1994.

[4] D.L. Brutsaert, N.M. de Clerck, M.A. Goethals, and P.R. Housmans. Relaxation of ventricular cardiac muscle. *J Physiol (Lond)*, 283:469–480, 1978.

[5] R. Cooke and E. Pate. The effects of adp and phosphate on the contraction of muscle fibers. *Biophys J*, 48(5):789–798, 1985.

[6] R. Cooke, H. White, and E. Pate. A model of the release of myosin heads from actin in rapidly contracting muscle fibers. *Biophys J*, 66(3 Pt 1): 778–788, 1994.

[7] A. Deussen, C.W. Flesche, T. Lauer, M. Sonntag, and J. Schrader. Spatial heterogeneity of blood flow in the dog heart. II. Temporal stability in response to adrenergic stimulation. *Pflugers Arch*, 432(3):451–461, 1996.

[8] E. Eisenberg and T.L. Hill. Muscle contraction and free energy transduction in biological systems. *Science*, 227(4690):999–1006, 1985.

[9] G. Gong, K. Ugurbil, and J. Zhang. Transmural metabolic heterogeneity at high cardiac work states. *Am J Physiol*, 277(1 Pt 2):H236–H242, 1999.

[10] A.B. Groeneveld, J.H. van Beek, and D.J. Alders. Assessing heterogeneous distribution of blood flow and metabolism in the heart. *Basic Res Cardiol*, 96(6):575–581, 2001.

[11] T.L. Hill. Theoretical formalism for the sliding filament model of contraction of striated muscle. Part I. *Prog Biophys Mol Biol*, 28:267–340, 1974.

[12] R. Hisano and G. Cooper. Correlation of force-length area with oxygen consumption in ferret papillary muscle. *Circ Res*, 61(3):318–328, 1987.
[13] P.J. Hunter, A.D. McCulloch, and H.E. ter Keurs. Modelling the mechanical properties of cardiac muscle. *Prog Biophys Mol Biol*, 69(2-3):289–331, 1998.
[14] P.M. Janssen and W.C. Hunter. Force, not sarcomere length, correlates with prolongation of isosarcometric contraction. *Am J Physiol*, 269(2 Pt 2):H676–H685, 1995.
[15] R.B. King, J.B. Bassingthwaighte, J.R. Hales, and L.B. Rowell. Stability of heterogeneity of myocardial blood flow in normal awake baboons. *Circ Res*, 57(2):285–295, 1985.
[16] P.M. Nielsen, I.J. Le Grice, B.H. Smaill, and P.J. Hunter. Mathematical model of geometry and fibrous structure of the heart. *Am J Physiol*, 260(4 Pt 2):H1365–H1378, 1991.
[17] E. Pate and R. Cooke. A model of crossbridge action: the effects of ATP, ADP and Pi. *J Muscle Res Cell Motil*, 10(3):181–196, 1989.
[18] V.A. Saks, Z.A. Khuchua, E.V. Vasilyeva, O.Y. u. Belikova, and A.V. Kuznetsov. Metabolic compartmentation and substrate channelling in muscle cells. role of coupled creatine kinases in in vivo regulation of cellular respiration – a synthesis. *Mol Cell Biochem*, 133-134:155–192, 1994.
[19] U. Schwanke, S. Cleveland, E. Gams, and J.D. Schipke. Correlation between heterogeneous myocardial flow and oxidative metabolism in normoxic and stunned myocardium. *Basic Res Cardiol*, 96(6):557–563, 2001.
[20] D.D. Streeter. Gross morphology and fiber geometry of the heart. In R.M. Berne, editor, *Handbook of physiology — The cardiovascular system I*, pages 61–122. Am. Physiol. Soc., Bethesda, MD, 1979.
[21] H. Suga. Ventricular energetics. *Physiol Rev*, 70(2):247–277, 1990.
[22] T.W. Taylor, Y. Goto, K. Hata, T. Takasago, A. Saeki, T. Nishioka, and H. Suga. Comparison of the cardiac force-time integral with energetics using a cardiac muscle model. *J Biomech*, 26(10):1217–1225, 1993.
[23] T.W. Taylor, Y. Goto, and H. Suga. Variable cross-bridge cycling-ATP coupling accounts for cardiac mechanoenergetics. *Am J Physiol*, 264(3 Pt 2):H994–1004, 1993.
[24] R. van Heuningen, W.H. Rijnsburger, and H.E. ter Keurs. Sarcomere length control in striated muscle. *Am J Physiol*, 242(3):H411–H420, 1982.
[25] M. Vendelin, P.H. Bovendeerd, J. Engelbrecht, and T. Arts. Optimizing ventricular fibers: uniform strain or stress, but not atp consumption, leads to high efficiency. *Am J Physiol Heart Circ Physiol*, 283(3):H1072–H1081, 2002.
[26] M. Vendelin, P.H.M. Bovendeerd, T. Arts, J. Engelbrecht, and D.H. van Campen. Cardiac mechanoenergetics replicated by cross-bridge model. *Ann Biomed Eng*, 28(6):629–640, 2000.
[27] M. Vendelin, O. Kongas, and V. Saks. Regulation of mitochondrial respiration in heart cells analyzed by reaction-diffusion model of energy transfer. *Am J Physiol Cell Physiol*, 278(4):C747–C764, 2000.
[28] J.R. Williamson, C. Ford, J. Illingworth, and B. Safer. Coordination of citric acid cycle activity with electron transport flux. *Circ. Res.*, 38(5 Suppl 1): I39–I51, 1976.

[29] A.Y. Wong. Mechanics of cardiac muscle, based on huxley's model: mathematical stimulation of isometric contraction. *J Biomech*, 4(6):529–540, 1971.

[30] J. Zhang and K.M. McDonald. Bioenergetic consequences of left ventricular remodeling. *Circulation*, 92(4):1011–1019, 1995.

# Towards Patient Specific Models of Cardiac Mechanics: A Sensitivity Study

Liesbeth Geerts[1], Roy Kerckhoffs[1], Peter Bovendeerd[1], and Theo Arts[1,2]

[1] Eindhoven University of Technology, PO Box 513, 5600 MB Eindhoven The Netherlands
[2] Maastricht University, PO Box 616, 6200 MD Maastricht, The Netherlands

**Abstract.** In the design of patient specific mathematical models of cardiac mechanics, the lack of patient specific input data leads to default settings of various model parameters. To estimate the potential errors thus introduced, we evaluated changes in predicted mechanics in a model of the left ventricle (LV) induced by changes in geometry, fiber orientation, heterogeneity of passive material behavior and triaxial active stress development.
Incorporation of measured heterogeneity of passive stiffness did not affect systolic mechanics. Incorporation of triaxial active stress development did significantly affect systolic mechanics, but knowledge on this mechanism is too limited to draw conclusions.
LV geometry variations covering the biological range changed the equatorial distribution of active myofiber stress and shortening by about 10 to 15%. Similar changes were found by variation of fiber orientation by 8° at maximum. Since this change in orientation is at the edge of the accuracy, with which myofiber orientation can be measured *in vitro*, and far below the accuracy, obtainable for *in vivo* measurements, we conclude that the benefit of accounting for patient specific geometry is questionable when using experimental data on fiber orientation. We propose to select myofiber orientation such, that myofiber load is distributed homogeneously across the cardiac wall.

## 1 Introduction

The pump function of the heart finds its origin in the contraction of the myofibers in the cardiac wall. The contribution of a myofiber to the cardiac pump function depends among others on the timing of its electrical activation, on the oxygen supplied through the coronary perfusion, on its intrinsic contractile properties, on its position and orientation in the cardiac wall, and on the mechanical load it experiences from its environment. The interplay between all contracting myofibers results in a three dimensional deformation of the cardiac wall, which can be assessed non invasively through Magnetic Resonance Tagging.

Cardiac pathologies, e.g. conduction disorders or regions of ischemia, may become manifest in abnormalities in the deformation pattern. Clinically, it would be desirable to be able to deduce the underlying pathology from deformation

I. Magnin et al. (Eds.): FIMH 2003, LNCS 2674, pp. 81–90, 2003.

abnormalities. Moreover, it would be interesting to know the associated abnormalities in the spatial distribution of myofiber stress and strain, since stress and strain are known to initiate tissue adaptation.

Mathematical models of cardiac mechanics can be used to perform this inverse analysis. In these models, the sensitivity of predicted cardiac deformation to the settings of the model parameters plays a crucial role. First, already in the healthy heart various model input parameters cannot be assessed directly and, consequently, one has to revert to default settings. It is important to know how sensitive model output is to errors in model input. Second, the sensitivity is needed in the inverse analysis, to guide an optimisation process in which the difference between measured and computed LV deformation is minimised.

In the present study we used an existing model of left ventricular wall mechanics [3,4] to investigate the sensitivity of the predicted myofiber stress and strain at the equator to changes in geometry, myofiber orientation, and material properties.

## 2 Methods

### 2.1 Description of the Model

In the model, the zero transmural pressure state in diastole was chosen as a reference. In this state, the LV endocardial and epicardial surfaces are approximated by truncated confocal ellipsoids (Fig. 1). The geometry is quantified by wall volume $V_w$, cavity volume $V_{cav}$, a common focal length of the ellipsoids $C$, and the height $h$, above the equator at which the ellipsoids are truncated. The ellipticity of the cavity $E_{cav}$, was defined as the ratio of the minor and major axis length of the inner ellipsoid.

Myofiber orientation in the reference state is quantified by the helix and transverse myofiber angles [16]. The helix angle, $\alpha_h$, was defined as the angle between the local circumferential direction and the projection of the myofiber direction on the plane normal to the local transmural direction. The transverse angle, $\alpha_t$, was defined as the angle between the local circumferential direction and the projection of the myofiber direction on the plane normal to the local long axis direction. Spatial variation of $\alpha_h$ and $\alpha_t$ over the myocardial wall is described as a function of a normalized transmural coordinate $\bar{\xi}$, and a normalized longitudinal coordinate $\bar{\theta}$ (Fig. 1). The helix angle is given by:

$$\alpha_h(\bar{\xi}, \bar{\theta}) = a_{h,0} + a_{h,1}\alpha_{h,ref}(\bar{\xi}, \bar{\theta}) \tag{1}$$

The setting of the reference distribution $\alpha_{h,ref}(\bar{\xi}, \bar{\theta})$ was taken from literature [13]. The coefficients $a_{h,0}$ and $a_{h,1}$ were introduced to enable change of slope and offset of $\alpha_h$ with respect to the reference setting. The setting of $\alpha_t(\bar{\xi}, \bar{\theta})$ was also adopted from literature [13].

Total Cauchy stress in the tissue is described as the sum of a passive component $\boldsymbol{\sigma}_p$, and an active component $\boldsymbol{\sigma}_a$. The passive Cauchy stress $\boldsymbol{\sigma}_p$ is derived from a strain energy function $W(\boldsymbol{E})$, composed of a transversely isotropic term

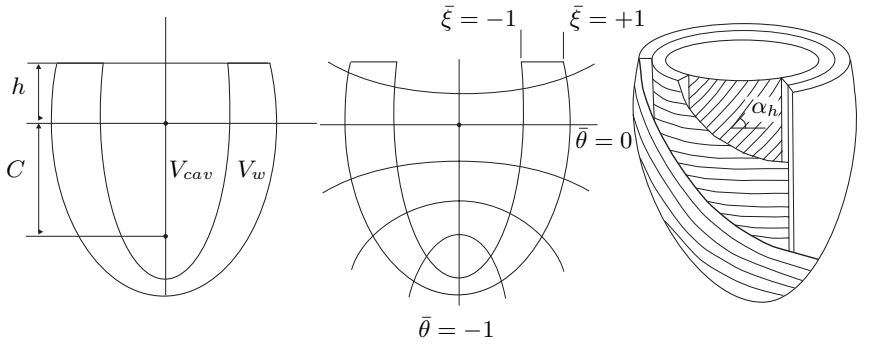


**Fig. 1.** Geometry and myofiber structure of the model of the left ventricle (LV); left: cross-section through the LV showing focal length $C$, truncation height above the equator $h$, wall volume $V_w$ and cavity volume $V_{cav}$; middle: cross-section through the LV showing normalized ellipsoid coordinates $\bar{\xi}$ and $\bar{\theta}$, the dotted lines indicate levels of constant $\bar{\theta}$; right: illustration of the helix angle, $\alpha_h$

$W_m$, associated with change in shape of the tissue, and an isotropic term $W_v$, associated with tissue volume change:

$$W(\boldsymbol{E}) = (a_{pas,0} + a_{pas,2}\,\xi^2)W_m(\boldsymbol{E}) + W_v(\boldsymbol{E}) \tag{2}$$

The expressions for $W_m$ and $W_v$ were taken from [20]. The function $a_{pas,0} + a_{pas,2}\,\xi^2$ was added to enable transmural variation of passive stiffness.

The active stress is modelled with an elastic element in series with a contractile element (see [3] for details). The first Piola Kirchhoff active stress $T_a$ is described as :

$$T_a = E_a T_{max}(l_s, l_c, t_s)(l_s - l_c) \tag{3}$$

with sarcomere length $l_s$, contractile element length $l_c$, time elapsed since activation $t_s$, and stiffness of the series elastic element $E_a T_{max}$. The function $T_{max}(l_s, l_c, t_s)$ was adopted from [3]:

$$T_{max} = T_1 f(l_c) g(t_s, l_s) \tag{4}$$

Here $T_1$ is a reference level of active stress, $f(l_c)$ describes the active stress-length relation, and $g(t_s, l_s)$ is related to force development during an isometric twitch, with stress decay depending on sarcomere length. The evolution of the contractile element length is described by:

$$\frac{dl_c}{dt} = (E_a(l_s - l_c) - 1)v_0 \tag{5}$$

The active stress tensor $\boldsymbol{\sigma}_a$ is described by:

$$\boldsymbol{\sigma}_a = T_a(l_s, l_c, t_s)\,(\lambda_f \boldsymbol{e}_f \boldsymbol{e}_f + a_{act}(\lambda_{cf1}\boldsymbol{e}_{cf1}\boldsymbol{e}_{cf1} + \lambda_{cf2}\boldsymbol{e}_{cf2}\boldsymbol{e}_{cf2})) \tag{6}$$

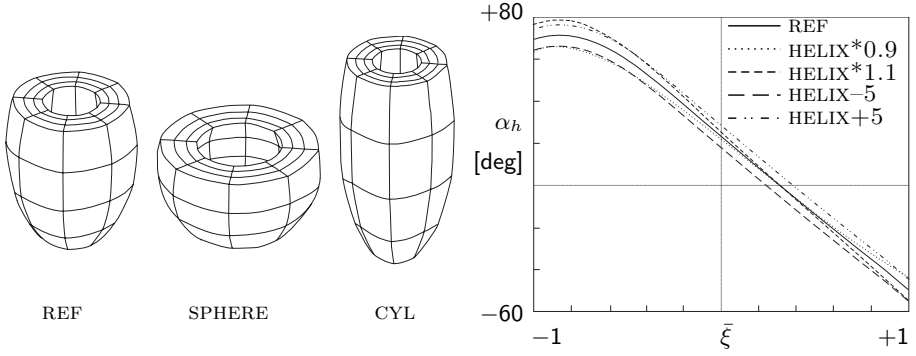


**Fig. 2.** Left: geometry variations; right: variation of the transmural course of the helix angle

where $\lambda_f$, $\lambda_{cf1}$ and $\lambda_{cf2}$ denote stretch ratios in myofiber and both cross-fiber directions. The factor $a_{act}$ enables stress development not only in the myofiber direction $\boldsymbol{e}_f$, but also in the cross fiber directions $\boldsymbol{e}_{cf1}$ and $\boldsymbol{e}_{cf2}$.

In the calculations, a complete cardiac cycle is simulated [3]. In each phase of the cycle, a uniform LV pressure is prescribed at the endocardium, while epicardial load equals zero. During diastolic filling, cavity pressure is prescribed to increase from 0 kPa to 1 kPa. The filling phase ends at $t = 200$ ms. At that moment, active stress development is initiated in all myofibers simultaneously. During isovolumic contraction, LV pressure is determined such, that it balances the increasing myofiber stress in the wall at a constant cavity volume. Ejection starts as soon as cavity pressure exceeds a prescribed pressure level, set at 10 kPa. During ejection, ventricular pressure and volume are determined from the interaction of the ventricle and the arterial system, simulated by an ideal aortic valve, in series with the aortic input impedance, represented by a 3 element Windkessel model [4,23]. The ejection phase ends as soon as the aortic flow becomes negative. During isovolumic relaxation, again cavity pressure is determined such that cavity volume remains constant.

Stresses and strains in the wall are determined from the equations of conservation of momentum. These equations were converted into a Galerkin-type finite element formulation, elaborated in triquadratic 27 node brick elements with three displacement components as nodal degrees of freedom. The left ventricular wall is represented by 108 elements. As a boundary condition, axial motion of all nodes in the basal plane and circumferential motion of four nodes in the endocardial basal ring are suppressed during the cardiac cycle.

### 2.2 Model Variations

In all models, $V_w$ and $V_{cav}$ were set to 140 ml and 40 ml, respectively. The base-to-equator distance $h$ was set to half the long axis of the endocardial ellipsoid. The reference model REF was defined setting $C = 43$ mm (yielding $E_{cav} = 0.35$),

$a_{h,1} = a_{pas,0} = 1$ and $a_{h,2} = a_{pas,2} = a_{act} = 0$. The effect of variation of geometry is studied in models SPHERE and CYL, obtained by variation of the focal distance $C$. The effect of variation of myofiber orientation is studied in models HELIX*1.1, HELIX*0.9, HELIX+5 and HELIX–5. The effect of variation of variation of material properties is studied in models HETER, mimicking the experimental observation that myocardial tissue stiffens near the endocardium and epicardium [11], and TRIAX incorporating the experimental finding of active stress development in cross-fiber direction [9,19]. Details of the models are shown in Fig. 2 and Table 1.

### 2.3 Presentation of Results

In each simulation, hemodynamics and spatial distribution of active myofiber stress and sarcomere length were calculated as a function of time during the cycle. For assessment of the effect of the model variations, we focussed on the transmural distribution active myofiber stress $s_a$, as averaged over time during the ejection phase, and sarcomere shortening $\Delta l_s$ during ejection. At the equatorial level, distributions $s_a$ and $\Delta l_s$ are characterized by the averages $\overline{s_a}$ and $\overline{\Delta l_s}$ and the coefficients of variation $cv(s_a) = SD(s_a)/\overline{s_a}$ and $cv(\Delta l_s) = SD(\Delta l_s)/\overline{\Delta l_s}$. For each model variation, the transmural change of $s_a$ and $\Delta l_s$ with respect to simulation REF is characterised in terms of the coefficients of a second order Legendre fit:

$$\begin{aligned} s_a(\bar{\xi}) - s_{a,ref}(\bar{\xi}) &\approx s_0 + s_1\bar{\xi} + s_2\,\tfrac{1}{2}(3\bar{\xi}^2 - 1) \\ \Delta l_s(\bar{\xi}) - \Delta l_{s,ref}(\bar{\xi}) &\approx d_0 + d_1\bar{\xi} + d_2\,\tfrac{1}{2}(3\bar{\xi}^2 - 1) \end{aligned} \tag{7}$$

It is noted that the coefficients $s_1$ and $d_1$ describe the redistribution of $\overline{s_a}$ and $\overline{\Delta l_s}$ between the subendocardial and subepicardial layers, while the coefficients $s_2$ and $d_2$ describe the redistribution between the midwall and superficial layers.

## 3 Results

Hemodynamics and sarcomere mechanics for simulation REF are shown in Fig. 3. Maximum LV pressure is 19.6 kPa, while stroke volume is 31.2 ml (Table 1). The time course of active myofiber stress and sarcomere length resembles that of LV pressure and volume, respectively. With a coefficient of variation of 4%, the transmural distribution of active myofiber stress is fairly homogeneous. The transmural distribution of sarcomere shortening has a coefficient of variation of 10% (Table 1). In subendocardial layers, shortening is larger than in subepicardial layers.

Due to a change of wall geometry, ventricular pump function is reduced in simulation SPHERE and remains virtually unaffected in simulation CYL. In both cases, the transmural distribution of active myofiber stress becomes less homogeneous. The difference is stress distribution with respect to simulation

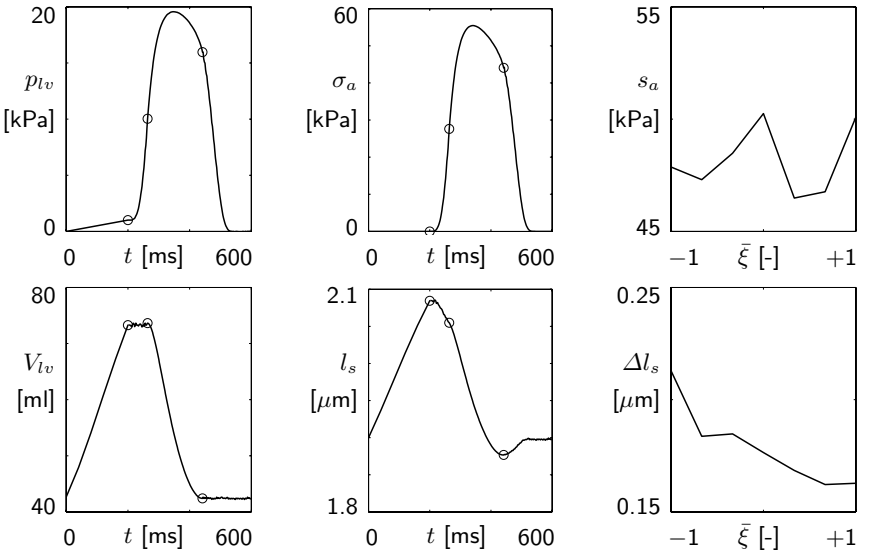


**Fig. 3.** Results from simulation REF: left: change of cavity pressure $p_{lv}$ and volume $V_{lv}$ as a function of time $t$, dots indicate transitions between the phases in the cycle; middle: temporal change of active myofiber stress $\sigma_a$ and sarcomere length $l_s$ at the equatorial midwall location; right: equatorial transmural variation of mean active myofiber stress during ejection $s_a$ and sarcomere shortening during election $\Delta l_s$

REF is characterised by $\|s_2\| > \|s_1\|$, indicating a redistribution between midwall and superficial layers. Midwall stress is increased in simulation SPHERE, and decreased in simulation CYL. Myofiber shortening becomes less homogeneous in simulation SPHERE, and more homogeneous in simulation CYL. With respect to simulation REF, shortening is redistributed between subendocardial and subepicardial layers. The transmural gradient of shortening becomes larger in simulation SPHERE, and is reduced in simulation CYL.

The changes in transmural distribution of the helix angle (simulations HELIX-5, HELIX+5, HELIX*1.1 and HELIX*0.9) hardly affect ventricular pump function. In all four cases, the transmural distribution of active myofiber stress becomes less homogeneous. The change in offset mainly affects the distribution of stress between subendocardial and subepicardial layers: a negative offset (simulation HELIX-5) promotes subendocardial stress while a positive offset (simulation HELIX+5) promotes subepicardial stress. Inhomogeneity of transmural distribution of myofiber shortening remains similar. Subendocardial shorting is increased in simulation HELIX-5 and decreased in simulation HELIX+5. The change in slope mainly affects the distribution of stress between midwall and superficial layers: increasing the slope (simulation HELIX*1.1) promotes midwall active stress, while a decrease of slope (simulation HELIX*0.9) has the opposite effect. Inhomogeneity of transmural myofiber shortening remains at the same level. The

**Table 1.** Simulation results: global cardiac function expressed in maximum LV pressure $p_{max}$ and stroke volume $V_{stroke}$; active equatorial myofiber stress averaged over the ejection phase, $s_a$, and sarcomere shortening during ejection $\Delta l_s$, represented by transmural averages ($\overline{s_a}$ and $\overline{\Delta l_s}$), coefficients of variation $cv(s_a)$ and $cv(\Delta l_s)$, and the coefficients of a Legendre polynomial fit $(s_1, s_2, d_1, d_2)$

| simulation | | hemodynamics | | active myofiber stress | | | | sarcomere shortening | | | |
|---|---|---|---|---|---|---|---|---|---|---|---|
| name | variation | $p_{max}$ [kPa] | $V_{stroke}$ [ml] | $\overline{s_a}$ [kPa] | $cv$ [%] | $s_1$ [kPa] | $s_2$ [kPa] | $\overline{\Delta l_s}$ [nm] | $cv$ [%] | $d_1$ [nm] | $d_2$ [nm] |
| REF | | 19.6 | 31.2 | 49.0 | 4 | – | – | 179 | 10 | – | – |
| SPHERE | $E_{cav} = 0.99$ | 17.7 | 24.5 | 44.1 | 14 | -1.5 | -9.0 | 172 | 25 | -37 | 5 |
| CYL | $E_{cav} = 0.20$ | 19.4 | 30.8 | 46.5 | 13 | -4.4 | 7.8 | 165 | 3 | 19 | -8 |
| HELIX–5 | $a_{h,0} = -5^\circ$ | 19.8 | 32.0 | 47.1 | 12 | -7.6 | -0.0 | 193 | 13 | -11 | -0 |
| HELIX+5 | $a_{h,0} = +5^\circ$ | 19.0 | 29.5 | 50.4 | 13 | 8.6 | 1.8 | 161 | 9 | 7 | -0 |
| HELIX*0.9 | $a_{h,1} = 0.9$ | 19.3 | 30.2 | 48.8 | 12 | -2.7 | 8.4 | 175 | 14 | -9 | 9 |
| HELIX*1.1 | $a_{h,1} = 1.1$ | 19.5 | 31.0 | 48.4 | 12 | 2.9 | -8.7 | 173 | 8 | 10 | -12 |
| TRIAX | $a_{act} = 0.4$ | 20.2 | 29.5 | 29.3 | 10 | -0.5 | -6.2 | 249 | 8 | 4 | -19 |
| HETER | $a_{pas,0} = 0.9$ $a_{pas,2} = 0.3$ | 19.7 | 31.5 | 49.6 | 4 | 0.1 | 0.0 | 179 | 10 | -2 | 0 |

redistribution of transmural myofiber shortening does not show a clear endo-epicardial of midwall-superficial pattern.

Incorporation of cross-fiber active stress development (simulation TRIAX), hardly affects ventricular pump function. Myofiber mechanics is strongly affected: with respect to simulation REF active stress in the myofiber direction decreases by about 40%, while myofiber shortening increases by about 40%. These changes are fairly evenly distributed across the wall, as indicated by the level inhomogeneity of about 10%. Still, myofiber stress and shortening increase in the midwall layers, and decrease in the subendo- and subepicardial layers.

Making the midwall tissue less stiff than the subendo- and subepicardial tissue (simulation HETER) has virtually no effect on ventricular pump function and wall mechanics.

## 4 Discussion

In the design of patient specific mathematical models of cardiac mechanics, the lack of patient specific input data leads to default settings of various model parameters. To estimate the potential errors thus introduced, in a model of LV mechanics we evaluated changes in predicted mechanics, induced by changes in geometry and myofiber orientation, and passive and active material behaviour.

The variations of geometry used in our simulations, with $E_{cav}$ ranging from 0.2 to 0.99, are considered to span the complete range of geometries, observed in

man. In healthy subjects, the shape parameter of the left ventricle is typically on the order of $E_{cav}$=0.35 [16]. In patients however, several pathologies have been identified for which left ventricular shape is significantly different from normal. In patients with idiopathic dilated cardiomyopathy for example, left ventricular geometry has been reported to be more spherical, with shape parameter $E_{cav}$ on the order of 0.64 [2]. Furthermore, patients with mitral regurgitation have been found to have more spherical chamber geometry both in systole and diastole [6,22]. More cylindrically shaped hearts have been reported in chronic aortic regurgitation [1].

The variations in myofiber orientation are 5° in simulations HELIX+5 and HELIX-5, and 8° at maximum in simulations HELIX*0.9 and HELIX*1.1. These variations are low as compared to the variation in reported experimental data on the helix angle [3], and just at the level of accuracy, with which myofiber orientation can be measured *in vitro*, using MRI Diffusion Tensor Imaging [5,7, 8,15]. Measurement*in vivo* is less accurate and limited to low resolution [12,17, 18].

Thus, our results indicate that variation of the geometry across the complete range of geometries, observed in man, affects the transmural distribution of myofiber stress and shortening at the equatorial level to the same extent as variation of the helix angle at the level of the *in vitro* accuracy of state-of-the-art measurement techniques.

The high sensitivity of LV wall mechanics to a parameter, myofiber orientation, that cannot be measured with sufficient accuracy, has led us to an inverse approach. For the normal LV, we optimized myofiber orientation such that heterogeneity in the distribution of active myofiber stress and shortening was minimized. The resulting orientation was within the range of reported experimental data [13,14,21]. This orientation was also used in simulation REF. The optimization strategy could also be adopted for hearts with patient specific geometries. The present simulations indicate that more spherical hearts would require a positive offset of the transmural distribution of the helix angle. For more cylindrical hearts, a negative offset would be required.

The physiological mechanism by which homogeneity of myofiber load is obtained might lie in small, random variations of the orientation of individual myofibers. Reorientation could be caused by a continuous process of creation and break down of the connections between the cell and its environment, a process has been shown to exist in the borderzone of rat myocardial infarcts [10]. In this process, the orientation which is, in some sense, optimal for the myofiber would statistically be most prevalent. The assumption that myofibers strive for the same optimum load, regardless of their position in the cardiac wall, then leads to the conclusion that heterogeneity of myofiber load is minimized.

Although development of active stress perpendicular to the myofiber direction has been experimentally measured [9], the underlying mechanism remains unclear. The implementation of triaxial stress development in simulation TRIAX was adopted from literature [19] and must be regarded as a best guess, considering the available data. The combination of increased contractile capacity and an

unchanged LV afterload was found to increase myofiber shortening and decrease myofiber stress.

The transmural variation of passive stiffness was based on experimental data [11]. The variation in stiffness is on the order of 30% and will lead to passive stress variations of a similar magnitude. Still, during systole levels of active myofiber stress are much larger than those of passive stress. This explains why systolic LV mechanics is hardly affected in simulation HETER.

## 5 Conclusion

LV geometry variations covering the biological range change the equatorial distribution of active myofiber stress and shortening by about 10 to 15%. Similar changes are found by variation of fiber orientation by 8° at maximum. Since this change in orientation is at the edge of the accuracy, with which myofiber orientation can be measured *in vitro*, and far below the accuracy, obtainable for *in vivo* measurements, we conclude that the benefit of accounting for patient specific geometry is questionable when using experimental data on fiber orientation. We propose to select myofiber orientation such, that myofiber load is distributed homogeneously across the cardiac wall.

## References

1. A.M. Abdulla, M.J. Frank, M.I. Canedo, and M.A. Stefadouros. Limitations of echocardiography in the assessment of left ventricular size and function in aortic regurgitation. *Circulation*, 61:148–155, 1980.
2. E.A. Bocchi, L.F. Moreira, A.V. de Moraes, G. Bellotti, M. Gama, N.A.G. Stolf, A.D. Jatene, and F. Pileggi. Effects of dynamic cadiomyoplasty on regional wall motion, ejection fraction and geometry of the left ventricle. *Circulation*, 86, supp II:II231–II235, 1992.
3. P.H.M. Bovendeerd, T. Arts, J.M. Huyghe, D.H. van Campen, and R.S. Reneman. Dependence of local left ventricular wall mechanics on myocardial fiber orientation: A model study. *J Biomech.*, 25:1129–1140, 1992.
4. P.H.M. Bovendeerd, J.M. Huyghe, T. Arts, D.H. van Campen, and R.S. Reneman. Influence of endocardial-epicardial crossover of muscle fibers on left ventricular wall mechanics. *J Biomech.*, 27:941–951, 1994.
5. L. Geerts, P.H.M. Bovendeerd, K. Nicolay, and T. Arts. Characterization of the normal cardiac myofiber field in goat measured with MR diffusion tensor imaging. *Am. J. Physiol.*, 283, H126–H138, 2002.
6. J.J. Gomez-Doblas, J. Schor, P. Vignola, D. Weinberg, E. Traad, R. Carrillo, D. Williams, and G.A. Lamas. Left ventricular geometry and operative mortality in patients undergoing mitral valve replacement. *Clin Cardiol*, 24:717–722, 2001.
7. J.W. Holmes, D.F. Scollan, and R.L. Winslow. Direct histological validation of diffusion tensor mri in formaldehyde-fixed myocardium. *Magn Reson Med.*, 44:157–161, 2000.
8. E.W. Hsu, A.L. Muzikant, S.A. Matulevicius, R.C. Penland, and C.S. Henriques. Magnetic resonance myocardial fiber-orientation mapping with direct histological correlation. *Am J Physiol.*, 274:H1627–H1634, 1998.

9. D.H.S. Lin and F.C.P. Yin. A multiaxial constitutive law for mammalian left ventricular myocardium in steady-state barium contracture or tetanus. *J Biomech Eng.*, 120:504–517, 1998.
10. T. Matsushita, M. Oyamada, K. Fujimoto, Y. Yasuda, S. Masuda, Y. Wada, T. Oka and, T. Takamatsu. Remodeling of cell-cell and cell-extracellular matrix interactions at the borderzone of rat myocardial infarcts. *Circ Res.*, 85:1046–1055, 1999.
11. V.P. Novak, F.C.P. Yin, and J.D. Humphrey. Regional and mechanical properties of passive myocardium. *J Biomech.*, 27:403–412, 1994.
12. T.G. Reese, R.M. Weisskoff, R.N. Smith, B.R. Rosen, R.E. Dinsmore, and V.J. Wedeen. Imaging myocardial fiber architecture in vivo with magnetic resonance. *Magn Reson Med.*, 34:786–791, 1995.
13. J. Rijcken, P.H.M. Bovendeerd, A.J.G. Schoofs, D.H. van Campen, and T. Arts. Optimization of cardiac fiber orientation for homogeneous fiber strain at beginning of ejection. *J Biomech.*, 30:1041–1049, 1997.
14. J. Rijcken, P.H.M. Bovendeerd, A.J.G. Schoofs, D.H. van Campen, and T. Arts. Optimization of cardiac fiber orientation for homogeneous fiber strain during ejection. *Ann Biomed Eng.*, 27:289–297, 1999.
15. D.F. Scollan, A. Holmes, R. Winslow, and J. Forder. Histological validation of myocardial microstructure obtained from diffusion tensor magnetic resonance imaging. *Am J Physiol.*, 275:H2308–H2318, 1998.
16. D.D. Streeter. Gross morphology and fiber geometry of the heart. In R.M.Berne, editor, *Handbook of physiology – The Cardiovascular system I.* American physiological society, 1979.
17. W.-Y.I. Tseng, T.G. Reese, R.M. Weisskoff, T.J. Brady, and V.J. Wedeen. Myocardial fiber shortening in humans: Initial results of MR imaging. *Radiology*, 216:128–139, 2000.
18. W.-Y.I. Tseng, T.G. Reese, R.M. Weisskoff, and V.J. Wedeen. Cardiac diffusion tensor MRI in vivo without strain correction. *Magn Reson Med.*, 42:393–403, 1999.
19. T.P. Usyk, R. Mazhari, and A.D. McCulloch. Effect of laminar orthotropic myofiber architecture on regional stress and strain in the canine left ventricle. *J. Elast.*, 61:143–164, 2000.
20. M. Vendelin, P.H.M. Bovendeerd, T. Arts, J. Engelbrecht, and D.H. van Campen. Cardiac mechanoenergetics replicated by cross-bridge model. *Ann Biomed Eng.*, 28:629–640, 2000.
21. M. Vendelin, P.H.M. Bovendeerd, J. Engelbrecht, and T. Arts. Optimizing ventricular fibers: uniform strain or stress, but not ATP consumption, leads to high efficiency. *Am. J. Physiol.*, 283:H1072–H1081, 2002.
22. P.S. Vokonas, R. Gorlin, P.F. Crhon, M.V. Herman, and E.H. Sonnenblick. Dynamic geometry of the left ventricle in mitral regurgitation. *Circulation*, 48:786–795, 1973.
23. N. Westerhof, G. Elzinga, and G.C. van den Bos. Influence of central and peripherical changes on the hydraulic input impedance of the systemic arterial tree. *Med Biol Eng.*, 11:710–723, 1973.

# Does the Collagen Network Contribute to Normal Systolic Left Ventricular Wall Thickening? A Theoretical Study in Continuum Mechanics

Jacques Ohayon[1], Christian Bourdarias[2], and Stéphane Gerbi[2]

[1] Laboratoire TIMC-IMAG, Equipe DynaCell, Domaine de la Merci
38706 Grenoble cedex, France
Jacques.Ohayon@imag.fr
http://timc.imag.fr/dynacell
[2] Université de Savoie, LAMA, 73376 Le Bourget-du-Lac, France

**Abstract.** Studies in mammalian hearts shown that left ventricular wall thickening is an important mechanism for normal systolic ejection, and that during contraction the myocardium develops a significant stress in the muscular cross-fiber direction. We suggested that the collagen network surrounding the muscular fibers could account for these two mechanical behaviors. To test this hypothesis, we developed a mathematical model for a large deformation response of an active, incompressible, hyperelastic and transversely isotropic cardiac tissue, in which we included a coupling effect between the connective tissue and the muscular fibers. The three-dimensional constitutive law containing this internal pseudo-active kinematic constraint is derived and applied to obtain solutions for the cases of a free contraction, uniaxial and equibiaxial extensions of a rectangular sample assuming negligible body forces and inertia effects. This model may explain the contribution of the collagen network to the two following mechanics: (i) the normal systolic wall thickening, and (ii) the developed pseudo-active tension in the cross-fiber direction.

## 1 Introduction

It is known, that the transverse shear along myocardial cleavage planes provides a mechanism for a normal systolic wall thickening [5]. Indirect evidences indicate that the characteristics of the passive extracellular connective tissue in the myocardium is an important determinant of ventricular function ([6], [10], [3]). An appropriate constitutive law for the myocardium should therefore incorporate the most important features of its microstructure. A sound theoretical formulation for material laws of the active myocardium is essential for an accurate mechanical analysis of the stresses in the ventricular wall during the whole cardiac cycle. The wall stress distribution is one of the main factors governing the myocardial energetic [11], the coronary blood flow [2], the cardiac hypertrophy [10], and the fetal heart growth [7]. To date we do not have any reliable technique

I. Magnin et al. (Eds.): FIMH 2003, LNCS 2674, pp. 91–100, 2003.

to evaluate the stress in the cardiac muscle, therefore, mechanical models are useful in cardiology to assess the functional capacities of the human heart. Several numerical models using a finite element (FE) analysis have been performed to simulate the left ventricular performance ([4], [13]). The mechanical behavior of the connective tissue is often assumed isotropic [8]. This last assumption is not in agreement with the experimental results obtained on a sample of active myocardial rabbit tissue. Lin and Yin [6] showed that, during an active equibiaxial stretch test, there are significant stresses developed in the cross-fiber direction (more than 40% of those in the fiber direction) that cannot be attributed to nonparallel muscle fibers (MF).

Therefore, the purpose of this paper is to suggest a realistic pseudo-active kinematic law coupling the passive connective tissue to the active MF, which may explain the contribution of the collagen network to the two following mechanisms: (i) the normal systolic wall thickening, and (ii) the developed pseudo-active tension in the cross-fiber direction. The three-dimensional constitutive law including this coupling effect, and considering the myocardium as an incompressible hyperelastic material is presented. Futhermore, the proposed constitutive law for living tissue was applied to simple cases as, free contraction, uniaxial and equibiaxial extensions of a rectangular sample assuming negligible body forces and inertia effects.

## 2 Microstructure of the Cardiac Tissue

### 2.1 Muscle Fiber Organization

Anatomical observations have shown that the cardiac muscle tissue has a highly specialized architecture [12]. This structure is composed primarily of cardiac muscle cells, or myocytes that are 80 to 100 $\mu$m in length and are roughly cylindrical with cross-sectional dimensions of 10 to 20 $\mu$m. These cells are arranged in a more or less parallel weave that we idealize as "muscle fibers" (MF). We shall denote the local direction of this group of cells by the unit vector $\mathbf{f}$ and refer to it also as the local "fiber" direction with the understanding that individual continuous MF do not really exist. Experimental measurements have shown that the MF direction field defines paths on a nested family or toroidal surfaces of revolution in the wall of the heart [12]. These results show a continuously changing orientation $\mathbf{f}$ of the MF through the wall, circumferential near the midwall and progressively more inclined with respect to the equatorial plane when moving toward either the epicardium or the endocardium.

### 2.2 The Cardiac Connective Tissue Organization

Myocytes and coronary blood vessels are embedded in a complex extracellular matrix which consists of collagen and elastin, mainly. Caulfield and Janicki [1] used the scanning electron microscope (SEM) to reveal the basic organization of this connective tissue network. Their studies on the connective tissue of mammalian heart muscle give the description of the extracellular structures and their

arrangement relative to cardiac muscle cells. They described the three following classes of connective tissue organization: (i) interconnections between myocytes, (ii) connections between myocytes and capillaries and, (iii) a collagen weave surrounding group of myocytes. When viewed by SEM, groups of myocytes can be seen to be encompassed by a rather prominent meshwork of fibrillard collagen, and short collagen struts attach the myocytes subjacent to this meshwork to it.

## 3 Constitutive Law in Continuum Mechanics

### 3.1 Coupling between Muscle Fibers and Collagen Network

Extrapolations from the MF arrangement to the myocardial stress are realistic if we take into account the effect of the connective tissue. Based on the previous SEM observations, we proposed a connective tissue organization illustrated in Fig. 1. We assume that the MF are roughly cylindrical, and that two adjacent MF running on the tangential plane of the ventricular wall are surrounded by inextensible collagen bundles. So, during the contraction, the MF diameter increases and because the collagen bundles are inextensible, the adjacent MF become closer. Thus, the pseudo-active kinematic relationship between the extension ratios in the fiber and cross-fiber directions (noted $\lambda_f$ and $\lambda_{cf}$=D'/D, respectively (see Fig.1) is given by $h(\lambda_f, \lambda_{cf}) = 0$ with:

$$h(\lambda_f, \lambda_{cf}) = 1 - \lambda_{cf} + (\pi - 2)(1 - \lambda_f^{-1/2})\frac{a}{D} \tag{1}$$

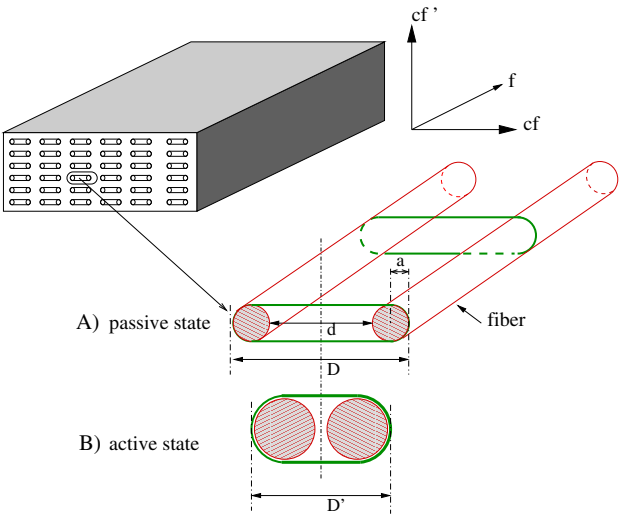


**Fig. 1.** Schematic illustrations of the sample of myocardium and the internal pseudo-active kinematic constraint induced by the collagen network surrounding the muscle fibers. A) Before contraction (or passive state). B) After or during contraction (or active state)

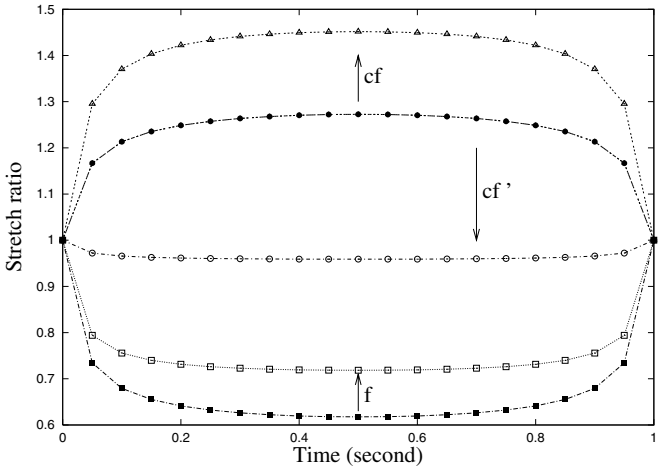


**Fig. 2.** Free contraction test with $\beta(t) = sin^2(\pi t)$: effect of the pseudo-active kinematic constraint. The empty and full symbols indicate that the coupling effect is acting or not, respectively. The fiber and cross-fiber directions are noted (f), (cf) and (cf ') and are defined in Fig. 1. Arrows show the curve modification when the pseudo-active kinematic constraint behaves

where $D = 4a + d$ in which $a$ is the initial MF radius and $d$ is the distance between the two adjacent MF.

### 3.2 Myocardium under Internal Pseudo-Active Kinematic Constraint

To be consistent with our mathematical formulation, the letter $\Phi$ is used for the non elastic gradient tensor and the letter $\mathbf{F}$ is used for the elastic gradient tensor. The activation of the MF changes the properties of the material and at the same time contracts the muscle itself. To have a continuous elastic description during the activation of the tissue, we used an approach similar to the one proposed by Taber [9], Lin and Yin [6]. From its passive state with zero residual stress $P$, the free activation of the muscle fibers is modelised by the following two transformations (Fig. 3): the first one (from state $P$ to virtual state $A_0$) changes the material properties without changing the geometry, and the second one (from $A_0$ to $A$) contracts the muscle without changing the properties of the material. Thus, the former is not an elastic deformation and is described by the gradient tensor $\Phi_{PA_0} = \mathbf{I}$ where $\mathbf{I}$ is the identity matrix. In that first transformation, only the strain energy function is modified using an activation function $\beta(t)$, where $t$ is the cardiac cycle time. The second transformation is an elastic deformation caused only by the active tension delivered by the fibers, and takes care of the internal kinematic constraint (Eq.(1)). This last transformation is described by the gradient tensor $\mathbf{F}_{A_0A}$. Thus the transformation from state $P$ to state $A$ is a non elastic transformation ($\Phi_{PA} = \Phi_{PA_0}\mathbf{F}_{A_0A}$), but can be

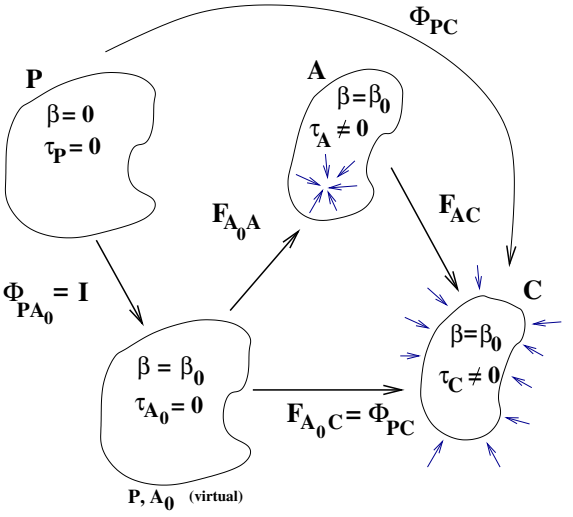


**Fig. 3.** Description of the active rheology in continuum mechanics (see text for more details)

treated mathematically as an elastic one because $\Phi_{PA} = \mathbf{F}_{A_0A}$. Finally, external loads are applied to state $A$ deforming the body through into $C$ (Fig. 3). The change of the material properties of the myocardium during the cardiac cycle is described by a time-dependent strain-energy function per unit volume of state $P$ noted $W(\mathbf{E}_{PH}, t)$:

$$W(\mathbf{E}_{PH}) = -\tfrac{1}{2}\, p_H(I_3(\mathbf{E}_{PH}) - 1) + W^*(\mathbf{E}_{PH}) + \delta_{AH}\, W_{\substack{pseudo\\active}}(\mathbf{E}_{PH}) \qquad (2)$$

$$\text{with} \qquad W^*(\mathbf{E}_{PH}) = W_{pas}(\mathbf{E}_{PH}) + \beta(t)\, W_{act}(\mathbf{E}_{PH}) \qquad (3)$$

where $\mathbf{E}_{PH}$ is the Green's strain tensor at an arbitrary state $H$ calculated from the zero-stress state $P$ (the state $H$ could be one of the states $A_0$, $A$ or $C$ shown in Fig. 3), $p_H$ is the Lagrangian multiplier resulting of the incompressibility condition $I_3(\mathbf{E}_{PH}) = \det \mathbf{C}_{PH} = 1$, where $\mathbf{C}_{PH}$ is the right Cauchy-Green strain tensor ($\mathbf{C}_{PH} = 2\mathbf{E}_{PH} + \mathbf{I}$), $W_{pas}$ represents the contribution of the surrounding collagen matrix and of the passive fiber components, $W_{act}$ arises from the change of rheology during muscular contraction, and $\beta(t)$ is an activation function equal to zero at end-diastolic state and equal to one at end-systolic state ($0 \leq \beta(t) \leq 1$). The scalar $\delta_{AH}$ is equal to one if state $H$ is the state $A$ and zero if the two states $H$ and $A$ are distinct. The pseudo-active strain energy function expressed in the last term of the right hand side of the Eq.(2) is introduced in order to satisfy the kinematic condition (Eq.(1)), and is given by:

$$W_{\substack{pseudo\\active}}(\mathbf{E}_{PH}) = -\frac{1}{2} q_H\, h(\mathbf{E}_{PH}) \qquad (4)$$

The scalar $q_H$ introduced in Eq.(4) is an additional indeterminate Lagrange multiplier. The function $h(\mathbf{E}_{PH})$ defined in Eq.(1), may be rewritten in terms

of the strain invariants as:

$$h(\mathbf{E}_{PH}) = 1 - I_6^{1/2} + (\pi - 2)\,(1 - I_4^{-1/4})\,\frac{a}{D} \tag{5}$$

where $I_4$ and $I_6$ are two strain invariants given by $I_4(\mathbf{E}_{PH}) = \mathbf{f}_P \cdot \mathbf{C}_{PH} \cdot \mathbf{f}_P$ and $I_6(\mathbf{E}_{PH}) = \mathbf{f}_P^{\perp} \cdot \mathbf{C}_{PH} \cdot \mathbf{f}_P^{\perp}$ in which the fiber and the perpendicular fiber directions are respectively characterized in state $P$ by the unit vectors $\mathbf{f}_P$ and $\mathbf{f}_P^{\perp}$. In an arbitrary deformed state $H$, the direction of these two unit vectors are noted $\mathbf{f}_H$ and $\mathbf{f}'_H$ and are respectively defined by $\mathbf{f}_H = \Phi_{PH} \cdot \mathbf{f}_P / \parallel \Phi_{PH} \cdot \mathbf{f}_P \parallel$ and $\mathbf{f}'_H = \Phi_{PH} \cdot \mathbf{f}_P^{\perp} / \parallel \Phi_{PH} \cdot \mathbf{f}_P^{\perp} \parallel$. The superscript '$T$' is used for transpose matrix and $\parallel\ \parallel$ stands for the euclidian norm. Note that $I_4$ and $I_6$ are directly related to the fiber and cross-fiber extension ratios ($I_4 = \lambda_f^2$ and $I_6 = \lambda_{cf}^2$). In our notations, $\lambda_f$ is related to the fiber direction $\mathbf{f}_H$, and $\lambda_{cf}$ to the cross-fiber direction $\mathbf{f}'_H$ (Fig. 1). We treat the myocardium as a homogeneous, incompressible, and hyperelastic material transversely isotropic with respect to the local MF direction. In this study, the passive strain-energy function is [6]

$$W_{pas}(\mathbf{E}_{PH}) = C_1^p(e^Q - 1) \tag{6}$$

$$\text{with} \qquad Q = C_2^p(I_1 - 3)^2 + C_3^p(I_1 - 3)(I_4 - 1) + C_4^p(I_4 - 1)^2 \tag{7}$$

For the active strain-energy we modified the function found by Lin and Yin [6] by substracting the "beating term":

$$W_{act}(E_{PH}) = C_1^a(I_1 - 3)(I_4 - 1) + C_2^a(I_1 - 3)^2 + C_3^a(I_4 - 1)^2 + C_4^a(I_1 - 3) \tag{8}$$

where $(C_i^p, \quad i = 1, \cdots, 4)$ and $(C_i^a, \quad i = 1, \cdots 4)$ are material constants and $I_1$ is the first principal strain invariant given by $I_1(\mathbf{E}_{PH}) = tr\,\mathbf{C}_{PH}$. The beating term is defined as the part of the active strain-energy function responsible for the change of geometry when the muscle is activated and submited to no external loading. To incorporate the beating behavior, the time-dependant beating tension $\beta(t)\,T^{(0)}$ was applied in the deformed fiber direction.

In our approach, the active loaded state $C$ of the myocardial tissue is obtained in two steps. In the first step, and at a given degree of activation $\beta$, we derived and quantified the internal pseudo-active stresses by looking the free contraction configuration of the tissue (state $A$, Fig. 3). Then, in a second step, we applied the external loads on the active myocardial tissue under the internal pseudo-active stresses previously found.

***Step 1: Determination of the Free Contraction State*** $A$

During the cardiac cycle and at a given degree of activation $\beta$, the Cauchy stress tensor in state $A$ (noted $\boldsymbol{\tau}_A$) is given by:

$$\boldsymbol{\tau}_A = -p_A\mathbf{I} + \Phi_{PA}\frac{\partial W^*(\mathbf{E}_{PA})}{\partial \mathbf{E}_{PA}}\Phi_{PA}^T + \beta(t)T^{(0)}\mathbf{f}_A \otimes \mathbf{f}_A + \boldsymbol{\tau}_A^{\substack{pseudo \\ active}} \tag{9}$$

$$\text{with} \qquad \boldsymbol{\tau}_A^{\substack{pseudo\\active}} = \boldsymbol{\Phi}_{PA} \frac{\partial W_{\substack{pseudo\\active}}(\mathbf{E}_{PA})}{\partial \mathbf{E}_{PA}} \boldsymbol{\Phi}_{PA}^T \tag{10}$$

where the symbol $\otimes$ denotes the tensor product. The postulated mechanical coupling law (Eq.(5)) induces, during the contraction, a pseudo-active stress tensor:

$$\boldsymbol{\tau}_A^{\substack{pseudo\\active}} = T_A^f \, \mathbf{f}_A \otimes \mathbf{f}_A + T_A^{cf} \, \mathbf{f}'_A \otimes \mathbf{f}'_A \tag{11}$$

These two stress tensor components $T_A^f$ and $T_A^{cf}$ are activation-dependent and behave as some internal tensions in the fiber and cross-fiber directions of unit vectors $\mathbf{f}_A$ and $\mathbf{f}'_A$, respectively. These pseudo-active tensions are defined by:

$$T_A^f = 2 \frac{\partial W_{\substack{pseudo\\active}}}{\partial I_4} \parallel \boldsymbol{\Phi}_{PA} \cdot \mathbf{f}_P \parallel^2 \quad ; \quad T_A^{cf} = 2 \frac{\partial W_{\substack{pseudo\\active}}}{\partial I_6} \parallel \boldsymbol{\Phi}_{PA} \cdot \mathbf{f}_P^{\perp} \parallel^2 \tag{12}$$

***Step 2: Determination of the Physiological Active Loaded State*** $C$
These previously found internal pseudo-active tensions $T_A^f$ and $T_A^{cf}$ were introduced in the expression of the stress tensor at loaded state $C$. Therefore, at a fixed time (or activation $\beta$) of the cardiac cycle, the Cauchy stress tensor in the physiological state $C$ (noted $\boldsymbol{\tau}_C$) is given by:

$$\boldsymbol{\tau}_C = -p_C \mathbf{I} + \boldsymbol{\Phi}_{PC} \frac{\partial W^* (\mathbf{E}_{PC})}{\partial \mathbf{E}_{PC}} \boldsymbol{\Phi}_{PC}^T + \left( \beta T^{(0)} + T_A^f \right) \mathbf{f}_C \otimes \mathbf{f}_C + T_A^{cf} \, \mathbf{f}'_C \otimes \mathbf{f}'_C \tag{13}$$

The suggested constitutive law for the active myocardium (Eqs.(2)-(13)) allows to simulate the left ventricle behavior during the whole cardiac cycle. Thus, in this law: (i) the anisotropic behavior is incorporated in the expressions of passive, active and pseudo-active strain energy functions by the terms $I_4$ and $I_6$, (ii) the kinematic contraction is accounted for by a beating tension $\beta T^{(0)}$ in the fiber direction, (iii) the change of properties is expressed by the active strain energy term $\beta(t) W_{act}$, and (iv) the coupling effect between the collagen network and the MF is accounted for by the two internal pseudo-active tensions $T_A^f$ and $T_A^{cf}$ in the fiber and cross fiber directions $\mathbf{f}_C$ and $\mathbf{f}'_C$, respectively.

## 4 Results and Discussion

We simulated the loading of a thin sample of living myocardium ($1.0 \times 1.0 \times 0.1$ cm$^3$) in which the MF are uniformly oriented in one direction. The coefficients involved in the strain energy-function are those of Lin and Yin [6]: $C_1^p$=0.292 kPa, $C_2^p$=0.321, $C_3^p$=-0.260, $C_4^p$=0.201, $C_1^a$=-3.870 kPa, $C_2^a$=4.830 kPa, $C_3^a$=2.512 kPa and $C_4^a$=0.951 kPa. For the beating tension, a good agreement between the previous experimental results and our theoretical solution is obtained for $T^{(0)}$=0.6 kPa. Nevertheless, the control simulation was performed with a/D=0.2

and $T^{(0)}$=35 kPa. This higher value of $T^{(0)}$ is more adapted to the description of the left ventricular performance [7].

***Influence of the Collagen Network on the Systolic Wall Thickening***
The free contraction test is performed with no external displacement or force on the boundaries of the sample, but just in activating the tissue. In this simulation we used the following time-dependent activation function : $\beta(t) = sin^2(\pi t)$. Compare to the case where the kinematic constraint is not taken into account, one can see an increase of the cross-fiber extension ratio which is in the tangential plane of the ventricular wall (Fig. 3). At the end-systolic state (i.e. when $\beta = 1$), this ratio goes from the value 1.25 if we neglect the coupling effect, to 1.45 when considering the kinematic constraint induced by the collagen. So, the connective tissue could account for 16 % of normal end-systolic wall thickness. This increase is clearly dependent of the geometrical parameter ratio $a/D$ and the maximal beating tension $T^{(0)}$.

***Influence of the Collagen Network on the Pseudo-active Tension***
Table 1 shows the effect of the geometrical parameter $a/D$ and the maximal active tension $T^{(0)}$, on the fiber and cross-fiber stresses (noted $\sigma_{11}$ and $\sigma_{22}$, respectively). These effects were given in the case of an equibiaxial extension loading ($\lambda_f = \lambda_{cf} = 1.2$) of an activated sample of myocardium ($\beta = 1$). These two stresses increase with $T^{(0)}$, but are not very sensitive to the geometrical ratio $a/D$. We can observe also, that by neglecting the interaction between the collagen network and the MF: (i) the cross-fiber stress is not affected by the amplitude of the beating tension, and (ii) the stress ratio $\sigma_{22}/\sigma_{11}$ decreases when $T^{(0)}$ increases. These results mean that the usual strain-energy functions considered for the myocardium are not able to generate any transverse pseudo-active tension.

Moreover, the results obtained for the uniaxial tests of an active or a passive sample, with or without the effect of the collagen on the MF, are shown in Fig. 4. Because the coupling effect between the collagen and the MF is an active mechanism, the passive stress-strain relations are not affected by the kinematic constraint. The mechanical properties of the active tissue, in the fiber and cross-fiber directions, become comparable when the coupling effect acts.

## 5 Conclusion

This study shows that the connective tissue skeleton in the normal and pathological left ventricle may have a large influence on the cardiac performance. A new constitutive law has been developed for large deformations of an incompressible hyperelastic, and anisotropic living myocardium. This work is based on the idea that the connective tissue is physically coupled to the muscle fibers which seems reasonable with regard to the available observations. Nevertheless, additional experimental works must be done in order to support this assumption and to study thoroughly the spatial organization of the myocardial collagen fibrils under normal and pathological conditions.

**Table 1.** Equibiaxial test: effect of active tension $T^{(0)}$ and geometrical parameter $a/D$

| $a/D$ \ $T_0$ $(kPa)$ | | 5 | 15 | 25 | 35 | 45 |
|---|---|---|---|---|---|---|
| 0.10 | $\sigma_{22}/\sigma_{11}$ (%) | 50.92 | 53.73 | 57.65 | 60.25 | 61.90 |
| | $\sigma_{22}$ $(kPa)$ | 5.94 | 11.44 | 17.78 | 24.32 | 30.88 |
| 0.15 | $\sigma_{22}/\sigma_{11}$ (%) | 51.44 | 54.56 | 58.60 | 61.30 | 63.01 |
| | $\sigma_{22}$ $(kPa)$ | 5.97 | 11.48 | 17.80 | 24.31 | 30.84 |
| 0.20 | $\sigma_{22}/\sigma_{11}$ (%) | 51.94 | 55.33 | 59.47 | 62.25 | 64.04 |
| | $\sigma_{22}$ $(kPa)$ | 6.00 | 11.51 | 17.79 | 24.25 | 30.73 |
| No kinematic constraint | $\sigma_{22}/\sigma_{11}$ (%) | 36.78 | 19.88 | 13.62 | 10.36 | 8.36 |
| | $\sigma_{22}$ $(kPa)$ | 4.32 | 4.32 | 4.32 | 4.32 | 4.32 |

**Acknowledgments.** This work was performed within the framework of the joint incentive action "Beating Heart" of the research group ISIS, ALP and MSPC of the French National Center for Scientific Research (CNRS). It is partly granted by the Région Rhône Alpes, through the AdéMO project and by the Lipha Santé Company, a subsidiary of the group MERCK KGaA.

## References

1. J. B. Caulfield and J. S. Janicki. Structure and function of myocardial fibrillar collagen. *Technology and Health Care.*, IOS Press (5):95–113, 1997.
2. R. S. Chadwick, A. Tedgui, J.B Michel, J. Ohayon, and B. I Levy. Phasic regional myocardial inflow and outflow : comparison of theory and experiments. *Am. J. Physiol.*, 258:H1687–1698, 1990.
3. K.D. Costa, P.J. Hunter, J.S. Wayne, L.K. Waldman, J.M. Guccione, and A.D. McCulloch. A three-dimensional finite element method for large elastic deformations of ventricular myocardium: Part II - Prolate spheroidal coordinates. *ASME J. Biomech. Eng*, 118:464–470, 1996.
4. J.M. Huyghe, D.H. van Campen, T. Arts, and R.M. Heethaar. A two-phase finite element model of the diastolic left ventricle. *J. Biomech.*, 24:527–538, 1991.

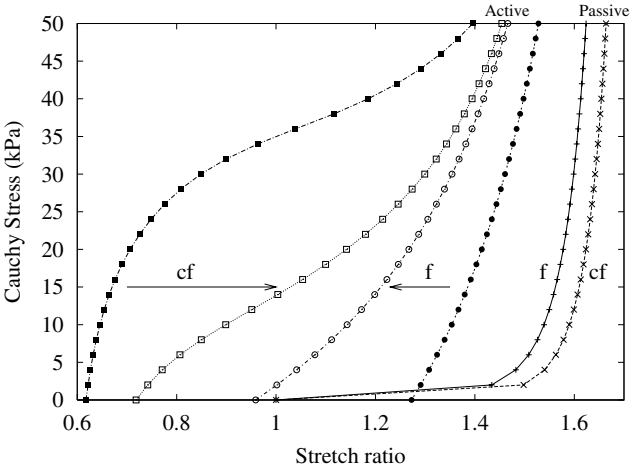


**Fig. 4.** Active and passive uniaxial extension tests: effect of the pseudo-active kinematic constraint. The empty and full symbols indicate that the coupling effect is acting or not, respectively. The fiber and cross-fiber directions noted (f) and (cf) are defined in Fig. 1. Arrows show the curve modification when the pseudo-active kinematic constraint behaves


5. I.J. LeGrice IJ, Y. Takayama, and J.W.J. Covell. Transverse shear along myocardial cleavage planes provides a mechanism for normal systolic wall thickening. *Circ. Res.*, 77:182–193, 1995.
6. D.H.S. Lin and F.C.P. Yin. A multiaxial constitutive law for mammalian left ventricular myocardium in steady-state barium contracture or tetanus. *J. Biomech. Eng.*, 120:504–517, 1998.
7. J. Ohayon, H. Cai, P.S. Jouk, Y. Usson, and A. Azancot. A model of the structural and functional development of the normal human fetal left ventricle based on a global growth law. *Comp. Meth. Biomech. Biomed. Eng.*, 2002.
8. J. Ohayon and R.S. Chadwick. Effects of collagen microstructure on the mechanics of the left ventricle. *Biophys. J.*, 54:1077–1088, 1988.
9. L.A. Taber. On a nonlinear theory for muscle shells: Part II- Application to the beating left ventricle. *J. Biomech. Eng.*, 113:63–71, 1991.
10. M.A. Rossi. Connective tissue skeleton in the normal left ventricle and in hypertensive left ventricular hypertrophy and chronic chagasis myocarditis. *Med. Sci. Monit.* 7(4):820–832, 2001.
11. S.J. Sarnoff, E. Braunwald, G.H. Jr. Welch, R. B. Case, W. N. Stainsby, and R. Macruz. Hemodynamic determinants of oxygen consumption of the heart with special reference to the tension-time index. *Am. J. Phsysiol.*, 192:148–156, 1958.
12. D.D. Streeter. Gross morphology and fiber geometry of the heart. In R. M. Berne et al., editor, *Handbook of physiology*, volume 1, pages 61–112, Bethesda MD, 1979. American Physiological Society.
13. T.P. Usyk, J.H. Omens, A.D. McCulloch Regional septal dysfunction in a three-dimensional computational model of focal myofiber disarray. *Am. J. Physiol. Heart Circ. Physiol.*, 281: H506–H514, 2001

# Regularization in Cardiac Source Imaging

Tuomas Lunttila[1], Jukka Nenonen[1,2], and Erkki Somersalo[3]

[1] Helsinki University of Technology, Laboratory of Biomedical Engineering
P.O. Box 2200, 02015 HUT, Espoo, Finland
Jukka.Nenonen@hut.fi
http://www.biomed.hut.fi
[2] Helsinki University Central Hospital, BioMag Laboratory
P.O. Box 340, 00029 HUCH, Helsinki, Finland
http://www.biomag.helsinki.fi
[3] Helsinki University of Technology, Institute of Mathematics
P.O. Box 1100, 02015 HUT, Espoo, Finland
Erkki.Somersalo@hut.fi
http://www.math.hut.fi

**Abstract.** Estimation of bioelectric currents in the heart involves the solution of an ill-posed inverse problem in electro- and magnetocardiography. The problem becomes *linear* in respect to current magnitudes when the equivalent sources are constrained into a pre-determined grid of reconstruction points. Still, a proper regularization is required to obtain physiologically meaningful results. This paper discusses the application of deterministic methods (such as Tikhonov or Wiener regularization) and statistical inversion. The deterministic methods require determination of an optimal regularization parameter, while the statistical inversion relies on application of a *prior* for the source distribution. Comparison of selected regularization methods is performed with simulated magnetocardiographic data.

## 1 Introduction

In the inverse problem of electrocardiography (ECG) and magnetocardiography (MCG), the aim is to estimate the current sources underlying measured extracardiac fields [1]. Progress in treatment of cardiovascular diseases has increased the demand for non-invasive localization and determination of the size of abnormally functioning regions in the heart. MCG has been applied for non-invasive studies of locating ischemic areas in patients with coronary artery disease and arrhyhmogenic regions in patients with tachycardias [2]. Current-density imaging was used to reconstruct an equivalent current density on the epicardial surface [3]. Besides MCG, numerous body surface potential mapping (BSPM) studies have been carried out to estimate the equivalent epicardial potential distribution [4,5], or to reconstruct the activation sequence on the heart surfaces [6]. The discrete forward problem in all above mentioned studies can be expressed as a linear system of the form

$$y = \mathbf{A}x + \eta \,. \tag{1}$$

Vector $x$ ($n \times 1$) characterizes a quantity that cannot be directly observed, such as bioelectric current density or the equivalent potential distribution in the heart; $n$ is the

I. Magnin et al. (Eds.): FIMH 2003, LNCS 2674, pp. 101–111, 2003.

number of nodes used for the reconstruction. Vector $y$ ($m \times 1$) in turn comprises values of noisy measurements outside of the body; $m$ is the number of MCG or ECG sensors. Leadfield matrix $\mathbf{A}$ ($m \times n$) is the transfer function from $x$ to $y$, and vector $\eta$ represents the unknown measurement noise.

The inverse problem here means estimating $x$ from Eq. (1). Solving the inverse problem is complicated by the fact that it is ill-posed: First, the problem may not have any solution. Second, if a solution exists, it may not be unique. Third, the solution of the problem does not depend continuously on the data, i.e. arbitrarily small errors in the measurements may cause large error in the calculated solution, making matrix $\mathbf{A}$ rank-deficient. Therefore, the usual approach is to limit the inverse problem by replacing the actual sources $x$ with equivalent generators in the body.

In many biomedical applications the inverse problem is underdeterministic, i.e. $m < n$ because in practice we have fewer measurement channels than the number of reconstruction points in the body. The conventional minimum norm solution of Eq. (1) can then be expressed as [1]

$$x_P = \mathbf{A}^\dagger y = \mathbf{A}^T(\mathbf{A}\mathbf{A}^T)^{-1}y \ , \tag{2}$$

where $\mathbf{A}^\dagger$ is the Moore-Penrose pseudo-inverse of $\mathbf{A}$ [7]. Still, the limited inverse problem is ill-posed, and measurement noise, inaccuracies in the modeling or even round-off errors in computer calculations cause large errors in the reconstructed $x$. Therefore, the problem has to be regularized. The most straightforward deterministic regularization method is the truncated singular value decomposition [1]. In the following, we discuss some advanced regularization methods and their role in the cardiac source imaging problem.

## 2 Deterministic Inversion

In the Tikhonov regularization a solution $x_T$ to the problem (1) is sought by adding a side constraint that drives the solution of the inverse problem towards a reasonable a priori assumption [8]. The general form of the Tikhonov regularization is

$$x_T = \min \|W(\mathbf{A}x - y)\|^2 + \lambda R(x) \tag{3}$$

where $W$ is the weighting operator, $R$ is the regularization functional, and $\lambda$ is a parameter controlling the weight given to the side constraint. Because of practical reasons, $R$ and $W$ are often of the form $R(x) = |\mathbf{R}x|^2$ and $W(x) = \mathbf{W}x$, where $\mathbf{R}$ and $\mathbf{W}$ are matrices of appropriate dimensions. Thereafter, the unique Tikhonov regularized solution is obtained as

$$x_T = \mathbf{W}\mathbf{W}^T\mathbf{A}^T(\mathbf{A}\mathbf{W}\mathbf{W}^T\mathbf{A}^T + \lambda\mathbf{R}^T\mathbf{R})^{-1}y. \tag{4}$$

The matrix inversion in the equation is possible for all $\lambda > 0$, provided that the regularization matrix $\mathbf{R}$ has full rank.

The weight $\mathbf{W}$ is usually a diagonal data scaling matrix that is used to adjust the importance of individual data points. The regularization operator $\mathbf{R}$ incorporates available a priori information about the solution. The most commonly used choices are the identity matrix and a discrete approximation of the Laplacian of the solution. These choices are

often called the zeroth and the second order Tikhonov regularization operators, respectively. The use of identity matrix tends to minimise the Euclidean norm of the solution, whereas the second order Tikhonov regularization favors smoothly varying solutions.

The proper choice of regularization parameter $\lambda$ is critical for the performance of Tikhonov regularization. If it is chosen too big, the solutions tend to be too smooth to reveal anything about the true current distribution in the heart. On the other hand, if the value is set too small, the solution will be seriously contaminated by noise. Several methods have been proposed for selecting the proper value of the regularization parameter, such as the generalized cross-validation, the discrepancy principle, the quasi-optimality criterion, and the $L$-curve method (e.g., [4,9]).

The zeroth-order Tikhonov regularization can be seen as a special case of the Wiener regularization, where the most optimal deterministic solution of Eq. (1) is [10]:

$$x_W = \mathbf{A}^\dagger y = \Gamma_x \mathbf{A}^T (\mathbf{A}\Gamma_x \mathbf{A}^T + \Gamma_n)^{-1} y \ , \tag{5}$$

where $\Gamma_x$ and $\Gamma_n$ are the covariance matrices of the $x$ and $\eta$, respectively. The covariances are assumed known a priori. The method has been used, e.g., in inverse electrocardiography: Martin et al. [11] applied Eq. (5) in reconstructing the epicardial potential. Later, van Oosterom [5] has presented a detailed treatment for the covariance derived from a uniform double-layer model. He demonstrated that the use of a proper covariance significantly improved the quality of reconstructed potential distributions. We have also applied the method in reconstructing current density in patients with exercise-induced myocardial ischemia [3].

## 3 Statistical Inference in Inverse Magnetocardiography

### 3.1 Posterior Probability Density

Next we turn our focus on statistical inversion methods which are based on the Bayesian inference. Statistical inversion methods were first used in the field of geophysics [12]. Since their introduction, they have been used in many fields. The biomedical applications include electrical impedance tomography [13] and electromagnetic source localisation in the brain [14,15].

All measured quantities are modeled as random variables with known probability distributions. The randomness can be thought of as reflecting our uncertainty about the true values of measured variables, mainly due to measurement noise. The measured variables are related to quantities of interest, that cannot be measured directly, through a more or less well known model. We may also have some prior information about the estimates, which is formulated as a probability distribution.

The solution of the statistical inverse problem is obtained as a posterior probability density from the Bayes theorem as

$$\pi_{post}(x) = \pi(x|y) \propto \pi(y|x)\pi(x) \ , \tag{6}$$

i.e., the posterior density is the conditional probability density of $x$ conditioned on $y$. Here $\pi(y|x)$ is known as the likelihood and $\pi(x)$ the prior density [13]. Assuming that $x$ and $\eta$ are independent, we can also write $\pi(y|x) = \pi_{noise}(y - f(x))$.

When the posterior probability distribution for the random variable $x$ has been obtained, the inverse problem has been solved in a statistical sense. However, for practical purposes one usually wants a single estimate of the sought quantity rather than a multidimensional probability distribution. Therefore it is necessary to calculate various point estimates for $x$ as well as a posteriori uncertainties for the estimates.

Assume that the posterior probability distribution is given in terms of probability density $\pi(x|y)$ as above and we have measured $y$. A commonly used estimate based on this density is the maximum a posteriori (MAP) estimate: $x_{MAP} = \max \pi(x|y)$. The MAP estimate does not need to be unique. The computation of the MAP estimate is an optimisation problem. Another commonly used estimator is the conditional expectation

$$x_{CE}(y) = \int_{\mathbf{R}^n} x\pi(x|y)\mathrm{d}x. \tag{7}$$

The conditional expectation estimate is unique, if it exists. Finding the conditional expectation is an integration problem, in contrast to the problem of finding the MAP estimate.

### 3.2 Markov Chain Monte Carlo Method

To compute conditional expectations and confidence regions from the posterior probability density it is often necessary to calculate various integrals over parameter spaces. The integrals can be evaluated analytically only in special situations. Also, since the dimension of the parameter space $\mathbf{R}^n$ is often large, numerical quadrature rules cannot be used effectively.

A frequently used method for computing high-dimensional integrals with respect to probability distributions is the Monte Carlo integration, where one generates samples $\{x^1, x^2, \ldots, x^n\}$ from distribution $\pi(x)$ and estimates the integral of $\pi(x)f(x)$ as

$$\int_{\mathbf{R}^n} f(x)\pi(x)\mathrm{d}x \approx \frac{1}{n}\sum_{k=1}^{n} f(x^k). \tag{8}$$

The problem remains, however, of generating samples $x_k$ distributed as $\pi(x)$. Direct drawing of independent samples is not possible, unless $\pi(x)$ is of special form, such as an $n$-dimensional Gaussian distribution.

The Markov chain Monte Carlo (MCMC) methods are used for generating samples from a probability distribution. The samples will not be independent, but it can be shown that a properly constructed MCMC method generates a sample ensemble such that (8) holds (e.g., [16,17]). The generation of the sample points with Metropolis–Hastings algorithm for this study is briefly described below (see also [13]).

First, we need to construct a Markov chain with invariant distribution given by density $\pi$. We define a probability transition kernel as

$$p(x, y) = K(x, y) + r(x)\delta(x - y) \tag{9}$$

i.e. $r(x)$ is the probability of remaining at point $x$, while $K(x, y)$ is the (differential) probability of moving from $x$ to $y$. We can further require that $K$ satisfies the balance equation

$$\pi(y)K(y, x) = \pi(x)K(x, y), \tag{10}$$

for all $x, y \in \mathbf{R}^n$. Equation (10) is the starting point in constructing a MCMC method known as the Metropolis–Hastings sampler. We start by choosing a candidate transition kernel $q$, i.e. a function from $\mathbf{R}^n \times \mathbf{R}^n$ to $\mathbf{R}^+$ with the property $\int_{\mathbf{R}^n} q(x,y)\mathrm{d}y = 1$, and try to choose a correction function $\alpha : \mathbf{R}^n \times \mathbf{R}^n \to [0,1]$ such that (10) holds for $K(x,y) = \alpha(x,y)q(x,y)$:

$$\alpha(x,y) = \min\left\{\frac{\pi(y)q(y,x)}{\pi(x)q(x,y)}, 1\right\}. \tag{11}$$

The correction term $\alpha(x,y)$ is called the acceptance probability: it can be seen as the probability with which the step from point $x$ to a point $y$ generated from the distribution given by density $q$ should be accepted.

The Metropolis–Hastings algorithm has the advantage that the acceptance probability (11) only depends on $\pi$ thorough ratios of form $\pi(y)/\pi(x)$, thus $\pi$ only needs to be known up to a normalising constant. This is an important property in the applications, since often the normalising constant is not known. Details on the practical implementation can be found e.g. in [13,17].

A method known as the random walk Metropolis–Hastings algorithm is obtained if we draw $z$ from a fixed distribution with density $f$ and use as a candidate $y = x + z$. This means choosing $q(x,y) = f(x-y)$. Another possibility is to choose candidate steps from a fixed density: $q(x,y) = f(y)$. In this case the acceptance probability is obtained as

$$\alpha(x,y) = \min\left\{\frac{w(x)}{w(y)}, 1\right\}, \tag{12}$$

where $w(x) = \pi(x)/f(x)$. This Markov chain obtained is called the independence Metropolis chain. The independence chain Metropolis–Hastings algorithm works well, if it is possible to choose density $f$ such that the weight function $w(x)$ is bounded, and preferably close to constant. Perhaps the most common choice for the density $f$ is the zero-mean Gaussian distribution. The covariance matrix should be such that about 20–30% of all generated steps are accepted [17].

### 3.3 Gaussian Priors

It is usually assumed that the measurement noise is additive and independent of the measurements. Often, it is further assumed that the measurement noise is a zero mean Gaussian distributed random vector with a positive definite covariance matrix $\mathbf{C}_n$. Then

$$\pi(x|y) \propto \pi_{pr}(x) e^{-\frac{1}{2}(y-\mathbf{A}x)^T \mathbf{C}_n^{-1}(y-\mathbf{A}x)}. \tag{13}$$

The simplest posterior probability density is obtained if the prior probability density is Gaussian:

$$\pi_{pr}(x) \propto e^{-\frac{1}{2}(x-x^*)^T \mathbf{C}_{sp}^{-1}(x-x^*)}, \tag{14}$$

with some estimated current density covariance matrix $\mathbf{C}_{sp}$ and mean $x^*$. The MAP-solution equals the Tikhonov regularised solution with $\mathbf{W} = (\frac{1}{2}\mathbf{C}^{-1})^{1/2}$, $\mathbf{R} = \mathbf{A}$ and $\lambda = 1$. Thus, the Tikhonov regularisation can be seen as MAP-estimation with Gaussian prior density.

Due to the symmetry of the posterior distribution it is easy to see that in the case of a Gaussian prior density the MAP-estimate and the conditional expectation coincide. By direct substitution it can be verified that also the Wiener estimate yields the same result.

### 3.4 Non-Gaussian Priors

A class of parametric non-Gaussian priors is obtained if we choose the prior density as

$$\pi_{pr}(x) \propto e^{-\alpha \|\mathbf{A}(x-x^*)\|_p}, \tag{15}$$

where $\|x\|_p = \sum_{i=1}^{n} \left(x_{i_1}^2 + x_{i_2}^2 + x_{i_3}^2\right)^{p/2}$. These types of priors can be seen as generalised Gaussian priors, since the choice $p = 2$ gives a Gaussian prior. Choosing $p = 1$ and $\mathbf{A} = \mathbf{I}$ we obtain the density known as the $L1$-prior or the impulse noise prior. It is concentrated around $x^*$, but also current distributions that have few large deviations with small support are quite probable.

We usually have a good idea of what the current density at one node should be, if we know the current elsewhere on the epicardial surface of the heart. This knowledge can be used to construct the complete a priori probability distribution using Markov Random Fields (MRF):

$$\pi(x) \propto e^{-\sum V_C(x)}, \tag{16}$$

where functions $V_C$ in subset $C \subseteq \{1 \dots n\}$ can be chosen arbitrarily subject to restrictions that each $V_C$ depends only on those coordinates $x_i$ of $x$ for which $i \in C$, and that the prior is integrable.

In this study, we applied two different MRF priors. First, the functions $V_C$ were selected so that the directions of neighbouring dipoles in $x$ are coupled. Strong coupling drives active dipoles to form clusters, whereas low coupling gives the dipoles more independence. This is the famous Ising model for ferromagnetism [18]. Second, the total variation prior was applied [13]. Total variation prior gives high probability to current distributions where the activated region has short, sharp edges.

## 4 Results

In order to illustrate differences between various regularization schemes, we carried out computer simulations to reconstruct equivalent current density from electric and magnetic fields observed on the body surface. First, we computed forward solutions for a focal current dipole at different locations in the multichannel MCG and ECG sensors employed in [3]. Random noise was added to the simulated data, with the RMS value of 2% from maximal MCG or ECG amplitude. Examples of the Tikhonov and Wiener regularizations, Eqs. (4)–(5), are shown in Fig. 1 for the deepest (posterior) dipole location. The optimal regularization parameter was defined with the L-curve method.

To test the statistical approach, we next computed forward solutions for different source current distributions in an array of magnetometer sensor coils. Figure 2 depicts the sensor array and the selected current distributions: a) a single dipole represents a focal activity, such as a starting point of a ventricular extrasystolic beat; b) a hypothetical

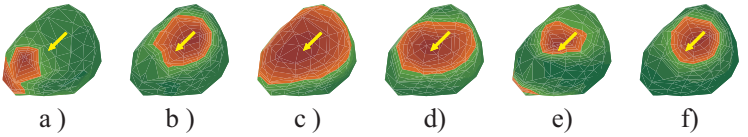


**Fig. 1.** Tikhonov and Wiener regularization for a single test dipole source in a homogeneous boundary-element torso. The triangulated epicardial surface is viewed from the posterior direction. The test dipole is indicated with a yellow arrow. The results $x_{T0}$ are shown on the left (a) MCG, b) ECG), $x_{T2}$ in the middle (c) MCG, d) ECG), and $x_W$ on the right (e) MCG, f) ECG). Fow $x_W$, diagonal covariance $\Gamma_x$ in Eq. (5) was estimated from the magnitudes of $x_{T2}$. The current-density magnitude is presented as colour maps, the deepest red indicates highest current density. The red-green boundary indicates that the current magnitude is 50% from the maximum

curved current density, c) a tail-to-tail dipole pair, which explains the epicardial potential pattern following a point stimulus in an anisotropic myocardium [19]; d) a hypothetical vortex current, which does not generate an electric potential in the volume conductor. Random noise was then added to the data, and inverse solutions were computed according to the statistical method using different priors. This time the body was approximated as a semi-infinite conducting medium with a plane boundary.

The total strength of the dipoles was the same in all four test cases. Before the reconstruction, uncorrelated Gaussian noise was added to the simulated measurements. The standard deviation of the noise was the same in all channels, 2% of the maximum MCG amplitude in test case 4. This resulted in relative noise levels between 1.5% and 4% with the highest relative noise level in case 3, where the measured signal is weakest, and the lowest in case 1 with the strongest signal. The noise covariance matrix used in constructing posterior probability density was the covariance matrix of the added noise.

In the inverse calculations, a single component random walk Metropolis–Hastings scheme was used. The variance of the proposal distribution was chosen such that the acceptance ratio of the sampler was approximately 30%. The algorithm was started from the zeroth order Tikhonov regularised solution. After the burn-in period of 10000 updates, 200000 samples were generated.

The conditional expectations according to Eq. 7 for four different priors are displayed in Figs. 3–6. Note that in this simple volume conductor, dipoles perpendicular to the plane boundary do not generate and magnetic field, and the potential distribution on the plane surface is obtained by rotating the $B_z$ distribution by $90^o$ [20]. Therefore, the ECG reconstructions for the cases of Fig. 2a-c are very similar than the MCG results.

## 5 Discussion

In this study we selected simplified forward modeling instead of incorporating detailed excitation models based on electrophysiology. Our approach is nevertheless sufficient for demonstrating similarities and differences between conventional (Tikhonov or Wiener) regularization and statistical inversion. Sometimes it is difficult to classify inversion methods as deterministic or statistical. Many conventional methods, such as Wiener regularization, use statistical assumptions about the sources and the measurement noise,

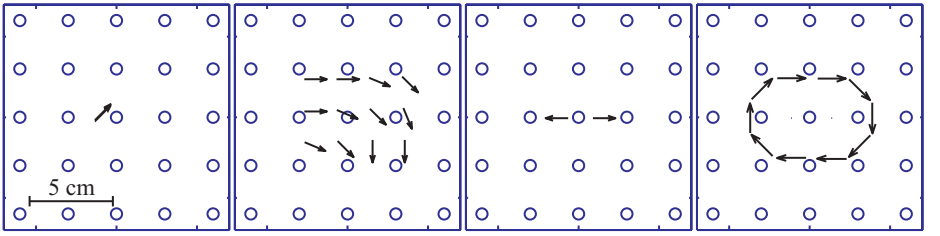


**Fig. 2.** Four dipole configurations used in computing the forward solutions. The tangential dipoles are in the same xy-plane at the depth of 5 cm from the surface. The circles show the locations of the magnetometers detecting the component $B_z$. The magnetometers are arranged on $xy$-plane 2 cm above the plane surface

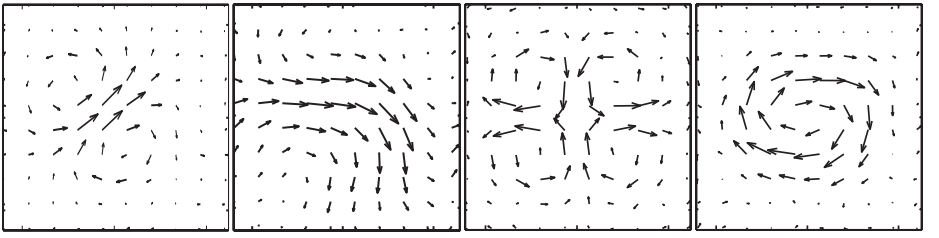

**Fig. 3.** Current densities reconstructed using Gaussian smoothness prior

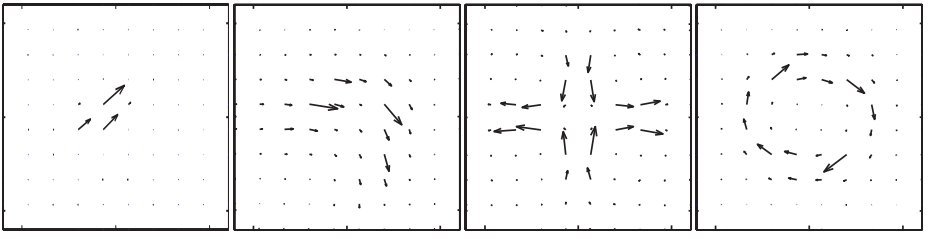

**Fig. 4.** Current density reconstructed with L1-norm prior

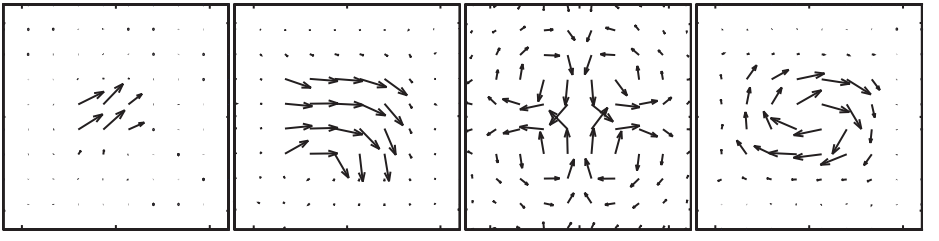

**Fig. 5.** Current density reconstructed using total variation prior

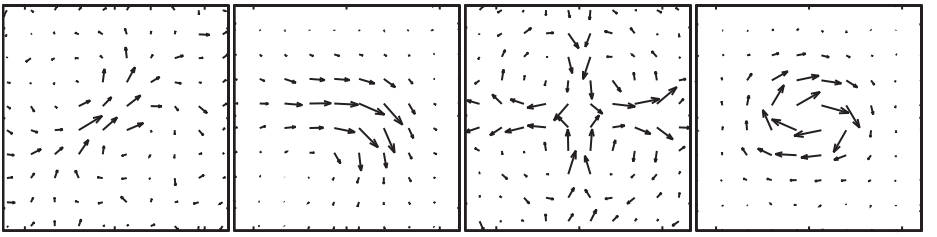

**Fig. 6.** Current density reconstructed using Ising prior

at least implicitly. Often the deterministic inversion methods can be seen as special cases of the statistical methods.

In the statistical methods the solution to the inverse problem is not a single estimate for $x$ but a probability distribution. Also, in the statistical inversion methods the role of the prior information is more explicit. After the inverse problem has been solved in the statistical sense, one usually calculates some point estimates and confidence regions from the posterior distribution. The interpretation of these results requires care, as it is easy to draw false conclusions.

Figures 1 and 3 show clearly that Tikhonov regularization, as well as Gaussian smoothness priors, tend to spread the source distribution. The $L1$-norm prior distribution gives very good results when applied to focal source configurations (a) and (c) (Fig. 4). When the source current is spread over a wider area, the $L1$-norm prior often fails to detect the true extent of activation. Total variation prior gives high probability to current distributions where the activated region has short, sharp edges. It can be seen that the total variation prior gives good results in case (b) (Fig. 5), where the source is well defined with short boundaries. The result for the focal source (a) is also satisfactory, although the reconstruction is not quite as localised as with $L1$-prior. The Ising prior (Fig. 6) works well on those source distributions that have a well defined large cluster of activated dipoles, notable in test case (b). On the other hand, localised sources in case (a) and especially in case (c) are not reconstructed very well.

So far, our experiments are rather tentative attempts than a covering answer to the inverse problem of ECG and MCG. To achieve new clinically useful functional source imaging tools, there are still several open questions. Various source models and regularization approaches have been suggested in the literature (e.g. [1]–[6]). Despite the Bayesian and Markov chain approaches have been extensively applied in image processing, to our knowledge the present study is the first attempt to apply statistical inversion methods in ECG and MCG studies. Our simulation results are illustrative in the sense that they reveal differences between the solution strategies of the inverse solutions. Still, more realistic prior densities are needed to make full use of the inversion methods. One needs to calculate the appropriate transfer matrix and define prior probabilities that reflect the physical, physiological and anatomical a priori information about the electrical activity in the heart. Finding suitable priors poses many challenges, but also provides new possibilities of more accurate inverse solutions.

## References


1. Hämäläinen, M., Nenonen, J.: Magnetic Source Imaging. In *Engineering Superconductivity*, P.J. Lee, ed. (Wiley, New York, 2001) 464–479
2. Nenonen, J.: Magnetocardiography. In: Braginski, A., Clarke, J., editors, *SQUID handbook*. Wiley-VCH Verlag, Berlin (2003)
3. Nenonen, J., Pesola, K., Hänninen, H., Lauerma, K., Takala, P., Mäkelä, T., Mäkijärvi, M., Knuuti, J., Toivonen, L., Katila, T.: Current-Density estimation of exercise-induced ischemia in patients with multivessel coronary artery disease. *J. Electrocardiol.* **34**(suppl.) (2001) 37–42
4. Horáček, B.M., Clements, J.: The inverse problem of electrocardiography: A solution in terms of single– and double–layer sources on the epicardial surface. *Math. Biosci.* **144** (1997) 119–154
5. van Oosterom, A.: The use of the spatial covariance in computing pericardial potentials. *IEEE Trans. Biomed. Eng.* **46** (1999) 778–787
6. Tilg, B., Fischer, G., Modre, R., Hanser, F., Messnarz, B., Schocke, M., Kremser, C., Berger, T., Hintringer, F., Roithinger, F.: Model-based imaging of cardiac electrical excitation in humans. *IEEE Trans. Med. Im.* **21** (2002) 1031–1039
7. Golub, G., van Loan, C.: *Matrix Computations (2nd edition)*. Johns Hopkins University Press, Baltimore (1989)
8. Tikhonov, A., Arsenin, V.: *Solutions of Ill-Posed Problems*. Winston & Sons, Washington (1977)
9. Hansen, P.: Analysis of doscrete ill-posed problems by means of the L-curve. *SIAM Review* **34** (1992) 561–580
10. Foster, M.: An application of Wiener-Kolmogorov smoothing theory to matrix inversion. *J. Soc. Ind. Appl. Math.* **9** (1961) 387–392
11. Martin, R., Pilkington, T., Morrow, M.: Statistically constrained inverse electrocardiography. *J. Soc. Ind. Appl. Math.* **22** (1975) 487–492
12. Tarantola, A.: *Inverse Problem Theory.* Elsevier, Amsterdam (1987)
13. Kaipio, J., Kolehmainen, V., Somersalo, E., Vauhkonen, M.: Statistical inversion and Monte Carlo sampling methods in electrical impedance tomography. *Inverse Problems* **16** (2000) 1487–1522
14. Ollikainen, J., Vauhkonen, M., Karjalainen, P., Kaipio, J.: A new computational approach for cortical imaging. *IEEE Trans. Med. Im.* **20** (2001) 325–332
15. Baillet, S., Mosher, J., Leahy R.: Electromagnetic brain mapping. *IEEE Signal Proc. Magazine* **18** (2001) 14–30
16. Tierney, L.: Markov Chains for exploring posterior distributions. *Ann. Stat.* **22** (1994) 1701–1762
17. Gilks, W., Roberts, G., George, E.: *Markov Chain Monte Carlo in Practice*. Chapman and Hall, London (1996)
18. Ising, E.: Beitrag zur Theorie des Ferromagnetismus. *Zeitschr. f. Physik* **31** (1925) 253–258
19. Colli-Franzone, P., Guerri, L., Viganotti, C., Macchi, E., Baruffi, S., Spaggiari, S., Taccardi, B.: Potential fields generated by oblique dipole layers modeling excitation wavefronts in the anisotropic myocardium. *Circulation Res.* **51** (1982) 330–346
20. Cuffin, N., Cohen, D.: Magnetic fields of a dipole in special volume conductor shapes. *IEEE Trans. Biomed. Eng.* **24** (1977) 372–381

# On the Influence of a Volume Conductor on the Orientation of Currents in a Thin Cardiac Tissue

R. Weber dos Santos[1,2] and F. Dickstein[2]

[1] Physikalisch-Technische Bundesanstalt, Berlin, Germany
rodrigo.weber@ptb.de
[2] Universidade Federal do Rio de Janeiro, Rio de Janeiro, Brazil

**Abstract.** In this work we study the influence of a volume conductor on the orientation of cardiac currents that generate magnetic field. Previous computer simulations have suggested currents to be transversal to the local action potential propagation direction [4,5]. Here we propose a new 2D model that accounts for the presence of a volume conductor in contact with a thin cardiac tissue. Our results using this tridomain model suggest that while part of the current spreads out to the volume conductor the orientation of the current in the cardiac tissue tends to align to the local cardiac fiber distribution.

## 1 Introduction

A useful approximation for ECG (Electrocardiogram) interpretation is to consider the body electrical current distribution as generated by current dipoles aligned with the cardiac wave front propagation direction. However, recent MCG (Magnetocardiogram) investigation ([4], [5]) has suggested that the primary currents that generate the measured magnetic field are rather transversal to the wave propagation direction. Such a difference arises from the fact both intra and extracellular currents are detectable by MCG, while only extracellular currents generate ECG.

In this paper we continue the investigation initiated in [4] and [5] by studying a thin piece of cardiac tissue in contact with a non-excitable volume conductor. We introduce a new two-dimensional cardiac model, which we call the tridomain model, that accounts for the interface effects of a volume conductor such as a perfusing bath or blood. We assume that the current which flows away from the cardiac tissue into the volume conductor (see Fig. 1) does not directly contribute to the measured magnetic field. The primary currents that generate the measured magnetic field are those that remain in the cardiac tissue, i.e., the sum of intracellular and extracellular cardiac currents. Our numerical results suggest that under the influence of a volume conductor the cardiac tissue current orientation is no longer transversal to the propagation direction. The presence of a volume conductor changes the cardiac current orientation by aligning it with the cardiac fiber orientation.

I. Magnin et al. (Eds.): FIMH 2003, LNCS 2674, pp. 111–121, 2003.

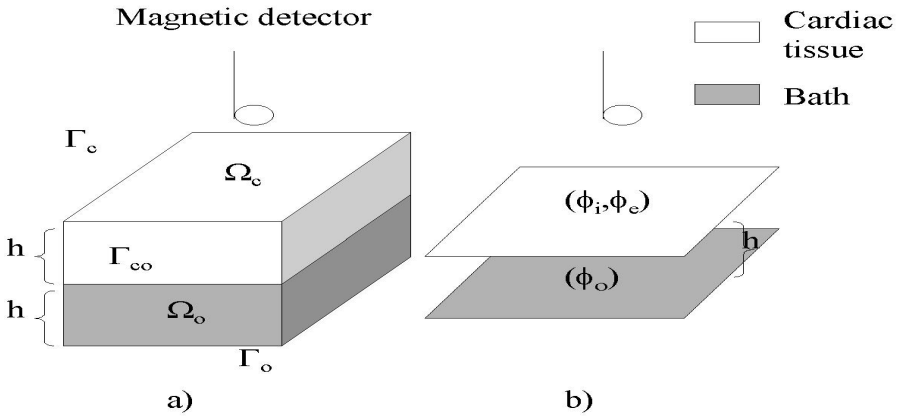


**Fig. 1.** a) A cardiac tissue slab ($\Omega_c$) is in contact ($\Gamma_{co}$) with a volume conductor ($\Omega_o$). Both have a thickness of $h$ and have external borders ($\Gamma_c$, $\Gamma_o$) electrically isolated. b) The equivalent cardiac and volume conductor planes of the tridomain model.

## 2 Tridomain: A 2D Model

In this section we develop a mathematical model for the propagation of electrical excitation in a thin piece of cardiac tissue in contact with an isotropic volume conductor. The situation considered here is similar to an *in vitro* animal experiment where the cardiac tissue is on the top of a perfusing bath, such as described in [2] and illustrated by Fig. 1. We stress, however, that we disconsider 3D effects by assuming the cardiac tissue to be thin enough. The bath is modeled by an isotropic conductor with conductivity $\sigma_o$. The electric potential $\phi_o$ in the interior of the bath ($\Omega_o$) satisfies

$$\sigma_o \Delta\phi_o(\mathbf{x},t) = 0, \mathbf{x} \in \Omega_o, \tag{1}$$

where $\mathbf{x} = (x, y, z)$. The cardiac tissue ($\Omega_c$) is simulated via the bidomain equations

$$\nabla.(\boldsymbol{\sigma_i}\nabla\phi_i(\mathbf{x},t)) = \chi\left(C_m\frac{\partial\phi(\mathbf{x},t)}{\partial t} + \frac{1}{R_m}f(\phi(\mathbf{x},t),n(\mathbf{x},t))\right), \tag{2}$$

$$-\nabla.(\boldsymbol{\sigma_e}\nabla\phi_e(\mathbf{x},t)) = \chi\left(C_m\frac{\partial\phi(\mathbf{x},t)}{\partial t} + \frac{1}{R_m}f(\phi(\mathbf{x},t),n(\mathbf{x},t))\right), \tag{3}$$

$$\frac{\partial n(\mathbf{x},t)}{\partial t} = g(\phi(\mathbf{x},t),n(\mathbf{x},t)), \tag{4}$$

$$\phi(\mathbf{x},t) = \phi_i(\mathbf{x},t) - \phi_e(\mathbf{x},t),\ \mathbf{x} \in \Omega_c. \tag{5}$$

where $\phi_i$, $\phi_e$ and $\phi$ are the intracellular, extracellular and transmembrane potentials; $n$ is the recovery variable; $\boldsymbol{\sigma_i}$ and $\boldsymbol{\sigma_e}$ are conductivity tensors of intracellular and extracellular spaces; $f$ and $g$ model ionic currents; $C_m$, $R_m$ and

$\chi$ are capacitance, transmembrane resistance and surface-volume ratio, respectively. Curved cardiac fibers are modeled by spatial variation of the conductivity tensors. The conductivity tensors $\boldsymbol{\sigma_i}$ and $\boldsymbol{\sigma_e}$ are of the form

$$\boldsymbol{\sigma_*} = \begin{pmatrix} \sigma_{*x} & \sigma_{*xy} & 0 \\ \sigma_{*xy} & \sigma_{*y} & 0 \\ 0 & 0 & \sigma_{*z} \end{pmatrix},$$

where $* = i$ or $e$. This means that we do not consider cardiac fiber curvature on the $z$ direction. We use the following boundary conditions for the bath to tissue interface (see [1]).

$$\phi_e(\mathbf{x}, t) = \phi_o(\mathbf{x}, t), \tag{6}$$

$$\boldsymbol{\sigma_e} \nabla \phi_e(\mathbf{x}, t).\eta = \sigma_o \nabla \phi_o(\mathbf{x}, t).\eta, \tag{7}$$

$$\boldsymbol{\sigma_i} \nabla \phi_i(\mathbf{x}, t).\eta = 0, \ \mathbf{x} \in \Gamma_{co}. \tag{8}$$

The other boundaries are assumed to be electrically isolated :

$$\boldsymbol{\sigma_i} \nabla \phi_i(\mathbf{x}, t).\eta = 0, \ \mathbf{x} \in \Gamma_c, \tag{9}$$

$$\boldsymbol{\sigma_e} \nabla \phi_e(\mathbf{x}, t).\eta = 0, \ \mathbf{x} \in \Gamma_c, \tag{10}$$

$$\sigma_o \nabla \phi_o(\mathbf{x}, t).\eta = 0, \ \mathbf{x} \in \Gamma_o. \tag{11}$$

Equations (1)-(11) constitute a 3D model. From these equations, we obtain a 2D model by assuming that both tissue and bath have a small thickness of $h$. We solve for the average over $z$, $\overline{\phi_*}(x, y) = 1/h \int_0^h \phi_*(x, y, z) dz$. Next we denote $\nabla = (\frac{\partial}{\partial x}, \frac{\partial}{\partial y})$, $\Delta = (\frac{\partial^2}{\partial x^2} + \frac{\partial^2}{\partial y^2})$ and

$$\overline{\boldsymbol{\sigma_*}} = \begin{pmatrix} \sigma_{*x} & \sigma_{*xy} \\ \sigma_{*xy} & \sigma_{*y} \end{pmatrix}.$$

Integrating (1) over $z$,

$$\sigma_o \Delta \overline{\phi_o}(x, y) + \frac{\sigma_o}{h} \left( \frac{\partial \phi_o(x, y, h)}{\partial z} - \frac{\partial \phi_o(x, y, 0)}{\partial z} \right) = 0. \tag{12}$$

Using (11),

$$\sigma_o \Delta \overline{\phi_o}(x, y) - \frac{\sigma_o}{h} \frac{\partial \phi_o(x, y, 0)}{\partial z} = 0. \tag{13}$$

Taking the average over $z$ for (2), using (9) and (8) we obtain that

$$\nabla.(\overline{\boldsymbol{\sigma_i}} \nabla \overline{\phi_i}) = \chi \left( C_m \frac{\partial \overline{\phi}}{\partial t} + \frac{1}{R_m} \int_{-h}^{0} f(\phi, n) dz \right). \tag{14}$$

Repeating this procedure with (3), using (10) and the interface conditions (7) we find that

$$\nabla.(\overline{\boldsymbol{\sigma_e}} \nabla \overline{\phi_e}) + \frac{\sigma_o}{h} \frac{\partial \phi_o(x, y, 0)}{\partial z} = -\chi \left( C_m \frac{\partial \overline{\phi}}{\partial t} + \frac{1}{R_m} \int_{-h}^{0} f(\phi, n) dz \right). \tag{15}$$

Finally, (4) implies that

$$\frac{\partial \overline{n}}{\partial t} = \int_{-h}^{0} g(\phi, n) dz. \tag{16}$$

Next we consider the following $O(h)$ approximations.

$$\frac{\partial \phi_o(x, y, 0)}{\partial z} \approx \frac{\overline{\phi_o}(x, y) - \overline{\phi_e}(x, y)}{h}, \tag{17}$$

$$\int_{-h}^{0} f(\phi, n) dz \approx f(\overline{\phi}, \overline{n}), \tag{18}$$

$$\int_{-h}^{0} g(\phi, n) dz \approx g(\overline{\phi}, \overline{n}). \tag{19}$$

Substituting (17)-(19) in (13)-(16) we obtain the 2D tridomain equations

$$\nabla.(\overline{\boldsymbol{\sigma_i}} \nabla \overline{\phi_i}) = \chi(C_m \frac{\partial \overline{\phi}}{\partial t} + \frac{1}{R_m} f(\overline{\phi}, \overline{n})), \tag{20}$$

$$\nabla.(\overline{\boldsymbol{\sigma_e}} \nabla \overline{\phi_e}) = -\chi(C_m \frac{\partial \overline{\phi}}{\partial t} + \frac{1}{R_m} f(\overline{\phi}, \overline{n})) - \frac{\sigma_o}{h^2}(\overline{\phi_o} - \overline{\phi_e}), \tag{21}$$

$$\sigma_o \Delta \overline{\phi_o} = \frac{\sigma_o}{h^2}(\overline{\phi_o} - \overline{\phi_e}), \tag{22}$$

$$\frac{\partial \overline{n}}{\partial t} = g(\overline{\phi}, \overline{n}), \tag{23}$$

$$\overline{\phi} = \overline{\phi_i} - \overline{\phi_e}. \tag{24}$$

We should mention an important difference among the model domains. The intra and extracellular domains of the cardiac tissue are spatially mixed, i.e., are on a same spatial plane. However, the bath plane is situated at a distance of $h$ from the tissue domain. Figure 1 shows this tridomain interpretation.

The numerical results presented in the next sections were obtained by solving the tridomain equations using a finite difference method on a regular space-time grid. The numerical scheme is semi-implicit and employs an operator splitting technique [6]. In the experiments we describe, we have considered a 1 cm size square for the cardiac tissue and for the bath, with thickness $h = 0.7$mm. The bidomain parameter values were extracted from [3]:

$$f(\phi, n) = c_1 \phi \, (1 - \phi/\Phi_t) \, (1 - \phi/\Phi_r) + c_2 \phi n, \tag{25}$$

$$g(\phi, n) = c_3(\phi - c_4 n), \tag{26}$$

with $c_1 = 0.5$, $c_2 = 0.02$, $c_3 = 0.015$, $c_4 = 0.005$. $C_m = 1\,\mu\text{F/cm}^2$, $\chi = 2000\,/\text{cm}$, $R_m = 1\,\text{k}\Omega\text{cm}^2$, $\Phi_t = 5$ mV, $\Phi_r = 100$ mV, $\sigma_{il} = 3.$ mS/cm, $\sigma_{it} = 0.31$ mS/cm, $\sigma_{el} = 2.$ mS/cm and $\sigma_{et} = 1.35$ mS/cm. In all simulations we set the spatial discretization to $\Delta x = 0.005$ cm and the time step to $\Delta t = 0.05$ ms.

## 3 Plane Waves

Consider the case of a plane wave that propagates in the $x$ direction and a cardiac tissue with straight fibers with an inclination of $\theta$ with $x$. This simple situation allows us to derive some interesting formulas for the cardiac current orientation and intensity. The conductivity tensors can be written as

$$\boldsymbol{\sigma_*} = \begin{pmatrix} \sigma_{*l}\cos^2\theta + \sigma_{*t}\sin^2\theta & (\sigma_{*l}-\sigma_{*t})\cos\theta\sin\theta \\ (\sigma_{*l}-\sigma_{*t})\cos\theta\sin\theta & \sigma_{*l}\cos^2\theta + \sigma_{*t}\sin^2\theta \end{pmatrix},$$

where $\sigma_{*l}$ and $\sigma_{*t}$ are longitudinal and transversal fiber conductivities. We consider the intracellular current density $\mathbf{J}_i = (J_{ix}, J_{iy}) = -\boldsymbol{\sigma_i}\nabla\phi_i$, the extracellular current $\mathbf{J}_e = (J_{ex}, J_{ey}) = -\boldsymbol{\sigma_e}\nabla\phi_e$, the bath current $\mathbf{J}_o = (J_{ox}, J_{oy}) = -\sigma_o\nabla\phi_o$, the total current $\mathbf{J} = \mathbf{J}_i + \mathbf{J}_e + \mathbf{J}_o = (J_x, J_y)$ and the cardiac current $\mathbf{J}_c = \mathbf{J}_i + \mathbf{J}_e = (J_{cx}, J_{cy})$. Since $\frac{\partial\phi}{\partial y} = \frac{\partial\phi_i}{\partial y} = \frac{\partial\phi_e}{\partial y} = \frac{\partial\phi_o}{\partial y} = 0$ it follows that $\mathbf{J}_* = (\sigma_{*x}\frac{\partial\phi_*}{\partial x}, \sigma_{*xy}\frac{\partial\phi_*}{\partial x})$ ($* = i$ or $e$) and $\mathbf{J}_o = (\sigma_o\frac{\partial\phi_o}{\partial x}, 0)$. The tridomain equations satisfy

$$-\frac{\partial J_{ix}}{\partial x} = \sigma_{ix}\frac{\partial^2\phi_i}{\partial x^2} = \chi(C_m\frac{\partial\phi}{\partial t} + \frac{1}{R_m}f(\phi, n)), \tag{27}$$

$$-\frac{\partial J_{ex}}{\partial x} = \sigma_{ex}\frac{\partial^2\phi_e}{\partial x^2} = -\chi(C_m\frac{\partial\phi}{\partial t} + \frac{1}{R_m}f(\phi, n)) - \frac{\sigma_o}{h^2}(\phi_o - \phi_e), \tag{28}$$

$$-\frac{\partial J_{ox}}{\partial x} = \sigma_o\frac{\partial^2\phi_o}{\partial x^2} = \frac{\sigma_o}{h^2}(\phi_o - \phi_e). \tag{29}$$

Summing up these equations we obtain that $\frac{\partial J_x}{\partial x} = 0$. The homogeneous boundary conditions then yield

$$J_x = -\sigma_{ix}\frac{\partial\phi_i}{\partial x} - \sigma_{ex}\frac{\partial\phi_e}{\partial x} - \sigma_o\frac{\partial\phi_o}{\partial x} = 0. \tag{30}$$

So the total current of the tridomain does not have a component on the direction of the propagation , as for the bidomain equations ([4], [5]). The transversal component, $J_y = -\sigma_{ixy}\frac{\partial\phi_i}{\partial x} - \sigma_{exy}\frac{\partial\phi_e}{\partial x}$, can be written in terms of the transmembrane potential $\frac{\partial\phi}{\partial x}$ and the volume conductor current $\mathbf{J}_o$. Using (30) and equations $\phi = \phi_i - \phi_e$, $J_{ox} = -\sigma_o\frac{\partial\phi_o}{\partial x}$, it follows that

$$J_y = \frac{(\sigma_{exy}\sigma_{ix} - \sigma_{ixy}\sigma_{ex})}{(\sigma_{ix} + \sigma_{ex})}\frac{\partial\phi}{\partial x} - \frac{(\sigma_{exy} + \sigma_{ixy})}{(\sigma_{ix} + \sigma_{ex})}J_{ox}. \tag{31}$$

Substituting $\sigma_{*x}$ by $\sigma_{*l}\cos^2\theta + \sigma_{*t}\sin^2\theta$ and $\sigma_{*xy}$ by $(\sigma_{*l} - \sigma_{*t})\cos\theta\sin\theta$ we obtain

$$J_y = \frac{\cos\theta\sin\theta\left((\sigma_{il}\sigma_{et} - \sigma_{el}\sigma_{it})\frac{\partial\phi}{\partial x} + (\sigma_{il} + \sigma_{el} - \sigma_{it} - \sigma_{et})J_{ox}\right)}{(\sigma_{il} + \sigma_{el})\cos^2\theta + (\sigma_{it} + \sigma_{et})\sin^2\theta}. \tag{32}$$

From (32) we note that the term $(\cos\theta \sin\theta)/((\sigma_{il}+\sigma_{el})\cos^2\theta+(\sigma_{it}+\sigma_{et})\sin^2\theta)$ intensifies the influence of the cardiac fiber orientation on the amplitude of the transversal currents. So the transversal currents are highly dependent on $\theta$.

Although there is no current $\mathbf{J}$ in the direction of propagation $x$, we assume that part of the current (the bath current) is away from the magnetic detector, so that the magnetic field is mainly generated by $\mathbf{J}_c$. By doing so, we already see the effect of the volume conductor, since current $\mathbf{J}_c$ is no longer transversal to the propagation direction,

$$\mathbf{J}_c = \mathbf{J} - \mathbf{J}_o = (-J_{ox}, J_y). \tag{33}$$

In fact, from the above equations it is possible to prove that the monodomain and bidomain models appear as particular cases of the tridomain formulation. If there is no volume conductor ($\sigma_o = 0$), $J_{ox} = 0$ and we reduce to the bidomain case, where $\mathbf{J}_c$ is transversal to the propagation direction independently of $\theta$. For of a volume conductor with infinite conductivity ($\sigma_o = \infty$) we are reduced to the monodomain model with $\mathbf{J}_c = -\mathbf{J}_o = \mathbf{J}_i = (J_{ix}, J_{iy})$. In this case, the current inclination $\gamma = \arctan(J_{iy}/J_{ix})$ satisfies

$$\gamma = \arctan((\sigma_{it} - \sigma_{il})\cos\theta \sin\theta/(\sigma_{il}\cos^2\theta + \sigma_{it}\sin^2\theta)). \tag{34}$$

So $|\gamma|$ varies from $0^o$ to $\max|\gamma_m(\theta)| = \arctan((\sigma_{il} - \sigma_{it})/(2\sqrt{\sigma_{il}\sigma_{it}}))$, which is attained for $\theta = \pm\arctan(\sqrt{\sigma_{il}/\sigma_{it}})$. For $\sigma_o > 0$ and finite, the current inclination $\gamma$ for the tridomain lies between this two limit cases. So both orientation and amplitude of the current that generates the magnetic field are dependent on the fiber orientation.

The above theoretical results give us an insight of what are the effects of a volume conductor on the currents in the cardiac tissue: the current orientation is no longer transversal to the propagation; and it depends on the local fiber orientation. In order to quantify such effects we numerically solve the system (27)-(29) for different values of $\theta$ and $\sigma_o$. Figure 2 shows the magnitude of the cardiac current, $\max||\mathbf{J}_c(x)||_2$, the amount of transversal current information, $r_y = \max|J_{cy}(x)|/\max||\mathbf{J}_c(x)||_2$, the current orientation with respect to $x$, $\gamma = \arctan(\max|J_{cy}(x)|/\max|J_{cx}(x)|)$, and $(\gamma - \theta)$ against $\theta$ for $\sigma_o = 0.2$, 2, 20 and 200 mS/cm. In all graphs, as we vary $\sigma_o$, we move from a behavior similar to the bidomain (low $\sigma_o$) to one similar to the monodomain situation (high $\sigma_o$). We note that for high $\sigma_o$, $||\mathbf{J}_c||_2$ is nearly independent on $\theta$ for values of $\theta$ up to $70^o$. This is the case for instance with $\sigma_o = 20$ mS/cm and $\sigma_o = 200$ mS/cm, which are in the normal range for perfusing bath, blood, and many body tissue conductivities. So, in the presence of such volume conductor the cardiac current intensity only significantly changes when cardiac fibers are almost orthogonal to the propagation direction. On the other side, $r_y$ and $\gamma$ become more dependent on $\theta$ for high $\sigma_o$. While for the bidomain case $\gamma = 0$ for all $\theta$, for the general case of the tridomain model $\gamma$ does depend on $\theta$. In addition, the graph of $\gamma_t - \theta$ shows that for $\sigma_o = 20$ mS/cm and $\sigma_o = 200$ mS/cm the current and fiber orientations are very close. Only for $\theta > 80^o$ they are significantly different. However, for these high values of $\theta$ the current intensity is very low, and therefore would not significantly affect the measured magnetic field.

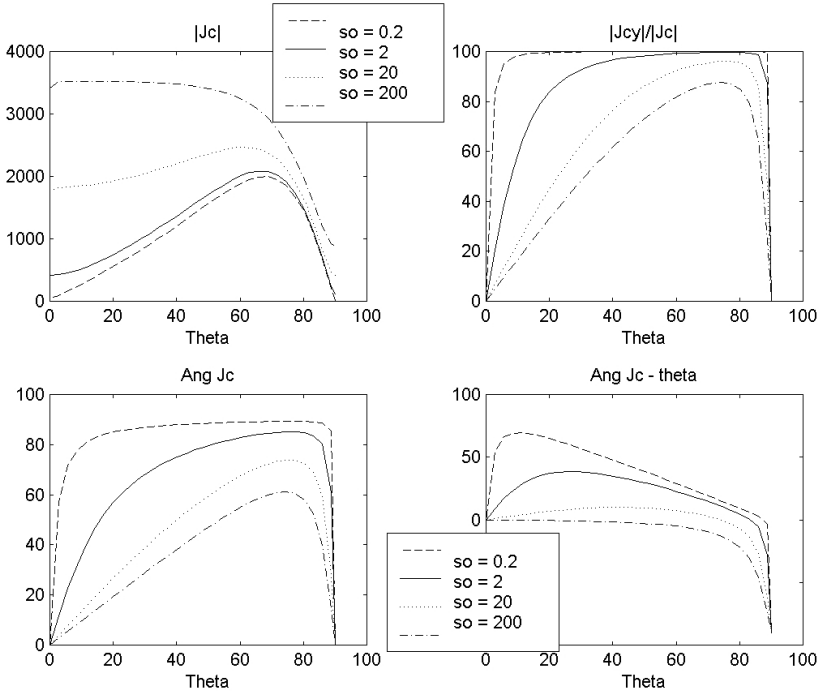


**Fig. 2.** Numerical results for plane wave simulation. The magnitude of the cardiac current, $\max ||\mathbf{J}_c(x)||_2$ ($|Jc|$), the amount of transversal current information, $r_y = \max |J_{cy}(x)| / \max ||\mathbf{J}_c(x)||_2$ ($|Jcy|/|Jc|$), the current orientation with respect to $x$, $\gamma = \arctan(\max |J_{cy}(x)| / \max |J_{cx}(x)|)$ (Ang $Jc$), and $(\gamma - \theta)$ against $\theta$ (theta), the cardiac fiber inclination, for $\sigma_o$ (so) = 0.2, 2, 20 and 200 mS/cm.

## 4 2D General Propagation

In this section we investigate the 2D general case of propagation in a cardiac tissue in contact with an isotropic volume conductor which has conductivity $\sigma_o = 20$ mS/cm. First we simulate a point stimulus on the middle left of a tissue with straight horizontal fibers, see Fig. 3. Figure 4 shows the distribution of $\mathbf{J}$, $\mathbf{J}_c$, $\mathbf{J}_o$ and the difference $\mathbf{J} - \mathbf{J}'$, where $\mathbf{J}'$ is the theoretical current based on formula (32). $\mathbf{J}$ tends to be perpendicular to $\nabla\phi$, while the bath current $\mathbf{J}_o$ tends to align to $\nabla\phi$. The orientation of $\mathbf{J}_c$ is basically horizontal, i.e., the same as the cardiac fiber orientation. Only when the fibers are close to orthogonal to the local propagation direction the cardiac current orientation changes. Nevertheless, these are very low intensity currents. The distribution of $\mathbf{J} - \mathbf{J}'$ shows that the transversal currents on the wave front are well approximated by (32). Most of the difference between $\mathbf{J}$ and $\mathbf{J}'$ is restricted to currents ahead of the wave front, the so-called return currents [7]. We warn the reader that in Figs. 4, and 6, the distribution of $\mathbf{J}$ and $\mathbf{J} - \mathbf{J}'$ are presented in different scales.

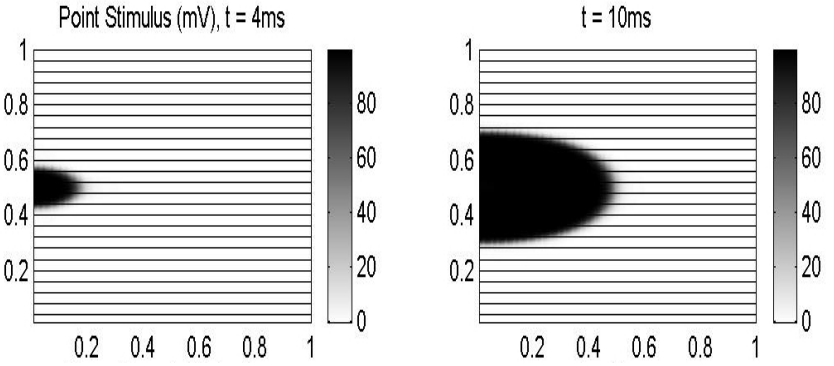


**Fig. 3.** Fiber orientation and transmembrane potential maps of two consecutive time instants for a point stimulus on a cardiac tissue with straight horizontal fibers.

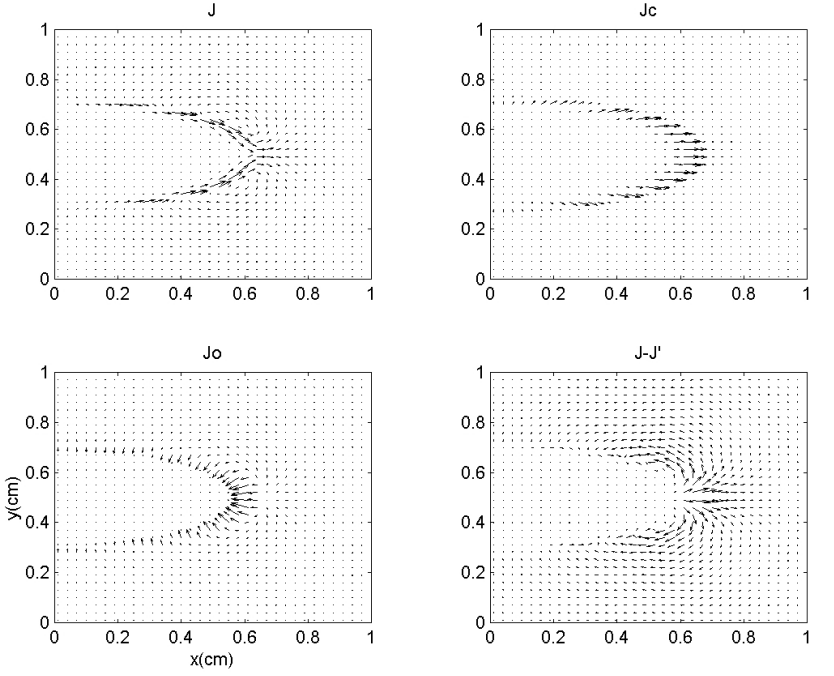


**Fig. 4.** Current distributions for the point stimulus experiment for $t = 10$ ms. The total current $\mathbf{J}$ is mainly transversal to $\nabla\phi$, but most of the cardiac current $\mathbf{J}_c$ is on the $x$ direction. $\mathbf{J}_o$ has the same direction of $\nabla\phi$. The difference $\mathbf{J} - \mathbf{J}'$ shows that the transversal currents on the wave front are well approximated by (32), except for return currents ahead of the wave front.

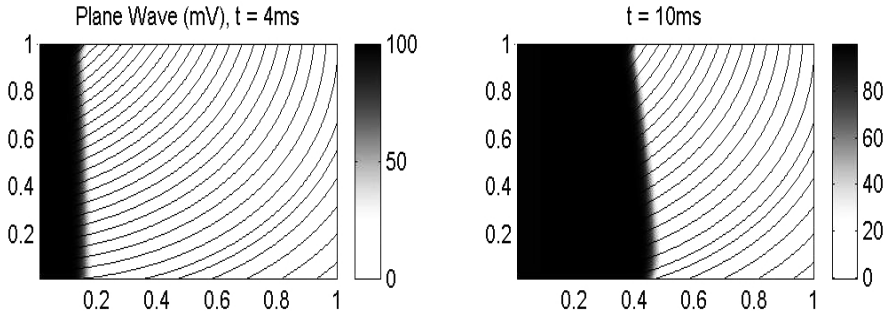


**Fig. 5.** Fiber orientation and transmembrane potential maps of two consecutive time instants for a plane stimulus on a cardiac tissue with curved fibers.

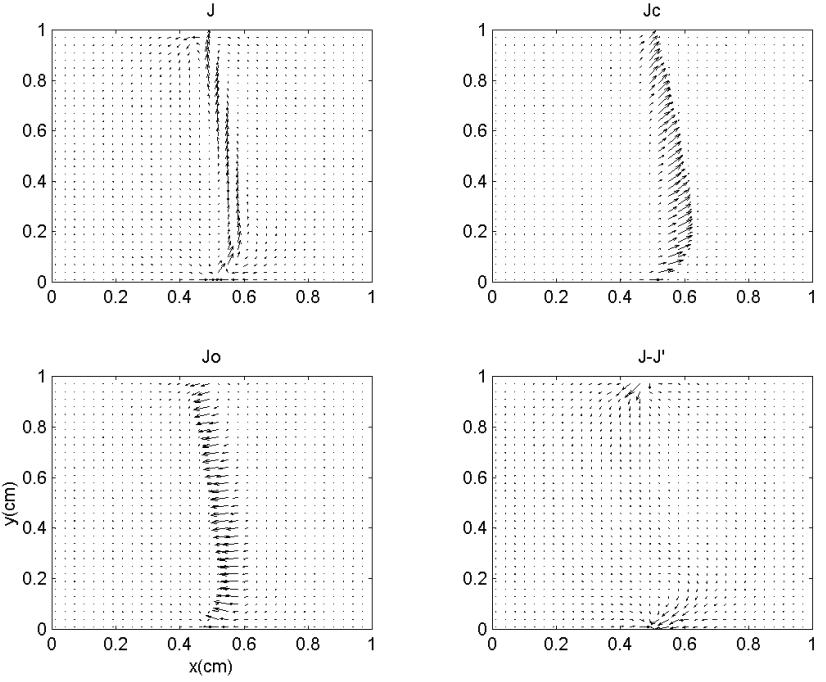


**Fig. 6.** Current distributions for the plane stimulus experiment for $t = 10$ ms. The total current $\mathbf{J}$ is mainly transversal to $\nabla\phi$, but the cardiac current $\mathbf{J}_c$ has the cardiac fiber orientation. $\mathbf{J}_o$ is on the direction of $\nabla\phi$. The difference $\mathbf{J}-\mathbf{J}'$ shows that the transversal currents on the wave front are well approximated by (32), except for reflected currents at the boundary.

We next simulate a plane current injection at the left boundary $x = 0$. The wave propagates on an electrically isolated tissue with spiral shaped fibers as those in the apex of the heart, see Fig. 5. Figure 6 shows the distribution of $\mathbf{J}$, $\mathbf{J}_c$, $\mathbf{J}_o$ and the difference $\mathbf{J} - \mathbf{J}'$. Once more, $\mathbf{J}$ tends to be perpendicular to $\nabla\phi$, the bath current $\mathbf{J}_o$ tends to align to $\nabla\phi$, and $\mathbf{J}_c$ and the local cardiac fibers $\theta$ have similar orientation. The distribution of $\mathbf{J} - \mathbf{J}'$ show that the currents on the wave front are well approximated by (32), except for the existence of reflected currents at the boundary which are not captured by $J'$.

We have performed various other experiments, with different current injection points and different fiber geometries, generating complex electrical distributions. The results were consistent with those described above.

## 5 Conclusions

In this work we have developed a new two-dimensional mathematical model that accounts for the influence of volume conductor on a thin cardiac tissue. Our numerical results show that a volume conductor may alter the cardiac current orientation by aligning it to the cardiac fiber direction. We would therefore expect that the currents that generate the magnetic field are no longer transversal to the propagation direction, as suggested by recent studies ([4], [5]). Our 2-D tridomain model may be considered a good approximation for various situations, such as *in vitro* experiments with thin cardiac tissue, electric propagation at the atrium and the interface ventricular-blood or ventricular-torso regions. Nevertheless, it contains all the limitations of a 2-D approximation. We are currently developing a tri-dimensional simulator to pursue this investigation on more general situations.

**Acknowledgments.** We gratefully acknowledge useful discussions with Hans Koch and Uwe Steinhoff and the support provided by Brazilian CAPES doctorate scholarship and by 13N8125 BMFT German ministry of research and technology.

## References

1. W. Krassowska, J. Neu *"Effective boundary conditions for syncytial tissues"*, IEEE Trans. on Biomed. Eng., vol 41, 2 (1994), 143–150.
2. E. Monteiro et al. *"Animal experimentation study of atrial activity propagation using a multi-channel SQUID system"*, Biomedizinische Technik, vol 46, 2 (2001), 70–72.
3. A. Muzikant, C. Henriquez *"Validation of three-dimensional conduction models using experimental mapping: are we getting closer?"*, Progress in Biophysics and Molecular Biology, 69 (1998), 205–223.
4. B. Roth, M. Woods *"The Magnetic Field Associated With a Plane Wave Front Propagating Through Cardiac Tissue"*, IEEE Trans. Biomed. Eng., vol 46, 11 (1999),1288–1292.

5. R. Weber dos Santos, F. Dickstein, D. Marchesin *"Transversal versus longitudinal current propagation on a cardiac tissue and its relation to MCG"*, Biomedizinische Technik, vol 47, 1 (2002), 249–252.
6. R. Weber dos Santos, F. Dickstein *"Splitting Techniques for Cardiac Models"*, in preparation.
7. J. Wikswo *"Tissue Anisotropy, the Cardiac Bidomain and the Virtual Cathode Effect"*, Cardiac Electrophysiology: From Cell to Bedside, Second Edition (W.B. Saunders, Orlando), D.P. Zipes and J. Jalife, Eds. (1994), 348–361.

# First 36-Channel Magnetocardiographic Study of CAD Patients in an Unshielded Laboratory for Interventional and Intensive Cardiac Care[1]

Donatella Brisinda, Anna Maria Meloni, and Riccardo Fenici

Clinical Physiology – Biomagnetism Research Center, Catholic University of Sacred Heart
L.A. Gemelli 8, 00168 Rome, Italy
feniciri@rm.unicatt.it

**Abstract.** The first 36-channel Magnetocardiographic (MCG) system, successfully installed in the Biomagnetism Research Center, Catholic University of Rome, has been tested to evaluate the reliability of this novel instrumentation for the study of patients with coronary artery disease (CAD), in an "unshielded" laboratory for interventional and emergency cardiac care. 13 patients, with coronary disease documented by angiography, 8 patients with abnormality of non-invasive studies (exercise-ECG or SPECT), and 13 healthy controls (age-matched) were investigated at rest. Other 6 cases were investigated, before and after stress test with a standard ergometer. The sensitivity of the system was 20 fT/√Hz, at 1Hz. After morphological evaluation, quantitative analysis of magnetocardiographic repolarization parameters was performed according to Hänninen et al. and Park et al. At rest, magnetocardiographic mapping has shown abnormality of repolarization in 95.2% of CAD patients, with sensibility of 92.6%, specificity of 92.3%, and predictive value 92.3%.

## 1 Introduction

In clinical practice, non-invasive evaluation of myocardial ischemia is usually performed with exercise-ECG, echocardiography or radionuclide imaging using SPECT (Single Photon Emission Computed Tomography) at rest and under stress. More recently, Positron emission tomography (PET) and Magnetic Resonance Imaging (MRI) are also increasingly used for more advanced functional imaging. However, such procedures are either expensive or, particularly echocardiographic imaging, highly dependent on the skill of the interpreter, or need radioactive tracers. Multichannel Magnetocardiography (MMCG) on the contrary is a method for non-invasive imaging of repolarization phenomena [1], which seems promising for quick, contactless screening of patients with myocardial ischemia [2–4]. Thus the interest of clinicians

[1] Supported by MIUR grants # 9906571299_001 and 2001064829_001. The authors are also grateful to Dr. Carl Rosner, Prof. Alexander Bakarev, Prof. Alexander Braginski, Dr. Nikolai Korsun, Dr. Karsten Sternickel and Dr. Jury Poliakov for continuous help in solving the problems for the CMI system installation and for the stimulating scientific cooperation. The significant support of Dr. Jukka Nenonen of the Helsinki University of Technology has been fundamental to this work. The dedication of Mrs. Viola Iacobini, our professional nurse, is outstanding and invaluable.

I. Magnin et al. (Eds.): FIMH 2003, LNCS 2674, pp. 122–131, 2003.

for MMCG, as an alternative for the detection of ischemia, is growing up continuously, and several studies have already evidenced that exercise-induced ischemia causes significant changes in the MCG of patients with coronary artery disease (CAD) [5–8]. It was recently suggested that MMCG enables the detection of viable myocardium after infarction [9] and provides three-dimensional (3D) localization and imaging of abnormal current flowing associated with ischemia [10–12].

So far MMCG was carried out with expensive systems requiring magnetically shielded rooms (MSRs), inadequate for the study of patients in whom an acute ischemia could require emergency intervention. Furthermore, in order to perform stress-MMCG custom, amagnetic ergometers had to be constructed [1,6,8], which performance is not fully standardized.

The purpose of this study was to evaluate whether or not unshielded MMCG, carried out in an hospital laboratory equipped with "electromagnetically noisy" instrumentation for intensive and interventional care of cardiac critical patients, could be still sensitive enough to detect ventricular repolarization abnormalities due to myocardial ischemia, using the quantitative parameters proposed by Hänninen et al [5] and by Park et al. [13].

Secondly, an attempt was made to evaluate the feasibility of combined stress ECG and MMCG, carried out with a conventional bicycle ergometer, at the minimal distance between MMCG system and the ergometer to avoid electromagnetic interference and artifacts.

## 2 Methods

### 2.1 The MCG Mapping System

The 36-channel MCG system operating in the unshielded catheterization laboratory of the Catholic University of Rome, *(CARDIOMAG IMAGING INC, USA)* measures, with a single data acquisition, the *z*-component of local magnetic fields at 36 positions in a plane (6 x 6 grid, covering an area of 20 x 20 cm), with 36 DC-SQUID sensors coupled to second-order axial gradiometers (55 mm baseline). The cylindrical cryostat doesn't affect the operational capability of the cardiologist during interventions. The intrinsic sensitivity of the system is 20 fT/√Hz in the frequency range of interest for clinical MCG *(1 to 100 Hz).* Signals are recorded with a Windows NT-based acquisition system *(24 bits A/D conversion, 1-4 kHz sampling frequency and automatic electronic noise rejection).* By shifting the patient couch from fluoroscopy to the MCG mapping system and viceversa, it is possible to fuse images obtained with MMCG, intracardiac mapping and bidimensional digital radiology. The standard mapping procedure requires 90 seconds.

Post processing is done with Windows NT-based PC software (*CMI*, *USA*) and UNIX-based X-MCG software *(NEUROMAG, FINLAND),* which provides functional source localization and imaging, with the Equivalent current dipole (ECD), Effective Magnetic Dipole (EMD) and distributed currents imaging (CDI) models, in less than 2 minutes, after the recording is finished. The inverse solution for localization and imaging is applied after MMCG raw data are filtered, baseline corrected and aver-

aged. Multimodal integration of the MMCG localization results is possible with fluoroscopy, MRI and 3D model images of the patient's torso and heart. A commercial bicycle-ergometer was used for stress test. The minimal distance between the ergometer and the MMCG system, to avoid electromagnetic interference, was experimentally identified. An overview of the laboratory set-up, for the study of CAD patients, is shown in Fig. 1.

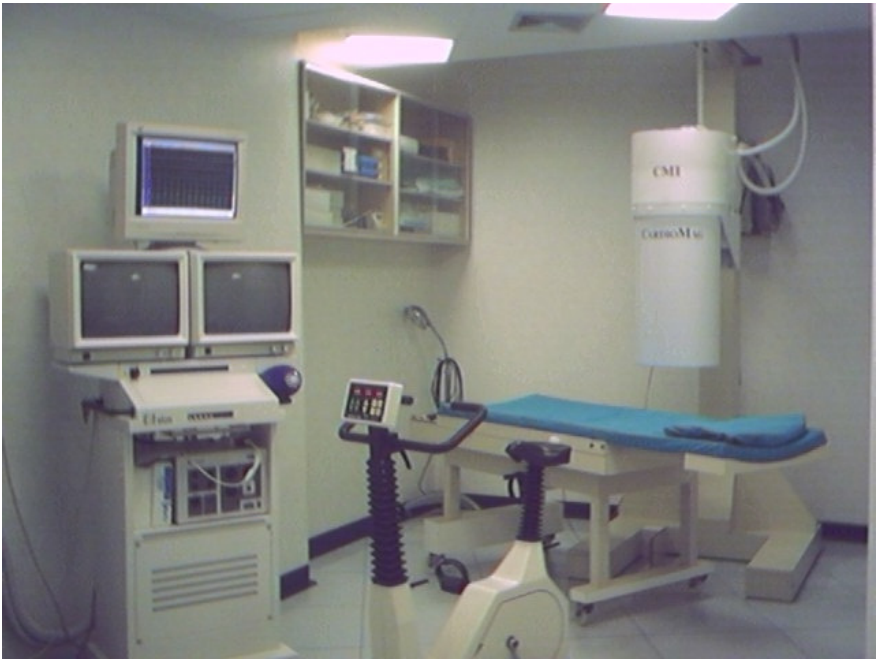

**Fig. 1.** Overwiev of the laboratory set-up for stress MMCG. The movable bed is behind the bicycle-ergometer. Immediately after the target rate has been reached, the patient lies down on the bed and is wheeled to the MMCG system. The time required to initiate the post-stress MMCG is 90 seconds.

## 2.2 Signal Analysis

The data were, independently, evaluated by two cardiologists; in case of different opinions, a consensus was achieved after data were submitted to a third investigator.

First evaluation of the MMCG study was done by morphological analysis of the time evolution of the magnetic field maps during the ST-T interval, then, quantitative data analysis, according to Hänninen et al. [5] and to Park et al. [13], was carried out.

With the first method [5], after automatic construction of the magnetic field maps (MFMs), two time points were discretionally identified by the cardiologist: the J point

and the T-wave apex, which defined the ST-segment. Then, for the determination of the magnetic field orientation at the two time-intervals of interest, the surface gradient method, based on the arrow maps, was applied. The location and direction of the largest spatial gradient of the signal distribution in the measurement plane was computed at two time-intervals: 1) the integral of the second quarter from the J-point to the T-wave apex, representing ST-segment, and 2) the T-wave apex. The MFM **angle α** was then calculated as the angle between the direction of the largest gradient and the patient's right-left line, for both intervals (ST-segment and T-wave apex) (Fig. 2).

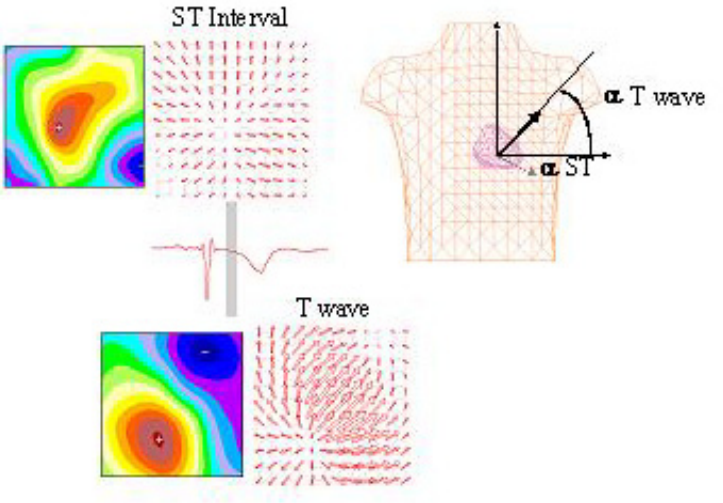


**Fig. 2.** Sequence of data processing for the calculation of the α angle at the second quarter of the ST interval and at the apex of the T-wave

The quantitative analysis according to Park et al. [13], was done with the CMI proprietary software. Three parameters were calculated and at least one of them had to change pathologically for diagnosis of ischemia: 1) pattern with at least two dipoles in the time interval between $S_{100}$ (the point in time 100 ms at the end of S-wave) and Tmax (apex of T wave); 2) the direction of current vector (CV) between – 20° + 110° for the same time interval; 3) if CV direction lies between + 110°and – 20°, one of these three parameters has to be satisfactory: a) change angle of CV > 60 in 30 ms of change angle of $S_{100}$ Tmax, b) change pole distance > 20 mm (in 30ms of $S_{100}$-Tmax), c) ratio MF poles strength > ± 0.3 (in 30 ms of $S_{100}$-$T_{max}$).

### 2.3 Patients

This study was aimed to test the reliability of MMCG as a new method for the investigation of myocardial ischemia, in an unshielded clinical setting, equipped with standard instrumentation for stress testing, intensive care and invasive interventions, and to optimize the operational protocol for stress-MMCG.

21 pts (15 male and 6 female, age 63+/-10 years) with documented coronary artery disease (17 by angiography and 4 by SPECT and exercise-test), who volunteered for this protocol, after written informed consent, were studied at rest. The MCG data of 13 healthy subjects (8 male and 5 female, age 54+/-8 years) were used for comparison. 6 additional patients, who volunteered, were studied both at rest, and after effort test, with bicycle ergometer. Stress MMCG was performed at: 90 seconds, 4 minutes, 7 minutes and 10 minutes after the end of the effort. Each recording was of 90 seconds.

### 2.4 Statistic Analysis

Data are reported as mean value +/- standard deviation (SD).

The calculation of sensitivity and specificity of the diagnostic test was made according to the following parameters:

a) fraction of pts with disease having a positive test result (true positive)
b) fraction of pts without disease having a positive test result (false positive)
c) fraction of pts with disease having a negative test result (false negative)
d) fraction of pts without disease having a negative test result (true negative).

The ***sensitivity*** was calculated as the number of true positive results divided by the number of pts having disease (as detected by the tests): a/(a+c).

The ***specificity*** was calculated as the number of true negative results divided by the number of pts without disease (as detected by the tests): d/(b+d).

It can also calculate how the probability that, with a positive diagnostic test result, the disease is actually present (***positive predictive value***): a/(a+b); and with a negative test result, the disease isn't present (***negative predictive value***): d/(d+c).

## 3 Results

With the system sensitivity of 20 fT/√Hz, in the frequency range of 1 to 100 Hz, the quality of MCG signals was good enough to quantify all the parameters of interest, after adaptive digital filtering of the 50 Hz noise, automatic averaging of 60-100 beats and construction of magnetic field maps.

At the morphological analysis, all the three cardiologists agreed that the magnetic field distribution during the ST interval was abnormal in all patients and in 4 controls out of 13. However, using the quantitative analysis proposed by Hänninen et al. [5], the magnetic field orientation of the integral of the second quarter from the J-point (**ST angle $\alpha$**) was abnormal (210 ± 129.3 SD), in 9/13 (69.2%) pts with abnormal

coronary angiography, and in 16/21 (76.2%) pts (212.9 ± 113 SD) studied with SPECT. The **T-wave apex angle α** was **abnormal** in 2/13 patients (15.3%) (59.1± 112 SD) with abnormal coronary angiography and in 4/21 patients (19%) (105.8 ± 114).

According to Park [13], at least one of three parameters was abnormal 17/21 (80.9%) pts, and in 11 of the 13 (84.6%) pts with abnormal coronary angiography.

By pooling the abnormalities found with either of the two methods, 20/21 (95.2 %) pts with CAD were correctly identified by MMCG (see Table 1). The same parameters were normal in 93.4% of control cases according to Hänninen [5], and in 100% according to Park [13]. Examples of normal and abnormal magnetic field patterns are shown in Fig. 3 and Fig. 4, respectively.

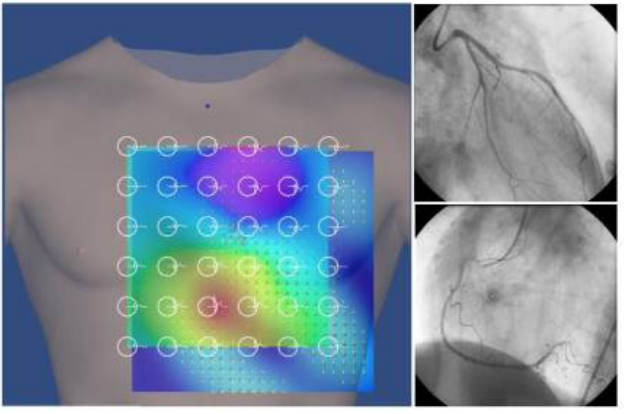

**Fig. 3.** Magnetic field distribution and current reconstruction, during the ST segment, in a patient with normal coronary angiography

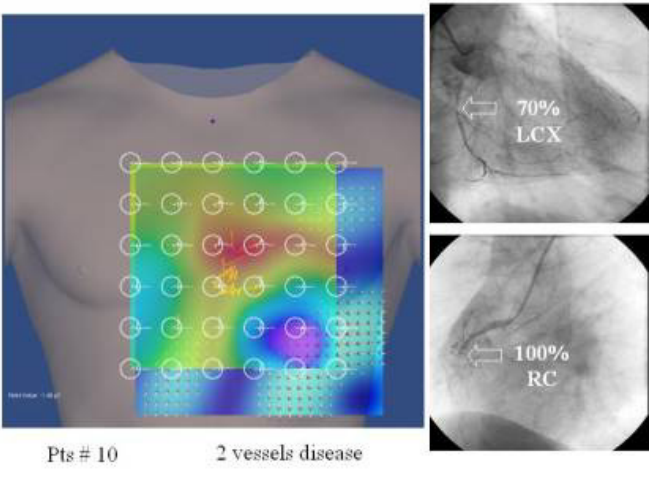


**Fig. 4.** Magnetic field distribution and current reconstruction, during the ST segment, in a patient with abnormal coronary angiography (two vessel disease)

**Table 1**. MCG findings of 21 CAD patients, 13 with positive coronary angiography. Stress ECG, and SPECT findings are also shown. (n.a. = not available. Abnormal ST and T alfa angle values are in italics)

| Pat. | Vessels | Stress | SPECT | Morfology | Hänninen et al [2] | | Park et al.[13] | | |
|---|---|---|---|---|---|---|---|---|---|
| # | # | ECG | | MCG | ST alfa | T alfa | 1 | 2 | 3 |
| 1 | 1 | + | n.a. | + | 58,3 | 33,5 | - | - | - |
| 2 | 1 | + | n.a. | + | *354,9* | 5,1 | + | + | + |
| 3 | 1 | + | + | + | 34,7 | 51,5 | + | - | + |
| 4 | 1 | - | n.a. | + | *90,5* | 84,4 | - | - | - |
| 5 | 1 | + | n.a. | + | 70,9 | 60,6 | - | - | + |
| 6 | 2 | + | n.a. | + | 44,8 | 59,1 | + | - | + |
| 7 | 2 | + | n.a. | + | *238,8* | 39,7 | + | + | + |
| 8 | 2 | + | + | + | *250,0* | 70,0 | + | - | + |
| 9 | 2 | + | + | + | *314,1* | 45,0 | + | - | + |
| 10 | 2 | + | + | + | *272* | 63,4 | + | + | + |
| 11 | 2 | + | + | + | *325,8* | *333,6* | + | + | + |
| 12 | 3 | + | n.a. | + | *355,8* | 44,3 | + | - | + |
| 13 | 3 | n.a. | n.a. | + | *324,6* | *353,2* | + | + | + |
| 14 | 0 | + | + | + | *125* | 67,8 | + | + | + |
| 15 | 0 | + | + | + | *303* | *300* | - | + | + |
| 16 | 0 | + | + | + | *325* | 31 | - | - | + |
| 17 | 0 | + | + | + | *220,8* | 68,3 | + | + | + |
| 18 | n.a. | + | + | + | *225* | 53,9 | - | - | - |
| 19 | n.a. | + | + | + | 60,5 | 57,5 | - | - | + |
| 20 | n.a. | + | + | + | *256* | *344* | + | + | + |
| 21 | n.a. | + | + | + | *220* | 55,5 | + | + | + |

Combined ECG and MCG stress test was feasible using a conventional bicycle ergometer. Therefore a standardized stress protocol was used. Out of 6 investigated patients, only one was positive for stress-induced ischemia at the ECG. MMCG in this patient reproduced the abnormal rotation of the magnetic field gradient during the ST interval as reported by Hänninen et al. [5] (Fig. 5).

## 4 Discussion

Previous studies had already suggested that MCG contains additional information not present in the ECG [1,14]. More recent work, carried out in magnetically shielded rooms, has given evidence that, in patients with different degree of CAD, exercise-

induced myocardial ischemia causes significant changes in the magnetocardiogram of the CAD patient, and that changes related to special phases of the cardiac repolarization enable approximate localization of the ischemic myocardial region [3, 5,10,11].

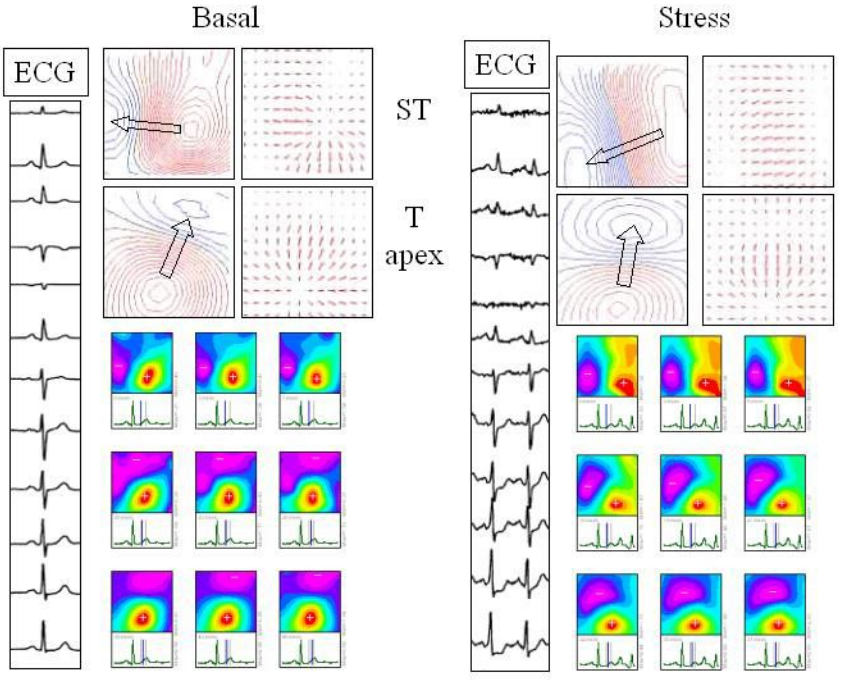


**Fig. 5.** Example of Stress MMCG, in one patient with inferior-lateral ischemia. The abnormal magnetic field distribution during the ST, already evident in basal state, impairs after effort (counterclockwise rotation of the Magnetic Field Gradient). The T wave α angle is only slightly modified. The rest ECG did not evidence any significant abnormality

According to Tsukada et al. [4], in the presence of ischemia, the current flow during ventricular repolarization becomes random, and the strength of the magnetic field becomes weaker, as compared to normal myocardium, where the current flow is almost uniform during repolarization. This might explain the difference between the ST magnetic field of CAD patients and normal controls (see Fig. 3 and Fig. 4). It has been reported that exercise-induced ischemia determines abnormalities in the ST-segment orientation of magnetic field, after cessation of stress, and that T-wave MFM orientation abnormalities appear later [5]. Furthermore the rotational change of T-wave magnetic field, after exercise, was useful to differentiate patients with right coronary artery disease from those with left descending anterior, and circumflex coronary arteries. Moreover MMCG seems to be more sensitive to detect inferior wall ischemia [5].

As compared with above mentioned studies, all carried out in magnetically shielded rooms, our study provides for the first time the demonstration that, with presently available technology, MMCG study of CAD patients, can be performed also in an unshielded hospital room fully equipped for intensive cardiac care and interventional cardiology, with quality good enough to detect and quantify ventricular repolarization abnormalities due to myocardial ischemia.

We have studied patients with coronary artery disease (true positive) and a case-control group (true negative). For quantitative analysis of ventricular repolarization we have used different parameters, to test their sensibility, specificity and predictive value. Indeed, although the number of patients at the moment is limited by the design of the study, which was primarily aimed to test the reliability of the MMCG system for the investigation of myocardial ischemia in an unshielded clinical setting, we have found that rest MMCG identifies repolarization abnormalities in almost 100% of patients with chronic CAD. In fact, MMCG at rest evidenced morphological abnormalities of the MFM during the ST-segment in 100% of pts, even in those with negative effort-ECG and normal ST angle α. As concerns the two method used for quantitative analysis [5,13], calculated parameters were abnormal in 95.2% of patients, with cumulative sensibility and specificity above 90%. Hänninen's criteria were slightly less sensitive than Park's ones (76.1% vs 80.9%, respectively), but more specific (92.3% vs 84.6%, respectively).

Furthermore, although the stress-MMCG protocol was only aimed to test the feasibility of the method, our results demonstrates that, with the 36-channel system designed for unshielded environment, stress-MMCG can be performed with a commercial bicycle-ergometer, without significant electromagnetic interference (see Fig. 1 and Fig. 5). This should facilitate clinical application of stress MMCG and provide a better standardization of the method, though full comparability with simultaneous ECG recording [9]. Especially in this preliminary phase, it is our opinion that simultaneous 12-lead ECG monitoring during the stress test is mandatory, because clinical experience with MCG waveforms and the quality of real time MCG signals are not adequate to safely monitor the patient's conditions otherwise. Interestingly a good agreement was found between stress ECG and MCG in all the 6 investigated cases; however further work is needed to define the respective predictivity of the two methods.

Finally, as the new 36-channel instrumentation allows true DC-MCG recording, MMCG might be able to detect, localize and image abnormal injury current flowing associated with ischemia and to study their potential arrhythmogenic effect [15, 16].

## References

1. Brockmeier, K., Schmitz, L., Bobadilla Chavez, J.D., Burghoff, M., Koch, H., Zimmermann, R., Trahms, L.: Magnetocardiography and 32-lead potential mapping: repolarization in normal subjects during pharmacologically induced stress. J Cardiovasc Electrophysiol. 18 (1997) 615–626
2. Nomura, M., Nakaya, Y., Fujino, K., Ishihara, S., Katayama, M., Takeuchi, A., Watanabe, K., Hiasay, Y., Aihara, T., Mori, H. : Magnetocardiographic studies of ventricular repolarization in old inferior myocardial infarction. Eur Heart J. 10 (1) (1989) 8–15

3. Sato, M., Terada, Y., Mitsui, T., Miyashita, T., Kandori, A., Tsukada, K. : Detection of myocardial ischemia by magnetocardiogram using 64-channel SQUID system. In: Nenonen, J., Ilmoniemi, R.J., Katila, T., (eds): Proceedings 12th International Conference on Biomagnetism, Helsinki Univ. of Technology, Espoo, Finland (2001) 523–526
4. Tsukada, K., Miyashita, T., Kandori, A., Mitsui, T., Terada, Y., Sato, M., Shiono, J., Horigone, H., Yamada, S., Yamaguchi, I.: An iso-integral mapping technique using magnetocardiogram and its possible use for diagnosis of ischemic heart disease. Int J Card Imaging 16 (1) (2000) 55–66
5. Hänninen, H., Takala, P., Mäkijärvi, M., Montonen, J., Korhonen, P., Oikarinen, L., Nenonen, J., Katila, T., Toivonen, L.: Detection of exercise induced myocardial ischemia by multichannel magnetocardiography in patients with single vessel coronary artery disease. Ann. Noninv Electrocardiology 5 (2) (2000) 147–157
6. Takala, P., Hänninen, H., Montonen, J., Makjiarvi, M., Nenonen, J., Oikarinen, L., Simeliu, K., Toivonen, L., Katila, T.: Magnetocardiographic and Electrocardiographic Exercise Mapping in Healthy Subjects. Annals of Biomedical Engineering 29 (2001) 501–509
7. Brockmeier, K., van Leeuwen, P.: Magnetocardiographic stress test investigations analyzing ventricular repolarization changes. In: Nenonen, J., Ilmoniemim R.J., Katila, T., (eds.): Proceedings 12th International Conference on Biomagnetism, Helsinki Univ. of Technology, Espoo, Finland (2001) 546–548
8. Brazdeikis, A., Taylor, A. A., Mahmarian, J. J., Xue, Y., Chu, C.W. Comparison of magnetocardiograms acquired in unshielded clinical environment at rest, during and after exercise and in conjunction with myocardial perfusion imaging. In: Nowak, H., Haueisen, J., Giessler, F., Huonker, R., (eds): Proceedings 13th International Conference on Biomagnetism, Jena. VDE Verlag (2002) 530–532
9. Leder, U., Novak, H., Haueisen, J. : Myocardial ischemia and viability. In: Nenonen, J., Ilmoniemi, R.J., Katila, T., (eds): Proceedings 12th International Conference on Biomagnetism, Helsinki Univ. of Technology, Espoo, Finland (2001) 518–522
10. Pesola, K., Hänninen, H., Lauerma, K.: Current density estimation on left ventricular epicardium: a potential method for ischemia localization. Biomed Tech. 44 (1999) 143–146
11. Leder, U., Pohl, H.P., Michaelsen, S., Fritschi, T., Huch, M., Eichhom, J., Muller, S., Nowak, H.: Noninvasive biomagnetic imaging in coronary artery disease based on individual current density maps of the heart. Int J Cardiol. 13 (1998) 83–92
12. Leder ,U., Haueisen, J., Huck, M., Nowak, H.: Non-invasive imaging of arrhythmogenic left-ventricular myocardium after infarction. Lancet 352 (1998) 1825
13. Park, J.W., Reichert, U., Malek, A., Klabes, M., Schafer, J., Jung, F.: Sensitivity and predictivity of Magnetocardiography for the Diagnosis of Ischemic Hearth Disease in Patients with Acute Chest Pain: Preliminary Results of the Hoyerswerda Registry Study" (personal communication)
14. Wikswo, J.P., Barach, J.P.: Possible sources of new information in the magnetocardiogram. Journal of Theoretical Biology 95 (1982) 721–729
15. Cohen, D., Kaufman, L.A.: Magnetic determination of the relationship between the ST segment shift and the injury current produced by coronary artery occlusion. Circ. Res. 36 (1975) 414–424
16. Janse, M.J., Moreina, H., Cinca, J.: Role of re-entry and currents of injury in early ischemic ventricular tachyarrhythmias: which properties should theoretically make a drug effective in the management of these arrhythmias? In: Sandoe, E., Julian, D.G., Bekll, J.W. (eds): Management of ventricular tachycardia- role of mexiletine. Excerpat Medica (1978) 183–196

# Heterogeneous Sinoatrial Node of Rabbit Heart – Molecular and Electrical Mapping and Biophysical Reconstruction

Henggui Zhang[1], Halina Dobrzynski[2], Arun V. Holden[2], and Mark R. Boyett[2]

[1]Biological Physics Group, Physics Department, UMIST, Manchester, M60 1QD, UK
[2]School of Biomedical Sciences, The University of Leeds, LS2 9JT, UK

**Abstract.** Electrophysiology and immunocytochemistry have been used to map the detailed properties of cells cross the pacemaker of the heart, the sinoatrial node. The electrical activities and expressions of various proteins across the sinoatrial node change smoothly with distance and so can be modelled by a gradient in parameter values. Experimental data have been integrated into computational models of the SA node at cellular and tissue levels and mechanisms underlying initiation and propagation of pacemaker activity of the heart identified.

## 1 Introduction

The sinoatrial node (SA node) is the pacemaker of the heart, which initiates a sequence of rhythmic action potentials propagating in the excitable cardiac tissue. The SA node is a heterogeneous tissue. Cells in the centre are smaller and have fewer and more poorly organised myofilaments than cells in the periphery [1,2,11]. Action potentials recorded in the centre of the intact SA node and from small tissues cut from the centre have more positive take-off potential, slower upstroke velocity, longer action potential duration, more positive maximum diastolic potential (also resting potential in quiescent tissue), and slower intrinsic pacemaker activity than those in the periphery [7,13]. Normally the action potential is first initiated in the centre and then conducted through the periphery of the SA node towards the atrial muscle anisotropically [1] (with a preferential conduction towards the up crista terminalis, but a slow conduction towards the atrial septum). Between the centre and atrial septum there is a special region within which action potential fails to propagate [1]. This special region is referred as conduction block zone. Both the mechanisms underlying the intrinsic inhomogeneous nature of the SA node and functional roles of this heterogeneity are unclear.

We are interested in the detailed structure and functions of the SA node, at the molecular, cellular and tissue levels. We approach the structure and functions of the SA node by combined techniques of immunocytochemistry and electrophysiology. We map the distributions of electrical properties of cells and expressions of various proteins across the SA node. These detailed experimental data were utilised to reconstruct computer models of the SA node to study how the tiny SA node drives the massive atrial muscle.

I. Magnin et al. (Eds.): FIMH 2003, LNCS 2674, pp. 132–140, 2003.

## 2 Heterogeneous Electrical Activity

Heterogeneous electrical activities of cells across the rabbit SA node have been investigated by various techniques, which include dissecting multicellular small balls from different regions of the SA node [7], isolating single cells across the SA node and relating their morphology with locations of origin [4]; and a lattice of arrayed electrodes recording action potentials from various sites across the intact SA node. Data from various techniques show consistently the smooth changes of electrical activities of cells across the SA node as shown in Fig. 1. In the figure panel (a) is a schematic illustration of the geometry and location of SA node of the rabbit heart. The asterisk represents the center of the SA node, i.e., the leading pacemaker site, where the action potential is first initiated. Once initiated, action potentials propagate from the center towards the periphery and then the atrial muscle. Conduction of action potentials within the SA node is anisotropic as shown by the isolines of activation times of excitation. Panel (b) shows superimpose spontaneous action potentials recorded from various positions of the SA node as indexed by 1–6 in panel (a). Action potential recorded from the center (labeled by 1) has a longer action potential duration, a smaller amplitude and a higher maximal diastolic potential than those recorded from positions distant from the center (labeled by 2, 3, 4, 5, 6). From the center towards the periphery, there are smooth changes in the action potential duration, amplitude and maximal diastolic potential. Stimulated action potentials from various positions show similar gradient features as shown in panel (c).

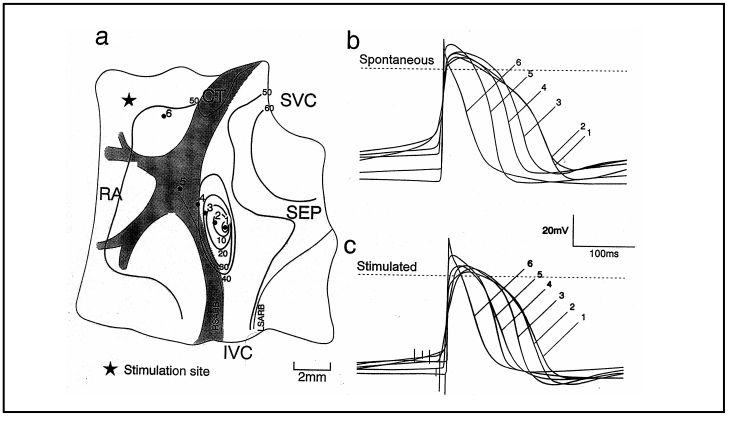


**Fig. 1.** Heterogeneous features of electrical activities of cells across the rabbit SA node and anisotropic conduction of excitation

## 3 Regional Differences in Ionic Current Densities

Though individual cells have not been isolated from specific regions to explore regional differences in the ionic current densities of cells across the SA node, we have studied the correlations between cell size and cell membrane ionic current densities. As morphological data suggested that cells from the center SA node are smaller than

cells from the periphery, it is reasonable to relate cell origin with its size. Single myocytes have been isolated from rabbit SA node and individual ionic current densities have been measured by voltage clamp technique [3–5, 8–10]. Experimental data show strong correlations between individual ionic current densities and cell sizes. Results obtained from rabbit SA node are summarized in Fig. 2.

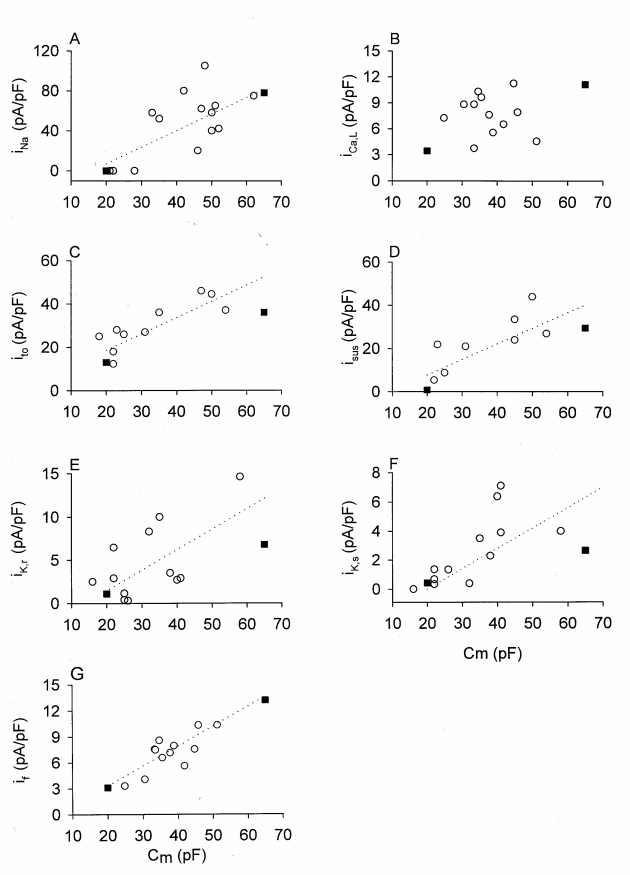


**Fig. 2.** Correlations between ionic current densities and cell sizes, which were indexed by cell membrane capacitances. Open symbol: experimental data. Solid symbol: data used to develop central and peripheral cell models in Zhang et al. (2000).

# 4 Heterogeneous Protein Expressions

## 4.1 Makeup of the SA Node

Two different models about the makeup of the SA node have been proposed to account for the electrical heterogeneity: the mosaic model [14] and the gradient model [15]. The mosaic model proposes that the observed electrical heterogeneity is due to a

mixing of atrial and SA node cells in the SA node and a smooth change in the ratio of the population of the atrial cell to SA node cells. However the gradient model claims there are no atrial cells in the SA node and the smoothly changes in electrical activities are results of a gradient in properties of the SA node cells, such as the ionic channel densities. In order to see if there are a large population of atrial cells intermingled with SA node cells we have used immunocytochemistry on the intact rabbit SA node.

A section of tissue through the crista terminalis and the intercaval region of the SA node was cut through the centre of the SA node. The tissue section was then labelled with different antibodies. The result is shown in Fig. 3.

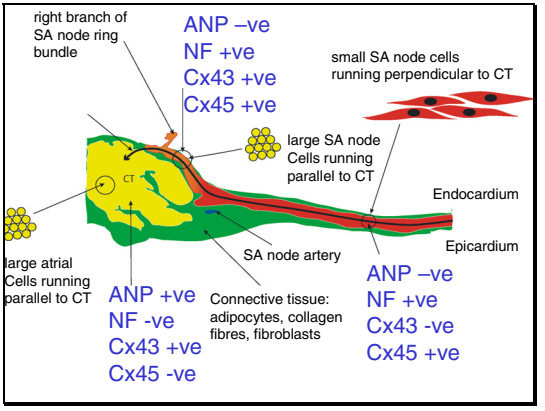


**Fig. 3.** Heterogeneous distributions of various protein expressions across the rabbit SA node

In Fig. 3 different expressions of atrial natriuretic peptide (ANP), neurofilament (NF), and connexins (Cx43 and Cx45) in a tissue were represented by different colours. It was shown that the SA node tissue (red and orange) of the intercaval region rises up the endocardial face of the crista terminalis and overlaps the atrial muscle (yellow). The atrial muscle (yellow) expresses ANP but not NF, whereas all the SA node tissue (red and orange areas) expresses NF but not ANP. NF is cytoskeletal protein found in nerve cells. The presence of NF in the SA node suggests that the SA node is neural in origin. Cx43 and Cx45 are components of gap junctions, which are responsible for electrical coupling. In the atrial muscle (yellow area) Cx43 is expressed but not Cx45. In contrast, in the centre of the SA node (red area) Cx45 is expressed but not Cx43. Intriguingly, in the periphery of the SA node (orange area), both Cx43 and Cx45 are expressed. Therefore, on the basis of these markers, three cell types can be identified: ANP-ve/NF+ve/Cx43-ve/Cx45+ve (red) in the centre of the SA node, ANP-ve/NF+ve/Cx43+ve/Cx45+ve (orange) in the periphery of the SA node and ANP+ve/NF-ve/Cx43+ve/Cx45-ve (yellow) in the atrial muscle of the crista terminalis. The use of ANP, NF and Cx43 and Cx45 markers provides no evidence of a mosaic of atrial and SA node in the SA node region. Instead in any one area the cells are uniform of one type.

### 4.2 Connective Tissue Barrier at the Junctional Border between SA Node and Surrounding Atrial Muscle

It is not clear how SA node is electrically connected to the atrium in the overlap region, which enables a small SA node to drive a large massive atrial muscle without its pacemaker activity being fully depressed (6). To investigate how the SA node is connected to the atrial muscle, a rabbit SA node preparation was cut and processed for histology. Figure 4 shows 1 μM semi-thin section cut through the leading pacemaker site and stained with Toluidene blue.

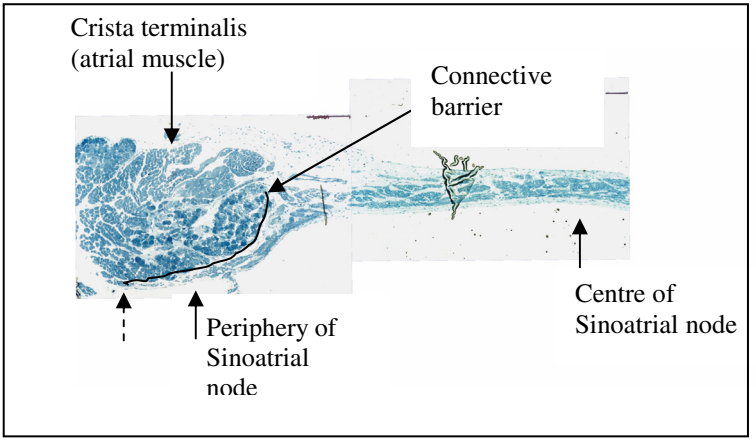


**Fig. 4.** Connective tissue between the SA node and the surrounding atrial muscle. Physical connection between SA node and the atrial muscle is indicated by the dashed arrow

Figure 4 is a low magnification montage of a Toluidene blue stained tissue section through the atrial muscle of the crista terminalis, the periphery of the SA node and the centre of the SA node. In the rabbit, the SA node rises up the crista terminalis and it terminates at the position marked by the arrow in the figure. Histology suggested that the SA node is not connected to the atrial muscle of the crista terminalis but is separated from it by a connective tissue as indicated by the black curve in the figure. There is a connective tissue barrier separating much of the periphery of the SA node from the crista terminalis. Data from this specific section suggested that the only point of contact between the SA node and the atrial muscle is at the termination of the SA node tissue as indicated by the arrow in the figure. Data from other sections showed similar results.

### 4.3 Morphology of Conduction Block Zone

Using Masson's trichrome technique the morphology of the block zone was investigated. A rabbit SA node preparation (similar to this) was processed for histology. 10 μM cross-sections were cut through the leading pacemaker site and stained with Masson's trichrome technique. The result is shown in Fig. 4.

Figure 5 is a low magnification montage of a Masson's trichrome stained tissue section through the atrial muscle and the intercaval region. The red arrow points at the block zone. The image on the left shows a close up view of the block zone of this section, whereas the image on the right shows a close up view of the block zone from another section. The myocytes are in purple and the connective tissue is in blue. Our histological data suggested that in the block zone there are fewer myocytes and thus low excitability of tissue in the region.

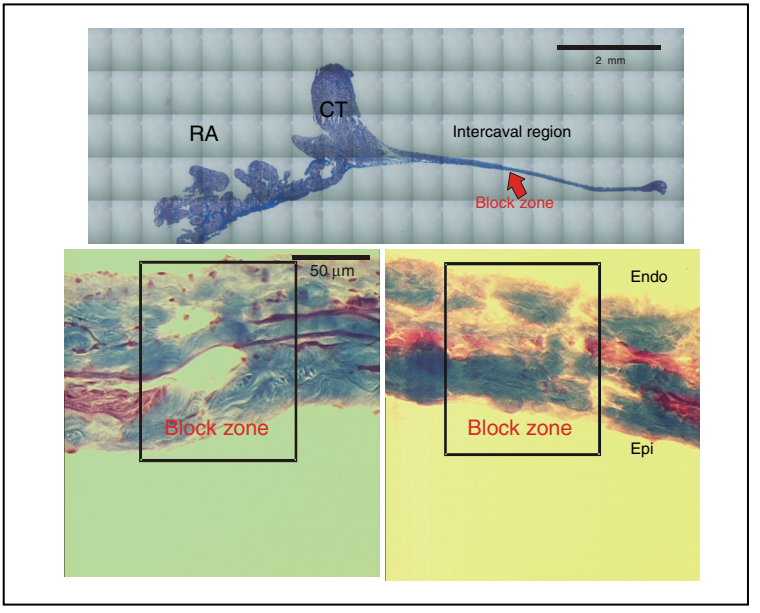


**Fig. 5.** Morphology of conduction block zone

## 5 Biophysical Models of the SA Node

### 5.1 Gradient Model of the SA Node

Based on experimental data about variation of cell sizes from centre to periphery, and the correlation between cell size (measured as cell capacitance) and ionic channel current densities, a 2-dimensional model of an intact SA model and atrial muscle has been constructed to simulate the initiation and propagation of action potential within the SA node. In the model, we assume that the cell size in the centre is 50 µm in length, and increases exponentially to 100 µm in the periphery towards both the crista terminalis and atrium septum directions. Cell diameter is 10 µm cross the whole SA node. In the model the width of the SA node is 6 mm. The centre of the SA node is at 3 mm distance from the border of the crista terminalis. The length of the SA node tissue varies from 9 mm in the centre to 18 mm in the periphery at both borders of

crista terminalis and atrial septum. In the SA node the cell capacitance changes from 20 pF in the centre to 65 pF in the periphery. SA node cells were modelled by the model of Zhang et al. (16) for the electrical activity. Ionic channel densities are functions of cells size cross the SA node as described by Honjo et al. (4). In the atrium cells are modelled by the Earm-Hilgemann-Noble model (12) for action potential. The 2D SA model is shown in figure 6A, which is superimposed with the physical scheme of the rabbit SA node tissue. At 1.5 mm distance from the centre of the SA node towards the atrium septum, there is a conduction block region of 0.3 mm × 6 mm, within which the tissue excitability was reduced by removing the $i_{Ca,L}$ channel density.

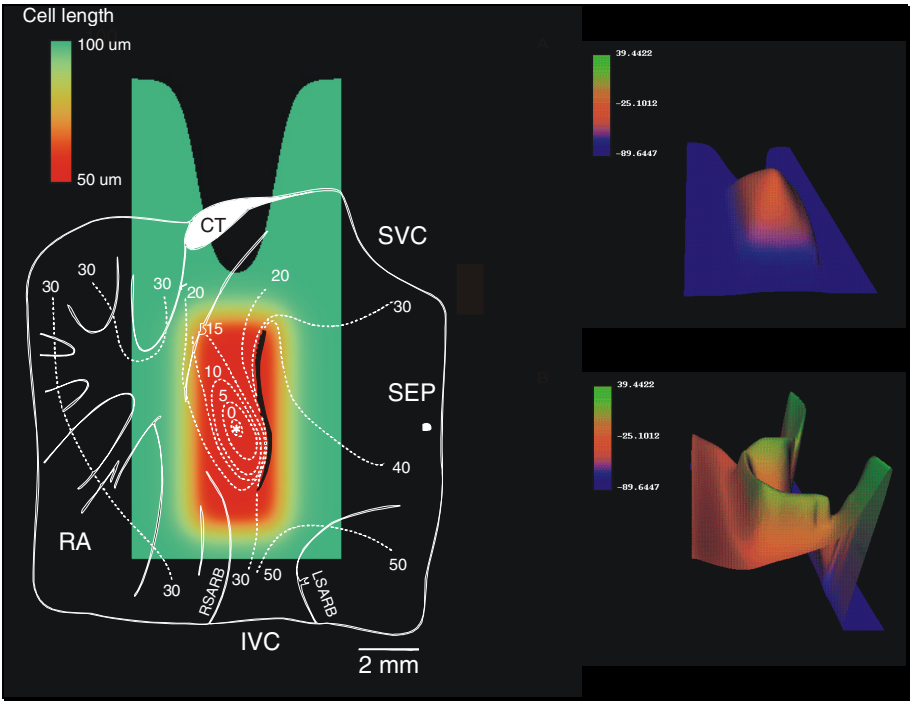


**Fig. 6.** 2D gradient model of an intact SA node and atrium. The model is physically superimposed with a physical scheme of the rabbit SA node tissue (left panel). (right top) Snapshot of action potential in the model at 50 ms from initial condition. (right bottom) Snapshot of action potential at 70 ms from initial condition

Right top and bottom panels show snapshots of action potentials spreading in the 2D gradient model of the intact SA node and atrial muscle. It was illustrated that in the model the action potential was first initiated in the centre of the SA node, and then propagated towards periphery (right top) in the direction of the crista terminalis. When the action potential reached the atrium, it evoked excitation wave that propagates rapidly in the atrium. Towards the atrium septum action potential failed to propagate in the conduction block zone. It encircled the zone via conducting pathways of the surrounding atrium. The simulated initiation and propagation of action potential is similar to that seen experimentally.

### 5.2 Functional Roles of Connective Tissue Barrier

Using computer models we investigated how does the SA node drive the atrium and the possible roles of the connective tissue barrier. To do this we have constructed an anatomical model of rabbit SA node and atrium. To investigate the functional role of connective tissue barrier, we systematically changed the length (content) of the connection between the SA node and atrial muscle and studied the effects of connection on initiation and propagation of action potentials. We found that whether the SA node is able to drive the atrial muscle depends on the content of electrical connection between the SA node and atrium. Depending on the size of electrical connection (L) between the SA node and the atrium, there are four different types of behaviour. The four behaviours can be classified as: a) the SA node is pacemaking but can not drive atrium; b) SA node is pacemaking and drive the atrium normally; c) exit block and d) full depression of the SA node. Data from immunocytochemistry indicated that the connective tissue barrier electrically separates the SA node and atrium, which suggests that the connective tissue barrier in the overlap region helps to prevent the SA node from being fully depressed by the atrial muscle.

## 6 Discussions

The SA node is the pacemaker of the heart, which initiates action potential and controls the rhythm of the heart. Due to its intrinsic complexity it is still unclear about the detailed makeup of the SA node and the functional roles of heterogeneity. Our experimental data from immunocytochemistry and electrophysiology have consistently shown smooth changes in the electrical properties of SA node cells and expressions of various proteins. These proteins determine the electrical properties of the SA node. Computer models of the intact SA node based on gradient changes of electrical properties of cells across the SA node can reproduce the correct activation sequence of propagating pacemaker activity, which supports the gradient model rather than the mosaic model of the SA node. These studies have provided fundamental insights about the detailed structure of the SA node and thus its functions in initiation and conducting pacemaker activity in the mammalian heart.

**Acknowledgements.** This work was supported by a programme grant from the British Heart Foundation.

## References

1. Bleeker, W.K., A.J.C. Mackaay, M. Masson-Pevet, L.N. Bouman, and A.E. Becker. Functional and morphological organization of the rabbit sinus node. *Circ. Res.* 46: 11-22, 1980.
2. Bleeker, W.K., A.J.C. Mackaay, M. Masson-Pevet, T. Op't Hof, H.J. Jongsma, and L.N. Bouman. Asymmetry of the sino-atrial conduction in the rabbit heart. *J. Mol. Cell. Cardiol.* 14: 633-643, 1982.

3. Boyett, M.R., H. Honjo, M. Yamamoto, R. Niwa, and I. Kodama. Regional differences in the effects of 4-aminopyridine within the sinoatrial node. *Am. J. Physiol.* 44: H1158-H1168, 1998.
4. Honjo, H., M.R. Boyett, I. Kodama, and J. Toyama. Correlation between electrical activity and the size of rabbit sinoatrial node cells. *J. Physiol.* 496: 795-808, 1996.
5. Honjo, H., M. Lei, M.R. Boyett, and I. Kodama. Heterogeneity of 4-aminopyridine sensitive current in rabbit sinoatrial node cells. *Am. J. Physiol.* 276: H1295-H1304, 1999.
6. Joyner, R.W. and F.J.L. van Capelle. Propagation through electrically coupled cells: how a small SA node drives a large atrium. *Biophys. J.* 50: 1157-1164, 1986.
7. Kodama, I. and M.R. Boyett. Regional differences in the electrical activity of the rabbit sinus node. *Pflügers Arch.* 404: 214-226, 1985.
8. Kodama, I., M.R. Boyett, M.R. Nikmaram, M. Yamamoto, H. Honjo, and R. Niwa. Regional differences in the effects of E-4031 within the sinoatrial node. *Am.J.Physiol.* 276: H793-H802, 1999.
9. Kodama, I., M.R. Nikmaram, M.R. Boyett, R. Suzuki, H. Honjo, and J.M. Owen. Regional differences in the role of the $Ca^{2+}$ and $Na^{+}$ currents in pacemaker activity in the sinoatrial node. *Am. J. Physiol.* 272: H2793-H2806, 1997.
10. Lei, M., H. Honjo, and M.R. Boyett. Characterisation of the transient outward current in rabbit sinoatrial node cells. Cardiovasc Res. 2000 Jun; 46(3):433-41.
11. Masson-Pévet, M.A., W.K. Bleeker, E. Besselsen, B.W. Treytel, H.J. Jongsma, and L.N. Bouman. Pacemaker cell types in the rabbit sinus node: a correlative ultrastructural and electrophysiological study. *J. Mol. Cell. Cardiol.* 16: 53-63, 1984.
12. Noble, D. Oxsoft manual version 4.8. Oxford . 1990.
13. Opthof, T., A.C.G. VanGinneken, L.N. Bouman, and H.J. Jongsma. The intrinsic cycle length in small pieces isolated from the rabbit sinoatrial node. *J.Mol.Cell.Cardiol.* 19: 923-934, 1987.
14. Verheijck, E.E., A. Wessels, A.C.G. van Ginneken , J. Bourier, M.W.M. Markman, J.L.M. Vermeulen, J.M.T. de Bakker, W.H. Lamers, T. Opthof, and L.N. Bouman. Distribution of atrial and nodal cells within rabbit sinoatrial node. Models of sinoatrial transition. *Circulation* 97: 1623-1631, 1998.
15. Zhang, H., A.V. Holden and M.R. Boyett. The gradient model vs the MOSAIC model. *Circulation* 103:584-588 2001
16. Zhang, H., A.V. Holden, I. Kodama, H. Honjo, M. Lei, T. Varghese and M.R. Boyett. Mathematical models of action potentials in the periphery and centre of rabbit sinoatrial node. *American Journal of Physiology (Heart and Circulation)* 279(1):H397-H421.

# Construction of a Cardiac Motion Atlas from MR Using Non-rigid Registration

A. Rao[1], G.I. Sanchez-Ortiz[1], R. Chandrashekara[1], M. Lorenzo-Valdés[1], R. Mohiaddin[2], and D. Rueckert[1]

[1] Visual Information Processing Group, Department of Computing
Imperial College of Science, Technology, and Medicine
180 Queen's Gate, London SW7 2BZ, United Kingdom
[2] Royal Bromptom and Harefield NHS Trust, Sydney Street
London, United Kingdom

**Abstract.** In this paper we present a technique for constructing a cardiac motion atlas using the myocardial motion fields derived from 4D MR image sequences of a series of subjects. This is achieved by transforming the motion field of each subject into a the coordinate system of a reference subject, and then averaging the transformed fields to give a vector field representing the mean motion of the heart. The motion fields of each subject are calculated by registering each of the frames in the sequence of tagged short-axis and long-axis MRI images to the end-diastolic frame using a non-rigid registration technique based on multi-level free-form deformations. The end-diastolic untagged short-axis images of each subject, which are acquired shortly after the tagged images, are registered to the corresponding image of a designated reference subject using non-rigid registration to determine reference-subject mappings, which are then used to transform the corresponding motion fields into that of the reference subject. Finally, the mean transformed motion field is calculated to give the cardiac motion atlas.

## 1 Introduction

Despite the advent of increasingly sophisticated cardiac imaging and surgery techniques, cardiovascular disease remains the leading cause of death in the western world [1]. It most frequently appears as coronary heart disease, in which an atherosclerosis of the coronary arteries reduces the oxygen supply to the muscles of the heart, causing them to become ischemic. This leads to a loss of function of the heart and a reduced contractility.

Tagged MRI imaging [2,3] provides a means to investigate the deformations that the heart undergoes through the cardiac cycle, and is thus a potential tool for coronary heart disease diagnosis. It relies on the perturbation of magnetisation in the myocardium in a specified spatial pattern at end-diastole. These appear as dark stripes or grids when imaged immediately after the application of the tag pattern, and, since the myocardial tissue retains this perturbation, the dark stripes or grids deform with the heart as it contracts, allowing local deformation parameters to be estimated. Recently, Chandrashekara et al [4] described a fully automated method for tracking the cardiac motion of a subject in a sequence of tagged MRI images using non-rigid registration. In this algorithm,

I. Magnin et al. (Eds.): FIMH 2003, LNCS 2674, pp. 141–150, 2003.

a sequence of free-form deformations is used to represent myocardial motion and the displacement motion field is extracted by maximising the mutual information between images in the cine sequence. The result of this algorithm is a set of motion fields for each time frame relative to the end-diastolic image.

Although visual inspection of the derived motion fields of a particular subject may allow us to assess the subject's cardiac function, we cannot directly compare the motion fields across several different subjects as calculated by the tracking algorithm described above because each of the motion fields will be defined with respect to the coordinate systems of the end-diastolic images used to calculate them, which in general will be different. Even allowing for this coordinate change, comparisons of the motion fields of different subjects do not directly enable us to infer the normality or otherwise of the cardiac motion of the subjects unless we have a cardiac motion model that in some sense represents the cardiac motion of a healthy heart. One possibility is to use the motion field of one of the subjects as our model motion field, but although each of the subjects may be considered 'normal', it is possible that any one of them may actually lie at the extremum rather than the centre of the normal distribution of motion fields. This would bias any evaluations of cardiac motion leading to false conclusions.

In a previous publication [5], we tackled the problem of different coordinate sytems for the motion fields by describing a technique that can be used to transform the motion fields of a subject $S$ into the coordinate system of a reference subject $R$. Firstly, the original (unmapped) myocardial motion fields were calculated using both short-axis and long-axis tagged MRI sequences as described by [4] to give a sequence of motion fields relating each frame of the sequence to the end-diastolic frame. The corresponding end-diastolic untagged short-axis images were then registered using non-rigid registration to determine an inter-subject mapping which was then used to transform the motion vectors of the subject into the coordinate system of the reference. In fact, the method we used only gives an approximation to the vectors in the transformed motion field which can be calculated exactly if the inverse of the inter-subject mapping is known. Unfortunately, the inverse cannot be easily calculated from the original mapping even if we use an alternative registration technique [6], while simply performing the registration in the opposite direction may yield a mapping that does not produce the identity transformation when composed with the original. On the other hand our method will degrade for points at which the untransformed motion vectors are large.

In this paper we describe a refinement of our earlier technique that uses the same motion fields and inter-subject mappings but increases the numerical accuracy of the motion vector transformation. We go on to address the problem of building a cardiac motion model and describe how we use a set of transformed motion fields of a series of subjects together with the motion field of the reference subject to produce a cardiac motion atlas.

In the next section we describe the non-rigid registration algorithm we used to determine the original myocardial motion fields and calculate the inter-subject mapping. We go on to describe in detail each of the stages of our technique, before showing the cardiac motion atlas obtained using a reference subject and eight other subjects in Sect. 5.

## 2 Non-rigid Registration

Image registration entails the determination of a transformation that maps points within one image to their corresponding points in another image. For our purposes we will require the mappings between corresponding points at different time frames of a sequence of MR images taken of a single subject, as well as the mappings between corresponding points of two MR images of different subjects. We model the transformations using the non-rigid registration technique of Rueckert et al. [7]. This algorithm expresses the required transformation as the sum of a global and local component:

$$\mathbf{T}(x, y, z) = \mathbf{T}_{global}(x, y, z) + \mathbf{T}_{local}(x, y, z)$$

$\mathbf{T}_{global}$ is modelled by an affine transformation that incorporates scaling, shearing, rotation and translation. $\mathbf{T}_{local}$, the local deformations, are modelled using a free-form deformation (FFD) model based on B-splines that manipulates an underlying mesh of control points $\phi$, thus changing the shape of the object. The resulting deformation can be expressed as the 3D tensor product of the standard 1D cubic B splines

$$\mathbf{T}_{local}(x, y, z) = \sum_{l=0}^{3} \sum_{m=0}^{3} \sum_{n=0}^{3} B_l(u) B_m(v) B_n(w) \phi_{i+1,j+m,k+n}$$

where $B_l$ denotes the $l$-th B-spline basis function. In our algorithm the optimal transformation $\mathbf{T}$ is found by maximising a voxel-based similarity measure, normalised mutual information [8], which measures the degree of alignment between images. The normalised mutual information of two images $A$ and $B$ is defined as

$$I(A, B) = \frac{H(A) + H(B)}{H(A, B)}$$

where $H(A)$,$H(B)$ are the marginal entropies of images $A$ and $B$, and $H(A, B)$ denotes the joint entropy of the combined images $A$, $B$. We are using normalised mutual information as a similarity measure because it only measures the statistical dependencies between the intensity distributions in both images and therefore can be used in tagged MR images where the image intensities can change as a result of tag fading.

### 2.1 Motion Modelling from Tagged MR Using Non-rigid Registration

The first step in our process requires the calculation of the myocardial motion fields for a subject $S$ that we will later map into the coordinate system of $R$, the reference subject. To facilitate this we must first choose an image in our tagged image sequence $S_i$, $i = 0, ..., n$, to be our temporal reference point, i.e. the one in whose coordinate system all calculated motion fields of $S$ will be expressed and will be relative to. We choose the end-diastolic image $S_0$ to be this reference because cardiac motion is minimal at this time, and we denote its coordinate system as the triple $(x', y', z')$. Similarly, we define the end-diastolic image of subject $R$, $R_0$, to be the analogous reference point for this subject, denoting its coordinate system as $(x, y, z)$. This makes $(x, y, z)$ the

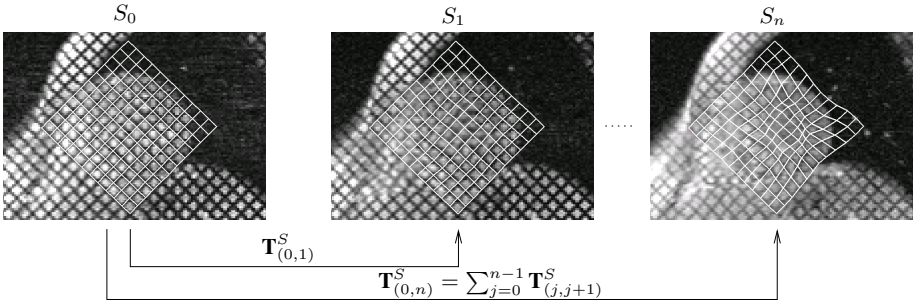


**Fig. 1.** Extraction of cardiac motion parameters for Subject $S$: A virtual tag grid which has been aligned with the tag pattern at time $t = 0$ is overlaid on different time frames of the tagged MR sequence to illustrate the tag tracking with non-rigid registration. As time progresses the virtual tag grid is deformed by the MFFD and follows the underlying tag pattern in the images. An animated colour version of this figure can be found at `http://www.doc.ic.ac.uk/~dr/projects/animations/MICCAI02`.

coordinate system to which we ultimately would like to map the myocardial motion fields of $S$.

To calculate the myocardial motion fields we are using an extension of the free-form deformation (FFD) model described in the previous section. In this extension a number of single-level FFDs are combined in a multi-level FFD framework [9]. This approach has been previously applied successfully for myocardial motion tracking in tagged MR images [4]. The estimation of the motion field proceeds in a sequence of registration steps: After registering the image $S_1$ to $S_0$ we obtain a multi-level FFD (MFFD) consisting of a single FFD representing the motion of the myocardium at time $t = 1$. To register volume $S_2$ to $S_0$ a second level is added to the sequence of FFDs and then optimised to yield the transformation at time $t = 2$. This process continues until all the volumes in the sequence are registered, allowing us to relate any point in the myocardium at time $t = 0$ to its corresponding point throughout the sequence. Note that here, each of the registrations are performed using only a local component to model the calculated transformation ie. the global component is set to zero in each case. The transformation between the end-diastolic time frame $S_0$ and the image $S_i$ at time frame $t = i$ is then given by:

$$\mathbf{T}^S_{(0,i)}(x', y', z') = \sum_{j=0}^{i-1} \mathbf{T}^S_{(j,j+1)}(x', y', z')$$

Figure 1 shows the short axis tagged images of a subject taken at different time frames overlayed with a virtual grid which has been aligned with the tag pattern of the end-diastolic frame. As time progresses, the virtual tag grid is deformed by the calculated MFFD and is seen to follow the underlying tag pattern in the images. This demonstrates the success of the tracking algorithm used.

The actual myocardial motion fields $\mathbf{D}^S_{(0,i)}(x', y', z')$ that we require are given by

$$\mathbf{D}^S_{(0,i)}(x', y', z') = \mathbf{T}^S_{(0,i)}(x', y', z') - (x', y', z')$$

Using the same approach we can calculate the myocardial motion fields $\mathbf{D}^R_{(0,i)}(x, y, z)$ for subject $R$.

Since the cardiac cycles of the subject $S$ and reference subject $R$ will be of different lengths, we determined and then applied an affine temporal mapping that aligns the end-diastolic and end-systolic frames of $R$ with the corresponding frames in the subject $S$ so that each motion field $\mathbf{D}^R_{(0,i)}(x, y, z)$ corresponds with motion field $\mathbf{D}^S_{(0,i)}(x, y, z)$ of the subject.

### 2.2 Non-rigid Registration of Untagged MR between Subjects

We now need to calculate a mapping between the end-diastolic MR images of subject and reference, $S_0$ and $R_0$, so that we can map the myocardial motion fields $\mathbf{D}^S_{(0,i)}$ into the coordinate system of $R$ , $(x, y, z)$. Since the untagged images are obtained shortly after the tagged images, the end-diastolic untagged frames of each subject are already aligned with the end-diastolic tagged frames of each subject that were used to define the coordinate systems of $R$ and $S$. This means that we can use the end-diastolic untagged images of each subject to calculate the inter-subject coordinate system mapping. The transformation between subjects $R$ and $S$ is determined using the non-rigid registration algorithm described in the introduction of Sect. 2, giving a mapping $\mathbf{F}_{(R,S)}$ between coordinate systems $(x, y, z)$ and $(x', y', z')$:

$$\mathbf{F}_{(R,S)} : (x, y, z) \longmapsto (x'(x, y, z), y'(x, y, z), z'(x, y, z))$$

In this case there will be a non-zero global component as we are registering between subjects. Note that here the registration algorithm is being used to calculate a transformation of coordinates of the reference anatomy that aligns it with the subject anatomy, in contrast to its use in Sect. 2.1 where it was used to calculate the motion of the heart in a fixed coordinate system. Figure 2 shows the short-axis end-diastolic image of a

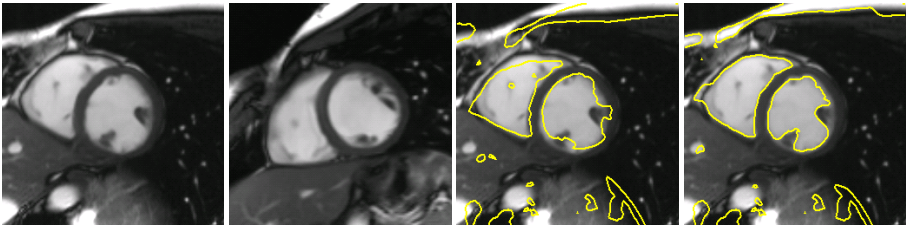

(a) (b) (c) (d)

**Fig. 2.** This figure illustrates the short axis views of a reference end-diastolic image (a), a subject end-diastolic image (b), the isolines of the subject image after global registration (c), and non-rigid registration (d)

reference subject (a), and of a second subject (b). In Figure 2(c) we see the isolines of equal intensity of the second subject overlayed on the reference subject anatomical image where the registration has been performed using only an affine global component, while Fig. 2(d) shows the contours if we include the local deformations in the registration. It is clear that the anatomies are much better aligned when we include local deformations in our registration.

## 3 Transformation of Myocardial Motion Fields

We are now in a position to transform the motion fields $\mathbf{D}^S_{(0,i)}(x', y', z')\ i = 1, ...n$ into the coordinate system of $R$, $(x, y, z)$. If the motion vector at a point $P$ with positional coordinate $\boldsymbol{x}'_0 = (x'_0, y'_0, z'_0)$ in the coordinate system of $S$ is equal to $\mathbf{d}^S$, this will transform to a vector $\tilde{\mathbf{d}}^S$ at the location $\boldsymbol{x}_0 = (x_0, y_0, z_0)$ in the coordinate system of $R$, where

$$\boldsymbol{x}_0 = \mathbf{F}^{-1}_{(R,S)}(\boldsymbol{x}'_0)$$

In order to determine $\tilde{\mathbf{d}}^S$, consider a path $\mathcal{L} : \boldsymbol{x}(\theta), \theta \in [0, 1]$ defined in the coordinate system of $R$ that represents the transformed motion vector ie.

$$\boldsymbol{x}(0) = \boldsymbol{x}_0, \boldsymbol{x}(1) = \mathbf{F}^{-1}_{(R,S)}(\boldsymbol{x}'_0 + \mathbf{d}^S)$$

By the fundamental theorem of calculus

$$\begin{aligned}\tilde{\mathbf{d}}^S = \boldsymbol{x}(1) - \boldsymbol{x}(0) &= \int_0^1 \frac{d\boldsymbol{x}(\theta)}{d\theta} d\theta \\ &= \int_0^1 J^{-1}(\boldsymbol{x}(\theta)) \frac{d\boldsymbol{x}'(\theta)}{d\theta} d\theta\end{aligned}$$

where $\boldsymbol{x}'(\theta)$ is $\mathcal{L}$ defined in the coordinate system of $S$ representing the untransformed motion vector $\mathbf{d}^S$ and $J(\boldsymbol{x}(\theta))$ is the Jacobian matrix of the transformation $\mathbf{F}_{(R,S)}$ evaluated along $\boldsymbol{x}(\theta)$:

$$J = \left[\begin{array}{ccc} \frac{\partial x'}{\partial x} & \frac{\partial x'}{\partial y} & \frac{\partial x'}{\partial z} \\ \frac{\partial y'}{\partial x} & \frac{\partial y'}{\partial y} & \frac{\partial y'}{\partial z} \\ \frac{\partial z'}{\partial x} & \frac{\partial z'}{\partial y} & \frac{\partial z'}{\partial z} \end{array}\right]\Bigg|_{\boldsymbol{x}=\boldsymbol{x}(\theta)}$$

which can be determined analytically. This integral can then be approximated by dividing the interval $[0, 1]$ into $n$ subintervals of length $\delta\theta$

$$\tilde{\mathbf{d}}^S \simeq \sum_{k=0}^{n-1} J^{-1}(\boldsymbol{x}^{(k)})(\boldsymbol{x}'^{(k+1)} - \boldsymbol{x}'^{(k)})$$

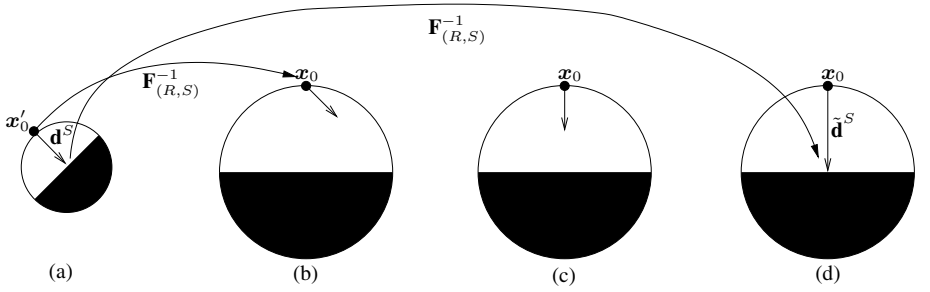


**Fig. 3.** This figure shows how the motion vector for a point in the smaller semi-filled circle (subject) can be transformed into a motion vector defined in the coordinate system of the larger semi-filled circle (reference). Figure (a) shows the subject and original untransformed motion vector $\mathbf{d}^S$ at the point with coordinates $\boldsymbol{x}'_0$ while (b) shows the reference and what happens if we place $\mathbf{d}^S$ in the corresponding reference location without any vector transformation. In (c) we additionally rotate $\mathbf{d}^S$ to align it with the reference, while (d) shows the fully transformed motion vector $\tilde{\mathbf{d}}^S$

where $\boldsymbol{x}'^{(k)} = \boldsymbol{x}'_0 + k\delta\theta\mathbf{d}^S$ and $\boldsymbol{x}^{(k)} = \mathbf{F}^{-1}_{(R,S)}(\boldsymbol{x}'^{(k)})$. In our previous work [5] we used precisely this formulation but with $n = 1$. Here we improve the approximation to the integral by setting $n > 1$ and evaluating the integral as

$$\tilde{\mathbf{d}}^S = \boldsymbol{f}(\boldsymbol{x}'^{(n)}) - \boldsymbol{x}_0$$

where $\boldsymbol{f}$ is the recursion formula

$$\begin{aligned}\boldsymbol{f}(\boldsymbol{x}'^{(0)}) &= \boldsymbol{x}_0 \\ \boldsymbol{f}(\boldsymbol{x}'^{(k+1)}) &= \boldsymbol{f}(\boldsymbol{x}'^{(k)}) + J^{-1}(\boldsymbol{f}(\boldsymbol{x}'^{(k)}))(\boldsymbol{x}'^{(k+1)} - \boldsymbol{x}'^{(k)})\end{aligned}$$

Figure 3 gives an illustration of what this motion transformation technique will produce for a synthetic example in which the subject and reference are semi-filled circles that differ in size and alignment: In Fig. 3(a) we see the subject and a motion vector $\mathbf{d}^S$ at the point $\boldsymbol{x}'_0$, each of which is defined in the coordinate system of the subject. Figure 3(b) shows the reference which we can see is a rotated, magnified version of the subject, and the calculated reference-subject mapping $\mathbf{F}_{(R,S)}$ has been used to place the subject motion vector in the correct location in the reference, without any vector transformation. Correcting just for the differences in alignment of the subject and reference gives the motion vector we see in figure 3(c), while using our motion transformation technique will give the vector $\tilde{\mathbf{d}}^S$ seen in 3(d) where the scaling has also been accounted for.

We applied our motion transformation technique to each of the motion fields of the subject to give us a set of transformed motion fields $\tilde{\mathbf{D}}^S_{(0,i)}(x, y, z)$.

## 4 Construction of the Cardiac Motion Atlas

We now repeat the steps described in Sects. 2.1-3 above to derive and transform each of the motion fields of $k$ healthy subjects $S^0, S^1, \ldots, S^{k-1}$ into the coordinate system

$(x, y, z)$ of our reference subject $R$. Since we require our cardiac motion atlas to encapsulate the variation in the cardiac motion fields of the healthy population, we treat the transformed motion fields as a representative sample of this population and produce our atlas $\mathbf{A}_{(0,i)}(x, y, z)\ i = 1, ...n$ by simply averaging the transformed motion fields of each of the $k$ subjects combined with that of the reference subject $R$:

$$\mathbf{A}_{(0,i)}(x, y, z) = \frac{1}{k+1}\left(\mathbf{D}^{R}_{(0,i)}(x, y, z) + \sum_{j=0}^{k-1} \tilde{\mathbf{D}}^{S^j}_{(0,i)}(x, y, z)\right)$$

The resulting cardiac motion atlas is thus a mean motion model of the healthy population.

## 5 Results and Discussion

We applied our technique using sets of untagged and tagged short-axis images of 9 healthy volunteers. The untagged and tagged MR images were acquired shortly after each other to minimise any motion between the image acquisitions. All images were acquired using a Siemens Sonata 1.5T scanner. For the tagged sequences, a cine breath-hold sequence with a SPAMM tag pattern was used to acquire ten short-axis slices covering the entire LV and a set of long-axis slices. For the untagged images a cine breath-hold TrueFisp sequence was used to acquire ten slices in the same anatomical planes as the tagged imaging planes. In both cases the images have a resolution of 256 x 256 pixels with a field of view ranging between 300 and 350mm depending on the subject and a slice thickness of 10mm. In both cases imaging was done at the end of exhalation and all images have been visually assessed to verify that there was minimal motion between the acquisitions.

Firstly, the myocardial motion fields of each subject relative to the end-diastolic frame in their respective sequence, were calculated using the tagged image sequences. The control point spacings in the mesh we used to perform the registration were 8mm by 8mm by 10mm. Our previous experiments [4] have shown that, using a manual tag tracking as the gold standard, the non-rigid registration algorithm is able to track the myocardial motion with an RMS of less than 0.5mm in simulated data and with an RMS error between 1 and 2mm on tagged MR images. One of the nine subjects was designated a reference subject, and the untagged end-diastolic images of the other were registered to this one using a mesh with a uniform control point spacings of 5mm. The calculated transformations were then used to map the myocardial motion fields of each of these eight subjects into the coordinate system of the reference subject. The cardiac atlas was then constructed using these transformed motion fields and the motion field of the reference subject.

In Fig. 4 we show the cardiac motion atlas describing cardiac motion between end-diastole and end-systole. We chose to show the motion fields at end-systole because this is when the deformation of the heart is greatest, and vectors are only shown for regions which we have manually segmented as belonging to the myocardium. Figure 4(a) shows a short-axis slice towards the base of the left ventricle of the heart, 4(b) shows a slice through the middle of the left ventricle, while 4(c) shows a slice towards the apex of the left ventricle. Vector magnitude is indicated by the length of the arrows. In each case, the

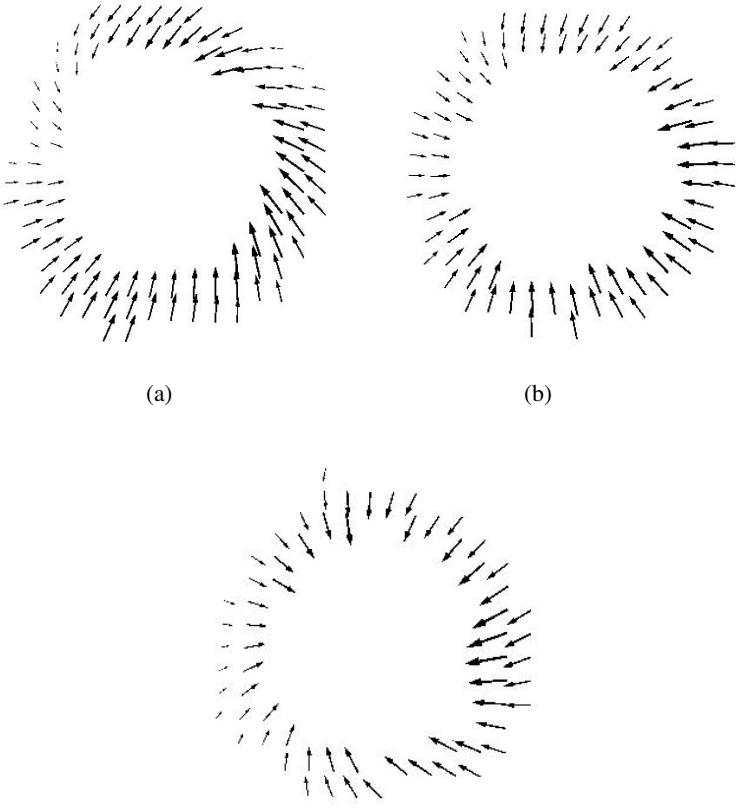


**Fig. 4.** The myocardial motion field at end-systole of the cardiac atlas on a short-axis slice towards the base of the left ventricle is shown in (a). Images (b) and (c) show the corresponding motion fields for parallel slices through the middle of the left ventricle and towards the apex of the left ventricle respectively. In each case, the motion fields have been projected onto the planes defined by the associated anatomical slice. Animations of these fields can be found at `http://www.doc.ic.ac.uk/~dr/projects/animations/FIHM03`.

motion fields have been projected onto the planes defined by the associated anatomical slice. All of the slices show a contraction of the left ventricle but we can also see that towards the base of the heart the atlas has a counter-clockwise twisting action while towards the apex it has a clockwise twist. The motion in the slice through the middle of the left ventricle has minimal twisting and is almost a pure contraction.

## 6 Conclusions and Future Work

In this paper we have developed a non-rigid registration based technique to produce a cardiac motion analysis that attempts to encapsulate the variation of cardiac motion across a healthy population. Such an atlas can potentially be used as a model to which the transformed motion fields of other healthy subjects can be compared for assessment of cardiac function. Although here we have only used eight subjects and one reference to build the atlas, the technique can be re-used as more subject data becomes available, thereby improving the accuracy of the atlas as a mean motion model.

Future work will focus on performing further stastistical analysis of the transformed motion fields used to build the atlas in order to extend the current model of cardiac motion. We intend to do this by performing a principal component analysis on the transformed vector fields in order to model the expected nature, and degree, of variability in cardiac motion. In addition, we will incorporate current research on the registration of 4D cardiac image sequences [10] which can be used to automatically align the cardiac cycles of the subjects used to build the atlas. This ensures that the motion fields we use relate corresponding parts of the cardiac cycle of each of the subjects.

## References

1. American Heart Association. Heart and stroke statistical update. `http://www.americanheart.org/`, 2002.
2. E. A. Zerhouni, D. M. Parish, W. J. Rogers, A. Yang, and E. P. Shapiro. Human heart: Tagging with MR imaging – a method for noninvasive assessment of myocardial motion. *Radiology*, 169(1):59–63, 1988.
3. L. Axel and L. Dougherty. MR imaging of motion with spatial modulation of magnetization. *Radiology*, 171(3):841–845, 1989.
4. R. Chandrashekara, R. H. Mohiaddin, and D. Rueckert. Analysis of myocardial motion in tagged MR images using non-rigid image registration. In *Proc. SPIE Medical Imaging 2002: Image Processing*, San Diego, CA, February 2002. In press.
5. A. Rao, G. I. Sanchez-Ortiz, R. Chandrashekara, M. Lorenzo-Valdes, R. Mohiaddin, and D. Rueckert. Comparison of cardiac motion across subjects using non-rigid registration. In *Fifth Int. Conf. on Medical Image Computing and Computer-Assisted Intervention (MICCAI '02)*, pages 722–729, 2002.
6. H. Johnson and G.E. Christensen. Consistent landmark and intensity-based image registration. *IEEE Transactions on Medical Imaging*, 21(5):450–461, 2002.
7. D. Rueckert, L. I. Sonoda, C. Hayes, D. L. G. Hill, M. O. Leach, and D. J. Hawkes. Non-rigid registration using free-form deformations: Application to breast MR images. *IEEE Transactions on Medical Imaging*, 18(8):712–721, August 1999.
8. C. Studholme, D. L. G. Hill, and D. J. Hawkes. An overlap invariant entropy measure of 3D medical image alignment. *Pattern Recognition*, 32(1):71–86, 1998.
9. J. A. Schnabel, D. Rueckert, M. Quist, J. M. Blackall, A. D. Castellano Smith, T. Hartkens, G. P. Penney, W. A. Hall, H. Liu, C. L. Truwit, F. A. Gerritsen, D. L. G. Hill, and D. J. Hawkes. A generic framework for non-rigid registration based on non-uniform multi-level free-form deformations. In *Fourth Int. Conf. on Medical Image Computing and Computer-Assisted Intervention (MICCAI '01)*, pages 573–581, Utrecht, NL, October 2001.
10. D. Perperidis, A.Rao, , M. Lorenzo-Valdes, R. Mohiaddin, and D. Rueckert. Spatio-temporal alignment of 4d cardiac mr images. In *Second International Workshop on Functional Imaging and Modeling of the Heart*, 2003. Submitted.

# Motion-Compensation of Cardiac Perfusion MRI Using a Statistical Texture Ensemble

Mikkel B. Stegmann[1,2] and Henrik B.W. Larsson[2,3]

[1] Informatics and Mathematical Modelling, Technical University of Denmark
Richard Petersens Plads, Building 321, DK-2800 Kgs. Lyngby, Denmark
mbs@imm.dtu.dk, http://www.imm.dtu.dk/~mbs/
[2] Danish Research Centre for Magnetic Resonance, H:S Hvidovre Hospital
Kettegaard Allé 30, DK-2650 Hvidovre, Denmark
[3] MR-Senteret, St. Olavs Hospital, Trondheim University
Olav Kyrres Gate 17, N-7006 Trondheim, Norway

**Abstract.** This paper presents a novel method for segmentation of cardiac perfusion MRI. By performing complex analyses of variance and clustering in an annotated training set off-line, the presented method provides real-time segmentation in an on-line setting. This renders the method feasible for e.g. analysis of large image databases or for live non-rigid motion-compensation in modern MR scanners. Changes in image intensity during the bolus passage is modelled by an Active Appearance Model augmented with a cluster analysis of the training set and priors on pose and shape. Preliminary validation of the method is carried out using 250 MR perfusion images, acquired without breath-hold from five subjects. Quantitative and qualitative results show high accuracy, given the limited number of subjects.

## 1 Introduction

Within the last decade magnetic resonance imaging has been proven able to assess myocardial perfusion in an accurate and safe manner, see e.g. [9]. While scanning times have improved drastically, the amount of manual post-processing remains to render the method prohibitive to clinical practice. A major part of this manual labour is spent by marking up points of correspondence on the myocardium, thus enabling compensation of any motion during a perfusion sequence. This paper present a novel approach aiming at replacing the tedious and error prone labour with an automatic image analysis method, which provides a structured way of collecting and applying expert knowledge given by medical doctors into a learning-based framework.

The paper is organised as follows. Section 2 describes the data used for this study. Section 3 begins by introducing the foundations of this work, namely myocardial perfusion imaging and active appearance modelling, and concludes by describing the proposed method. Section 4 presents a preliminary experimental validation. Finally, Sects. 5 and 6 serve a discussion of the obtained results and draw some concluding remarks.

I. Magnin et al. (Eds.): FIMH 2003, LNCS 2674, pp. 151–161, 2003.

## 2 Data Material

The data material comprises 250 myocardial perfusion, short-axis, magnetic resonance images (MRI). For each of five subjects, 50 sequential images were acquired before, during and after the bolus of contrast. The used contrast agent was gadolinium diethylenetriaminopentaacetic acid (Gd-DTPA). Breath-hold was not used and the time-gap between images was approximately three seconds. Registration relative to the heart-cycle (end-diastole) was obtained using ECG-triggered acquisition from a whole-body MR unit, Siemens Vision, operating at 1.5 T. We used an inversion recovery turbo-FLASH (fast low-angle shot) MR-sequence. Matrix size was 128x128 pixels. Slice thickness was 10 mm. The endocardial and epicardial contours of the left ventricle (LV) were annotated in all images by manually placing 66 landmarks. To fix rotation around the LV long-axis, the right ventricle (RV) was annotated using 12 landmarks.

## 3 Methods

### 3.1 Myocardial Perfusion Imaging

Developments in MR-technology during the past decade have made it possible to acquire physiological information about dynamic processes in the human body. As an example of such, myocardial perfusion imaging encompasses assessment of myocardial perfusion at rest and during stress (e.g. pharmacological). By injecting a bolus of contrast the myocardial perfusion mechanism can be quantified, which is essential in ischemic heart diseases. As the contrast agent tags the blood stream and amplifies the MR signal, areas of the myocardium served by diseased arteries show a delayed and attenuated response. Acquisition is carried out dynamically and registered to the heart cycle using ECG-triggering. Images are typically acquired from one or more short-axis slices every $n$-th heartbeat, trading through-plane resolution for temporal resolution. If the time-window is sufficiently short (typically $< 40$ secs), breath-hold can be used to remove respiration artefacts. Another source of unwanted variation is erroneous ECG-triggering, giving an erroneous heart-phase and destroying trough-plane (z-axis) correspondence, due to the long-axis movement of the LV during the heart cycle.

### 3.2 Active Appearance Models

Active Appearance Models (AAMs) [7,4] was introduced as a method for segmentation and interpretation of face images. This was carried out by building models based on a set of annotated images without any ordering. By being a generic approach, medical applications were soon to follow. These include segmentation of knee cartilage MRI [6], short-axis cardiac MRI [11,14], metacarpal radiographs [15], diaphragm dome CT [1], echocardiogram time series [3], and corpus callosum in brain MRI [13].

Formally, AAMs establish a compact parameterisation of object variability, as learned from a representative training set. The modelled object properties are

usually shape and pixel intensities. The latter is henceforward denoted *texture*. From these quantities new images similar to the training set can be generated. Objects are defined by marking up each example with points of correspondence (i.e. landmarks) over the set either by hand, or by semi- to completely automated methods. Using a learning-based optimisation strategy, AAMs can be rapidly fitted to unseen images, thus providing image segmentation and analysis.

Variability is modelled by means of a Principal Component Analysis (PCA), i.e. an eigen analysis of the dispersions of shape and texture. Let there be given $Q$ training examples for an object class, and let each example be represented by a set of $N$ landmark points and $M$ texture samples. The shape examples are aligned to a normalised common mean using a Generalised Procrustes Analysis. The texture examples are warped into correspondence using a piece-wise affine warp, normalised, and subsequently sampled from this *shape-free* reference. Typically, this geometrical reference frame is the Procrustes mean shape. Let $\mathbf{s}$ and $\mathbf{t}$ denote a synthesised shape and texture and let $\bar{\mathbf{s}}$ and $\bar{\mathbf{t}}$ denote the corresponding sample means. New instances are now generated by adjusting the PC scores, $\mathbf{b}_s$ and $\mathbf{b}_t$ in

$$\mathbf{s} = \bar{\mathbf{s}} + \boldsymbol{\Phi}_s \mathbf{b}_s \quad , \quad \mathbf{t} = \bar{\mathbf{t}} + \boldsymbol{\Phi}_t \mathbf{b}_t \tag{1}$$

where $\boldsymbol{\Phi}_s$ and $\boldsymbol{\Phi}_t$ are eigenvectors of the shape and texture dispersions estimated from the training set. To obtain a combined shape and texture parameterisation, $\mathbf{c}$, the values of $\mathbf{b}_s$ and $\mathbf{b}_t$ over the training set are combined into

$$\mathbf{b} = \begin{bmatrix} \mathbf{W}_s \mathbf{b}_s \\ \mathbf{b}_t \end{bmatrix} = \begin{bmatrix} \mathbf{W}_s \boldsymbol{\Phi}_s^{\mathrm{T}} (\mathbf{s} - \bar{\mathbf{s}}) \\ \boldsymbol{\Phi}_t^{\mathrm{T}} (\mathbf{t} - \bar{\mathbf{t}}) \end{bmatrix}. \tag{2}$$

A suitable weighting between pixel distances and pixel intensities is carried out through the diagonal matrix $\mathbf{W}_s$. To recover any correlation between shape and texture the two eigenspaces are usually coupled through a third PC transform

$$\mathbf{b} = \boldsymbol{\Phi}_c \mathbf{c} = \begin{bmatrix} \boldsymbol{\Phi}_{c,s} \\ \boldsymbol{\Phi}_{c,t} \end{bmatrix} \mathbf{c} \tag{3}$$

obtaining the combined appearance model parameters, $\mathbf{c}$, that generate new object instances by

$$\mathbf{s} = \bar{\mathbf{s}} + \boldsymbol{\Phi}_s \mathbf{W}_s^{-1} \boldsymbol{\Phi}_{c,s} \mathbf{c} \quad , \quad \mathbf{t} = \bar{\mathbf{t}} + \boldsymbol{\Phi}_t \boldsymbol{\Phi}_{c,t} \mathbf{c}. \tag{4}$$

The object instance, $(\mathbf{s}, \mathbf{t})$, is synthesised into an image by warping the pixel intensities of $\mathbf{t}$ into the geometry of the shape $\mathbf{s}$ and applying the current pose parameters $\mathbf{p} = [\ t_x\ t_y\ s\ \theta\ ]^{\mathsf{T}}$ where $t_x$, $t_y$ and $\theta$ denotes in-plane translation and rotation, and $s$ denotes the shape size.

Given a suitable similarity measure the model is matched to an unseen image using an iterative updating scheme based on a fixed Jacobian estimate [5] or a principal component regression [4]. For further details on AAMs refer to [4,5,6].

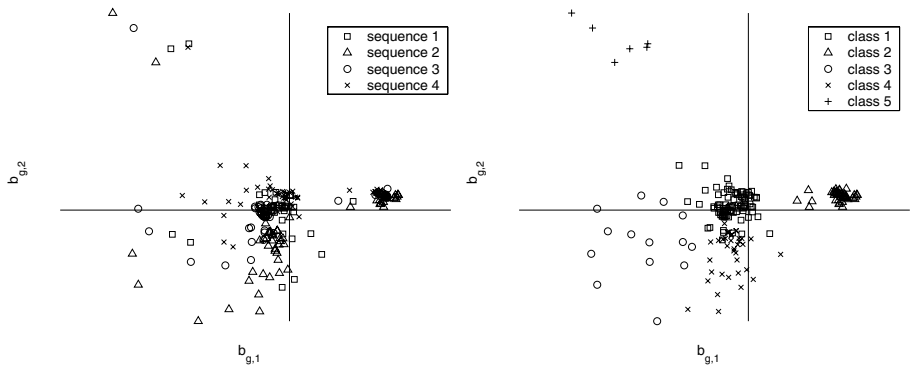


**Fig. 1.** First versus second principal component of 200 texture vectors from four perfusion sequences (left). Unsupervised classification result using five classes (right)

### 3.3 Modelling of Perfusion Time-Series

Since perfusion MRI sequences differ in structure from the single-image oriented AAMs, this section will discuss the issue of data modelling.

Treating each perfusion sequence as one observation (as in [10]) is not feasible due to random fluctuations in pose and shape induced by the variation sources mentioned in Sect. 3.1. However, texture variability – decoupled from changes in shape and pose – can be modelled as one observation per sequence providing a more specific model. Unfortunately, to model this behaviour properly, far more training sequences would be required compared to taking each frame as an observation. Consequently, given the low number of sequences, we will treat each image in a sequence as an observation. Circumventing the need for large training sets unfortunately violates the basic assumption in AAMs, that the variation in texture is well modelled by a multivariate Gaussian. Due to the radical changes in intensity during contrast uptake this is clearly not the case. On a coarse level we can split the sequence into i) pre-contrast arrival, ii) contrast agent entering the RV, iii) LV, and iv) the myocardium.

Figure 1 (left) shows the two most significant texture parameters of the texture model shown in Eq. (1), $b_{g,1}$ versus $b_{g,2}$, from the first four sequences in the data set.[1] Here it is verified that the expected clustering is very conspicuous. Modelling this distribution of textures with a multivariate Gaussian gives rise to several problems. Most problematic is that the resulting model is not very specific and can easily generate textures that are not plausible to occur during a perfusion bolus passage.

[1] Since the signal variation of the LV and RV is very small prior to contrast arrival and thus leading to little contrast, the standardisation of texture vectors normally used in AAM would result in severe amplification of scanner noise. Hence, we have only removed the texture mean in all models presented in this paper.

### 3.4 Adding Cluster Awareness

In order to model the distribution of textures above we propose an unsupervised learning approach that models texture variation using an ensemble of linear subspaces. Alternatively, these subspaces could have been given by an operator, which identifies different phases of each bolus passage. However, to reduce, i) the tedious burden of training set generation, and ii) inter- and intra-observer variability, supervised learning was rejected. Further, since we believe that no canonical number of subspaces exists, we would like to evaluate different ensemble sizes, which would have been very tedious in the case of manual labelling.

Though machine learning literature offers an abundance of classification methods, it is generally agreed upon that no *silver bullet* exists. We have chosen a $k$-means classification [8] combined with a Monte Carlo simulation scheme where several classifications are carried out, based on different initial random class centres. The final classification is chosen using a minmax criterion, i.e. having the smallest maximum distance to its class centre.

The obtained classification using five classes ($k = 5$) of the data set is shown in Fig. 1 (right). From this classification, a set of linear texture subspaces, $\{\boldsymbol{\Phi}_{t,i}\}_{i=1}^{k}$, is obtained directly by $k$ separate texture PCAs. A corresponding set of texture parameter update matrices, $\{\mathbf{R}_{t,i}\}_{i=1}^{k}$, is obtained following the procedure in [5]. As changes in texture over the sequence is assumed to be uncorrelated with shape, building a joint shape model, $\boldsymbol{\Phi}_s$, from all sequences yields the best estimate of inter- and intra-subject shape variability. We call this a model a *Cluster-aware AAM* (CAAM).

Fitting a CAAM to unseen images now involves choosing the appropriate texture subspace. As a reasonable choice for $k$ is very low, model selection is performed by exhaustively trying all models and selecting the model producing the best fit, subject to a set of constraints given later in this paper. To increase performance during model fitting, model selection could be accomplished by a classification of the texture vector into the set of training classes.

To choose $k$ prior knowledge can employed. However, being an optimisation problem in one positive integer variable, we would prefer a data-driven method. Here, the optimal $k$ is estimated using cross-validation on the training set.

### 3.5 Estimating and Enforcing Pose and Shape Priors

The fact that changes in pose and shape are uncorrelated with the change of texture is highly useful for initialising and constraining the model fitting process. Further, it can validate the final segmentation results. Thus, if it is possible to obtain reliable estimates of the shape and pose in a subpart of the sequence these can be used in the remains of that sequence. This is the case in the latter part of a bolus passage where the contrast agent has been washed out of the RV and LV, only leaving the subtle changes stemming from the perfusion mechanism in the myocardium. Hence, we propose to estimate prior distributions of pose and shape from the latter part of a perfusion sequence of $P$ frames.

Let $\kappa$, $\gamma$, $D_{max}$ denote a set of user-selectable constants controlling the influence of the priors. Then, let $\boldsymbol{\Sigma}$ denote the dispersion matrix of the pose

parameters and let $\boldsymbol{\sigma}$ denote the standard deviations of the shape parameters. How these two quantities are estimated is treated in Appendix A. Further, let $\mathbf{F}_t$ denote the $t$-th frame. Let the set of frames $\{\mathbf{F}_t\}_{t=1}^{S-1}$ denote the unstable period, and the frames $\{\mathbf{F}_t\}_{t=S}^{P}$ denote the stable period. Then, an algorithm for exploiting these priors can be formulated as:

**Algorithm 1** Sequence prior augmented AAM search

**Require:** $S$, $\kappa$, $\gamma$, $D_{max}$, $\boldsymbol{\Sigma}$ and $\boldsymbol{\sigma}$
1: $\overline{\mathbf{p}}$ = initialisation
2: $\overline{\mathbf{b}}_s$ = initialisation
3: **for** $t = P$ down to $S$ **do**
4: $\quad\{\mathbf{p}_t, \mathbf{b}_{s,t}\}$ = CAAM search started at $\{\overline{\mathbf{p}}, \overline{\mathbf{b}}_s\}$ in $\mathbf{F}_t$
5: $\quad\overline{\mathbf{p}} = \frac{1}{P-t+1}\sum_{j=t}^{P}\mathbf{p}_j$ *)
6: $\quad\overline{\mathbf{b}}_s = \frac{1}{P-t+1}\sum_{j=t}^{P}\mathbf{b}_{s,j}$ *)
7: **end for**
8: **for** $t = S-1$ down to 1 **do**
9: $\quad\{\mathbf{p}_t, \mathbf{b}_{s,t}\}$ = Constrained CAAM search started at $\{\overline{\mathbf{p}}, \overline{\mathbf{b}}_s\}$ in $\mathbf{F}_t$
(constrain using $\kappa$, $\gamma$, $D_{max}$, $\boldsymbol{\Sigma}$, $\overline{\mathbf{b}}_s$, $\boldsymbol{\sigma}$)
10: **end for**
*) Notice that this is carried out most efficiently by using provisional means.
This circumvents the need for storing past observations when calculating the mean.

During CAAM search in the unstable period, pose and shape priors are used to stabilise parameter updates by limiting the maximal update step. To simplify notation, the time index $t$ is omitted from this point on. Let $\Sigma_{ij}$ denote the element in the $i$-th row and $j$-th column of $\boldsymbol{\Sigma}$, and let $p_i$ denote the $i$-th element of $\mathbf{p}$. Pose parameter updates can now be constrained using the following simple clamping approach:

$$\delta p_i = \begin{cases} \kappa\sqrt{\Sigma_{ii}} & \text{if } \delta p_i > \kappa\sqrt{\Sigma_{ii}} \\ \delta p_j & \text{otherwise.} \end{cases} \tag{5}$$

The constant $\kappa$ acts thus as a clamping constant given in units of standard deviations of pose variation as estimated from the training sequences. In all experiments we have used $\kappa = 0.5$. Likewise, we also exploit the prior knowledge of shape variation, $\boldsymbol{\sigma}$, (as obtained from the training set) in a similar clamping approach,

$$b_{s,i} = \begin{cases} b_{s,i} + \text{sign}(b_{s,i} - \overline{b}_{s,i})\gamma\sigma_i & \text{if } b_{s,i} - \overline{b}_{s,i} > \gamma\sigma_i \\ b_{s,i} & \text{otherwise,} \end{cases} \tag{6}$$

where $\gamma$ denotes the maximally accepted distance from the mean in units of standard deviations. In our experiments we have used $\gamma = 3$.

After ended CAAM search in the unstable period, pose prior enforcement is determined by testing the Mahalanobis distance to the pose distribution:

$$\{\mathbf{p}, \mathbf{b}\} = \begin{cases} \{\overline{\mathbf{p}}, \overline{\mathbf{b}}\} & \text{if } D_{max}^2 < (\mathbf{p} - \overline{\mathbf{p}})^{\mathsf{T}}\boldsymbol{\Sigma}_p^{-1}(\mathbf{p} - \overline{\mathbf{p}}) \\ \{\mathbf{p}, \mathbf{b}\} & \text{otherwise} \end{cases} \tag{7}$$

Under the assumption of normal distributed pose parameters, we have chosen to use $D_{max} = 3$. Hence, implausible pose solutions are discarded and replaced with the maximum likelihood of the prior; the mean configuration.

## 4 Experimental Results

To evaluate the proposed method a Cluster-aware AAM was built using four sequences of 50 frames each. Our software was implemented in C++ (see [14]) and executed on an 1.2 GHz Athlon PC. The stable period was set manually as the last 25 frames of each sequence, i.e. $S = 26$. Using hold-out evaluation the model was tested on the remaining fifth sequence. The model was manually initialised in the $P$-th frame. Table 1 shows segmentation results for five different values of $k$. Double-mean landmark errors were calculated as the mean of all landmark points (for both RV and LV) and the mean over all frames. Not surprisingly, we found that the error was above average before and during the bolus passage. Segmentation results for $t = \{1, 12, \ldots, 17, 50\}$ are shown in Fig. 2.

**Table 1.** Segmentation results for different values of $k$

| $k$ | Pose rejects | Pt.pt.[1)] [pixels] | Pt.crv.[2)] [pixels] | Time [sec] |
|---|---|---|---|---|
| 1 | 3 | 2.19±0.35 | 1.33±0.19 | 0.5 |
| 2 | 3 | 2.26±0.41 | 1.38±0.20 | 0.7 |
| 3 | 0 | 1.81±0.38 | 1.03±0.15 | 1.2 |
| 4 | 2 | 2.13±0.60 | 1.19±0.17 | 1.5 |
| 5 | 0 | 2.13±0.49 | 1.24±0.18 | 1.8 |

[1)]Pt.pt. measures the Euclidean distance between corresponding landmarks of the model and the ground truth. [2)]Pt.crv. measures the shortest distance to the ground truth curve in a neighbourhood of the corresponding landmark.

To hint the behaviour of the method given a large training set, contrary to the four sequences used in the above, we have performed a leave-all-in evaluation where a CAAM was built using all 250 images from the five sequences, and the tested on the fifth sequence. Consequently, the model had a full representation of the test sequence, except for the regularisation of the texture and shape eigenspaces in an AAM [4]. The results given in Table 2 show a trend of decreasing landmark error with increasing class numbers. Though being rather positively biased, the results also hints the lower bound on the landmark error.

## 5 Discussion

As observed in the previous section, the addition of cluster-awareness seems to increase segmentation accuracy. However, as the set of training sequences is very limited, conclusions would always remain premature and fragile. By design

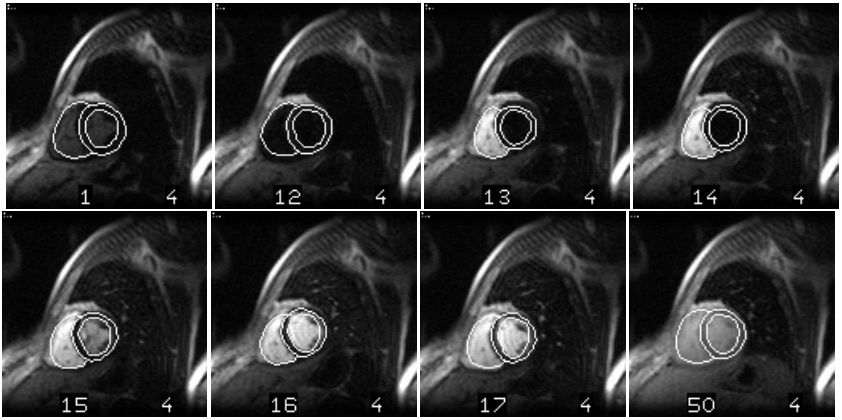


**Fig. 2.** Segmentation results before, during and after the bolus passage, $k = 3$

**Table 2.** Leave-all-in segmentation results

| $k$ | Pose rejects | Pt.pt. [pixels] | Pt.crv. [pixels] | Time [sec] |
|---|---|---|---|---|
| 1 | 0 | 1.80±1.20 | 0.89±0.52 | 0.8 |
| 2 | 1 | 1.70±1.17 | 0.89±0.65 | 1.0 |
| 3 | 1 | 1.30±0.80 | 0.67±0.37 | 1.7 |
| 4 | 0 | 1.50±0.93 | 0.77±0.40 | 1.9 |
| 5 | 0 | 1.13±0.46 | 0.61±0.24 | 2.5 |

cluster-awareness adds specificity in the texture, which is a very important property for a generative model. In other words, the chance of synthesising implausible images from a cardiac perfusion sequence is drastically reduced. However, the cost turns up as a need for more training examples to reliably estimate a cluster texture model.

Typically, cardiac perfusion images are acquired for several slices in the apex-basal direction. An extension of our approach is straightforward to implement by concatenating texture vectors to obtain one joint multi-slice texture model.

As touched upon earlier, a classification approach could be used instead of a brute-force evaluation of all models. This would lead to a segmentation time corresponding roughly to using one cluster. However, as the initial texture sample is only close to the correct subspace, misclassification is likely to happen. This would need to be dealt with, if a further increase in speed is required.

Compared to a recent approach to segmentation of perfusion cardiac MRI [12] our method offers a 20 times speed-up. Unfortunately, the approach described in [12] is restricted to breath-hold sequences, why a modification would be needed to enable a comparable study using non breath-hold perfusion sequences. Segmentation of perfusion MRI was also reported in [2] where a non-rigid transformation was used compared to our deformable approach.

To let our method generalise to new data, very few assumptions concerning the data content have been made. Except for a few scalar parameters (most of these being indices relating to the actual data), all values are estimated from training data, rather than being hard-coded into a computer framework. We believe this to be a very fruitful approach, as the method easily adapts to new expert knowledge given by medical doctors. Knowledge, that typically already exists in the form of hand-annotated training data from previous studies.

Finally, contrary to most other segmentation methods and due to the inherent representation of texture vectors in AAMs, we mention that motion-compensated images are directly obtained by projecting each texture vector in the shape-free reference frame. Thereby a correspondence for each pixel over the complete perfusion sequence is obtained, ready to be fed into a perfusion model as e.g. [9]. In future studies, we aim at validating our method on much larger data sets. As a natural performance benchmark, we will compare estimated perfusion parameters as obtained from automatic versus hand-segmented sequences.

## 6 Conclusion

We have described a novel, data-driven method for motion-compensation of cardiac perfusion MRI. Preliminary validation of the method showed high segmentation accuracy, considering the small number of subjects available. We anticipate a substantial increase in accuracy when more training data becomes available. The running time of the method using a standard PC is below two seconds for a 50-frame perfusion sequence and can easily be sped up. Thus, the method provides means for segmentation in an on-line setting, e.g. analysis of large image databases or for live motion-compensation in MR scanners.

## References

1. R. Beichel, S. Mitchell, E. Sorantin, F. Leberl, A. Goshtasby, and M. Sonka. Shape- and appearance-based segmentation of volumetric medical images. *IEEE International Conference on Image Processing*, 2:589–592, 2001.
2. L.M. Bidaut and J.P. Vallee. Automated registration of dynamic MR images for the quantification of myocardial perfusion. *Magn Reson Imag*, 13(4):648–655, 2001.
3. J.G. Bosch, S.C. Mitchell, B.P. Lelieveldt, F. Nijland, O. Kamp, M. Sonka, and J.H. Reiber. Fully automated endocardial contour detection in time sequences of echocardiograms by three-dimensional active appearance models. *Medical Imaging 2002: Image Processing, San Diego CA, SPIE*, pages 452–462, 2002.
4. T.F. Cootes, G.J. Edwards, and C.J. Taylor. Active appearance models. In *Proc. European Conf. on Computer Vision*, volume 2, pages 484–498. Springer, 1998.
5. T.F. Cootes, G.J. Edwards, and C.J. Taylor. Active appearance models. *IEEE Trans. on Pattern Recognition and Machine Intelligence*, 23(6):681–685, 2001.
6. T.F. Cootes and C.J. Taylor. *Statistical Models of Appearance for Computer Vision.* Tech. Report. Feb 2000, University of Manchester, 2000.
7. G.J. Edwards, C.J. Taylor, and T. F. Cootes. Interpreting face images using active appearance models. In *Proc. 3rd IEEE Int. Conf. on Automatic Face and Gesture Recognition*, pages 300–5. IEEE Comput. Soc, 1998.

8. E. Forgey. Cluster analysis of multivariate data. *Biometrics*, 21:768, 1965.
9. Henrik B.W. Larsson, Thomas Fritz-Hansen, Egill Rostrup, Lars Søndergaard, Poul Ring, and Ole Henriksen. Myocardial perfusion modeling using MRI. *Magnetic Resonance in Medicine*, 35:716–726, 1996.
10. S. Mitchell, B. Lelieveldt, R. Geest, H. Bosch, J. Reiber, and M. Sonka. Time continuous segmentation of cardiac MR image sequences using active appearance motion models. In *Medical Imaging 2001: Image Processing, San Diego CA, SPIE*, volume 1, pages 249–256. SPIE, 2001.
11. S. Mitchell, B. Lelieveldt, R. Geest, J. Schaap, J. Reiber, and M. Sonka. Segmentation of cardiac MR images: An active appearance model approach. In *Medical Imaging 2000: Image Processing, San Diego CA, SPIE*, volume 1. SPIE, 2000.
12. L. Spreeuwers and M. Breeuwer. Automatic detection of the myocardial boundaries of the right and left ventricle in mr cardio perfusion scans. *Proceedings of SPIE – The International Society for Optical Engineering*, 4322(3):1207–1217, 2001.
13. M.B. Stegmann and R.H. Davies. Corpus callosum analysis using MDL-based sequential models of shape and appearance. In *Medical Image Computing and Computer-Assisted Intervention - MICCAI.*, LNCS. Springer, 2003 (submitted).
14. M.B. Stegmann, B K. Ersbøll, and R. Larsen. FAME – a flexible appearance modelling environment. *IEEE Trans. on Medical Imaging*, 2003 (to appear).
15. M.B. Stegmann, R. Fisker, and B.K. Ersbøll. Extending and applying active appearance models for automated, high precision segmentation in different image modalities. In *Proc. 12th Scandinavian Conference on Image Analysis – SCIA 2001*, volume 1, pages 90–97, 2001.

## A Estimation of $\boldsymbol{\Sigma}$ and $\boldsymbol{\sigma}$

The dispersion matrix of the pose parameters, $\boldsymbol{\Sigma}$, and the standard deviations of the shape parameters, $\boldsymbol{\sigma}$, can be estimated from the stable period. However, in order to obtain more reliable estimates we propose to use the training sequences, since much more samples are available. To avoid confusion of inter- and intra-sequence variability, we filter out sequence-specific information (such as mean shape size) prior to the estimation. Now, let $R$ denote the number of sequences, each containing $P$ frames. Further, let $\odot$ denote the Hadamard, i.e. element-wise, product. Then the estimation of $\boldsymbol{\Sigma}$ and $\sigma$ can be specified as:

**Algorithm 2** Estimation of pose and shape variation

1: **for** $i = 1$ to $R$ (for each training sequence) **do**
2: $\quad \mathbf{p}_t \leftarrow \mathbf{p}_t \odot (\frac{1}{\bar{s}}[\ 1\ 1\ 1\ \bar{s}\ ]^\mathsf{T})\ \ \forall\ \ t$ — Normalise pose w.r.t. mean size
3: $\quad \overline{\mathbf{p}}_i = \frac{1}{P}\sum_{t=1}^{P}\mathbf{p}_t$ — Estimate pose mean
4: $\quad \boldsymbol{\Sigma}_i = \frac{1}{P-1}\sum_{t=1}^{P}(\mathbf{p}_t - \overline{\mathbf{p}}_i)(\mathbf{p}_t - \overline{\mathbf{p}}_i)^\mathsf{T}$ — Estimate pose dispersion matrix
5: $\quad \overline{\mathbf{b}}_{s,i} = \frac{1}{P}\sum_{t=1}^{P}\mathbf{b}_{s,t}$ — Estimate shape mean
6: $\quad \boldsymbol{\sigma}_i = \sqrt{\frac{1}{P-1}\sum_{t=1}^{P}(\mathbf{b}_{s,t} - \overline{\mathbf{b}}_{s,i}) \odot (\mathbf{b}_{s,t} - \overline{\mathbf{b}}_{s,i})}$ — Estimate shape std. dev.
7: **end for**
8: $\boldsymbol{\Sigma} = \frac{1}{R}\sum_{i=1}^{R}\boldsymbol{\Sigma}_i$ — Calculate pooled estimate for all sequences
9: $\boldsymbol{\sigma} = \frac{1}{R}\sum_{i=1}^{R}\boldsymbol{\sigma}_i$ — Calculate pooled estimate for all sequences

Further, to maintain simplicity, normalisation w.r.t. rotation has not been included in the above algorithm. However, if sequences differ in orientation, this should be taken into account when estimating $t_x$ and $t_y$. Finally, during CAAM search, appropriate normalisation and de-normalisation using the stable period mean size (and orientation) must be carried out.

# Measuring Myocardial Deformations in Tagged MR Image Sequences Using Informational Non-rigid Registration

Caroline Petitjean[1], Nicolas Rougon[1], Françoise Prêteux[1], Philippe Cluzel[2], and Philippe Grenier[2]

[1] ARTEMIS Project Unit, Institut National des Télécommunications, Evry, France
[2] Service de Radiologie, Groupe Hospitalier Pitié-Salpêtrière, Paris, France

**Abstract.** We address the problem of quantifying myocardial deformations from tagged MRI sequences. We develop a two-step method comprising (i) a motion estimation step using a novel variational non rigid registration technique based on generalized information measures, and (ii) a measurement step, yielding local and segmental deformation parameters over the whole myocardium. Experiments performed on healthy and pathological data originating from various imaging devices demonstrate that this method delivers, within a reasonable computation time and in a robust and fully unsupervised way, reliable measurements for normal subjects and provide quantitative pathology-specific information.

## 1 Introduction

Cardio-vascular (CV) diseases are the leading cause of mortality in industrialized countries, and therefore a major public health challenge. Magnetic Resonance Imaging (MRI) is recognized as a relevant modality for dynamically imaging the heart anatomy and function. It provides a valuable investigation tool for early diagnosis and clinical/therapeutical follow-up, capable of delivering, in single examination, all the necessary information for assessing a large variety of CV pathologies, including those related to morphology and flow rate of coronary arteries, cardiac function, and myocardial perfusion/viability.

The reference MR modality for imaging myocardial strain is tagged MRI [16,2]. Measuring myocardial deformations from tagged MR sequences relies on estimating a dense displacement field consistent with the motion of the structured tagging pattern. Classical approaches can be classified into three groups: (i) differential optical flow-based methods [12,5], which often require knowing acquisition parameters, and fail to deal with large deformations due to their local nature; (ii) phase-based optical flow methods such as HARP, which are best suited to 1D tagging patterns [1]; (iii) three-step methods consisting of tag segmentation, sparse motion estimation along the tagging pattern, and dense motion interpolation over the whole image domain [9,8,6,4,3,1]. For the latter class, the critical segmentation step is made complex by tag/background constrast attenuation over time due to demagnetization phenomena (tag fading out),

I. Magnin et al. (Eds.): FIMH 2003, LNCS 2674, pp. 162–172, 2003.

and tag topology variations induced by blood flows within the cardiac chambers. Consequently, a certain degree of supervision is usually required either to guide the segmentation process or to correct segmentation errors.

To overcome these limitations, a variational non rigid registration (NRR) approach based on generalized information measures is presented in Sect. 2. It does not require preliminary tag segmentation and directly delivers dense displacement estimates in a robust and non-supervised way. These estimates are then used to compute local and segmental deformation parameters over the myocardium, as described in Sect. 3. Section 4 presents results on healthy and pathological data, and demonstrates performances for estimating heart motion.

## 2 NRR Using Generalized Information Measures

### 2.1 Generalized Information Measures

Let $X$ and $Y$ denote continuous random variables (RV) over a state space $\Omega$ with p.d.f. $p^X$ and $p^Y$, respectively, and let $p^{X,Y}$ be the p.d.f. of the joint RV $(X, Y)$ over $\Omega^2$. The classical tool for measuring the reduction of uncertainty of $Y$ given $X$ (and *vice-versa*) is mutual information (MI), defined as:

$$I(X,Y) \;:=\; H_S(X) + H_S(Y) - H_S(X,Y) \;=\; D_{\mathrm{KL}}((X,Y) \parallel X \times Y) \;\; .$$

Here, $H_S$ denotes Shannon entropy which measures the information content of a RV: $H_S(X) := -\int_\Omega p^X(x) \log(p^X(x))\, dx$, and $D_{\mathrm{KL}}$ is the (non symmetric[1]) statistical similarity measure, refered to as Kullback-Leibler (KL) divergence:

$$D_{\mathrm{KL}}(X \parallel Y) \;:=\; \int_\Omega p^X(x) \log \frac{p^X(x)}{p^Y(x)}\, dx \;\; .$$

Hence, MI measures the information gain resulting from observing $X$ and $Y$ jointly compared to observing them independantly. This measurement is based on the Kullback metrics $f_{\mathrm{KL}}(x) := x \log x$.

It is known that MI leads to optimal decision when uncertainty measurement is constrained to be additive and no assumption is made about RV statistics. Relaxing these hypotheses, extensions of the Shannon framework to more general metrics yielding generalized information gain measures have been proposed [15]. In this paper, we confine ourselves to integral[2] $f$-informations $I_f$ defined as:

$$I_f(X,Y) \;:=\; D_f\big((X,Y) \parallel X \times Y\big) \;=\; \int_{\Omega^2} p^X(x) p^Y(y) f\left(\frac{p^{X,Y}(x,y)}{p^X(x)p^Y(y)}\right) dxdy \;\; .$$

where $f$ is a convex continuous mapping over $\mathbb{R}^+$, and $D_f$ is a generalized statistical similarity measure, refered to as integral $f$-divergence, such that:

$$D_f(X \parallel Y) \;:=\; \int_\Omega p^Y(x) f\left(\frac{p^X(x)}{p^Y(x)}\right) dx \;\; .$$

[1] This asymmetry is reflected by the notation $X \parallel Y$ to denote $D_{\mathrm{KL}}$ arguments.
[2] Non-integral $f$-informations are addressed in [11,13].

It can be related to a generalized entropy measure $H_f$ (integral $f$-entropy): $H_f(X) := -\int_\Omega f(p^X(x))\,dx$. Choosing $f = f_{\mathrm{KL}}$ yields KL divergence and Shannon entropy. Other metrics allow to tune the measurement of uncertainty.

### 2.2 Variational NRR Using Generalized Information Measures

Given a pair of images $I_1$ and $I_2$ defined over a domain $D \subset \mathbb{R}^n$, registering $I_2$ onto $I_1$ consists in finding a transformation $\phi : D \to D$ within some functional space $\mathcal{T}$ so that $I_2 \circ \phi$ is similar to $I_1$ according to some predefined criterion. Equivalently, the problem can be expressed in terms of a displacement field $\mathbf{u}$ such that $\phi = \mathrm{Id} + \mathbf{u}$. That is, for any $\mathbf{x} \in D$, we are looking for $\mathbf{u}$ such that $I_2^{\mathbf{u}}(\mathbf{x}) := I_2(\mathbf{x} + \mathbf{u}(\mathbf{x}))$ is similar to $I_1(\mathbf{x})$. The space $\mathcal{T}$ is a space of sufficiently smooth mappings which can be parametric or not. We here restrict to non parametric motion models. The parametric case is detailed in [13].

The problem is ill-posed and must be regularized. A classical deterministic approach defines a solution as a minimizer $\mathbf{u}^*$ over $\mathcal{T}$ of a cost functional $\mathcal{J}$ such that $\mathcal{J}(\mathbf{u}) = \mathcal{S}(\mathbf{u}) + \alpha\mathcal{R}(\mathbf{u})$, where:

- $\mathcal{S}$ is a similarity functional which quantifies the discrepancy between $I_1$ and $I_2^{\mathbf{u}}$. In this paper, $\mathcal{S}$ is chosen as the opposite of a generalized information measure: $\mathcal{S}(\mathbf{u}) = -I_f(I_1, I_2^{\mathbf{u}})$, $I_1$ and $I_2^{\mathbf{u}}$ being modeled as probability distributions with marginal p.d.f. $p^{I_1}$ and $p^{I_2^{\mathbf{u}}}$, and joint p.d.f. $p^{I_1, I_2^{\mathbf{u}}}$.
- $\mathcal{R}$ is a stabilizing functional ensuring (almost everywhere) regular solutions. Here, we consider first-order stabilizers involving the Jacobian $\nabla\mathbf{u}$ of $\mathbf{u}$.
- $\alpha > 0$ is a regularization parameter which controls the trade-off between data consistency and smoothing.

Minimizing $\mathcal{J}$ over $\mathcal{T}$ by gradient descent yields the flow: $\frac{\partial \mathbf{u}}{\partial t} = -\partial_{\mathbf{u}}\mathcal{J}(\mathbf{u})$ ($\mathbf{u}(t = 0) = \mathbf{0}$), where $\partial_{\mathbf{u}}\mathcal{J}$ is the Gâteaux derivative of $\mathcal{J}$. Computing the Gâteaux derivative of the similarity functional $\mathcal{S}$ under closed form is here the central issue. To this end, non parametric Parzen-Rozenblatt estimation is used to derive analytical estimates of p.d.f.. That is, the p.d.f. of a RV $X$ over $D$ is approximated as: $p^X(X_0) = \frac{1}{\mu(D)}\int_D \mathcal{K}(X(\mathbf{x}) - X_0)\,d\mathbf{x}$, where $\mathcal{K}$ is a density kernel with the same dimension as $X$ and $\mu(D)$ is the volume of $D$. The gradient flow of integral $f$-information criteria is then shown to be [11,13]):

$$\partial_{\mathbf{u}} S(\mathbf{u}) = \frac{-1}{\mu(D)} \left\{ \left[ \mathcal{K}_2 \star \frac{\partial L_1^{\mathbf{u}}}{\partial i_2} \right] \left(I_1(\mathbf{x}), I_2^{\mathbf{u}}(\mathbf{x})\right) + \mathrm{E}_{I_1}\left( \left[ \mathcal{K}_1 \star \frac{\partial L_2^{\mathbf{u}|i_1}}{\partial i_2} \right] (I_2^{\mathbf{u}}(\mathbf{x})) \right) \right\} \nabla I_2^{\mathbf{u}}(\mathbf{x})$$

where $\mathrm{E}_{I_1}(\cdot)$ denotes expectation w.r.t. the RV $I_1$ and the symbol $\star$ is the 2D (resp. 1D) convolution operator over the intensity space $\Omega^2$ (resp. $\Omega$). In addition, denoting by $\rho^{\mathbf{u}}(i_1, i_2) := \frac{p^{I_1, I_2^{\mathbf{u}}}(i_1, i_2)}{p^{I_1}(i_1)\, p^{I_2^{\mathbf{u}}}(i_2)}$ the so-called deviation from independance ratio, one has: $L_1^{\mathbf{u}} := f'(\rho^{\mathbf{u}})$, $L_2^{\mathbf{u}} := f(\rho^{\mathbf{u}}) - \rho^{\mathbf{u}} f'(\rho^{\mathbf{u}})$ and $L_2^{\mathbf{u}|i_1}(\cdot) := L_2^{\mathbf{u}}(i_1, \cdot)$, $\forall i_1 \in \Omega$. It is then easily shown that: $\frac{\partial L_2^{\mathbf{u}|i_1}}{\partial i_2} = -\rho^{\mathbf{u}} \frac{\partial L_1^{\mathbf{u}}}{\partial i_2}$.

Notice that the flow is along $\nabla I_2^{\mathbf{u}}$. Thus, constant intensity areas remain unaltered and are deformed only through interactions along their boundaries. The flow is driven: (i) locally, by the contrast of $I_2^{\mathbf{u}}$, and (ii) globally, by the variation of the statistical coupling between $I_1$ and $I_2^{\mathbf{u}}$ induced by perturbing $I_2^{\mathbf{u}}$. Statistical dependance is modeled via the deviation from independance ratio $\rho^{\mathbf{u}}$ and analyzed via the estimators $L_1^{\mathbf{u}}$ and $L_2^{\mathbf{u}}$. Variations are estimated in a regularized way by linear filtering against Parzen kernels, and measured via the metrics $f$. Interestingly, $L_2^{\mathbf{u}}$ is informationless when $f = f_{\mathrm{KL}}$, producing a zero contribution to the associated MI flow [7]. In contrast, using non Shannon metrics allows to exploit the information content of $I_2^{\mathbf{u}}$ in a more extensive fashion.

### 2.3 Gradient Flow of Normalized Generalized Information Measures

Computing $p^{I_1,I_2^{\mathbf{u}}}$ is restricted to the overlapping part $D \cap \phi(D)$ of the domains of $I_1$ and $I_2^{\mathbf{u}}$. This makes information measures sensitive to the image overlap [10,14]. In the Shannon framework, normalized information measures have been proposed to overcome this problem, such as the *entropy correlation coefficient* [10] and the *normalized mutual information* [14]. A non normalized measure has also been suggested [10]. These various measures can be extended to generalized information metrics in a consistent fashion with the Shannon case as follows [13]:

– *Generalized entropy correlation coefficient:*

$$ECC_f(X,Y) := 2\,\frac{I_f(X,Y)}{I_f(X,X)+I_f(Y,Y)} \quad \longrightarrow \quad \mathcal{S}(\mathbf{u}) = -ECC_f(I_1, I_2^{\mathbf{u}})$$

– *Generalized normalized mutual information:*

$$\bar{I}_f(X,Y) := \frac{I_f(X,X)+I_f(Y,Y)}{I_f(X,X)+I_f(Y,Y)-I_f(X,Y)} \quad \longrightarrow \quad \mathcal{S}(\mathbf{u}) = -\bar{I}_f(I_1, I_2^{\mathbf{u}})$$

– *Generalized exclusive information:*

$$Z_f(X,Y) := I_f(X,X)+I_f(Y,Y)-2I_f(X,Y) \quad \longrightarrow \quad \mathcal{S}(\mathbf{u}) = Z_f(I_1, I_2^{\mathbf{u}})$$

The gradient flows for the induced similarity criteria are of the generic form [11]:

$$\partial_{\mathbf{u}} S(\mathbf{u}) \;=\; -\alpha(I_1, I_2^{\mathbf{u}})\big[w_1(I_1, I_2^{\mathbf{u}})\;\partial_{\mathbf{u}} I_f(I_1, I_2^{\mathbf{u}}) - w_2(I_1, I_2^{\mathbf{u}})\;\partial_{\mathbf{u}} I_f(I_2^{\mathbf{u}}, I_2^{\mathbf{u}})\big]$$

where, assuming integral $f$-information, we have:

$$\partial_{\mathbf{u}} I_f(I_2^{\mathbf{u}}, I_2^{\mathbf{u}}) \;=\; \frac{1}{\mu(D)}\left\{\left[\mathcal{K}_1 \star \frac{\partial L_3^{\mathbf{u}}}{\partial i_2}\right]\left(I_2^{\mathbf{u}}(\mathbf{x})\right)\right\}\nabla I_2^{\mathbf{u}}(\mathbf{x})$$

with $L_3^{\mathbf{u}} := 2f'\left(\frac{1}{p^{I_2^{\mathbf{u}}}}\right)p^{I_2^{\mathbf{u}}} - f'\left(\frac{1}{p^{I_2^{\mathbf{u}}}}\right)$ and global weights $\alpha(I_1, I_2^{\mathbf{u}})$, $w_1(I_1, I_2^{\mathbf{u}})$ and $w_2(I_1, I_2^{\mathbf{u}})$ defined in Table 1.

**Table 1.** Weights involved in the flow for generalized normalized information measures

| | $w_1(X,Y)$ | $w_2(X,Y)$ | $\alpha(X,Y)$ |
|---|---|---|---|
| $ECC_f$ | 2 | $ECC_f(X,Y)$ | $\frac{1}{I_f(X,X)+I_f(Y,Y)}$ |
| $\bar{I}_f$ | $\bar{I}_f(X,Y)$ | $\frac{\bar{I}_f(X,Y)ECC_f(X,Y)}{2}$ | $\frac{\bar{I}_f(X,Y)}{I_f(X,X)+I_f(Y,Y)}$ |
| $Z_f$ | 2 | 1 | 1 |

### 2.4 First-Order Regularization

Non-parametric motion models require explicit regularization. Following [7], we have considered the Nagel-Enkelmann oriented smoothness constraint such that: $\mathcal{R}(\mathbf{u}) := \frac{1}{2}\int_D \mathrm{Tr}\left(\nabla\mathbf{u}^t\, T_{I_1}\nabla\mathbf{u}\right) d\mathbf{x}$ . Its Gâteaux derivative is given by:

$$-\partial_{\mathbf{u}}\mathcal{R}(\mathbf{u}) = \nabla\cdot\left(T_{I_1}\nabla\mathbf{u}\right)$$
$$T_{I_1} = \frac{1}{||\nabla I_1||^2 + 2\beta}\left[\left(\beta + ||\nabla I_1||^2\right)\mathbb{I}\mathrm{d} - \nabla I_1 \nabla I_1^t\right]$$

where $\beta > 0$ is a contrast parameter. This stabilizer induces limited regularizing effects in low motion areas, yielding more localized field estimates than the classical linear elasticity constraint or discontinuity-preserving stabilizers.

## 3 Quantifying Myocardial Deformations

Myocardium has a complex architecture: fibers in the mid wall are circumferential whereas subendocardial fibers are longitudinally directed. This results in inhomogeneous and complex contraction patterns, correlated to fiber structure. In particular, the left ventricle (LV) deformations comprise radial thickening, circumferential shortening, torsion, and longitudinal shortening.

According to the laws of continuous mechanics, local deformation information are encoded pointwise in the strain tensor $\mathbf{E}(\mathbf{u}) := \frac{1}{2}\left(\nabla\mathbf{u} + \nabla\mathbf{u}^t + \nabla\mathbf{u}^t\nabla\mathbf{u}\right)$, which can be numerically computed from $\mathbf{u}^*$ using finite differences. Various deformation parameters can be derived from $\mathbf{E}$, including eigenvalues/eigenvectors which define maximal stretching and shortening magnitudes/directions, and directional strains $Q_{\mathbf{d}} := \mathbf{d}^t\mathbf{E}\,\mathbf{d}$ along some unit vector $\mathbf{d}$. In particular, choosing $\mathbf{d}$ as the normal ($\mathbf{n}$) or tangential ($\mathbf{t}$) vector field to myocardial boundaries yields estimates of radial/circumferential contraction. In addition, the component of $\mathbf{u}^*$ along this normal/tangential field yields a radial contraction/torsion attribute. In practice, the fields $\mathbf{n}$ and $\mathbf{t}$ are derived from the gradient of the distance function over binary masks of the myocardium extracted from cine-MR data.

Averaging these various parameters over each region of a layered regional model of the myocardium yields segmental descriptions of the deformation.

## 4 Results and Discussion

The developed computational framework has been applied to a cardiac MRI database, comprising healthy and pathological data. Tagged MR data were acquired during multiple breath holds on a 1.5T GE scanner using the SPAMM technique[3]. For each patient, three base-to-apex short-axis slice sequences were captured. For myocardium segmentation purpose, cine-MR sequences were also acquired at the same slice levels in identical conditions.

NRR using $I_\alpha$-exclusive information ($\alpha = 1.5$) has been performed between successive images pair in each sequence. The total computation time per examination varies from 15 to 30 minutes on a standard Pentium3 platform. Using $I_\alpha$-exclusive information instead of $I_\alpha$-information results in speeding up convergence. Myocardium segmentation, required for visualization purpose, was performed on the cine-MR data using mathematical morphology operations.

Results demonstrate that the developed NRR technique allows to estimate reliable frame-to-frame displacements, but also large-magnitude deformations such as systolic motions (Fig. 3). The matching proves to be accurate along tags, and consistent in such extent that systolic fields were found very close to the composition of frame-to-frame motion estimates during systole. Registration accuracy can be appreciated by warping a binary grid corresponding to the undeformed tagging pattern from starting frame to the target frame. The technique appears to perform robustly w.r.t. to tag fading out and imaging technology, as observed from additional experiments on CSPAMM and DANTE data. By contrast, applying such intensity-based non registration method as the "daemons" algorithm fails. Moreover, the proposed approach is far more computationally efficient than fluid registration.

**Non-pathological Data.** Figure 1 shows radial contraction and torsion for a healthy heart. Radial contraction mostly takes place during protosystole, on the right part of the LV (inferior and lateral walls mainly), in particular near apex. The propagation of deformation is visible: (i) on each slice, it moves clockwise from lateral to inferior wall, (ii) in each segment, it seems to propagate from apex to base. The latter behaviour may be linked to electrical activation: the electrical impulse is travelling from base to apex in the septal wall, and from apex to base in ventricular walls, causing ventricles to contract. Another remark concerns septum which still contracts in telesystole and early diastole while free walls start dilating. This seems to be linked to the right ventricle motion.

Torsion, shown on Fig. 2, differs at apex and base. The wringing motion in mid-systole is induced by a basal clockwise rotation, and an apical counterclockwise rotation.

These various observations prove to be in accordance with well-established results regarding heart anatomy.

[3] The acquisition parameters were as follows: 285mm field of view, $256 \times 128$ acquisition matrix and $1.4 \times 1.4$mm in-plane resolution. The number of images per sequence ranged from 15 to 21 ($\approx$ 45ms time interval) depending on the heart beat.

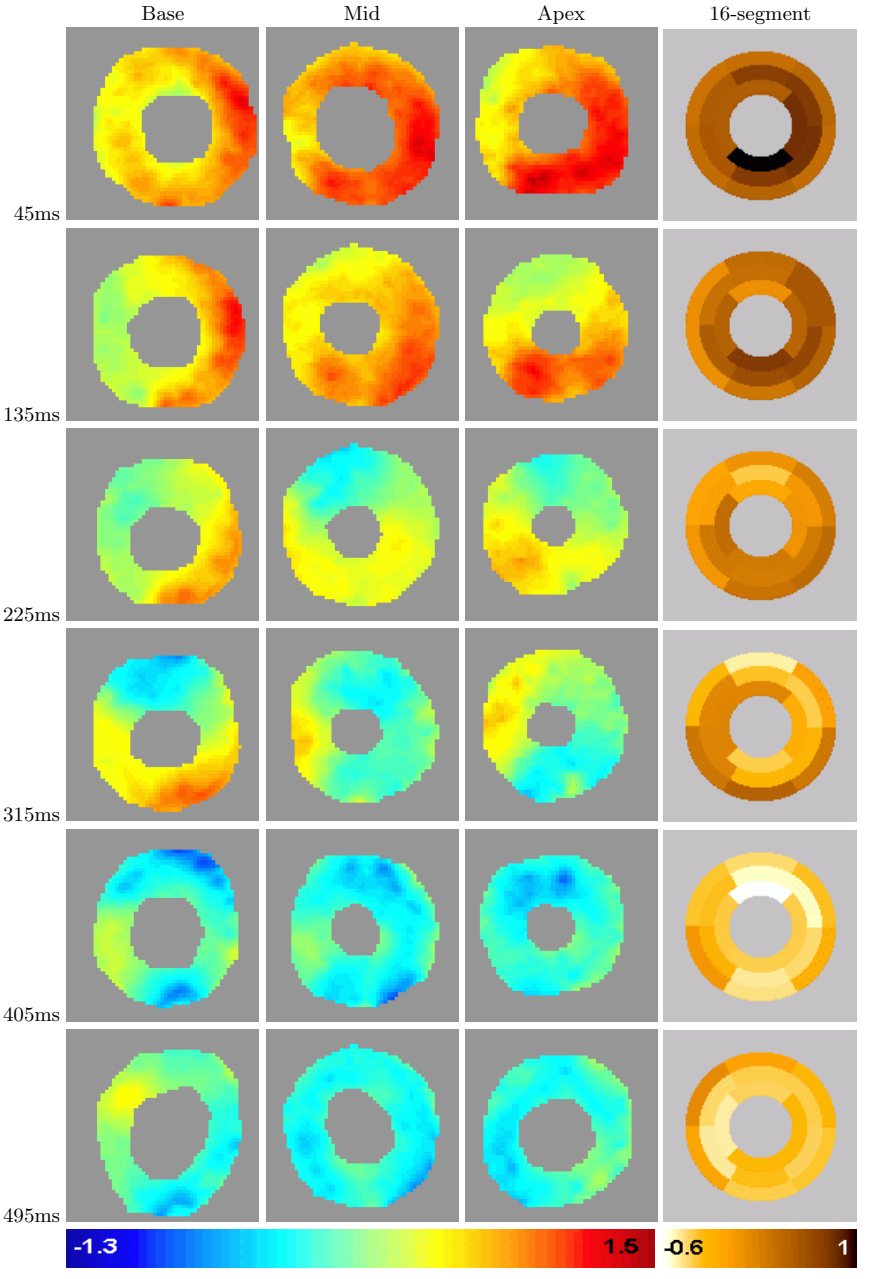


**Fig. 1.** Local and segmental radial contraction maps (shown as pseudocolor) for a healthy heart at basal, mid and apical slice levels

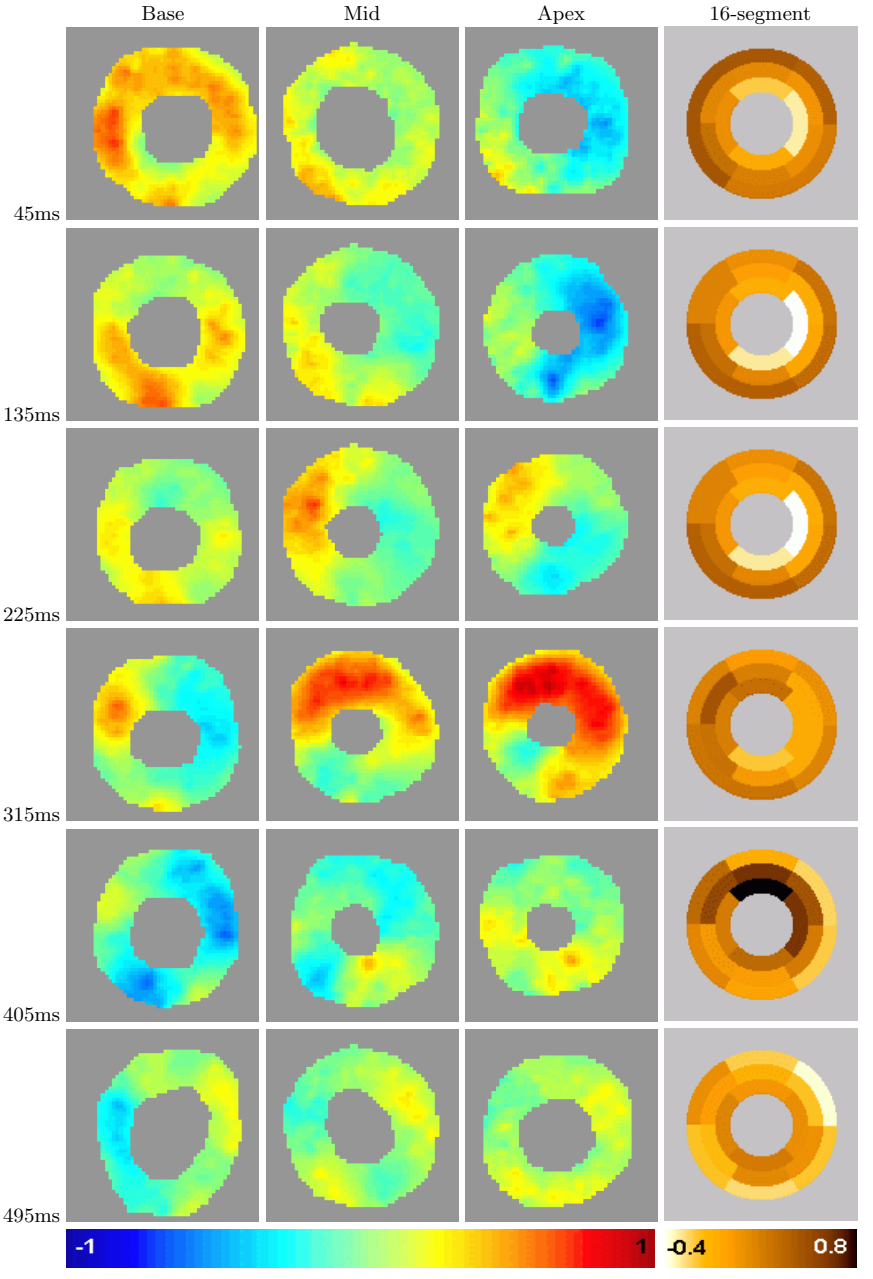


**Fig. 2.** Local and segmental torsion maps (shown as pseudocolor) for a healthy heart at basal, mid and apical slice levels

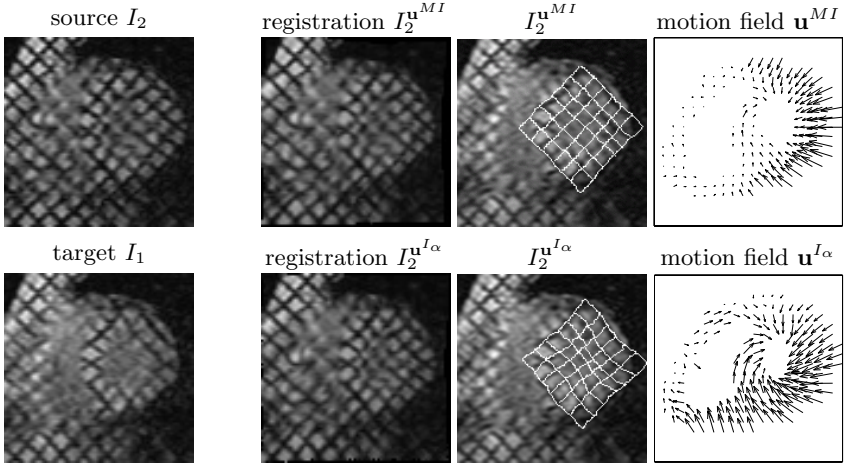


**Fig. 3.** NRR of tagged MR data using (*top row*) MI *vs.* (*bottom row*) $I_\alpha$-exclusive information ($\alpha = 1.5$). A grid warped by $\mathbf{u}^*$ has been overlaid to enhance tag deformation recovery

**Pathological Cases.** The method has been applied to a patient with dilated cardiomyopathies (DCM). Figures 4 and 5 show the evolution during a cardiac cycle of averaged contraction and torsion for this pathology, compared to healthy data mean values. One first notices that healthy curves corroborate the observations made on dense maps: one can clearly see the global homogeneity of radial contraction, whereas torsion is much more inhomogeneous. Notice the late contraction of septum (the curves are decreasing more slowly) and the wringing motion (decreasing at the apex, increasing elsewhere). The DCM case shows very little radial contraction, whereas torsion is enhanced and prolonged.

## 5 Conclusion and Perspectives

We have developed a non-supervised and robust method for quantifying myocardial deformations from tagged-MR data, which delivers accurate and consistent measurements that accounts for regional inhomogeneities of wall motion and velocity distribution. Future work includes: (i) extensive study of the dilated/hypertrophic cardiomyopathies, as well as sarcoidosis cases; (ii) incorporation of long-axis images to derive 3D motion estimates, (iii) joint study of contraction/perfusion and contraction/activation via multimodal registration, which the current technique is readily suited for.

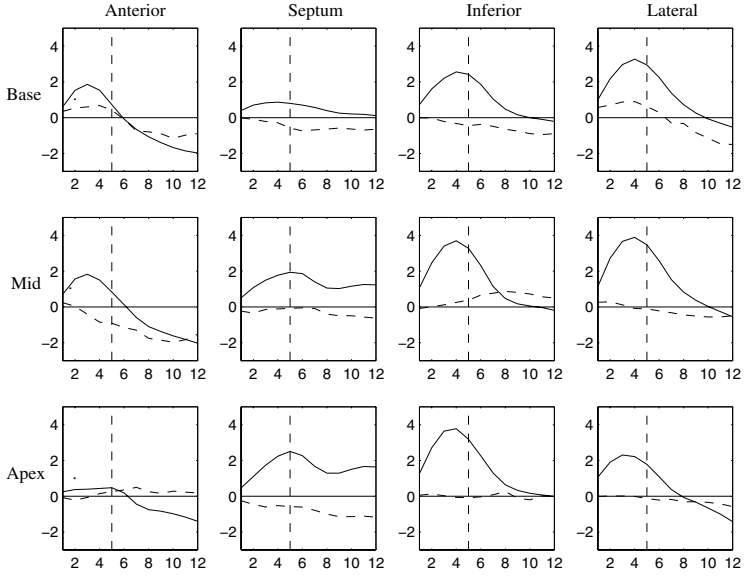


**Fig. 4.** Radial displacement (in mm) of LV segments during cardiac cycle for the mean of healthy data (plain line) and DCM (dashed line)

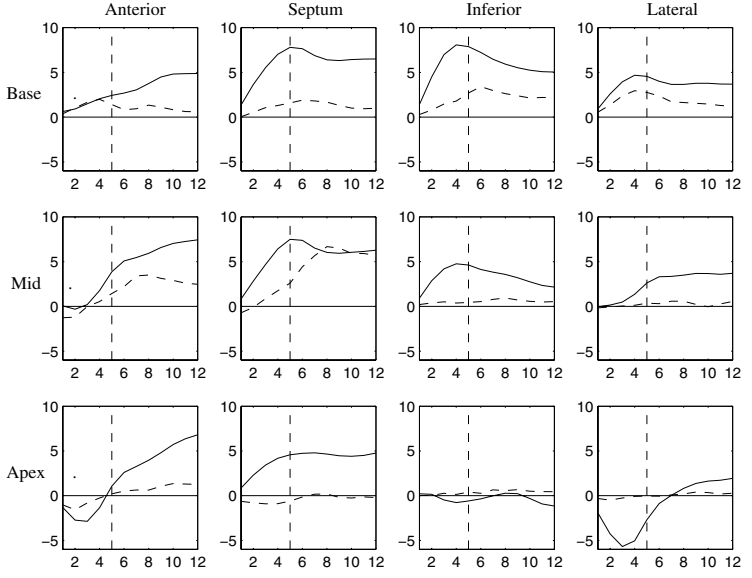


**Fig. 5.** Torsion (in degrees) of LV segments during cardiac cycle for the mean of healthy data (plain line) and DCM (dashed line)

## References


1. A.A. Amini, J.L. Prince, "Measurement of cardiac deformations from MRI: Physical and mathematical models", *Kluwer Academic Publishers, Dordrecht*, 2001.
2. L. Axel, L. Dougherty, "MR imaging of motion with spatial modulation of magnetization", *Radiology*, 1989, 171(3):841–845.
3. P. Clarysse, C. Basset, L. Khouas, P. Croisille, D. Friboulet *et al.*, "Two-dimensional spatial and temporal displacement and deformation field fitting from cardiac magnetic resonance imaging", *Medical Image Analysis*, 2000, 4:253–268.
4. J. Declerck, "Etude de la dynamique cardiaque par analyse d'images tridimensionnelle", *Ph.D. Dissertation Université de Nice-Sophia-Antipolis*, France, 1997.
5. S.N. Gupta, J.L. Prince, S. Androutsellis-Theotokis, "Bandpass Optical Flow for Tagged MRI", *Proceedings of IEEE ICIP*, San Diego, CA, 1997, 3:364–367.
6. M. Guttman, J.L. Prince, E.R. McVeigh, "Tag and contour detection in tagged MR images of the left ventricle", *IEEE TMI*, 1994, 13(1):74–88.
7. G. Hermosillo, "Variational methods for multimodal image matching", *Ph.D. Dissertation Université de Nice-Sophia-Antipolis*, France, 2002.
8. D. Kraitchman, A. Young, C.N. Chang, L. Axel, "Semi-Automatic Tracking of Myocardial Motion in MR Tagged Images", *IEEE TMI*, 1995, 14(3):422–433.
9. S. Kumar, D. Goldgof, "Automatic tracking of SPAMM grid and the estimation of deformation parameters from cardiac MR images", *IEEE TMI*, 1994, 13:122–132.
10. F. Maes, A. Collignon, D. Vandermeulen *et al.*, "Multimodality image registration by maximization of mutual information", *IEEE TMI*, 1997, 16(2):187:198.
11. C. Petitjean, N. Rougon, F. Prêteux, "Non rigid image registration using generalized information measures", *Research Report 02001 INT, France*, March 2002.
12. J.L. Prince, E.R. McVeigh, "Motion estimation from tagged MR images sequences", *IEEE TMI*, 1992, 11(2):238–249.
13. C. Petitjean, N. Rougon, F. Prêteux, Ph. Cluzel, Ph. Grenier "A non rigid registration approach for measuring myocardial contraction in tagged MRI using exclusive f-information", *To appear in Proceedings of ICISP'2003.*
14. C. Studholme, D.L. Hill, D. Hawkes, "An overlap invariant entropy measure of 3D medical image alignment", *Pattern Recognition*, 1999, 32(1):71–86.
15. I. Vajda, "Theory of statistical inference and information", *Kluwer Academic Publisher, Dordrecht*, 1989.
16. E. Zerhouni, D. Parish, W. Rogers *et al.*, "Human heart: Tagging with MR imaging-A method for non invasive assessment of myocardial motion", *Radiology*, 1988, 169(1):59–63.

# Parametric Analysis of Main Motion to Study the Regional Wall Motion of the Left Ventricle in Echocardiography

C. Ruiz Dominguez[1,2], F. Frouin[1], O. Gérard[2], P. Lim[1], B. Diebold[3], and A. Herment[1]

[1] U494 INSERM, CHU Pitié-Salpêtrière, Paris, France
ruiz@imed.jussieu.fr
[2] PRF, Philips Research France, Suresnes, France
[3] Service d'échocardiographie, HEGP, Paris, France

**Abstract.** Parameters which are related to the wall motion of the left ventricle are estimated from the time signal amplitude curves of the pixels of an echocardiographic image sequence. They yield parametric images, which are interpreted by clinicians. Factor analysis of the left ventricle in echocardiography is such a method. Its theoretical limits are first listed. To overcome them, a generalized method, the parametric analysis of main motion (PAMM), is proposed in this paper. The new parameters are computed as the projections of the time signal amplitude curves on a set of curves, which are generated by translation and scale transformations of a mother curve. This mother curve represents a generic motion curve. The PAMM method has been tested on a simulated sequence and applied to patients. Results demonstrate the theoretical interest of the method and show its potential contribution to clinical studies.

## 1 Introduction

Echocardiography is a commonly used exam to analyze the wall motion of the left ventricle at rest and under stress. It mainly contributes to the diagnosis of myocardial ischemia and infarction. Segmental wall motion scores which are derived from this exam have a high predictive value for the prognosis. At the present time, the analysis of the contraction is mainly visual.

Several means including acoustic techniques and image processing have been developed to make the evaluation of the wall contraction more automatic, but none of them is fully satisfactory. The "Color Kinesis" approach [1], which segments the RF signal into myocardium and cavity analyses only the endocardial motion. Other techniques based on Doppler Tissue Imaging (DTI) allow to measure the motion, according to the direction of the ultrasound beam [2].

Several post processing methods analyse 2D+t echographic image sequences, by making use of the temporal analysis of the left ventricle motion. This *a priori* information has been used for segmentation and contour follow-up techniques [3] [4], as well as denoising procedures [5]. Moreover the temporal dimension is

I. Magnin et al. (Eds.): FIMH 2003, LNCS 2674, pp. 173–183, 2003.

the basis of motion estimation and motion detection methods, which have been proposed for cardiac ultrasound [6] [7].

Some parametric imaging methods are directly based on the temporal evolution of signal amplitude inside each pixel. Among them, the Fourier first harmonic [8], widely used in radionuclide cardiac studies, provide some parametric phase images that can help the diagnosis of pathological motion. Similarly, a method based on factor analysis of the left ventricle has been proposed for echocardiography [9], which provides a less restrictive hypothesis on the shape of the gray level evolution (see Fig. 4) than Fourier analysis does. It provides a three color parametric image, which is easily interpreted by clinicians. First results are promising to detect abnormal motion pattern. But the discrimination between akinetic and hypokinetic regions remains to be improved.

In this paper, the formulation of this factor analysis approach is first recalled. The theoretical limits of the factor analysis, which are due to the restrictive model used to describe the motion, are then listed. A new approach, called Parametric Analysis of Main Motion (PAMM), is then proposed to overcome these limits. Some preliminary results using this new method are shown and discussed.

## 2 Material and Method

### 2.1 Material

An image sequence was simulated to mimic the left ventricle motion in echography. A binary image was generated from the contours of the endocardium and the epicardium, drawn from a end-diastolic image of a real echocardiographic image sequence. Simplified motion was simulated by morphological transforms (directional erosions) applied to this reference image. The sequence was corrupted by a typical ultrasound speckle pattern, positioning points scatters at random within the myocardial wall, and convolving with a separable point spread function. Twenty-three images were generated, which represent a whole cardiac cycle.

Echocardiographic image sequences were acquired in 2D harmonic gray scale, using a HDI 5000 device (Philips Ultrasound), corresponding to a normal subject (two-chamber view) and to a patient (four-chamber view) with complete left bundle branch block (LBBB). The views were acquired during several cardiac cycles. The best cycle, that is the one which presented the better superimposition of images between the beginning and the end of the cycle, corresponding to end diastolic images, was selected. This was done to limit the undesirable sources of motion, due to breathing or probe motion. A fixed mask was applied on the valve region of the sequences.

Those three sequences (the simulated and two echocardiographic data) will be used as illustration in the remainder of this paper.

### 2.2 Factor Analysis of the Left Ventricle in Echocardiography

Factor analysis of medical image sequences is a method which is commonly used to analyse an image sequence acquired to study the time variations of a contrast

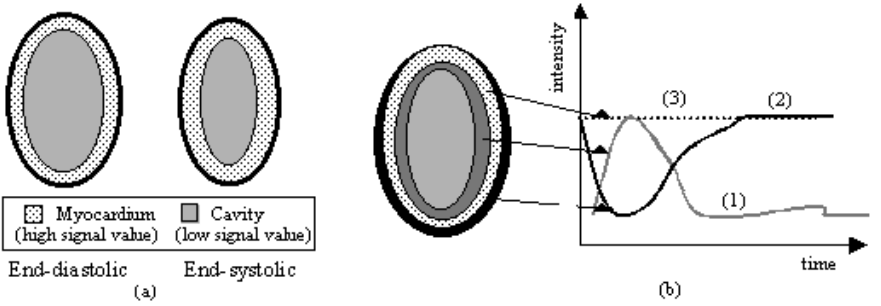


**Fig. 1.** Schematic representation of endocardial-epicardial motion. TSAC of a pixel initially in the cavity, near the endocardial wall: signal increases then decreases due of endocardial motion (1). TSAC of a pixel initially in the myocardium, near the epicardial wall decreases then decreases due of epicardial motion (2). Pixels inside myocardium and cavity present flat intensity variations (3)

agent [10]. It discriminates the different spatial structures (the factor images) according to their contrast kinetics curves (the factors). The main hypothesis of the method is that these structures do not move during the observation time. In that sense, its adjustment to the estimation of the wall motion is innovative.

The main hypothesis is thus the following: the major time variations of the signal amplitude in each pixel are due to the motion of the ventricle (see Fig. 1).

The underlying model states that the time signal amplitude curves (TSAC) of each pixel are a linear combination of two curves (factors) estimated from the TSAC [9]. The first factor estimates the DC component of the curves. It is associated to the pixels which show only small variations of the signal during the cardiac cycle (mainly the pixels which stay inside the myocardium or the left cavity during the whole cycle) (see Fig. 1). The second factor estimates the AC component: it increases during systole, then decreases during diastole. It represents the pixels which have a large variation of intensity (see Fig. 1).

The factor analysis method expresses the signal amplitude $p(x, y, t)$ of each pixel $(x, y)$ at time $t$:

$$p(x, y, t) = \sum_{i=1}^{2} f_i(t) I_i(x, y) + e(x, y, t) \quad x = 1, ..., M \quad y = 1, ..., N \qquad (1)$$

The time functions $f_i(t)$ are the factors, and the weighting coefficients $I_i(x, y)$ are the factor images, $M$ and $N$ are the row and column numbers of the images and $e(x, y, t)$ is the residual error.

The factors are estimated by a two-step procedure, using Pixies software (`http://www.apteryx.fr`). The first step is a global orthogonal analysis. The second one is an "oblique" analysis, that is an estimation under constraints in the subspace which has been generated by the two first principal components. Some *a priori* information is introduced in order to have a unique solution to

the oblique analysis. The first factor is the projection of the flat curve with "1" values. The second factor is called "contraction-relaxation" factor: it has zero for minimal value, one for maximal value and first increases then decreases [9].

Factor images are finally estimated from raw data and factors, such as to minimize the global least-squared error:

$$E_{FA} = \sum_{t=1}^{T} \sum_{x=1}^{M} \sum_{y=1}^{N} \left[ p(x,y,t) - \sum_{i=1}^{2} f_i(t) I_i(x,y) \right]^2 \tag{2}$$

In a matrix form, this is equivalent to:

$$I = PF^T(FF^T)^{-1} \tag{3}$$

$F$ being the $(2,T)$ matrix of factors, $I$ the $(M \times N, 2)$ matrix of factors images and $P$ the $(M \times N, T)$ matrix of raw data.

The first factor image has positive values, the second factor image has positive or negative values, with intensities related to the ones in the raw image sequence [9]. The three-color superposition of these images (green color scale for the first factor image $I_1$, red scale for the positive values and blue scale for the negative values of the second factor image $I_2$) is interpreted by the clinician.

### 2.3 Application and Limits of Factor Analysis of the Left Ventricle in Echocardiography

In a first clinical study, a four level score for wall motion (normal, hypokinetic, akinetic and dyskinetic) was attributed by three clinicians to each segment according to the distribution of the factor images inside the segment [9]. Results on 500 segments have shown that in 90% of them, the quotation is correct with one level of tolerance, but is exact in only 65%. This results could be improved.

Moreover, some inherent limitations of the factor analysis approach can be noticed in the underlying model. If large asynchronous motion found in dyskinetic segments can be easily shown in factor images (reversal of red and blue colours), minor asynchronous wall motion cannot be described adequately by a unique global motion factor.

To illustrate it, a regional factor analysis was performed. The 2-chamber view was cut into 7 regions, according to the model proposed by the ASE [11]. The segmentation was performed interactively, by asking the user to define 3 points (apex and valves) on an end-diastolic image.

Seven regional factor analyses were performed, yielding seven contraction-relaxation factors. Mean transit time (MTT) and second central moment (SCM) of these factors were computed for each segment $(s)$.

$$MTT(s) = \frac{\sum_{t=1}^{T} t f_2^s(t)}{\sum_{t=1}^{T} f_2^s(t)} \quad SCM(s) = \frac{\sum_{t=1}^{T} (t - MTT(s))^2 f_2^s(t)}{\sum_{t=1}^{T} f_2^s(t)} \tag{4}$$

The factor analysis of the left ventricle was applied to the real echocardiographic study on the global field of view and on the seven regions defined by

**Table 1.** MTT and square root of SCM obtained for the different contraction relaxation regional factors

| Segment (s) | MTT (ms) | $\sqrt{SCM}$ (ms) |
|---|---|---|
| Apex | 386.8 | 213.9 |
| Apical anterior (AA) | 374.4 | 220.0 |
| Mid anterior (MA) | 387.6 | 232.8 |
| Basal anterior (BA) | 490.4 | 247.0 |
| Apical inferior (AI) | 418.4 | 184.7 |
| Mid inferior (MI) | 443.3 | 182.4 |
| Basal inferior (BI) | 568.8 | 226.7 |
| Global | 428.1 | 204.7 |

the segmentation of the myocardium. The MTT and SCM of each contraction relaxation factor (Table 1) depend on the localisation of the region.

These results show that the local variation of duration in the contraction-relaxation curve cannot be described adequately by a unique global motion factor.

### 2.4 Parametric Analysis of Main Motion

To overcome the theoretical limitations of the factor analysis method and to better describe the time signal amplitude curves which are related to the wall motion, a generalized approach, called parametric analysis of main motion (PAMM) was proposed.

The basic idea is to better describe the motion, which is globally estimated by the "contraction-relaxation" factor in the factor analysis approach. This factor represents the "main motion", from which we derive a parametric analysis.

The same model structure is used (with the linear combination of two components). However, the second curve is modified by two parameters which are pixel location dependent. A set of possible curves is generated from a contraction-relaxation mother curve by allowing translation and scale transformations of this mother curve, according to the following equation:

$$p(x,y,t) = g_1(t)J_1(x,y) + g_2\left(\frac{t-\mu(x,y)}{\sigma(x,y)}\right)J_2(x,y) + e(x,y,t) \qquad (5)$$

The curve $g_1(t)$ corresponds to the flat curve previously introduced in the factor analysis model, and the curve $g_2(t)$ is the relaxation-contraction mother curve. The coefficients $\mu(x,y)$ and $\sigma(x,y)$ represent the adjustable translation and scale parameters applied to the mother curve, the coefficients $J_1(x,y)$ and $J_2(x,y)$ being linear amplitude coefficients. Using this formulation, $\mu(x,y)$ is related to MTT and $\sigma(x,y)$ to the square root of SCM.

The mother curve $g_2$ is assumed to represent a generic wall motion curve. Two approaches have been proposed to generate this curve. The first one is data driven, with the mother curve being the global "contraction-relaxation" factor,

as estimated by the factor analysis (with $g_1(t) = f_1(t)$ and $g_2(t) = f_2(t)$). The second one is model driven, since it considers that the mother curve $g_2$ is an analytically defined curve (with $\forall t \ g_1(t) = 1$). Bloc function model has been tested ($g_2(t) = 1$ for $t \in [\mu(x,y) - 0.5\sigma(x,y), \mu(x,y) + 0.5\sigma(x,y)]$, and $g_2(t) = 0$ elsewhere).

*Resolution of the PAMM Model*

Equation (5) is solved by a discrete approach, in order to transform the non linearity problem, which is introduced by the parameters $\sigma$ and $\mu$ into a finite set of linear equations. These parameters are supposed to belong to a finite subset of values $(\mu_j, \sigma_k)$:

$$\text{where } \mu_j = \{\mu_{min} + \tfrac{j}{J}(\mu_{max} - \mu_{min})\} \text{ with } j = 0, ..., J$$

$$\text{and } \sigma_k = \{\sigma_{min} + \tfrac{k}{K}(\sigma_{max} - \sigma_{min})\} \text{ with } k = 0, ..., K$$

The parameters values were established according to the temporal features of the cardiac cycle.

Practically, they were defined from two characteristic times, $t_1$ and $t_2$, defined as follows: $t_1(x,y) = \mu(x,y) - 0.5\sigma(x,y)$ and $t_2(x,y) = \mu(x,y) + 0.5\sigma(x,y)$. Both values have been determined according to the systolic and diastolic phases. The time $t_1$ roughly corresponds to the beginning of contraction in one pixel location, the second time $t_2$ roughly corresponds to the end of the contraction at the same location. These parameters were expressed as integer values, corresponding to a number of images in the raw image sequence, and the bounds were defined as follows: $t_{1min} = 1, t_{1max} = int(T * 0.3)$, $t_{2min} = int(T * 0.25), t_{2max} = T$, $T$ being the total number of echographic images of the cardiac cycle, and *int* the nearest integer function. These values were used to determine $\mu_{min}$, $\mu_{max}$, $\sigma_{min}$ and $\sigma_{max}$ in order to define the possible set of values for $\mu_j$ and $\sigma_k$, with a step equal to one time sample.

Each couple of admissible solutions $(\mu_j, \sigma_k)$ determines the function $g_2$ and (5) is reduced to a linear system. Thus, the coefficients $J_1^{j,k}(x,y)$ and $J_2^{j,k}(x,y)$ can be estimated similarly to the coefficients $I_1(x,y)$ and $I_2(x,y)$ of (3):

$$\forall(\mu_j, \sigma_k) \quad j = 0, ..., J \quad k = 0, ..., K$$

$$J^{j,k} = P(G^{j,k})^T (G^{j,k}(G^{j,k})^T)^{-1} \tag{6}$$

$$G^{j,k} = \begin{bmatrix} g_1(t) \\ g_2(\frac{t-\mu_j}{\sigma_k}) \end{bmatrix} \quad J^{j,k} = \begin{bmatrix} J_1^{j,k}(x,y) \\ J_2^{j,k}(x,y) \end{bmatrix} \tag{7}$$

For each pixel $(x,y)$, the optimal values $(\mu_j^*, \sigma_k^*)$ are computed as the values which minimize the least-squared error:

$$E_{PAMM} = \sum_{t=1}^{T} \sum_{x=1}^{M} \sum_{y=1}^{N} [p(x,y,t) - p_{j,k}(x,y,t)]^2$$

$$\text{with} \quad p_{j,k}(x,y,t) = g_1(t)J_1^{j,k}(x,y) + g_2(\frac{t-\mu_j}{\sigma_k})J_2^{j,k}(x,y) \tag{8}$$

From this estimation, four parametric images are computed, which correspond to amplitude coefficients $J_1(x,y)$ and $J_2(x,y)$, and to parameters $\mu(x,y)$ and $\sigma(x,y)$. Characteristic systolic times $t_1(x,y)$ and diastolic times $t_2(x,y)$ can be represented as an alternative to $\mu$ and $\sigma$. The two non-linear parametric images are only represented where these parameters are significant (this condition is expressed as a threshold value on $J_2(x,y)$ coefficient) and are filtered with a median 3x3 filter in order to be less noisy.

## 3 Results

The PAMM method was applied to the numerical simulation of a contraction relaxation motion, which was described in Sect. 2.1. The parametric images showing the systolic times $t_1$ (see Fig. 2(a)) and the diastolic times $t_2$ (see Fig. 2(b)) present some successive layer pattern. They well describe the variation of the systolic and diastolic times in colours, according to the distance of the pixel to the cavity.

The $t_1$ and $t_2$ parametric images obtained using the data driven and the model driven (bloc function) approaches in the normal subject (see Fig. 3) show the same successive layer pattern as the numerical simulation one. Figure 4 shows the time signal amplitude curve fit for two pixels being alternatively in the cavity and in the myocardium, using the factor analysis approach and the PAMM approach. The fit is clearly improved by both PAMM approaches. A different pattern is obtained for the patient with LBBB (see Fig. 5), for which the sytolic and diastolic images show some delay at the level of the interventricular septum. The visual analysis of the sequence confirms the presence of an early systolic paradoxal motion followed by a delayed inward end-systolic motion.

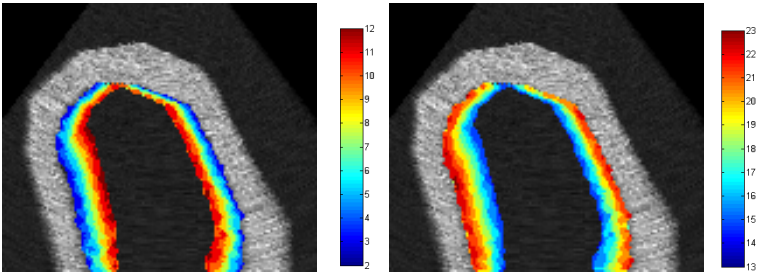


(a) (b)

**Fig. 2.** Parametric images of the systolic time $t_1$ (a) and the diastolic time $t_2$ (b) in case of the numerical simulation using the model driven approach (bloc function)

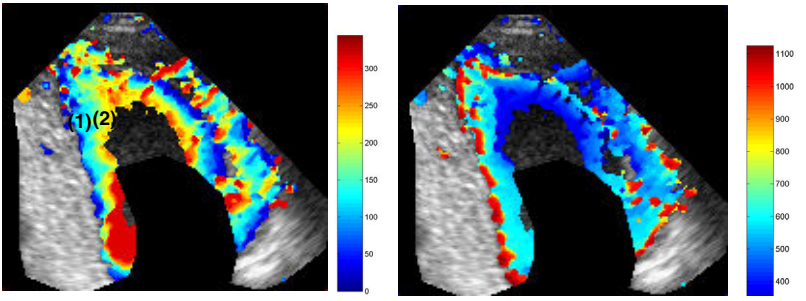


(a) (b)

**Fig. 3.** Example of parametric images of systolic time $t_1$ (a) and diastolic time $t_2$ (b) obtained for the real exam obtained using the model driven PAMM approach

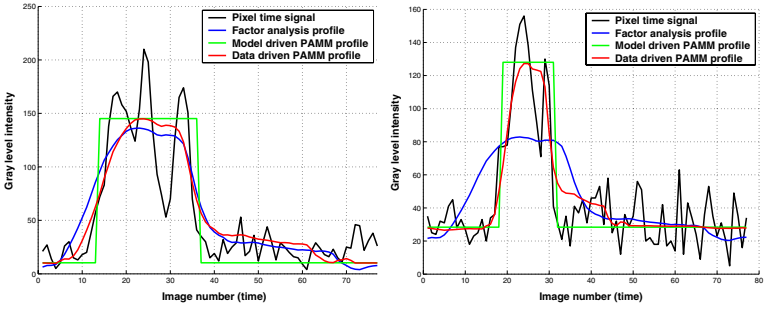


**Fig. 4.** Time signal amplitude curve and corresponding FA and PAMM approaches for two pixels being alternatively in the cavity and in the myocardium denoted (1) and (2) on Fig. 3

**Table 2.** Relative variation error of data driven and model driven PAMM compared to the factor analysis for the simulation and echocardiographic sequences

| Method | Simulation data | Echocardiographic data |
|---|---|---|
| PAMM Data driven | 4% | 31% |
| PAMM Model driven | 28% | 34% |

Finally, the relative variation error compared to the factor analysis (FA) approach (2) has been computed for the simulation and the real echocardiographic case (Table 2) as follows: $Er = (E_{FA} - E_{PAMM})/E_{FA}$. It clearly demonstrates that the PAMM method reduces more the fit error than the FA method.

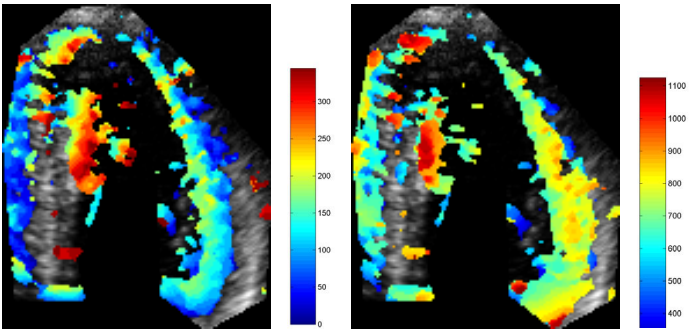


(a) (b)

**Fig. 5.** Example of parametric images of systolic time $t_1$ (a) and diastolic time $t_2$ (b) obtained for the real complete left bundle branch block exam obtained using the model driven PAMM approach

## 4 Discussion and Conclusion

The application of the factor analysis approach to different regions of the left ventricle has shown some asynchronous motion between the apex and the base. Moreover, the time signal amplitude curves have a variable duration, according to the inner or outer position of the considered pixel compared with the cavity (see Fig. 4).

These two phenomena have been taken into account by a new model (Parametric Analysis Main Motion), which proposes a generalization of the basic factor analysis model. Two additional parameters: systolic times and diastolic times, which respectively correspond to the increase and decrease times of the time signal amplitude curves, have been introduced. This yields to four parametric images: two amplitude images, one systolic time image, and one diastolic time image. Compared to the factor images, absolute amplitude values obtained with the PAMM methods vary (see Fig. 4), but their spatial and relative redistribution appear to be similar. The $t_1$ and $t_2$ parametric images are related to the spatio-temporal displacement of the myocardium. Filtering and thresholding of these images is necessary to represent only significant regions.

Compared to the Fourier approach, which computes the phase and the amplitude of the first harmonic of the time signal amplitude curve, the PAMM approach is more flexible. Indeed, the model of a sinusoidal curve, with a frequency equal to the cardiac frequency is not the best model to describe profiles (see Fig. 4). Compared to the factor analysis approach [9], the PAMM model enables us to reduce the global error by a factor of about 30%-35%.

Both model driven and data driven approaches give encouraging results. For the case that was considered in the paper, the global error is smaller with the model driven method, using a bloc function, than with the data driven approach.

However, it can be locally opposite. Some consistent statistical criteria could be defined in order to choose the best approach. One additional contraint is the computing time, which is much shorter with the model driven method, using a bloc function.

From a clinical point of view, the new concept of PAMM has to be tested on a large well-documented database. This database already exists [9] and the evaluation is currently under investigation. Beside the amplitude images, which are assumed to give information close to that contained in the two factor images, the informative part of the parametric time images remains to be investigated. Some successful results are expected in the detection of tardokinesia, which is difficult to visually apprehend and could be more easily readable on the parametric time images.

The method is sensitive to the global motion of the heart, as DTI or Color Kinesis approach. This is particulary true for patients with the left bundle branch block or pace maker. However, for PAMM method registration, a procedure can be undertaken as a first processing step, just after the image acquisition.

Finally, the method could be generalized without theoretical difficulties to real-time three dimensional echocardiographic data. However, a synthetic representation of parametric volumes would be then necessary, in order to facilitate the diagnosis. The next goal is also to derive some quantitative indices derived from the parametric images, obtained with the PAMM approach.

## References

1. Mor-Avi, V., Vignon P., Koch R., et al.: Segmental analysis of color kinesis images: new method for quantification of the magnitude and timing of endocardial motion during left ventricular systole and diastole. Circulation **95** (1997) 2082–2097.
2. Sutherland, G.R., Stewart M.J., Groundstroem K.W. et al.: Color Doppler myocardial imaging: a new technique for the assessment of myocardial function. J. Am. Soc. Echocardiogr. **7** (1994) 441–458.
3. Mulet-Parada, M., Noble, J.A.: 2D+T acoustic boundary detection in echocardiography. Medical Image Analysis **4** (2000) 21–30.
4. Jacob G., Noble J.A., Mulet-Parada M., Blake A.: Evaluating a robust contour tracker on echocardiographic sequences. Medical Image Analysis **1** (1999) 63–75.
5. Evans, A.N., Nixon, M.S.: Biased motion-adaptative temporal filtering for speckle reduction in echocardiography. IEEE Trans. Med. Imag **15**(1996) 39–50.
6. Ledesma-Carbayo, M.J.,Kybic J., Suhling M., et al.: Cardiac ultrasound motion detection by elastic registration exploiting temporal coherence. In: Proceedings of 2002 IEEE ISBI, (Washington D.C.) 585–588.
7. Yeung F., Levinson S.F., Fu D., Parker K.J.: Feature-adaptative motion tracking of ultrasound image sequences using a deformable mesh. IEEE Trans. Med. Imag. **17** (1998) 945–956.
8. Hansen A., Krueger C., Hardt S.E., Haass M., Kuecherer H.F.: Echocardiographic quantification of left ventricular asynergy in coronary artery disease with Fourier phase imaging. Int. J. Cardiovasc. Imaging. **17** (2001) 81–8.
9. Frouin F., Delouche A., Abergel E., Raffoul H., Diebold H., Diebold B.: Factor analysis of left ventricular contraction disorders at echocardiography. J. Radiol. **83** (2002) 1835–1841.

10. Janier M.F., Mazzadi A.N., Lionnet M. et al.: Factor analysis of medical image sequences improves evaluation of first-pass MR imaging acquisitions for myocardial perfusion. Acad Radiol. **9** (2002) 26–39.
11. Cerqueira M.D., Weissman N.J., Dilsizian V., et al.: Standardized myocardial segmentation and nomenclature for tomographic imaging of the heart. Int. J. Cardiovasc. Imaging. **18** (2002) 539–542.

# Modeling and Tracking of the Cardiac Left Ventricular Motion by a State Space Harmonic Model in MRI Sequence

Mohammed Oumsis[1,2], Quoc-Cuong Pham[2], Abdelaziz D. Sdigui[1], Bruno Neyran[2], and Isabelle E. Magnin[2]

[1] Laboratory of Computer Sciences, ENSIAS, Mohammed V University Souissi Rabat, Morocco
[2] CREATIS, INSA, Batiment Blaise Pascal, 69621 Villeurbanne Cedex, France
mohammed.oumsis@creatis.insa-lyon.fr

**Abstract.** We present a new method for modeling the left ventricular motion of the heart from a magnetic resonance imaging (MRI) sequence. We propose to model the 3D time-space trajectory of the points of the endocardial regions of the left ventricle (LV) using an harmonic model of movement, which is linear and describes the dynamics of the left ventricle throughout the cardiac cycle. This new state space model is based on the assumption of quasi-periodicity of the cardiac cycle. We describe our method to obtain the state canonical vector and the corresponding state equations of the harmonic state model (HSM). A Kalman filter is used on this harmonic state model as an estimation tool of the filtered trajectory of the LV. It allows to obtain a robust estimation of the state vector which contains the measured parameter and its derivatives. Thus, a robust estimation of the instantaneous velocity of the LV region is computed using the whole information of the sequence included in the harmonic model. The model is validated on real cardiac sequences. We detail how to get the 3D time-space trajectories of the LV edge points. The results obtained are particularly interesting because they demonstrate the capability of our method to understand and discriminate normal cases from pathological cases.

## 1 Introduction

Cardiac pathologies such as ischemia modify the kinetics of the heart motion [1]; necrosed regions do not beat anymore while contractility decreases in ischemic regions. Estimation and analysis of the 3D heart motion, through cardiac imaging, is a powerful tool for evaluating the functional consequences of the cardiac disease. Advanced motion estimation techniques provide 3D dense displacement fields of the heart and derived parameters of myocardial motion that allow to quantify the cardiac function. In this context an increasing number of studies are currently investigated to model, track and analyze cardiac motion from 3D sequences [2]. In most approaches, the processing is mainly divided into three stages [3]: 1) myocardial wall segmentation from 3D successive images of the sequence, 2) estimation of the motion parameters by direct measurements or adapted modeling, and 3) analysis of the extracted motion parameters to separate the healthy from pathological cardiac behaviour [4]. In

I. Magnin et al. (Eds.): FIMH 2003, LNCS 2674, pp. 184–193, 2003.

this work we focus on steps two and three. Our objective is to model and analyze the motion of the heart's left ventricle (LV). Several authors already proposed such models. We distinguish three classes. The first one based on an harmonics decomposition of motion. It is based on the assumption of a quasi-periodic heart rhythm that can be decomposed into a harmonics series [5,6]. Such harmonic models approximate the heart movement but does not present a dynamic form. The second class of models concerns linear dynamic models. They are characterized by a state vector and a transition matrix completely describing the LV system [7–9]. We find classical models of movement with constant velocity or constant acceleration [7,9], but they are unable to track and model the real cardiac motion because the velocity and acceleration are not constant in reality. Another approach makes the hypothesis of a sinusoidal movement [10]. Models of the first and second class are only temporal models (1D) that can be merged with a 2D or 3D spatial model to supply spatio-temporal behaviour [11,12]. They belong to the third class of movement models. In this class, the other approaches use laws of movement bound to the structure of the 3D model [2,4]. Only some studies suggest to take into account the temporal continuity and the possible periodicity of the movement [13,14].

In this work we present a new method for modeling and analyzing the left ventricular motion from 3D magnetic resonance imaging (MRI) data. Our technique is based on the development of a new dynamic model of movement, which is harmonic, linear and can describe the dynamics of the left ventricle throughout the cardiac cycle. This new model is based on the assumption of quasi-periodicity of the cardiac cycle and presents a state form that allows to use a Kalman filter as an estimation tool. It leads to a robust estimation of the state vector which contains the measured parameter and its derivatives. Thus, a robust estimation of the instantaneous velocity of the LV region is computed using the whole information of the sequence included in an harmonic model. This model combines three important characteristics: i) the possibility to select the physical attributes providing the best quantification of the cardiac function, ii) account the dynamics throughout the whole cardiac cycle and iii) a high robustness to noisy data.

The method is described in Sect. 2. Section 3 presents the application of the method on real data. A discussion and conclusions are drawn up in Sect. 4.

## 2 Theoretical Model

### 2.1 Modeling the Left Ventricular Motion

By observing the quasi-periodicity of the heart rhythm, we can make the hypothesis that the motion of the left ventricle is also quasi-periodic. Let *s(t)* be an attribute of the left ventricle extracted from a temporal 3D cardiac image sequence. The attribute can be for example the 3D coordinates of a point of the LV wall. This attribute possesses a value which periodically evolves and which evolution trajectory can be considered as a continuous signal. This signal can be decomposed in the Fourier domain into a sum of harmonics according to equation (1):

$$s_n(k) = s_n(t) = \bar{s} + A_1 \sin(\omega t + \varphi_1) + .... + A_n \sin(n\omega t + \varphi_n) \quad (1)$$

where *s(t)* is the trajectory of the attribute considered as a signal. $A_1 \ldots A_n$ are weighting coefficients, $\omega$ is the pulsation and $\varphi_1 \ldots \varphi_n$ the phases. We consider a linear state model according to the following equation (2)

$$S(k+1) = F \;\; S(k) + \zeta(k) \tag{2}$$

where *k* is the temporal variable, *S(k)* is the state vector that describes the *s(t)* attribute at time *k*, *F* is the transition matrix of the vector state *S(k)* from sample *k* (respectively time *t*) to sample *k+1* (respectively time $t+\Delta t$), and $\zeta(k)$ is a zero mean gaussian noise of covariance matrix *Q(k)* [7,9].

### 2.1.1 Choice of a State Vector for the Model

For the sample *k* corresponding to time *t*, the motion of the LV is described by equation (1). The sample *k+1* corresponds to time $t+\Delta t$. It comes

$$\begin{aligned} s_n(k+1) = s_n(t+\Delta t) = \bar{s} + A_1 \sin(\omega(t+\Delta t) + \varphi_1) \\ + \cdots + A_n \sin(n\omega(t+\Delta t) + \varphi_n) \end{aligned} \tag{3}$$

which can be expressed as :

$$\begin{aligned} s_n(t+\Delta t) = \bar{s} + A_1 \sin(\omega t + \varphi_1)\cos(\omega \Delta t) + A_1 \cos(\omega t + \varphi_1)\sin(\omega \Delta t) + \cdots \\ + A_n \sin(n\omega t + \varphi_n)\cos(n\omega \Delta t) + A_n \cos(n\omega t + \varphi_n)\sin(n\omega \Delta t) \end{aligned} \tag{4}$$

Our objective here is to find a state vector $S_n$ containing the element $s_n$ so as to be able to calculate $s_n(t+\Delta t)$ according to $s_n(t)$. We observe from equation (1) that $s_n(t)$ is a linear combination of the terms $A_i \sin(i\omega t + \varphi_i)$ and from equation (4) that $s_n(t+\Delta t)$ is also expressed as a linear combination of the terms $A_i \sin(i\omega t + \varphi_i)$ and $A_i \cos(i\omega t + \varphi_i)$.

Consequently, it is clear that $s_n(t)$ is continuous function, infinitely differentiable. Let us note $s_n^{(i)}(t)$ the derivatives $s_n(t)$ at the order *i* with respect to *t*, we can write the following system of equations:

$$\begin{cases} s_n(t) = \bar{s} + A_1 \sin(\omega t + \varphi_1) + \ldots + A_n \sin(n\omega t + \varphi_n) \\ s_n^{(2)}(t) = -\omega^2 A_1 \sin(\omega t + \varphi_1) - \ldots - (n\omega)^2 A_n \sin(n\omega t + \varphi_n) \\ \vdots \\ s_n^{(2(n-1))}(t) = (-1)^{n-1} \omega^{2(n-1)} A_1 \sin(\omega t + \varphi_1) + \ldots \\ \qquad + (-1)^{n-1} (n\omega)^{2(n-1)} A_n \sin(n\omega t + \varphi_n) \end{cases} \tag{5}$$

This linear system of *n* equations has *n* unknowns represented by the vector $V_n(t)$:

$$V_n(t) = (A_1 \sin(\omega t + \varphi_1), \cdots, A_n \sin(n\omega t + \varphi_n))^T \tag{6}$$

The resolution of this system allows to write every element of the vector $V_n(t)$ as a linear combination of the elements of the *n+1* dimensional vector

$(\bar{s}, s_n(t), s_n^{(2)}(t), s_n^{(4)}(t), \cdots, s_n^{(2(n-1))}(t))^T$. Let $\bar{r}_i$ and $r_{i,j}$ $(i = 1,\ldots,n\ ,\ j = 0,\ldots,n-1)$ be the coefficients of this combination:

$$A_i \sin(i\omega t + \varphi_i) = \bar{r}_i \bar{s} + \sum_{j=0}^{n-1} r_{i,j} s_n^{(2j)}(t) \tag{7}$$

By deriving equation (7), we obtain the expression of $A_i \cos(i\omega t + \varphi_i)$:

$$A_i \cos(i\omega t + \varphi_i) = \frac{\sum_{j=0}^{n-1} r_{i,j} s_n^{(2j+1)}(t)}{i\omega} \tag{8}$$

If we replace in (4) the elements $A_i \sin(i\omega t + \varphi_i)$ and $A_i \cos(i\omega t + \varphi_i)$ by their expressions obtained in (7) and (8), the result is an expression of $s_n(t+\Delta t)$ function of the $2n+1$ dimensional vector $S_n(t) = (\bar{s}, s_n(t), s_n^{(1)}(t), s_n^{(2)}(t), \cdots, s_n^{(2(n-1))}(t), s_n^{(2n-1)}(t))^T$. Let $\bar{a}_1$ and $a_{1,j}$ $(j = 0,\ldots,2n-1)$ be the coefficients of this linear relation, it can be written:

$$s_n(k+1) = s_n(t+\Delta t) = \bar{a}_1 \bar{s} + \sum_{j=0}^{2n-1} a_{1,j} s_n^{(j)}(t) = \bar{a}_1 \bar{s} + \sum_{j=0}^{2n-1} a_{1,j} s_n^{(j)}(k) \tag{9}$$

By successive derivation of equation (4) and repetition of the same process, we derive $s_n^{(i)}(t + \Delta t)$ $(i = 1,..,2n-1)$, as a function of vector $V_n(t)$ and thus as a function of vector $S_n(t)$. Therefore, we build a set of linear relations corresponding to the state model (2). Note that for an Harmonic State Model (HSM) of order $n$, the vector $S_n(t)$ of dimension $2n+1$ can be chosen as the state vector.

$$S_n(t) = (\bar{s}, s_n(t), \ldots, s_n^{(2n-1)}(t))^T \tag{10}$$

### 2.1.2 Computation of the Transition Matrix

Let the state equation of the HSM with order $n$ be:

$$S_n(t + \Delta t) = F_n \ S_n(k) + \zeta(k) \tag{11}$$

The transition matrix $F_n$ can be directly calculated by solving system (5). This system provides the expression of the vector $V_n(t)$, *as a* function of the vector $S_n(t)$. Therefore, by replacing in equation (4), and also in its derivatives, the elements of vector $V_n(t)$ by their expressions versus vector $S_n(t)$, we can directly compute the elements of the transition matrix $F_n$.

The transition matrix $F_n$ of the harmonics state model with order $n$, can also be recursively determined from the transition matrix of the harmonics state model of order $n-1$. In that case, calculations are simplified. We give here the final system allowing the transformation from the model at order $n$ to the model at order $n+1$:

$$
\begin{aligned}
s_{n+1}(t+\Delta t) = & \left[ \bar{a}_1 - \bar{r} \sum_{j=0}^{n-1} (-1)^j a_{1,2j} ((n+1)\omega)^{2j} + \bar{r} \cos((n+1)\omega\ \Delta t) \right] \bar{s} \\
& + \sum_{i=0}^{n-1} \left[ a_{1,2i} - r_i \sum_{j=0}^{n-1} (-1)^j a_{1,2j} ((n+1)\omega)^{2j} + r_i \cos((n+1)\omega\ \Delta t) \right] s_{n+1}^{(2i)} \\
& + \sum_{i=0}^{n-1} \left[ a_{1,2i+1} - r_i \sum_{j=0}^{n-1} (-1)^{j+1} a_{1,2j+1} ((n+1)\omega)^{2j+1} + r_i \frac{\sin((n+1)\omega\ \Delta t)}{(n+1)\omega} \right. \\
& + \left[ - r_n \sum_{j=0}^{n-1} (-1)^j a_{1,2j} ((n+1)\omega)^{2j} + r_n \cos((n+1)\omega\ \Delta t) \right] s_{n+1}^{(2n)}(t) \\
& + \left[ - r_n \sum_{j=0}^{n-1} (-1)^{j+1} a_{1,2j+1} ((n+1)\omega)^{2j+1} + r_n \frac{\sin((n+1)\omega\ \Delta t)}{(n+1)\omega} \right] s_{n+1}^{(2n+1)}
\end{aligned}
\tag{12}
$$

This expression gives the second line of the matrix $F_{n+1}$. The expressions $s_{n+1}^{(i)}(t+\Delta t)$ are calculated by derivation of equation (12) with respect to $\Delta t$. In conclusion we have determined the coefficients connecting the vector $s_{n+1}^{(i)}(t+\Delta t)$ to the vector $s_{n+1}^{(i)}(t)$. These coefficients constitute the elements of the transition matrix $F_{n+1}$.

The state model obtained this way is a canonical model which presents the advantage that its state vector is formed by the successive temporal derivatives (velocity, acceleration …) of the observed parameter. It differs from a model where the components of the state vector are composed only by the juxtaposition of the state model of the various harmonics.

### 2.2 Recursive and Optimal Estimation of the Model Parameters

The measurements obtained from the cardiac sequences are characterized by a low signal to noise ratio which makes the direct exploitation of these measures very difficult. To minimize the impact of noise, Kalman's filter is built from the harmonics state model (HSM) calculated in the previous paragraph. The filter estimates the state vector components [7,8,9,10]. The complete state model of the linear system is given by the state equation (2) and the measure equation which connects the state vector with the measurements. in our case only the variable *s(k)*:

$$
\begin{aligned}
S(k+1) &= F S(k) + \zeta(k) \\
s_z(k) &= H S(k) + \eta(k)
\end{aligned}
\tag{13}
$$

With $H = (0,1,0,....,0)$, $\zeta(k)$ is a zero main additive gaussian noise of covariance matrix $Q(k)$. $s_z(k)$ is the measurement vector which includes the observations at sample *k*. In our case, this vector has only one component: the measurement of the *s(k)* attribute. The optimal estimate $\tilde{s}(k)$ is generated by filtering data with respect to

time with a Kalman filter [7,9]. This dynamic filter converges to a periodic stable estimate even from an ambiguous initialization point. So, after convergence on a sufficient number of periods (at least 4), the information contained in the state vector, i.e. the successive derivatives of the estimated parameter, allows to describe the temporal evolution of this parameter (Fig. 1). Only the value of the studied parameter is measured, thus the matrix *R(k)* is reduced to a matrix *1*1* of a single element. This element represents the variance of the measured noise. This value is estimated during the detection of the outlines of the LV. The matrix *Q( k)* is chosen as diagonal matrix *(2n+1* 2n+1)*, witch elements represent the noise present in the system. They can be adjusted to provide various levels of temporal smoothing.

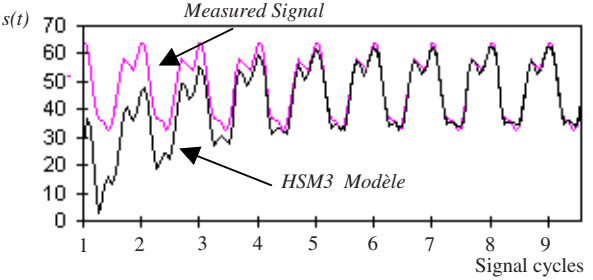


**Fig. 1.** Behaviour of the filter built from a HSM model of order 3, from the initialisation time, to convergence. We observe that the model converges after a learning phase. The selected attribute is the radius of the LV and its evolution throughout the cardiac cycle

## 3 Results

### 3.1 Image Acquisition

The cardiac MR images were acquired using breath-hold techniques at 10 slice levels and 10 instants of cardiac cycle. These acquisitions provide, cine-3D image sequence magnitude data within several minutes at a spatial resolution of 1.5 x 1.5 x 5mm$^3$. A 3D volume is calculated afterward by linear interpolation of the 10 acquired slices. The sequences concern healthy volunteers as well as pathological patients. Figure 2.a shows two successive instants of one of the studied sequences.

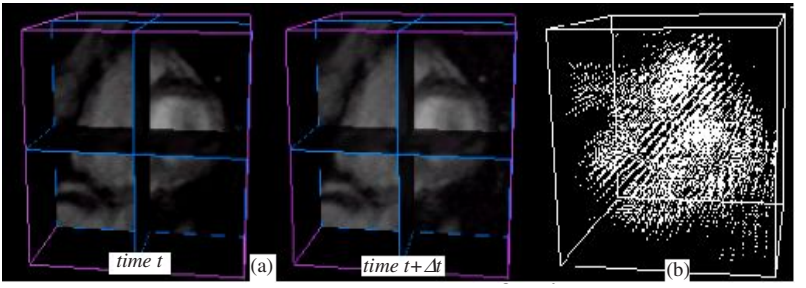


**Fig. 2.** (a): 3D MRI interpolated data volumes (2 successive instants). (b): 3D velocity field

### 3.2 Image Segmentation

In all images of the 3D sequence, the inner and outer walls of the LV have been previously delimited by B-spline contours. The control points of the B-splines are manually selected by two experts. The difference between measures experts allows to estimate a quadratic segmentation error for all points of contours, which will be considered in the model as the noise of measures.

### 3.3 Surface Reconstruction of the Myocardium

The surface of the LV is obtained from the segmented images. It is a very simple 3D geometrical model provided by a shape-based interpolation of the binarised data [15]. A more sophisticated model could be used, but it is not necessary here to assess the 3D motion model.

### 3.4 3D Motion Estimation

For every point of the interpolated data volume, and for every instant of the cardiac cycle, we estimate the velocity vector by a 3D optical flow method applied on two successive volumes [16,17]. Figure 2.b shows the velocity field of the LV for a normal heart data set.

### 3.5 Point to Point Tracking

The matching between a point $P_i$ of the LV wall at time $t$ and the same point at the time $t+\Delta t$ is obtained by the intersection of the line directed as the velocity vector of point $P_i$ at time $t$ and the LV surface extracted at time $t+\Delta t$. However, the repetition of this step for all the pairs of images of the sequence leads to an accumulation of errors in the trajectory of the considered point. The position of a point $P_i$ at time $t$ depends on its 3D coordinates at time $t-\Delta t$. the accuracy depends on the precision of the previous point and the current calculation. Thus, the confidence in the trajectory decreases according to the tracking. To limit this effect, the tracking is realized forwards and backwards: a direct following the real motion of the LV, and the inverse according to the inverse motion. At time $t$, linear weighting coefficients take into account in a linear way, the time distance from the initial point in the direct and the reverse direction.

$$P_{i,k} = \frac{((N-k)+1)p_{i,k}^{direct} + (k-1)\ p_{i,(N-k)+2}^{inverse}}{N} \text{; avec } k \in [1;N] \tag{14}$$

The points $P_{i,k}$ *(i=1,…,M and k=1,…,N)* include the trajectory of $M$ points of the inner or outer walls of the LV during all the cycle. Each trajectory describes the dynamics of a region of the LV and will be modeled with the aim of analyzing its movement and discriminate its behavior, normal or pathological.

### 3.6 Results

From the motion information estimated by the state harmonic model, we propose motion analysis of two sequences: a healthy case and a pathological case. The myocardium global shift with the chest throughout the cardiac cycle have a confounding influence on the quantification of the intrinsic cardiac motion. To minimize this problem, the distance between each control points of LV to the main axis of the LV is studied throughout the cardiac cycle. Parametric images of the velocity were created to visualize instantaneous endocardial motion. Figures 3 and 4 show the variation of the velocity parameter for each control point of the endocardium during the cardiac cycle respectively for a normal and a pathological heart.

**- *Normal Case:*** we observe that the motion begins in the apex and propagates regularly towards the base. We also see that the septal motion is weaker than in the other regions. It results from a weak mobility of this region because of its neighborhood with the right ventricle.

**- *Pathological Case:*** the gradual propagation of the motion from the apex to the base is no more observed, all the lateral regions contract almost at the same time. The diastolic phase is relatively long compared with the normal case. A global translation of the Apical region can be also observed but no local pathologies are present. The clinical diagnosis for this patient reports an Hypertrophic LV, that is a global dysfunctionary of the LV.

We demonstrated that it is possible, with our model, to enhance a significant difference in the behaviour of these two selected cases (a healthy case and a pathological case). We now plan to validate the model on a large MRI cardiac data base including normal and pathological cases.

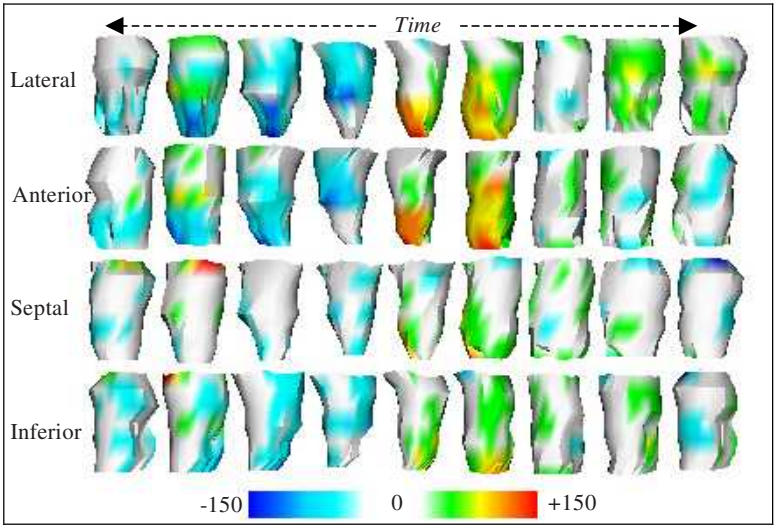


**Fig. 3.** Regional velocity of normal myocardium through cardiac cycle

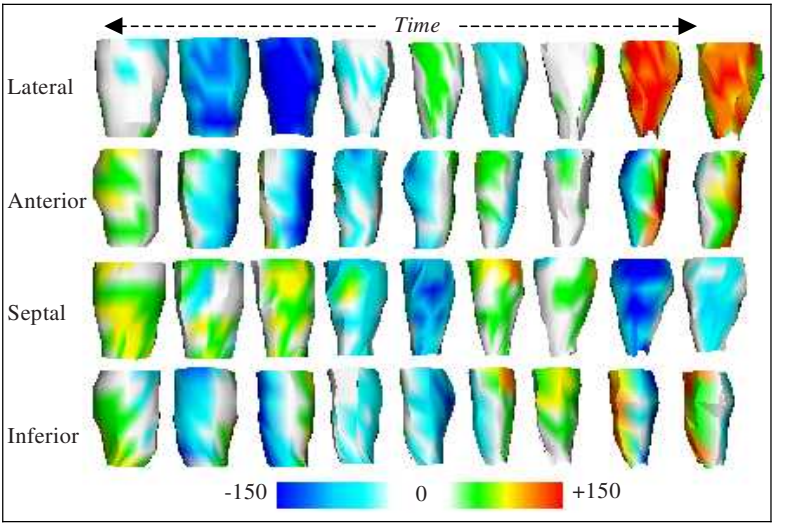


**Fig. 4.** Regional velocity of pathological myocardium through cardiac cycle

## 4 Discussion and Conclusion

In this work, we proposed a new temporal modeling of the left ventricle 3D deformation. It is a generic approach that can be used to estimate and model any pseudo-periodic evolution. The periodicity of the behaviour is the main hypothesis that leads to a harmonic model. Our contribution consists of the introduction of a state form of the harmonic model (HSM) of any order, with a state vector in the canonical form, i.e. composed of the successive derivatives of the observed parameter. This HSM allows to use a Kalman filter in order to obtain a robust estimation of the measured parameter and its derivatives. To ensure the Kalman filter convergence, the periodicity is also used to duplicate the measure of a single period of the cardiac cycle, which is then modeled. The choice of the cardiac sequences to be analyzed is done by the clinician. The elements of the HSM state vector present the major interest to have a physical meaning (position, velocity, acceleration...) directly interpretable for the analysis of the normal and pathological motion. The parameters extracted from the model allowed to discriminate the healthy regions from the pathological ones from cardiac MRI sequences. The results obtained on a normal and a pathological case confirmed the capabilities of our model to detect motion abnormalities. Such preliminary result demonstrate the feasibility and the interest of the method but a larger clinical validation is requested for further medical assessment. The proposed study exploited the temporal dimension of the model. We note that the periodicity of LV boundaries (closed curves) would allow a direct transposition of the model in the spatial dimension and so allow to introduce constraints on shape and smoothing. This double characteristic still enhances the potential interest of such a model, for the 4D tracking of the LV wall from spatio-temporal images sequence.

**Acknowledgments.** This work was supported by a FFI collaboration Morocco-French program. It is partly granted by the région Rhône Alpes. The authors would like to thank Pierre Croisille, radiologist, for acquisition and expertise of the MRI data.

## References

1. Tennant R., Wiggers C.J., The effect of coronary occlusion on myocardial contraction, *Am. J. Physiol.*,Vol. 112, pp,351–361, 1935.
2. Alejandro F. Frangi, Wiro J. Niessen, Max A. Viergever, Three-dimensional modeling for functional analysis of cardiac images: a review, IEEE Transactions on Medical Imaging, vol. 20, n° 1, pp. 2–25, Jan. 2001.
3. Magnin I.E., Analyse et modélisation 3D du comportement dynamique du cœur en imagerie multimodalité, Revue de l'ACOMEN, vol. 5, n° 2, pp. 191–196, 1999.
4. Clarysse P., Han M., Croisille P., Magnin I.E., Exploratory analysis of the spatio-temporal deformation of the myocardium during systole from tagged MRI, IEEE Transactions on Medical Imaging, vol. 49, n° 11, pp. 1328–1339, Nov. 2002.
5. Declerck J., Etude de la dynamique cardiaque par analyse d'images tridimensionnelles, Thèse de doctorat, Université de Nice Sophia-Antipolis, 1997, 253p.
6. Zhu Y.D., Drangova M., Pelc N.J., Fourier tracking of myocardial motion using Cine-PC velocity data, Magnetic Resonance in Medicine, 1996 35:471–480.
7. Radix J.C., Filtrage et lissage statistiques optimaux linéaires, Cepadues-Editiond 1984.
8. Kalman R.E., Bucy R.S., New results in linear filetring and prediction theory, transactions, ASME, J. Bas. Eng., 83(D), pp. 95–108, 1961.
9. Oumsis M., Sdigui A.D., Neyran B., Magnin I.E., Modélisation et suivi par modèle d'état harmonique du mouvement ventriculaire gauche du cœur en Imagerie par résonance Magnétique, Traitement du Signal, Vol. 17, n° 5/6, pp. 501–516, 2000.
10. Meyer F.G., Constable R.T., Sinusas A.J, Duncan J.S., Tracking Myocardial Deformation Using Phase Contrast MR Velocity Fields: A Stochastic Approach, IEEE Transactions on Medical Imaging, Vol. 15, n° 4, pp. 453–465, 1996.
11. Nastar C., Modèles physiques déformables et modes vibratoires pour l'analyse du mouvement non-rigide dans les images multidimensionnelles, Thèse de doctorat, Ecole Nationale des Ponts et des Chaussées, 181p, 1994.
12. Zhu D., Drangova M., Pelc N.J., Estimation of deformation gradient and strain from Cine-PC velocity data, IEEE Transactions on Medical Imaging, vol. 16, n° 6, pp. 840–851,1997.
13. McEachen J., Nehorai A., Duncan J., A recursive filter for temporal analysis of cardiac motion, IEEE workshop on Biomedical Image analysis, pp. 124–133, 1994.
14. Todd R. C., Rath K., A. Sinusas, J. Gore, Development and evaluation of tracking algorithms for cardiac wall motion analysis using phase velocity MR imaging, Magnetic Resonance in Medicine, vol. 32, pp. 33–42, 1994.
15. Grevera G. j., Udupa K. J., Shape-based interpolation of multidimensional grey-level images, IEEE Transactions on Medical Imaging, vol. 15, n° 6, pp. 881–891, 1996.
16. Song M., Leahy R. M., Computation of 3D velocity fields from 3D cine CT images of a human heart, IEEE Transactions on Medical Imaging., vol. 10, pp. 295–306, Sept. 1991.
17. Gorce J.-M., Friboulet D., Magnin I. E., Estimation of three-dimensional cardiac velocity fields: Assessment of a differential method and application to three-dimensional CT data, Medical Image Analysis, Vol. 1, n°3, pp. 245–261, 1997.

# A Strategy to Quantitatively Evaluate MRI/PET Cardiac Rigid Registration Methods Using a Monte Carlo Simulator

Nicoleta Pauna[1,5], Pierre Croisille[1], Nicolas Costes[2], Anthonin Reilhac[2,3], Timo Mäkelä[1,4], Onuc Cozar[5], Marc Janier[1,2], and Patrick Clarysse[1]

[1] CREATIS, INSA, Batiment Blaise Pascal, 69621 Villeurbanne Cedex, France
{Nicoleta.Pauna,Pierre.Croisille}@creatis.insa-lyon.fr
{Marc.Janier,Patrick.Clarysse}@creatis.insa-lyon.fr
[2] CERMEP, Neurological Hospital, 59 boulevard Pinel, F-69003 Lyon, France
Nicolas.Costes@cermep.fr
[3] McGill University/McConnel Brain Imaging Centre, Montreal Neurological Institute, WB - 315, 3801 University Street, Montreal, Quebec, H3A 2B4, Canada
[4] Laboratory of Biomedical Engeeniering, Helsinki University of Technology P.O.B. 2200, FIN-02015 HUT, Finland
[5] Department of Physics, Babes-Bolyai University, I. Kogalniceanu, 3400, Cluj-Napoca, Romania

**Abstract.** The goal of this work is to present a strategy to validate cardiac MRI/PET registration methods. The strategy relies on a MRI/PET image reference data set including a computer generated PET data set of the thorax and its structures. This data set was produced using a Monte Carlo simulator from segmented T1-weighted MRI thorax data. From the reference data set as a *gold standard*, test transformations are randomly generated and used to quantify registration accuracy. The validation approach has been applied to our own rigid registration method with three different similarity measures: Correlation Ratio, Correlation Coefficient and Mutual Information. In this study, we observed that the Correlation Ratio gave better results both for thorax and heart image registration.

## 1 Introduction

Cardiac viability studies rely on the concurrent analysis of complementary functional and anatomical information acquired in multimodality imaging. The cardiac anatomy and function can be analyzed from Magnetic Resonance Imaging (MRI) while myocardial metabolism can be evaluated from Positron Emission Tomography (PET). In order to assess the reliable integration of useful data obtained from separate modalities, accurate multi-modal image registration is required. Improving the registration accuracy is an important goal, but without a thorough validation no registration method can be accepted as a clinical tool. The accuracy of a registration technique depends on the specific application, the involved imaging modalities, and the anatomical regions under study. The

I. Magnin et al. (Eds.): FIMH 2003, LNCS 2674, pp. 194–204, 2003.

most commonly accepted strategy for validation is to compare the registration result against a gold standard, which is defined as a reference multimodal data set with known accuracy [3]. This is a non-trivial problem for the simple reason that a gold standard is generally lacking with in-vivo data. Evaluations of a registration method in terms of accuracy and precision (and other criteria) may be achieved at different levels [6], [8]: with synthetic data, with physical phantoms, with software phantoms, and with clinical data. The merit of software phantoms, which are obtained through computation emulating the clinical acquisitions, includes the availability of a *ground truth* and the fact that realistic image degrading factors can be controlled. Moreover, some simulators have obtained a very high degree of realism. In this paper we present a methodology for the evaluation of cardiac registration methods using a PET simulator in the special case of FDG studies. Note that the use of realistic simulated data has already been presented for the validation of brain registration methods [1]. We developed our proper affine registration method in order to better control the pertinence of our validation strategy. This also allows us to better control each component of the registration algorithm. The data, the evaluation strategy and the registration method are presented in Sect. 2. Results are presented in Sect. 3 and commented in Sect. 4. This latter section also discusses the perspectives of the validation strategy and the improvements we are currently conducting.

## 2 Material and Methods

Our validation approach relies on the building of a reference PET-MRI data set that will first be presented. Then, we describe the procedure to evaluate the accuracy of affine registration methods. This procedure is applied to our own implementation of a rigid registration method.

### 2.1 PET-MRI Reference Data Set

For validation purpose, the idea is to obtain a MRI data set and a PET data set that are in perfect correspondence from the start. To this aim, a 3D MR thorax acquisition has been performed on a healthy volunteer. The thorax and cardiac structures have been identified to construct a 3D anatomical model that constitutes the input of a PET image simulator.

**MR Thorax Data.** The MR images were generated at the Cardiological Hospital of Lyon on a 1.5T scanner (Magneton Vision, Siemens, Erlangen, Germany). A series of 15 T1 weighted contiguous transaxial images was acquired with a multislice singleshot TSE HASTE sequence (TR = 872 ms and TE = 120 ms) during a breathhold with phased-array body coil on a healthy volunteer (Fig. 1a). The pixel size and the slice thickness were 0.97 x 0.97 mm and 8 mm, respectively and the image data were reconstructed to a 512 x 512 matrix. Nine ECG-gated breathhold short axis (SA) slices covering the ventricles were also acquired using a cine fast low-angle shot two-dimensional sequence (TR = 650 ms and

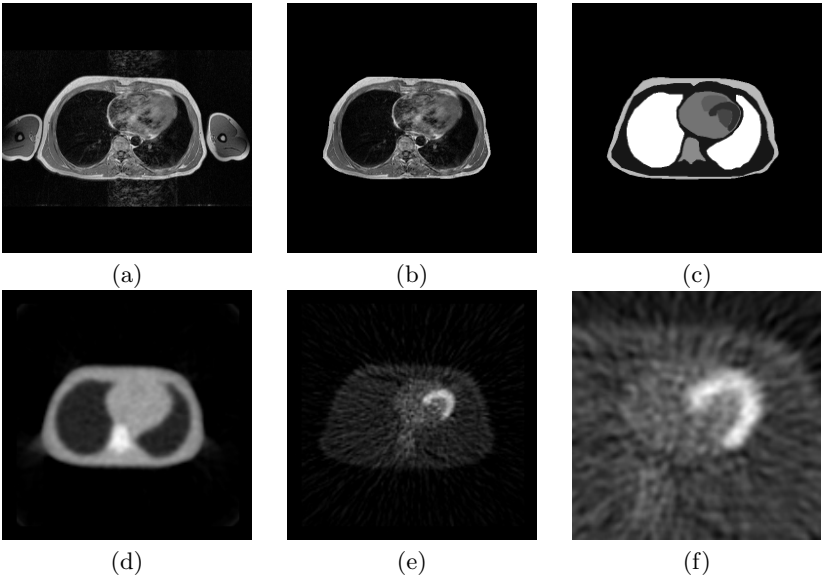

**Fig. 1.** (a) transaxial MR image with arms, (b) transaxial MR image without arms, (c) segmented MR image. Simulated PET (d) thorax transmission, (e) thorax emission and (f) heart emission images

TE = 4.8ms). The pixel size for SA slices was 1.093 x 1.093 mm and the slice thickness was 8 mm.

**3D Anatomical and Metabolic Model.** Arms were masked out from the thorax transaxial MR image (Fig. 1b) because in cardiac PET image acquisition, patient held hands above head to avoid extra attenuation in the heart area. Transaxial MR image was segmented into nine tissue classes (muscle, lungs, liver, fat, spine (bone), left ventricle (LV), the cavity of the LV, right ventricle (RV), the cavity of the RV) and background (Fig. 1c). A special radioactivity (Bq/cc) is attributed to each class. We also defined the attenuation media: air, fat, muscle, lung, bone and water.

**PET Simulated Data.** Both PET emission and transmission images were simulated from the 3D anatomical and metabolic model using the SORTEO (Simulation Of Realistic transmission and Emission Object) software [10,11]. SORTEO is a Monte Carlo simulator which uses a realistic phantom with labeled tissue classes to simulate spatial distribution of the tracer and attenuation properties of the tissue classes. The simulator includes technical characteristics such as typical PET voxel sampling, a 3D spatially-varying resolution function modeled from the PET scanner and realistic noise. PET emission image simulation was performed using [$^{18}$F]FDG as a radioactive tracer and PET transmission image simulation

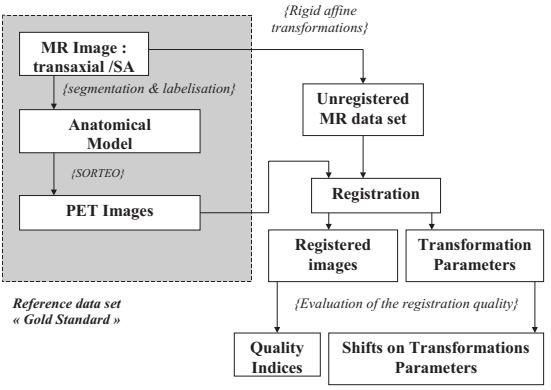


**Fig. 2.** Evaluation Strategy of MR-PET image registration methods

was done using $^{68}$Ge as an external radioactive source. Fluorodeoxyglucose PET imaging is considered as a gold standard to determine viable areas of the heart [2] and it provides images with a reasonably good resolution. In the tomographic reconstruction of the simulated images, Filtered Back Projection algorithm with Hanning filter (kernel=6 mm) was used. Thorax simulated PET transmission and emission images have a pixel size and slice thickness of 3.52 x 3.52 mm and 2.43 mm, respectively (Fig. 1d and 1e). Heart simulated PET emission image has a pixel size and a slice thickness of 1.76*1.76 and 2.43 mm, respectively (Fig. 1f). PET transmission and emission images were reconstructed to a 128 x 128 x 63 matrix.

### 2.2 Evaluation Strategy

Our evaluation strategy is based on the evaluation of the ability of a registration algorithm to recover a series of transformations randomly generated from the reference data set presented in the previous subsection. The principle is illustrated in Fig. 2.

The accuracy of registration can be evaluated qualitatively by visual inspection, by looking at the appearance of the joint histograms, and comparing similarity measures before and after registration although this interpretation may be delicate. The accuracy can be more interestingly analyzed quantitatively. Since the rigid transformation is known *a priori* it can be used as a *gold standard* to test the output of the registration algorithm.

**Average RMS Error:**

- **RMS Error for a Given Test Transformation:** The difference between two rigid transformations can be measured in order to assess the accuracy and robustness of registration methods. This measurement should not be

biased by selection of certain key points (such as the corners of a cube). One such measure is the RMS deviation measure described in [4] and [5]. It provides an average error over the expected heart volume (taken to be a sphere of radius $R$).
The transformations are quantitatively compared using the $d_{RMS}$ deviation between the composite transformation $T \cdot A$ and the identity $I$, where $A$ represents the geometrical transformation to be recovered applied to one image and $T$ is the registration transformation.

$$d_{RMS} = \sqrt{\frac{1}{5}R^2 Trace(M^T M) + t^T t}, \tag{1}$$

where $\begin{pmatrix} M & t \\ 0 & 0 \end{pmatrix} = T \cdot A - I$, $M$ is the $3 \times 3$ rotation and scaling matrix and $t$ is the $3 \times 1$ translation vector.

- **Global RMS Error:** For a set of $n$ test transformations, the performance of a method is evaluated through the computation of the mean and standard deviation of $d_{RMS}$. It can also be represented using box and whiskers plots.

**Intrinsic Errors:**

- For rigid transformations, the 3 rotations and 3 translations are derived and compared to the true values. For the set of $n$ test transformations, the $n$ corresponding errors for each transformation parameters are represented using boxplot and whiskers. It is accepted that evaluation of translations and rotations is not straightforward as these two transformations interact [7].

### 2.3 Registration Method

We implemented our own rigid registration method. Formally, the registration problem consists in finding the transformation $T$ that best aligns a reference image $I^r$ to another "floating" image $I^f$. The optimal transformation $T^*$ minimizes a certain cost function $C$:

$$T^* = \underset{T \in S_T}{argmin} C(I^r, I^f oT), \tag{2}$$

where $S_T$ is the transformations search space. Therefore, the main components of a registration method are the transformation $T$, the cost function $C$ which is based on some similarity measure, and the minimization method. The transformation we are searching for is rigid. In the context of multimodal registration, we investigated 3 intensity-based similarity measures: the correlation ratio (CR), the correlation coefficient (CC) and the mutual information (MI). The measures are maximal when the images are correctly aligned. More details about their definitions and behaviors can be found in [12]. The optimization of the cost functions was achieved using the Powell's multidimensional direction set method [9]. B-spline interpolation of degree 0 was performed using the algorithm of the affine transformation function developed by P. Thevenaz (http://bigwww.epfl.ch/).

## 3 Results

The evaluation strategy is demonstrated for the rigid registration of both thorax and heart images using the registration algorithm. A set of 100 theoretical transformations were generated by randomly sampling a 6 parameter transformation vector (3 translations and 3 rotations) using two Gaussian distributions (one for translations and one for rotations). The experts estimated that for the thorax imaging examinations in PET and MRI the rotation of the patient around the $Z$-axis is not more than 5 degrees, and rotations around $X$ and $Y$-axis are less than 3 degrees. The standard deviation for all the rotations was set to 2°. The maximum translation for thorax images was set to $\pm$ 4 cm = 26 voxels (standard deviation of 8 voxels) and it was set to $\pm$ 3 cm = 15 voxels (standard deviation of 5 voxels) for SA images.

**Thorax Image Registration.** We evaluated the registration of the thorax MR transaxial images with the PET transmission images using the MI, CC and CR as similarity measures and the nearest neighbour interpolation. We applied transformations on the PET transmission volume. Visually, we observed that the registered images are in good agreement (Fig. 3).

Intrinsic errors in translations (voxels) and rotations (degrees) are represented in Fig. 5a–c using boxplots. The lower and upper limits of the box corresponds to the first and third quartile, respectively. The line inside the box represents the median value. Outliers marked with stars are data with values beyond the whiskers. The mean and standard deviation of the global RMS error calculated for all the transformations and for the three similarity measures are given in Fig. 4a. We also represented using boxplot and whiskers the $d_{RMS}$ for the three similarity measures.

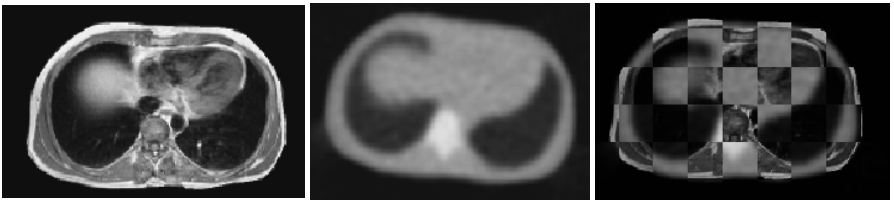

(a) (b) (c)

**Fig. 3.** Registration of transaxial MR-PET thorax volumes (a) transaxial MR image (b) transformed thorax PET transmission image with rotation around the Z-axis (5 degrees) and a translation along the X-axis (8 mm) (c) registered PET transmission image. The recovered parameters after the registration were -7.86 mm for the translation and 4.75 degrees for the rotation. The correlation ratio before and after registration was 0.4 and 0.8, respectively

.

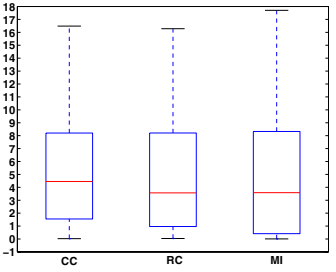


| *Similarity Measures* | *RMS(mm)* |
|---|---|
| Correlation Coefficient | 5,31±4,3 |
| Correlation Ration | 4,9±4,41 |
| Mutual Information | 4,69±4,68 |

(a)

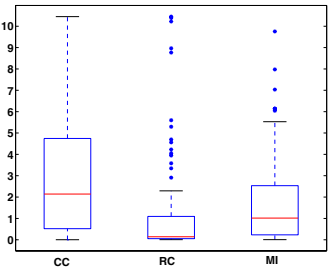


| *Similarity Measures* | *RMS(mm)* |
|---|---|
| Correlation Coefficient | 2,84±2,79 |
| Correlation Ration | 1,2±2,35 |
| Mutual Information | 1,78±2,04 |

(b)

**Fig. 4.** $d_{RMS}$ and global RMS error for the three similarity measures (a) for the thorax images (b) for the heart images

**Heart Image Registration.** The direct registration of the heart PET (simulated) and MRI short axis images did not lead to satisfactory results as the algorithm was not able to converge. We then used the orientation information available in the SA MR header information to pre-align the images.

Moreover, due to the very different content of both images, we selected a volume of interest (VOI) that includes the LV both in the MR and PET images. The VOI is included into a larger volume in order to avoid the border cutting effect when applying geometrical transformations (Fig. 6).

The accuracy test was applied to 100 image pairs. In each case, the target image was the MR data and the source image was the transformed PET image both having isotropic voxel dimension (1.093 mm). The starting position for the optimization process was zero on all axis.

There is an obvious improvement of the similarity measure values after the registration compared with its value before registration. So, the selection of the VOI affects the similarity measure convergence: anatomical features that do not appear in both images can contribute to the registration solution, leading to inaccurate registration. The errors with respect to the transformations parameters and the RMS are represented in Fig. 5d–f and Fig. 4b, respectively.

## 4 Discussion and Conclusion

We developed an evaluation strategy that exploits the output information of a registration method considered as a black box. This goal was achieved using a PET simulator which gives access to a *gold standard*. We also developed a rigid registration method for better testing the evaluation approach. Quantita-

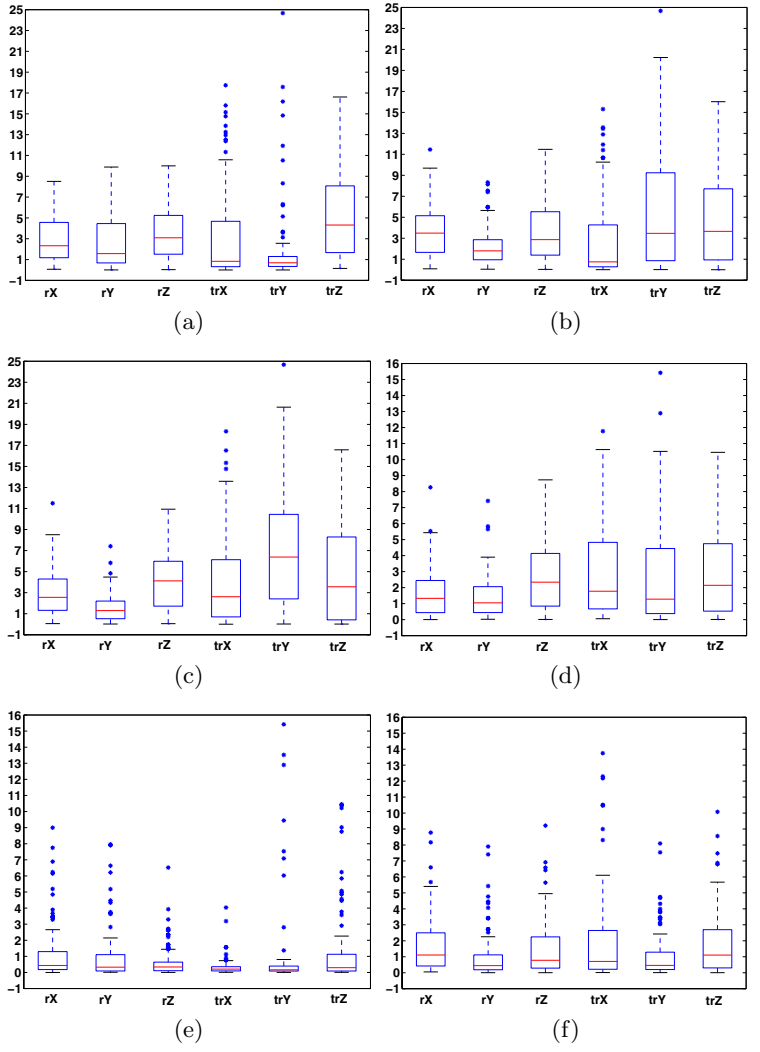


**Fig. 5.** Registration errors for thorax image registration using (a) CC (b) RC and (c) MI and for heart image registration using (d) CC (e) RC and (f) MI. Translation errors are in voxels, rotation errors are in degrees

tive results for the registration method were ascertained using an accuracy test by comparing registrations obtained using various, but known, initial starting positions of a given image.

Our evaluation approach was applied on two types of data: transaxial thorax and SA cardiac images. To examine various aspects of the registration results, we used the global RMS measure and boxplot and whiskers representations.

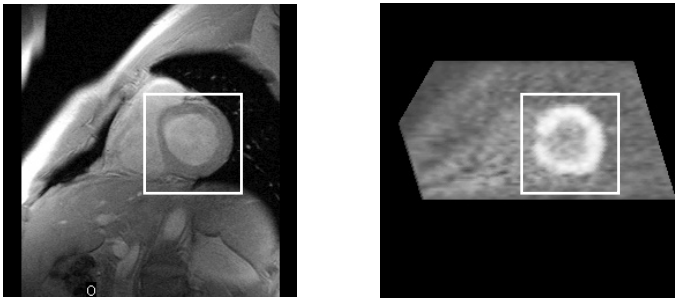

(a) (b)

**Fig. 6.** (a) SA MR heart slice, (b) corresponding simulated PET slice with the VOI contours.

For the thorax based registration, as shown in Fig. 4a, the global RMS error for CC is $5.31 \pm 4.3$ mm while for RC and MI the errors are very closed $4.9 \pm 4.41$ mm and $4.69 \pm 4.68$ mm, respectively. We can observe this in the representation of Fig. 4a. One can see from Fig. 5a–c that the median errors of translations in $X, Y, Z$ directions are 3.66, 4.31 and 6.38 voxels with RC, CC and MI similarity measures, respectively. The dispersion of errors in translation is lowest for CC and highest for MI. Regarding the estimation of rotations, the median errors of $X, Y, Z$ rotations are 3.09, 3.49 and 4.12 degrees for CC, RC and MI, respectively. The dispersion of errors in rotations is higher for RC and MI in the $Z$ direction. We conclude that RC gave the best results in this study.

For the heart based registration, the global RMS error is lowest for the RC measure and highest for the CC measure, $1.2 \pm 2.35$ mm and $2.84 \pm 2.79$ mm, respectively. This is confirmed by boxplot and whiskers representation in Fig. 4b. The algorithm better retrieves the *ground truth* transformation for the RC and MI measures (yielding median errors of 0.43 degree, 0.5 voxel and 1 degree, 1 voxel, respectively) and it converges to a local maximum (yielding median errors of 2.5 voxels and 2.5 degrees) for the CC measure. RC similarity measure proved to be the most performant measure in this case.

The boxplot and whiskers representation helps us to choose the best similarity measure adapted for registering cardiac data set. For a deeper evaluation of a registration method, the accuracy with which the parameters of the rigid transformation is recovered depends on the symmetry of the object to register. Boxplots in Fig. 5 compare the accuracy for each transformation parameter. Such representations better illustrate the dispersion of the results. The results for the thorax registration are similar for all the registration measures. Accuracy differences are more obvious for the heart registration case (Fig. 5d–f) but it still not allows to highlight clear differences parameters by parameters. Changing only one parameter at a time when holding the remaining parameters constant, can reveal some information about the influence of this parameter on the overall error. This is what we plan to do in the near future. These tests also showed that

the similarity measures based on different grey value relationships influence the convergence of the registration in a different way. In the case of heart registration, we observed that much better results are obtained if a VOI is preliminary selected. The interpolation method has also a great impact on the registration results as the PET and MRI resolutions are different In this study, the simple nearest neighbour interpolation was used. Such an evaluation strategy will allow us to thoroughly quantify the effect of different interpolation schemes. It will also be used to compare different registration methods and could also be applied to other modalities. The accuracy evaluation is one aspect of the validation problem which implies other criteria as well [6]. Aspects such as robustness and precision remain important areas for further work. Motion due to the breathing and the different acqusition times between PET and MRI imaging were not taken into account in this study. This is surely a limitation of the current approach that we would like to address in future work.

## References


1. C. Grova, A. Biraben, J.-M. Scarabin, P. Jannin, I. Buvat, H. Benali, and B. Gibaud. A methodology to validate MRI/SPECT registration methods using realistic simulated SPECT data. In W.J. Niessen and M.A. Viergever, editors, *Lecture Notes in Computer Science 2208: MICCAI01*, pages 275–282, 2001.
2. J. Hartiala and J. Knuuti. Imaging of heart by MRI and PET. *Ann. Med.*, 27:35–45, 1995.
3. D.L.G. Hill and D.J. Hawkes. *Handbook of Medical Imaging: Processing and Analysis*, chapter Across-modality registration using intensity-based cost functions, pages 537–553. Academic Press, 2000.
4. M. Jenkinson. Measuring transformation error by RMS deviation. Technical Report 3741, 1999.
5. M. Jenkinson and S. Smith. A global optimisation method for robust affine registration of brain images. *Medical Image Analysis*, 5:143–156, 2001.
6. J. B. A. Maintz and M. A. Viergever. A survey of medical image registration. *Medical Image Analysis*, 2(1):1–36, 1998.
7. C. Nikou, F. Heitz, and J.P. Armspach. Robust voxel similarity metrics for the registration of dissimilar single and multi-modal images. *Pattern Recognition*, 32:1351–1368, 1999.
8. S. Pallotta, M. C. Gilardi, V. Bettinardi, G. Rizzo, C. Landoni, G. Striano, R. Masi, and F. Fazio. Application of a surface matching image registration technique to the correlation of cardiac studies in positron emission tomography by transmission images. *Physics in Medicine and Biology*, 40:1695–1708, 1995.
9. W. H. Press, S. A. Teukolsky, W. T. Vetterling, and B. P. Flannery. *Numerical Recipes in C: The art of scientific computing 2nd Edition*. Cambridge Univ. Press, Cambridge, 1992.
10. A. Reilhac, M. C. Gregoire, N. Costes, F. Lavenne, C. Pierre, A. Diou, and J.-F. Pujol. A PET Monte Carlo simulator from numerical phantom: Validation against the EXACT ECAT HR+ scanner. *In Proc. IEEE Nuclear Sciences Symposium, Seattle, Washington, USA*, 3:1527–1531, 1999.

11. A. Reilhac, C. Lartizien, N. Costes, S. Sans, C. Comtat, and A. Evans. Accounting for singles rates related phenomena in PET Monte Carlo based simulations. *In Proc. IEEE Nuclear Sciences Symposium and Medical Imaging Conference, Norfolk*, 2002, accepted.
12. A. Roche, G. Malandain, X. Pennec, and N. Ayache. Multimodal image registration by maximizaton of the correlation ratio. Research Report 3378, INRIA, 1998.

# Spatio-temporal Alignment of 4D Cardiac MR Images

Dimitrios Perperidis[1], Anil Rao[1], Maria Lorenzo-Valdés[1], Raad Mohiaddin[2], and Daniel Rueckert[1]

[1] Visual Information Processing Group
Department of Computing
Imperial College of Science, Technology and Medicine
180 Queen's Gate, London SW7 2BZ, United Kingdom
[2] Royal Brompton and Harefield NHS Trust
Sydney Street, London, United Kingdom

**Abstract.** A 4D registration method for the spatio-temporal alignment of cardiac MR image sequences has been developed. The registration algorithm has the ability not only to correct any spatial misalignment between the image sequences but also any temporal misalignment which maybe the result of differences in the cardiac cycle between subjects and differences in the temporal acquisition parameters. The algorithm uses a 4D transformation model which is separated into a spatial and a temporal component: the spatial component is a 3D affine transformation which corrects for any misalignment between the two image sequences. The temporal component uses an affine transformation which corrects the temporal misalignment caused by differences in the initial acquisition offset and length of the two cardiac cycles. The method was applied to seven cardiac MR image sequences from healthy volunteers. The registration was qualitatively evaluated by visual inspection and quantitatively by measuring the volume difference and overlap of anatomical regions between the sequences. The results indicated a significant improvement in the spatio-temporal alignment of the sequences.

## 1 Introduction

Cardiovascular diseases are the leading cause of death in the UK [1]. Their early diagnosis and treatment is crucial in order to reduce mortality and to improve patients' quality of life. Recent advances in the development of non-invasive imaging modalities are enabling the high resolution imaging of the cardiovascular system. Among these modalities, magnetic imaging (MR) is playing an increasingly important role. MR imaging allows not only the acquisition of 3D images which describe the cardiac anatomy but also the acquisition of 4D cardiac image sequences which describe the cardiac anatomy as well as function.

These recent advances in the development of cardiac imaging modalities have led to an increased need for cardiac image registration methods (see the paper by Mäkelä et al. [2] for recent review of cardiac image registration methods or [3,4,5] for a general review of image registration). In general, cardiac image registration is a very complex problem due to the complicated non-rigid motion of the heart and the thorax as well as the low resolution in which the cardiac images are usually acquired. In recent years cardiac image registration has emerged as an important tool for cardiac or respiratory

I. Magnin et al. (Eds.): FIMH 2003, LNCS 2674, pp. 205–214, 2003.

motion correction [6,7] and cardiac motion estimation [8]. Cardiac image registration also plays an important role for the fusion of information from a number of different image modalities such as CT, MR, PET and SPECT [9,10]. In addition, cardiac image registration is crucial for the comparison of images of the same image modality, e.g. before pharmacological treatment or surgical intervention and after the treatment. Other applications include the inter-subject registration of cardiac image sequences to the same coordinate space (anatomical reference) in order to enable a direct comparison between the cardiac anatomy and function of different subject [11,12]. Such inter-subject registration is the essential for the development of an anatomical and functional atlas of the cardiovascular system similar to atlases that have already been developed for the human brain [13].

In this paper we develop a novel 4D cardiac MR image registration method using voxel-based similarity measures. This method will not only bring a number of sequences of cardiac images acquired from different subjects or from the same subject (for example short and long axis cardiac image sequences) into the same spatial coordinate frame but also into the same temporal coordinate system. The key difference of this registration algorithm is its ability not only to correct any spatial misalignment between the image sequences but also any temporal misalignment due to differences in the cardiac cycles of the subjects and differences in the temporal acquisition parameters. This does not only allows direct comparison between the cardiac anatomy of different subjects to be made but will also allow comparisons between the cardiac function to be made. The remainder of the paper is organised as follows: Sect. 2 provides a brief review of related work while Sect. 3 describes the proposed 4D image registration algorithm and its advantages for the registration of MR cardiac image sequences over existing methods. In Sect. 4 we present the results of the experiments performed in order to demonstrate the applicability of our method. Finally, Sect. 5 describes the conclusions from this work and future work as the construction of a cardiac atlas.

## 2 Related Work

While a large number of registration techniques exists for cardiac images, most of these techniques focus on 3D images and ignore any temporal misalignment of the images. Klein et al. [14] investigated a 12 parameter global affine motion model for the registration of different respiratory gates in an end diastolic cardiac PET sequence. In order to obtain robust motion estimates, a 4D registration model was produced which encourages smoothly varying motion between adjacent frames. Similarly to their earlier work [15],[16], this approach assumes that the motion of the heart from one frame to the other is likely to follow a uniform motion. The approach uses priori knowledge of the cardiac motion during the registration of two respiratory gated images and as a result there is significant reduction of noise and blurring in the registered image.

Faber et al. [17] developed an approach for the spatial and temporal registration of cardiac SPECT and MR images. Their method uses an automatic surface detection algorithm to detect the left ventricle (LV) in both the MR and the SPECT images.The surface detection algorithm is applied to all frames of the sequences. After the automatic surface detection algorithm, the best transformation for the spatial registration of the end-

systolic (ES) and end-diastolic (ED) frames of the SPECT and MR images is determined. The ES and ED frames are determined by using the surface representation of the LV. For the spatial registration, only translations and rotations were considered. After the spatial registration, the ES and ED frames of the SPECT and MR images are considered registered. Then, linear interpolation is used in order to generate new SPECT frames which correspond to the MR frames between the ES and DS frames. A drawback of this methods is that ignores all the spatial information contained in the images between the end-systolic and end-diastolic frames.

Outside cardiac image analysis, Caspi and Irani [18] developed an approach for the spatio-temporal alignment of image sequences. Their paper studies the problem of establishing correspondence in both the temporal and the spatial domains between two video sequences of the same scene. They solve the alignment problem by dividing it into two components: the spatial misalignment which is caused by the external and internal calibration parameters and the temporal misalignment which is caused when the two image sequences have a time shift or different frame rates. Hence, the transformation they used has two parts: a temporal and a spatial part. The spatial part of the transformation is a 2D affine and the temporal part of the transformation is an 1D affine transformation in time [18]. They have developed two different sequence to sequence alignment methods: the first method aligns the two sequences by aligning the trajectories of manually marked points while the other one uses the only grey level information of the two sequences.

## 3 Spatio-temporal Registration of 4D Cardiac Image Sequences

Since the heart is undergoing a constant non-rigid motion during the cardiac cycle, 4D cardiac image registration algorithms are required when registering two cardiac MR image sequences. Spatial alignment of corresponding frames of the image sequences (e.g. the second frame of one image sequence with the second frame of the other) is not enough since these frames may not correspond to the same position in the cardiac cycle of the image sequences. Spatio-temporal alignment of cardiac MR image sequences will resolve spatial ambiguities which occur when there is not sufficient common appearance in the two 3D MR cardiac images.Furthermore, it can also improve the results of the registration because it is not restricted only to the alignment of existing frames but it can also use sub-frame information.

A 4D cardiac image sequence can be represented as sequence of $n$ 3D images $I_k(x, y, z)$ with a fixed field of view $\Omega_I$ and an acquisition time $t_k, t_k < t_{k+1}$, in the temporal direction. The resulting image sequence can be viewed as 4D image $I(x, y, z, t)$ defined on the spatio-temporal domain $\Omega_I \times [t_1, t_n]$. The goal of 4D image registration described in this paper is to relate each point of one image sequence to its corresponding point of the reference image sequence. In this case the transformation $\mathbf{T} : (x, y, z, t) \rightarrow (x', y', z', t')$ maps any point of one image sequence $I(x, y, z, t)$ into its corresponding point in the reference image sequence $I(x', y', z', t')$. The 4D mapping used in this paper is of the form:

$$\mathbf{T}(x, y, z, t) = (x'(x, y, z), y'(x, y, z), z'(x, y, z), t'(t)) \quad (1)$$

and can be of a subvoxel displacement in the spatial domain and of a sub-frame displacement in the temporal domain. The 4D mapping can be resolved into decoupled spatial

and temporal components $\mathbf{T}_{spatial}$ and $\mathbf{T}_{temporal}$ respectively where

$$\mathbf{T}_{spatial}(x, y, z) = (x'(x, y, z), y'(x, y, z), z'(x, y, z))$$

and

$$\mathbf{T}_{temporal}(t) = t'(t)$$

each of which we choose to be one-to-one mappings. One consequence of this decoupling is that each temporal frame $t$ in image sequence $I$ will map to another temporal frame $t'$ in image sequence $I'$, ensuring causality and preventing that different regions in a 3D image $I_k(x, y, z)$ will be warped differently in the temporal direction by $T_{temporal}$.

### Temporal Alignment of 4D Image Sequences

The alignment of the two 4D cardiac MR images involves a temporal alignment and a spatial alignment. The temporal alignment of two image sequences aims try to find the transformation function $\mathbf{T}_{temporal}$ which established correspondences between time $t$ in one image sequence and the corresponding time $t'$ in the reference image sequence, thereby establishing a correspondence between corresponding time points in two cardiac cycles. In addition to differences in the length of the cardiac cycle, the temporal alignment of two image sequences is further complicated by the fact that the acquisition of cardiac MR images typically depends on two parameters: the first parameter describes the delay $t_{delay}$ after the R-wave after which the MR acquisition starts while the second parameter $\Delta t$ describes the temporal resolution of the image sequence. Figure 1 demonstrates how a typical ECG-gates cardiac MR image sequence is acquired. Together with the differences in the length of cardiac cycle between different subjects, differences of the acquisition parameters across different acquisitions account for the temporal misregistration of the image sequences.

In our current implementation the temporal transformation, $\mathbf{T}_{temporal} : (t) \rightarrow (t')$, is represented as an affine transformation of the following form:

$$\mathbf{T}_{temporal}(t') = \alpha t + \beta \tag{2}$$

Here $\alpha$ accounts for scaling differences between the two image sequences while $\beta$ accounts for differences in the translation between the two image sequences.

### Spatial Alignment of 4D Image Sequences

The aim of the spatial part of the transformation is to relate each spatial point of an image to a point of the reference image, i.e. $\mathbf{T}_{spatial} : (x, y, z) \rightarrow (x', y', z')$ maps any point $(x, y, z)$ of a particular time frame $t$ in one image sequence into its corresponding point $(x', y', z')$ of another particular time frame $t'$ of the reference image sequence. The simplest choice of $\mathbf{T}_{spatial}$ is a rigid transformation which has six degrees of freedom corresponding to translation and rotation. We choose an affine transformation which is a more general class of transformations with 12 degrees of freedom utilising scaling and

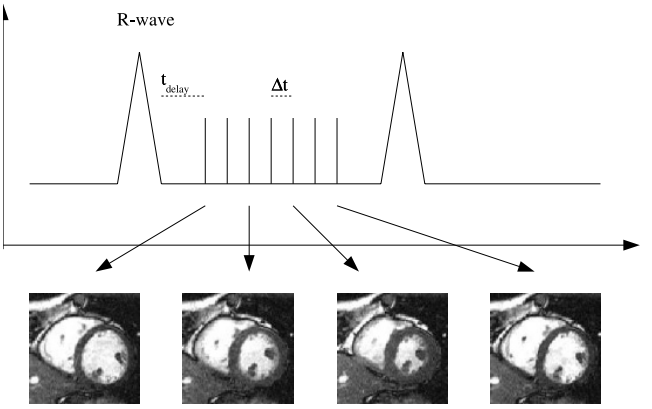


**Fig. 1.** An example of an ECG-gated acquisition of a cardiac MR image sequence: The parameter $t_{delay}$ describes the delay after the R-wave after which the MR acquisition starts while $\Delta t$ describes the temporal resolution of the image sequence

shearing in addition to translation and rotation. Such an 3D affine transformation can be written as:

$$\mathbf{T}_{spatial}(x, y, z) = \begin{pmatrix} \theta_{11} & \theta_{12} & \theta_{13} \\ \theta_{21} & \theta_{22} & \theta_{23} \\ \theta_{31} & \theta_{32} & \theta_{33} \end{pmatrix} \begin{pmatrix} x \\ y \\ z \end{pmatrix} + \begin{pmatrix} \theta_{14} \\ \theta_{24} \\ \theta_{34} \end{pmatrix} \tag{3}$$

where the coefficients $\theta$ parameterise the twelve degrees of freedom of the transformation.

### Similarity Measures for 4D Image Sequences

The optimal transformation is found by maximising a voxel based similarity measure. The use of a voxel-based similarity measure eliminates the need for any feature detection and segmentation of structures such as the epi- or endocardial surfaces. We choose normalised mutual information (NMI) [19] as a measure of spatio-temporal alignment which has been previously used successfully for mono- and multi-modality image registration. The normalised mutual information of two image sequences can be written as

$$I(A, B) = \frac{H(A) + H(B)}{H(A, B)} \tag{4}$$

where $H(\cdot)$ denotes the marginal entropy of an images sequence and $H(\cdot, \cdot)$ is the joint entropy of two image sequences. The normalised mutual information of the two image sequences can be calculated directly from the joint intensity histogram of the two sequences over the spatio-temporal domain of overlap $\Omega_{I_A} \times [t_{A1}, t_{An}] \bigcap \mathbf{T}(\Omega_{I_B} \times [t_{B1}, t_{Bn}])$. During the optimisation new voxel values are generated in the temporal

domain using linear interpolation and trilinear interpolation in the spatial domain. The optimisation is carried out using an iterative downhill descent algorithm to calculate the optimal transformation:

$$\arg \max_{\alpha,\beta,\Theta} I(A, T(B)) \tag{5}$$

where $A$ is the reference image sequence and $\mathbf{T}(B)$ is the transformed image sequence $B$.

## 4 Results and Discussion

To evaluate the spatio-temporal registration algorithm we have acquired cardiac MR image sequences from seven volunteers. All image sequences used for our experiments were acquired on a Siemens Sonata 1.5T scanner using a TrueFisp pulse sequence. For the reference subject 32 different time frames were acquired (cardiac cycle of length 950msec). Each 3D image of the sequence had a resolution of $256 \times 192 \times 46$ with a pixel size of 0.97mm, 0.97mm and a slice thickness of 3mm. Six 4D cardiac MR images were registered to the reference subject. The length of the cardiac cycle of these six images varied from 300msec to 800msec. The temporal part of the 4D transformation is described by Eq. (2), i.e. only temporal scaling and translation will be taken into account, while the spatial part of the transformation uses the affine transformation (Eq. (3)). An initial estimate of the temporal part 4D transformation was provided due to the large differences in the length of the cardiac cycle of each image. The temporal part of transformation was initially calculated in order to match the temporal ends of the two 4D cardiac MR images.

Figure 3 provides an example of the registration. In the first row of figure 3 (a,b,c) are the short axis (a) and the long axis (b) views of particular slices of the reference sequence and also a temporal view of a short axis line (c) of the reference sequence. The middle row and last contains the corresponding views of the corresponding slices before and after the registration respectively. In the images of the middle and bottom row the anatomy contours of the reference subject are also overlayed. The figure shows a large improvement in the alignment of the images after the registration. In the images i,f,c we can see how well the temporal alignment of the two sequences has been achieved. Initially, the temporal domains of the images sequences are completely misaligned, while the alignment of the sequences after the registration has been greatly improved.

To assess the quality of the registration quantitatively we have calculated the volume difference of the left ventricle (manually segmented by an expert observer) between the two image sequences as measured by the following equation:

$$\Delta(T, S) = \frac{V_T - V_S}{V_T} \times 100\% \tag{6}$$

Here $\Delta$ is the absolute volume difference between the two images, $V_T$ is the volume of the target and $V_S$ the volume of the source image. We found that the mean volume difference of the left ventricle between two image sequences before the registration was 29.55% and after the registration reduced to 13.90%. The mean error of the time where the

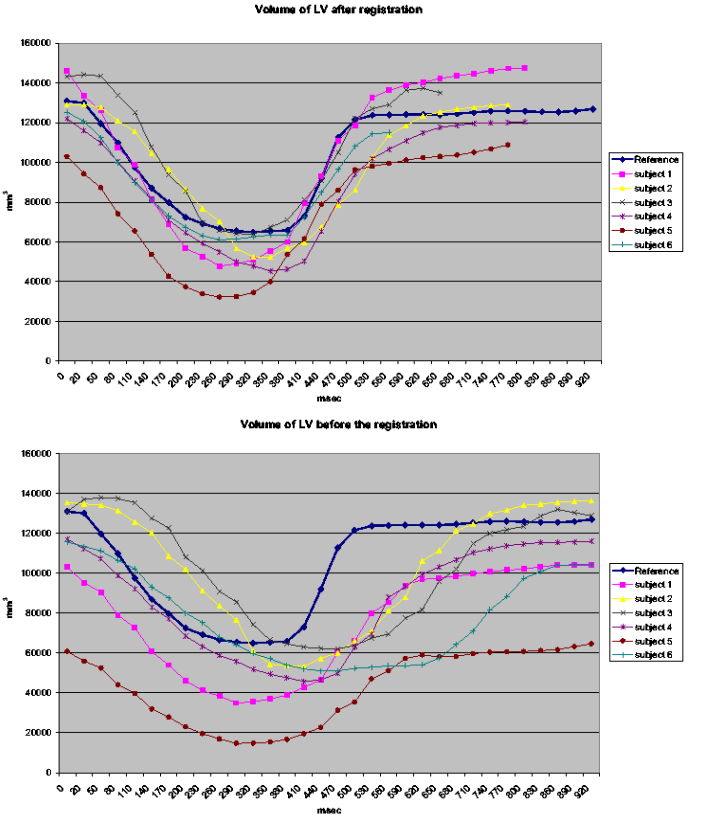


**Fig. 2.** The volume curves of the reference image and the subjects images (a) after the 4D registration, (b) before the 4D registration (with the use of the initial estimate)

maximum contraction of the left ventricle is achieved was 80 msec before the registration (taking into account that the temporal resolution of the target, $\Delta$, is 30msec, this error corresponds to 2.6 frames) while after the registration the was reduced to 40 msec (which corresponds to an error of 1.3 frames). This can also be observed in the volume curves of the left ventricle before and after the registration shown in Fig. 2. The figure clearly shows that the temporal features of the volume curves are significantly better aligned after registration even though no segmentation of the left ventricle was used during the registration. In addition to the volume difference between image sequences, we have also evaluated the quality of the registration by calculating the volume overlap for the left and right ventricle as well as for the myocardium (defined by an expert observer). The volume overlap for an object $O$ is defined as:

$$\Delta(T,S) = \frac{|T \bigcap S|}{|T|} \times 100\% \tag{7}$$

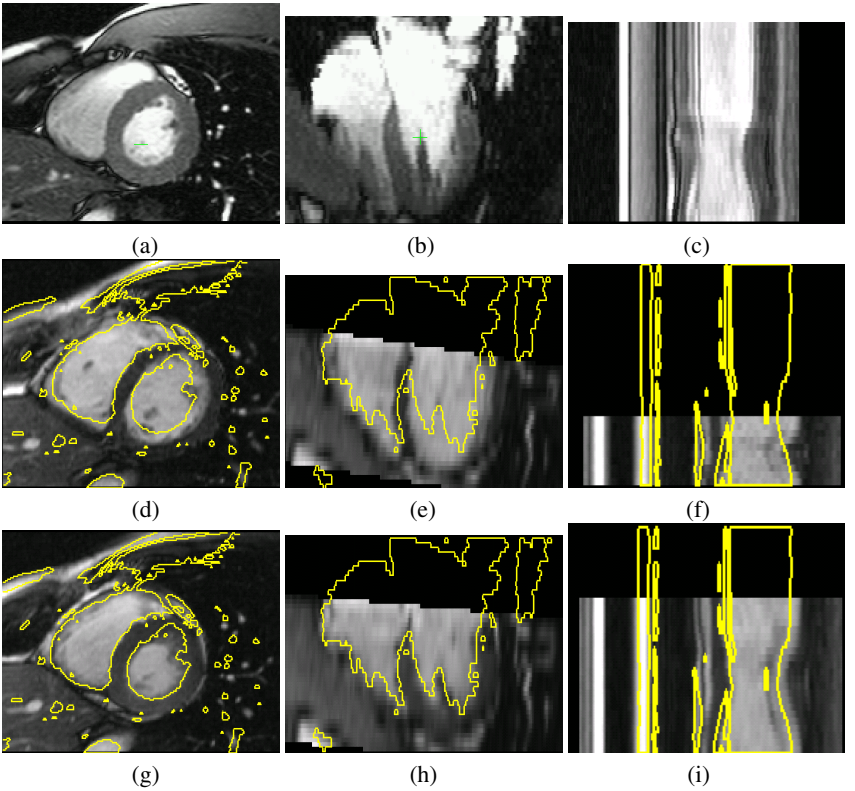


**Fig. 3.** Results of the 4D cardiac MR registration algorithm (a) shows the short axis view of the reference subject, (b) shows the long axis view of the reference subject (c) a temporal view of a short axis line of the reference subject (d-e) shows the corresponding short axis and long axis views before the registration (f) shows the corresponding temporal view of a short axis line before the registration (g)-(i) show the corresponding images after the 4D registration

**Table 1.** The mean volume overlap before and after the 4D registration

| Volume overlap | Before registration (SD) | After registration (SD) |
|---|---|---|
| **Left ventricle** | 49.84% (24%) | 75.34% (7.09%) |
| **Right ventricle** | 48.07% (20.95%) | 65.23% (6.92%) |
| **Myocardium** | 44.86% (21.87%) | 61.32% (5.05%) |

Here $T$ denotes the voxels in the reference (target) image part of object $O$ and $S$ denotes the number of voxels in the other image part of object $O$. Table 1 shows the mean volume overlap for each anatomical region before and after registration. The results clearly show an improvement of the overlap measures after registration.

It is not expected that the images would be perfectly aligned either temporal domain or in the spatial domain. This is due to the nature of the temporal and spatial components of the 4D transformation. For example, the mapping of the cardiac anatomy of two

different subjects most likely requires a non-rigid transformation. This can be modelled to a certain extend by the current $\mathbf{T}_{spatial}$. The temporal transformation (Eq. (2)) can only scale and translate the entire image sequence. It can not scale parts of the cardiac cycle differently. Therefore, it would not be able to address the temporal misalignment caused by differences in the dynamic properties of the contraction and relaxation phases of the cardiac cycle (one heart may have longer contraction phase than relaxation phase). An example of a temporal misalignment that can not be recovered by the current $\mathbf{T}_{temporal}$ can been seen in the volume diagrams (Fig. 2). In this figure, the volume of the left ventricle in the reference image (Fig. 2a,b) appears stable after a certain time period, while this is not true for all the other images (Fig. 2b).

## 5 Conclusions and Further Work

A 4D transformation model which consists of decoupled spatial and temporal components has been used in an iterative registration approach for the spatio-temporal alignment of two cardiac MR image sequences. The proposed registration approach uses mutual information as a measure of image sequence alignment and enables the comparisons of the anatomy and the cardiac function of a number of MR cardiac image sequences. The transformation model corrects both the temporal misalignment (caused by differences in initial offset and in the length of the two cardiac cycles) and the spatial misalignment (caused by spatial differences of affine nature between the two image sequences). The spatio-temporal alignment can be further improved by employing a more complex transformation in which the spatial component will be modelled by a 3D free form transformation based on B-Splines [20] and the temporal part will also be a similar B-Spline model. Hence, the spatial part of the transformation, $\mathbf{T}_{spatial}$, will correct the misalignment caused by the non-rigid differences while the temporal transformation,$\mathbf{T}_{temporal}$ will align cardiac motion patterns with complicated dynamic properties. This registration method will be used for the inter-subject spatio-temporal alignment of a number of cardiac MR image sequence in order to construct a probabilistic atlas of cardiovascular system.

## References

1. American Heart Association. Heart and stroke statistical update. `http://www.americanheart.org/`, 2002.
2. T. Mäkelä, P. Clarysse, N. Sipila, O.and Pauna, and Q. C. Pham. A review of cardiac image registration methods. *IEEE Transcactions on Medical Imaging*, 21(9), 2002.
3. J.B.A Maintz and M.A. Viergever. A survey of medical image registration. *Medical Image Analysis*, 2(1):1–37, 1998.
4. D.L.G. Hill, P.G. Batchelor, M. Holden, and D.J. Hawkes. Medical image registration. *Physics in Medical Biology*, 46(3):R1–R45, 2001.
5. H. Lester and S. Arridge. A survery of hierarchical non-linear medical image registration. *Pattern Recognition*, 32(1):129–149, 1999.
6. D. Manke, P. Rosch, K. Nehrke, P. Bornert, and O. Dossel. Model evaluation and calibration for prospective respiratory motion correction in coronary MR angiography based on 3D image registration. *IEEE Transcactions on Medical Imaging*, 21(9), 2002.

7. K. McLeish, D.L.G Hill, D. Atkinson, J.M. Blackall, and R. Razavi. A study of the motion and deformation of the heart due to respiration. *IEEE Transcactions on Medical Imaging*, 21(9), 2002.
8. R. Chandrashekara, R. Mohiaddin, and D. Rueckert. Analysis of myocardial motion in tagged MR images using non-rigid image registration. In *Proc. SPIE Medical Imaging 2002: Image Processing*, San Diego, CA, 2002.
9. M.C. Gilardi, G. Rizzo, A. Savi, C. Landoni, V. Bettinardi, C. Rosseti, G. Striano, and F. Fazio. Correlation of SPECT and PET cardiac images by a surface matching registration technique. *Computerized Medical Imaging and Graphics*, 22(5):391–398, 1998.
10. T. G. Turkington, T. R. DeGradom, M. W. Hanson, and E. R. Coleman. Alignment of dynamic cardiac PET images for correction of motion. *IEEE Transaction on Nuclear Science*, 44(2):235–242, 1997.
11. L.M. Bidaut and J.P. Vallëe. Automated registration of dynamic MR images for the quantification of myocardial perfusion. *Journal Of Magnetic Resonance Imaging*, 13(4):648–655, 2001.
12. A. Rao, G.I. Sanchez-Ortiz, R. Chandrashekara, M. Lorenzo-Valdés, R. Mohiaddin, and D. Rueckert. Comparison of cardiac motion across subjects using non-rigid registration. In *Proceedings: Medical Image Computing Assisted Intervention, MICCAI 2002*, " Tokyo, Japan", 2002.
13. J.C. Mazziotta, A.W. Toga, A. Evans, P. Fox, and J. Lancaster. A probabilistic atlas of the human brain:theory and rationale for its development. The international consortium for brain mapping. *Neuroimage*, 2:89–101, 1995.
14. G.J. Klein, B.W. Reutter, and R.H. Huesman. Four dimensional affine registration models for respiratory-gated PET. *IEEE Transactions on Nuclear Science*, 48(3):756–760, 2001.
15. G.J. Klein. Four dimensional processing of deformable cardiac PET data. In *workshop on Mathematical Methods in Biomedical Image Analysis June 11-12 2000*, pages 127–134, Hilton Head Island, SC, 2000.
16. J.K. Klein and R.H Huesman. Four dimensional processing of deformable cardiacd PET data. *Medical Image Analysis*, 6(1):29–46, 2002.
17. T.L. Faber, R.W. McColl, R.M Opperman, J.R. Corbett, and R.M. Peshock. Spatial and temporal registration of cardiac SPECT and MR images: Methods and evaluation. *Radiology*, 179(3):857–861, 1991.
18. Y. Caspi and M. Irani. Spatio-temporal alignment of sequences. *IEEE Transactions on Pattend Analysis and Machine Intelligence*, 24(11):1409–1424, 2002.
19. C. Studholme, D.L.G. Hill, and D.J. Hawkes. An overlap invariant entropy measure of 3D medical image alignment. *Pattern Recognition*, 32:71–86, 1999.
20. D. Rueckert, L.I. Sonoda, C. Hayes, D.L.G. Hill, M.O. Leach, and D.J Hawkes. Non-rigid registration using free-form deformations: Application to breast MR images. *IEEE Transactions on Medical Imaging*, 18(8):712–721, 1999.

# Automatic Registration of MR First-Pass Myocardial Perfusion Images

Luc Bracoud[1,2], Fabrice Vincent[1], Chahin Pachai[1],
Emmanuelle Canet[2], Pierre Croisille[2], and Didier Revel[2]

[1] THERALYS S.A., 29 rue Bellecombe, 69006 Lyon, France
{bracoud,vincent,pachai}@theralys.com
[2] CREATIS, INSA, Bâtiment Blaise Pascal, 69621 Villeurbanne Cedex, France
{Emmanuelle.Canet,Pierre.Croisille,Didier.Revel}
@creatis.insa-lyon.fr

**Abstract.** Magnetic resonance perfusion imaging has become a technique of choice in the evaluation of patients with suspected coronary artery disease (CAD). In order to improve the quantification of perfusion parameters (such as signal intensity amplitude and upslope), an automatic registration technique is proposed. The results are compared to manually registered perfusion sequences. Perfusion maps computed from original and registered data sets are also compared. Automatic registration can be efficiently used as a post-processing technique to improve further qualitative and quantitative evaluation strategies.

## 1 Introduction

Magnetic resonance (MR) myocardial first-pass perfusion imaging has become a technique of choice in the evaluation of patients with suspected coronary artery disease (CAD) [1-4]. Perfusion indices such as upslope, time to peak and maximum signal intensity variation computed from signal-versus-time curves are increasingly used to quantitatively evaluate and precisely locate ischemically challenged areas of the myocardium.

The evaluation of myocardial perfusion images may suffer from respiratory motion during the acquisition procedure even when the patient is asked to hold breath. In order to improve the visual (qualitative) assessment and provide a more robust strategy for quantitative evaluation of perfusion data, an automated image registration technique is proposed in this paper. A multi-resolution, mutual information (MI)-based registration technique is used. After the selection of a reference image for each slice of a given perfusion sequence and the definition of a rectangular region of interest (ROI) including the heart, the algorithm automatically registers all the images of the corresponding dynamic sequence.

The overall efficacy of the proposed algorithm was evaluated both qualitatively, by visual assessment of original and registered dynamic images, and quantitatively by comparing the results with manually registered image data. The impact of such correction as a post-processing technique on the quality of perfusion maps is also displayed and discussed in this paper.

I. Magnin et al. (Eds.): FIMH 2003, LNCS 2674, pp. 215–223, 2003.

## 2 Material and Method

### 2.1 MRI Perfusion Data

Short axis slices from MR perfusion sequences of five patients with stable CAD were used for the validation of the registration technique. The patients were prospectively enrolled in a clinical trial with MRI, X-ray coronarography and SPECT examinations after giving written informed consent.

The acquisition parameters were: field strength 1.5T (Magnetom Vision, Siemens Medical Systems), number of short axis slices: 3, number of time frames per slice: 30, Repetition Time: 3.5 ms, Echo Time: 1.7 ms, in-plane resolution: 1.56 mm, 256×256 matrix, slice thickness: 12 mm.

### 2.2 Automatic Registration

In order to improve the quality of first-pass signal-versus-time curves prior to the generation of perfusion maps, an automatic registration technique was used. This algorithm was used to correct for the movements induced by breathing during the acquisition. Provided a reference time-point in a given perfusion sequence and a rectangular ROI, the algorithm automatically registered all the images of that sequence.

A two-dimensional, multi-resolution, MI-based registration technique was used. The implementation was based on several routines available in the ITK library [5]. The algorithm is described in this section.

#### Registration Framework

For a given perfusion sequence, the inputs of the registration algorithm were the reference image (also called target image) and any other image of the same sequence (also called source image). For any couple of target and source images, the registration algorithm must therefore provide a geometric transformation to correct for the heart movements. The registration framework classically includes four basic elements:

- Transformation
- Similarity measure (or metric), which indicates how well the target image matches the source image.
- Interpolation, which is used to resample image data every time a transformation is applied.
- Optimization, which consists in maximizing the value of the similarity measure to search for an optimal solution (transformation).

A multi-resolution, coarse-to-fine strategy was adopted. It is well known that the smoothing effect of such strategy improves and accelerates the convergence of the optimizer, and increases the robustness of the matching strategy by initially emphasizing on global, large-scale image structures prior to further refinement based on small image details. The registration starts at the lowest resolution level. Once convergence is reached at this level, the algorithm is initialized with the resulting solution for the next finer resolution level within an iterative scheme.

**Implementation, Parameter Settings, and Initialization**

In this work, a rigid 2D transformation (only 2D translations and rotations without scaling) was used, the process being performed independently for each level of slice. The similarity measure was MI, implemented following Viola and Wells recommendations detailed in [6-8]. MI is well suited for our problem, as the dependency between image intensities varies along the sequence according to bolus circulation. Linear interpolation was used, as well as a simple gradient descent method for optimization.

The whole perfusion sequence was dynamically observed in a cine-loop display window to define the extent of a rectangular ROI including both ventricles, over which the registration algorithm was performed. Defining such a ROI was necessary to focus on heart registration and discard, if possible, the impact of other surrounding organ movements on final motion estimation. The size of the ROI was not critical for the algorithm performance as long as it was close enough (under ten pixels approximately) to the heart. Therefore, this interactive step of ROI definition was not time consuming.

Two resolution levels were obtained including the initial image resolution and a coarser level by dividing the initial resolution in two. Considering that the extent of the ROI over which the registration was performed was about 80x70 pixels, two levels sufficed to smooth out local minima and enhance registration results. The similarity measure, which estimates the goodness of fit, was computed over a fixed number of samples to accelerate the registration (50 equally distributed pixels, in this setting). The gradient descent optimizer iterated 1000 times for each resolution level, which ensured us to reach an optimal solution for either small or large movements to compensate.

The initialization included the choice of a reference image for a given perfusion sequence. This reference image was selected among the last images of the dynamic sequence, after the contrast agent washout and where the signal-intensity is nearly constant.

Registration took approximately 8 minutes for each level of slice (30 images), when run on an Athlon 1.8GHz working under Linux.

## 3 Validation

### 3.1 Qualitative Evaluation

A dedicated graphical user interface was developed to perform a qualitative validation of the registration algorithm. Source, target and registered images were simultaneously displayed, along with a so-called checkerboard image frame to efficiently assess the continuity of anatomical structures on two different images, before and after registration (checker-like combination of two images, with “white squares” filled with the corresponding parts of the first image, and “black squares” with the corresponding parts of the second image). All image frames were bound together in terms of window/level, zoom factor and slice number settings.

Joint two-dimensional histograms were also generated before and after registration. The dispersion on these joint histograms, which can be assessed qualitatively

and quantitatively, provided useful information on the goodness of fit. A reduced dispersion can indeed be associated with a successful registration (the ideal case of an image registered with itself would correspond to the first bisector of the histogram).

Figure 1 simultaneously displays original and registered images of one perfusion sequence. The heart movements can be assessed with respect to the myocardium contours drawn by a medical expert. Maximum signal intensity variation and upslope perfusion maps are also displayed for original and registered perfusion sequences. Right and left ventricles clearly overlap with the myocardium region (as defined on the reference image, Fig. 1f), over the dynamic sequence and reduce the accuracy of the corresponding perfusion maps.

**Strategy**

The results of the registration algorithm were quantitatively assessed by a medical expert by mean of a manual registration software specially designed for this study. This software allowed to interactively quantify the misregistration of the heart in a dynamic sequence by drawing and translating contours on images. Both original and registered dynamic sequences were processed by the expert with this software.

The principles of the interactive quantification of the misregistration were the following:

For each dynamic sequence, either registered or original, the medical expert:

1. Chose an image where myocardial contours could be easily delineated.
2. Outlined epicardial and endocardial contours on the selected image. These contours were then automatically copied on all the images of the dynamic sequence.
3. Translated, if necessary, the manually outlined contours to match the myocardial contours on each image of the dynamic sequence.

The rotation component of the motion was not assessed. Indeed, its impact on the misregistration is, according to the expert, of lesser importance than the translation component, at least on the sequence set processed in this paper. It was also noted that the automatic registration algorithm results showed a negligible rotation component.

The previous procedure produced two vectors $X^s=(x_1,\ldots,x_n)$ and $Y^s=(y_1,\ldots,y_n)$ describing the translation in the x and y directions with respect to the reference image (with n the number of images per dynamic sequence, i.e. n=30). The mean position of the myocardium $(\bar{x},\bar{y})$ was then computed in order to derive the vectors $X_r^s$ and $Y_r^s$ describing the translation with respect to the mean position:

$$X_r^s = (x_1 - \bar{x},\ldots, x_n - \bar{x}) \;;\; Y_r^s = (y_1 - \bar{y},\ldots, y_n - \bar{y}) \quad (1)$$

The vectors $X_r^s$ and $Y_r^s$ are good measures of the misregistration of the heart in a dynamic sequence (with the assumption of negligible rotation) since they represent the motion of the heart with respect to a mean position and do not depend on the choice of the reference image as $X^s$ and $Y^s$ do.

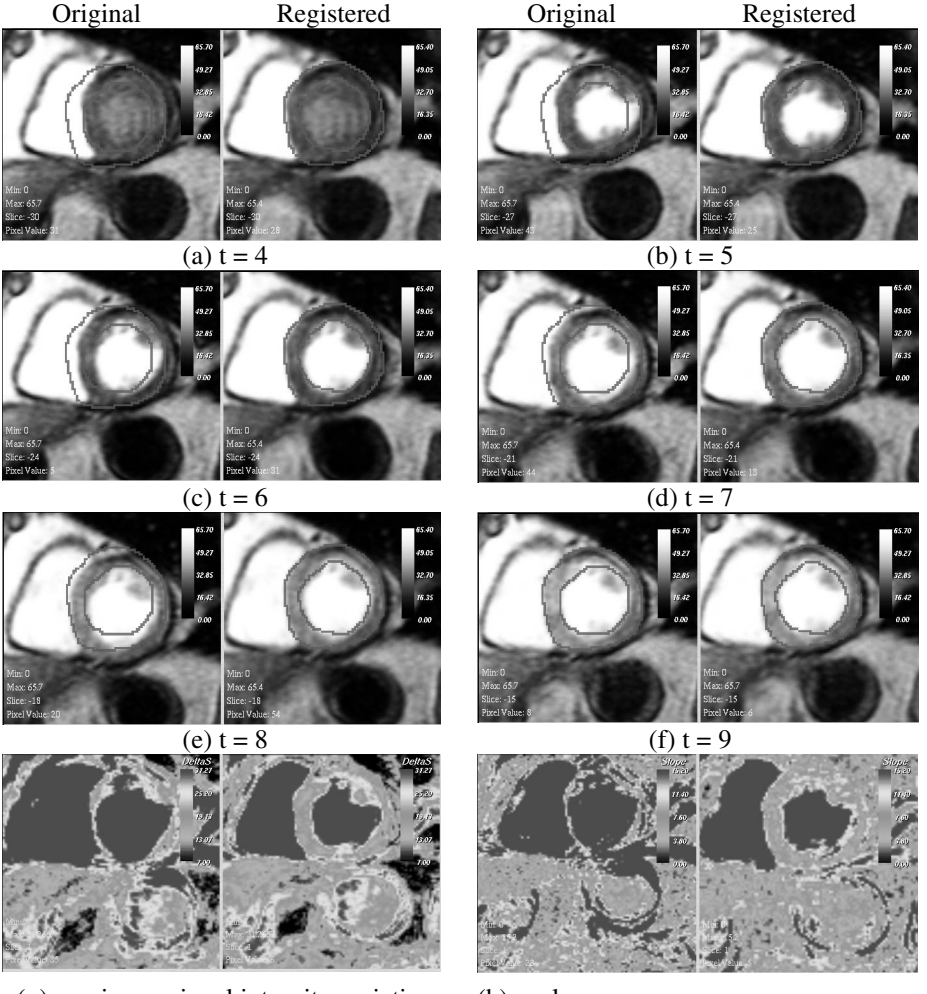


**Fig. 1.** Six consecutive images of a dynamic sequence are displayed (a-f). Each window includes both the original (left) and the registered image (right). Epicardial and endocardial contours are manually drawn by a medical expert on time-point t = 9 (f). These contours are then copied on all other images of the dynamic sequence. The heart movements can be easily observed with respect to the myocardium contours from time-point t = 4 (a) to time-point t = 8 (e) on original images. The resulting perfusion maps are also displayed for original and registered images: maximum signal intensity variation (g) and up-slope (h). Perfusion maps computed from registered images (right) have a much better quality than those computed from original images (left)

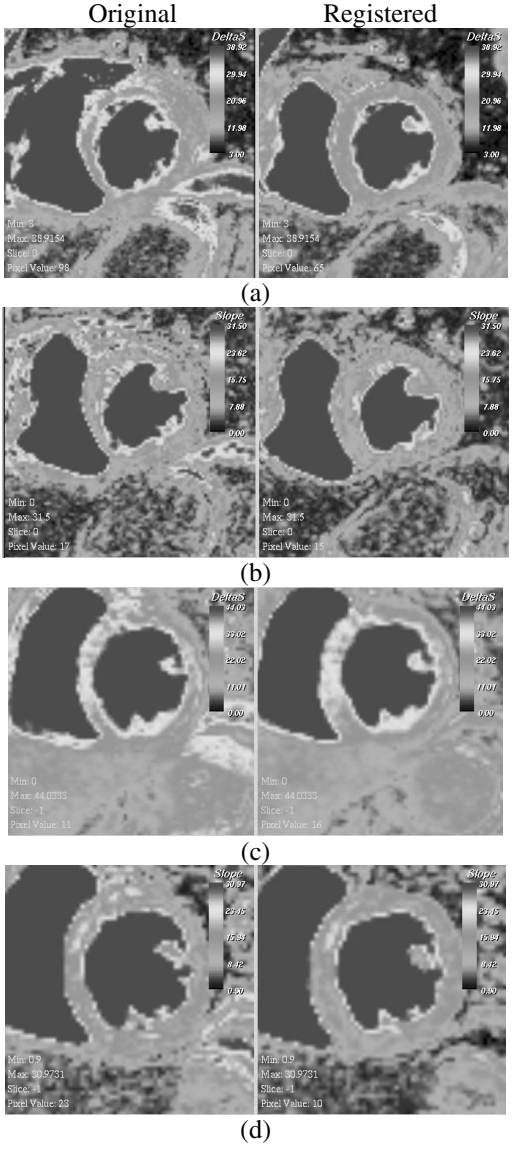


**Fig. 2.** Perfusion maps maximum amplitude variation (a and c) and up-slope (b and d) are computed from short-axis slices of two patients from original images (left column) and registered images (right column). The color-maps are identical for original and registered perfusions maps for a given perfusion parameter. The myocardium is "thinned" on perfusion maps computed from original images where respiratory movements reduce the accuracy of signal-time curves

### 3.2 Quantitative Evaluation

The distance vector $D_r^s$, measuring the distance of the myocardium with respect to the mean position, was also computed:

$$D_r^s = (d_1,...,d_n) \text{ with } d_i = \sqrt{(x_i - \bar{x})^2 + (y_i - \bar{y})^2} \quad (2)$$

**Results**

A set of 10 dynamic sequences (30 images per sequence, i.e. 300 images) from 5 patients (a rest and a stress sequence for each patient) were processed with the registration algorithm which produced a new set of dynamic sequences. The two sets, named *0* (original) and *R* (registered), of dynamic sequences were then analyzed with the manual registration software as previously described. The manual registration was performed with an accuracy of one pixel. This accuracy was considered as satisfactory by the medical expert.

A statistical analysis was carried out over all 300 images for original and registered sets. That is, for all the sequences belonging to the same set (*s* in *O* or *s* in *R*) we respectively concatenated the vectors $X_r^s$, $Y_r^s$ and $D_r^s$ to construct the global vectors, respectively $X_r$, $Y_r$ and $D_r$.

Mean and standard deviation for these two vectors are provided in Fig 3, along with scatter plots representing the magnitude of heart motion.

The following observations can be made:

1. The magnitude of heart motion in original dynamic sequences was important. It often exceeded several millimeters and had the same order of magnitude as the myocardium thickness. This result clearly justified the need for a registration step before any further analysis of MR myocardial perfusion sequences.
2. 
3. The automatic registration algorithm efficiently corrected for an important part of the motion: the mean distance of the myocardium with respect to the average position fell from 3.87 (± 2.45) mm in the original sequences to 1.10 (± 1.54) mm in the registered sequences. This result is visually confirmed in Fig 3, where the dispersion of points in the scatter plot is decreased by the registration process. It is important to note that the mean motion in the registered sequences is less than the size of the pixel (1.56 mm)

## 4 Conclusion

Other authors addressed the issue of image registration in the context of myocardial MR perfusion imaging [9-10]. The technique described in this paper provided an automatic way to correct for heart movements and improved the context of qualitative and quantitative analysis of myocardial MR perfusion images.

| | X motion around average position Xr (mm) | | Y motion around average position Yr (mm) | | Distance to average position (Dr) | |
|---|---|---|---|---|---|---|
| | mean | std | mean | std | mean | std |
| Original images | 0,00 | 2,75 | 0,00 | 3,67 | 3,87 | 2,45 |
| Registered images | 0,00 | 1,31 | 0,00 | 1,37 | 1,10 | 1,54 |

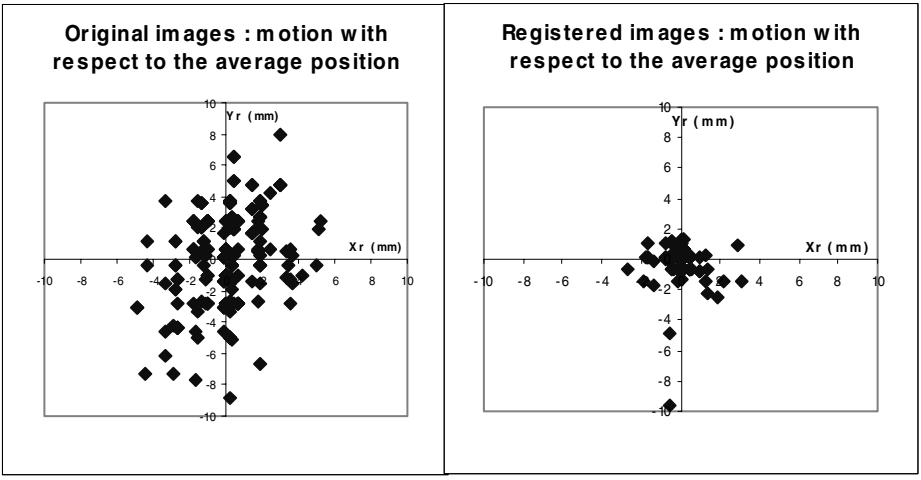


**Fig. 3.** Comparison of heart motions assessed by the expert in original and registered dynamic sequences (10 dynamic sequences, 300 short-axis slices): registration dramatically decreases the magnitude of heart motion

The registration technique was robust since it was not based on other image features than gray level. Its accuracy with respect to manual registration was less than the pixel size.

The registration algorithm improved the quality of perfusion maps, which can be noted in Fig. 1. The algorithm clearly led to a visual improvement of the perfusion maps and therefore increased the diagnostic value of such technique for the assessment of patients with suspected CAD.

## References

1. Schwitter J., Nanz D., Kneifel S., Bertschinger K., Buchi M., Knusel P.R., Marincek B., Luscher T.F., von Schulthess G.K.: Assessment of myocardial perfusion in coronary artery disease by magnetic resonance: a comparison with positron emission tomography and coronary angiography. Circulation **103(18)** (2001) 2230–2235

2. Bertschinger KM., Nanz D., Buechi M., Luescher TF., Marincek B., von Schulthess GK., Schwitter J.: Magnetic resonance myocardial first-pass perfusion imaging: parameter optimization for signal response and cardiac coverage. Magn Reson Imaging **14(5)** (2001) 556–562
3. Al-Saadi N., Nagel E., Gross M., Bornstedt A., Schnackenburg B., Klein C., Klimek W., Oswald H., Fleck E.: Noninvasive detection of myocardial ischemia from perfusion reserve based on cardiovascular magnetic resonance. Circulation **101(12)** (2000) 1379–1383
4. Plein S., Ridgway J.P., Jones T.R., Bloomer T.N., Sivananthan MU.: Coronary artery disease: assessment with a comprehensive MR imaging protocol--initial results. Radiology **225(1)** (2002) 300–307
5. ITK, National Library of Medicine Insight Segmentation and Registration Toolkit www.itk.org
6. Wells W.M. 3rd, Viola P., Atsumi H., Nakajima S., Kikinis R. : Multi-modal volume registration by maximization of mutual information. Med. Image Anal. **1(1)** (1996) 35–51.
7. Viola P.: Alignment by Maximization of Mutual Information. PhD thesis, Massachusetts Institute of Technology (1995)
8. Viola P. and Wells III W.: Alignment by Maximization of Mutual Information. International Journal of Computer Vision **24(2)** (1997) 137–154
9. Bidaut L.M., Vallee J.P.: Automated registration of dynamic MR images for the quantification of myocardial perfusion. J. Magn. Reson. Imaging **13(4)** (2001) 648–655
10. Delzescaux T., Frouin F., De Cesare A., Philipp-Foliguet S., Zeboudj R., Janier M., Todd-Pokropek A., and Herment A.: Adaptive and self-evaluating registration method for myocardial perfusion assessment. Magma **13** (2001) 28–39

# Evaluation and Comparison of Surface and Intensity Based Rigid Registration Methods for Thorax and Cardiac MR and PET Images

Timo Mäkelä[1,2,6], Mika Pollari[1], Jyrki Lötjönen[3], Nicoleta Pauna[2], Anthonin Reilhac[4,5], Patrick Clarysse[2], Isabelle E. Magnin[2], and Toivo Katila[1,6]

[1] Laboratory of Biomedical Engineering, Helsinki University of Technology
P.O.B. 2200, FIN-02015 HUT, Finland
{Mika.Pollari,Timo.Makela,Toivo.Katila}@hut.fi
[2] CREATIS, INSA, Batiment Blaise Pascal, 69621 Villeurbanne Cedex, France
{Nicoleta.Pauna, Patrick.Clarysse, Isabelle.Magnin}@creatis.insa-lyon.fr
[3] VTT Information Technology, P.O.Box 1206, FIN-33101 Tampere, Finland
Jyrki.Lotjonen@vtt.fi
[4] Centre d'Exploration et de Recherche Médicales par Emission de Positons,
Neurological Hospital, 59 boulevard Pinel, F-69003 Lyon, France
[5] McGill University/McConnell Brain Imaging Centre
Montreal Neurological Institute, WB-315, 3801 University Street
Montreal, Quebec, H3A 2B4, Canada
anthonin@bic.mni.mcgill.ca
[6] BioMag Laboratory, Helsinki University Central Hospital, P.O.B. 503
FIN-00029 HUS, Finland

**Abstract.** In this paper an evaluation and a comparison of surface and image intensity based (mutual information, normalized mutual information and correlation ratio) rigid registration methods for cardiac magnetic resonance and positron emission tomography images are presented. In both types of rigid image registration methods, PET transmission image was used as a linking mediator to register corresponding PET emission image to MR image coordinates. Also direct rigid registration of PET emission image to MR image coordinates was tested. Methods were evaluated with simulated and ten patient MR-PET images and with three optimization methods. Results indicated that NMI and CR methods with simplex optimization provided the most robust and accurate results.

## 1 Introduction

Cardiac image registration is a more difficult problem than brain image registration because of the mixed movement of the heart and thorax structures and, also, because the heart exhibits fewer accurate anatomical landmarks than brain. A recent review of cardiac image registration approaches can be found in [1]. Methods are often based on automatic registration of heart or thorax structures [2].

I. Magnin et al. (Eds.): FIMH 2003, LNCS 2674, pp. 224–233, 2003.

Another category of methods relies on the registration of image intensities. In the literature, there are very few papers concerning the registration of cardiac or thorax images using modern image intensity based methods such as Mutual Information (MI) or Normalized Mutual Information (NMI) [3], [4], [5]. To our knowledge, Correlation Ratio (CR) has been reported to be used only for brain image registration [6].

In this work we present an evaluation and a comparison of rigid surface and image intensity based registration methods for cardiac Magnetic Resonance (MR) and Positron Emission Tomography (PET). Surface and image intensity based registration methods are both based on the registration of PET transmission image to the coordinates of transaxial MR image to obtain registration parameters to register PET emission image to MR image coordinates. Surface based registration method uses deformable model based automatic segmentation of the thorax and lungs surfaces from transaxial MR and transmission PET image [7]. Surface based registration method was presented in detailed in [2]. Image intensity based methods (MI, NMI and CR) are used as an alternative for surface based registration method. To find the optimum of the algorithms, Powell [8], simplex [8] and grid based [2] optimization methods were used. Methods were evaluated with simulated images and tested with ten patients MR-PET images. The data are presented in Sect. 2 and methods in Sect. 3. The registration results are presented in Sect. 4 and discussed in Sect. 5.

## 2 Cardiac Image Data

### 2.1 Simulated Data

In order to evaluate the registration methods, a reference PET-MRI data set was build up [9]. Thorax transaxial MR images were acquired on a healthy volunteer with a 1.5 T Siemens Magnetom Vision Imager (Siemens, Erlangen, Germany) at the Cardiological Hospital of Lyon. A series of 15 T1 weighted ECG-gated contiguous transaxial images covering heart area was acquired during breath hold sequence with the body array coil (Fig. 1a). The pixel size and the slice thickness were 0.97 x 0.97 mm and 8 mm, respectively. MR images were segmented and labeled (Fig. 1b). Arms were excluded from the segmentation. The result was inputted into a PET simulator. Simulated PET images (Fig. 1c and Fig. 1d) and original MR image provided the gold standard for registration.

PET transmission and emission images were simulated using the SORTEO (Simulator Of Realistic Three-dimensional Emitting Objects) PET simulator [10,11]. SORTEO is a Monte Carlo simulator which uses a 3-D realistic phantom based on the segmented MR images into 9 classes (muscle, lungs, liver, fat, spine (bone), heart left ventricle (LV), the cavity of the LV, right ventricle (RV), the cavity of the RV). It takes into account the specific activity and attenuation of each tissue. The Monte Carlo method simulates photons one by one and tracks them until they are detected or lost, accounting then for all the sources of biases and noises. PET emission image simulation was performed using an F-18 radioactive tracer. Fluorodeoxyglucose (FDG) PET imaging is considered

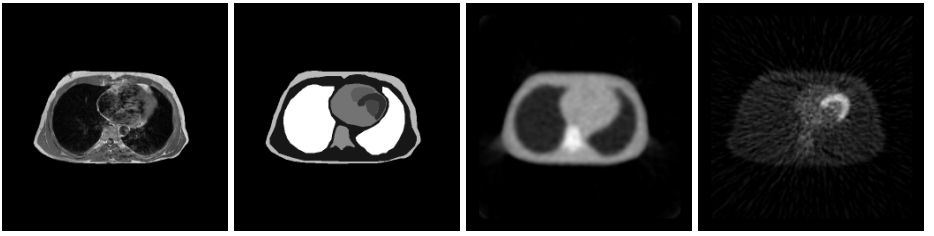

(a) (b) (c) (d)

**Fig. 1.** (a) MR image, (b) segmented MR image, simulated PET (c) transmission and (d) emission images

as a golden standard to determine viable areas of the heart [12]. A PET transmission image simulation was obtained using Ge-68 as an external radioactive source. Reconstructed simulated PET transmission and emission images (FBP with Hanning filter) had pixel sizes and slice thickness of 3.52 x 3.52 $mm^2$ and 2.43 mm, respectively. Both MR and simulated PET images were interpolated (trilinear interpolation) to the same 256 x 256 x 15 matrix with voxel size 1.95 x 1.95 x 8 mm. Also isotropic volumes were created with 256 x 256 x 58 matrix size and 1.95 $mm^3$ voxel size.

### 2.2 Patient Data

The cardiac patient data consisted of MR and PET images of ten patients suffering from three vessels coronary artery disease, diagnosed with coronary angiography and regional dyskinesia in cineangiograms [13]. All patients underwent MR and fluorine-18-deoxyglucose (FDG) PET imaging within 10 days.

The MR imaging was performed at the Department of Radiology of Helsinki University Central Hospital with a 1.5 T Siemens Magnetom Vision imager (Siemens, Erlangen, Germany). A series of 39 ECG-gated contiguous transaxial images was acquired during free respiration using TurboFLASH sequence (Fig. 2a). The pixel size and the slice thickness were 1.95 x 1.95 $mm^2$ and 10 mm, respectively. Also five ECG-gated breath-hold cine SA sections were also acquired (Fig. 2b). In this work only transaxial images were used.

Static PET imaging was performed using a Siemens ECAT (Siemens/CTI, Knoxville, USA) PET scanner. A series of 16 contiguous transmission and emission images was acquired. The pixel size and the slice thickness were 2.41 x 2.41 $mm^2$ and 6.75 mm, respectively (Fig. 2c,d).

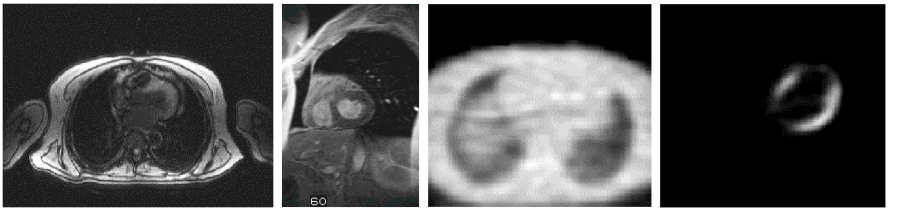

(a) (b) (c) (d)

**Fig. 2.** (a) Transaxial and (b) SA MR images, (c) transmission and (d) emission PET images

## 3 Methods for PET-MR Image Registration

### 3.1 Registration of MR-PET Patient Images

**Surface Based Registration.** The method for surface based registration for MR and PET images was fully described in [2]. It minimizes the distance between the point set from segmented PET transmission image surfaces and a distance map [14] built upon the segmented transaxial MR surfaces. The thorax and lungs surfaces are segmented from transaxial MR and transmission PET images by using the deformable model based segmentation method presented in [7]. Here three optimization methods, Powell [8], simplex [8] and non-standard grid based method [2] (notated as grid optimization method in this paper) were used to find minimum of registration algorithms. Grid method evaluates function value iteratively in a user defined amount of points $T$ and their local neighborhood $\pm\sigma(t)T$, where $\sigma(t)$ is step size for every search direction (6 parameters in rigid registration). The algorithm then chooses from these points the winning nodes (N=2 in this work) for next iteration with smaller local neighborhood. Iterations are repeated until the cost function or local neighborhood reaches a user-predefined value [2] .

**Image Intensity Based Registration.** Image intensity based method uses MI, NMI or CR measures for registration. The similarity measurements for MI and NMI are described in Eqs. (1)–(2) as a function of marginal probabilities $p(a)$, $p(b)$ and a joint probability $p(a, b)$

$$MI(A,B) = \sum_a \sum_b p(a,b) \log \frac{p(a,b)}{p(a)p(b)}, \tag{1}$$

$$NMI(A,B) = \frac{\sum_a p(a) \log p(a) + \sum_b p(b) \log p(b)}{\sum_{a,b} p(a,b) \log p(a,b)}. \tag{2}$$

The CR measure [6] is based on the minimization of the following equation:

$$\mu(A|B) = \frac{Var\left[E(A|B)\right]}{Var(A)}. \tag{3}$$

The idea of the image intensity based registration algorithm is similar for the one presented in [15]. Registered images were first scaled and interpolated (trilinear interpolation) by using voxel dimensions. Simulated images had the same dimensions before registration and scaling was not needed. With patient images, PET image was interpolated to isotropic MR image voxel dimensions with trilinear interpolation. To initialize registration, mass center of the image spaces were registered. During iterative registration procedure, partial volume interpolation was used. Optimization of the registration was done with two standard methods, Powell [8] and simplex [8], and a non standard grid optimization method [2] (see above for a short explanation of grid method). Multiresolution approach was tested with image intensity based registrations, but in practice, only one resolution level was used in this work.

### 3.2 Evaluation Method

The evaluation of PET-MR image registration relies on the simulated data set presented in Sect. 2.1 [9]. Fifty transformations, obtained by randomly sampling the 6 parameter transformation vector, were applied to PET data. The translations were limited to ± 5 cm along each of the three axis (*x, y, z*) and rotations around each axis ranged between ± 5 °. The selection of transformations followed Gaussian distribution and obeyed the previous constraints; N(0, 1.67)) cm for translations and N(0,1.67) degrees for rotations.

The fifty transformed simulated PET transmission images (and emission images) were registered with the MR images by using the surface or intensity based methods described in Sect. 3.1. The registration accuracy is evaluated by computing a Root Mean Square (RMS) error on a set of points belonging to the whole image, the thorax, the heart or the LV, respectively. The RMS error was obtained from the equation;

$$RMS = \sqrt{\frac{1}{n}\sum_{i=1}^{n} \parallel P_i - \hat{I}(T(P_i)) \parallel^2}, \tag{4}$$

where $P_i$ is a voxel-point, $T(P_i)$ is the transformed voxel-point using the known transformations $T$, and $\hat{I}$ is the evaluated registration transformation calculated using the surface or image intensity based registration method.

## 4 Results

### 4.1 Evaluation Using Simulated MR-PET Image

Results for surface and image intensity based registration using simulated images are presented in Table 1. Evaluation method was described in Sect. 3.2. Both mean and SDV values of RMS-error (in mm) were calculated for four areas: whole image, thorax area, heart area and LV. Powell, simplex and grid methods were used for optimizations. In the grid based optimizations the search space was limited to ± 5 cm translations for all 3 directions (*x, y, z*) and ± 5° of rotations around all three axis.

**Table 1.** Registration accuracy (RMS-error in mm) of simulated images with surface and image intensity based registration methods. For each optimization method both an average error of all registrations and an average value over successful registrations (marked with *) are given. The registration was considered to be successful if the registration did reduce RMS error of the misregistered image. Initial misregistrations were selected from gaussian distributions as described in Sect. 3.2. In the Table, best cases are marked in bold (Surf.=Surface, Pow.=Powell, Simp.=Simplex)

| | | Image RMS | Thorax RMS | Heart RMS | LV RMS |
|---|---|---|---|---|---|
| | | $Mean \pm SDV$ | $Mean \pm SDV$ | $Mean \pm SDV$ | $Mean \pm SDV$ |
| **Surf. Pow.** | (50/50) | $22.16 \pm 14.56$ | $15.40 \pm 10.40$ | $11.32 \pm 8.17$ | $11.03 \pm 7.70$ |
| Surf. Pow. | (43/50) | $17.33 \pm 6.97$ | $12.13 \pm 4.63$ | $9.00 \pm 3.55$ | $9.14 \pm 3.91$ |
| Surf. Simp. | (50/50) | $27.32 \pm 14.99$ | $20.90 \pm 12.89$ | $17.45 \pm 12.87$ | $16.90 \pm 13.08$ |
| Surf. Simp.* | (35/50) | $20.23 \pm 7.25$ | $14.82 \pm 5.06$ | $11.92 \pm 5.38$ | $12.08 \pm 6.48$ |
| Surf. Grid | (50/50) | $25.78 \pm 15.16$ | $19.30 \pm 12.31$ | $14.13 \pm 11.63$ | $13.13 \pm 11.57$ |
| Surf. Grid* | (37/50) | $19.31 \pm 8.58$ | $14.24 \pm 6.11$ | $10.27 \pm 4.73$ | $9.94 \pm 5.04$ |
| MI Simp. | (50/50) | $246.24 \pm 184.91$ | $114.82 \pm 89.11$ | $98.55 \pm 105.45$ | $103.05 \pm 113.76$ |
| MI Simp.* | (5/50) | $6.74 \pm 2.50$ | $5.95 \pm 2.71$ | $4.83 \pm 1.52$ | $5.48 \pm 2.30$ |
| MI Grid | (50/50) | $95.21 \pm 37.08$ | $51.17 \pm 21.33$ | $37.54 \pm 29.05$ | $36.42 \pm 30.22$ |
| MI Grid* | (39/50) | $19.72 \pm 6.40$ | $18.07 \pm 8.89$ | $17.59 \pm 7.14$ | $17.41 \pm 6.10$ |
| NMI Pow. | (50/50) | $475.52 \pm 252.88$ | $271.95 \pm 149.71$ | $164.16 \pm 88.96$ | $218.96 \pm 124.45$ |
| NMI Pow.* | (39/50) | $4.88 \pm 2.55$ | $4.11 \pm 2.24$ | $4.33 \pm 2.41$ | $4.42 \pm 2.47$ |
| **NMI Simp.** | (50/50) | $6.96 \pm 2.40$ | $5.02 \pm 1.32$ | $4.57 \pm 1.43$ | $4.36 \pm 1.89$ |
| **CR Simp.** | (50/50) | $6.98 \pm 14.89$ | $5.82 \pm 14.60$ | $5.35 \pm 15.48$ | $5.46 \pm 16.05$ |
| CR Simp.* | (49/50) | $4.85 \pm 2.19$ | $3.72 \pm 1.12$ | $3.12 \pm 0.71$ | $3.15 \pm 0.80$ |

### 4.2 Registration of Ten MR-PET Patient Images

Results for ten patient MR-PET image registrations are presented in Table 2. Patient images were first registered with surface or image intensity based registration methods to obtain registration parameters. Registration parameters were then used to transform corresponding manually segmented PET transmission image (point set from PET transmission image surface) to the coordinates of manually segmented MR image. Mean distance of point set from PET transmission image surface and manually segmented MR image surface was calculated using chamfer distance map algorithm [14]. With patient image registrations also three different optimization methods were used (Powell, simplex and grid). Grid optimization used limited search space as in the case of simulated images.

## 5 Discussion and Conclusion

For simulated images CR and NMI image intensity based registrations with simplex minimization (Table 1) had smaller RMS-errors for all areas than biggest voxel size (8 mm in the z-dimension). Best result was obtained using NMI with simplex minimization and mean RMS error of all fifty registrations was for heart area $4.57 \pm 1.43$ mm (mean $\pm$ SDV). Both NMI and CR with simplex optimization proved also to be very robust; NMI method gave successful registration for

**Table 2.** Registration results of ten patient images for surface and image intensity based registration methods. Error term quantifies the mean distance of the surfaces (manually segmented images) after registration of manually segmented images with the parameters obtained from surface or image intensity based registration methods. In the results which were marked with (*) some cases were excluded if they were visually unsatisfactorily registered (and mean error was more than 30 mm). Best results are marked in bold

| | | $Mean \pm SDV(inmm)$ |
|---|---|---|
| Surface Powell* | (8/10) | $14.23 \pm 2.99$ |
| Surface Simplex* | (8/10) | $11.62 \pm 3.73$ |
| **Surface Grid** | (10/10) | $7.46 \pm 2.46$ |
| **MI Powell*** | (9/10) | $7.17 \pm 3.05$ |
| MI Grid* | (9/10) | $7.93 \pm 1.67$ |
| MI Simplex* | (9/10) | $9.94 \pm 5.50$ |
| NMI Powell* | (9/10) | $10.68 \pm 5.62$ |
| NMI Simplex* | (9/10) | $9.98 \pm 5.33$ |
| **CR Powell** | (10/10) | $9.85 \pm 5.19$ |
| CR Simplex* | (9/10) | $9.60 \pm 5.36$ |

all cases and CR method was unsuccessful in only one case. The registration was considered to be successful if the registration did reduce RMS error of the misregistered image (measured from whole image area). MI registration with simplex minimization method was unsuccessful 45 times out of 50. In the case of Powell optimization, both MI and CR registrations methods were unsuccessful every time (not marked in the Table 1) and NMI registration was unsuccessful 11 times out of 50. We added also additional noise (gaussian) to the simulated images (1%, 5%, 10% and 20%) and tested image intensity based methods. The adding of gaussian noise seemed to increase registration accuracy and robustness especially with MI and NMI registration methods. Additional noise might smooth the cost function and thus improve registration results. In the image intensity based registration methods there can also be small interpolation effects which can also effect to the results. We tested the method presented by Holden *et al.* [16] to reduce interpolation errors. However, the effect of interpolation error seemed to be small compared to the registration error.

Results of the surface based registration with simulated images (Table 1) showed that the mean registration error for surface based method was greater than the voxel size of the registered images (8 mm in the z-direction) with all optimization methods. Best results for surface based registration was obtained with the Powell optimization method with a mean RMS error of $11.32 \pm 8.17$ mm for the whole heart area (for all fifty cases). Powell optimization was also the most robust optimization algorithm of surface based methods with 43 successful registrations (in RMS sense) over fifty registrations.

When registering emission images (simulated images) directly with MR images using image intensity based methods, only about fifth of the cases succeeded (in RMS sense). When considering all registrations (50/50) error values for heart

area were 61.02 ± 71.05 mm, 66.46 ± 34.91, 87.54 ± 63.25 for NMI, CR and MI registrations, respectively. With succeeded cases (in RMS sense) errors for heart area were 7.85 ± 1.21 mm (15/50 succeeded), 6.83 ± 1.38 (10/50) and 8.47 ± 3.57 (8/50) for NMI, CR and MI registrations, respectively. With patient images, results were similar (only visual verification was used). Thus, results indicated that the use of transmission image as a linking mediator is more accurate and reliable way to register PET image and MR image. The problem while using PET transmission image as a linking mediator to register PET emission image to MR image coordinate is that there might be movement artifacts between (or during) PET transmission and emission imaging. Two transmission images, one before and one after emission imaging, could help to reduce this type of movement artefacts.

Registration methods were also tested using simulated images with isotropic voxel sizes. Original image had 256 x 256 x 15 matrix size with voxel size of 1.95 x 1.95 x 8 mm and isotropic image (trilinear interpolation) had 256 x 256 x 58 matrix size with isotropic voxel size of 1.95 $mm^3$. Best results with isotropic voxel sizes were obtained with NMI ($2.89 \pm 0.44$ mm) and CR ($2.89 \pm 0.41$ mm) image intensity based methods (error of all fifty registrations in heart area using simplex minimizations) while with non-isotropic voxel sizes errors were respectively 4.57 ± 1.43 (NMI) and 5.35 ± 15.48 mm (CR). With surface based registration the registration error in heart area (all fifty cases with grid minimizations) was for isotropic voxel size image 8.23±2.28 mm and with non-isotropic voxel sizes image 11.32±8.17 mm. Results indicated, that the use of isotropic voxel sizes might help both image intensity and surface based registration methods. However, execution time of registration with image intensity based method was with isotropic voxel sizes about five times more than with original image dimensions.

When using intensity based methods, the registration time of 256 x 256 x 15 matrix size simulated images was about 25 minutes with grid minimization and about 4 minutes with Powell and simplex minimizations (1.3 GHz PC). In surface based registration of simulated images, the registration time of Powell and simplex optimizations was 1-3 seconds and for the grid optimization about 1 minute. With surface based registration method a point set of about 1000 points from surface or PET transmission image was registered with MR image surface. Surface based registration needed also automatic segmentation of the MR and PET images which both took about 3 minutes for both MR and PET images.

For patient image registration we estimated in our previous work [2] the quality of surface based registration method using surface distance error after registration. Deformable model based segmentation of surfaces was used for both defining surface based registration parameters and for calculating the surface distance error after registration. Surface distance error with grid optimization was 2.8 ± 0.5 mm. In this work, we also used deformable model based method for segmentations of patient images and to obtain surface based registration parameters, but resulting registrations parameters were then used to transform corresponding manually segmented PET transmission images (point set from PET transmission image surface) to the coordinates of manually segmented MR

images. The distance error term of registered manually segmented images was then calculated (Table 2). The computed surface distance error term quantify also the difference between segmentation results of PET and MR thorax images but gives also a reasonable index of the quality of the patient image registration. Results of surface distance errors of patient images indicated that image intensity based methods performed all pretty well but CR with the Powell optimization was the most robust. Results with simulated images and patient images were a little bit contradictory with Powell optimization methods (Powell optimization did not work well with simulated images). MI registration did not work well with simulated images but did perform well with patient images. The noise in the patient MR and PET images might smooth the cost function of MI and help it not to be attracted to a local minima. With surface based registration of patient images grid based optimization gave smallest error values and was also the most robust. Probable reason for this was the limited search space of grid optimization allowing only reasonable results. Results of image intensity based CR method with Powell optimization and surface based registration method with grid optimization were also visually satisfying in 9 of the 10 cases. In one PET image registration, unexpected artifacts in the PET emission image was observed and the visual assessment of that registration result was difficult to confirm; the PET transmission image was visually well registered also in that case.

Image intensity based methods do not need *a priori* extraction of registered structures (e.g. segmentation of surfaces) and are thus promising methods for the automatic registration of images. Still, image intensity based methods need *a priori* knowledge of the nature of registered images to find proper cost function and optimization method for registration. Surface based methods can be sometimes efficient methods when registered structures are clearly visible and easy to segment. For cardiac MR and PET image registrations, it seems that NMI and CR methods with simplex optimizations are more reliable than MI or Powell optimizations. Patient and simulated image registration results were nevertheless slightly contradictory, especially with MI registrations. Surface based methods, with optimization methods allowing limited search space, gave also robust results. Limited search space could also be used with image intensity based registration methods. Also elastic transformations would be good to use e.g. to reduce the effect of breathing in the registration of patient images and will be considered in our future studies.

## References

1. Mäkelä, T., Clarysse, P., Sipilä, O., Pauna, N., Pham, Q., Katila, T., Magnin, I.E.: A review of cardiac image registration methods. IEEE Trans. Med. Imaging, **21** (2002) 1011–1021.

2. Mäkelä, T. J., Clarysse, P., Lötjönen, J., Sipilä, O., Lauerma, K., Hänninen, H., Pyökkimies, E.-P., Nenonen, J., Knuuti, J., Katila, T., and Magnin, I. E.: A new method for the registration of cardiac PET and MR images using deformable model based segmentation of the main thorax structures. In Niessen, W. and Viergever, M., editors, *Lecture Notes in Computer Science 2208:MICCAI01*, (2001) 557–564.
3. Carrillo, A., Duerk, J., Lewin, J., Wilson, D.: Semiautomatic 3-D image registration as applied to interventional MRI liver cancer treatment. IEEE Trans. Med. Imaging **19** (2001) 175–185.
4. Slomka P. J., Dey D., Przetak C., and Baum R.: Automated nonlinear 3-D registration of 18-F FDG wholebody PET with thoracic CT, *J. Nucl. Med.*, **42**:5 (2001) 11P.
5. Zhenghong, L., Berridge, M.S.: PET imaging-based evaluation of aerosol drugs and their delivery devices: nasal and pulmonary studies. IEEE Trans. Med. Imaging **21** (2002) 1324–1331.
6. Roche A. and Pennec X. and Malandain G. and Ayache N.: Rigid Registration of 3-D Ultrasound With MR Images: A New Approach Combining Intensity and Gradient Information. IEEE Trans. Med. Imaging **20** (2001) 1038–1049.
7. Lötjönen J., Reissman P.-J., Magnin I.E. and Katila T.: Model extraction from magnetic resonance volume data using the deformable pyramid. Medical Image Analysis, **4** (1999) 387–406.
8. Press, W.H., Teukolsky, S.A., Vetterling, W.T., and Flannery, B.P.: *Numerical Recipes in C: The art of scientific computing 2nd Edition*. Cambridge Univ. Press, Cambridge, (1992).
9. Pauna N., Croisille P., Costes N., Reilhac A., Mäkelä T., Onuc C., Janier M., Clarysse P.: A strategy to quantitatively evaluate MRI/PET cardiac registration methods using a Monte Carlo simulator. Accepted to FIMH2003.
10. Reilhac A., Gregoire M.-C., Costes N., Lavanne, F., Pierre C., Diou A., and Pujol J.-F.: A PET Monte Carlo simulator from numerical phantom: Validation against the EXACT ECAT HR+ scanner. In *Proc. IEEE Nuclear Sciences Symposium*, vol. 3 (1999) 1527–1531.
11. Reilhac A., Lartizien C., Costes N., Sans S., Comtat C., Evans A.: Accounting for singes rates related phenomena in PET Monte-Carlo based simulations. In *IEEE Nuclear Sciences Symposium*, (2002), in press.
12. Hartiala, J. and Knuuti, J.: (1995). Imaging of heart by MRI and PET. *Ann. Med.*, **27** (1995) 35–45.
13. Lauerma K., Niemi P., Hänninen H., Janatuinen T., Voipio-Pulkki L., Knuuti J., Toivonen L., Mäkelä T., Mäkijärvi M. A. , Aronen H. J.: Multimodality MR imaging assessment of myocardial viability: combination of first-pass and late contrast enhancement to wall motion dynamics and comparison with FDG-PET. Radiology, **217** (2000) 729–736.
14. Borgefors G.: Hierarchical chamfer matching: A parametric edge matching algorithm. IEEE Trans. Pattern Anal. Machine Intell., **6** (1988) 849–865.
15. Maes F., Collignon A., Vandermeulen D., Marchal G. and Suetens P.: Multimodality Image Registration by Maximization of Mutual Information. IEEE Trans. Med. Imaging **16**:2 (1997) 187–198.
16. Holden M., Hill D., Denton E., Jarosz J., Cox T., Rohlng T., Goodey J., Hawkes D.: Voxel similarity measures for 3-D serial MR brain image registration. IEEE Trans. Med. Imaging **19**:2 (2000) 94–102.

# Left Ventricular Flow Dynamics and Transmural Gradients in Myofiber Shortening with MRI-Tagging

T. Arts[1], T. Delhaas[2], A. van Susteren[1], G. Snoep[3], and F.W. Prinzen[2]

Departments of [1]Biophysics and [2]Physiology, Cardiovascular Research Institute
Maastricht University, 6200MD Maastricht, The Netherlands
[3]Department of Radiology, Academic Hospital Maastricht
6202AZ Maastricht, The Netherlands

**Abstract.** Most cardiac diseases are related to non-uniformities in contractile function. Such regional non-uniformities can be recognized conventionally, but transmural gradients in mechanical function cannot be determined that easily. We propose a method to assess transmural differences in myofiber shortening, using MRI-tagging of the heart. Midwall motion of 5 short-axis slices of the left ventricle was determined non-invasively. Using a model of cardiac motion, the transmural distribution of deformation of the left ventricular wall was determined. On the basis of remodeling rules, the transmural course of myofiber orientation was estimated. From deformation and fiber orientation data transmural differences in myofiber shortening were calculated. The method appears sensitive to distinguish patients with aortic stenosis from healthy volunteers.

## 1 Introduction

Most cardiac diseases are related to non-uniformities in mechanical function. Regional non-uniformities in contractile function, e.g. due to coronary artery stenosis, can be recognized conventionally with 2-D echocardiography, or more indirectly, by mapping coronary perfusion or metabolic uptake using a gamma camera. Theoretically as well as in animal experiments, in sick hearts often also transmural gradients in coronary perfusion, metabolic uptake, and in mechanical function are to be expected.

Common clinical techniques are not designed to recognize transmural differences in function. With MRI-tagging [1] regional motion of a cross-section of the heart can be determined with a resolution on the order of the distance between the tags, which is generally about 6 mm for human applications. In a straightforward approach transmural differences of contractile function in the wall of the left ventricle may be determined from measurements of local deformation and myofiber orientation. However, the resolution of deformation measurement is limited. In principle, MRI diffusion tensor imaging [2] may have sufficient resolution to determine differences in function in the beating heart. However, the amount of scanning time and the presence of motion of heart and patient during the scan makes mapping of fiber orientation cumber-

I. Magnin et al. (Eds.): FIMH 2003, LNCS 2674, pp. 234–241, 2003.

some. Thus, the straightforward approach to measure transmural differences in function is not likely to work with currently available techniques.

In the present study we propose to use MRI-tagging in such a way that the inherent technical problems are circumvented, and available information is used optimally. Midwall motion of the cardiac wall can be measured with MRI tagging. The transmural resolution of MRI-tagging is considered insufficient. Therefore, a kinematic model is proposed to transmurally extrapolate midwall motion to a map of deformation of the whole wall. Since measurement of myofiber orientation is difficult, an model of myofiber adaptation has been used to estimate fiber orientation [3]. The latter model uses adaptation rules for myofiber orientation in cardiac tissue, subject to a known chronic pattern of deformation [4]. As a result we estimate transmural differences in myofiber shortening non-invasively in patients.

## 2 Methods

### 2.1 Image Acquisition

MRI experiments were performed at 1.5 T (Gyroscan NT, Philips Medical Systems, Best, The Netherlands) on human subjects. Images were acquired using ECG-triggering while subjects hold breath over about 12 s. Five parallel short-axis images of the heart were obtained, evenly distributed from apex to base (Fig. 1). One non-tagged cine image was used for contouring about 150 ms after peak ECG. Series of line-tagged images from the same slices were obtained with time intervals of 18-22 ms, using spatial modulation of the magnetization [1] over a period of about 80% of the cardiac cycle. Used parameter settings: echo time 10 ms, slice thickness 8 mm, field of view 200-250 mm, image size 256 x 256 pixels.

### 2.2 Image Analysis

To quantify motion of the tags MR-images were analyzed off-line, using homemade software for MATLAB 5.3.1 (or 6.0; The MathWorks Inc., Natick, Massachusetts). In the reference cine-image, the LV wall was manually outlined for each slice. Papillary muscles were excluded from the wall. The horizontally tagged images were spatially band filtered around the line tag frequency (spatial frequency 0.17 $mm^{-1}$, ratio of bandwidth to center frequency 1.0). With the use of a correlation method previously applied for pulsed ultrasonic echo signals [5], from the successive images with horizontal tag lines, vertical displacement maps were calculated for each time interval. Similarly, the images with vertical tags were used to obtain horizontal displacement maps. Per slice, the midwall circle and wall area were determined from the delineated wall contours in the cine-image.

### 2.3 Model of 3D Motion in the Cardiac Wall

Motion around midwall was determined with high precision. Near the inner and outer boundaries of the wall, motion appeared however less accurately determined, probably due to boundary effects. We modeled the motion field near the equator by that of an incompressible thick-walled cylinder, subject to circumferential and axial shortening, and torsion. Torsion is an axial gradient of circumferential rotation of the wall. It was defined quantitatively by the axial-circumferential shear ($\varepsilon_{zc}$) at midwall (Fig. 1).

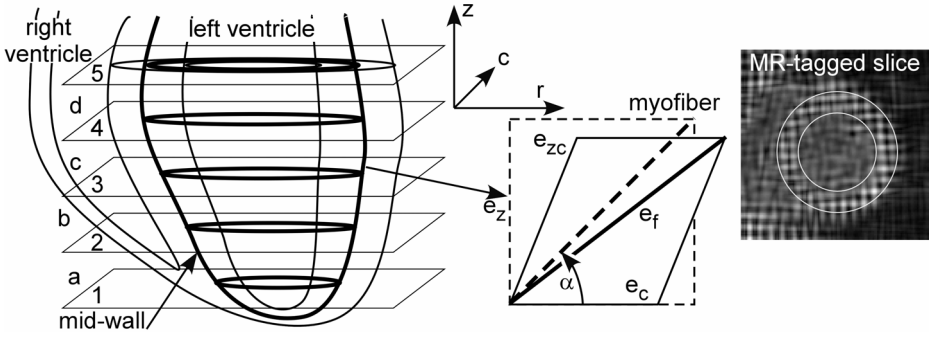


**Fig. 1.** Schematic representation of the heart. Short axis slices of the heart are imaged from apex to base, numbered 1-5. Deformations are estimated between the slices, indicated by letters a-d. The image at the right shows the sum of horizontally and vertically band filtered tagged images, together with the epicardial and endocardial contours of the left ventricle. Symbols [r, c, z] refer to the radial, circumferential and axial coordinate. An originally rectangular surface (broken line) deforms by axial ($e_z$) and circumferential ($e_c$) extension, and shear $\varepsilon_{zc}$. The myofiber follows the diagonal, having a helix angle $\alpha$ with the circumference. Myofiber extension has been indicated by $e_f$.

In the reference state, the shape was defined by midwall enclosed area ($A_{mRef}$) and wall area ($A_{wRef}$). Furthermore, both midwall enclosed area ($A_m$) and midwall shear ($\varepsilon_{zc}$) were considered to be known as a function of time. Fifty percent area division of the wall has defined Midwall. Midwall myofibers are directed circumferentially [6]. Thus, at midwall myofiber extension ($e_{fm}$) is equal to circumferential extension ($e_{cm}$), which depends on the enclosed area ($A_m$) by:

$$e_{fm} = e_{cm} = \sqrt{A_m / A_{mRef}} \tag{1}$$

In the normal heart, the myofiber structure is likely to adapt so that myofiber strain during ejection is homogeneous [4]. Mean myofiber extension $e_{fMean}$ depends on the ratio of cavity volume ($V_{cav}$) to wall volume ($V_w$). Using that midwall volume ($V_m$) encloses the cavity and half of the wall, it is found [7]:

$$e_{fMean} = \frac{1+3\dfrac{V_{cav}}{V_w}}{1+3\dfrac{V_{cav\,Ref}}{V_w}} = \frac{\dfrac{V_m}{V_w}-\dfrac{1}{6}}{\dfrac{V_{m\,Ref}}{V_w}-\dfrac{1}{6}} \tag{2}$$

For a cylinder the ratio $V_m/V_w$ is equal to the ratio $A_m/A_w$. Assuming that wall volume is constant during deformation, wall area $A_w$ is inversely proportional to axial extension $e_z$. Thus, by setting midwall myofiber extension (Eq. 1) equal to mean myofiber extension (Eq. 2), it follows:

$$\frac{\left(\dfrac{A_m}{e_z A_{w\,Ref}}-\dfrac{1}{6}\right)}{\left(\dfrac{A_{m\,Ref}}{A_{w\,Ref}}-\dfrac{1}{6}\right)} = \sqrt{\frac{A_m}{A_{m\,Ref}}} \tag{3}$$

From Eq. (3), axial extension $e_z$ can be solved as a function of measured areas. The radius of a material point in the wall depends on the fractional depth h in the wall and $A_m$:

$$r(h, A_m) = \sqrt{\frac{A_m + hA_{w\,Ref}}{\pi e_z}} \qquad \text{with } |h|<0.5 \tag{4}$$

In the reference state, in Eq. (4) it should be substituted $A_m=A_{mRef}$. Thus for circumferential extension $e_c$ it is found:

$$e_c = \frac{r(h, A_m)}{r(h, A_{m\,Ref})} \tag{5}$$

Torsion, defined as the axial gradient of rotation, induces shear $\varepsilon_{zc}$. In experiments, during the ejection phase, the midwall shear to shortening ratio SSRmid was determined by linear regression as the slope of midwall shear $\varepsilon_{zc}$ as a function of the natural logarithm of midwall myofiber extension $e_{fm}$ (Eq. 1). Conform a model of cardiac wall motion [8]; we assume wall shear $\varepsilon_{zc}$ to be constant across the wall. Thus, local myofiber extension $e_f$ may be expressed as a function of $A_m$, $A_{mRef}$, $A_{wRef}$, SSRmid, depth in the wall h, and helix angle $\alpha$:

$$e_f = fu\left(A_m, A_{m\,Ref}, A_{w\,Ref}, SSRmid, h, \alpha(h)\right) = \frac{}{\sqrt{(e_z \sin\alpha)^2 + (e_c \cos\alpha + \varepsilon_{zc} e_z \sin\alpha)^2}} \tag{7}$$

From anatomical studies [6, 9] the myofiber helix angles at the endocardium ($\alpha_{endo}$) and epicardium ($\alpha_{epi}$) are known to be about +1 rad and –1 rad, respectively. We assume that in the normal heart myofiber extension during ejection is uniformly distributed over the wall. Knowing cardiac deformation characteristics, Eq. (7) and Eq. (2) are combined to solve $\alpha(h)$ for all slices i by minimizing

$$\sum_i E(\alpha_i, h_i) = \sum_i \left(e_f(\alpha_i, h_i) - e_{fMean}\right)^2 \quad \text{with } |h_i|<0.5 \qquad (8)$$

The values of $h_i$ were uniformly distributed in the range $-0.5<h_i<+0.5$. For deformation of the average young volunteer heart [10] it was found experimentally as shown in column 'Ref' of the table.

Midwall enclosed area at mid ejection has been used as reference: $A_{mRef}=\sqrt{(A_{mbe}*A_{mee})}$. Applying 7 shells, for the helix angles it was found $\alpha_i$= [0.70, 0.51, 0.30, 0.09, -0.15, -1.09, -1.07]. After substitution of these angles in Eq. (7), the transmural course of myofiber extension $e_f$ was calculated for examples of a healthy volunteer and an aortic stenosis patient.

Natural myofiber strain $\varepsilon_f$ has been defined as the natural logarithm of myofiber extension $e_f$. Parameter TransDif has been defined as the epi-endo difference of natural myofiber strain, as normalized to mean natural myofiber strain. Its value is calculated by linear regression over the shells i in the wall:

$$\text{TransDif} = \frac{\sum_i \varepsilon_{f,i} h_i}{\bar{\varepsilon}_{f,i} \sum_i h_i^2} \quad \text{with } \varepsilon_f = \ln(e_f) \qquad (9)$$

| | | Ref | Example Fig. 2 | Aortic Stenosis |
|---|---|---|---|---|
| Midwall area at begin ejection ($mm^2$) | $A_{mbe}$ | 3050 | 3310 | 3050 |
| Midwall area at end ejection ($mm^2$) | $A_{mee}$ | 2410 | 2528 | 2410 |
| Wall area at mid ejection (reference) ($mm^2$) | $A_{wRef}$ | 2295 | 3092 | 2807 |
| Midwall Shear to Shortening Ratio | SSRmid | 0.524 | 0.760 | 1.070 |
| TransDif (calculated) | | 0.0 | 0.125 | 0.857 |

## 3 Results

In Fig. 2, midwall cross-sectional area is shown as a function of time for 5 short-axis slices. Near the equator, these areas were maximum. Areas of all slices follow the same pattern, i.e. a decrease during ejection and an increase during the fast filling phase. In the negative time derivative of mean slice area, aortic volume flow and early mitral inflow can be recognized. Rotation of the slices is also shown as a function of time.

In Fig. 2 at the right, midwall mechanics are summarized. The top tracings show midwall circumferential natural strain ($\varepsilon_{ccm}= \ln[\sqrt{(A_m/A_w)}]$). The shape of these curves is qualitatively similar to that of midwall enclosed area. Midwall shear $\varepsilon_{zc}$ represents torsional deformation between the slices. The midwall shear to shortening ratio SSRmid has been defined as the slope of $\varepsilon_{zc}$ versus midwall circumferential natural strain $\varepsilon_{ccm}$ between the slices during the ejection phase. For the reference state, TransDif (Eq. 9) equals zero by definition. The values of TransDif, as determined in the healthy volunteer of Fig. 2 and for an aortic stenosis patient are shown in the table.

## 4 Discussion

Applying image analysis to the sequence of tagged MRI-images, in 5 slices rotation and midwall enclosed area were determined as a function of time during the cardiac cycle. Wall area was determined by manual contouring in one regular cine MRI-image of the cross-section of the left ventricle. In short-axis cross-sections, the midwall contour could be followed using motion data as derived from analysis of time series of MR-tagged images. Using the property of incompressibility of the cardiac wall, motion in the whole cardiac wall was estimated. Myofiber orientation was estimated with adaptation rules of cardiac tissue structure subject to chronic regular deformation [4]. Thus, myofiber strain was estimated as a function of time during the cardiac cycle. In the healthy volunteer, transmural differences in myofiber strain were little. The analysis showed that in an aortic stenosis patient subendocardial myofiber shortening was found to be less than subepicardial myofiber shortening.

Changes in cavity area were determined by measurement of radial tissue flux across the midwall contours. These area changes were determined with so little noise that the time derivative of mean cavity area (dA/dt) was a clear signal (Fig. 2). During ejection, the time course of dA/dt was similar to the negative of a familiar aortic flow signal. During diastole, the time course of the fast mitral filling phase could be recognized as well. For a secure volume flow calibration, analysis of base to apex motion of the left ventricle should be added to the analysis.

Transmural gradients of deformation tensor components such as shear and shortening could not easily be determined directly. And even if the local deformation gradient could be determined accurately, the problem remains how to deduct myofiber shortening from local myofiber orientation and this local deformation. For estimating myofiber strain, an angular accuracy of about $\pm 10°$ is required. Since within the cardiac wall the helix angle ($\alpha$) varies transmurally by about 10°/mm, a resolution of 1 mm is needed for matching the deformation field to the field of myofiber orientation. With current measuring techniques this condition cannot be met easily. The proposed modeling method circumvents the problem to determine motion and myofiber orientation with a high resolution. Thus, the latter method is likely to be preferred over a direct measurement.

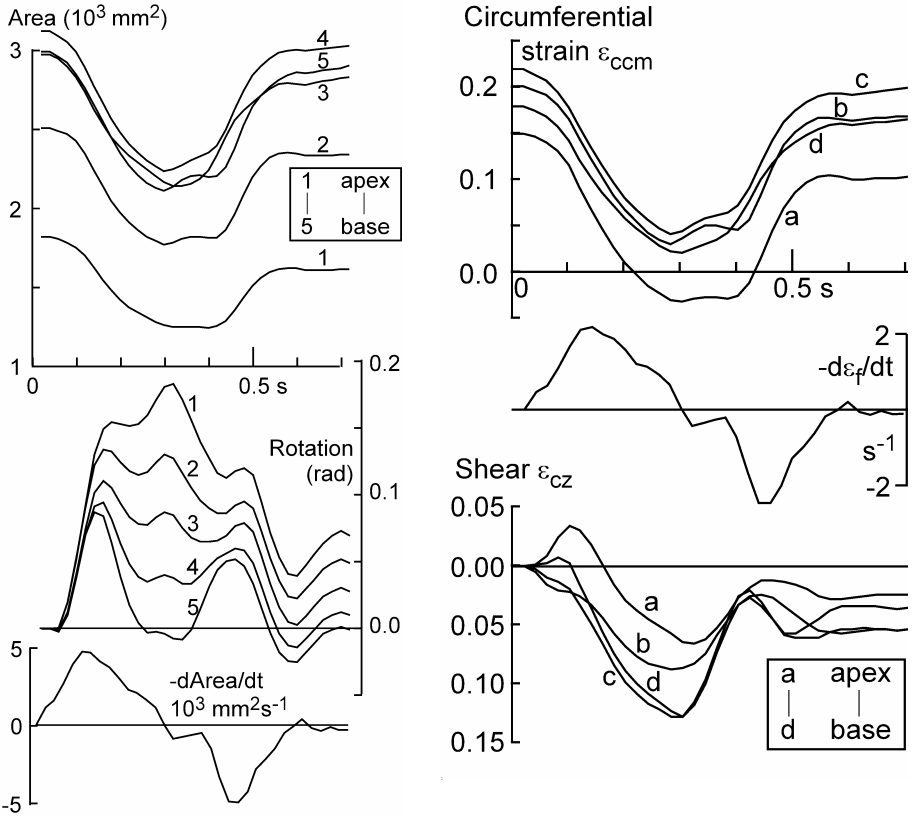


**Fig. 2.** Left: Midwall enclosed area and rotation of 5 short axis slices (1-5) as a function of time during the cardiac cycle. The time derivative of area reflects aortic outflow and mitral inflow. Right: Cardiac deformation (a-d) in the sections between the slices is shown by midwall circumferential strain $\varepsilon_{ccm}$ and shear $\varepsilon_{zc}$. Natural myofiber strain rate $d\varepsilon_f/dt$ is very similar to the time derivative of area.

## 5 Conclusion

With MRI-tagging motion of the heart can be followed in time. Transmural differences in wall motion do not easily reflect transmural differences in contractile function. However, using modeling techniques, transmural differences in myofiber function were quantified from measured motion of the midwall region without the need to detect transmural differences in motion. On the basis of remodeling rules, the transmural course of myofiber orientation was estimated. Midwall motion was extrapolated to predict motion inside the whole wall. From the ratio of torsional shear and contraction together with the ratio of cavity area to wall area transmural differences in

myofiber shortening could be estimated. The method appears sufficiently sensitive to distinguish a patient with aortic stenosis from a healthy volunteer.

**Acknowledgement.** The work has been supported by the Netherlands Heart Foundation (NHS), grants 98.035 and 2000.T036.

## References

1. Axel, L. and L. Dougherty. MR imaging of motion with spatial modulation of magnetization. Radiology, 1989. 171: 841-845.
2. Tseng, W.Y., T.G. Reese, R.M. Weisskoff, T.J. Brady, and V.J. Wedeen. Myocardial fiber shortening in humans: initial results of MR imaging. Radiology, 2000. 216: 128-39.
3. Rijcken, J., P.H.M. Bovendeerd, A.J.G. Schoofs, D.H. van Campen, and T. Arts. Optimization of cardiac fiber orientation for homogeneous fiber strain during ejection. Ann Biomed Eng, 1999. 27: 289-297.
4. Arts, T., F.W. Prinzen, L.H.E.H. Snoeckx, J.M. Rijcken, and R.S. Reneman. Adaptation of cardiac structure by mechanical feedback in the environment of the cell, a model study. Biophys J, 1994. 66: 953-961.
5. De Jong, P.G.M., T. Arts, A.P.G. Hoeks, and R.S. Reneman. Determination of tissue motion velocity by fast correlation of pulsed ultrasonic echo signals. Ultrasonic Imaging, 1990. 12: 84-98.
6. Geerts, L., P. Bovendeerd, K. Nicolay, and T. Arts. Characterization of the normal cardiac myofiber field in goat measured with MR Diffusion Tensor Imaging. Am J Physiol, 2002. 283: H139-H145.
7. Arts, T., P.H.M. Bovendeerd, F.W. Prinzen, and R.S. Reneman. Relation between left ventricular cavity pressure and volume and systolic fiber stress and strain in the wall. Biophys J, 1991. 59: 93-103.
8. Arts, T., W.C. Hunter, A.S. Douglas, A.M.M. Muijtjens, and R.S. Reneman. Description of the deformation of the left ventricle by a kinematic model. J Biomech, 1992. 25: 1119-1128.
9. Streeter, D.D. Gross morphology and fiber geometry of the heart, in The cardiovascular system, the heart, R.M. Berne, Editor. 1979, Am Physiol Soc: Bethesda, Maryland, USA. 61-112.
10. Van der Toorn, A., P. Barenbrug, G. Snoep, F.H. Van der Veen, T. Delhaas, F.W. Prinzen, and T. Arts. Transmural gradients of cardiac myofiber shortening in aortic valve stenosis patients using MRI-tagging. Am J Physiol, 2002. 283: H1609-1615.

# Intravascular Ultrasound Images Vessel Characterization Using AdaBoost

Oriol Pujol[1], Misael Rosales[1], Petia Radeva[1], and Eduard Nofrerias-Fernández[2]

[1] Computer Vision Center, Universitat Autònoma de Barcelona, Edifici O, Campus UAB, Bellaterra. Spain
{oriol,misael,petia}@cvc.uab.es
[2] Hospital Universitari Germans Trias i Pujol, Can Ruti. Barcelona. Spain

**Abstract.** This paper presents a method for accurate location of the vessel borders based on boosting of classifiers and feature selection. Intravascular Ultrasound Images (IVUS) are an excellent tool for direct visualization of vascular pathologies and evaluation of the lumen and plaque in coronary arteries. Nowadays, the most common methods to separate the tissue from the lumen are based on gray levels providing non-satisfactory segmentations. In this paper, we propose and analyze a new approach to separate tissue from lumen based on an ensemble method for classification and feature selection. We perform a supervised learning of local texture patterns of the plaque and lumen regions and build a large feature space using different texture extractors. A classifier is constructed by selecting a small number of important features using AdaBoost. Feature selection is achieved by a modification of the AdaBoost. A snake is set to deform to achieve continuity on the classified image. Different tests on medical images show the advantages.

## 1 Introduction

Intravascular Ultrasound Images (IVUS) are an excellent tool for direct visualization of vascular pathologies and evaluation of the lumen and plaque in coronary arteries. However, visual evaluation and characterization of plaque require integration of complex information and suffer from substantial variability depending on the observer. This fact explains the difficulties of manual segmentation prone to high subjectivity in final results.

Automatic segmentation will save time to physicians and provide objective vessel measurements [6]. Nowadays, the most common methods to separate the tissue from the lumen are based on gray levels providing non-satisfactory segmentations. This leads to use more complex measures to discriminate lumen and plaque. One of the most wide spread methods in medical imaging for such task is texture analysis. The problem of texture analysis has played a prominent role in computer vision to solve problems of object segmentation and retrieval in numerous applications [4,5]. This approach, encodes the textural features of our image, and provide a feature space in which a classification based on such primitives is easier to perform.

I. Magnin et al. (Eds.): FIMH 2003, LNCS 2674, pp. 242–251, 2003.

In general, two approaches are used for texture analysis: supervised and unsupervised analysis. Our scheme will use supervised texture analysis. Texture analysis has an important problem in both approaches, the precise location of textured object boundaries. Previous works in segmentation of IVUS images have shown different ways to segment lumen and to classify tissues [7,8,9]. However, these approaches usually are semi-automatic, and very sensitive to image artifacts.

The classification process is critical step in any image segmentation problem. Recently, arcing and boosting techniques have been applied successfully to different computer vision areas [1]. In this paper we analyze the relevance of boosting techniques, and in particular AdaBoost in Intravascular Ultrasound Image analysis for a dual task, creation of a strong classifier and feature selection. This process is integrated in an automatic framework for discrimination of lumen and plaque. The method is divided in 4 steps, corresponding to preprocessing step, feature extraction, feature selection and classification, and higher level organization of data using deformable models. An objective evaluation of the different approaches is made and validated by the physicians in patients with different pathologies and images with different topologies. The paper is organized as follows: Sect. 2 introduces the AdaBoost procedure for feature selection and classification assembling of "weak" classifiers; Sect. 3 describes the framework in which the AdaBoost is integrated, pre-processing considerations, the feature space selected and deformable models; Sect. 4 shows the results of the methods and Sect. 5 discuss the future lines.

## 2 AdaBoost for Feature Selection and Classification

Considering the general problem of texture analysis without any *a priori* information about the scale, orientation, ... a high dimensional feature space is generated, involving texture descriptors of different scales, orders, orientation, etc. Nowadays, there are different kinds of feature spaces that try to encode the texture information: Gabor filters responses, derivatives of Gaussian filters, wavelets, co-occurrence matrices measures, fractal spaces, Markov random fields, ... Therefore, a lot of processing time is invested in the characterization of the texture and the decision of the feature space. This problem emphasizes the importance of relevant feature selection, allowing subsequent reduction of time processing in the classification step. On the other hand, the decision of a classifier is not an easy task. Recently, arcing procedures (Adaptative reweighing and combining) have been credited to lead to very high classification ratios using "weak" learning processes [15,1,2]. Boosting allows the use of "weak" classifiers with accuracy on the training set greater random classification. The goal is to create a high performant classifier ensemble of "weak" classifiers.

### 2.1 AdaBoost Procedure

Adaptative Boosting (AdaBoost) is an arcing method which allows the designer to continue adding "weak" classifiers until some desired low training error has

been achieved. A weight is assigned to each of the feature points. These weights measure how accurate the feature point is being classified. If it is accurately classified, then its probability of being used in subsequent learners is reduced, or emphasized otherwise. This way, AdaBoost focuses on difficult features.

To address both problems: feature selection and classification process, a weak learning algorithm is designed to select the single features which best separate the different classes. In our problem, the different classes are tissue and blood. For each feature, the weak learner determines the optimal classification threshold function, so that the minimum number of feature points is misclassified. The weak classifier, $h_j(x)$ consists of a feature $f_j$, and the parameters of the classifier $\Theta_j$. Those parameters are a threshold $\theta_j$, a parity $p_j$ and $W_j$, a classifier trained by linear discriminant analysis. Although the threshold separates the two classes it is not enough to identify which class is in either side of the threshold. Therefore a parameter $p_j$ (parity) is needed to indicate the direction of the inequality sign when classifying:

$$h_j(x) = \begin{cases} 1 & \text{if } p_j f_j(x) < p_j \theta_j \\ 0 & \text{otherwise} \end{cases}$$

The algorithm is described as follows

- Determine a supervised set of feature points $\{x_i, c_i\}$ where $c_i = \{-1, 1\}$ is the class associated to each of the features classes (blood and tissue respectively)
- Initialize weights $w_{1,i} = \frac{1}{2m}, \frac{1}{2l}$ for $c_i = \{-1, 1\}$ respectively, where $m$ and $l$ are the number of feature points for each class.
- For $t = 1..T$:
  - Normalize weights
    $$w_{t,i} \leftarrow \frac{w_{t,i}}{\sum_{j=1}^{n} w_{t,i}}$$
    so that $w_t$ is a probability distribution.
  - For each feature, $j$ train a classifier, $h_j$ which is restricted to using a single feature. The error is evaluated with respect to $w_t$, $\epsilon_j = \sum_i w_i |h_j(x_i) - c_i|$.
  - Choose the classifier, $h_t$ with the lowest error $\epsilon_t$.
  - Update the weights:
    $$w_{t+1,i} = w_{t,i} \beta_t^{e_i}$$
    where $e_i = 1$ for each well-classified feature and $e_i = 0$ otherwise. $\beta_t = \frac{\epsilon_t}{1-\epsilon_t}$. Calculate parameter $\alpha_t = -log(\beta_t)$.
- The final "strong" classifier is:

$$h(x) = \begin{cases} 1 & \sum_{t=1}^{T} \alpha_t h_t(x) \geq 0 \\ 0 & \text{otherwise} \end{cases}$$

Therefore, the strong classifier is the ensemble of a series of simple classifiers ("weak"). Parameter $\alpha_t$ is the weighting factor of each of the classifiers. The loop ends whether the classification error of a "weak" classifier is over 0.5, the

estimated error for the whole "strong" classifier is lower than a given error rate or if we achieve the desired number of "weaks". The final classification is the result of the weighted classifications of the "weaks". The process is designed so that if $h(x) > 0$, then pixel $x$ belongs to class "tissue".

### 2.2 Weak Classifiers

The weak classifier has an important role in the procedure. Different approaches can be used, however it is relatively interesting to center our attention in low time-consuming classifiers.

The first approach we have tried is a classical learner, modelling the feature points as Gaussian distributions. This is an easy scheme which allow us to introduce the weights easily, simply calculating the weighed mean and covariance of the classes at each step of the process:

$$\mu_{i,t}^{j} = \sum w_{i,t} x_i \qquad \Sigma_{i,t}^{j} = \sum w_{i,t} (x_i - \mu_{i,t}^{j})^2$$

for each $x_i^j$ point in class $C_j$. $W_{i,j}$ are the weights for each data point.

This classifier, though it leads to fairly good results is highly constrained to the N features of the N-dimensional feature space. If N is not enough large, the procedure could not improve its performance. Therefore we propose another classifier for relatively low dimensional spaces (2 magnitude orders). Because the selection of a single feature for each of the classifiers is quite a hard constraint, we can look for the most significant pair of features which discriminates better the blood and the tissue.

For each pair of features of our space we use linear discriminant analysis to find the transformation which leads to the most discriminant axis. We chose the pair of features with the lowest error. We can describe this "weak" classifier as follows.

$$h(x) = \begin{cases} 1 & \text{if } p_j W_j^t x < p_j \theta_j \\ 0 & \text{otherwise} \end{cases}$$

where $p_j$ and $\theta_j$ are the parity and threshold parameters and $W_j$ is defined as follows:

$$W_j = \Sigma_j^{-1} (\mu_{-1,j} - \mu_{1,j})$$

which is the canonical variate. $W_j$ is the principal axis of the solution of the linear discriminant analysis system which maximizes

$$J(W) = \frac{W^t S_B W}{W^t S_W W},$$

where $S_B$ is the between-class scatter $S_B = \sum_{i=1}^{C} N_i (\mu_i - \mu)(\mu_i - \mu)^t$ and $S_W$ is the within-class scatter$S_W = \sum_{i=1}^{C} \sum_{x \in C_i} (x - \mu_i)(x - \mu_i)^t$, where $\mu$ is the mean value of the whole data, c is the number of classes and $N_i$ is the number of samples in class $i$.

# 3 Integration Framework

## 3.1 Cartesian to Polar Conversion

Intravascular Ultrasound Images are usually displayed as a cartesian image although the transducer acquires the echoes while rotating. This gives an accurate description of the physiology of the artery, but it also has some disadvantages. Due to the fact that the transducer casts rays at a definite angular speed, not all the space can be covered. That means that the image shown is inaccurate because of the interpolation process performed to fill the distance between rays. The interpolation process creates false structures, which are seen as long circular areas with similar intensities, while the real structure has not such length.

This press us to work with the polar representation of the data, keeping just the rays with information. Figure 1 shows an example of the process. On the left, the polar image, which the physicians see, and on the right side the polar conversion of the image. Since we do not have access to the raw data from the transducer, or to some technical specifications of the same, we have chosen a 360 degrees representation of the image.

## 3.2 Feature Extraction

The input of the feature extraction module is the transformed image. The response of the method is a feature vector. The texture feature spaces selected for our approach is twofold: the co-occurrence matrices space and the cumulative moments space. They both provide good representation of the texture space for our problem.

The Gray Level Co-occurrence Matrix is a well-known statistical tool for extracting second-order texture information from images [10]. In the co-occurrence method, the relative frequencies of gray level pairs of pixels at certain relative displacement are computed and sorted in a matrix, the co-occurrence matrix $P$. For $G$ gray levels in the image, P will be of size $G \times G$. If $G$ is large, the number of pixel pairs contributing to each element, $p_{i,j}$ in $P$ is low, and the statistical significance poor. On the other hand if the number of gray levels is low, much of the texture information may be lost in the image quantization. The element

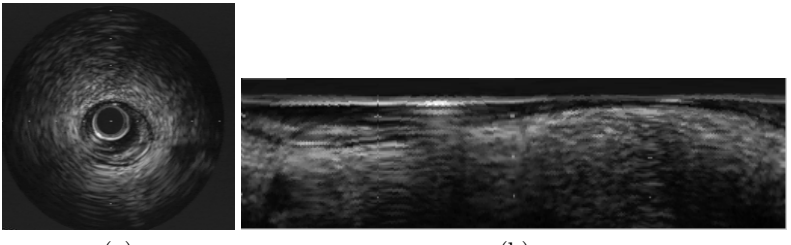

(a) (b)

**Fig. 1.** (a) Original image. (b) Polar transformed image

values in the matrix, when normalized are bounded by $[0, 1]$, and the sum of all element values is equal to 1.

$$P(i, j, D, \theta) = P(I(l, m) = i \text{ and } I(l + Dcos(\theta), m + Dsin(\theta)) = j)$$

where $I(l, m)$ is the image at pixel $(l, m)$, $D$ is the distance between pixels and $\theta$ is the angle. As suggested by other researchers [11,12] the nearest neighbor pairs at orientations $\theta = \{0^o, 45^o, 90^o, 135^o\}$ will be used in the experiments. To describe this two-dimensional probability density function, several features are computed. We will consider six of the most used measures: Energy, Entropy, Inverse Differential Moment, Shade, Promenance and Inertia, for each of the orientations.

Geometric moments have been used effectively for texture segmentation in many occasions [13]. Actually, any set of parameters obtained by projecting an image onto a 2D polynomial basis are called moments. Then, since different sets of polynomials up to the same order define the same subspace, any complete set of moments up to given order can be obtained from any other set of moments up to the same order. A fast computation set of moments is the accumulation local moments. Two kind of accumulation local moments can be computed, direct accumulation and reverse accumulation. Since direct accumulation is more sensitive to round off errors and small perturbations in the input data [14], the reverse accumulation moments are used.

The reverse accumulation moment of order $(k-1, l-1)$ of matrix $\mathbf{I}_{ab}$ is the value of $\mathbf{I}_{ab}[1, 1]$ after bottom-up accumulating its column $k$ times (i.e., after applying $k$ times the assignment $\mathbf{I}_{ab}[a-i, j] \leftarrow \mathbf{I}_{ab}[a-i, j] + \mathbf{I}_{ab}[a-i+1, j]$, for $i = 0$ to $a-1$, and for $j = 1$ to $b$), and accumulating the resulting first row from right to left $l$ times (i.e., after applying $l$ times the assignment $\mathbf{I}_{ab}[1, b-j] \leftarrow \mathbf{I}_{ab}[1, b-j] + \mathbf{I}_{ab}[1, b-j+1]$, for $j = 1$ to $b-1$). The reverse accumulation moment matrix is defined so that $\mathbf{R}_{mn}[k.l]$ is the reverse accumulation moment of order $(k-1, l-1)$.

Once the image is represented in the feature space, the next step is the classification process and feature selection, explained in detail in the former section.

### 3.3 Snake-Based Accurate Location of Borders

The result after the classification step is a clear image in which the main structures are clearly visible, but there is no connection among them. This is a good example in which a snake can be useful. The basic target of active contours [16,17,18] is to find a parameterized curve that minimizes the weighted sum of its internal energy and external energy. Given a traditional snake curve $\mathbf{x}(s) = (x(s), y(s)), s \in [0, 1]$, the snake can be formulated as the minimization of the equation $S(\mathbf{x}) = \int_0^1 (\alpha|\mathbf{x}'(s)|^2 + \beta|\mathbf{x}''(s)| + E_e)ds$; where $\alpha$ and $\beta$ are weighting factors and $E_e$ the external energy.

The typical potential function designed to lead a deformable contour toward step edges is $P(x, y) = -\gamma|\nabla[G_\sigma(x, y) * I(x, y)]|^2$ where $\nabla$ is the gradient operator, $\gamma$ is a weighting parameter, $G_\sigma(x, y)$ is the gaussian filter of standard

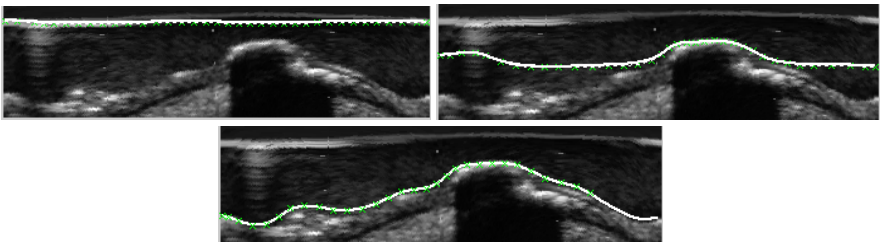

**Fig. 2.** Evolution of a snake on the IVUS image

deviation $\sigma$, and $I(x, y)$ is the image data. As can be observed greater $\sigma$ will increase the attraction range but the edges will blur. In our experiments the snake is initialized at the top row of the image and is attracted by the classification edges; therefore $I(x, y)$ will be the resulting classification image.

Figure 2 shows the deformation process of a snake. The snake is initialized on the top row of the image and deforms to the contours of the classification map. Parameters $\alpha$ and $\beta$ has been kept constant during all the experiments at a value of 0.3 each.

## 4 Experimental Results

We have used images from five different patients to build the training set. Segmentation of those images in the training step has been manually guided by experts. The test set is composed by different images of 5 different patients. The feature space is composed of the Co-occurrence matrices space with number of gray levels $G = \{256, 64\}$, neighborhoods of $N = [5 \times 5]$, $N = [8 \times 8]$ , and distances $D = \{2, 3\}$; and cumulative moments $N = 3$ and maximum order $(k, l) = (9, 9)$. As a result we have a $24 \times 4$ space for co-occurrence matrices and a 81 dimensional space for cumulative moments. The analysis of the resulting features after the feature selection is quite significative since the 85% of the features selected by the AdaBoost are from the co-occurrence space. This encourages us to find work with the co-occurrence space, applying our second "weak" classifier for feature pairs. The results with the "weak" classifier restrict the feature space to half of the feature space, reducing the processing time in the test step to a half.

Figure 3 shows the typical behavior of the training process of the AdaBoost classifier for a mixed set of feature spaces and a simple "weak" classifier approach. Figure 3 (top) shows the error rate of each of the "weak" classifiers. Each time a "weak" is assembled, feature are more difficult to classify due to the weights influence, therefore the "weak" classification error increases. However, 3 (bottom) shows how the joint error of the ensemble of the "weak" classifiers (the "strong" classifier) decreases as more "weaks" are assembled. Figure 3 (right) illustrates the test error. Note that after the 20th "weak" assemble the method overfits. Although theoretically the training error in the AdaBoost methods asymptoti-

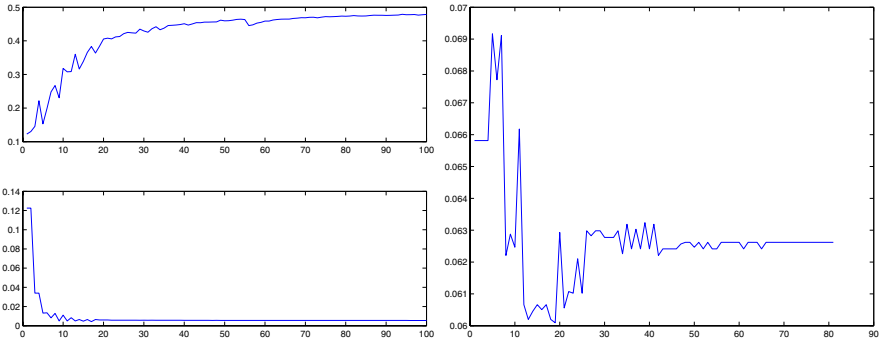

**Fig. 3.** Training error of the process for a mixed set of feature spaces. Weak classification error (top). Strong classification error (bottom). Test classification error (right)

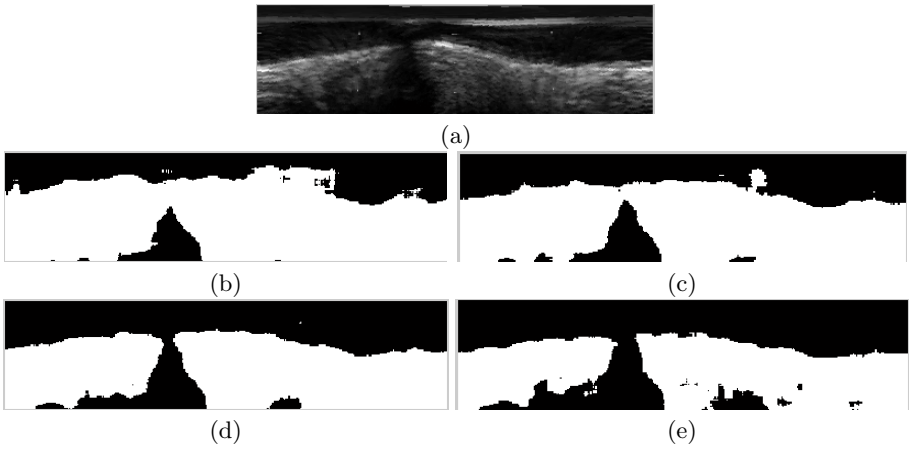


**Fig. 4.** Test classification images at different stages of the strong classifier. (a) Original image (b) "Strong" with 3 "weaks" (c) "Strong" with 7 "weaks" (d) "Strong" with 17 "weaks" (e) "Strong" with 22 "weaks"

cally tend to zero, in practical applications it has been shown that it does not necessarily converge to any desired error-rate [3]; this is most certain in high noise scenarios. IVUS images are one of these high noise image data. However the method can be applied successfully to create fast classifiers.

Figure 4 shows the evolution of the classification image. It can be seen that the classification tends to be better the most classifiers are assembled. However it must be said that most of the time it tends to overfit or to stabilize in a fixed error rate; hence, the number of the reliable "weak" classifiers for the application must be found. This can be done using cross-validation processes.

We have applied this fully automatic integration framework described in the former section to different sequences from 5 patients, for validation of the methodology. The mean error rate for the estimated contours in our experiments

is $0.18 \pm 0.04$ mm. and maximum error rate of $0.43 \pm 0.06$ mm. This error rates are comparable to the detection schemes found in literature. However, the classification step is performed in very little time, allowing this kind of schemes apt for real-time detection processes.

## 5 Conclusion and Future Lines

We have presented an integration framework for tissue-blood segmentation in IVUS images using an classifier ensemble with Adaboost. The Adaboost process is also used for feature selection so the feature extraction process is accelerated in the testing step. The classifier found is apt for real time classification. The method has convergence problems with high noise images, this emphasizes the necessity of a regularization scheme for better performance of the method. The future work lead us to investigate in fast tissue characterization for IVUS images, a very important problem due to the fact that any patient study needs segmenting of about thousand of images that takes about an hour to the medical experts. This method is robust to blood area size. Therefore occlusive plaques can be segmented correctly. The method can be used in future with suitable descriptors of the plaque to segment the plaque from the normal tissue.

**Acknowledgements.** This work was partially supported by the project TIC2000-1635-C04-04 of CICYT, Ministerio de Ciencia y Tecnologia of Spain.

## References

1. R.E. Schapire: "The Boosting Approach to Machine Learning. An Overview." MSRI Workshop on Nonlinear Estimation and Classification. 2002.
2. P. Viola and M. Jones: "Rapid Object Detection using a Boosted Cascade of Simple Features". Accepted Conference on Computer Vision and Pattern Recognition 2001.
3. G. Ratsch, T. Onoda, and K.-R. Muller: "Soft Margins for AdaBoost". NeuroColt2 Technical Report Series. NC-TR-1998-021.
4. J. Malik, S. Belongie, T. Leung, and J. Shi: "Contour and Texture Analysis for Image Segmentation". International Journal of Computer Vision. 43(1),7–27,2001.
5. J. Puzicha, T. Hoffman, and J. Buhmann: "Unsupervised texture segmentation in a deterministic anhealing framework". Trans. on Pattern Recognition and Machine Intelligence. 20(8):803–818,1998.
6. M. Sonka, X. Zhang, M. Siebes et al.: "Segmentation of intravascular ultrasound images: A knowledge based approach". IEEE Trans. on Medical Imaging.14: 719–732. 1995.
7. X. Zhang, C.R. McKay, and M. Sonka: "Tissue Characterization in intravascular ultrasound images". IEEE Trans. on Medical Imaging. 17: 889–899. 1998.
8. C. von Birgelen, A. van der Lugt, A. Nicosia et al.: "Computerized assessment of coronary lumen and atherosclerotic plaque dimensions in three-dimensional intravascular ultrasound correlated with histomorphometry". Amer. J. Cardiol. 78: 1202–1209, 1996.

9. J.D. Klingensmith, R. Shekhar, and D.G. Vince: "Evaluation of Three-Dimensional Segmentation Algorithms for Identification of Luminal and Medial-Adventitial Borders in Intravascular Ultrasound Images", IEEE Trans. on Medical Imaging, 19(10): 996–1011,2000.
10. R. Haralick, K. Shanmugam, and I. Dinstein: "Textural Features for Image Classification". IEEE Trans. System, Man, Cybernetics. 3:610–621. 1973.
11. P.P. Ohanian and R.C. Dubes: "Performance Evaluation for Four Classes of Textural Features". Pattern Recognition. 25(8),819–833, 1992.
12. Trygve Randen and John H. Husoy: "Filtering for Texture Classification: A Comparative Study". Pattern Recognition. 21(4):291–310. 1999.
13. M. Turceyan: "Moment Based texture segmentation". Pattern Recognition Letters. 15:659–668. 1994.
14. J. Martinez and F. Thomas: "Efficient computation of local geometrical moments". Submitted to IEEE Trans. on Image Processing.
15. Richard O. Duda, Peter E. Hart, and David G. Stork: "Pattern Classification". Wiley-Interscience, 2001. 2nd Ed.
16. M. Kass, A. Witkin, and D. Terzopoulos: "Snakes, Active contour models". Int. J. Computer Vision, 1(4): 321–331. 1987.
17. V. Caselles, F. Catte, T. Coll, and F. Dibos: "A geometric model for active contours". Numerische Mathematik. 66:1–31, 1993.
18. T. McInerney and D. Terzopoulos: "Deformable models in medical images analysis: a survey". Medical Image Analysis. 1(2):91–108, 1996.

# Motion Analysis of 3D Ultrasound Texture Patterns

Weichuan Yu[1], Ning Lin[2], Ping Yan[3], Kailasnath Purushothaman[1,3], Albert Sinusas[1,4], Karl Thiele[5], and James S. Duncan[1,2]

[1] Department of Diagnostic Radiology, Yale University
[2] Department of Electrical Engineering, Yale University
[3] Department of Mechanical Engineering, Yale University
[4] Department of Internal Medicine, Yale University
[5] Philips Medical Systems, 3000 Minuteman Road, Andover, MA 01810

**Abstract.** We model the process of imaging soft tissues with a 3D ultrasound probe using a linear convolution model, and obtain analytical expressions of both the ultrasound image and its spectrum. We use this model to study the ultrasound decorrelation caused by tissue motion both in the spatial domain and spectral domain. Finally, we propose a spectral-feature-based algorithm to analyze tissue motion. The comparison with intensity-based algorithm shows promising results.

## 1 Introduction

Ultrasound imaging is widely used in the clinic because it is non-invasive, portable, and affordable. Echocardiography is such an example of using ultrasound imaging for the diagnosis of heart diseases. Currently, echocardiographic images are acquired almost in real time and image quality keeps improving. Analysis of these images, however, still remains tedious and difficult. For example, quantitative analysis of left ventricular (LV) deformation is known to be a sensitive index of myocardial ischemia and injury [1]. But no objective algorithm is yet available to directly analyze LV deformation from echocardiographic images. Although strain and strain rate imaging provides some promising results [2], this methodology is Doppler-based and does not exploit the underlying image information.

The difficulty of analyzing echocardiographic images lies in the complexity of the ultrasound imaging process. Thus, it is essential to understand the ultrasound imaging process before we can reasonably analyze echocardiographic images. One of the special characteristics of ultrasound is the appearance of speckle patterns, which are the result of constructive or destructive interference of different back-scattering waves [3]. The speckle patterns are the unique signatures in static images. Speckle tracking has been used within the framework of pattern correlation techniques for motion analysis [4, 5]. Unfortunately, current speckle tracking techniques work only if the object motion is translational or the displacement small. For more complicated motion like the non-rigid LV motion with large displacements, the speckle patterns will change and lead to *decorrelation* between successive images. Under these circumstances, the motion estimated from speckle tracking fails to represent the underlying tissue motion.

In this paper, we study the relation between tissue motion and the variation of speckle texture patterns in 3D spatial and spectral domains. Some pioneering work has already

I. Magnin et al. (Eds.): FIMH 2003, LNCS 2674, pp. 252–261, 2003.

been done in this direction. Meunier and Bertrand [6] studied the relation between tissue dynamics and image mean gray level changes. Maurice and Bertrand [7] used a Lagrangian model to restore intensity patterns after 2D tissue motion. The decorrelation of speckle-tissue motion has also been explored experimentally using 3D simulation [8]. Also, spectral information has been used in the field of 1D strain imaging [9]. In the blood flow measurement [10] and strain imaging [11], 3D motion estimation from ultrasound data has been proposed without studying the reason of decorrelation.

The rest of the paper is organized as follows: In Sect. 2, we describe a linear model of the ultrasound imaging process. In Sect. 3, we analyze the intensity variation of both a raw *radio frequency* (RF) image and a *B-scan* image under different tissue motion. Subsequently, in Sect. 4 we derive the energy spectra of RF and B-scan images and further justify the use of local band-pass energy as a feature in motion tracking. The experimental results are presented in Sect. 5. Finally, we conclude the paper in Sect. 6.

## 2 Model of Ultrasound Imaging Process

Both radio frequency (RF) image and B-scan (envelope) image have been used for the purpose of motion tracking. Thus, here we derive the analytical expressions of echocardiographic images in both forms. Following the development in [8], we define the point spread function (PSF) in the far field of the transducer as a 3-D Gaussian enveloped cosine function

$$H(\boldsymbol{X}) = e^{-\frac{1}{2}\boldsymbol{X}^T \Gamma \boldsymbol{X}} \cdot \cos(2\pi \boldsymbol{X}^T \boldsymbol{U}_0). \tag{1}$$

Here $\boldsymbol{X} = (x, y, z)^T$ denotes the spatial coordinates with positive $z$ denoting the wave propagation direction, $\boldsymbol{U}_0 = (0, 0, u_{z0})^T$ denotes the spatial frequency of the ultrasound wave, and $\Gamma = \begin{pmatrix} \frac{1}{\sigma_x^2} & 0 & 0 \\ 0 & \frac{1}{\sigma_y^2} & 0 \\ 0 & 0 & \frac{1}{\sigma_z^2} \end{pmatrix}$. The variances of the Gaussian ($\sigma_x$, $\sigma_y$, and $\sigma_z$) are not necessarily the same. We set the location of the transducer at $(0, 0, 0)$ in the 3D spatial space.

During the imaging process, the tissue region can be decomposed into a discrete set of resolution cells, each of which has a number of tissue scatterers to back-scatter the ultrasound wave. We also assume that each tissue scatterer is very small with respect to the wavelength of the acoustic wave so that it can be represented as a Dirac function [8]

$$T_n(\boldsymbol{X}) = a_n \delta(\boldsymbol{X} - \boldsymbol{X}_n), \tag{2}$$

where $\boldsymbol{X}_n = (x_n, y_n, z_n)^T$ denotes randomly distributed center of each scatterer. The echogenicity of the scatterers is represented by $a_n (\geq 0)$. In each resolution cell, the RF image is then the sum of a set of $T_n(\boldsymbol{X})$ convolved by $H(\boldsymbol{X})$, yielding

$$I(\boldsymbol{X}) = \sum_{n=1}^{N} a_n e^{-\frac{1}{2}(\boldsymbol{X}-\boldsymbol{X}_n)^T \Gamma (\boldsymbol{X}-\boldsymbol{X}_n)} \cdot \cos(2\pi(\boldsymbol{X} - \boldsymbol{X}_n)^T \boldsymbol{U}_0). \tag{3}$$

In a commercial ultrasound system, a RF image is usually converted into a B-scan image before displaying on the screen. Ideally, this process can be described as converting the RF signal into an *analytical signal* and then extracting the magnitude of the analytical signal (see [12] for details about the analytical signal). The analytical signal of $I(\boldsymbol{X})$ reads

$$I_A(\boldsymbol{X}) = \sum_{n=1}^{N} [a_n e^{-\frac{1}{2}(\boldsymbol{X}-\boldsymbol{X}_n)^T \Gamma (\boldsymbol{X}-\boldsymbol{X}_n)} \cdot e^{-j2\pi \boldsymbol{X}_n^T \boldsymbol{U}_0}] \, e^{j2\pi \boldsymbol{X}^T \boldsymbol{U}_0}. \tag{4}$$

Correspondingly, the B-scan image is

$$I_B(\boldsymbol{X}) = |I_A(\boldsymbol{X})| = |\sum_{n=1}^{N} a_n e^{-\frac{1}{2}(\boldsymbol{X}-\boldsymbol{X}_n)^T \Gamma (\boldsymbol{X}-\boldsymbol{X}_n)} \cdot e^{-j2\pi \boldsymbol{X}_n^T \boldsymbol{U}_0}|. \tag{5}$$

Note that $|e^{j2\pi \boldsymbol{X}^T \boldsymbol{U}_0}| = 1$.

## 3 Intensity Variation under Tissue Motion

The speckle patterns caused by interference are *unique signatures* in static images. Therefore, many researchers tried to analyze tissue motion by tracking speckle patterns [13,7]. But these patterns are not always invariant with respect to tissue motion. Several authors have experimentally studied the relation between the pattern decorrelations and tissue motion (e.g. [14]). Here we would like to study the use of an analytical model to predict and eventually compensate for the speckle decorrelations caused by tissue motion.

As both RF image and B-scan image have been used in speckle tracking, we would like to study the temporal variations of both images under different forms of tissue motion. Let us assume the non-rigid tissue motion dynamics can be locally approximated as affine motion

$$\boldsymbol{X}_n^{'} = \boldsymbol{D} + M\boldsymbol{X}_n, \tag{6}$$

where $\boldsymbol{X}_n^{'}$ denotes positions of tissue scatterers after motion, $\boldsymbol{D} = (d_x, d_y, d_z)^T$ is a translation vector, and $M$ is a $3 \times 3$ matrix which can describe rotation, scaling change, shearing and their combinations. We start with the most simple case – pure translation, in which $\boldsymbol{X}_n$s at time $t = 0$ are uniformly shifted to $\boldsymbol{X}_n + \boldsymbol{D}$ at time $t = \Delta t$. Correspondingly, the intensity patterns in both the RF image and the B-scan image do not change except the translation of image coordinates. For more complicated non-translational motion ($\boldsymbol{X}_n^{'} = M\boldsymbol{X}_n$ with $M$ a $3 \times 3$ matrix), we lose these nice

relations:

$$
\begin{aligned}
I(\boldsymbol{X}, \Delta t) &= \sum_{n=1}^{N} a_n e^{-\frac{1}{2}(\boldsymbol{X}-M\boldsymbol{X}_n)^T \Gamma (\boldsymbol{X}-M\boldsymbol{X}_n)} \cdot \cos(2\pi(\boldsymbol{X}-M\boldsymbol{X}_n)^T \boldsymbol{U}_0) \\
&= \sum_{n=1}^{N} a_n e^{-\frac{1}{2}(M^T\boldsymbol{X}-\boldsymbol{X}_n)^T M^T \Gamma M (M^T\boldsymbol{X}-\boldsymbol{X}_n)} \\
&\qquad \cdot \cos(2\pi(M^T\boldsymbol{X}-\boldsymbol{X}_n)^T M^T \boldsymbol{U}_0) \\
&\neq I(M^T\boldsymbol{X}, 0). \qquad (7) \\
I_B(\boldsymbol{X}, \Delta t) &= |\sum_{n=1}^{N} a_n e^{-\frac{1}{2}(\boldsymbol{X}-M\boldsymbol{X}_n)^T \Gamma (\boldsymbol{X}-M\boldsymbol{X}_n)} \cdot e^{-j2\pi(M\boldsymbol{X}_n)^T \boldsymbol{U}_0}| \\
&= |\sum_{n=1}^{N} a_n e^{-\frac{1}{2}(M^T\boldsymbol{X}-\boldsymbol{X}_n)^T M^T \Gamma M (M^T\boldsymbol{X}-\boldsymbol{X}_n)} \cdot e^{-j2\pi \boldsymbol{X}_n^T M^T \boldsymbol{U}_0}| \\
&\neq I_B(M^T\boldsymbol{X}, 0). \qquad (8)
\end{aligned}
$$

The above expressions clearly indicate that the deformation of the tissue does not result in the same deformation of image intensities. As a result, intensity-based tracking algorithm does not work well under these circumstances. The only exception is the axial rotation case, which we will demonstrate later in Sect. 5. Actually, this is a common limitation of intensity correlation-based techniques used in speckle tracking [8] or elastography [15], where small displacement assumption often has to be made to approximate the actual motion with pure translation. One may suggest that we can compensate for the intensity variation using the above explicit expression. This idea, however, is infeasible in the practice because we generally do not know the values of $\boldsymbol{X}_n$ (location of scatterers) and $a_n$ (echogenicity coefficients of scatterers).

When we think of the speckle pattern tracking as a texture motion analysis problem, it is possible to find suitable texture features in the spectral domain (e.g. [16,17]). Thus, we shall study the spectra of both images and their variations under tissue motion.

## 4 Local Spectral Analysis of Ultrasound Images

The energy spectrum of the RF image is straightforward (Here $\tilde{I}$ denotes the spectrum of $I$ and $\otimes$ denotes convolution)

$$
\begin{aligned}
|\tilde{I}(\boldsymbol{U})| &= (2\sqrt{\pi})^3 |\Gamma^{-1}|^{\frac{1}{2}} e^{-\boldsymbol{U}^T \Gamma^{-1} \boldsymbol{U}} \sum_{n=1}^{N} a_n e^{-j2\pi \boldsymbol{X}_n^T \boldsymbol{U}} \\
&\qquad \otimes \frac{1}{2}[\delta(\boldsymbol{U}-\boldsymbol{U}_0) + \delta(\boldsymbol{U}+\boldsymbol{U}_0)] e^{-j2\pi \boldsymbol{X}_n^T \boldsymbol{U}} \\
&= 4\pi^{\frac{3}{2}} |\Gamma^{-1}|^{\frac{1}{2}} [e^{-(\boldsymbol{U}-\boldsymbol{U}_0)^T \Gamma^{-1} (\boldsymbol{U}-\boldsymbol{U}_0)} \\
&\qquad + e^{-(\boldsymbol{U}+\boldsymbol{U}_0)^T \Gamma^{-1} (\boldsymbol{U}+\boldsymbol{U}_0)}] |\sum_{n=1}^{N} a_n e^{-j2\pi \boldsymbol{X}_n^T \boldsymbol{U}}|. \qquad (9)
\end{aligned}
$$

The energy spectrum of the B-scan image, however, is more complicated since extracting magnitude of the analytical signal is a non-linear operation. Here we try to derive the spectrum of the B-scan image from the spectrum of the analytical signal. Concretely, the analytical signal $I_A(\boldsymbol{X})$ in Eq. (4) can be reformulated as

$$I_A(\boldsymbol{X}) = I_B(\boldsymbol{X})e^{j\phi(\boldsymbol{X})} \tag{10}$$

with $I_B(\boldsymbol{X}) \geq 0$ a real function of $\boldsymbol{X}$ and $\phi(\boldsymbol{X})$ denoting the phase. In general, the explicit form of $\phi(\boldsymbol{X})$ is unknown, which makes explicit spectrum of $I_B(\boldsymbol{X})$ a difficult task. In some specific cases, however, we can simplify the problem. For example, if all $\boldsymbol{X}_n$s are assumed lying on a plane perpendicular to the positive $z$ axis so that all of $\boldsymbol{X}_n^T\boldsymbol{U}_0$s equal to a constant $C_0$, we can simplify the unknown phase term in Eq. (10) as (cf. Eq. (4))

$$e^{j\phi(\boldsymbol{X})} = e^{-j2\pi C_0}e^{j2\pi\boldsymbol{X}^T\boldsymbol{U}_0}. \tag{11}$$

From Eqs. (10) and (11) we derive the Fourier transform of $I_A(\boldsymbol{X})$ as

$$\tilde{I}_A(\boldsymbol{U}) = \tilde{I}_B(\boldsymbol{U})e^{-j2\pi C_0} \otimes \delta(\boldsymbol{U} - \boldsymbol{U}_0). \tag{12}$$

From Eq. (4) we also obtain

$$\tilde{I}_A(\boldsymbol{U}) = [(2\sqrt{\pi})^3|\Gamma^{-1}|^{\frac{1}{2}}e^{-\boldsymbol{U}^T\Gamma^{-1}\boldsymbol{U}}e^{-j2\pi C_0}\sum_{n=1}^{N}a_n e^{-j2\pi\boldsymbol{X}_n^T\boldsymbol{U}}] \otimes \delta(\boldsymbol{U} - \boldsymbol{U}_0). \tag{13}$$

Comparing Eq. (13) and Eq. (12) yields

$$\tilde{I}_B(\boldsymbol{U}) = (2\sqrt{\pi})^3|\Gamma^{-1}|^{\frac{1}{2}}e^{-\boldsymbol{U}^T\Gamma^{-1}\boldsymbol{U}}\sum_{n=1}^{N}a_n e^{-j2\pi\boldsymbol{X}_n^T\boldsymbol{U}}. \tag{14}$$

The corresponding energy spectrum reads

$$\tilde{E}_B(\boldsymbol{U}) = |\tilde{I}_B(\boldsymbol{U})| = \underbrace{(2\sqrt{\pi})^3|\Gamma^{-1}|^{\frac{1}{2}}e^{-\boldsymbol{U}^T\Gamma^{-1}\boldsymbol{U}}}_{\text{3D Gaussian}} \Big|\sum_{n=1}^{N}a_n e^{-j2\pi\boldsymbol{X}_n^T\boldsymbol{U}}\Big|. \tag{15}$$

The first part of the above expression is just a 3D Gaussian function and the second part is the magnitude of the sum of a set of complex vectors. It should be noted that this equation is derived from a simplified assumption that all scatterers in the local neighborhood are lying on the same plane. For the scatterers in the far field of the transducer which contribute to the constructive inference, this simplification is a fair assumption (Intuitively, the scatterers contributing to the constructive inference should have approximately the same phase). But this may not be true for all possible distributions of scatterers. As the constructive inferences are the most significant parts in the speckle texture pattern, we simply use this assumption in the rest of the paper. The limitations and possible improvements of this assumption remain to be addressed.

If we apply the same assumption of $\boldsymbol{X}_n^T\boldsymbol{U}_0 = C_0$ in the spatial domain, Eqs. (3) and (5) turn out to the simple summation of echogenicity weighted Gaussians times a constant – only the constructive inference effects in the RF and the B-scan images are described, as we have explained in the spectral domain. This assumption does not affect the intensity variation analysis of the RF and the B-scan images in the spatial domain (cf. Eqs. (7) and (8)).

### 4.1 Spectral Variation under Tissue Motion

If tissue scatterers undergo pure translation, the only difference between the spectra before and after the translation is the uniform phase shift. The corresponding energy spectra are identical. For more complicated tissue dynamics $\boldsymbol{X}_n^{'} = M\boldsymbol{X}_n$ (cf Eq. (6)), we obtain the energy spectra of both RF and B-scan image as

$$|\tilde{I}_{M\boldsymbol{X}_n}(\boldsymbol{U})| = 4\pi^{\frac{3}{2}}|\Gamma^{-1}|^{\frac{1}{2}}\left[e^{-(\boldsymbol{U}-\boldsymbol{U}_0)^T\Gamma^{-1}(\boldsymbol{U}-\boldsymbol{U}_0)} + e^{-(\boldsymbol{U}+\boldsymbol{U}_0)^T\Gamma^{-1}(\boldsymbol{U}+\boldsymbol{U}_0)}\right] \\ |\sum_{n=1}^{N} a_n e^{-j2\pi\boldsymbol{X}_n^T M^T\boldsymbol{U}}| \tag{16}$$

$$\tilde{E}_{B,M\boldsymbol{X}_n}(\boldsymbol{U}) = (2\sqrt{\pi})^3|\Gamma^{-1}|^{\frac{1}{2}}e^{-\boldsymbol{U}^T\Gamma^{-1}\boldsymbol{U}}|\sum_{n=1}^{N} a_n e^{-j2\pi\boldsymbol{X}_n^T M^T\boldsymbol{U}}|. \tag{17}$$

It is known that the variance parameters $\sigma_x$, $\sigma_y$, and $\sigma_z$ in Eq. (3) are very small (not larger than several voxels) comparing to the window size we choose for local Fourier transform. Correspondingly, the Gaussian function in the spectral domain has very large covariance parameters. We can approximately assume that the 3D Gaussians in Eqs. (9) and (15) do not change much inside the observation window after the deformation and their variation can be ignored ( This assumption can be indirectly verified by the fact that the high-frequency components of the local spectrum are not smoothed out by the Gaussian filter). Based on this approximation, we obtain the following relations after comparing Eq. (9) with (16) and comparing (15) with (17)

$$\begin{cases} |\tilde{I}_{\boldsymbol{X}_n}(M^T\boldsymbol{U})| &= |\tilde{I}_{M\boldsymbol{X}_n}(\boldsymbol{U})| \\ \tilde{E}_{B,\boldsymbol{X}_n}(M^T\boldsymbol{U}) &= \tilde{E}_{B,M\boldsymbol{X}_n}(\boldsymbol{U}) \end{cases}, \tag{18}$$

Unlike Eqs. (7) and (8), the above expressions state clearly that the deformation of soft tissue results in the deformation of the energy spectrum. Hence, it is possible to compensate for the tissue-motion-caused variation directly in the spectral domain, even without knowing the exact values of the parameters $\boldsymbol{X}_n$ and $a_n$. For example, if we can find a matrix $\hat{M}$ to manipulate $\tilde{E}_{B,\boldsymbol{X}_n}(\boldsymbol{U})$ so that $\tilde{E}_{B,\boldsymbol{X}_n}(\hat{M}^T\boldsymbol{U}) = \tilde{E}_{B,M\boldsymbol{X}_n}(\boldsymbol{U})$ can be satisfied, then $\hat{M}$ is a good estimation of $M$.

This idea, however, is not implemented in this paper because it needs very large searching space and is computationally burdensome (just think of all possible variations of the matrix $\hat{M}$). Instead, we choose the computationally more efficient local band-pass energy as the spectral feature in the motion analysis. Intuitively, spectral components at low-frequencies are not very useful in characterizing the texture patterns and those components at high-frequencies are in general corrupted by noise. Thus, using components from the band-pass region is a reasonable choice. Also, the LV deformation mainly consists of translation, rotation and small scaling change. The local band-pass energy is robust against translation and rotation (rotation of the spectral coordinates does not change their distances to the spectral origin. Therefore, a band-pass component still remains in the same pass-band, only with different orientation). Further, if we choose the pass-band carefully, the scaling change of the major LV texture patterns (characterized as sliding up/down along the radial axis in the spectral domain) can also be covered by the pass-band as well.

It should be noticed that using band-pass energy has been initially described by Heeger [18] in the estimation of optical flow. Recently, Yeung et al [17] proposed to use pass-band energy as a feature in the tracking of 2D ultrasound images. In the following section, we would like to further extend their approach to 3D space.

## 5 Experiment

Generally, tracking can be done by minimizing the sum-of-square-distance (SSD) function

$$SSD(\boldsymbol{D}) = \sum_{\boldsymbol{X} \in \mathcal{N}(\boldsymbol{X}_0)} (F(\boldsymbol{X}, t) - F(\boldsymbol{X} + \boldsymbol{D}, t + \Delta t))^2, \tag{19}$$

where $F$ means feature, $\boldsymbol{D}$ denotes the displacement vector and $\mathcal{N}(\boldsymbol{X}_0)$ denotes the local neighborhood of candidate $\boldsymbol{X}_0$. The feature can be intensity (i.e. $F(\boldsymbol{X}, t) = I(\boldsymbol{X}, t)$) [4,8] or pass-band energy [18,17]. In oder to extract the pass-band energy, we modify the spatio-temporal Gabor filter in [18] into a 3D ring-Gabor filter $G$, whose impulse response in the spectral domain reads (here $\tilde{G}$ denotes the spectrum of $G$)

$$\tilde{G} = \sum_{i=1}^{N} exp\{-\frac{C^2\ (|\boldsymbol{U}| - u_i)^2}{2\ u_i^2}\}. \tag{20}$$

This is a sum of multiple Gabor-rings with different mid-frequency parameters $u_i (i = 1, \cdots, N)$. The covariance parameter of each Gabor-ring is defined as $\sigma = u_i / C$ with $C$ a constant. The motivation behind this modification is that it is more efficient to apply a filter with a ring-shape than to apply multiple filters at different orientation and then sum up the filter responses (like in [18,17]). It should also be noticed that the above complicated construction of multiple Gabor-rings does not mean that we have to apply multiple filters like in [18,17]. Once the construction is done, we only need to apply the single filter $G$ to band-pass the intensity image. The benefit of introducing multiple Gabor-rings is the flexibility of adjusting the relative importance of different frequency components and sharp stop-edges at low- and high-frequency. The band-pass energy at fixed location $\boldsymbol{X}_0$ is then obtained as (here $\otimes$ denotes convolution)

$$F(\boldsymbol{X}_0) = \sum_{\boldsymbol{X} \in \mathcal{N}(\boldsymbol{X}_0)} |G(\boldsymbol{X}) \otimes I(\boldsymbol{X})|^2 \quad \text{or} \quad \sum_{\boldsymbol{X} \in \mathcal{N}(\boldsymbol{X}_0)} |G(\boldsymbol{X}) \otimes I_B(\boldsymbol{X})|^2. \tag{21}$$

In this paper, we choose $N = 6$, $C = 0.5$, and $u_i \in [\frac{\pi}{4}, \frac{1.4\pi}{4}, \frac{1.8\pi}{4}, \frac{2.2\pi}{4}, \frac{2.6\pi}{4}, \frac{3\pi}{4}]$. One example of the ring-Gabor filter in the spectral domain is shown in Fig. 1.

In our lab, we are using a Philips Sonos 5500 Imaging System with a 3D omniprobe transducer to acquire 3D images in the polar coordinates. In order to solve the problem of anisotropical sampling, we rotate the transducer with a small angular interval of $1^\circ$ during the acquisition. Then, the 3D image volume in the polar coordinates is converted into the Cartesian coordinates and resampled on the Cartesian grids. During this process, a "nearest neighbor" interpolation method is used. In the experiment, we excise a rat heart, fix it into a cup with gel, and cover it with water. The water cup is installed on

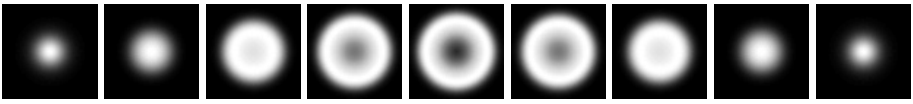

**Fig. 1.** Impulse response of 3D Gabor filter in the spectral domain. Here white pixels denote large weighting coefficients and dark pixels denote small coefficients. The slices are arranged from left to right with the slice in the middle as the central part of the 3D volume

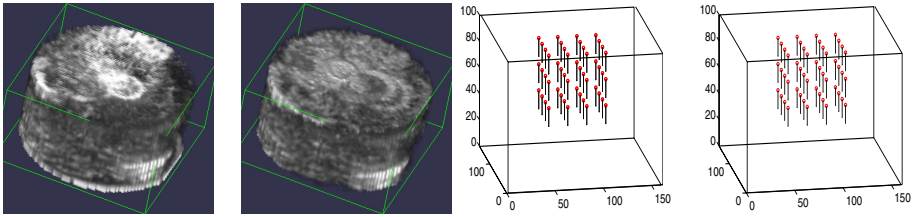


**Fig. 2.** Two phantom volumes before (column 1) and after (column 2) axial translation of 1.27mm. The displacement needle maps of the axial translation are shown in column 3 (using intensity) and column 4 (using pass-band energy)

a round table which can be rotated. The ultrasound transducer is fixed on a pole which can be shifted in three different directions precisely. Its tip is under the water surface to image the heart before and after the motion.

We start with the axial translation. We keep the round table static and take one acquisition. Then, we move the transducer along its axial direction by 1.27mm and image the same volume again. The intensity- and pass-band energy-based tracking algorithms provide almost perfect performances (Fig. 2). In another example, we observe the change of texture patterns after the laterial translation. This observation indicates that the dense sampling of the angular space does not solve the decorrelation problem. It is different as Meunier's model [8], but similar to the experimental results in [10]. At this moment, we are uncertain if the new linear-array transducer will solve this problem.

Then we continue the validation with an axial rotation example, in which the round table is rotated by 15 degrees around the transducer axis between two acquisitions. Our model explains that there is a slight decorrelation after the axial rotation: the matrix $M$ in the axial rotation is simplified to have only one variable $\alpha$, i.e. $M = \begin{pmatrix} \cos(\alpha) & -\sin(\alpha) & 0 \\ \sin(\alpha) & \cos(\alpha) & 0 \\ 0 & 0 & 1 \end{pmatrix}$. Since we are using the sectorial transducer, all orientation in the laterial plane is uniformly treated. Thus, we have $\sigma_x = \sigma_y$ (cf. Sect. 2). Then, the $M^T \Gamma M$ term in Eq. (8) turns out to be $\Gamma$. The only difference between $I_B(\boldsymbol{X}, \Delta t)$ and $I_B(M^T \boldsymbol{X}, 0)$ is the rotated spectral axes (i.e. $U \rightarrow M^T U$), which causes some decorrelation. However, if the rotation angle is small, the decorrelation is minor. This explains why the intensity-based approach still provides reasonable results.

According to our analysis in Sect. 4.1, the band-pass energy feature is robust against rotation. Therefore, it should have better performance than intensity. Although it is

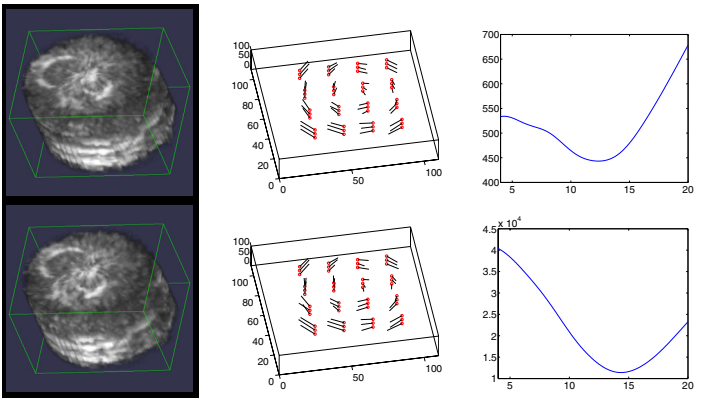

**Fig. 3. Column 1:** Rendering images of 3D heart volumes before (top) and after (bottom) the axial rotation of $15^\circ$ . **Column 2:** Tracking trajectories using intensity (top) and pass-band energy (bottom). **Column 3:** Eq. (22)-based SSD function value vs. rotation angle. The function values are not normalized as we are only interested in the positions of minimal values. For intensity-based SSD function (top), the minimal value is at $\alpha = 12.4^\circ$, while for band-pass energy the minimum is at $\alpha = 14.4^\circ$ (bottom).

hard to confirm this conclusion using the similar tracking trajectories in Fig. 3, we can quantitatively compare the performance of both features from another perspective. The SSD function in Eq. (19) is based on the assumption that the image feature (either intensity or band-pass energy) does not change before and after the motion. In the specific example of axial rotation, we know the location of the rotation axis and the ground truth of rotation angle. Thus, we can extract a volume centered at the rotation axis and apply geometric transform directly on the candidate volume. By searching in the $\alpha$-space for the best match between geometrically transformed image volume before the rotation and the original volume after the rotation, we obtain an estimated rotation angle for each feature. This procedure is described mathematically in the following modified SSD function

$$SSD(\alpha) = \sum_{\boldsymbol{X} \in \mathcal{N}(\boldsymbol{X}_0)} (F(M(\alpha)^T \boldsymbol{X}, t) - F(\boldsymbol{X}, t + \Delta t))^2. \tag{22}$$

In Fig. 3, we present the plots of SSD function values using intensity and band-pass energy as feature. The band-pass energy is clearly superior to the intensity in tracking.

## 6 Conclusion

We follow a common model to describe the ultrasound imaging process and derive an explicit relation between tissue motion and image variation both in the spatial domain and spectral domain. This relation justifies the use of band-pass energy in tracking motion from ultrasound images. Primary tests show that the estimation result using the band-pass energy is as good as the result using intensity in the case of axial translation and

is closer to the ground truth in the case of axial rotation. In the future work, we plan to further compare the band-pass energy feature with the intensity feature using laterial rotation and different combinations of translation and rotation.

## References


1. Shi, P., Sinusas, A., Constable, R., Ritman, E., Duncan, J.: Point-tracked quantitative analysis of left ventricular surface motion from 3-D image sequences. IEEE Trans. Medical Imaging **19(1)** (2000) 36–50
2. D'hooge, J., Bijnens, B., Thoen, J., Van de Werf, F., Sutherland, G., Suetens, P.: Echocardiographic strain and strain-rate imaging: A new tool to study regional myocardial function. IEEE Trans. Medical Imaging **21(9)** (2002) 1022–1030
3. Wagner, R., Smith, S., Sandrik, J., Lopez, H.: Statistics of speckle in ultrasound B-scans. IEEE Trans. Sonics and Ultrasonics **30(3)** (1983) 156–163
4. Meunier, J., Bertrand, M.: Ultrasonic texture motion analysis: Theory and simulation. IEEE Trans. Medical Imaging **14(2)** (1995) 293–300
5. Bohs, L., Geiman, B., Anderson, M., Gebhart, S., Trahey, G.: Speckle tracking for multidimensional flow estimation. Ultrasonics **38** (2000) 369–375
6. Meunier, J., Bertrand, M.: Echographic image mean gray level changes with tissue dynamics: A system-based model study. IEEE Trans. Biomedical Engineering **42(4)** (1995) 403–410
7. Maurice, R., Bertrand, M.: Lagrangian speckle model and tissue-motion estimation ó theory. IEEE Trans. Medical Imaging **18(7)** (1999) 593–603
8. Meunier, J.: Tissue motion assessment from 3d echographic speckle tracking. Phys. Med. Biol. **43** (1998) 1241–1254
9. Konofagou, E., Varghese, T., Ophir, J., Alam, S.: Power spectral strain estimators in elastography. Ultrasound in Med. & Biol. **25(7)** (1999) 1115–1129
10. Bashford, G.R., von Ramm, O.T.: Ultrasound three-dimensional velocity measurements by feature tracking. IEEE Trans. Ultrasonics, Ferroelectrics, and Frequency Control **43(3)** (1996) 376–384
11. Krueger, M., Pesavento, A., Ermert, H., Hiltawsky, K., Heuser, L., Rosenthal, H., Jensen, A.: Ultrasonic strain imaging of the female breast using phase root seeking and threedimensional "optical flow". In: IEEE Ultrasonics Symposium. (1998) 1757–1760
12. Granlund, G.H., Knutsson, H.: Signal Processing for Computer Vision. Kluwer Academic Publishers (1995)
13. Wagner, R., Insana, M., Smith, S.: Fundamental correlation lengths of coherent speckle in medical ultrasonic images. IEEE Trans. Ultrasonics, Ferroelectrics, and Frequency Control **35(1)** (1988) 34–44
14. Friemel, B., Bohs, L., Nightingale, K., Trahey, G.: Speckle decoorelation due to twodimensional flow gradients. IEEE Trans. Ultrasonics, Ferroelectrics, and Frequency Control **45(2)** (1998) 317–327
15. Bilgen, M., Insana, M.: Error analysis in acoustic elastography. I. displacement estimation. Journal of the Acoustical Society of America **101(2)** (1997) 1139–1154
16. Bovik, A.C., Clark, M., Geisler, W.S.: Multichannel texture analysis using localized spatial filters. IEEE Trans. Pattern Analysis and Machine Intelligence **12(1)** (1990) 55–73
17. Yeung, F., Levinson, S., Fu, D., Parker, K.: Feature-adaptive motion tracking of ultrasound image sequences using a deformable mesh. IEEE Trans. Medical Imaging **17(6)** (1998) 945–956
18. Heeger, D.J.: Optical flow using spatiotemporal filters. International Journal of Computer Vision **1(4)** (1988) 279–302

# Estimation of the Diastolic Intraventricular Relative Pressures Using MRI Acceleration Measurements

Fanny Balleux[1], Odile Jolivet[1,2], Alain De Cesare[1], Alain Herment[1], Jean-Pierre Tasu[2], and Elie Mousseaux[1]

[1] U494 INSERM, Paris, France
[2] UMR 8081 CNRS, CIERM, Le Kremlin-Bicêtre, France

**Abstract.** This paper presents a method to determine noninvasively relative pressures from magnetic resonance (MR) acceleration and velocity data. The technique is based on the complete Navier-Stokes equation associated with the direct measurement of the total acceleration, defined as the sum of the velocity derivative vs. time and the convective acceleration. It consists of determinining relative pressures by constructing a minimization problem of a quadratic energy function. The original ways of discretisation and computation allow to estimate relative pressures independently of a path of integration. The algorithm is applied to compute relative pressures over the diastolic filling of the left ventricle (LV) within a region of interest delineating the left atrium (LA) and the LV.

## 1 Introduction

Blood pressure is a fundamental physiological parameter for the study of the ventricular function. Many years ago, an early diastolic intraventricular pressure gradient was described between the left ventricular (LV) base and apex using catheters [5]. Ever since, further studies have suggested the importance of the diastolic intraventricular pressure gradients for adequate LV filling [2]. At the moment, blood pressure measurements are most commonly made using a manometer, which gives an absolute pressure at one spatial point. Because of the cost and risk associated to catheter technique, non-invasive flow imaging methods such as Doppler ultrasound or magnetic resonance imaging (MRI) have been proposed to estimate blood pressure.

The most currently used method is based on fluid dynamics and uses either the complete Navier-Stokes (NS) equation or simplified versions of it (Euler equation or Bernouilli equation). Using MRI, calculation of cardiovascular pressure gradients or relative pressures from 2D or 3D time-resolved blood velocity measurements have yet been studied [7,8,9,10]. The methods described by Urchuk et al. are based on measurements of vascular compliance and vessel distension, which are determined from a correlation of spatial and temporal velocity derivatives and the mean velocity gradient in the direction of the flow. Only time-dependent pressure variations can be estimated accross a vessel area

I. Magnin et al. (Eds.): FIMH 2003, LNCS 2674, pp. 262–271, 2003.

in the direction of the flow. Tyszka et al. proposed then an extension of the method until they compute time-dependent pressure variations along the axis of the vessel using MR velocity data in three spatial and one temporal dimensions. Yang et al. proposed a more general method based on the Euler equation. The method permits to determine the pressure distribution in a flow field but the results of the computation are very dependant of the chosen path of integration what is not very desirable. Furthermore, all the methods used derivatives velocity data, vs. time and space, to compute pressures. Making deratives introduce noise in the data and in sufficient spatial or temporal resolution in the MRI experiment will result in faulse estimations of the pressure gradients.

Unlike other methods of measuring fluid motion, such as Doppler, MRI provides measurements of total acceleration [1]. Recently, [6] reported how to estimate pressure gradients in a pulsatile flow using the NS equation with input MR acceleration encoding. Pressures are computed in one dimension, along the direction of the flow. Showing the ability to compute pressure variations from acceleration data, the authors suggested to calculate the distribution pressure within the cavities containing flowing fluid by integrating pressure gradient over space.

In this paper a method is proposed to estimate relative blood pressures using the fundamental fluid dynamics and an original way of computation. The technique uses the complete NS equation associated with both acceleration and velocity MR data to assess relative pressure. The problem is discretized and posed as an optimization problem of a quadratic energy function. The method is illustrated from 2D simultaneous acceleration and velocity data in the case of the estimation of the intraventricular relative pressures during the diastolic filling of the LV. The spatial relative pressures of a healthy subject are presented at each time frame over the diastolic period.

## 2 Methods and Materials

### Theory

The problem of determining the intraventricular pressures given velocity and acceleration data is formulated within the framework of fundamental fluid dynamics. The technique is developed assuming that the moving blood in cardiac chambers is incompressible and Newtonian. The kinematics of such a fluid is governed by the following NS equation:

$$\nabla P = -\rho\Big(\frac{\delta \boldsymbol{v}}{\delta t} + \boldsymbol{v}.\nabla \boldsymbol{v}\Big) + \rho \boldsymbol{g} + \mu \nabla^2 \boldsymbol{v} \tag{1}$$

where

$\boldsymbol{g}$ = gravitational body-force
$\boldsymbol{v}$ = velocity vector
$\mu$ = dynamic viscosity of the blood
$\rho$ = blood density
P = local pressure

The sum $(\frac{\delta \boldsymbol{v}}{\delta t} + \boldsymbol{v}.\nabla \boldsymbol{v})$ represents the fluid inertial forces $\boldsymbol{\gamma}$ (or total acceleration) where the terms of the sum respectively denote the temporal and convective contributions to the fluid acceleration.

The NS equation holds everywhere in the cardiac chambers where the Newtonian assumption remains valid.

The NS equation is typically solved for $(\boldsymbol{v}, \boldsymbol{\gamma}, P)$ given the initial and boundary conditions. The problem here is to obtain the pressure $P$ given velocity and acceleration fields. Then, we have to solve:

$$\nabla P = \boldsymbol{\mathcal{A}} \tag{2}$$

where $P$ is also the potential of the vector field $\boldsymbol{\mathcal{A}}$, which is given by:

$$\boldsymbol{\mathcal{A}} = \rho \boldsymbol{\gamma} + \rho \boldsymbol{g} + \mu \nabla^2 \boldsymbol{v} \tag{3}$$

Because of the additive noise included in both acceleration $\boldsymbol{\gamma}$ and velocity $\boldsymbol{v}$ data, the vector field $\boldsymbol{\mathcal{A}}$ is contaminated by noise and do not verify the Laplace equation (it means that $\boldsymbol{rot}(\boldsymbol{\mathcal{A}}) \neq \boldsymbol{0}$). The problem of determining $P$ given $\boldsymbol{\mathcal{A}}$ based on (2) is thus an ill-posed problem because of the incompatibility between the projections of Eq. (2) on the three axes X, Y and Z. Hence, a straightforward integration of equation (2) to obtain the local pressures $P$ will give different spatial distributions of pressure according to the path of integration in each direction (X, Y and Z).

To avoid this problem of integration, the calculation of the local pressures is thus formulated as an optimization problem where the pressure variations are given by the minimization of the $\mathcal{L}_2$-norm (4). The optimization criterion $\mathcal{E}$ is:

$$\mathcal{E} = \arg\min_{P} \left\{ \parallel \nabla P - \boldsymbol{\mathcal{A}} \parallel^2 \right\} \tag{4}$$

**Discretization of the Problem.** The numerical resolution of the optimization problem requires discretization of the variables. Considering the cartesian form of the NS equation, equation (1) is written as follows:

$$\frac{\delta P_i}{\delta i} = -\rho \gamma_i + \rho g_i + \mu \Big( \frac{\delta^2 v_i}{\delta x^2} + \frac{\delta^2 v_i}{\delta y^2} + \frac{\delta^2 v_i}{\delta z^2} \Big) \qquad \text{i=x,y,z} \tag{5}$$

In order to solve the problem in $\mathcal{N}$, we propose to discretize it as an oriented $2\mathcal{N}$-connex graph on which nodes are the local pressures P and correspond to the pixels of the image, and arcs are the pressure gradient values $\mathcal{A}$.

**Resolution of the Inverse Problem.** The quadratic and positive semi-definite energy function given by the equation (4) is developed using the oriented graph and the optimization criterion is written as follows:

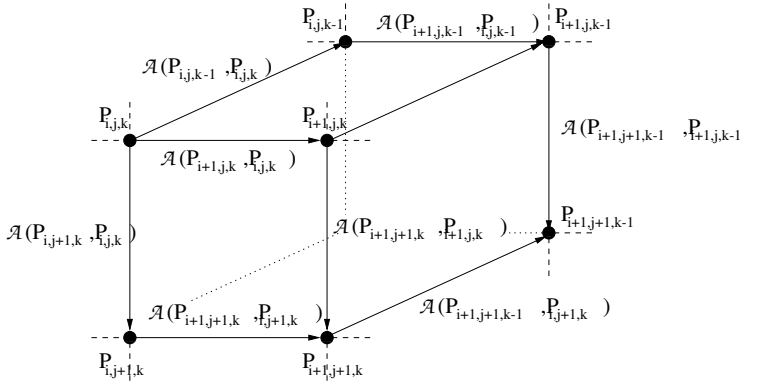


**Fig. 1.** Discretization of the problem as an oriented 4-connex graph: nodes represent the local pressures P and arcs the pressure gradient values $\mathcal{A}$

$$
\begin{aligned}
E = \arg\min_{P} \Big\{ & \sum_{i=1}^{I-1} \big((P_{i+1,j,k} - P_{i,j,k}) - \mathcal{A}(P_{i+1,j,k}, P_{i,j,k})\big)^2 \\
& + \sum_{j=1}^{J-1} \big((P_{i,j+1,k} - P_{i,j,k}) - \mathcal{A}(P_{i,j+1,k}, P_{i,j,k})\big)^2 \\
& + \sum_{k=1}^{K-1} \big((P_{i,j,k+1} - P_{i,j,k}) - \mathcal{A}(P_{i,j,k+1}, P_{i,j,k})\big)^2 \Big\}
\end{aligned}
\tag{6}
$$

N, M and L are the sizes of the considered volume for the estimation of the pressures. Minimizing this criterion leads to minimizing $\boldsymbol{rot}(\boldsymbol{\mathcal{A}})$ at each square pattern of the graph. Expression (6) assumes that the errors $\big[(P_{i+1,j,k} - P_{i,j,k}) - \mathcal{A}(P_{i+1,j,k}, P_{i,j,k})\big]$, $\big[(P_{i,j+1,k} - P_{i,j,k}) - \mathcal{A}(P_{i,j+1,k}, P_{i,j,k})\big]$ and $\big[(P_{i,j,k+1} - P_{i,j,k}) - \mathcal{A}(P_{i,j,k+1}, P_{i,j,k})\big]$ at each point $P_{i,j,k}$ are $\mathcal{G}$aussian and independant of each other points.

The criterion is minimized by using a conjugate gradient method. The pressure distribution can be computed at each time frame of an image sequence but can only be obtained up to an integration constant because the pressure enters the NS equation only through its gradient. This integration constant is not the same one for every time frame of the sequence. Local pressures thus can only be estimated up to a constant offset.

## Materials and Methods

To illustrate the method described above, we studied the intraventricular pressures in 9 healthy volonteers. In this clinical application, we assumed that the transmitral flow propagates along a main streamplane through the cardiac chamber, from the bottom of the LA to the end of the LV. This realistic assumption makes 2D acquisitions possible that shorten the acquisition time with respect to

3D acquisitions. This reduce significantly artifacts due to cardiac cycle irregularities or patient breathing.

**Data Acquisitions.** MR imaging exams were performed with a 1.5 T imaging system (GE Medical Systems, Milwaukee, WI) using a maximum gradient strength of 22 mT/m and a slew rate of 77 mT/m/s. Each acquisition was ECG-gated and performed in a double oblique slice on a three cardiac chambers view, oriented in the plane of the flow propagation between the LA and the LV.

Velocity and acceleration data were encoded using the method proposed by Bittoun et al. [1]. But in order to shorten the acquisition time, components of the flow velocity and acceleration were not simultaneously measured. A first acquisition was performed to simultaneously encode flow velocity in the two spatial directions of the flow. A second acquisition was performed to simultaneously encode the total acceleration in the two directions. Imaging parameters for both velocity and acceleration mapping were 8 mm slice thickness, $30^o$ flip angle, a 36 cm field-of-view, $128 \times 256$ matrix, NEX=1. The encoding velocity and acceleration were respectively $v_{enc}$=180 cm/s (which corresponds to an echo-time TE=7.6 ms) and $\gamma_{enc}$=5000 cm/s$^2$ (TE=13.8 ms). The temporal resolution was TR=22 ms.

To encode velocity (*resp.* acceleration) a bipolar (*resp.* tripolar) gradient was added to the standard imaging sequence. By incrementing the amplitude of this flow-encoding gradient, the phase which is proportional to the velocity (*resp.* acceleration) is progressively rotated and can be assimilated to a frequency shift. This frequency shift was estimated using the mean frequency estimator described in [1] to reconstruct velocity and acceleration maps.

For a pulsation rate of 80 beats per minute, data acquisitions required approximatively 12 minutes.

**Data Analysis.** All MR data were transfered to a UNIX workstation cluster for reconstruction. Velocity and acceleration maps and their corresponding anatomical amplitude images were analysed at each time frame throughout the cardiac cycle.

Before pressure distribution computation, segmentation of the velocity and acceleration images was required to delineate the flow region (LA-LV) and the path of the transmitral blood flow (see Fig. 2a). This process was performed interactively by the operator using the magnitude images to identify anatomical structures. This step permitted to obtain a region mask which was used to compute intraventricular pressures.

The spatial pressure variations in the left part of the heart were computed at each time frame over the diastolic period in the region of interest (LA-LV). The subjects being studied in a supine position, the gravitational force term has been neglected in our computation because perpendicular to the slices. The vector field $\boldsymbol{\mathcal{A}}$ was then equal to $\boldsymbol{\mathcal{A}} = -\rho\boldsymbol{\gamma} + \mu\nabla^2\boldsymbol{v}$, with $\rho$=1060 kg/m$^3$ and $\mu$=0.0035 kg/m/s. The problem was solved by using a 4-connex oriented graph. Due to the fact that solutions were defined up to a constant, a zero-value pressure

point was imposed at the apex for each time frame. Pressure variations were thus measured in relation to this point all over the diastolic period. Temporal changes of the relative pressures were then estimated along the path of the transmitral flow. Besides the computation of the spatial pressure variations maps in the left ventricle, spatio-temporal maps of pressure variations were built by aligning pressure profiles estimated at each time frame along the curve following the intracavitar flow (2).

## 3 Results

Estimations of the intraventricular relative pressures of one of our healthy subjects are presented. Figure 2a illustrates an example of a magnitude image segmentation: the LA-LV chamber and the path of the transmitral flow are surrounded in yellow. In Fig. 2b, spatial pressure variations computed in the flow region (LA-LV) are shown at each time frame over the diastolic period. Time frame images corresponding to the systolic period are not shown because during this period the mitral valve is closed and the two left chambers do not communicate. The NS equation is then independently verified in the LA and the LV. There is a discontinuity of pressure between the two chambers at the level of the valve which can not be determinated until the relative pressures are obtained up to a unknown constant. Over the diastolic period, the mitral valve is opened; the two chambers communicate.

Figure (3) represents the corresponding spatio-temporal pressure map. This kind of representation allows an easier visualization of the changes of the relative pressures over the time. Over the period of time between the opening of the mitral valve and about 65 ms after, there is an important pressure difference between the LA and the apex ($\Delta P = 4.89 \pm 1.6$ mmHg). It corresponds to the fast filling period of the ventricle. Then the pressure difference is reversed: the pressure becomes higher in the LV than in the LA ($\Delta P = 2.5 \pm 0.6$ mmHg) that corresponds to the period of the slow filling.

## 4 Discussion

In this paper, we have presented a method to assess non-invasively flow pressure variations from MR acceleration and velocity data. Our approach is based on the Navier-Stokes equation and on an original way of computation since pressure differences are obtained by solving an $\mathcal{L}^2$ optimization problem. This method permits to estimate relative pressures in $\mathcal{N}$ dimensions independently of a path of integration. It allows to determine intraventricular relative pressures but it is not limited to this application and can be applied to other images as long as the given images obey the incompressibility and Newtonian conditions. However it must be emphasized that *relative* blood pressures and *not absolute* pressures are obtained using this technique.

In clinical cardiology, the Euler equation or simplified versions of it have been widely used for the estimation of the pressure variations from 1-dimensional

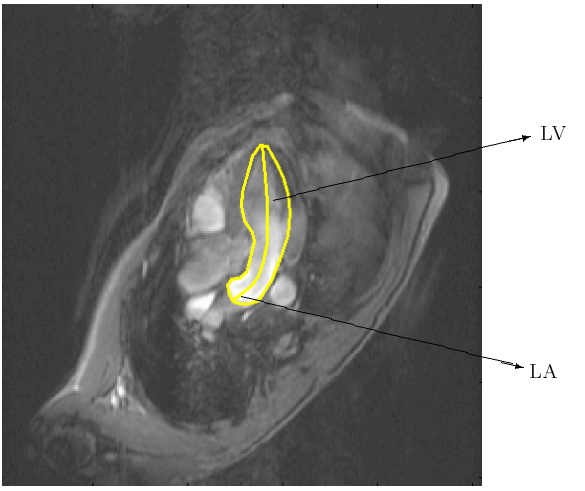


(a)

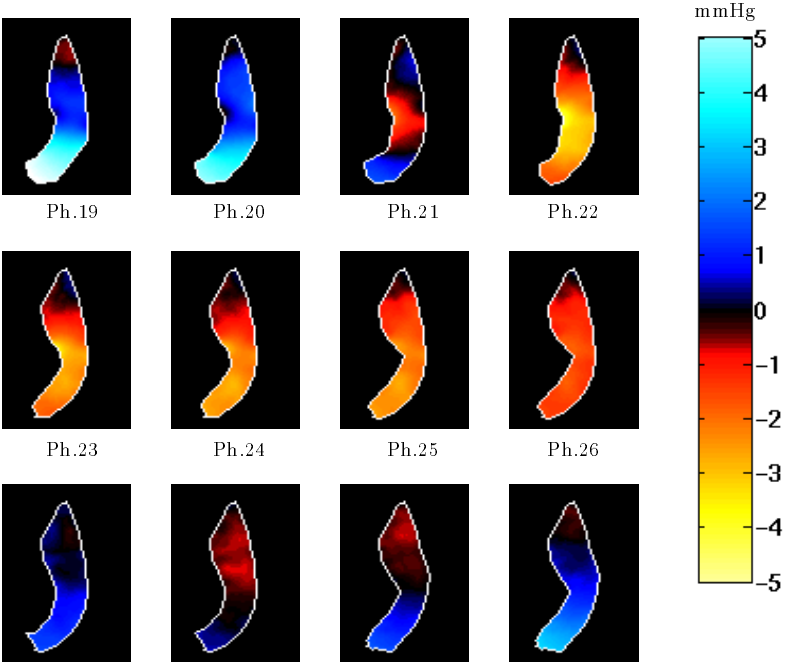


(b)

**Fig. 2.** Intraventricular pressure maps over the cardiac cycle. (a) The operator surrounds the region described by the left atrium and the left ventricle on the anatomical images. (b) Pressure variations are computed in the ROI in relation to the reference pressure point defined at the apex. They are represented here over the diastolic period of the cardiac cycle. Ph=Phase

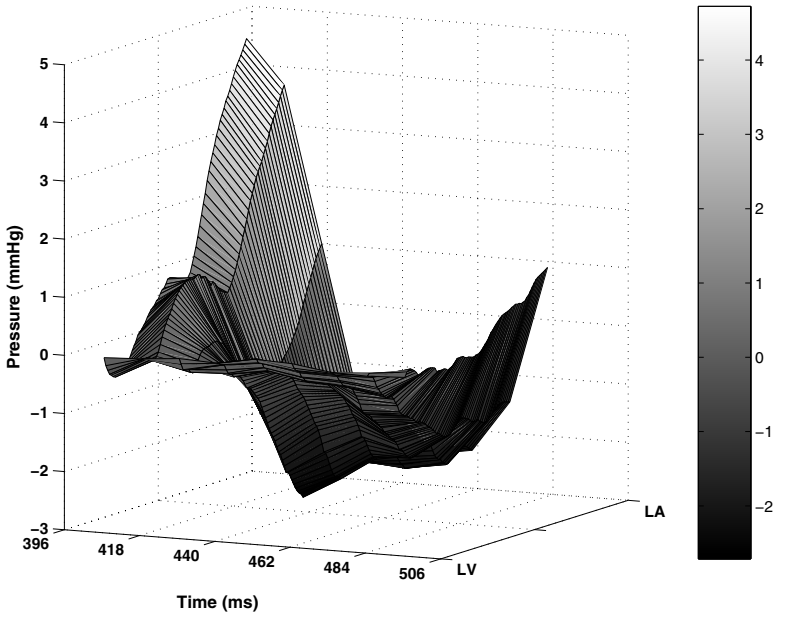


**Fig. 3.** A spatio-temporal pressure map over the diastolic period of a cardiac cycle. This representation allows to make qualitative diagnostic about the changes of the intraventricular pressure differences in time

data acquired by Doppler ultrasounds or from velocity data using time-resolved MRI. Many studies were performed using MRI modality in the case of pulsatile flow pressure estimations [7,10] but none has been proposed to compute the spatial distribution of the intraventricular pressures. In contrast, it has been done by using color Doppler M-mode technique [3,4] but it seems to have a few limitations. Indeed, the application of such an equation with velocity ultrasound data assumes that inflow is laminar and that the ultrasound scanline closely coincides with the inflow streamline. The assumption of laminar flow is verified in the case of a normal mitral valve but is no longer valid for a mitral stenosis valve and, inflow throught a normal mitral valve is rather typically directed laterally, following the curvature of the LV wall. Application of the Euler equation also assumes that transmitral viscous forces are neglected. This term seems yet to be significant as well in regions close to the wall of the arteries as in the case of prosthetic valve flow. Furthermore, the accuracy of these treatments of the discretized equation strongly depends on both temporal and spatial resolutions due to the numerical differentiations of velocity data vs. time and space.

In our approach, the NS equation, which provides a complete description of the hemodynamics, was solved to calculate pressure gradients from a vector field using MR acceleration and velocity data. Employing MR acceleration data avoids

the need for spatial or temporal velocity derivations [6], since both the inertial and the convective terms of the acceleration are encoded in the acquisitions. Although the viscous term can be neglected in case of normal mitral vlave, the simultaneous acquisitions of acceleration and velocity data allow to take it into account for flow through prosthetic valves, for which viscous forces can be large.

The relative pressures are calculated by constructing a optimization problem. It is an original and simple method. No parameter trimming is required and the estimation of the local pressures in the region of interest is global in the contrary of previous stepwise methods which used heuristic parameters to find the optimal path of integration to calculate local pressures from pressure gradients. The minimization of our quadratic criterion (Eq. (4)) gives a optimal solution of the intraventricular pressure distribution up to an unknown constant.

In our application the criterion has been minimized by using a method of conjugate gradients. We suggest to formulate the problem in matricial terms and resolve it by using a sparse matrix algorithm in order to compute faster. Indeed the matrix which contains the second degree terms, called Q, will be a sparse symetric matrix due to the discretization of the region of interest as a oriented graph. The pentadiagonal (resp. heptadiagonal) structure of the matrix Q for 2D (resp. 3D) implementation would be very interesting for the memory space and computation time.

The method requires an operator to draw the regions of interest. However, this step allows to accurately track the flow which is typically directed laterally following the curvature of the LV wall for a normal valve. Moreover, the accuracy of the region outline also has less impact on the local pressure results. Thus, the error generated by taking into account a non-flow value is propagated as a decreasing exponential so that only an area immediately around the non-flow pixel is affected. The privileged path of the inflow track is thus free of such errors.

This method allows the estimation of relative pressures. The changes of the pressure variations over time can be quantitatively measured according to the apex which was arbitrarily defined as a zero-value point pressure all over the diastole. We know that the pressure at the apex changes [2] so that monitoring the changes in the apex pressure remains a subject of continuing research. However, relative pressure changes over time seems to be potentials of additional informations that it can be provided on cardiovascular physiological studies and pathophysiological diagnostics.

In the study we have done, only volunteers have received the MR exam. We have computed pressure variations with and without the viscous term of the Navier-Stokes equation and verify, in vivo that the term $\mu\nabla^2\boldsymbol{v}$ can be neglected in the case of normal mitral valve.

This new application in MRI in the field of cardiology we proposed here seems to provide additional informations for diagnostics. MRI using cine-acquisition sequences is nowdays considered to be the reference method for estimating cardiac chamber volume and the ejection fraction. Combining these measurements with estimations of the intraventricular pressures could give a complete information

on the LV relaxation and compliance. Apply this method over the systolic period during the ejection could also give more cardiac informations.

## References


1. J. Bittoun, O. Jolivet, A. Herment, E. Itty, E. Durand, E. Mousseaux, and J.P. Tasu. Multidimensional mr mapping of mutiple components of velocity and acceleration by fourier phase encoding with a small number of encoding steps. *Magn Reson Med*, 44:723–730, 2000.
2. M. Courtois, S. Kovács, and P. Ludbrook. Transmitral pressure-flow velocity relation. *Circulation,* 78:661–671, 1988.
3. M. Firstenberg, P. Vandervoort, N. Greenberg, N. Smedira, P. McCarthy, M. Garcia, and J. Thomas. Noninvasive estimation of transmitral pressure drop across the normal mitral valve in humans: importance of convective and inertial forces during left ventricular filling. *J Am Coll Cardiol,* 36:1942–49, 2000.
4. N. Greenberg, P. Vandervoort, M. Firstenberg, M. Garcia, and J. Thomas. Estimation of diastolic intraventricular pressure gradients by doppler m-mode echocardiography. *Am J Physiol Heart Circ Physiol,* 280:H2507–H2515, 2001.
5. D. Ling, J.S. Rankin, C.H. Edwards, P.A. McHale, and R.W. Anderson. Regional diastolic mechanics of the left ventricle in the conscious dog. *Am J Physiol,* 236:H323–H330, 1979.
6. J.P. Tasu, E. Mousseaux, A. Delouche, C. Oddou, O. Jolivet, and J. Bittoun. Estimation of pressure gradients in pulsatile flow from magnetic resonance acceleration measurement. *Magn Reson Med,* 44:66–72, 2000.
7. J. Tyszka, D. Laidlaw, J. Asa, and J. Silverman. Three-dimensional, time-resolved (4d) relative pressure mapping using magnetic resonance imaging. *JMRI,* 12:321–329, 2000.
8. S.N. Urchuk, E.F. Fremes, and D.B. Plewes. In vivo validation of mr pulse pressure measurement in an aortic flow model: preliminary results. *Magn Reson Med,* 38:215–223, 1997.
9. S.N. Urchuk and D.B. Plewes. Mr measurement of time-dependent blood pressure variations. *Magn Reson Med,* 5:621–627, 1995.
10. G.Z. Yang, P.J. Kilner, N.B. Wood, S.R. Underwood, and D.N. Firmin. Computation of flow pressure fields from magnetic resonance velocity mapping. *Magn Reson Med,* 36(4):520–526, 1996.

# Magnetic Resonance Fusion Imaging of Chronic Myocardial Ischemia

M. Nahrendorf[1,2], K.-H. Hiller[1], Andreas Greiser[1], Sascha Köhler[1], Thomas Neuberger[1], K. Hu[2], C. Waller[2], G. Ertl[2], A. Haase[1], and W.R. Bauer[2]

[1]Physikalisches Institut (EP5), Universität Würzburg, Am Hubland, 97074 Würzburg
[2]Medizinische Universitätsklinik Würzburg, Josef Schneider Str. 2, 97080 Würzburg, Germany

**Abstract.** Aim of the study was to evaluate the concept of fusion imaging by magnetic resonance spectroscopy and imaging in the model of chronic coronary stenosis in the rat. 3D coronary angiograms were fused with ATP metabolite maps, which were acquired by $^{31}$P localized MR spectroscopy in the isolated rat heart.

Stenosis was induced by a ligation including a 300µm wire placed next to the left coronary artery. The wire was taken away imediately after the suture was closed. 2 weeks later localized 3D $^{31}$P Chemical Shift imaging was performed in 8 isolated perfused hearts on a Bruker 12 T AMX. (voxel size 4 x 4 x 6 mm). $^{1}$H gradient echo images were acquired to correlate position of the stenotic region in the metabolite maps and the angiography data, which was segmented and used for volume correction of spectroscopy. PCr/ATP was determined in a control and the ischemic region. MR angiography was performed with a flow weighted 3D gradient echo (TE 1.0ms, matrix $128^3$). Metabolite maps of ATP were fused with the coronary angiogram using the Amira software. After MR, fraction of scarring within ischemic region was determined in histology.

3D MRA enabled detection of coronary stenosis. In the ischemic region, PCr/ATP was decreased when compared to control region (1.24 ± 0.38 vs 1.45±-0.49, $p<0.05$). Fraction of fibrosis in histology was 12.8±1.4%, and was correlated to ATP signal reduction in the ischemic region ($r=0.71$, $p<0.05$).

In future this kind of image fusion might be of help in fast characterisation of the severity of a stenosis and might aid decision making concerning revascularisation, because not only anatomy, but also metabolic information can be given at a glance.

## 1 Introduction

In coronary heart disease, diagnostic procedures aim at either description of pathologic anatomy (x ray coronary angiography) or assessment of altered metabolism (for instance PET). We suggest to deliver both parts of information, that so far had to be integrated in the physicians head, in one single image. This strategy will deliver the two facts that guide decision making concerning therapy in coronary artery disease

I. Magnin et al. (Eds.): FIMH 2003, LNCS 2674, pp. 272–277, 2003.

simultaneously: not only the pathological anatomy of the narrowed coronary artery but also the metabolic state of myocardium is given within one image.

Fusion of coronary angiography and szintigraphy data has been proposed before (1). In our work, both images may be aqcuired with magnetic resonance techniques.

## 2 Methods

### 2.1 MR Spectroscopy

Stenosis was induced by a ligation including a 300µm wire placed next to the left coronary artery. The wire was taken away imediately after the suture was closed. In 8 rats 2 weeks after induction of coronary stenosis, hearts were excised and localized $^{31}$P MR spectroscopy was performed in the Langendorff perfusion mode (2) on a Bruker 11.75 T AMX. The rats were anesthetized by pentobarbital sodium i.p. (Narcoren; Rhone Merieux GmbH, Laupheim, FRG, 160mg/kg). Hearts were rapidly excised, immersed in ice-cold buffer and perfused within 2 min (Langendorff mode with non-recirculating 37°C Krebs-Henseleit buffer equilibrated with 95% $O_2$ and 5% $CO_2$ (pH=7.4) at constant perfusion pressure (100 mmHg). A drain pierced through the left ventricular apex drained flow from thebesian veins. A water filled Latex balloon was inserted in the left ventricle and connected to a Statham P23XL pressure transducer to measure left ventricular pressure, which was recorded by a PC to trigger MRI-pulse sequences.

The custom-built double-resonant crosscage probe enabled the detection of $^{1}$H and $^{31}$P signals in one setup. An accumulation-weighted 3D phase-encoded $^{31}$P Chemical Shift Imaging (awCSI) experiment (3) was performed. The number of accumulations at each phase-encoding step was calculated according to a Hanning window in k-space, which resulted in a significantly lower signal contamination of neighbouring voxels. The field of view of the 3D awCSI experiment was 40 x 40 x 60 mm, the nominal voxel size was 4 x 4 x 6 mm. In an overall experiment time of about 60 minutes the average SNR for PCr in the local spectra at the nominal voxel size of 96 µl, determined from the Cramer-Rao lower bounds in the spectral fit, was 7.6 in the sham hearts, 6.5 in the ischemic regions of hearts with coronary narrowing and 9.4 in the remote regions. Anatomical multi-slice $^{1}$H gradient echo (GE) images were acquired to correlate the position of the stenotic region in the $^{31}$P CSI metabolite maps and the coronary angiography data. By segmentation of these images a mask was generated and used for volume correction of spectroscopic data during post-processing. As the voxel size in the CSI experiment was in the range of the LV wall thickness, every awCSI voxel is only partially filled with myocardium. Therefore, the signal levels in the local $^{31}$P spectra are attenuated by a spatially dependent factor $k_{PVE}(\vec{r})$ reflecting to the so-called ‚Partial Volume Effect' (PVE). As a consequence, the absolute signal amplitudes of the metabolite resonances in the local spectra from different positions in the same heart cannot be compared. To correct for the PVE, the 3D segment mask derived from the $^{1}$H GE image data was folded with the simulated 3D Spatial Response Function of the spectroscopic experiment. The resulting matrix was used to calculate local correction factors $k_{corr}^{PVE}(\vec{r}) = 1 / k_{PVE}(\vec{r})$ for the $^{31}$P CSI

data. Only voxels that had a correction factor $k_{corr}^{PVE}(\vec{r})< 2.5$ were corrected. All other positions were set to zero. With this correction, local signal levels in the same heart could be compared in a quantitative manner. A correction for local $B_1$ field variations was not included due to the high homogeneity of the crosscage resonator ($\Delta B_1/B_1<5\%$). Local spectra from 4 different positions in a mid-ventricular transversal slice, one in the stenosis area and 3 equally-spaced in remote regions, were extracted from the 3D awCSI dataset. All spectra were fitted with the AMARES time domain fitting routine (4). To determine a correction factor for $T_1$ saturation, heartbeat-triggered (TR ~ 200 ms) and fully relaxed (TR ~ 10s) global $^{31}$P spectra were acquired. The peak area ratios were used to calculate the saturation correction factors for each individual metabolite. The signal amplitudes and PCr/ATP ratios were derived from the peak areas in the local spectra. The same protocol and processing was applied to sham operated animals (n=4). The complete protocol was performed in a physiological time window of 90 minutes.

### 2.2 3D MRA

MR angiography was performed in isolated hearts as described by Bauer et al. (5, 6) immediately after spectroscopy using 3D time of flight (TOF) angiography. A segmented flow-compensated 3D-FLASH sequence with a TR/TE of 3.0/1.3 ms and a flip angle of 30° was used. With a matrix of 128 x 128 x 128 and a FOV of 18 x 18 x 18 mm, an isotropic resolution of 140 µm was achieved. Eight phase encoding steps were acquired during one heart beat. The total acquisition time for a 3D-TOF data set was approximately 7 minutes. For visualization of the vessel structure surface rendering was used (Amira Graphics Software Package, www.amiravis.com), after zero-filling of the raw data.

The metabolite maps of the PCr and the γ-ATP resonance were fused with the coronary angiogram using the Amira software on a SGI workstation. Because the coordinate system of both imaging procedures was identical, information of the gradients used for spatial encoding was employed for data fusion with the result of exact position of the metabolite map within the 3D angiography dataset. The original spectroscopy slice thickness of 6mm was reduced to generate a 2D metabolite map, which was positioned in the middle of the imaging slice and than fused with the angiography. The software enables only the visual fusion of the datasets, and both datasets have their original and therefore different spatial resolution.

### 2.3 Histology

The hearts were excised and fixed in distended form in 3.4% buffered formalin. They were dehydrated in alcohol, washed in xylene and embedded in paraffin. Transverse serial sections of 3 µm thickness were obtained from the midventricular region. The sections were mounted and stained with hematoxilin eosin. The slices were scanned by a sony video scanner and the following areas were determined planimetrically: the region associated to the stenosed vessel containing fibrotic islets, islets of fibrotic tissue within the region associated to the narrowed artery, and the entire area of the myocardial ring (Scan Pro, Jandel Software).

# 3 Results

## 3.1 MR Spectroscopy

A significant reduction in the PCr/ATP ratio ($p<0.05$) was found in the region associated to the stenosis (1.09±0.09) when compared to the average of the remote positions (1.27±0.08) and to the control hearts (1.43±0.08), whereas the reduction of the PCr/ATP ratio in remote areas of hearts with stenosis did not reach level of significance when compared to average values in the control hearts. Within hearts with coronary stenosis, the signal of PCr in the ischemic region was reduced by 19.1±5.7% ($p<0.05$) and the signal of ATP by 5.8±2.9% (p=ns) when compared to the mean value of three remote regions in the same heart.

## 3.2 MRA

The 3D dataset can be fully rotated around the z-axis. Vessels with a cross sectional diameter of more than 140µm were clearly detectable. Ligation was performed on a main branch or directly on the left coronary artery, therefore the effect was clearly within the diagnostic range of imaging. In hearts with MI the signal ceased completely at the site of ligation. In hearts with coronary stenosis a short signal void with returning signal distal from the location of the coronary narrowing was found. Since we used a "time of flight" sequence, the signal in the vessel depends on flow. Within the stenotic segment, the turbulent flow leads to a lower signal. Because stenosis was induced by ligation, the result is a rather short stenotic segment.

Figure 1 shows the metabolite distribution for phosphocreatine in a mid-ventricular transversal slice of a heart with coronary stenosis. The 2D $^{31}$P metabolite map was fused with the maximum intensity projection of the angiography data set. There is an PCr signal reduction in the ischemic region that can be correlated to the stenosis seen in the corresponding vessel.

## 3.3 Histology

The fibrotic islets had a fraction of 12.8±1.4% within the area associated to coronary stenosis, which was 28.3±4% of the whole myocardial ring. The fraction of fibrosis within the region associated to the narrowed coronary was correlated to the ATP signal reduction from control region to the ischemic region in spectroscopy ($r=0.71$, $p<0.05$), whereas there was no correlation between PCr signal change and this area.

# 4 Discussion

For the first time MR coronary angiography and metabolite maps acquired by MR spectroscopy were fused. In future this kind of image fusion might be of help in fast characterisation of the severity of a stenosis and might aid decision making concerning revascularisation, because not only anatomy, but also metabolic information can be given simultaneously.

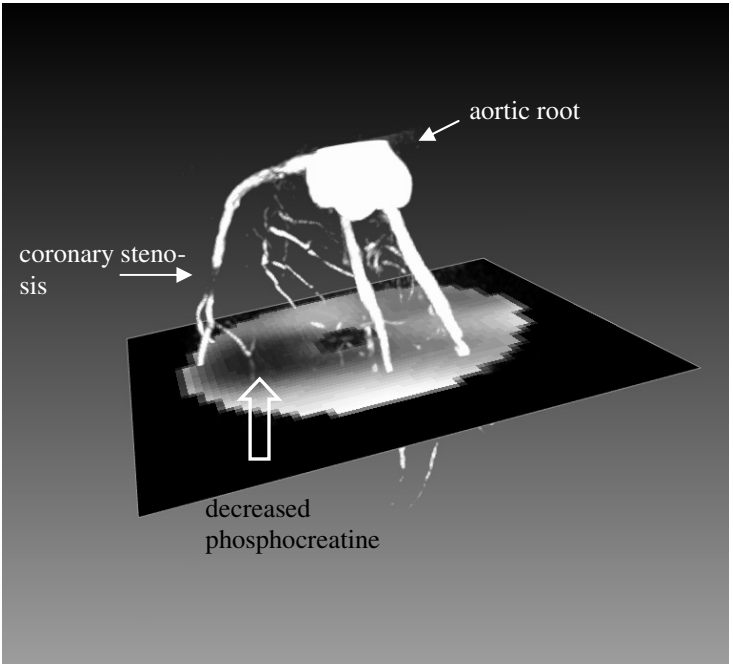


**Fig. 1.** Fusion image of coronary angiography and PCr metabolite map. Resolution of angiography 140 x 140 x 140 µm, of spectroscopy 1 x 1 mm

In accordance with reports of decreased PCr/ATP ratios in remote regions of infarcted hearts (7, 8), we found a trend for a reduction of that ratio between sham rats and the remote zone of rats with coronary stenosis (not significant).

The PCr signal and PCr/ATP ratio in the region associated with coronary stenosis were significantly reduced. This alteration in energy metabolism in chronic ischemia is comparable to the extent reported by Zhang et al. in acute ischemia (9, 10). The diminished PCr/ATP ratio and the PCr signal reduction suggest that viable myocardial portions are in a chronically ischemic state such as hibernation (11). Because only little fibrosis was seen in histology, PCr reduction is likely to be caused by ischemia.

We found a correlation of histologically determined fraction of fibrosis with ATP signal reduction. This finding corresponds with a study by Friedrich et al., who found a direct relation between viable tissue mass and the ATP signal in chronically infarcted rat hearts (7). In a clinical study, Yabe et al. reported diminished concentrations of ATP in patients with a fixed, but not in patients with a reversible thallium defect (11). In line with these studies, reduction of ATP therefore likely represents reduced viability in the rat model of chronic coronary artery stenosis.

Despite of the good quality of the coronary angiogram with visualization of even small side branches of the vascular bed, the degree of coronary narrowing could not

be quantitated. It would be desirable to have a more exact morphological characterisation of the lesion.

Spatial resolution of spectroscopy was limited. This led to an underestimation of viability loss when compared to histology (5.8% decline in ATP signal versus 12.8% of fibrosis within area associated to stenosis). However, reducing the slice thickness in MR spectroscopy (6 mm in our study) with the used technique would mean to prolong acquisition time beyond acceptable limits for valid metabolic studies.

This study may serve as evidence for the value of a single cardiac MR investigation integrating different modalities to thoroughly assess a patient's heart problem. The proposal to fuse the results of different modalities into one image may further add to the advantages of a "one stop shop" MR examination for cardiac diagnostics.

## References


1. Schindler T.H., Magosaki N., Jeserich M., Nitzsche E., Oser U., Abdollahnia T., Nageleisen M., Zehender M., Just H., Solzbach U: 3D assessment of myocardial perfusion parameter combined with 3D reconstructed coronary artery tree from digital coronary angiograms. Int J Card Imaging. 2000 Feb; 16(1):1–12.
2. Langendorff O.: Untersuchung am überlebenden Säugetierherzen. Pflügers Arch. 1895; 61: 291–332.
3. Mareci T.H., Brooker H.R.: Essential considerations for spectral localization using indirect gradient encoding of spatial information. J. Magn. Res., 1991; 92:229–246.
4. Vanhamme L., van den Boogaart A., Van Huffel S.: Improved method for accurate and efficient quantification of MRS data with use of prior knowledge. J. Magn. Res. 1997; 129(1):35–43.
5. Bauer W.R., Hiller K,-H., Roder F., Neubauer S., Fuchs A., Große Boes C., Lutz R., Gaudron P., Hu K., Haase A., Ertl G.: Investigation of Coronary Vessels in Microscopic Dimensions by Two- and Three-dimensional NMR Microscopic Imaging in the Isolated Rat Heart. Visualization of Vasoactive Effects of Endothelin 1. Circulation 1995; 92:968–977
6. Roder F., Hiller K.H., Henz P., v. Kienlin M., Bauer W.R., Ertl G., Haase A.: Three-dimensional coronary angiography of the perfused rat heart. JMRI 1997; 7:316–320.
7. Friedrich J., Apstein C.S., Ingwall J.S.: 31P Nuclear magnetic resonance spectroscopic imaging of regions of remodeled myocardium in the infarcted rat heart. Circulation 1995; 92:3527–3538.
8. Neubauer S., Horn M., Naumann A., Tian R., Hu K., Laser M., Friedrich J., Gaudron P., Schnackerz K., Ingwall J.S.: Impairment of energy metabolism in intact residual myocardium of rat hearts with chronic myocardial infarction. J Clin Invest 1995 Mar; 95(3):1092–100
9. Zhang J., Ishibashi Y., Zhang Y., Eijgelshoven M.H., Duncker D.J., Merkle H., Bache R.J., Ugurbil K., From A.H.: Myocardial bioenergetics during acute hibernation. Am. J. Physiol. 1997; 273:H1452–H1463.
10. Zhang J., Ugurbil K., From A.H., Bache R.: Myocardial oxygenation and high-energy phosphate levels during graded coronary hypoperfusion. Am. J. Physiol. Heart Circ. Physiol. 2001; 280:H318–H326.
11. Yabe T., Mitsunami K., Inubushi T., Kinoshita M.: Quantitative measurements of cardiac phosphorus metabolites in coronary artery disease by $^{31}$P magntetic resonance spectroscopy. Circulation 1995; 92:15–23.

# The Relationship between Regional Integrated Backscatter Levels and Regional Strain in Normal, Acutely Ischemic, and Reperfused Myocardium

Jan D'hooge[1,2,3], Oliver Turschner[2], Christoph Dommke[2], Piet Claus[2], Bart Bijnens[2], Jan Thoen[3], Frans Van de Werf[2], George Sutherland[2], and Paul Suetens[1]

[1] Medical Image Computing, Department of Electrical Engineering
Catholic University of Leuven, Leuven, Belgium
jan.dhooge@uz.kuleuven.ac.be
http://www.medicalimagecomputing.be
[2] Department of Cardiology, Catholic University of Leuven, Leuven, Belgium
[3] Laboratorium voor akoestiek en thermische fysica, Department of physics
Catholic University of Leuven, Leuven, Belgium

**Abstract.** Integrated backscatter (IB) and its cyclic variation (CV) are echocardiographic parameters often used for myocardial tissue characterization. Prior work has suggested that IB is directly related to regional scatterer density while its CV could be induced by local myocardial strain. The purpose of this study was to further test this hypothesis by simultaneously recording cyclic changes in IB and myocardial strain in normal, acutely ischemic and reperfused myocardium.

In ten closed-chest pigs, acute myocardial ischemia was induced by inflating a PTCA balloon in the left circumflex coronary artery. Radiofrequency (RF) M-mode data of the ischemic region of the posterior wall were acquired before, during and immediately after the balloon occlusion. IB and regional radial strain were estimated from the same RF data sets. End-systole was defined on a simulataneously recorded left ventricular pressure trace. The negative radial strain (NRS) was plotted on top of the IB curve.

At baseline, both the NRS and IB pattern paralleled and showed to be minimum at end-systole. During acute ischemia, marked post-systolic thickening was observed which resulted in a post-systolic peak in both the NRS and IB traces: the overall minimum in both curves was phase shifted, i.e. time-delayed. Moreover, the mean IB level increased acutely. Finally, at reperfusion, both the NRS and IB patterns returned to baseline with a minimum at end-systole. However, NRS showed some remaining characteristics of acute ischemic myocardium in contrast to the IB pattern that merely showed a hyperemic but normal response.

IB and NRS thus paralleled over the whole cardiac cycle in normal and acutely ischemic myocardium. At reperfusion the IB curve normalized immediately while the NRS showed some remaining ischemic characteristics. These observations are in concordance with the hypothesis that changes in integrated backscatter are induced by regional three-dimensional strain.

I. Magnin et al. (Eds.): FIMH 2003, LNCS 2674, pp. 278–286, 2003.

# 1 Introduction

Myocardial tissue characterization based on processing the raw backscattered data has been investigated by many research groups [1]. The parameter extracted from the radiofrequency (RF) data that has been studied most thoroughly is the integrated backscatter (IB). IB is calculated by integrating the power spectrum of the received signal over the meaningful bandwidth of the transducer. This implies that it is a measure for the mean backscattered ultrasonic energy from a particular region of tissue.

Extensive evaluation of the properties of IB has demonstrated that its magnitude correlates with the state of the myocardial tissue and can be used to differentiate normal from pathological myocardium. It has been shown that during acute ischemia, the mean IB level raises [2]. Moreover, IB exhibits a cardiac-cycle dependent variation (CV) in normal myocardium. Typically, a variation of 3 to 5 dB was found with a maximum at end-diastole and a minimum at end-systole [1]. However, more recent work showed that increasing the sampling frequency of the IB curve could resolve CV values up to 9-10 dB [3]. Extensive clinical evaluation of CV has demonstrated that the magnitude and the timing of peak and trough IB levels are all influenced by a wide range of disease processes. The magnitude of the CV has been suggested to be an index of contractile performance and to decrease during acute myocardial ischemia over a period of 5 to 60 minutes [4].

However, no consensus has been reached on the origin of this cyclic variation. Some investigators would hold that regional anisotropy produced by local changes in both scatterer density and angle of insonation can account wholly for the CV and its changes during ischemia and that CV is thus simply a measure of regional changes in wall thickness during the cardiac cycle [5]. Others would argue that CV represents more than wall thickness changes and point to the evidence for the return in CV in a myocardial segment following reperfusion which precedes the return of changes in wall thickness [6]. Both theories might, at least in part, by merged by the hypothesis that CV is related to regional three-dimensional strain rather than wall thicknening alone [7]. Although this hypothesis has been tested in normal myocardium [7], it had not been verified in acutely ischemic and reperfused myocardium. The purpose of this study was thus to further test this IB-strain hypothesis by simultaneously recording cyclic changes in IB and myocardial strain in normal, acutely ischemic and reperfused myocardium.

# 2 Material and Methods

## 2.1 Animal Preparation

Ten domestic pigs, weighting 25 to 35 kg, were premedicated with Ketamin (10-20 mg/kg intra-muscular) and anaesthetised with a combination of Propofol 2% (12-20 mg/kg/hour intra-venous) and Fentanyl (0.5 $\mu$g/kg/min). The animals were intubated and ventilated with a mixture of air and oxygen to maintain their

arterial blood gas values in the physiologic range during the study. All animals were treated according to the National Institute of Health Guide for the care and use of laboratory animals.

The left main coronary artery was catheterized under fluoroscopic guidance using an 8F Judkins left catheter via the left carotid artery. A percutaneous transluminal coronary angioplasty balloon (3.5 mm) was placed in the mid-segment of the circumflex artery. Via the right carotid artery, a micromanometer-tipped catheter (Millar Instruments, Houston, Texas) was introduced into the left ventricular cavity.

### 2.2 Ultrasonic Data Acquisition

Cardiac ultrasound IQ data (in-phase quadrature sample RF data) were acquired using an ultrasound scanner (Toshiba, PowerVision 6000, Otawara, Japan) equipped with a digital RF interface for research purposes. During apnoea, M-mode data were recorded over 3 to 5 consecutive cardiac cycles using a 5 MHz phased array transducer (Toshiba, PSM-50AT) from the "at risk" posterior wall segment at a pulse repetition frequency of 5 kHz. Data were transferred to a workstation for off-line analysis.

### 2.3 Experimental Monitoring

A continuous 3-lead electrocardiogram was recorded. Left ventricular pressure (P) and its first temporal derivative (dP/dt) were measured continuously. To avoid acoustic artifacts, care was taken to exclude the catheter from the ultrasonic beam when acquiring ultrasound data. All the above signals were digitized on-line and transferred to a workstation with a commercially available software package (Powerlab/Chart, ADInstruments, Mountain View, California).

### 2.4 Experimental Protocol

Echocardiographic and haemodynamic data were obtained at baseline, immediately following acute coronary artery occlusion (that was maintained for 20 seconds) and immediately following reperfusion. These measurements were repeated three times in each animal with five minutes intervals.

### 2.5 Data Processing

RF data were reconstructed from the IQ data set. Local myocardial velocities were estimated using a cross-correlation method of temporally successive RF segments for all M-mode lines over the relevant image depth as previously described [8]. The length of the kernel was chosen to be 32 RF samples in a search region of 96 samples (corresponding to 612 and 1836 $\mu$m respectively). Window overlap was set at 50%. The normalized cross-correlation function was used as a distance measure [9].

Endo- and epicardial borders were manually identified on the reconstructed gray scale M-mode images. Both borders were moved inwards by 25% of the manually defined wall thickness in order to avoid artifacts from the specular reflections occurring at the endo- and epicardial borders. The instantaneous strain rate was subsequently calculated as the slope of a linear fit through all velocity estimates within these borders [10]. Temporal integration of the strain rate curve resulted in the regional radial (natural) strain pattern [10].

Subsequently, IB was calculated as the average squared RF amplitude within the myocardial borders. In order to reduce the intrinsic variance of the IB estimates due to the stochastic properties of the RF signals [11], temporal smoothing was introduced by averaging the values over 50 consecutive RF lines. The traces were converted in a decibel scale using "1" as a reference value. The CV was subsequently calculated as the end-diastolic minus the end-systolic IB value.

End-diastole and end-systole were defined as the onset of the QRS-complex on the ECG and 20 ms before the minimum of the first derivative of the left ventricular pressure $(dP/dt)_{min}$ respectively [12].

The negative radial strain and IB curves were averaged over all acquisitions and over all animals. Hereto, both systole and diastole were interpolated separately in order to have the same number of samples. An average cardiac cycle was then obtained by merging the average systolic and average diastolic traces.

## 3 Results

Figures 1a–c show respectively the mean IB and negative radial strain curve at baseline, during acute ischemia and during subsequent reperfusion over one R-R interval. Some specific values are given in Table 1.

At baseline, both the NRS and the IB pattern parallel and reach their maximal and minimal value at end-diastole and end-systole respectively (Fig. 1a). During acute ischemia, the radial strain curve reveals early systolic thinning, reduced end-systolic thickening and marked post-systolic thickening (Fig. 1b). The overall minimum of both curves is phase shifted, i.e. delayed in time, by approximately 8% of the average R-R interval. Moreover, the mean IB level acutely increases by approximately 2 dB (Table 1). Finally, at reperfusion, both the NRS and the IB patterns return to their baseline characteristics with a minimum at end-systole (Fig. 1c). However, although the radial strain curve resembles its baseline pattern, it still shows some acute ischemic characteristics with some early systolic thinning, reduced end-systolic thickening (compared to baseline;

**Table 1.** Mean integrated backscatter (IB), its cyclic variation (CV) and end-systolic radial strain at baseline, during acute ischemia and during reperfusion

| | Mean IB (dB) | CV (dB) | end-systolic strain (-) |
|---|---|---|---|
| Baseline | 50.3 | 8.6 | 53% |
| Acute ischemia | 52.5 | 6.3 | 28% |
| Reperfusion | 49.8 | 9.8 | 47% |

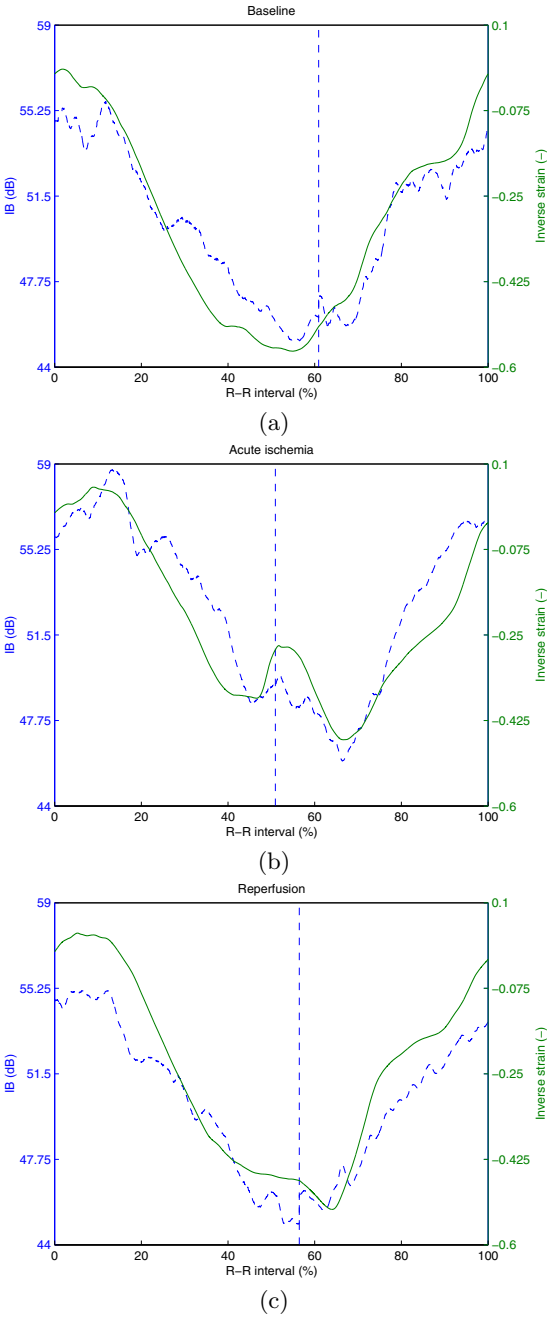


**Fig. 1.** Average integrated backscatter (dashed) and negative radial strain curve (solid) at baseline (a), during acute ischemia (b) and during reperfusion (c)

compared to ischemia there is recovery) and some remaining post-systolic thickening. This is in contrast to the characteristics of the IB trace that shows an increase in CV compared to baseline.

## 4 Discussion

Both the characteristics of normal myocardial deformation and the changes in deformation that are associated with acute myocardial ischemia have been described extensively in the literature. Although normal myocardium shows systolic thickening and diastolic thinning, acutely ischemic myocardium is characterized by early systolic thinning, reduced systolic thickening and continuous thickening after aortic valve closure, i.e. post-systolic thickening [13]. All of these characteristics were observed in our data (Figs. 1a and b). Moreover, acutely ischemic myocardium was shown to restore its normal radial deformation pattern within 20 seconds of reperfusion [13]. In our study, the radial deformation pattern returned to normal although the typical changes associated with acute ischemia were still visible. This was most likely due to the fact that our reperfusion data sets were taken at the onset of the reperfusion period, i.e. before the deformation pattern could normalize itself completely.

The properties of the integrated backscatter curve closely matched those of the radial deformation. For normal myocardium, IB was maximal at end-diastole and minimum at end-systole. During acute ischemia, the mean IB level raised by 2.2 dB and its CV was blunted. These results are in concordance with results found in the literature [1]. Moreover, the early systolic thinning, the reduced systolic thickening and the post-systolic thickening were associated with corresponding changes in IB. Finally, at reperfusion, the mean IB level returned to baseline levels while its CV increased above baseline. However, the phase of the IB curve returned to baseline.

All of the results on IB can be explained in the IB-strain hypothesis. Indeed, if the assumption is made that collagen fibers are the main scattering sites within the myocardium, then normal systolic thickening will be associated with a lower instantaneous fiber density in the echocardiographic resolution cell [7]. This is schematically illustrated in Fig. 2 by comparing the left and right sub-figures. As a result, the average reflected ultrasonic energy decreases with wall thickening. It has been shown that acute ischemia is associated with a decrease in myocardial wall thickness [14]. The density of collagen fibers within the resolution cell of the imaging system thus increases and the mean IB level as well. As a consequence, post-systolic thickening is associated with a phase shift of the IB curve.

Myocardial wall thickening can however not explain the results found during reperfusion in which the IB pattern immediately returned to baseline while the radial deformation still showed signs of acute ischemia. However, due to mechanical stress differences across the myocardial wall, sub-endocardial layers are more sensitive to ischemia than the sub-epicardial ones. Functional recovery after acute ischemia can thus be expected to occur first in the sub-epicardial layers. As these fibers are merely oriented longitudinally, hyperemia in these layers

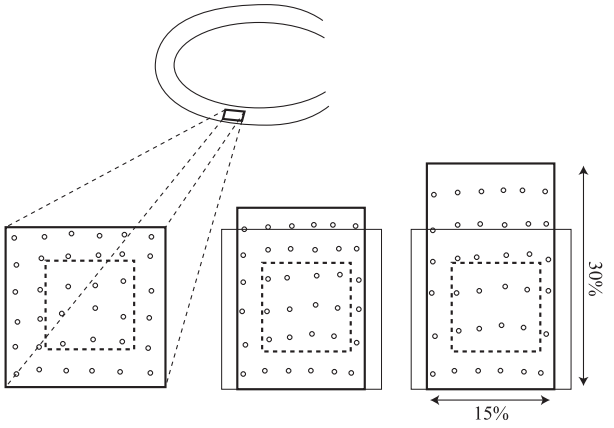


**Fig. 2.** Schematical illustration of the contraction of the posterior wall. The scatterers (collagen fibers) just before systole (left) will be re-organized during contraction. During reperfusion, longitudinal strain is dominant in early systole due to local fiber orientation and transmural ischemic stress differences, resulting in an initial increase in scatterer density (middle). In mid-late systole radial strain is more important (right), resulting in a decrease in scatterer density

initially increases longitudinal shortening rather than radial thickening (which is merely induced by mid-myocardial, circumferential fibers). This principle is schematically illustrated in Fig. 2. CV in IB thus returns above baseline levels, while the radial deformation pattern still shows signs of acute ischemia. These results support the hypothesis that changes in integrated backscatter are related to regional three-dimensional myocardial strain.

## 5 Conclusions

In this paper the relationship between changes in integrated backscatter and regional myocardial strain was further investigated in an animal model of normal, acutely ischemic and reperfused myocardium. Changes in integrated backscatter closely parralleled changes in regional strain. These results further support the hypothesis that changes in tissue reflectivity during the cardiac cycle are induced by regional myocardial strain.

**Acknowledgments.** This work was supported by the Fund for Scientific Research – Flanders (FWO). The authors would like to thank Dr. Joerg Schlegel, Toshiba Medical Systems, for his technical assistance of the project.

## References


1. J.E. Perez, V.G. Dávila-Román, and J.G. Miller. Assessment of myocardial viability by ultrasonic tissue characterization. *Coronary Artery Disease*, 6(8):613–618, 1995.
2. B. Bijnens, J. D'hooge, M. Schrooten, S. Pislaru, C. Pislaru, B. De Man, J. Nuyts, P. Suetens, F. Van de Werf, G.R. Sutherland, and M.C. Herregods. Are changes in myocardial integrated backscatter restricted to the ischemic zone in acute induced ischemia ? an in-vivo animal study comparing localized with widespread ischemia. *J. Am. Soc. Echo.*, 13(4):306–315, 2000.
3. J. D'hooge, B. Bijnens, F. Jamal, C. Pislaru, J. Thoen, P. Suetens, F. Van de Werf, C. Angermann, F. Rademakers, M.C. Herregods, and G.R. Sutherland. High frame rate myocardial integrated backscatter. does this change our understanding of this acoustic parameter? *Eur. J. Echocard.*, 1(1):32–41, 2000.
4. J.G. Miller, J.E. Perez, S.A. Wickline, S.L. Baldwin, B. Barzilai, V. Davila-Roman, R.J. Fedewa, A.E. Finch-Johnston, C.S. Hall, S.M. Handley, F.D. Hockett, M.R. Holland, A. Kovacs, G.M. Lanza, S.H. Lewis, J.N. Marsh, J. Mobley, D.E. Sosnovik, R.L. Trousil, K.D. Wallace, and K.R. Waters. Backscatter imaging and myocardial tissue characterization. *Proceedings IEEE Ultrasonics Symposium*, pages 1373–1383, 1998.
5. H. Rijsterborgh, F. Mastik, C.T. Lancee, A.F.W. Van der Steen, L.M.A. Sassen, P.D. Verdouw, J. Roelandt, and N. Bom. Ultrasonic myocardial integrated backscatter and myocardial wall thickness in animal experiments. *Ultrasound in Medicine & Biology*, 16(1):29–36, 1990.
6. M.R. Milunski, G.A. Mohr, K.A. Wear, B.E. Sobel, J.G. Miller, and S.A. Wickline. Early identification with ultrasonic integrated backscatter of viable but stunned myocardium in dogs. *JACC*, 14(2):462–471, 1989.
7. J. D'hooge, F. Jamal, B. Bijnens, J. Thoen, F. Van de Werf, P. Suetens, and G.R. Sutherland. The relationship between regional integrated backscatter levels and regional strain. *Proceedings IEEE Ultrasonics Symposium*, pages 1325–1328, 1999.
8. J. D'hooge, J. Schlegel, P. Claus, B. Bijnens, J. Thoen, F. Van de Werf, G.R. Sutherland, and P. Suetens. Evaluation of transmural myocardial deformation and reflectivity characteristics. *Proceedings IEEE Ultrasonics Symposium*, pages 1185–1188, 2001.
9. S. Langeland, J. D'hooge, H. Torp, B. Bijnens, and P. Suetens. A simulation study on the performance of different estimators for two-dimensional velocity estimation. *Proceedings IEEE Ultrasonics Symposium*, page In press, 2002.
10. J. D'hooge, B. Bijnens, J. Thoen, F. Van de Werf, G.R. Sutherland, and P. Suetens. Echocardiographic strain and strain-rate imaging: a new tool to study regional myocardial function. *IEEE Transactions on Medical Imaging*, 21(9):1022–1030, 2002.
11. B. Bijnens, J. D'hooge, G.R. Sutherland, M.C. Herregods, J. Nuyts, P. Suetens, and F. Van de Werf. Robustness of integrated backscatter for myocardial tissue characterization. *Ultrasound in Medicine & Biology*, pages 95–103, 1999.
12. P. Theroux, J. Ross, D. Franklin, W.S. Kemper, and S. Sasyama. Regional myocardial function in the conscious dog during acute coronary occlusion and responses to morphine, propranolol, nitroglycerin and lidocain. *Circulation*, 53(2):302–314, 1976.

13. F. Jamal, M. Szilard, T. Kukulski, X.S. Liu, J. D'hooge, B. Bijnens, F. Rademakers, L. Hatle, I. De Scheerder, and G.R. Sutherland. Changes in systolic and postsystolic wall thickening during acute coronary occlusion and reperfusion in closed-chest pigs: implications for the assessment of regional myocardial function. *J. Am. Soc. Echo.*, 14(7):691–697, 2001.
14. O. Turschner, J. D'hooge, C. Dommke, P. Claus, E. Verbeken, I. De Scheerder, B. Bijnens, and G.R. Sutherland. The sequential changes in systolic and postsystolic thickening which occur during acute infarction, infarct reperfusion and the expression of reperfusion injury. *European Heart Journal*, page (Submitted), 2003.

# Why Ischemic Hearts Respond Less to Cardiac Resynchronisation Therapy. A Modeling Study

Piet Claus[1], Bart Bijnens[1], Ole-Alexander Breithardt[2], and George R. Sutherland[1]

[1] Department of Cardiology, K.U.Leuven, University Hospitals Gasthuisberg
Herestraat 49, B-3000 Leuven, Belgium
Piet.Claus@uz.kuleuven.ac.be
http://www.kuleuven.ac.be/cardim/
[2] Department of Cardiology, University Hospital Aachen
D-52057 Aachen, Germany

**Abstract.** Cardiac Resynchronisation Therapy (CRT) by means of simultaneous biventricular or multisite leftventricular pacing is a new technique for improving left ventricular systolic performance in patients with heart failure and conduction abnormalities (e.g. left bundle branch block). However, different pathological cases do react differently to CRT and the underlying mechanisms are poorly understood. This paper presents a study of the mechanical effects of delayed activation on ejection and regional deformation using a simplified mathematical model. These effects are studied in normal and dilated hearts, and ischemic non-dilated and dilated hearts. From these simulations we derive dependencies of regional performance parameters on delayed activation and discuss why ischemic hearts do respond less to CRT.

## 1 Introduction

Cardiac Resynchronisation Therapy (CRT) is a relatively new treatment option for patients with heart failure and delayed intraventricular activation[1,2] by means of simultaneous right ventricular (apical) and left-ventricular (lateral) stimulation. In this way, delays in intra-ventricular activation are restored. Currently, patient selection criteria for CRT are based on (i) the New York Heart Association (NYHA) classification which classifies cardiac patients according to their overall physical activity capabilities and on the (ii) QRS duration. Large-scale controlled clinical trials have demonstrated both the acute and long-term clinical effects of CRT in selected patients [3,4,5]. The study of regional cardiac deformation is the closest we can get to study regional cardiac function non-invasively by means of echocardiographic strain rate imaging or cardiac magnetic resonance imaging using tagging. Therefore it is useful to study the changes in deformation that occur with delayed activation and resynchronisation. Ultimately, if these changes are well understood they may provide a better way of recruiting patients. In some patients the late activated region is ischemic and these patient are shown to respond less to CRT.

I. Magnin et al. (Eds.): FIMH 2003, LNCS 2674, pp. 287–294, 2003.

In order to have a better understanding of functional changes induced by delayed activation and/or (regional) ischemia we have set out a mathematical modeling study to simulate changes in regional deformation. This model is an effective macroscopic simulation model in the sense that it is simplified to a model dependent on a small number of parameters describing regional heterogeneity (both temporal and spatial) in contractile and/or elastic properties of interacting myocardial segments. This model is an extention of the model described in [6]. As opposed to a complete 'biophysical' model such a model is more effective in probing the moduli space, because of its limited number of parameters.

To cover a range of patients, four groups of simulations have been performed mimicking normal (N), dilated (DCM), regionally ischemic non-dilated (I) and regionally ischemic dilated hearts (ICM). Regional ischemia occurs in the late activated region and is modeled by a reduced and prolonged active force generation. This model of ischemic force development has been supported by findings on shortening profiles of unloaded ischemic cells. [6] In all the groups radial deformation has been simulated for a clinical range of delayed activation times.

Post-systolic thickening, i.e. thickening after Aortic Valve Closure has been identified both in hearts with left bundle branch block as well as in ischemic segments. Post-systolic thickening in normally activated ischemic segments can be shown to be passive deformation due to interaction with neighbouring segments. However, this post-systolic thickening can occur due to late activation and is not associated solely with ischemia.

The paper is organized as follows. Section+2 describes the simplified model and outlines discusses how the model parameters have been taken for the different groups. The derived parameters (describing the ejection and post-systolic phase) are explained. In Sect. 3 the results are presented and Sect. 4 summarizes the conclusions.

## 2 Methods

### 2.1 Description of the Simplified Model

The model used has been described earlier [6] and has been adapted to simulated delayed activation times.

**Model Geometry.** A mid-wall short-axis slice of the left ventricle is effectively described by a ring of discrete segments. The model allows for the simulation of variable-sized contiguous segments. Assuming conservation of myocardial volume, the segmental 'thickness' $w$ is taken to be inversely proportional to the segmental length $\ell$.

**Force Balance.** The dynamic equation to be solved is the balance of the internal (elasticity, contractile force and segment interaction forces) and external (cavity pressure) forces for each segment.

The *elastic force* (passive response to strain) is described by a non-linear stress ($T$) – strain ($\lambda$) relation on the segments

$$T = \frac{C}{K}\left(e^{K\lambda} - 1\right), \qquad \text{where} \qquad \lambda = \frac{\ell(t) - \ell(0)}{\ell(0)}, \tag{1}$$

where $\ell(t)$ is the instantaneous length and $\ell(0)$ is the diastolic length of the segment. $C$,$K$ are elasticity constants.

The *active contraction stress* is approximated by a Gaussian curve, which peaks at 1/3 of systole. This active stress profile has been adopted from experiments of active tension measurements with physiological loading conditions[7]. This active force is parametrised by three parameters, i.e. the onset (O), duration (D) and amplitude (A) and acts in the circumferential direction. One side of the myocardial short-axis slice (identified as the septal wall) is activated first and the activation spreads with a constant velocity along the segments to the other side of the slice (the lateral wall) in a time period that is variable. This myocardial activation time is variable.

The interaction forces ($F_R$) or "*shear forces*" , which occur between two segments, labeled $i$ and $j$, of different thickness can be described effectively by a simple Hookean relation, i.e.

$$F_{iR} = -k(w_i - w_j), \tag{2}$$

where $k$ is an 'elasticity' constant determining the relative strength of the interaction.

The left-ventricular *cavity pressure* ($P$), which is acting radially, i.e. orthogonal to the segments, was derived from the left-ventricular pressure traces recorded in patients. These pressure traces were interpolated to match the mechanical event timings of the simulations.

**The Subdivision of the Cardiac Cycle and the Solution Method.** The cardiac cycle was defined to have a fixed length (800 ms). This is equivalent to a heart rate of 75 beats/min. The cycle was divided into a pre-ejection period (defined from mechanical activation to Aortic Valve Opening (AVO) (duration 80 ms), ejection (AVO to Aortic Valve Closure (AVC) (duration 250 ms), isovolumetric relaxation period (AVC to Mitral Valve Opening (MVO) (duration 50 ms). The remainder of the cycle was ascribed to diastole. The model described above was implemented in Matlab (The MathWorks, Inc., Natick, Massachusetts, USA). For all simulations the number of segments was set to 400, with a variable diastolic cavity diameter.

The dynamics of the resulting coupled system is solved by integration of the equations of motion (Euler method), with time-steps of 1 ms.

### 2.2 Simulations

**Model Parameters for the Simulation of Normal Regional Myocardial Deformation.** Independent of the segment location in the myocardium, the

peak active tension occurs early in ejection (at about 1/3 of systole).[7] At this point in the cycle, the cytosolic calcium has returned to diastolic levels and the crossbridges start to break down (this is the onset of biochemical relaxation). As a result, the active tension gradually returns to zero.

The values of the force parameters in the model for normal myocardium were set to: $K = 4$, $C = 20$kPa, $k = .5$kPa, $A = 68$kPa, $D = 200$ms. The duration of the activation wave is set to 60 ms. The maximal systolic pressure was 90mmHg. The end-diastolic cavity diamater in normal human hearts was taken to be 4.8 cm.

**Model Parameters in the Pathological Groups.** To mimick the clinical situations of normal non-dilated (N) and dilated (DCM) hearts and regionally ischemic non-dilated (I) and dilated hearts (ICM), we have performed four sets of simulations.

Ischemia was simulated by reducing the normal active contraction force by a factor of 3 and prolonging the active contraction force by a factor of 2.

The activation delay between the septal (first activated) and lateral (last activated) wall has been varied from 60ms to 120ms with steps of 5 ms. This range corresponds to a clinical range from normal to patients with Left Bundle Branch Block. This range of activation delays has been introduced in 4 groups of simulations.

*Normal Size – Normal Myocardium.* The range of delayed activation described above was implemented in the model with normal force development and size.

*Dilated Hearts – Normal Myocardium.* Dilatation was simulated by changing the end-diastolic diameter from 4.8 cm (normal) to 9 cm (dilated). However, the active stress development remained unchanged.

*Normal Size – Regionally Ischemic Myocardium.* The range of delayed activation was implemented in a model with ischemia in site of latest activation. The size of the ischemic insult is taken to be 30% of the circumference and positioned in the lateral wall.

*Dilated Hearts – Regionally Ischemic Myocardium.* The ischemic simulation was repeated in hearts with a end-diastolic diameter of 9 cm.

### 2.3 Derived Parameters

Two systolic parameters have been derived from the simulation results. The *end-systolic radial strain* ($ESS$), i.e. the amount of thickening at end-ejection and the *regional stroke volume* ($RSV$), derived as the relative change in segmental cavity size. The short axes slice of the ventricle has been divided into 8 pie-shaped sectors, with there tip at the center of the cavity at end diastole. The area change of these sectors from end diastole to end systole has been computed, keeping the tip at the same position. This is taken as a measure of regional stroke volume, i.e. the contribution of the individual wall segments to the global stroke volume.

Two parameters describing timing changes in radial deformation w.r.t. normal deformation are the *Post-Systolic Strain* ($PSS$), which is the amount of thickening after aortic valve closure and the *time to maximal strain* ($T_{PS}$) measured from the time of aortic valve closure.

## 3 Results and Discussion

The results of the simulations are summarized in Figs. (1, 2 and 3). In the remainder of this paper, the terminology 'septal' wall is used for the earliest activated segment and 'lateral' wall for the latest activated segment.

In Fig. 1 radial strain during systole and the first part of diastole is depicted for the different delays and groups. In all cases the delayed activation induces post-systolic thickening in the lateral wall. However, this seems more pronounced for the small ventricles than for the dilated ventricles. Though the contractility for the dilated ventricles was kept the same (ignoring effects on contractility by fibre stretching as in the Frank-Starling mechanism), these ventricles exhibit reduced strain values in all the walls. This can be explained by the fact that the circumferential wall-stress due to the pressure increases in these ventricles, or otherwise put, the myocardium has to develop a larger active force to produce the same pressure in the cavity (following the law of Laplace).

Looking closer to the systolic parameters (Fig. 2), the magnitude of the end-systolic strain decreases with regional ischemia, and decreases further with dilatation. There is a marked decrease in the dependence of end-systolic strain on delay (slope of the curves) for dilatation which is not so pronounced for ischemic normal-sized hearts.

In contrast, the regional stroke volume of the late activated and/or ischemic segments behaves quite simular for non-ischemic hearts. They exhibit a higher dependency on delays than ischemic hearts which do almost not depend on the delays (zero-slopes). The reason why dilated hearts can maintain their stroke volume, with less deformation is the simple fact that 'most of the volume of a sphere sits at the boundary'. For regional stroke volume there is a marked difference for ischemic versus normal hearts.

Ischemic hearts show a larger dependency of post-systolic strain on delays than non-ischemic hearts (Fig. 3). This can be explained by the fact that two components play a role in the post-systolic thickening in regionally ischemic myocardium. First the ischemic segments have a reduced and prolonged active force development compared to the normal segments. This leads to a regional heterogeneity in amplitude and duration of active force development, causing non-homogeneous thickening in neighbouring segments. This differential thickening induce segmental interaction forces which produce passive thickening after aortic valve closure. However, the delayed activation shifts the tail of the active force development in ischemic hearts into the isovolumetric relaxation period. This then amplifies the passive effect already described above. In non-ischemic hearts the delayed activation causes post-systolic thickening in

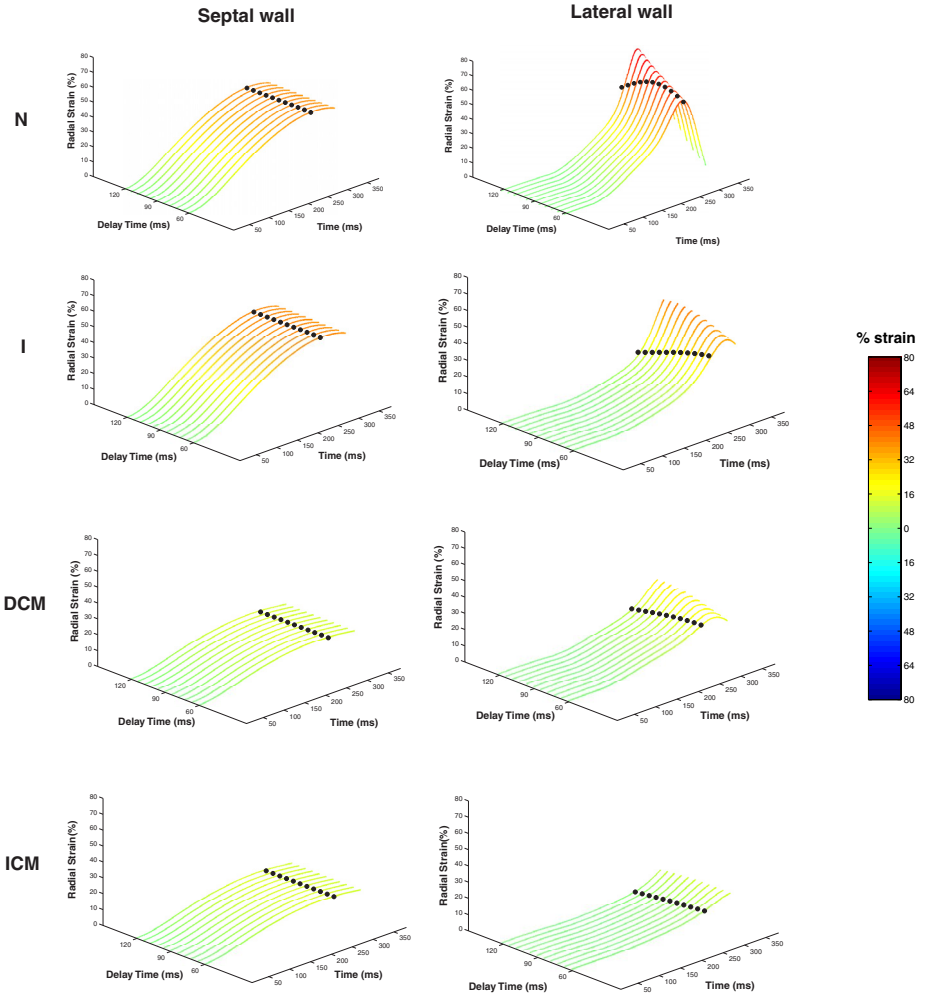


**Fig. 1.** Regional deformation curves as a function of delayed activation time for all four groups of simulations. The left column represents the septal wall which is activated first and always non-ischemic. The right column represents the radial strain at the point in the lateral wall which is activated last and is ischemic in the ischemic simulations. The black dots represent the timing of Aortic Valve Closure

the lateral wall, again due to passive segmental interaction forces induced by temporal heterogeneity in thickening.

## 4 Conclusions

Using an effective simplified model, we have been probing the underlying mechanisms of delayed activation times in hearts with different sizes (dilated vs.

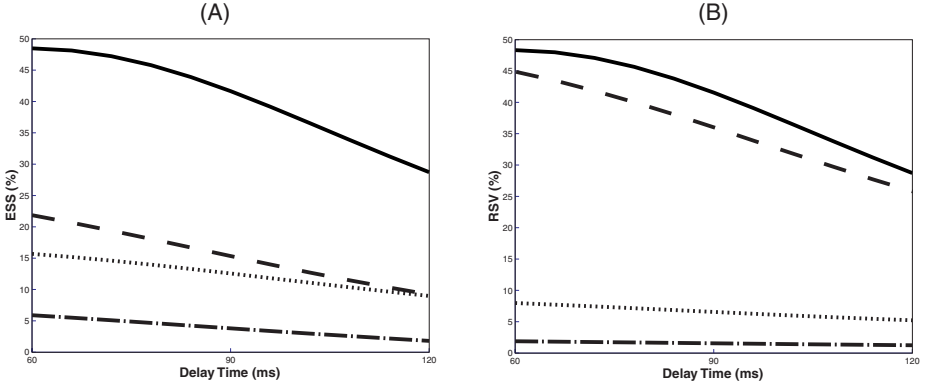


**Fig. 2.** Dependency of the systolic paramaters: (A) end-systolic strain and (B) regional stroke volume in the lateral wall. Solid line: Normal, Dotted line: Ischemic, Dashed line: Dilated, Dash-dotted line: Ischemic Dilated

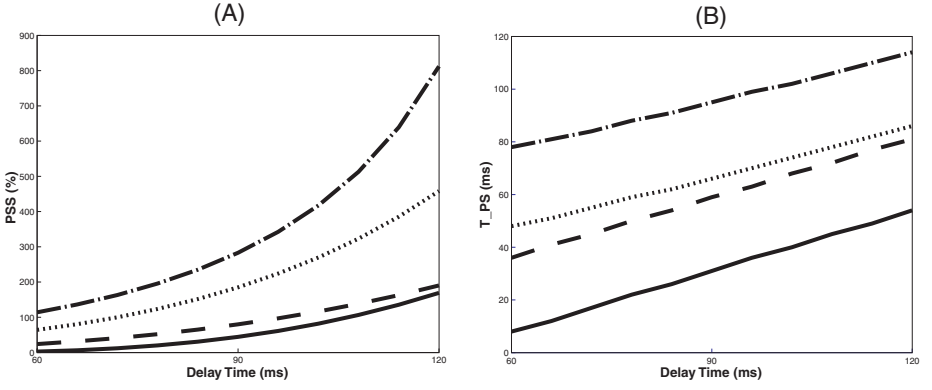


**Fig. 3.** Dependency of the post systolic paramaters in the lateral wall: (A) post systolic strain and (B) timing of post systolic strain. Solid line: Normal, Dotted line: Ischemic, Dashed line: Dilated, Dash-dotted line: Ischemic Dilated

non-dilated) and different regional contractility (ischemic vs. non-ischemic). The general findings from this modeling study are that by resynchronising the ventricles different amounts of systolic performance can be recruited for normal versus ischemic myocardium. With resynchronisation, ischemic segments would not increase their regional stroke volume, as a measure of ejection performance, significantly. Moreover, in dilated ischemic hearts also the end-systolic strain could not be improved by resynchronising, but only reduce the amount of post-systolic strain which is not contributing to the ejection. Therefore, Cardiac Resynchronization Therapy would have little effect on the systolic performance in regionally ischemic dilated hearts.

To conclude, this paper also shows that simplified macroscopic models can be useful in explaining clinical findings.

## References

1. S. Cazeau, D. Graz, A. Lazarus, P. Ritter and J. Mugica. Multisite stimulation for correction of cardiac asynchrony. *Heart* 84(6) 2000 579–581.
2. S. Cazeau, C. Leclerq, T. Lavergne, S. Walker, C. Varma, C. Linde, S. Garrigue, L. Kappenberger, G.A. Haywood M. Santini and C. Bailleul. Effects of multisite biventricular pacing in patients with heart failure and intraventricular conduction delay. *N. Engl. J. Med.* 344(12) (2001) 873–80.
3. A. Auricchio, C. Stellbrink, S. Sack, M. Block, J. Vogt, P. Bakker, C. Huth, F. Schondube, U. Wolfhard, D. Bocker, O. Krahnefeld and H. Kirkels. Long-term clinical effect of hemodynamically optimized cardiac resynchronization therapy in patients with heart failure and ventricular conduction delay. *J. Am. Coll. Cardiol.* 39(12) (2002) 2026–2033.
4. C. Linde, C. Leqlercq, S. Rex, S. Garrigue, T. Lavergne, S. Cazeau, W. McKenna, M. Fitzgerald, J.C. Deharo, C. Alonso, S. Walker, F. Braunschweig, C. Bailleul and J.C. Daubert. Long-term benefits of biventricular pacing in congestive heart failure: results from the MUltisite STImulation in Cardiomyopathy (MUSTIC) study. *J. Am. Coll. Cardiol.* 40(1) (2002) 111–118.
5. W.T. Abraham, W.G. Fisher, A.L. Smith , D.B. Delurgio, A.R. Leon,E. Loh, D.Z. Kocovic,M. Packer,A.L. Clavell, D.L. Hayes, M. Ellestad, R.J. Trupp, J. Underwood, F. Pickering, C. Truex, P. McAtee and J. Messenger. Cardiac resynchronization in chronic heart failure. *N. Engl. J. Med.* 346(24) (2002) 1845–1853.
6. P. Claus, B. Bijnens, F. Weidemann, C. Dommke, V. Bito, F. Heinzel, K. Sipido, I. De Scheerder, F.E. Rademakers and G.R. Sutherland. Post-systolic thickening in ischemic myocardium: A simple mathematical model for simulating regional deformation. In T. Katila, J. Nennonen, I.E. Magnin et al., eds, *Functional Imaging and Modeling of the Heart: fisrt international workshop*, volume 2230 of *Lecture Notes in Computer Science* (2001) 135–139.
7. J.M. Guccione, G.S. Le Prell, P.P. de Tombe and W.C. Hunter. Measurements of active myocardial tension under a wide range of physiological loading conditions. *J. Biomechanics* 30(2) (1997) 189–192.c

# Finite Element Models for Mechanical Simulation of Coronary Arteries

Javier Rodríguez, José Mª Goicolea, Juan C. García, and Felipe Gabaldón

E.T.S.I. Caminos, Canales y Puertos, Depto. Mecánica de Medios Continuos
Universidad Politécnica de Madrid (UPM), Madrid, 28040, Spain
jrs@mecanica.upm.es
http://w3.mecanica.upm.es

**Abstract.** Mechanical simulation of tissue in the walls of coronary arteries may provide valuable quantitative information for medical practice, such as understanding the evolution of stenosis, angioplasty processes, and placement of stents and possible restenosis. The material constitutive models which represent the mechanical response to strain are highly nonlinear as well as anisotropic, thus precluding standard finite element formulations with isotropic or linear elastic materials. Further, in order to study phenomena such as stenosis or restenosis, they must include essential phenomena in biological soft tissues such as growth and remodeling, as well as the consideration of initial stresses and strains. This paper discusses these issues and proposes some mathematical models for their mechanical simulation within a finite element framework. Some preliminary applications to the study of clinical cases are shown.

## 1 Introduction

Diseases in coronary arteries are strongly affected by mechanical factors such as stress and strain states. Computer simulation of the mechanical behaviour of coronary arteries is possible through the use of advanced mathematical models and numerical algorithms, implemented in a nonlinear finite element setting. This simulation enables a detailed analysis which may aid in the understanding and prevention of desease (stenosis, atherosclerosis, angina), as well as in planning of interventions (angioplasty, placement of stents).

A basic characteristic in soft tissue, which provides important challenges from a mathematical and numerical point of view, is an adequate representation of the highly nonlinear material behaviour (constitutive models). The models employed must include large deformations, strains and rotations. Furthermore, the material response exhibits a strong anisotropic behaviour, governed by the different properties of collagen fibers, elastin and smooth muscle cells.

An important feature whose relevance is enhanced by nonlinearity is the presence of initial stresses and deformations in vessel walls for the physiological state. A significant change in behaviour is obtained due to these initial stresses, which may be explained by using nonlinear material models. Furthermore, other

I. Magnin et al. (Eds.): FIMH 2003, LNCS 2674, pp. 295–305, 2003.

relevant aspects are biological growth and remodelling of tissues, as well as time or rate-dependence of the response.

Standard Finite Element formulations are not suitable for these problems, being generally limited to linear or isotropic material behaviour, and not considering the nonlinear features from initial strains or remodelling.

In this paper we discuss material constitutive models formulated within a basic hyperelastic setting, which includes anisotropy induced by the presence of collagen fibres. Within this setting a model for incorporating growth and remodelling of tissues is developed, extending the theorical framework proposed by Rodr´Ωguez [1] for general 3D geometries. Also, motivated by the presence of residual stresses and preloading in physiological states measured in-vivo, a scheme for the introduction of initial stress is discussed. Finally, some preliminary representative numerical simulations obtained with finite elements are shown.

## 2 Hyperelastic Material Models for Arterial Walls

### 2.1 Basic Assumptions

For the sake of completeness, we define below some basic concepts used in this work, following standard theories of continuum mechanics [2]. The deformation mapping is defined by $\boldsymbol{x} = \boldsymbol{\varphi}(\boldsymbol{X})$, where $\boldsymbol{x}$ and $\boldsymbol{X}$ are the position vectors of a particle in the reference configuration $\mathcal{B}_0$ and the deformed configuration $\mathcal{B}_t$ respectively (Fig. 1a).

The basic assumption for hyperelastic materials is the existence of a stored energy function $W(\boldsymbol{F})$ at each point $\boldsymbol{X}$ of the reference configuration, which depends only on the deformation gradient $\boldsymbol{F} = \mathrm{Grad}\,\boldsymbol{\varphi}$. Invariance with respect to frame of observation allows this stored energy to be expressed as $W(\boldsymbol{F}) = \hat{W}(\boldsymbol{C})$, where $\boldsymbol{C} = \boldsymbol{F}^{\mathrm{T}}\boldsymbol{F}$ (right Cauchy-Green tensor) is independent of rotations of the observer. Stresses (Fig. 1b) are determined by $\boldsymbol{S} = 2\partial\hat{W}/\partial\boldsymbol{C}$, where $\boldsymbol{S}$ is the second Piola-Kirchhoff stress tensor, related to the Cauchy (true) stress

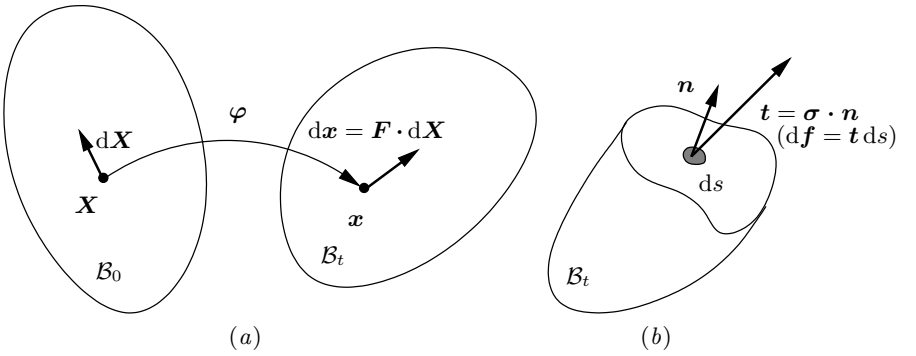


**Fig. 1.** Reference and deformed configuration $(a)$. Stresses $(b)$

tensor $\boldsymbol{\sigma}$ by $\boldsymbol{S} = J\boldsymbol{F}^{-1}\boldsymbol{\sigma}\boldsymbol{F}^{-\mathrm{T}}$, with $J = \det \boldsymbol{F}$. Tangent elastic moduli tensors, necessary for solution algorithms in any numerical setting such as a finite element scheme, are also determined from $\hat{W}$. In particular, the linearised relation is $\delta\boldsymbol{S} = \mathbb{C}\mathbf{:}\frac{1}{2}\delta\boldsymbol{C}$, where the tensor of elastic moduli is $\mathbb{C} = 4\partial^2\hat{W}/\partial\boldsymbol{C}\partial\boldsymbol{C}$.

### 2.2 Isotropic Hyperelasticity

Isotropic hyperelastic materials exhibit an invariant response for rotation in the reference configuration, i.e. $W(\boldsymbol{F}) = W(\boldsymbol{F}\boldsymbol{Q})$ for any rotation tensor $\boldsymbol{Q}$. In this case, $W$ can be expressed as a function of the Jordan invariants of $\boldsymbol{C}$, i.e. $W = \check{W}(I_1, I_2, I_3)$, where $I_1 = \operatorname{tr}\boldsymbol{C}$, $I_2 = \frac{1}{2}\left((\operatorname{tr}\boldsymbol{C})^2 - \operatorname{tr}\boldsymbol{C}^2\right)$ and $I_3 = \det\boldsymbol{C}$. Stresses are obtained by

$$\boldsymbol{S} = 2\sum_{p=1}^{3}\frac{\partial\check{W}}{\partial I_p}\frac{\partial I_p}{\partial\boldsymbol{C}}. \tag{1}$$

Further, due to the unique relation between invariants and eigenvalues of $\boldsymbol{C}$ ($\lambda_1^2$, $\lambda_2^2$, $\lambda_3^2$), $W$ may also be defined as $W = \bar{W}(\lambda_1, \lambda_2, \lambda_3)$.

A convenient material model for arterial walls is due to Ogden, formulated in terms of the principal streches,

$$W = \frac{K}{2}\log^2 J + \sum_{p=1}^{3}\left(\frac{\mu_p}{\alpha_p}\sum_{q=1}^{3}\tilde{\lambda}_q^{\alpha_p}\right), \quad \text{where } \tilde{\lambda}_q = J^{-1/3}\lambda_q.$$

As in this model, it is common to express $W$ as a sum of two contributions, $W = W_{\mathrm{vol}}(J) + W_{\mathrm{iso}}(\tilde{\boldsymbol{F}})$. The first term accounts for the volumetric response (function of $J$). Soft tissues generally exhibit a nearly incompressible response [1]. The second term is a function of $\tilde{\boldsymbol{F}} = J^{-1/3}\boldsymbol{F}$ which represent the volume preserving component of the deformation. As such, it is not affected by multiplications of $\boldsymbol{F}$ by scalars (equivalent to pure alterations of volume). Material parameters $\{\mu_p\}$ and $\{\alpha_p\}$ are determined from experimental tests for the range of loads which the material will be subject to. In this sense, one of the major advantages in Ogden's model is to allow an adequate increase of stiffness with deformation generally exhibited in soft biological tissues [3]. Further, stability conditions (see, e.g., [4]) are to be taken into account. Assuming linear external potentials for the principal stretches, this results in some restrictions: $\mu_p \geq 0$ if $\alpha_p > 1$ and $\mu_p \leq 0$ if $\alpha_p < 1$.

### 2.3 Anisotropic Hyperelasticity

Arterial walls are strongly anisotropic due to the presence of collagen fibres, taking into account the large difference in stiffness with elastin and smooth

[1] In order to avoid numerical locking for incompressible behaviour a mixed finite element formulation for the three field Simó-Taylor-Pister variational principle is usually adopted.

muscle cells. Collagen fibres appear in layers disposed mainly in two different directions.

Hyperelastic materials with *two preferential directions* may be considered within the framework proposed by Spencer [5], based on the fiber orientations determined in the reference configuration by unit vectors $\boldsymbol{a}_0$ and $\boldsymbol{b}_0$. These directions originate the the scalar parameters (called *pseudo-invariants*) $I_4 = \boldsymbol{a}_0 \cdot \boldsymbol{C} \cdot \boldsymbol{a}_0$, $I_5 = \boldsymbol{a}_0 \cdot \boldsymbol{C}^2 \cdot \boldsymbol{a}_0$, $I_6 = \boldsymbol{b}_0 \cdot \boldsymbol{C} \cdot \boldsymbol{b}_0$, $I_7 = \boldsymbol{b}_0 \cdot \boldsymbol{C}^2 \cdot \boldsymbol{b}_0$, $I_8 = (\boldsymbol{a}_0 \cdot \boldsymbol{b}_0)\boldsymbol{a}_0 \cdot \boldsymbol{C} \cdot \boldsymbol{b}_0$ and $I_9 = (\boldsymbol{a}_0 \cdot \boldsymbol{b}_0)^2$, in such a way that $W$ can be writen as $W(\{I_p\}, p = 1, \ldots, 9)$. The stress tensor $\boldsymbol{S}$ is determined similarly to (1) extending the summation index from 1 to 9.

A suitable model for arterial walls within the above setting has been proposed by Holzapfel [6],

$$W = \frac{K}{2} \log^2 J + \frac{c}{2}(\tilde{I}_1 - 3) + \frac{k_1}{2k_2} \sum_{p=4,6} \left( \exp(k_2(\tilde{I}_p - 1)^2) - 1 \right),$$

where $\{\tilde{I}_p\}$ are the (pseudo-)invariants of $\tilde{\boldsymbol{F}}$, and $K$, $c$, $k_1$ and $k_2$ are positive material parameters. The first term with large $K$ values is introduced for pseudo-incompressibility (as in the Ogden model). The second term represents the behaviour of the matrix (mainly determined by smooth muscle cells and elastin). The third term includes the response of collagen fibres as a sum of exponential functions which represent adequately the increase with the deformation. This is motivated from micromechanics and phenomenological results. We wish to remark that, due to stability considerations, this material should have a positive stretch along the preference directions, i.e. $I_4 \geq 1$ and $I_6 \geq 1$. Otherwise, this would produce convergence problems in a calculation e.g. from a zero-stress state. The above model has the advantage over the classical Fung-type models [11] of being more consistent with the micromechanics of the arterial wall.

For general 3D geometries, some assumptions are needed to assign the fiber directions in the mesh. We consider a distribution with cylindrical symmetry with respect to the virtual axis of the artery. Given $(O, \boldsymbol{u}_z)$ a point and unit tangent vector which define the virtual axis, for each material point $P$, referred to the local cylindrical base vectors, the directions are mapped to

$$\boldsymbol{a}_0 = \boldsymbol{u}_z \cos\phi + \boldsymbol{u}_\theta \sin\phi \quad \text{and} \quad \boldsymbol{b}_0 = \boldsymbol{u}_z \cos\phi - \boldsymbol{u}_\theta \sin\phi,$$

where $\phi$ is the average angle between the axis of the artery and the collagen fibres (see Fig. 2).

As an example, let us consider the stress state typical of physiological states, with initial stretches $\lambda_z$ and $\lambda_\theta$ in longitudinal and circumferential directions respectively, corresponding to a deformation gradient $\boldsymbol{F} = \lambda_\theta \boldsymbol{u}_\theta \otimes \boldsymbol{u}_\theta + \lambda_z \boldsymbol{u}_z \otimes \boldsymbol{u}_z + (\lambda_\theta \lambda_z)^{-1} \boldsymbol{u}_r \otimes \boldsymbol{u}_r$. For an incompressible material ($K \to \infty$), the induced Cauchy stress tensor results $\boldsymbol{\sigma} = (\tilde{\sigma}_\theta + \sigma')\boldsymbol{u}_\theta \otimes \boldsymbol{u}_\theta + (\tilde{\sigma}_z + \sigma')\boldsymbol{u}_z \otimes \boldsymbol{u}_z + \sigma' \boldsymbol{u}_r \otimes \boldsymbol{u}_r$,

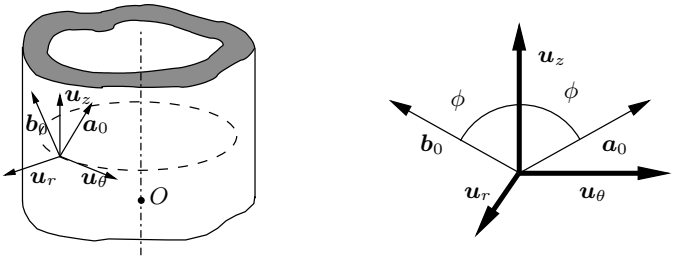


**Fig. 2.** Definition of preferential directions in the material

where

$$\tilde{\sigma}_\theta = c\left(\lambda_\theta^2 - (\lambda_\theta\lambda_z)^{-2}\right) + 4k_1\lambda_\theta^2 \exp\left(k_2(\lambda_\theta^2 \sin^2\phi + \lambda_z^2\cos^2\phi - 1)^2\right) \left(\lambda_\theta^2 \sin^4\phi + \lambda_z^2(\cos^2\phi - \cos^4\phi) - \sin^2\phi\right)$$

and

$$\tilde{\sigma}_z = c\left(\lambda_\theta^2 - (\lambda_\theta\lambda_z)^{-2}\right) + 4k_1\lambda_z^2\cos^2\phi \exp\left(k_2(\lambda_\theta^2 \sin^2\phi + \lambda_z^2\cos^2\phi - 1)^2\right)\left(\lambda_\theta^2 \sin^2\phi + \lambda_z^2\cos^2\phi - 1\right).$$

The term $\sigma'$ is related to pressure $p$ through $\sigma' = -p + \frac{1}{3}(\tilde{\sigma}_\theta + \tilde{\sigma}_z)$, being undetermined for a purely incompressible model.

## 3 Remodeling

*Remodeling* constitutes a key feature in order to interpret stenosis and atherosclerosis in vessel walls. It is defined as is the change of either geometry (*growth*, i.e. alterations in mass or shape) or mechanical properties with respect to a so-considered homeostatic reference state, motivated by the persistence of external loads. A usual hypothesis is that first the deformed geometry is determined by elastic properties and growth, and subsequently mechanical properties adapt, with the objective of maintaining the level of compliance (functionality) of the artery. This interpretation highlights the importance of considering growth in analysis of atherosclerotic and post-operatory processes.

Several models have been developed for growth, mostly considering global parameters of the artery (for simplified geometries and loads, [7], [8] and [9]). In this work, a non-local generalized model based on the theoretical framework in [9] and [1] is developed.

Let us consider an intermediate state due to pure local growth (free of stress) where compatibility conditions need not be fulfilled (Fig. 3). It is proposed that the deformation gradient be multiplicatively split as $\boldsymbol{F} = \boldsymbol{F}_{\mathrm{e}}\boldsymbol{F}_{\mathrm{g}}$, where $\boldsymbol{F}_{\mathrm{e}}$ is the elastic contribution and $\boldsymbol{F}_{\mathrm{g}}$ the part due to growth. The component $\boldsymbol{F}_{\mathrm{g}}$ is not uniquely defined, as the rotation term $\boldsymbol{R}_{\mathrm{g}}$ in the polar decomposition

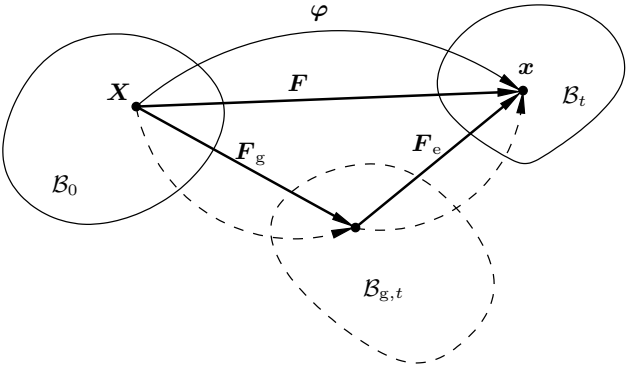


**Fig. 3.** Multiplicative decomposition for growth

$\boldsymbol{F}_{\rm g} = \boldsymbol{R}_{\rm g}\boldsymbol{U}_{\rm g}$ is undetermined due to the lack of compatibility restrictions; thus, it is assumed (with no loss of generality) that $\boldsymbol{F}_{\rm g}$ equals $\boldsymbol{U}_{\rm g}$. In case of incompressibility it is imposed $\det \boldsymbol{F}_{\rm e} = 1$.

The Cauchy stress tensor depends only upon $\boldsymbol{F}_{\rm e}$, verifying

$$\boldsymbol{\sigma} = (\det \boldsymbol{F}_{\rm e})^{-1}\boldsymbol{F}_{\rm e}\boldsymbol{S}_{\rm e}\boldsymbol{F}_{\rm e}^{\rm T} \;\text{ with }\; \boldsymbol{S}_{\rm e} = 2\frac{\partial \hat{W}(\boldsymbol{C}_{\rm e})}{\partial \boldsymbol{C}_{\rm e}} \;\text{ and }\; \boldsymbol{C}_{\rm e} = \boldsymbol{F}_{\rm e}^{\rm T}\boldsymbol{F}_{\rm e}.$$

In a so-called *simple material* [10], the growth law relates the rate of growth stretch $\boldsymbol{U}_{\rm g}$ to the stress state $\boldsymbol{\sigma}$, i.e. $\dot{\boldsymbol{U}}_{\rm g} = \boldsymbol{\phi}(\boldsymbol{\sigma})$. From objectivity (frame indifference) considerations it is needed that $\boldsymbol{\phi}(\boldsymbol{\sigma}) = \boldsymbol{\phi}(\boldsymbol{Q}\boldsymbol{\sigma}\boldsymbol{Q}^{\rm T})$ for any proper orthogonal tensor $\boldsymbol{Q}$. Hence, $\boldsymbol{U}_{\rm g}$ depends only on the co-rotational Cauchy stress tensor $\hat{\boldsymbol{\sigma}} = \boldsymbol{R}^{\rm T}\boldsymbol{\sigma}\boldsymbol{R}$, where $\boldsymbol{R}$ is the rotation in $\boldsymbol{F}_{\rm e}$.

In our model it is assumed that the growth in arteries at a point $\boldsymbol{X}$ depends on the local stress and on the (non-local) shear sensed by the intima (assumed to be a smooth surface in the reference configuration, denoted by $\mathcal{I}$). This results in a material which is not considered simple in the sense of [10]. We consider the non-local influence is provided through magnitudes on the nearest point in the intima $\boldsymbol{X}_{\rm npi}$ to $\boldsymbol{X}$, in the reference configuration (subindex $(\bullet)_{\rm npi}$ indicates *nearest point in the intima*). In particular, magnitudes in $\boldsymbol{X}_{\rm npi}$ considered are the stress state $\boldsymbol{\sigma}_{\rm npi}$, a normal unit vector $\boldsymbol{n}_{\rm npi}$ and the mean curvature $H_{\rm M,npi}$ (trace of the Weingarten operator) for $\mathcal{I}$ (so, it is geometrically determined).

Another assumption is to consider no change of the eigenvectors of $\boldsymbol{U}_{\rm g}$ in time (they are established as constant material properties). In the case of two preferential directions for the hyperelastic model, those eigenvectors, called $\boldsymbol{u}$, $\boldsymbol{v}$ and $\boldsymbol{w}$, may be taken as the vectors $\boldsymbol{u}_\theta$, $\boldsymbol{u}_z$ and $\boldsymbol{u}_r$, respectively, considered in Sect. 2.3.

With the above considerations, the growth law proposed here is:

$$\dot{\boldsymbol{U}}_{\rm g} = \boldsymbol{U}_{\rm g}\left(\boldsymbol{\mathcal{A}}\boldsymbol{:}(\hat{\boldsymbol{\sigma}} - \hat{\boldsymbol{\sigma}}_0) + (\tau_{\rm npi} - \tau_{0,{\rm npi}})\boldsymbol{A}\right), \tag{2}$$

$$\text{where }\; \hat{\boldsymbol{\sigma}}_0 = \sigma_0\,\boldsymbol{u}\otimes\boldsymbol{u}, \quad \tau_{\rm npi} = |(\boldsymbol{1} - \boldsymbol{n}_{\rm npi}\otimes\boldsymbol{n}_{\rm npi})\cdot(\boldsymbol{\sigma}_{\rm npi}\cdot\boldsymbol{n}_{\rm npi})|,$$

$$\boldsymbol{\mathcal{A}} = \frac{1}{\sigma_0}\left(\frac{1}{T_\theta}\boldsymbol{u}\otimes\boldsymbol{u} + \frac{1}{T_r}\boldsymbol{w}\otimes\boldsymbol{w}\right)\otimes\boldsymbol{u}\otimes\boldsymbol{u} \text{ and}$$

$$\boldsymbol{A} = \frac{1}{\tau_{0,\mathrm{npi}}}\frac{1}{T'_\theta}\exp\left(-2\alpha H_{\mathrm{M,npi}}\,|\boldsymbol{X}_{\mathrm{npi}} - \boldsymbol{X}|\right)\boldsymbol{u}\otimes\boldsymbol{u}.$$

The material parameters $\sigma_0$ and $\tau_{0,\mathrm{npi}}$ are stress magnitudes at equilibrium, $T_\theta$, $T_r$ and $T'_r$ are time material parameters and $\alpha$ is a non-dimensional factor related to the loss of the signal along the path from the intima to be determined experimentally. In (2) the factor $\boldsymbol{U}_{\mathrm{g}}$ has been introduced (differing from the model in [1]), in order to consider growth for the new material generated.

We remark that elasticity tensors for the configurations $\mathcal{B}_0$ and $\mathcal{B}_{\mathrm{g},t}$, $\mathbb{C}$ and $\mathbb{C}_{\mathrm{g},t}$ respectively, are related by (in cartesian components, following standard implied sum convention) $\mathcal{C}_{ABCD} = (\det \boldsymbol{U}_{\mathrm{g},t})U^{-1}_{\mathrm{g},AP}U^{-1}_{\mathrm{g},BQ}\mathcal{C}_{\mathrm{g},PQRS}U^{-1}_{\mathrm{g},CR}U^{-1}_{\mathrm{g},DS}$.

## 4 Initial Stresses

Reference configurations for arteries are not usually *stress-free*, on the contrary they generally have significant levels of *pre-stress* in the physiological state. Geometric data for our biomechanical predictions in soft tissues must be obtained in-vivo, with the material loaded circumferentially with the physiological pressure and also longitudinally. Moreover, in a unloaded configuration the existence of *residual stresses* is well known [11], related to the remodeling behaviour. These assumptions motivate the modifications of constitutive models for a realistic analysis. Additionally, a convenient practical side-effect of a proper consideration of such initial stresses is that it avoids material instabilities which may cause otherwise lack of convergence in the numerical model for (unrealistic) unstressed states.

The model may be formulated from the consideration of a virtual zero-stress state $\mathcal{B}_{\mathrm{z.s.}}$ (see Fig. 4) for which the deformation gradient of the reference configuration $\mathcal{B}_0$ is denoted by $\boldsymbol{F}_0$. Note that a continuum map from $\mathcal{B}_{\mathrm{z.s.}}$ to $\mathcal{B}_0$ is not granted (the field $\boldsymbol{F}_0$ is not generally integrable), for which reason the state $\mathcal{B}_{\mathrm{z.s.}}$ is termed *virtual*.

Considering a strain energy function $W$ in $\mathcal{B}_{\mathrm{z.s.}}$, the initial stress in the reference configuration $\boldsymbol{\sigma}_0$ is obtained as a function of $\boldsymbol{F}_0$. Similarly, the total real stress $\boldsymbol{\sigma}_{\mathrm{r}}$ in $\mathcal{B}_t$ is obtained as a function of the deformation gradient $\boldsymbol{F}_{\mathrm{r}} = \boldsymbol{F}\boldsymbol{F}_0$. From the mechanical equilibrium problem stresses that produce the deformation from $\mathcal{B}_{\mathrm{z.s.}}$ to $\mathcal{B}_0$ are not generally known, however the problem can be established in $\mathcal{B}_0$ (where new loads and stresses are applied) by considering constitutive equations expressed in the form $\boldsymbol{\sigma}(\boldsymbol{F}) = \boldsymbol{\sigma}_{\mathrm{r}}(\boldsymbol{F}_{\mathrm{r}}) - \boldsymbol{\sigma}_0$.

Finally, following a similar framework as described in the previous section for growth, elasticity tensors for the configurations $\mathcal{B}_0$ and $\mathcal{B}_{\mathrm{z.s.}}$, $\mathbb{C}$ and $\mathbb{C}_{\mathrm{z.s.}}$ respectively, are related in terms of cartesian components by

$$\mathcal{C}_{ABCD} = (\det \boldsymbol{F}_0)^{-1}F_{0,AP}F_{0,BQ}\mathcal{C}_{\mathrm{z.s.},PQRS}F_{0,CR}F_{0,DS}.$$

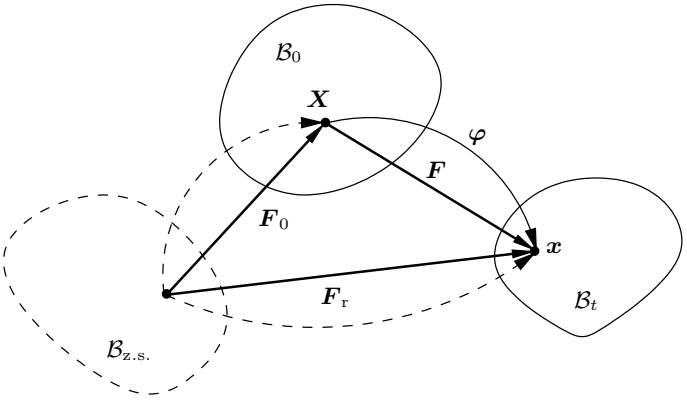


**Fig. 4.** Multiplicative decomposition for initial stress

## 5 Application

The above models have been implemented in a finite element framework [12] and are being applied to cases obtained from clinical studies. As a preliminary example, we present a study of the right coronary artery of a stenotic patient. The geometry was obtained from in-vivo angiography and IVUS (Intravascular Ultrasound System) cardiovascular images [13]. It was assumed that the media accounts for two thirds of the total thickness of the wall. Loads on the artery were obtained from a previous computational fluid dynamics (CFD) calculation [13], assuming blood as a newtonian fluid [14], rigid walls and a physiological pressure [2] of 100 mmHg. The map of shear stresses on the intima (input loads to the artery), obtained from the CFD analysis, is shown in Fig. 5.

The constitutive model considered is anisotropic (ect. 2.3), with the parameters proposed by [6], as follows, where subindex $(\bullet)_{\mathrm{M}}$ is used for the media and $(\bullet)_{\mathrm{A}}$ for the adventitia: $c_{\mathrm{M}} = 27.0$ kPa, $k_{1\mathrm{M}} = 0.64$ kPa, $k_{2\mathrm{M}} = 3.54$, $K_{\mathrm{M}} = 10^4$ kPa, $\phi_{\mathrm{M}} = 80^{\mathrm{o}}$, $c_{\mathrm{A}} = 2.7$ kPa, $k_{1\mathrm{A}} = 5.1$ kPa, $k_{2\mathrm{A}} = 15.4$, $K_{\mathrm{A}} = 10^4$ kPa and $\phi_{\mathrm{A}} = 50^{\mathrm{o}}$. The mesh comprises 5184 hexahedral elements with 7040 nodes and 20352 degrees of freedom. Displacements at the ends are restricted.

As an example of results, the contour fill of major principal stresses in the middle section is presented in Fig. 6, for the deformed configuration. The stress-states obtained may activate growth and so the model proposed by the authors could be applied.

[2] Note that in reality the in-vivo measured reference configuration is already loaded, however for the purpose of this application the physiological pressure is applied on it.

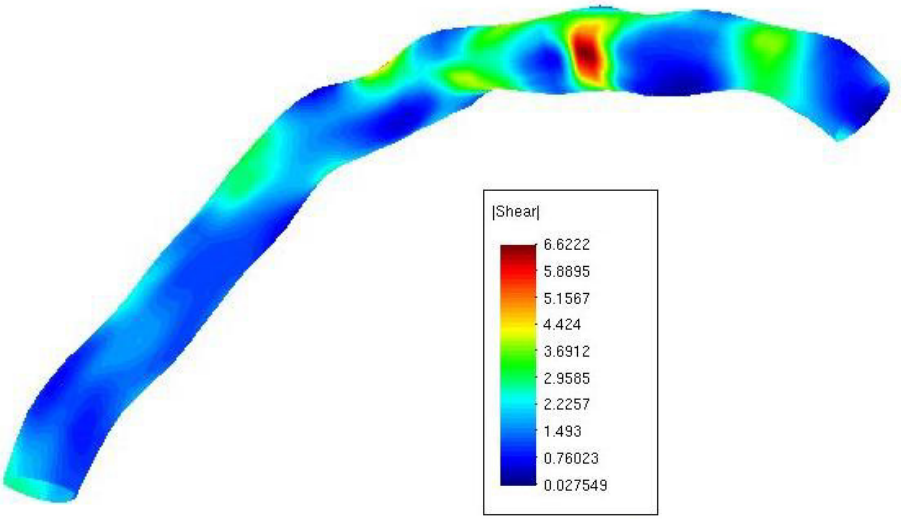


**Fig. 5.** Contour fill of tangential shear stresses [Pa], obtained from CFD analysis of blood flow

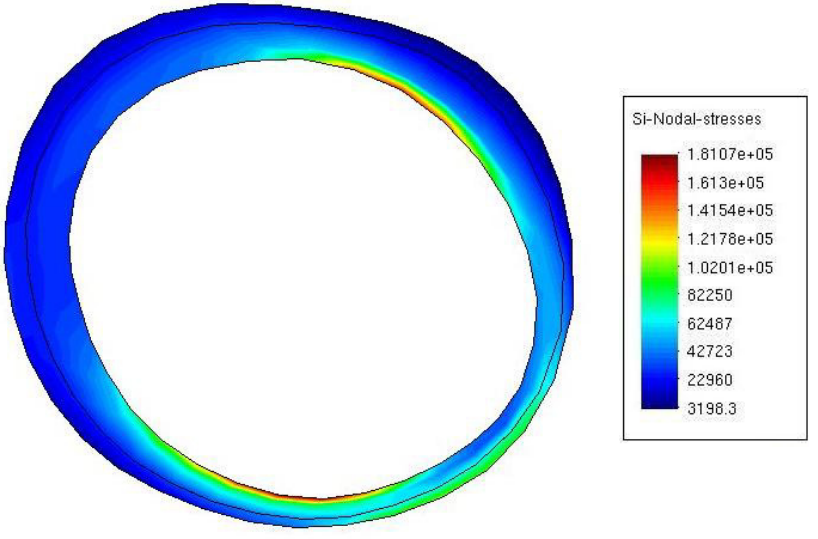


**Fig. 6.** Boundary fill of major principal stresses in the middle section [Pa]

## 6 Conclusions

We have discussed some of the major issues for a finite element detailed interpretation of the behaviour of tissue in coronary arteries, in which the material (constitutive) models play a major role. A basic anisotropic nonlinear elastic framework is followed, with preferential directions from collagen fibers. Furthermore, essential aspects to be modelled for realistic predictions are the growth and remodelling, and the initial stresses and strains in the measured in-vivo geometries. Some constitutive models which incorporate the above aspects have been shown. The authors have proposed an original model for remodeling in arbitrary 3D geometries obtained from in-vivo measurements, as a generalization of Taber's approach.

Other models of interest but not discussed in this paper are viscoelasticity and pseudo-elasticity (showing an important role in damage processes as angioplasty). Further work needs to be done on coupling effects of growth, viscoelasticity and pseudo-elasticity for arterial walls with real geometries (obtained by combination of angiography and IVUS), pre-loaded and with residual stresses.

**Acknowledgements.** Authors thank the rest of the members of their research group, specially F.J. Calvo, J.J. Arribas, and I. Romero. Support was provided by the Spanish Ministry for Science and Technology through the MOTRICO TIC2000-1635-CO4-03 project, and by our university through the research grant UPM-14585.

## References

1. Rodríguez, E., Hoger, A. and McCulloch, A.: Stress-dependent finite growth in soft elastic tissues. J. Biomech. **27** (1994) 455–467.
2. Marsden, J.E. and Hughes, T.J.R.: Mathematical foundations of elasticity. Dover Publications, inc. (1983).
3. Humphrey J.D.: Mechanics of the arterial wall: review and directions. Critical Reviews$^{RM}$ in Biomedical Engineering **23** (1995) 1–162.
4. Ball, J.: Constitutive inequalities and existence theorems in nonlinear elastostatics. Nonlinear analysis and mechanics: Heriot-Watt Symposium **1** (1977) 189–241.
5. Spencer, A.: Continuum theory of the mechanics of fibre-reinforced composites. CISM **282** (1984) 1–32.
6. Holzapfel, G.A. and Gasser C.G.: A new constitutive framework for arterial wall mechanics and a comparative study of material models. J. Elast. **61** (2000) 1–48.
7. Rachev, A.: Theorical study of the effect of stress-dependent remodeling on arterial geometry under hypertensive conditions. J. Biomech. **30** (1997) 819–827.
8. Fung, Y.: Biomechanics. Motion, flow, stress and growth. Springer (1990).
9. Taber, L.: A model for aortic growth based on fluid shear and fiber stresses. Journal of Biomechanical Engineering **120** (1998) 348–354.
10. Truesdell, C.: A first course in rational continuum mechanics: volume I, general concepts. Academic Press (1977).
11. Fung, Y.: Biomechanics. Mechanical properties of living tissues. Springer (1993).

12. Taylor, R.L.: FEAP, Finite Element Analysis Program, version 7.3, University of California Berkeley (2000).
13. Goicolea, F.J., Sanmartin, M., Crespo, A., Garcia, J.: Three-dimensional reconstruction and flow analysis in coronary artery, report MOTRICO project (2002).
14. Milnor, R.: Hemodynamics. William & Wilkins (1989).

# Author Index


Arts, T. 72, 81, 234
Axel, L. 1

Balleux, F. 262
Bauer, W.R. 272
Bijnens, B. 278, 287
Boldak, C. 39
Boulmier, D. 39
Bourdarias, C. 91
Bovendeerd, P.H.M. 72, 81
Boyett, M.R. 132
Bracoud, L. 215
Breithardt, O.-A. 287
Brisinda, D. 122

Canet, E. 215
Chandrashekara, R. 141
Charnoz, A. 52
Chen, M. 30
Clarysse, P. 194, 224
Claus, P. 278, 287
Clayton, R.H. 30
Cluzel, P. 162
Costes, N. 194
Cozar, O. 194
Croisille, P. 194, 215

D'hooge, J. 278
De Cesare, A. 262
Delhaas, T. 234
Dickstein, F. 111
Diebold, B. 173
Dobrzynski, H. 132
Dominguez, C.R. 173
Dommke, C. 278
Duncan, J.S. 252

Engelbrecht, J. 72
Ertl, G. 272

Fenici, R. 122
Frangi, F. 18
Frouin, F. 173

Gérard, O. 173
Gabaldón, F. 295
García, J.C. 295
Garreau, M. 39
Geerts, L. 81
Gerbi, S. 91
Glänzel, K. 62
Goicolea, J. 295
Greiser, A. 272
Grenier, P. 162

Haase, A. 272
Herment, A. 173, 262
Hiller, K.-H. 272
Holden, A.V. 30, 132
Hu, K. 272

Janier, M. 194
Jolivet, O. 262

Köhler, S. 272
Katila, T. 224
Kerckhoffs, R. 81
Kohl, P. 8

Lötjönen, J. 224
Larralde, A. 39
Larsson, H.B.W. 151
Lim, P. 173
Lin, N. 252
Lingrand, D. 52
Lorenzo-Valdés, M. 141, 205
Lunttila, T. 101

Mäkelä, T. 194, 224
Magnin, I.E. 184, 224
Markhasin, V.S. 8
Meloni, A.M. 122
Mohiaddin, R. 141, 205
Montagnat, J. 52
Mousseaux, E. 262

Nahrendorf, M. 272
Nenonen, J. 101
Neuberger, T. 272
Neyran, B. 184
Niessen, W.J. 18
Nofrerias-Fernández, E. 242

Ohayon, J. 91
Oumsis, M. 184

Pachai, C. 215
Pauna, N. 194, 224
Perperidis, D. 205
Petitjean, C. 162
Pham, Q.-C. 184
Pollari, M. 224
Prêteux, F. 162
Prinzen, F.W. 234
Pujol, O. 242
Purushothaman, K. 252

Radeva, P. 242
Rao, A. 141, 205
Reilhac, A. 194, 224
Revel, D. 215
Rodríguez, J. 295
Rolland, Y. 39
Rosales, M. 242
Rougon, N. 162
Rueckert, D. 18, 141, 205

Sachse, F.B. 62
Saks, V. 72
Sanchez-Ortiz, G.I. 141
Schnabel, J.A. 18
Sdigui, A.D. 184
Seemann, C. 62
Sinusas, A. 252
Snoep, G. 234
Solovyova, O. 8
Somersalo, E. 101
Stegmann, M.B. 151
Suetens, P. 278
Sutherland, G.R. 278, 287

Tasu, J.-P. 262
Thiele, K. 252
Thoen, J. 278
Toumoulin, C. 39
Tucker, J.V. 30
Turschner, O. 278

Van de Werf, F. 278
Van Susteren, A. 234
Vendelin, M. 72
Vikulova, N. 8
Vincent, F. 215

Waller, C. 272
Weber dos Santos, R. 111

Yan, P. 252
Yu, W. 252

Zhang, H. 132